Winter 1990

The analysis and design of brushless DC motors

Steven Ronald Prina
University of New Hampshire, Durham

Order Number 9119143

The analysis and design of brushless DC motors

Prina, Steven Ronald, Ph.D.

University of New Hampshire, 1990

U·M·I
300 N. Zeeb Rd.
Ann Arbor, MI 48106

THE ANALYSIS AND DESIGN OF BRUSHLESS DC MOTORS

BY

STEVEN RONALD PRINA

B.S., University of New Hampshire, 1983
M.S., University of New Hampshire, 1986

A DISSERTATION

Submitted to the University of New Hampshire
in Partial Fulfillment of
the Requirements for the Degree of

Doctor of Philosophy

in

Engineering

December 1990

This dissertation has been examined and approved.

Dissertation Director, Charles K. Taft
Professor of Mechanical Engineering

Barry K. Fussell
Assistant Professor of Mechanical Engineering

L. Gordon Kraft
Professor of Electrical Engineering

David E. Limbert
Professor of Mechanical Engineering

Loren D. Meeker
Professor of Mathematics

November 16, 1990
Date

DEDICATION

This work is dedicated in loving memory to my father, who always believed in me.

ACKNOWLEDGEMENTS

I would like to express my sincerest thanks to my committee members. Special thanks go to Dr. Charles K. Taft, my advisor, for his continued support, friendship and guidance during the period of research documented in this thesis, and Dr. David E. Limbert, for his helpful insights during the early stages of this work.

In addition, I would like to express my appreciation to Dr. Timothy J. Harned of the Parker Motor Design Center, Portsmouth. I am deeply indebted to Tim for providing me with materials and prototype motors, as well as his suggestions, comments and ideas during the course of this research. I would also like to thank Steve Huard, my office-mate for listening to me on many occasions and helping to separate the good ideas from the bad ones.

My thanks also go to all those members of the Dynamic Systems Modeling Group, past and present. Their friendship and the shared learning experience helped to make this work very enjoyable.

I thank my family and friends, and, above all, I would like to thank my wife Barbara, for her support and patience over the years.

TABLE OF CONTENTS

LIST OF TABLES

LIST OF FIGURES

LIST OF SYMBOLS

a_k ≡ Fourier series sine coefficient

$\vec{\mathbf{A}}$ ≡ magnetic vector potential

A_z ≡ scalar magnetic potential in z direction

A ≡ number of rotor north poles on rotor

A_e ≡ area of flux tube

A_g ≡ area of airgap perpendicular to flux

A_m, A_{mag} ≡ area of magnet perpendicular to flux

A_s ≡ area of a stator slot

A_{sa} ≡ available area of stator slot

A_{sn} ≡ necessary slot area

A_t ≡ average area of airgap over a tooth pitch

A_{TOT} ≡ average total area of magnet/airgap region perpendicular to flux

A_{wt} ≡ total coated area of a strand of copper wire

b_k ≡ Fourier series cosine coefficient

b_t ≡ back iron thickness

b_{tr}, b_{ts} ≡ rotor and stator back iron thickness

$\vec{\mathbf{B}}$ ≡ flux density vector

$|B|$ ≡ magnitude of **B**

$\tilde{B}$ ≡ square of the magnitude of B

B_{coil} ≡ flux density due to coil

B_{crad} ≡ radial component of flux density due to coil

B_e ≡ flux density in element e

B_{max} ≡ maximum allowable flux density in steel

B_r ≡ residual flux density

B_{ro} ≡ residual flux density at 25^0C

B_{rad}, B_θ ≡ r,θ components of flux density, $\vec{B}$

B_x, B_y ≡ x,y components of flux density, $\vec{B}$

C ≡ commutation factor

C_T ≡ reversible temperature coefficient of magnet

C_{TM} ≡ reversible temperature coefficient of resistive material

D_m ≡ ratio of stator torque period to detent torque period

D_r ≡ diameter of rotor

e ≡ wire axial overhang

{E} ≡ temporary vector

f ≡ excitation frequency

ff ≡ slot fill factor

F(U) ≡ energy functional

$\mathcal{F}$ ≡ mmf drop

$\vec{F}$ ≡ Lorentz force

F_{ave} ≡ average mmf of magnet over a flux tube

F_r, F_θ ≡ r,θ components of Lorentz force

F_x, F_y ≡ x,y components of Lorentz force

F_o, F_m ≡ magnet mmf

$\vec{H}$ ≡ magnetic intensity vector

H_e ≡ field intensity of element

H_c ≡ coercive force of magnet

Δh ≡ change in magnet length in direction of magnetization

i ≡ phase current

i_i ≡ current in phase i

$i_{j,kf}$ ≡ final current at state j, phase k

$i_{j,ki}$ ≡ initial current at state j, phase k

i_m, I_m ≡ equivalent magnetization current

Δi_k ≡ equivalent magnetization current for element pair k

IL ≡ stator iron losses

I_{max} ≡ maximum coil current

I_{stall} ≡ stall current

$\mathbf{J}$ ≡ vector current density

J_z ≡ current density in z direction

J_{back} ≡ inertia of rotor back iron

J_k ≡ inertia of rotor section k

J_{mag} ≡ inertia of magnet section

J_r ≡ rotor inertia

J_{se} ≡ inertia of shaft extension

J_{shaft} ≡ inertia of shaft

J_{sp} ≡ specified inertia of rotor

k ≡ Fourier series index

k_o, k_1, k_2 ≡ iron loss coefficients

K_{bexp} ≡ experimentally determined back emf constant

K_t ≡ motor torque constant

$\bar{K}_t$ ≡ normalized torque constant

K_{t0} ≡ torque constant predicted by finite element model 0

K_{t1} ≡ torque constant predicted by finite element model 1

K_{t2} ≡ torque constant predicted by finite element model 2

K_{t3} ≡ torque constant predicted by finite element model 3

K_{texp} ≡ experimentally determined motor torque constant

K_{tFEM} ≡ torque constant predicted by finite element model

K_{t2exp} ≡ experimentally determined K_t for second prototype motor

K_{t2FEM} ≡ finite element predicted torque constant for second prototype motor

K_{tess} ≡ effective torque constant for skewed stack motor

K_{tls} ≡ torque constant for long stack skewed motor

K_{tns} ≡ torque constant for nonskewed motor

K_{tss} ≡ torque constant for single stack skewed motor

$\vec{l}$ ≡ path of integration

ℓ ≡ scalar path of integration

ℓ_g ≡ length of airgap in direction of flux

ℓ_{ge} ≡ conbined length of magnet/airgap

ℓ_e ≡ length of element

ℓ_m ≡ length of magnet in direction of flux

ℓ_t ≡ length of a turn of wire

ℓ_z ≡ length of stator stack

L ≡ motor phase inductance

L_i ≡ inductance of phase i

L_{coil} ≡ inductance of a coil

L_{cs} ≡ cross-slot leakage inductance

L_{gap} ≡ inductance due to flux crossing the airgap

L_p ≡ inductance of a phase

L_k ≡ length of magnet in direction of magnetization to node k

L_s ≡ loss per pound

L_w ≡ length of a wire

M_i ≡ mutual inductance of phase i

N ≡ total number of turns of a coil

Nk ≡ total number of turns associate with mmf source k

$N_k i_k$ ≡ mmf produced by coil k

Ni_{cp} ≡ mmf per coil pole

N_n ≡ dimension of system of equations

N_i ≡ shape function

N_p ≡ number of rotor poles

N_{ps} ≡ maximum number of parallel strands

N_s ≡ number of staggered segments

N_t ≡ number of stator teeth

N_{TOT} ≡ maximum number of turns for a 2 pole motor

N_{wp} ≡ number of windings per coil

$\vec{p}$ ≡ vector distance from segment of current carrying wire to point P

P_{ij} ≡ elements of Jacobian matrix, [P]

P_s ≡ stall power dissipation

R ≡ resistance of a phase

R_i ≡ resistance of phase i

r_1 ≡ inner radius of back iron

r_2 ≡ inner radius of magnet

r_3 ≡ outer radius of magnet

r_4 ≡ inner radius of stator

r_5 ≡ inner radius of slot

r_6 ≡ outer radius of slot

r_7 ≡ outer radius of stator

r_{ave} ≡ average radius of sheet current

r_{ik} ≡ inner radius of rotor section

r_{ok} ≡ outer radius of rotor section

r_{mave} ≡ average radius of magnet

r_{save} ≡ average radius of stator slot

$\mathcal{R}$ ≡ reluctance of an element

$\mathcal{R}_e$ ≡ effective sturable reluctance of circuit

$\mathcal{R}_g$ ≡ reluctance of effective airgap

$\mathcal{R}_{mave}$ ≡ effective average reluctance of the magnet circuit

$\mathcal{R}_{cp}$ ≡ reluctance of coil flux path

$\mathcal{R}_{eff}$ ≡ effective reluctance of magnet circuit

$\mathcal{R}_s$ ≡ Reluctance of a slot

$\mathcal{R}_\ell$ ≡ cross-slot leakage reluctance

$\mathcal{R}_t$ ≡ reluctance of tooth face

$\mathcal{R}_{tth}$ ≡ reluctance of a single tooth gap

$\mathcal{R}_{tl}$ ≡ reluctance of left side of tooth face

$\mathcal{R}_{tr}$ ≡ reluctance of right side of tooth face

S_{ij} ≡ elements of matrix, [S]

S ≡ surface area

ΔT ≡ change in temperature of magnet and coil

t ≡ time

t_ℓ ≡ thickness of slot liner material

tt ≡ stator tooth tip thickness

T ≡ torque

T_ℓ ≡ applied load torque

T_f ≡ friction torque

T_{stall} ≡ stall torque of motor

T_D ≡ magnitude of detent torque vector for a magnet segment

T_{ds} ≡ detent torque for skewed motor

T_{peak} ≡ peak torque value of torque angle curve

T_s ≡ magnitude of stator torque vector for a magnet segment

T_{tot} ≡ total stator torque

U ≡ approximation to magnetic potential

U_z ≡ approximate magnetic potential

V_a ≡ unknown mmf potential at node a

V_{bemf} ≡ back emf voltage

V_{bi} ≡ back emf voltage of phase i

V_{drv} ≡ diode reverse bias breakdown voltage

V_{dfv} ≡ diode forward bias voltage drop

V_e ≡ volume of element e

V_j ≡ elements of residual vector, {V}

V_k ≡ voltage supplied to phase k

V_{smax} ≡ maximum supply voltage

V_{trv} ≡ transistor reverse bias breakdown voltage

V_{tfv} ≡ transistor forward bias voltage drop

V_{ubpd} ≡ upper transistor leg breakdown voltage for positive current with blocking diodes

V_{lbpd} ≡ lower transistor leg breakdown voltage for positive current with blocking diodes

V_{ubpn} ≡ upper transistor leg breakdown voltage for positive current without blocking diodes

V_{lbpn} ≡ lower transistor leg breakdown voltage for positive current with blocking diodes

V_{ubnd} ≡ upper transistor leg breakdown voltage for negative current with blocking diodes

V_{lbnd} ≡ lower transistor leg breakdown voltage for negative current with blocking diodes

V_{ubnn} ≡ upper transistor leg breakdown voltage for negative current without blocking diodes

V_{lbnn} ≡ lower transistor leg breakdown voltage for negative current without blocking diodes

Vol ≡ volume of motor

w ≡ distance between two infinitely long wires

w_s ≡ slot width

w_t ≡ width of a tooth

wtd ≡ width to diameter ratio

W(U) ≡ magnetic energy density

W_c ≡ magnetic coenergy

W_{ce} ≡ coenergy of lumped element

x,y ≡ location of P from a length of wire

z ≡ axial length of rotor/stator

α, β ≡ integration variables indicating geometry to determine flux density at point P

α_s ≡ magnet segment stagger angle

Δ_e ≡ area of a finite element triangle

ε ≡ incremental skew angle between adjacent laminations

ϕ ≡ magnetic flux

ϕ_{coil} ≡ flux through a coil

ϕ_c, ϕ_m ≡ flux through coil, flux through magnet

ϕ_{ck} ≡ flux through tooth k

ϕ_{ctth} ≡ coil flux through a single tooth

ϕ_{mtth} ≡ magnet flux through a single tooth

ϕ_e ≡ flux through lumped element

$\phi_t, \phi_{tl}, \phi_{tr}$ ≡ flux through tooth face, left side face and right side

Φ ≡ total flux through surface of integration

ϕ_{maxtot} ≡ max total flux through a tooth

γ ≡ skew angle over motor length

γ_c ≡ phase winding half pitch

γ_m ≡ magnet pole pitch

γ_s ≡ span of flat top region of ideal flux density distribution

γ_t ≡ span of transition region of ideal flux density distribution

λ ≡ flux linkage

λ_c ≡ flux linking coil due to coil

λ_m ≡ flux linking coil due to magnet

λ_o ≡ initial condition of flux linkage

λ_t ≡ total flux linkage for a coil

μ ≡ permeability of material

μ_o ≡ permeability of free space

μ_r ≡ relative permeability

η ≡ ratio of magnet length to rotor outer radius

$\mathcal{P}$ ≡ permeance

$\mathcal{P}_{eff}$ ≡ effective permeance of a circuit

ρ_k ≡ density of rotor section k

ρ_{pf} ≡ resistivity per foot of wire

ρ_{pfo} ≡ resistivity per foot of wire at 25^0C

ρ_s ≡ density of steel

η ≡ length to rotor radius ratio

τ ≡ dummy integration variable

τ_t ≡ tooth pitch

τ_s ≡ stator torque period

τ_d ≡ detent torque period

θ ≡ rotor position

$\dot{\theta}_{max}$ = maximum rotor speed

$\dot{\theta}_c$ ≡ maximum continous operating speed of motor

ν ≡ reluctivity

ω ≡ rotor speed

$\dot{\omega}$ ≡ rotor acceleration

$\dot{\omega}_{max}$ ≡ max acceleration of motor

ω_o ≡ rotor steady state speed

Ω ≡ finite element area integration variable

χ ≡ slot width ratio

ζ ≡ location of differential flux tube being integrated

ABSTRACT

THE ANALYSIS AND DESIGN
OF
BRUSHLESS DC MOTORS

by

Steven Ronald Prina
University of New Hampshire, December 1990

This work is concerned with the magnetic analysis of brushless DC motors, and, with the development of a method of designing brushless DC motors which have symmetric windings and rotors without any iron saliency. A two-dimensional nonlinear finite element magnetic model is used to analyze the magnetic behavior of the motor. Methods of using the finite element solution(s) to predict motor characteristic performance parameters, such as the torque-angle curve, detent torque-angle curve, torque constant, back emf constant and inductance are discussed in detail. It is shown that three-dimensional effects can make significant contributions to the motor inductance, making inductance prediction difficult. It is also shown that the prediction of detent torque can be extremely sensitive to the permanent magnet model.

A simple means of understanding the effects of rotor magnet arc width and winding distribution on the stator torque-angle curve shape is presented. In addition, methods of reducing detent torque by altering magnet arc width are discussed.

Finally, simple lumped models that allow one to predict motor performance characteristics as a function of important dimensions, magnet residual flux density, and phase current are developed and checked against finite element results. These models are used as a basis for an approach to designing brushless DC motors.

CHAPTER 1

INTRODUCTION

DC machines have been in existance since 1831 when Michael Faraday invented the first homopolar electromagnetic generator[1]. This generator was a copper disc placed in an axially directed permanent magnet, (PM), field. Brushes were used to pick up the emf voltage generated between the inner and outer radii as the disk spun. The first rotating machines using a commutator invented by Ampere, were developed in 1833[1]. While these machines were first developed as generators, it was discovered that they also functioned as motors. In fact, DC machines can work as generators when they are connected to a prime mover, or as motors when connected to a power supply, or as brakes when used as a generator with the generated voltage dissipated across a resistance.

The basic design of these DC machines has remained relatively unchanged since their conception. The most recent and significant change has come in the form of the DC machine commutator. The brushless DC motor, (BLDCM), was invented by eliminating the commutator segments and brushes and replacing them with some form of position sensor. Commutation is performed electronically with transistors and logic circuits.

Brushless commutation is used primarily in small DC machines, (mostly subfractional horsepower machines), rather than large DC machines. This is due to the fact that the power electronics required

to handle the large currents used in industrial class machines are too expensive.

There are several advantages gained by using brushless motors: 1) With no brushes breakdown due to brush failure is overcome. This usually increases the life span of the motor to the lifespan of the bearings. In addition, there are no wear particles generated that might cause a failure in an application where a clean enviroment is necessary. 2) The absence of brush arc makes the brushless motor advantageous in volatile environments. 3) Electromagnetic noise, generated by the combination of winding shorting and inductive effects during the passage of the brush from one commutator bar to the next, is eliminated. 4) Brush motors are speed limited by back emf voltage arcing across the insulation between commutator bars; this is not true for BLDCMs. Therefore, they can be operated at higher speeds. 5) The stator, which is the wound or current carrying member, does not rotate so it can be mounted to a heat sink. This allows for better heat transfer which will ultimately result in a cooler running motor and prolonged bearing life.

Unfortunately, the combination of position sensor and power electronics usually makes the brushless motor more expensive than the conventional brush DC motor, BDCM. Therefore, the brushless motor is used mostly in applications requiring a high performance motor, or in applications where brush arc and brush wear are important issues. Recently, however, decreasing costs in electronics and integrated circuit packaging have made the brushless DC motor a more viable alternative to conventional DC motors.

Although brushless DC motors can come in a variety of forms, all consist of three basic elements: the stator, the permanent magnet (PM) member, and the position sensing elements, or assembly, necessary for commutation. The stator, where the coils are placed, may consist of a number of iron teeth around which the coils are wound. Alternatively, the stator can consist of coils that are surface mounted to some piece of backing iron which serves as a magnetic return path. The PM member can comprise a number of individual PM segments resulting in a multi-pole rotor, or, a single magnet piece with alternating north and south poles polarized on its surface. The position sensor can consist of something as simple as a set of Hall sensors designed to sense the presence of a magnetic field. These are used either to sense the rotor magnets directly, or they are used to sense an additional magnet assembly mounted to the rotor. Other, more sophisticated and more accurate forms of position sensing are also used. Resolvers being a common example.

There are several basic forms of brushless DC motors. There is the axial airgap winding type, shown in Figure I-1. In this motor, the stator windings are wound on bobbins made of a nonmagnetic material, such as nylon. These windings are then located in the airgap of the motor, between the PM rotor and the back iron. The field induced by the stator coils is oriented in the axial direction. The permanent magnet field is also axially oriented. This design is used where a low-height, low cost package is desirable, such as in floppy disc drives.

Another type of brushless DC motor is the radial airgap winding type, as shown in Figure I-2. Like the axial airgap winding motor, the

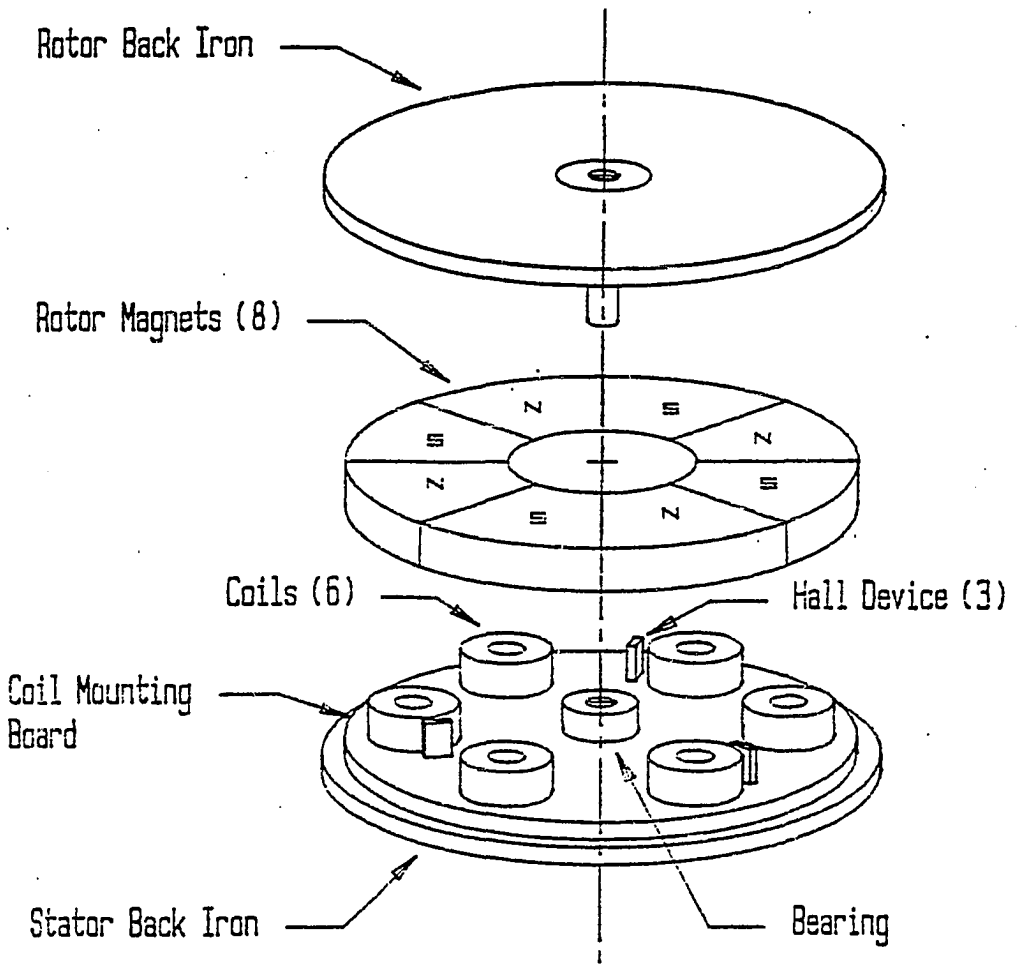

Figure I-1
Axial Airgap Brushless DC Motor

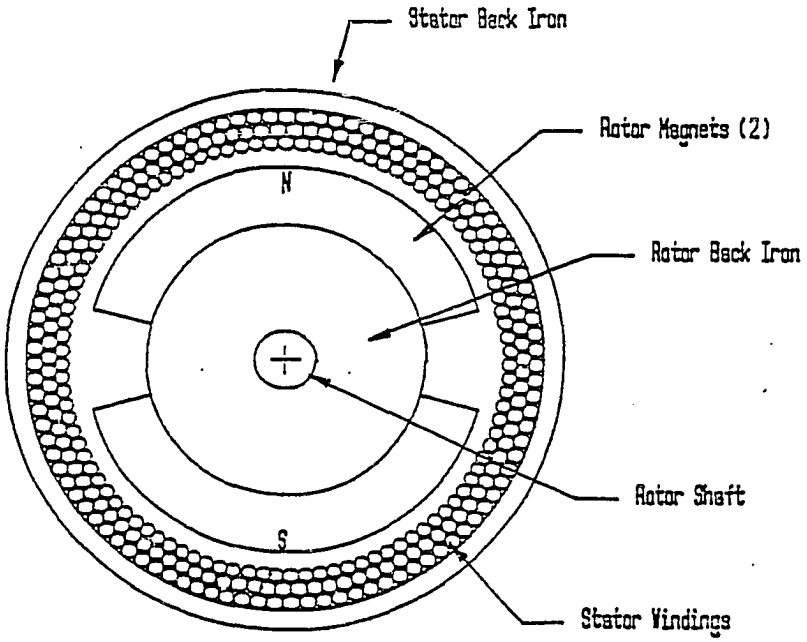

Figure I-2
Cross-Sectional View of
Radial Airgap Winding Brushless DC Motor

windings of this machine are also located directly in the airgap of the motor and not placed in the slots of a stator made of ferromagnetic material. This design has fast dynamic capabilites because of its characteristically small inductance.

Probably the most common type of brushless DC motor is the salient poled, or slotted, stator variety. In this type of motor the stator coils are wound around the teeth of a slotted stator. The stator is made from ferromagnetic materials so that a more efficient magnetic structure is obtained. There are two types of slotted stator brushless DC motors. The conventional type has a permanent magnet rotor which lies on the inside of the stator, as shown in Figure I-3a. An alternate type has the permanent magnet rotor on the outside of the stator, as shown in Figure I-3b. The latter type is often used in computer hard disc spindle drives. In addition, there is also a linear version of the BLDCM, Figure I-4. Similar to the rotary motor, either the slotted stator or the PM member could be the moving part.

The intent of this thesis was to develop a better understanding of the relationship between physical motor parameters, (such as magnet geometry, coil windings, and overall motor dimensions), and performance parameters such as the torque constant, the torque-angle waveform shape, detent torque, and phase inductance. Once this understanding was achieved, the results could be coupled to previous work relating the aforementioned performance parameters to dynamic simulations[2],[3]. This combination would result in a design package that would allow a motor designer to specify motor geometries, materials, and windings and be able to predict the torque-speed capabilities of the design as well as other performance indicators,

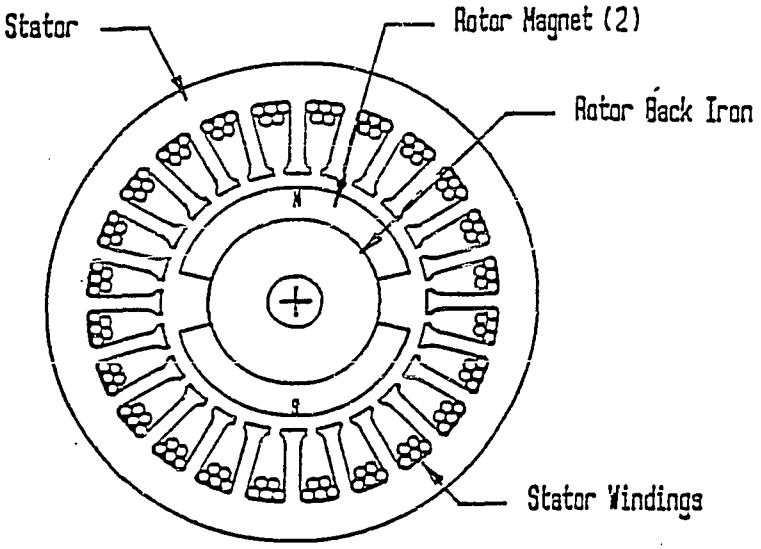

Figure I-3a
Cross-Sectional View of
Conventional Slotted Stator Brushless DC Motor

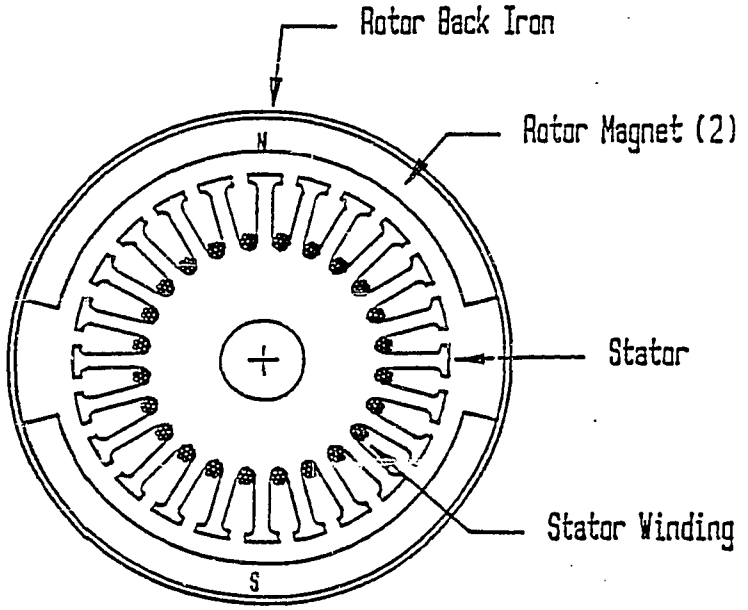

Figure I-3b
Cross-Sectional View of Spindle
Drive Type Slotted Stator Brushless DC Motor

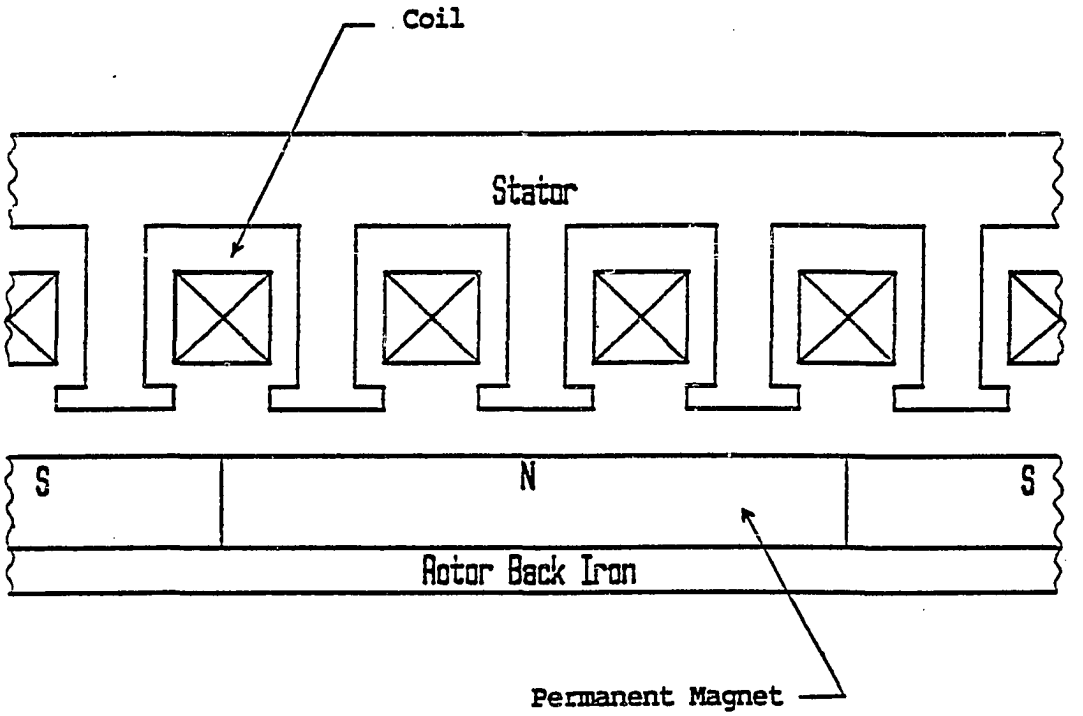

Figure I-4
Cross-Sectional View of Linear Motor

i.e: inductive time constants, torque to inertia ratio, and other figures of merit.

The research documented in this thesis focused on the conventional slotted stator BLDCM of Figure I-3a, although much of what was developed also directly applies to the type shown in Figure I-3b and I-4. The intent of this work was to use a nonlinear, two-dimensional, magnetic finite element analysis, FEA, as a basis for investigating various aspects of motor design. First, however, it was necessary to evaluate the accuracy of the FEA. As a means to that end, a prototype BLDCM was constructed and its characteristic parameters, such as the torque angle curve, torque constant and back emf constant, were measured. Then, a finite element model, FEM, of the prototype motor was developed and used to predict the same characteristic parameters. Finally, a comparison was made between the FEM predicted parameters and the measured ones. From the results of this comparison we were able to learn which parameters could be predicted accurately by the FEM. We could also decide whether it was possible to use the FEM as a substitute for prototyping motors. Using the FEM as a means of exploring motor design is attractive from several standpoints. 1) It is faster to implement and evaluate design changes. 2) It is less costly than prototyping. 3) It allows one to analyze the consequences of different designs in much greater detail and depth than one could by prototyping. 4) It provides a much more detailed picture of the magnetic field inside the machine than any prototype could yield, providing information that can not be measured easily.

Overview of Chapters

In Chapter II the prototype BLDC motor used to verify finite element and lumped parameter models is described. The experimental methods used to determine the characteristic parameters of the prototype motor are discussed and the results of those determinations are presented. Those results show, among other things, that the prototype motor has a large detent torque, and that the permanent magnet causes a significant degree of saturation. This saturation is present even though the torque-current characteristic for the motor is linear.

In Chapter III the finite element analysis process is described. First, the development of the finite element model is discussed. This includes the development of the finite element mesh and the modeling of the permanent magnet and nonlinear iron parts. In addition, the details of using the finite element results to find the characteristic parameters of the motor are also discussed. The parameters predicted by the finite element model are compared to the ones measured experimentally. It is found that the FEM does not predict either the detent torque or the inductance very accurately. This failure causes one to doubt the high degree of accuracy with which it predicts peak one-phase-on stator torque. The chapter concludes with a list of potential causes for the observed errors in prediction.

In order to address the questions raised in Chapter III, further finite element analysis is performed in Chapter IV. This includes: further checking of the FEM model of the permanent magnet rotor; alterations of the magnet model; investigating the sensitivity of the detent torque to the FEM; finite element analysis of other prototype

rotors. It is shown that end effects exist in the real motor that are not accounted for in the FEM and can result in fairly large errors in predicting inductance.

Chapter V addresses torque angle curve shape and detent torque. Several methods of reducing or eliminating detent torque in BLDCM's are discussed. It is also shown that motor detent torque can be very sensitive to the magnet model. Under the assumption of linear magnetics, the Lorentz force equation is used to determine the effects of magnet shape on the one-phase-on stator torque-angle curve. A method of easily evaluating the effects of winding distribution on the torque-angle curve shape is also included.

In Chapter VI the basic equations for lumped parameter magnetic circuit analysis are derived. This is done to identify fundamental assumptions. Then, some simple lumped magnet models are created to predict the airgap flux density due to either the coil or the permanent magnet rotor. It is shown that while the peak stator torque and torque angle waveform can be predicted reasonably well from simple models, prediction of the inductance requires more complicated models. It is also shown that prediction of the detent torque by a lumped parameter model requires a very complex model and therefore is impractical.

The purpose of developing a very simple lumped magnetic model to predict the motor characteristic parameters is to construct a set of equations that can be used to develop a motor design method. Chapter VII outlines a method for designing brushless DC motors. The design method described assumes that an inertia and torque constant for the motor have been specified. The motor designer must specify the number

of rotor poles and stator teeth, as well as several different wire sizes to use for the winding. The method then allows the designer to view and compare resulting designs, (motor geometries and characteristic parameters), for a variety of different winding wire sizes and/or different combinations of rotor poles and stator teeth. Parameters calculated include the phase resistance and inductance, iron losses, motor diameter, length, volume and motor weight. Torque-speed analysis is also included as part of the design process.

In Appendix A, the development of the two-dimensional nonlinear magnetic finite element model is presented. This appendix includes the derivation of the partial differential equation describing the static magnetic field, as well as the derivation of the FEM using a variational approach. A general expression for the individual entries in the final matrix equation is given.

Appendix B addresses the process of solving the nonlinear matrix equation formulated in Appendix A. Application of the Newton-Raphson solution method is detailed for the equations given in Appendix A.

In Appendix C, a derivation of the equations necessary for simulation of the torque-speed behavior, given a 3 phase, wye-node-open drive, is presented. The simulation process described includes handling of diode effects during the switching of phase energizations, i.e. the commutation points.

CHAPTER II

EXPERIMENTAL DETERMINATION OF MOTOR PARAMETERS

II.1 Motor Description

The motor used in this investigation was a prototype BLDC motor that had a 24 slot stator, was wound as a three phase device, and used a 4 pole rotor that consisted of arc segments of Neodymium-Iron-Boron, (Nd-Fe-B), rare earth magnets. A cross-sectional view of the motor is shown in Figure II-1. There were several reasons for using the prototype motor rather than an 'off the shelf' motor: 1) It was easy to make changes to the motor and evaluate the effects of those changes. 2) Rare earth magnet technology is rapidly developing. Presently, rare earth magnets are only being used in high performance applications. However, as magnet costs are decreasing in the future, one would expect to see an increase in the use of rare earth magnets in more ordinary applications. 3) Rare earth magnets have certain characteristics that are easier to model; such as a magnetic recoil permeability approximately equal to that of air, and a second quandrant demagnetization curve that is linear. This allows one to concentrate on other aspects of the design. In addition, the magnet is not subject to partial demagnetization if it is removed from the stator structure.

Due to the high cost of obtaining single quantities of rare earth magnet pieces manufactured to specific dimensions, several 'off the shelf' arc segments were obtained from Indiana General Technologies.

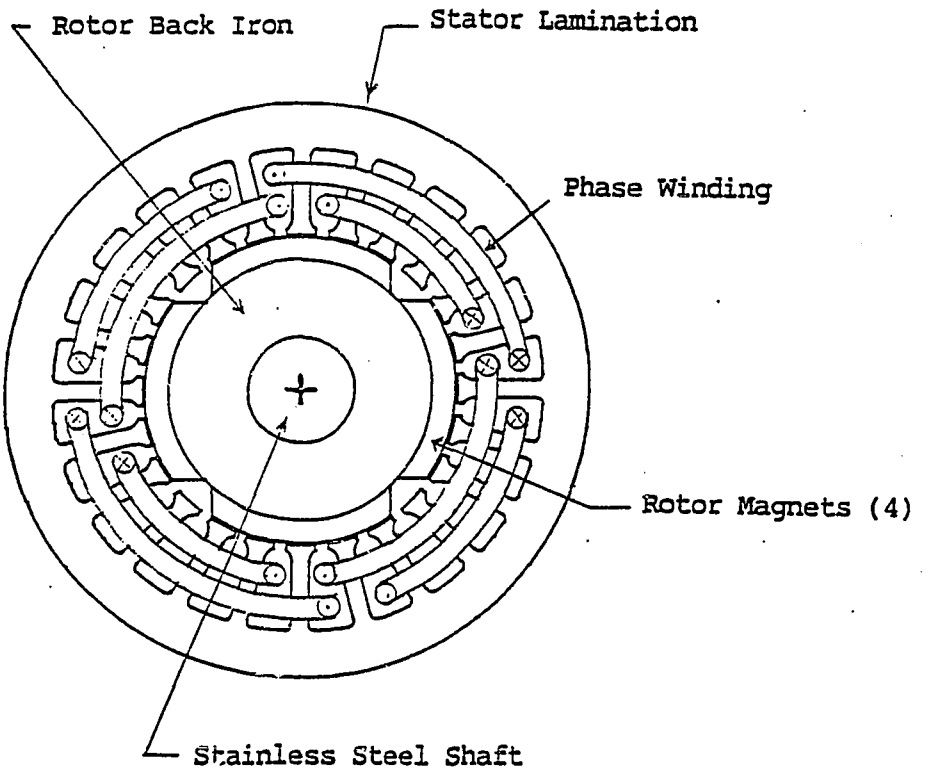

Figure II-1
Cross-Sectional View of Prototype BLDCM

The material type was a Nd-Fe-B material denoted as NeIGI27. The manufacturer's B-H curves for the material are shown in Figure II-2a. Some tabulated data for the material is shown in Figure II-2b.

A stator lamination that was of the appropriate size for the arc shaped magnets was selected from a lamination catalogue. The lamination drawing is shown in Figure II-3. This is a 24 slot lamination made of M19 electrical grade steel. A 24 slot lamination was selected because it is a common lamination used in BLDC motors. The magnet arc segments were mounted on a soft iron rotor and the outer diameter, (OD), was ground to fit the stator lamination. The rotor drawing is shown in Figure II-4b. Stator laminations were cemented together and fit into an aluminum housing and, with the addition of end caps, the motor was completed.

Once the motor was constructed, several characteristic parameters were measured that could be used to verify FEM results. These characteristic parameters were: the detent torque angle curve, the one-phase-on torque angle curve as a function of phase current, the torque constant, the back emf waveform, the back emf constant, and the coil flux linkage as a function of phase current. The experimental procedures used to determine these characteristics are described in the following sections.

II.2 Detent Torque Measurements

The interaction of the stator field with the permanent magnet is not the only source of torque produced in the motor. There is also a detent or 'cogging' torque produced due to the presence of the stator iron teeth in the permanent magnet field. A torque acts on the rotor

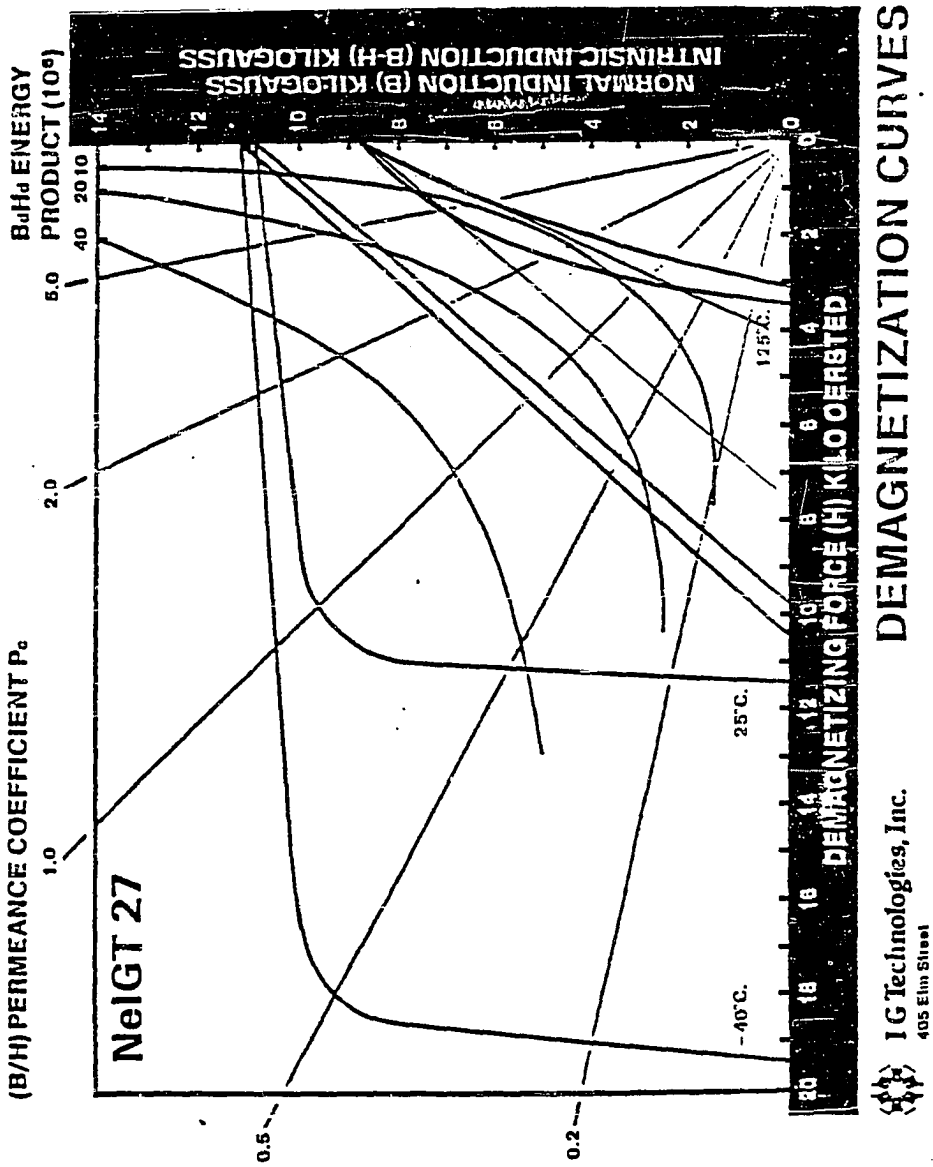

Figure II-2a
Manufacturer's B-H Curve
for Magnet Material

		NeIGT 27
Magnetic Characteristics		
Residual Induction - Br	(kG)	10.8
	(mT)	1080
Coercive Force - Hc	(kOe)	9.8
	(kA/m)	780
Intrinsic Coercive Force - Hci	(kOe)	11.0
	(kA/m)	920
Peak Energy Density (BdHd) max	(MGOe)	27
	(KJ/m^3)	218
Magnetizing Force - Hs	(kOe)	>30.0
	(kA/m)	>2765
Hk (H @ .9 Br)	(kOe)	9.5
Recoil Permeability	($\Delta B/\Delta H$)	1.1
Reversible Temperature Coefficient for Bd (%/C.)		-.11
Magnetic Orientation*		A
Material Characteristics		
Density	(lb/in^3)	.268
	(g/cm^3)	7.4
Curie Temperature (C.)		310
Temperature Affecting Material (C.)		200
Rockwell Hardness FI		C58
Electrical Resistivity of Material (at 25 C.)	(microohm cm)	150
Coefficient of Thermal Expansion (x 10 °/C.)	(I // M)	3
	(I ⊥ M)	5
Tensile Strength	(10^3 psi)	11.5

* U - Unoriented A - Axial
R - Transverse I - Isostatic

Relative Br vs. Magnetizing Field H for NeIGT

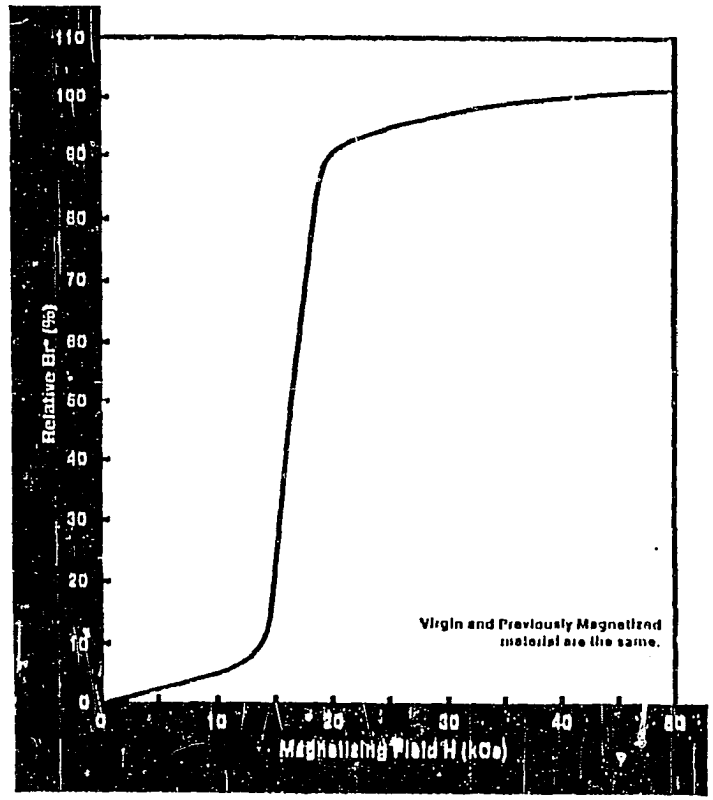

*Br after magnetizing in 50,000 Oe field is taken as the 100% value.

Figure II-2b
Manufacturer's Tabulated Data
for Magnet Material

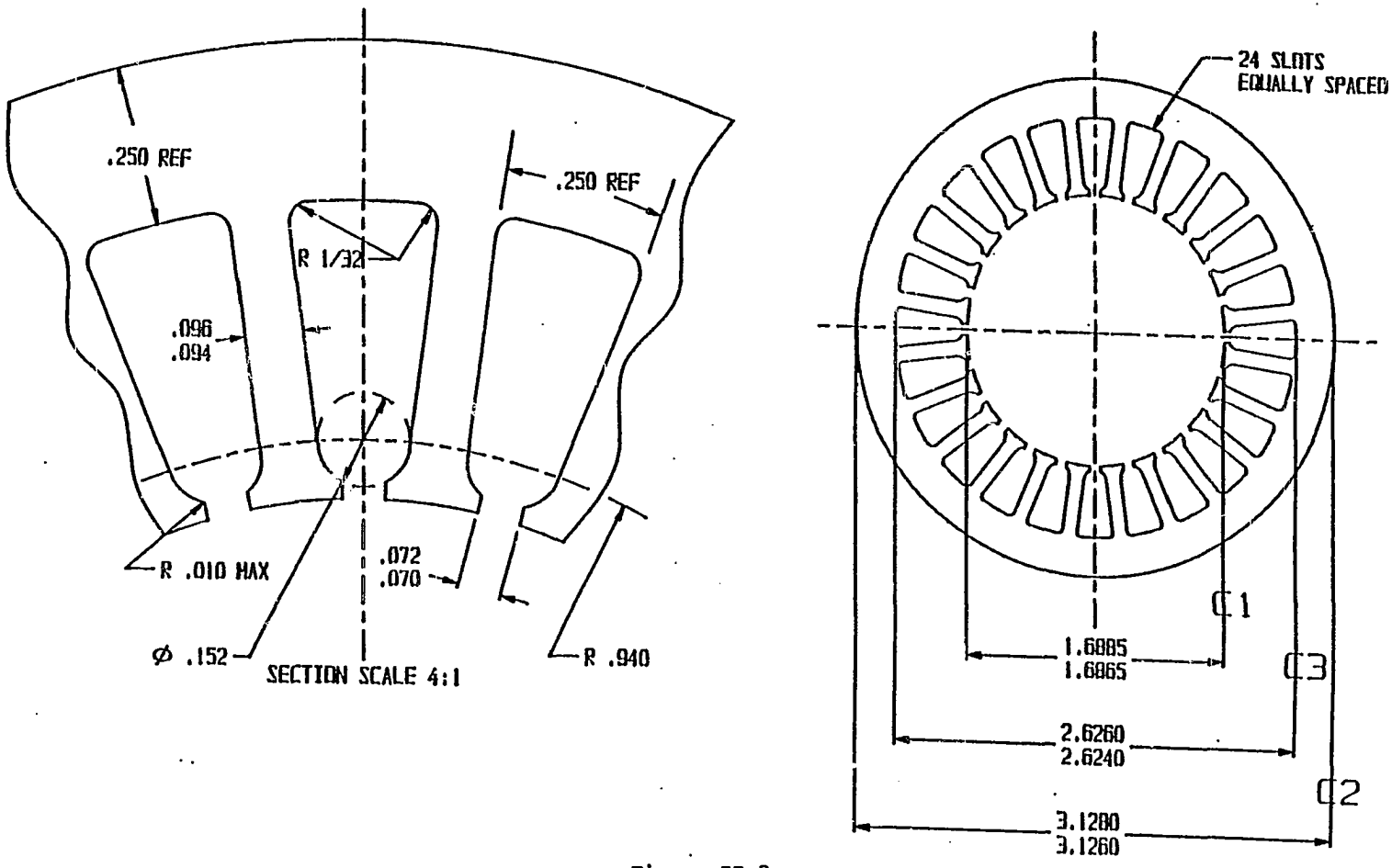

Figure II-3
Stator Lamination Drawing
(All Dimensions Shown Are in Inches)

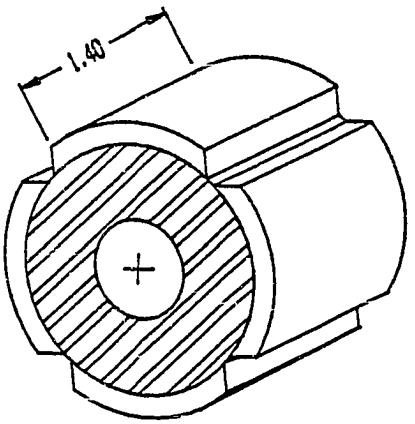

Figure II-4a
Oblique Projection of Prototype Rotor
(All Dimensions Shown Are in Inches)

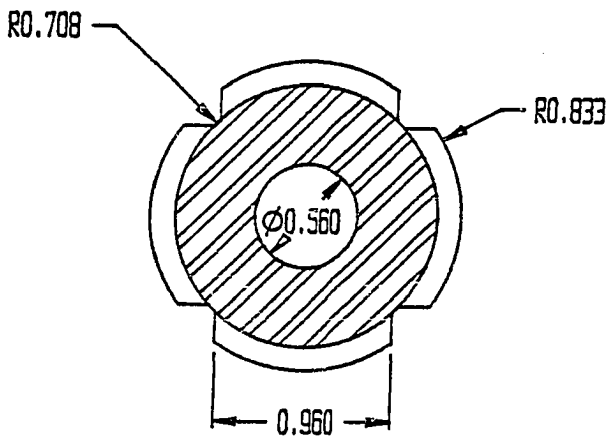

Figure II-4b
Rotor Drawing
(All Dimensions Shown Are in Inches)

to align it with the stator poles in a position that minimizes the magnetic field energy. This torque is called detent torque and is usually an unwanted phenomena because its presence causes torque ripple, resulting in speed ripple during the operation of the motor. For this reason, detent torque is an important issue in the consideration of the design of BLDC motors and will be discussed further in Chapter V.

The detent torque in this device was measured using an automated torque-angle measurement system. This system consists of a Berger-Lahr gear head stepping motor, a Dynamics Research Corporation 7200 count per revolution incremental optical encoder, a Vibrac 400 oz-in torque transducer and a Digital Equipment Corporation Micro-11 microcomputer to control the experimental system. This system is shown in Figure II-5. Angle accuracy is +/- .05 degrees, and torque accuracy is +/- 0.4 oz-in. This system samples and stores motor rotor angle, detent torque, instrumentation torque, and total torque due to both phase energization and detent. This allows one to subtract instrumentation torque from the total torque on a point by point basis. Thus, the original accuracy of the torque transducer is improved. The system also allows one to subtract the detent torque from the total torque on a point by point basis; thereby allowing one to view just the one-phase-on stator torque alone.

The detent torque produced by the prototype motor is shown in Figure II-6. The data shown starts at a stable equilibrium detent position and was taken over 180 mechanical degrees - which corresponds to twelve cycles of the detent torque. The average peak value is 61.8

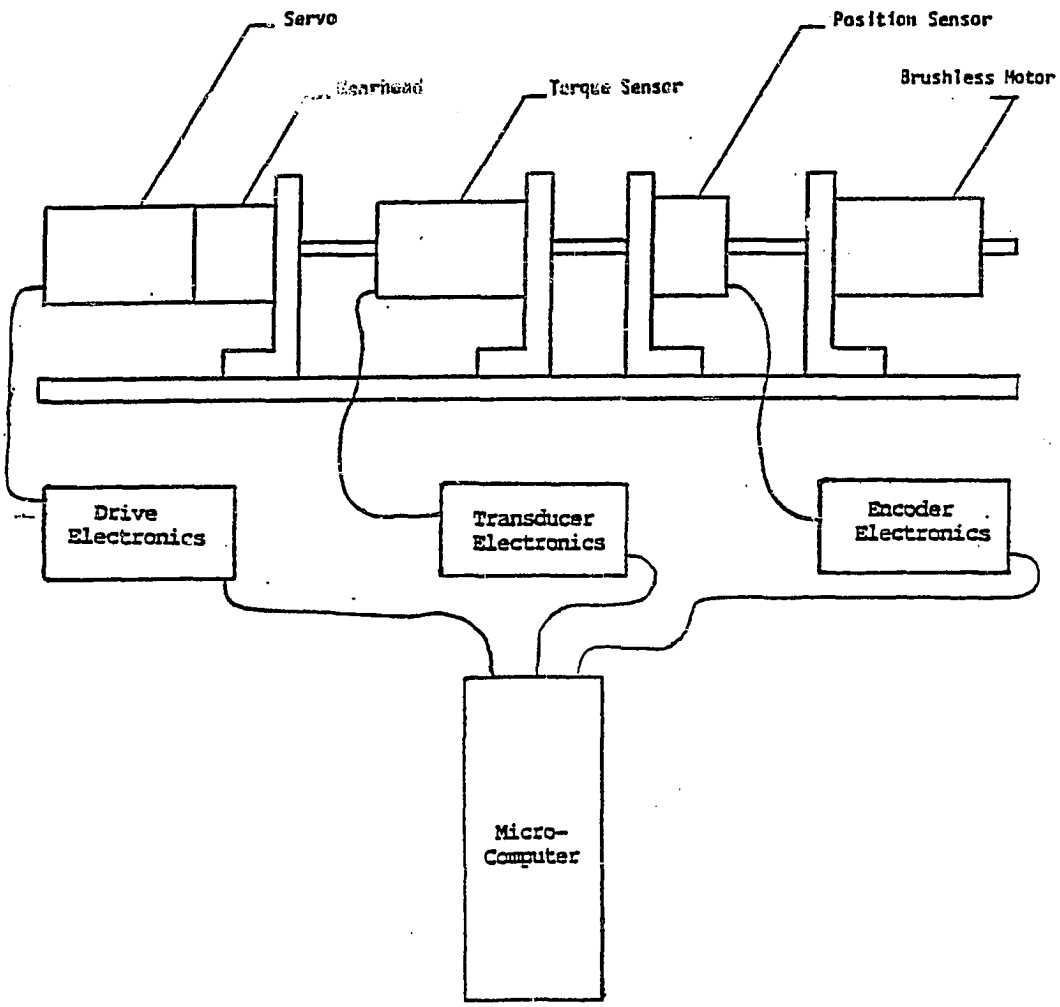

Figure II-5
Torque-Angle Measurement System

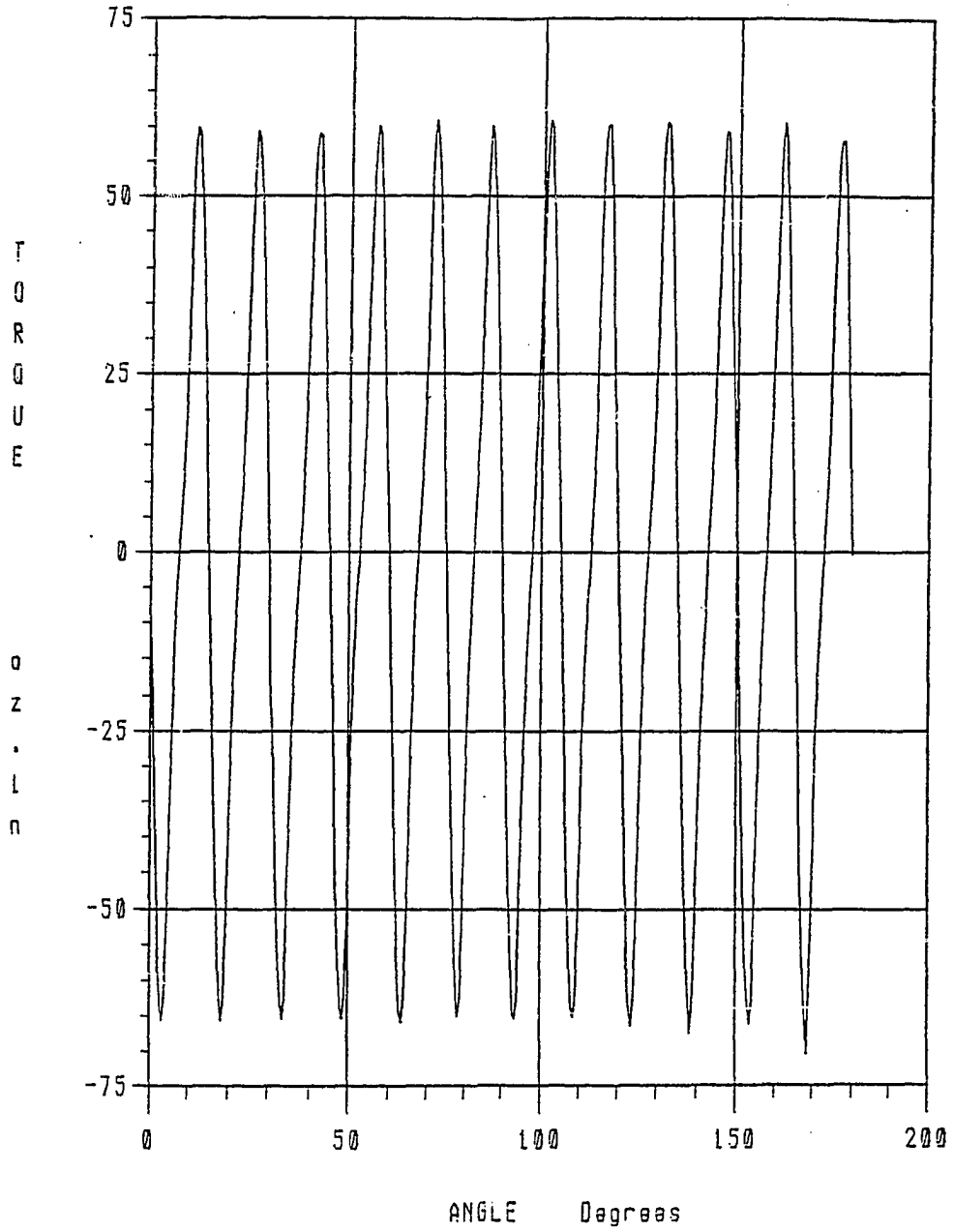

Figure II-6
Detent Torque Produced by Prototype BLDCM

oz-inches. The period of the detent torque is 15 mechanical degrees. This corresponds to one tooth pitch of the 24 slot stator.

II.3 Stator Torque-Angle Curve Measurement

In order to determine the one-phase-on stator torque, first the total torque must be determined. Total torques for the motor were measured in the same manner as the detent torque. The total torque consists of the net torque due to both the stator phase currents and the detent torque. The one-phase-on torque is produced by the interaction of the stator field and permanent magnet field. The detent torque is produced by the interaction of the permanent magnet field with the stator iron poles. Knowing the one-phase-on torque is important because it represents the controllable torque produced by the motor. Furthermore, the stator laminations are often 'skewed' to eliminate the detent torque. Hence, if detent torque can be eliminated, the total torque output of the motor will be just the one-phase-on torque. 'Skewing' is the term applied to describe a twisting of the stator stack so that the edge of a stator tooth is not parallel to the edge of a magnet. The concept of skewing and its effects will be discussed in detail in Chapter V.

The one-phase-on torque angle curves produced by energization of one phase of the prototype BLDCM, are shown in Figure II-7. Nine stator torque curves for nine different current levels are shown in this figure. The current levels start at 0.25 amps and are incremented by 0.25 amps to a final value of 2.25 amps. As stated previously, the one-phase-on torque-angle curves are obtained by measuring both the total torque-angle curves and the detent torque curves and then subtracting the detent torque from the total torque,

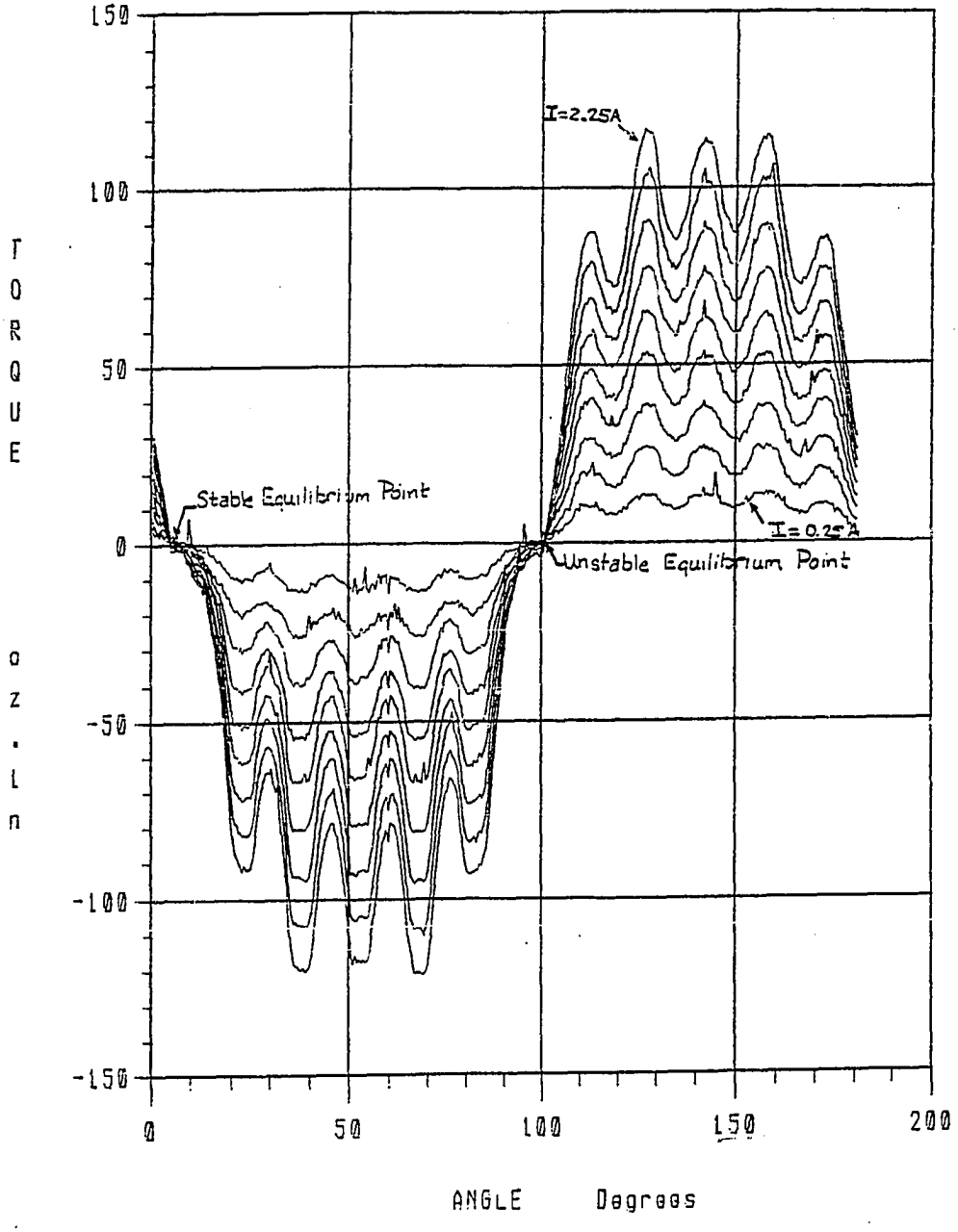

Figure II-7
Stator Torque-Angle Curves
for One-Phase-On Energization

on a point by point basis. This process assumes that no magnetic saturation has occured. Therefore, the principal of superposition can be applied to separate the two torque components. Assuming that superposition applies, one sees in this figure that an additional harmonic component exists in the stator torque angle curve that is of the same period as the detent torque. This is due to the fact that the coil induced flux density distribution that exists in the region of the magnet, has a harmonic of this period which is caused by the stator slots. This also will be addressed further in Chapter V.

II.4 Torque Constant

The torque constant, K_t, of a motor, is a parameter which is used to relate the magnitude of the torque-angle curve to the current. It is commonly used in brush DC motor technology. In that technology one usually thinks of the motor as a 'black box' and uses its terminal characteristics. If a constant, unidirectional current is injected into the terminals of the device, a unidirectional torque is obtained which is proportional to the current. Suppose, however, that the commutation process is interrupted. If current is applied to one of the rotor windings through one of the commutator bars, and prevented from switching to a different set of commutator bars as the rotor moved, one could then measure a torque angle curve for the BDCM. There would be a phase shifted torque angle curve for each set of commutator bars connected to supply by the brushes.

In brush DC motors there are usually a large number of commutators which results in a large number of phase shifted torque-angle curves. This is unlike the BLDCM which often has only three phases or, at

best, six torque-angle curves. Because of the large number of phases in a BDCM one commutates, (switches from one torque angle curve to another), over a very narrow range around the peak of the torque angle curve. Hence, the net static torque angle curve for a commutated BDCM is a DC level with some small amount of ripple. (See Figure II-8). The average value of this torque is proportional to the input current. This constant of proportionality is referred to as the torque constant, and is a figure of merit for the device. One can compare torque constants of similar machines to judge their torque producing capabilities.

A BLDCM has fewer phases and hence, a larger torque ripple. In addition, one often has the flexibility of altering the commutation angle or the number of phases which are energized, either of these can alter the average commutated torque. Since a torque constant relating terminal input current to the average commutated torque is not independent of these parameters, the torque constant concept is not as useful as it was for the BDCM. Instead, we select the constant of proportionality relating the peak of the one-phase-on torque angle curve to the phase current. See Equation II-1. This is independent of commutation angle and phase connection scheme.

$$T_{peak} = K_t i \qquad \text{(II-1)}$$

The torque constant can be found by determining the peak torque values obtained from the stator torque versus angle curves and then applying a linear least squares fit analysis to the torque-current data. Often, the torque-angle curve is approximately sinusoidal or trapeziodal and so the peak torque occurs at the 90 electrical degree point. Hence, one can simply measure the torque-current relation at

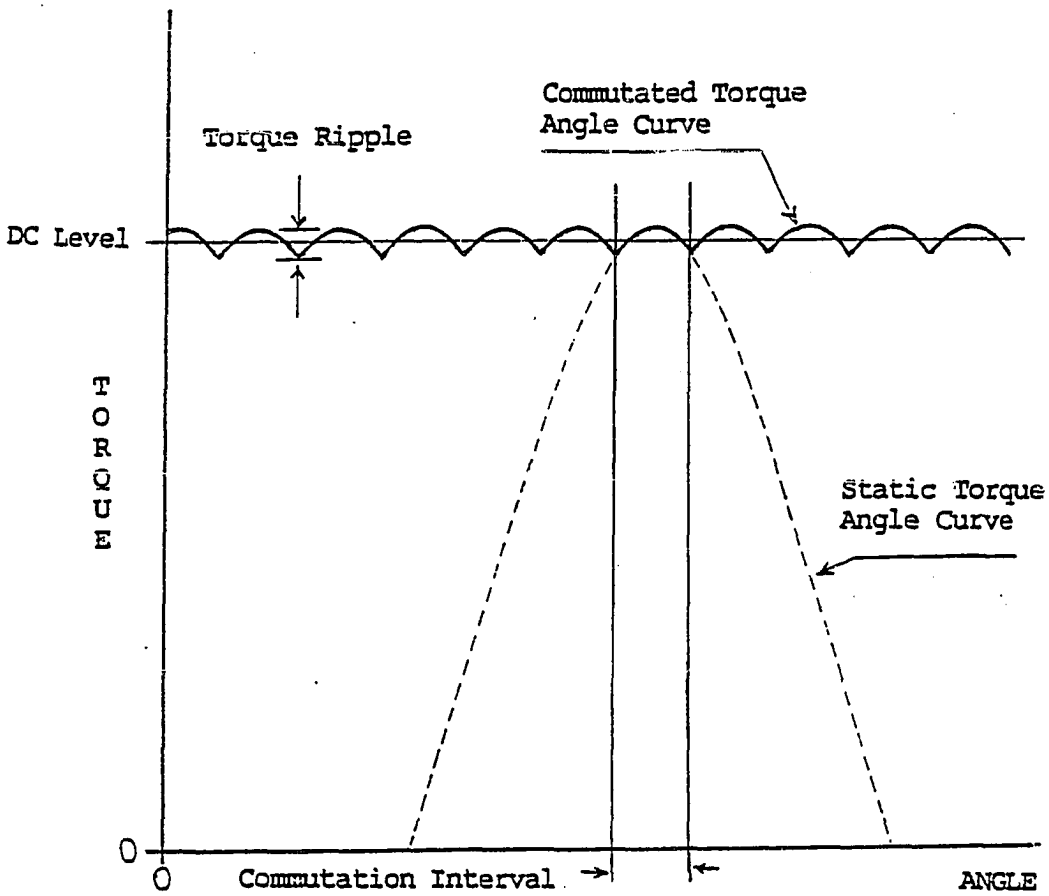

Figure II-8
Commutated Torque-Angle Curve

the peak torque position. Unfortunately, for a motor such as this prototype motor, which has a large amount of ripple in the torque angle curve, the peak torque value doesn't always coincide with the 90 electrical degree point. Two alternative approaches might be taken: 1) One might take the 'average' peak torque if the ripple were removed, (as might occur by skewing, for example). 2) One might take the value found at the 90 electrical degree point.

The data shown in Figure II-9 uses method 2. This was done because the experimental data will be compared to finite element results obtained from the 90 electrical degree point. This will allow a common basis of comparison. The torque constant is equal to the slope of the line shown in Figure II-9.

$$K_{texp} = 50.23 \text{ oz-in/Amp}$$

One can see from Figure II-9 that the torque-current relation is linear. One might infer that the stator and rotor back iron are not being driven into magnetic saturation by the coil. However, it will be shown that the permanent magnet is strong enough to saturate the iron even when the stator phase current is zero.

II.5 Back Emf Waveform

Whenever the motor rotor has some velocity, the stator coils enclose a time varying magnetic flux. This changing flux causes a back emf voltage, V_{bemf}, to be induced in the coils. The relationship is expressed mathematicallly in Equation II-2.

$$V_{bemf} = -\frac{d\lambda_t}{dt} = -N\frac{d\phi}{dt} \qquad \text{(II-2)}$$

Where: $N \equiv$ number of turns of the coil

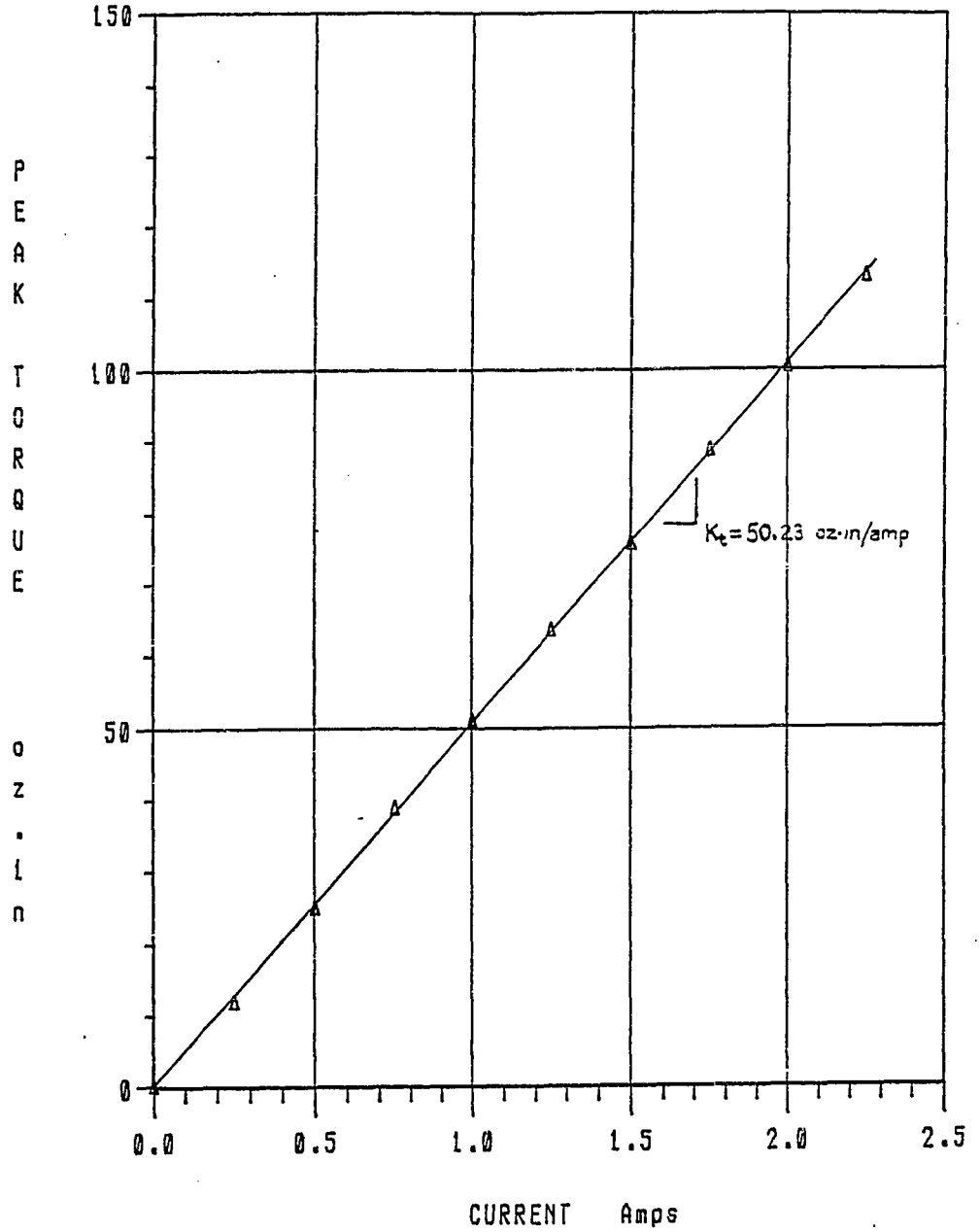

Figure II-9
One-Phase-On Peak Stator Torque
versus Current

$\phi \equiv$ total flux linking all N turns

$\lambda_t \equiv$ total flux linkages for the coil

The flux is a function of rotor angle, θ, which is a function of time:

$$\phi = f(\theta(t)) \qquad \text{(II-3)}$$

Application of the chain rule to Equations II-2 and II-3 yields:

$$V_{bemf} = -N \frac{\partial \phi}{\partial \theta} \omega_o \qquad \text{(II-4)}$$

Where: $\omega_o = \frac{d\theta}{dt}$

If the rotor is driven at a constant speed, ω_o, the voltage waveform that appears across the phase is proportional to the angular rate of change of flux linking the coil.

The back emf waveform was measured by driving the prototype BLDCM at a constant speed with a DC motor. The motor speed and the voltage that appeared across one of the open circuited phases were measured. Figure II-10 shows the waveform.

II.6 Back Emf Constant

Similar to the torque constant, (described in Section II.4), the back emf constant of a BLDCM is a constant of proportionality relating the peak voltage of the back emf waveform to the rotor speed. The back emf waveform was measured by driving the motor at a constant speed and recording the voltage waveform that appeared across a phase, (Figure II-10). The flux derivative, $\partial\phi/\partial\theta$, versus angle waveform is proportional to this voltage. (See Equation II-4).

The back emf constant was determined by measuring the magnitude of

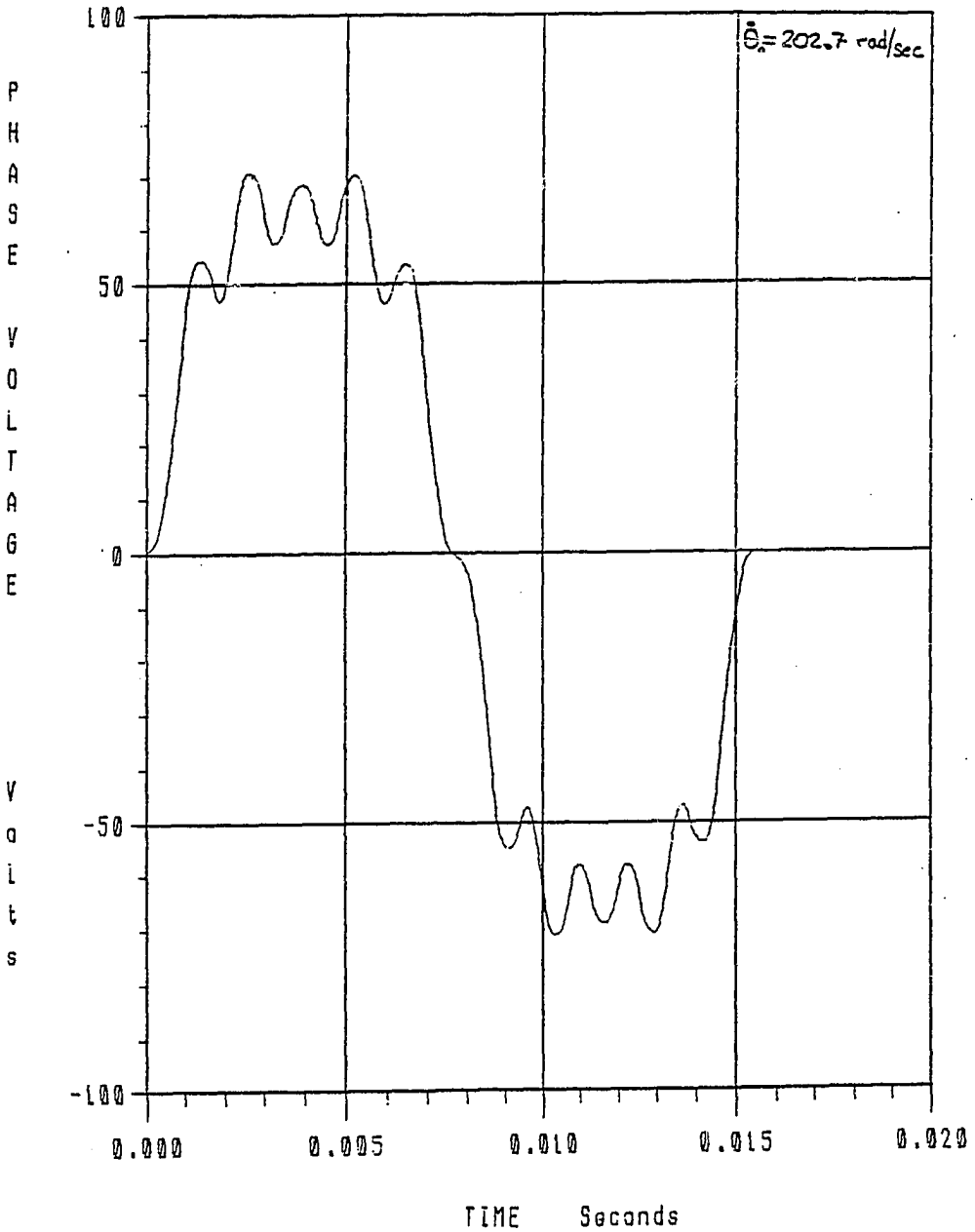

Figure II-10
Back Emf Voltage Waveform
at Motor Speed of 202.7 rad/sec

the back emf voltage that appeared across a phase while the motor was driven at a wide variety of constant speeds. The resulting plot is shown in Figure II-11.

Normally, the peak of the back emf voltage, like the peak torque, occurs at the 90 electrical degree point of the waveform. This is desirable because we can then compare back emf and torque constants, knowing that they were determined from data taken at the same rotor positions. While the peak voltage does not occur at the 90 degree point for the prototype BLDCM, one can see from Figure II-10 that the peak voltage is approximately equal to the voltage at the 90 degree point. Therefore, the slope of the envelope, (shown in Figure II-11), was used to find the back emf constant.

$$K_{bexp} = 0.332 \text{ Volts/rad/sec} \qquad \text{(II-5)}$$

II.7 Flux Linkage versus Current

Suppose that a simple one dimensional magnetic circuit is used to model the flux linking the magnet and coil. This circuit consists of two sources, the magnet and the coil, and an effective reluctance for airgap, magnet and steel parts of the circuit. Hence, the flux is simply equal to the sum of the mmfs divided by the effective reluctance. The total flux linkages for the N turn coil in this circuit, is given by:

$$\lambda_t = N\phi = \frac{N^2 i - NF_m(\theta)}{\mathcal{R}_e(\lambda_t)} \qquad \text{(II-6)}$$

Where: $\lambda_t \equiv$ total flux linkages of coil

$\phi \equiv$ total flux for circuit

$F_m \equiv$ mmf provided by magnet, a function of angle, θ

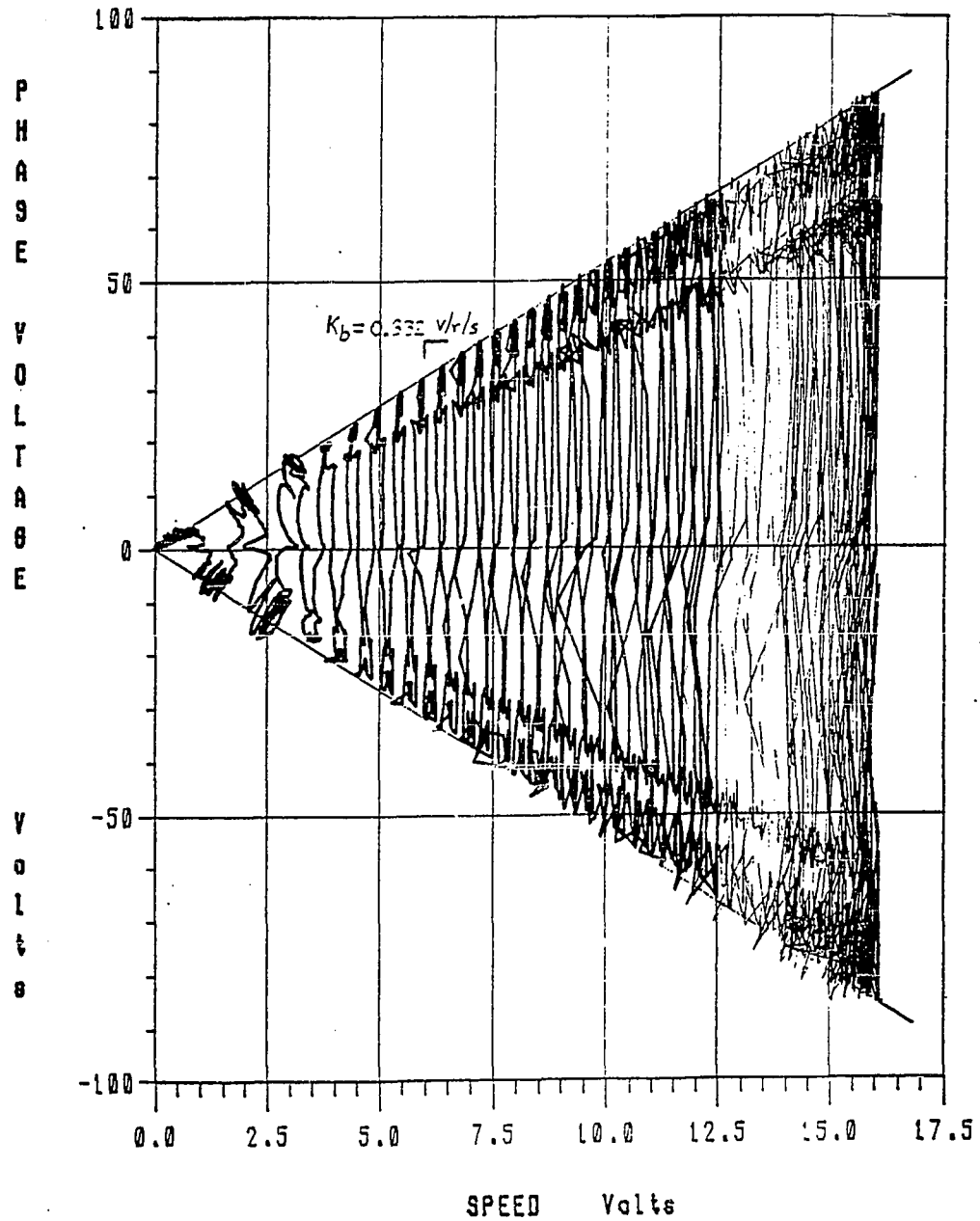

Figure II-11
Back Emf Voltage versus Speed
(Tachometer Sensitivity = 16.0 rad/sec/Volt)

$\mathcal{R}_e$ ≡ effective saturable reluctance of circuit, a function of the total flux linkages

N ≡ number of coil turns

i ≡ coil current

The effective reluctance of the circuit has been assumed to be saturable and therefore is a function of the total flux linking the circuit. The total flux linkage of the circuit can be separated into two components: λ_c, caused by the coil, and λ_m, caused by the magnet.

$$\lambda_t = \lambda_c + \lambda_m \tag{II-7}$$

$$\lambda_c = \frac{N^2 i}{\mathcal{R}_e(\lambda_t)}, \qquad \lambda_m = \frac{N F_m}{\mathcal{R}_e(\lambda_t)} \tag{II-8a,8b}$$

Equations II-8a and 8b show that only λ_c is a function of current if there is no saturation and $\mathcal{R}_e$ is a constant. In that case the slope of the flux linkage-current characteristic is constant and independent of λ_m.

If the magnet is the principal source of flux linkage and cause of saturation, then the slope of the flux linkage-current characteristic will change with the presence, (or strength), of the permanent magnet. If the coil is the principal cause, the flux linkage-current characteristic would not be linear. The slope would decrease with increasing current.

The flux linkage versus current characteristic of the motor is determined by recording the locked rotor current response to a step change in applied voltage. The difference between the applied voltage and the iR drop is numerically integrated with respect to time to yield the flux linkage as a function of time. (See Equation II-9).

$$\lambda(t) = \int_0^t (V(\tau)-Ri(\tau))d\tau + \lambda_o \qquad \text{(II-9)}$$

λ_o is equal to the flux linking the coil due to the permanent magnet. Although λ_o is unknown, it is simply set to zero. The only effect this has is to remove the DC bias from the flux linkage-current characteristic.

Once the flux linkage is calculated, both the current and corresponding flux linkage values are known for any instant in time. Flux linkage then can be plotted versus current. Figure II-12 shows two flux linkage-current curves, (1) and (2). Curve (1) was calculated from data obtained with the rotor magnets mounted on the rotor back iron. Curve (2) was calculated from data obtained with just the rotor back iron in place and no rotor magnets. As was shown in Equations II-8a&b, if there was no saturation in the stator iron then the slope of these two curves would be the same. (Neglecting the fact that the magnet is 10% more permeable than air.

Figure II-12 shows that for this motor the magnet is the principal cause of saturation. The presence of the magnet causes a 40% decrease in the slope of the flux linkage-current curve. If the permeability of the magnet is accounted for, the presence of the magnet has caused close to a 50% decrease in slope. This decrease must be due to saturation effects.

The preceeding discussion and measurements have shown that determining the flux linkage-current characteristic of the motor provides one with information relating to the degree and source of magnetic saturation present in the motor. In addition, the flux linkage-current characteristic can also be used to determine the

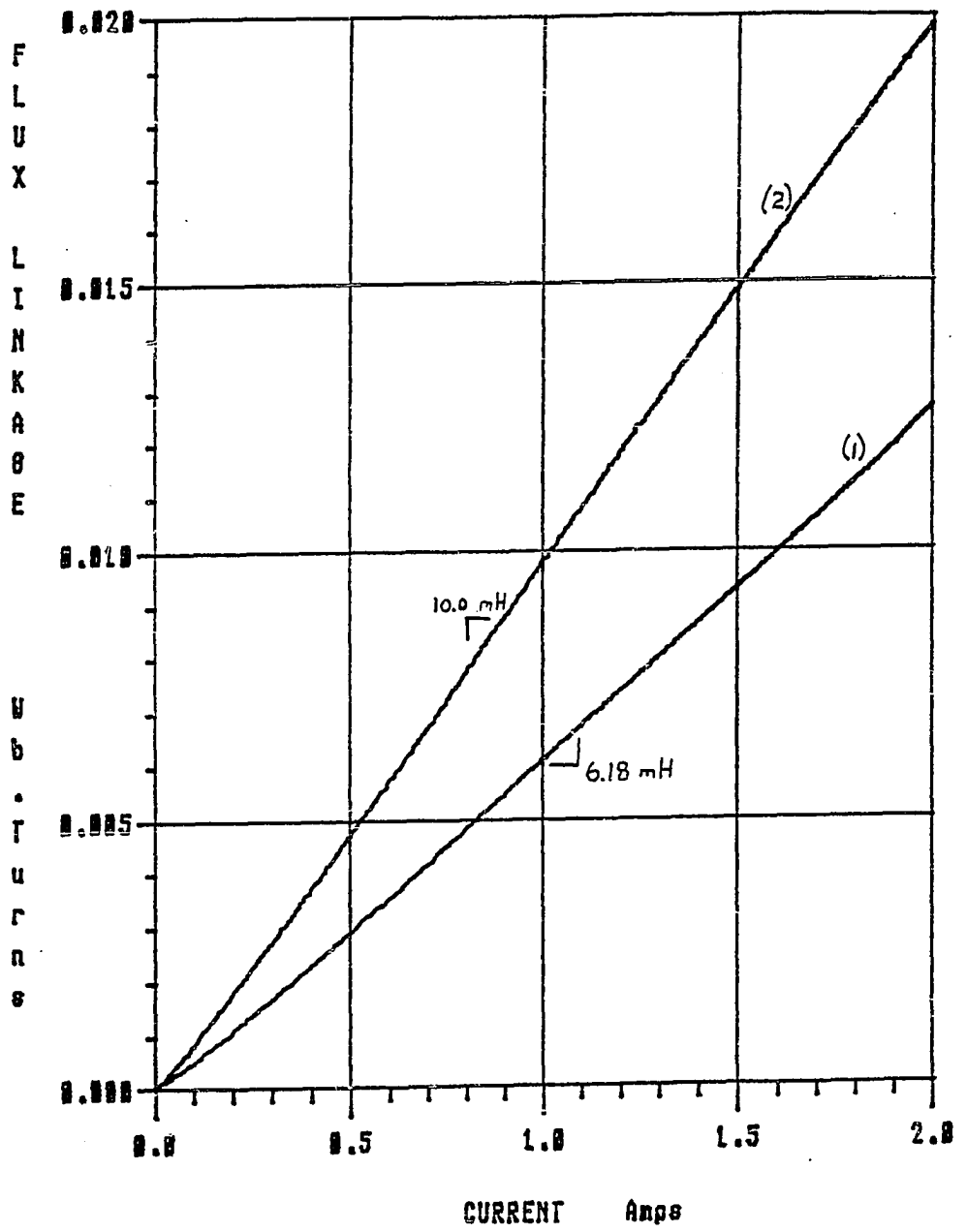

Figure II-12
Coil Flux Linkage versus Current,
Curve (1) - With Permanent Magnets on Rotor
Curve (2) - Without Permanent Magnets on Rotor

electrical inductance of the motor. From Faraday's law:

$$V = iR + \frac{d\lambda_t}{dt} \qquad \text{(II-10)}$$

Applying the chain rule:

$$V = iR + \frac{\partial\lambda_t}{\partial i}\frac{di}{dt} + \frac{\partial\lambda_t}{\partial\theta}\frac{d\theta}{dt} \qquad \text{(II-11)}$$

It is obvious from the form of Equation II-11 that the partial derivative of λ_t with respect to current is the inductance of the circuit. If the flux linkage-current characteristic is linear, as in the experimental case, then this parameter is a constant, and would be equal to the inductance determined from the locked rotor current response to a step change in voltage.

The step response method was used to determine the inductance of the motor with the magnets present and also with them removed. In Table II-1 the results of those measurements are compared to the slopes of the flux linkage-current characteristics of Figure II-12. It is obvious that the determination of the flux linkage-current curve is an effective means of determining inductance. It has the added feature of revealing saturation information.

Table II-1
Comparison of Flux Linkage-Current Slope to Measured Inductance

	Step Response Inductance (mH)	λ-i slope (mH)	%difference of slope from Step Response
With magnet	6.3	6.18	-1.9
No Magnet	10.6	10.00	-5.7

II.8 Summary

In this chapter, characteristic parameters of the prototype motor were determined. In determining these, several points became evident that will have to be addressed in any redesigns: 1) The magnitude of the detent torque is approximately 60 oz-in. This is extremely large compared to the peak one-phase-on torque, 100 oz-in, at the thermally rated current of 2.0 amps. If the detent torque is not eliminated, or at least significantly reduced, the resulting velocity ripple induced would be very large. 2) The one-phase-on stator torque has a large ripple component. If this torque ripple is not eliminated or reduced, it will cause a large velocity ripple in many applications. 3) The rotor magnets cause enough magnetic saturation so that the slope of the coil flux linkage vs current curve obtained at the stable equilibrium position, changes by 40% if the magnets are in place. Since it can be shown with simple magnetic circuit models that there is a direct correlation between the torque constant and the flux-current slope, the torque constant could be increased if the saturation condition was relieved. In order to relieve the saturation it might be necessary to make the teeth wider and/or the rotor and stator back irons thicker. This will result in a larger and heavier motor.

CHAPTER III

FINITE ELEMENT ANALYSIS

A two-dimensional nonlinear finite element model using triangular first order finite elements was used to analyze the static magnetic field produced within the prototype motor. The derivation of this finite element model is shown in Appendix A. The Newton-Raphson process used to solve the resulting set of nonlinear algebraic equations is shown in Appendix B.

This chapter is divided into two principal sections. In the first section, aspects of the finite element model are discussed, such as the mesh creation, modelling the nonlinearities in the iron, and modelling the permanent magnet. In the second section, the results of the finite element analysis are discussed.

In motor magnetic analysis, questions are not answered by simply obtaining the solution to the finite element model. In motor analysis, one is usually concerned with determining the motor characteristic parameters such as the torque constant, back emf waveform, energized torque-angle curve, detent torque-angle curve and flux linkage-current curve. The determination of some of these characteristics represents a large amount of post processing and many finite element solutions. Methods of determining these parameters are presented in this chapter. Where possible, methods are presented which require fewer finite element solutions and streamline the calculations.

The calculated parameters are then compared to the experimental ones found in Chapter II and the overall accuracy of the finite element model is evaluated. It is shown that two-dimensional finite element analysis seems to predict the torque constant and torque-angle characteristic well but is deficient in predicting inductance and detent torque. Questions are raised as to the cause of these discrepencies and are addressed further in Chapter IV.

III.1 The Finite Element Model

III.1a Mesh Development

The mesh that was created was a 'regular', first order triangular mesh. By 'regular' it is meant a mesh that is formed by first creating a grid as shown in Figure III-1. This grid can be in either a cartesian or a polar coordinate system. Grid increments, or spacing, is selected in advance depending upon the geometry of the problem being modeled. After the grid is created, individual nodes can be moved slightly so that the mesh fits the problem geometry better. Triangular first order elements are automatically formed during the generation of the regular mesh. In this particular code, the triangular elements are formed by placing a diagonal between the upper left and lower right corner of each square formed by the grid.

There are advantages and disadvantages to this type of mesh. Its principal advantage lies in the ease with which a mesh can be created. By simply specifying the number of nodes on the top and side boundaries, as well as the spacing of those nodes, the entire mesh is created. Then, one simply needs to map the material properties of the problem onto the mesh. Care should be exercised when specifying the

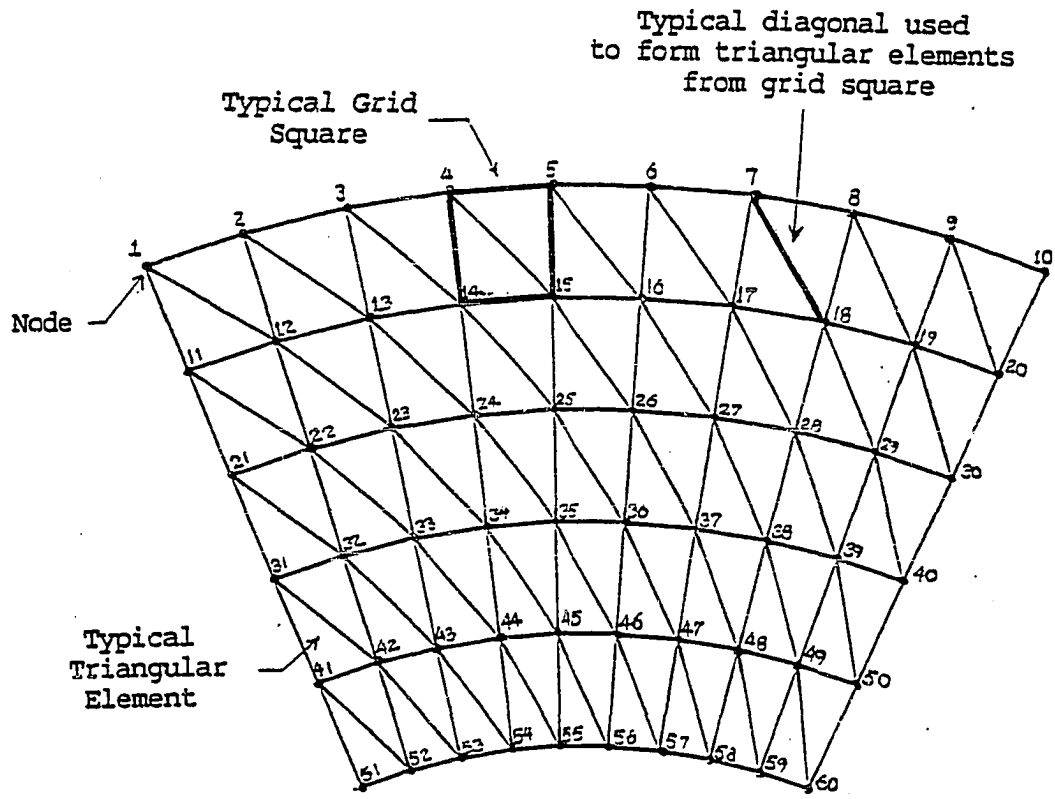

Figure III-1
'Regular' Finite Element Mesh

node spacing so as not to exceed aspect ratios for the triangles of 5:1. This is because the finite element formulation results in a matrix which has as its components, cotangents of the element angles. A 5:1 aspect ratio gives a margin of safety so that the included angles do not become too small and cause numerical errors when the cotangents are formed[4].

The grid type nature of the mesh leads to a node numbering scheme that is also very regular. The nodes are numbered sequentially by row starting at the upper left corner of the grid and ending at the bottom right corner of the grid. This numbering scheme allows easy manipulation of the mesh properties because the relation between indicies for adjacent nodes remains fixed. It also results in a sparse matrix which can be solved rapidly. In addition, algorithms for various types of pre- and post- processing operations can be developed with relative ease. This was an important factor, since we were exploring many different ideas to aid in the creation of mesh models for motors -as well as different ideas for post processing operations to answer questions that were specific to motor performance.

One of the primary disadvantages of this type of meshing is that it is not possible to refine the mesh by placing a large number of elements in a local area without also refining the mesh in other areas as well. In general, a higher number of first order elements is necessary to obtain the same level of accuracy as could be obtained with a smaller number of higher order elements. Although even with higher order elements, one needs to keep the element size small because the permeability is usually assumed constant over the higher order element. This assumption can be a source of error in higher

order formulations.

The mesh created for the prototype motor is too detailed to show with clarity in this text. However, an outline for the quarter section modelled is shown in Figure III-2. This mesh has 90 divisions in the theta direction, equally spaced at 1 degree intervals. The mesh has 55 divisions in the radial direction. Those divisions and the sections of the motor they correspond to are shown in Table III-1.

III.1b Modelling the Permanent Magnet

The basic premise in most models of permanent magnets used in finite element magnetic models is that the permanent magnet can be represented by an equivalent coil. This premise is derived from the fact that on an atomic level, magnetic dipole moments are caused by spinning electrons[5]. These spinning electrons are equivalent to current loops on an atomic scale. Therefore, it is reasonable to assume that the magnetization of a permanent magnet can be described by equivalent volume and surface currents[6],[7]. The magnitude of the currents used in the equivalent coil depends on the strength of the permanent magnet, i.e: its residual flux density level and permeability, the thickness of the permanent magnet, and the direction and uniformity of its magnetization. Ampere's circuitial law is used to determine the values of these currents[8],[9].

$$i = \int \vec{H} \cdot d\vec{l} \qquad \text{(III-1)}$$

If the permanent magnet is uniformly magnetized, then it can be represented in the finite element model by sheet currents at its edges. This is demonstrated as follows. Suppose one is modelling the segment of permanet magnet, shown in Figure III-3, and that the

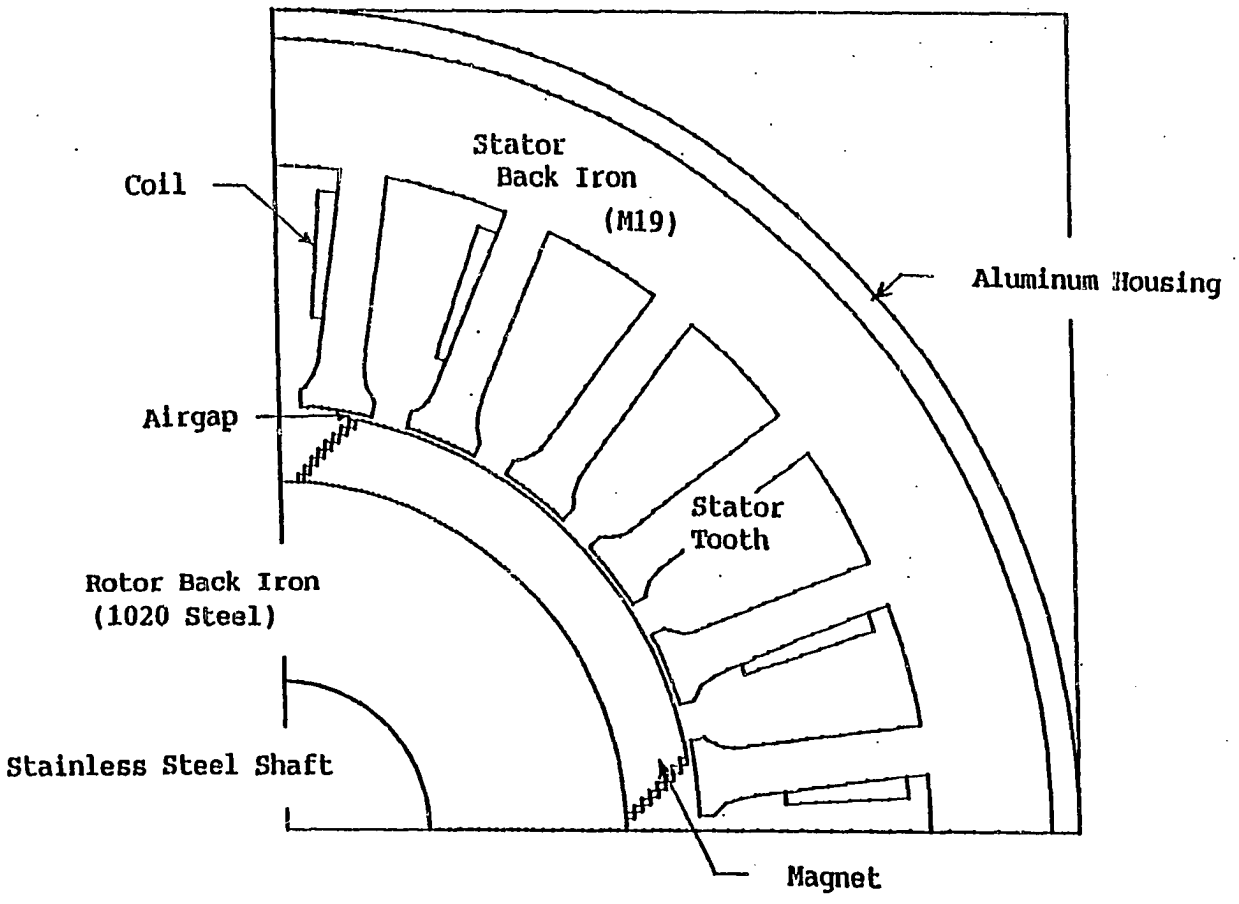

Figure III-2
Outline of Quarter Section of
Finite Element Mesh

Table III-1
Radial Grid Locations and Corresponding Motor Sections

Grid Division Radial Location (inches)	Motor Section
1.620 E-00	Housing
1.563 E-00	
1.500 E-00	
1.450 E-00	Stator Back Iron
1.400 E-00	
1.350 E-00	
1.3135 E-00	
1.27 E-00	
1.11 E-00	
1.08 E-00	
1.05 E-00	
1.02 E-00	
9.9000 E-01	Stator Tooth
9.6000 E-01	
9.3000 E-01	
9.0000 E-01	
8.7000 E-01	
8.4375 E-01	
8.3813 E-01	Airgap
8.3250 E-01	
8.1693 E-01	
8.01375E-01	
7.8581 E-01	
7.7025 E-01	Magnet
7.5468 E-01	
7.39125E-01	
7.2356 E-01	
7.0800 E-01	

(Continued)

Grid Division Radial Location (inches)	Motor Section
7.0800 E-01	
6.9250 E-01	
6.7500 E-01	
6.5750 E-01	
6.4000 E-01	
6.2000 E-01	
6.0000 E-01	
5.8000 E-01	
5.6000 E-01	
5.4000 E-01	Rotor Back Iron
5.2000 E-01	
5.0000 E-01	
4.8500 E-01	
4.7000 E-01	
4.5500 E-01	
4.4000 E-01	
4.2500 E-01	
4.1000 E-01	
3.9000 E-01	
3.7500 E-01	
3.7000 E-01	
3.5000 E-01	
3.3000 E-01	
3.1000 E-01	
2.9000 E-01	

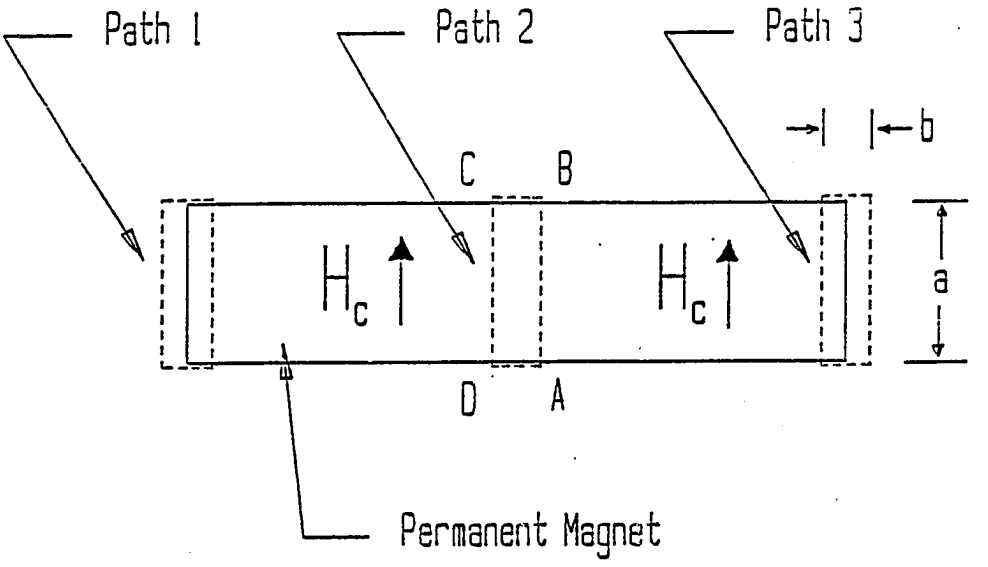

Figure III-3
Example Permanent Magnet

permanent magnet is uniformly magnetized so that the $\vec{H}$ field within the permanent magnet is uniformly directed and constant in magnitude. To find an equivalent current by Equation III-1, an integration path must be selected. Three sample paths are shown in the figure. First the equivalent current in the interior of this magnet is easily shown to be zero. Apply Equation III-1 to path 2 in Figure III-3; if one starts at point A and evaluates the line integral in the counter clockwise direction for each of the four line segments, Equation III-2a results. There is no contribution from line segment BC or DA because each of these is perpendicular to H. Contributions for line segments AB and CD are equal in magnitude and opposite in sign, leaving a net magnetization current of zero.

$$i = \int_A^B H\,dl + \int_B^C H\,dl + \int_C^D H\,dl + \int_D^A H\,dl \qquad \text{(III-2a)}$$

$$i_2 = H_c a + 0 - H_c a + 0 \qquad \text{(III-2b)}$$

This example can be extended to show that anywhere on the interior of the uniformly magnetized magnet, the equivalent magnet current is zero. In fact, only paths which enclose an edge of the magnet will have nonzero contributions. This is demonstrated by applying Equation III-1 to path 1 of Figure III-3. If one starts at point A of path 1 and applies Equation III-1 the resulting equivalent current magnitude is:

$$i_1 = H_c a + 0 + 0 + 0 = H_c a \qquad \text{(III-3)}$$

Similarly for path 3:

$$i_3 = 0 + 0 - H_c a + 0 = -H_c a \qquad \text{(III-4)}$$

The same result is obtained if the analysis is applied to the prototype motor magnets, which are arc shaped and radially oriented.

These magnetization sheet currents on the edges are distributed as current densities in the edge elements.

III.1c Including the Magnetic Nonlinearities of the Iron

The nonlinear nature of the stator iron was accounted for by using the virgin magnetization B-H curve to find reluctivity, (the inverse of permeability), versus flux density data for M19 electrical grade steel. Similarly, the B-H curve for 1020 soft steel was included in the model for the rotor back iron. The B-H and reluctivity versus B curves are shown in Figures III-4a through III-4d. Cubic splines are used to interpolate values between the specified data points.

Magnetic hysteresis is not included since it would require knowledge of local magnetic history. This is not practical to implement.

III.2 Finite Element Results

Each finite element solution provides the user with the values of the magnetic vector potential at every node. From this information the flux density, reluctivity, field intensity and coenergy of every element can also be determined. The vector potential solution is used to plot lines of constant vector potential. Figure III-5 is an example finite element solution plot of the contours of constant magnetic potential which occur when the rotor is at the peak torque position and the coil is energized. The direction of the flux density at any point is always tangent to a line of constant potential[10].

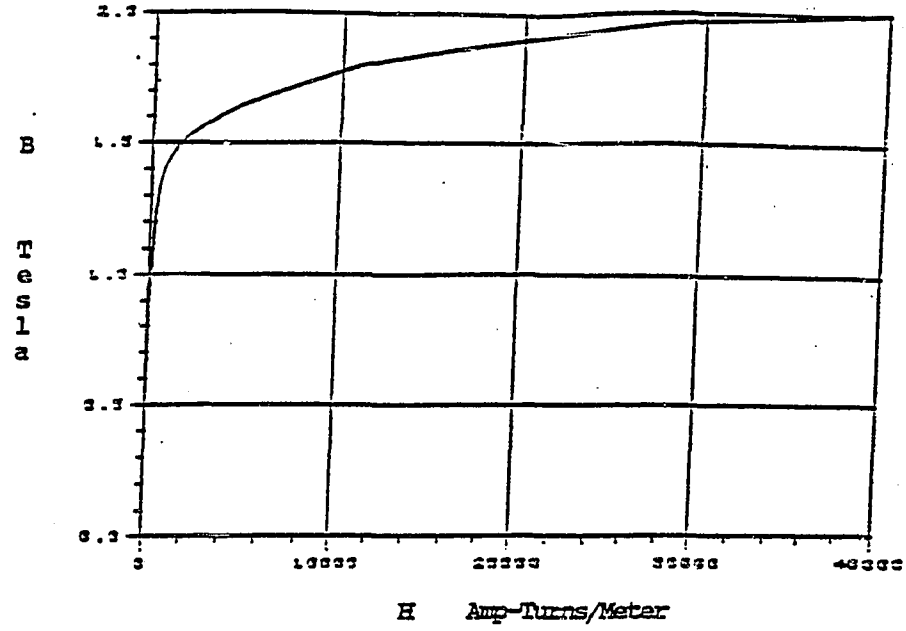

Figure III-4a
B-H Characteristic for 1020 Steel

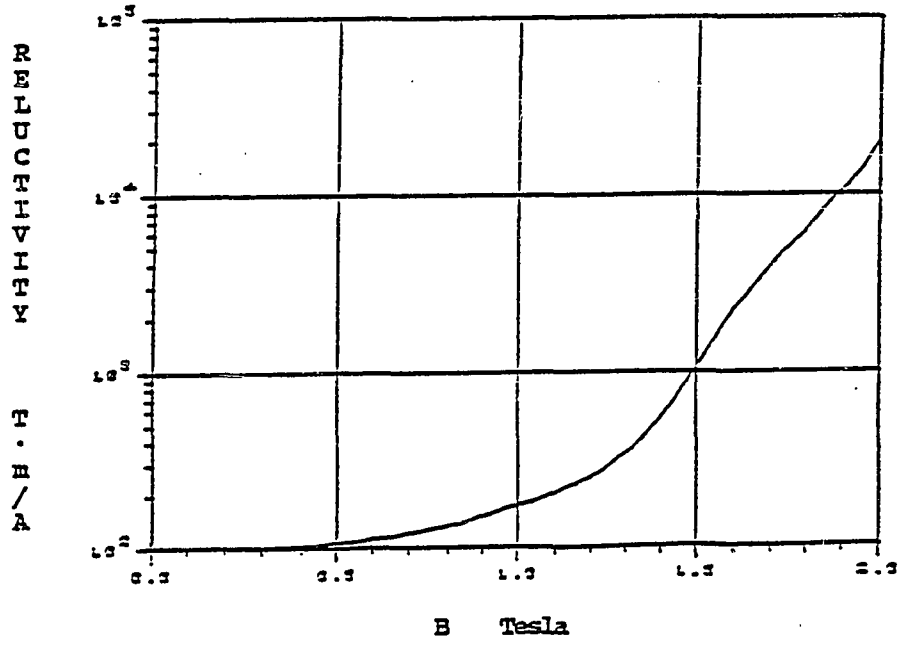

Figure III-4b
v-B Characteristic for 1020 Steel

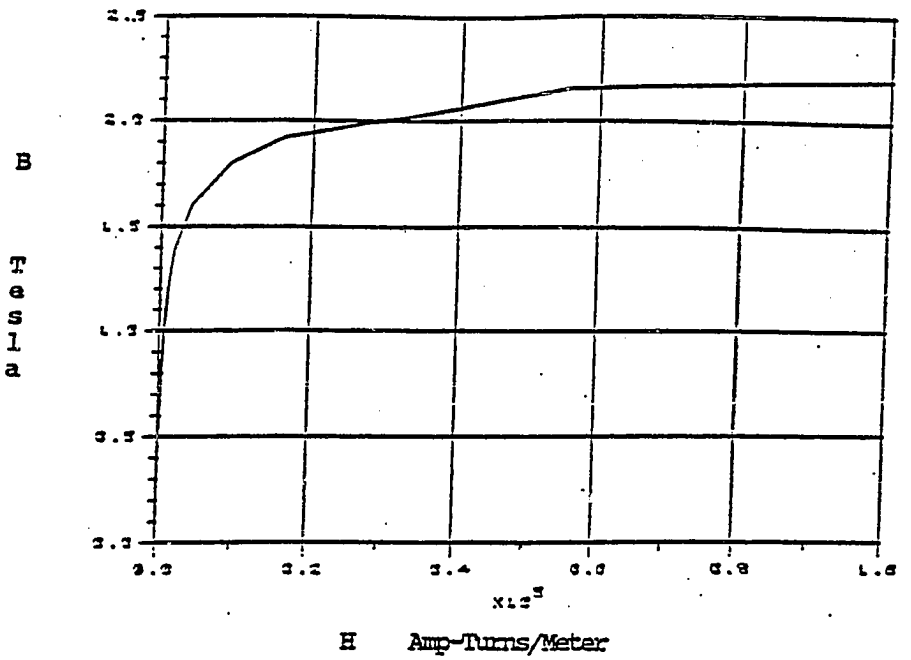

Figure III-4c
B-H Characteristic for M19
Electrical Grade Steel

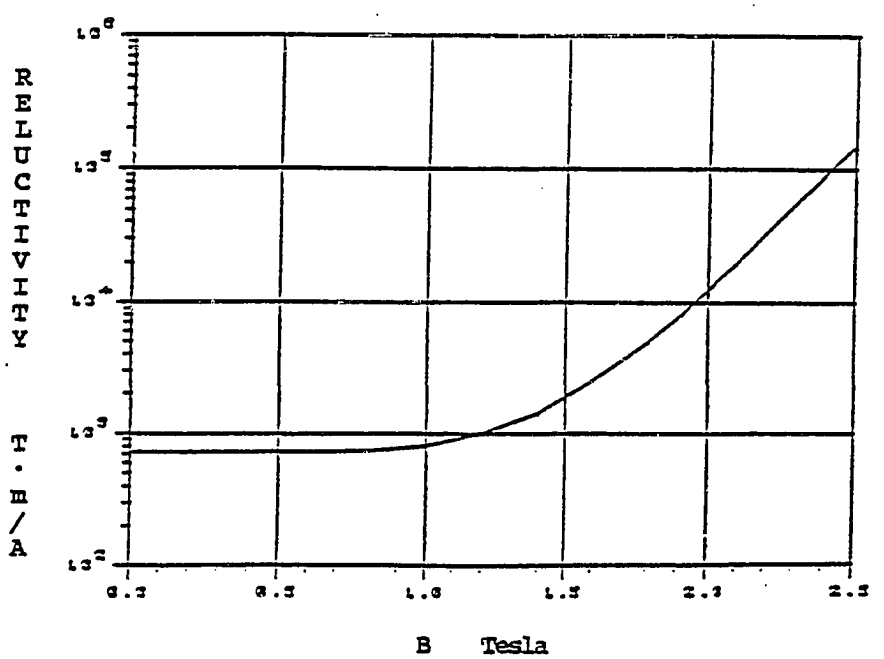

Figure III-4d
v-B Characteristic for M19
Electrical Grade Steel

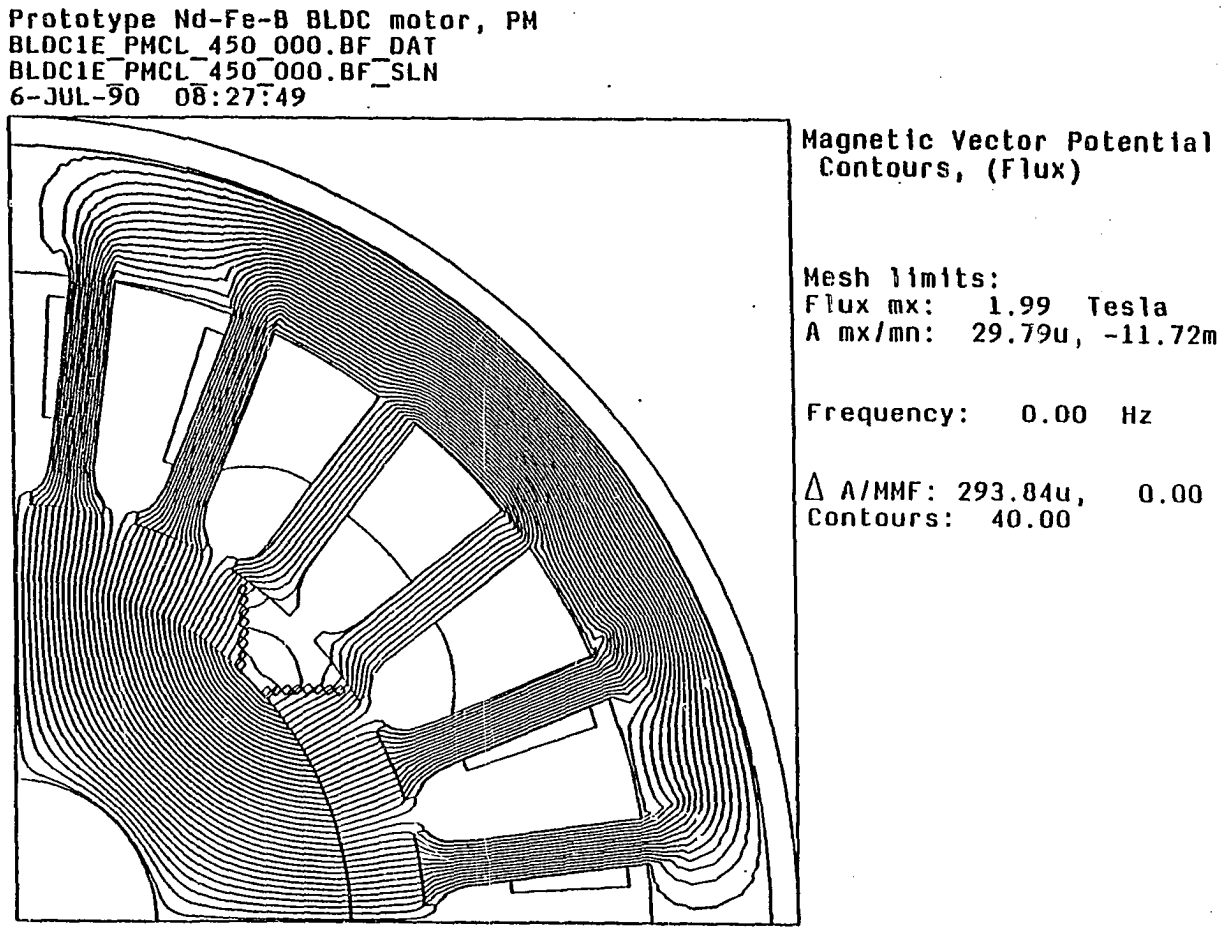

Figure III-5
Finite Element Solution Contour Plot

This allows the user to visualize flux paths within the motor, which will make it possible to design simpler lumped parameter models. The flux density information allows the user to identify regions of high flux density where magnetic saturation of iron material might occur. Thus, the motor designer can use this information to alter the geometry of the design to decrease saturation and perhaps increase the torque producing capability of the device.

In Figure III-5, the line spacing is indicative of the magnitude of the flux density. The flux between any two points is equal to the product of their potential difference and the distance between them, (to be shown later in this chapter). Since the potential contours drawn are of equal increments, the flux between any two contour lines is the same. Thus, the flux density is higher in regions where the contours are closer together. In areas where there are few or no contours drawn, such as in the airgap region between the teeth, the flux density is low.

The contours shown in Figure III-5 can also be drawn in color. As it passes through an element, each contour can be colored in a manner which would indicate the magnitude of a field parameter, such as flux density, field intensity, reluctivity or coenergy. Alternatively, elements, instead of contours, could be colored according to the magnitude of any of these field parameters. This latter scheme is the one most often used in many commercially available finite element packages.

In addition to the visual feedback and insight obtained from a plot like the one shown in Figure III-5, the vector potential solution can be used to calculate the characteristic motor parameters that were

described in Chapter II. The various methods of calculation used to determine those parameters are discussed in the following sections. In motor design, these post processing operations are often more important than knowing what the field solution looks like. In motor design, one is primarily interested in knowing how much torque the motor can produce, or the shape of the torque-angle curve, or the winding inductance.

III.2a Calculation of Torque

Torque can be calculated from the finite element results by several methods; Virtual Work[11], Maxwell Stress Tensor[12], Magnetizing Current[13], are a few of these. The one which is most commonly used is the virtual work method or 'coenergy' method. Torque is approximated by the change in magnetic coenergy for a change in angle, under the constraint of constant current.

$$T = \left.\frac{\partial W_c}{\partial \theta}\right|_i \approx \frac{\Delta W_c}{\Delta \theta} \qquad \text{(III-5)}$$

While this method is reasonably accurate, its primary disadvantage is that it requires two solutions. These solutions must be obtained from two slightly different rotor positions. (Recent work[14] shows that a coenergy change can be found from a single solution.)

Another method is the application of the Maxwell stress tensor. In this approach the total force on a body is determined by the integration of magnetic stress over a closed surface. This method usually suffers accuracy problems whenever first order triangular

elements are used. This is because its accuracy depends on the accuracy of the FEM in predicting the direction of B, which is necessarily constant over a first order triangular element.

Another method exists which can be used to find force, provided one is trying to find the forces on permanent magnets mounted on a non-salient back iron. This method uses the Lorentz force equation. In the FEA it was found that the magnet could be modeled as an equivalent coil and treated as a coil in almost every respect. This includes the manner in which forces are generated on the magnet. The force on a current carrying conductor in an external magnetic field is given by the Lorentz force equation, shown in Equation III-6.

$$\vec{F} = I \, d\vec{l} \times \vec{B} \qquad \text{(III-6)}$$

This equation can be used on the equivalent sheet currents used to model the PMs. While this expression is always valid, one needs to remember that it might not yield the total force being generated on a rotor member. Forces can also be generated due to variable reluctance effects. These forces are not taken into account by Equation III-6 and other methods, such as the coenergy method, or the magnetizing current method, must be used instead.

The Lorentz forces on the permanent magnets can be broken down into two components: F_x or F_θ, and F_y or F_r. These relations are given by:

$$F_{x,\theta} = i \, l \, B_{x,\theta} \qquad \text{(III-7)}$$

$$F_{y,r} = i \, l \, B_{y,r} \qquad \text{(III-8)}$$

The vector relation indicated in Equation III-6 is already taken into account because the current and flux density directions are always perpendicular in the two dimensional finite element model. Torque is calculated by multiplying the tangential component of force by the average radius of the element under consideration.

Data obtained from the FEA using this method was calculated and compared to data obtained using the coenergy method. A comparison is shown in Figure III-6. The method using the Lorentz force equation, (refered to hereafter as the IxB method), is denoted by O's, the coenergy method is denoted by Δ's.

One sees that the torque produced by the IxB method appears to have a DC level. In either the unstable or stable equilibrium positions the net torque produced by the motor should be zero. In order for the IxB method to accurately predict this, the B field found in elements containing one set of magnet edge currents must be identical in magnitude and opposite in sign to the B field found in the other set of edge current elements. Unfortunately, while the type of FEA used gives good overall average results in terms of the field solution, local errors occur. These local errors are due to a combination of the first order formulation and the fact that all triangular elements are created by placing a diagonal from upper left corner to bottom right corner of a grid square. The latter results in an asymmetric mesh that the former is not quite accurate enough to compensate.

The average DC level at the zero torque points is a good approximation for the average DC level of the waveform. If this value is subtracted from each point found on the curve, the results compare

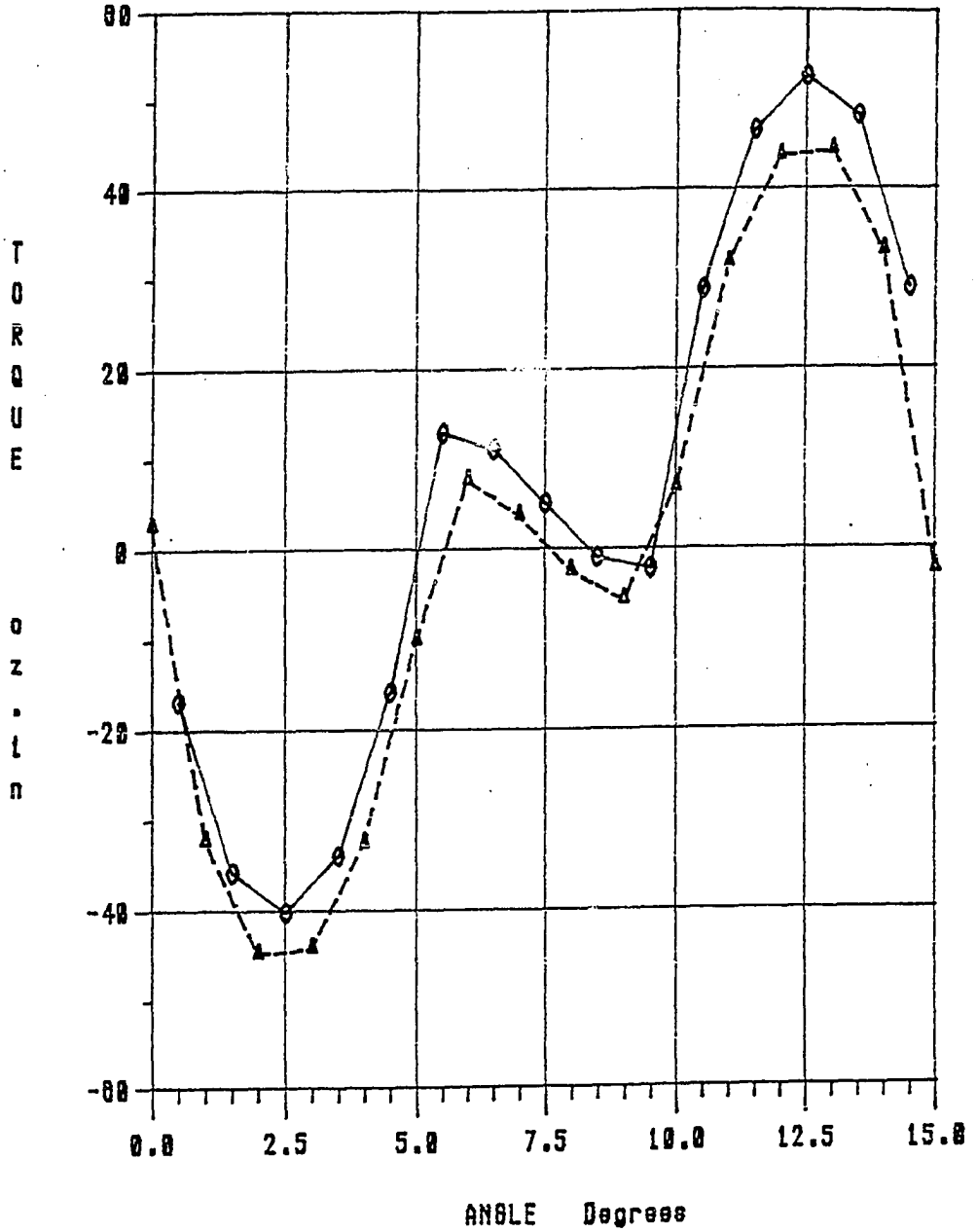

Figure III-6
Comparison of The Detent Torque-Angle
Curve Calculated by IxB, (Solid Line),
and Change in Coenergy, (Dashed Line)

well with the coenergy solution. The IxB data with the DC level removed is denoted by X's in Figure III-7. The coenergy data is again denoted by 'Δ's.

In the IxB method, the torque was found for each of fourteen rotor positions. These rotor positions were in 1 degree increments from 0.5 to 14.5 degrees. In the coenergy method, the coenergy values from two solutions 1 degree apart were used to find the torque at the average rotor position of the two solutions. While the aproach used does not allow a rigorous quantitative comparsion of the torques at each solution position, it does provide a qualitative comparison and shows that the two methods produce comparable results. Throughout most of the rest of this work, the IxB method will be used because of the advantage of calculating torque values from a single FEM solution.

III.2a1 Detent Torque Prediction

A comparison of the calculated detent torque versus angle curve and experimental detent torque versus angle curve is shown in Figure III-8. The solid line is the experimentally obtained detent torque as a function of angle. The symbol 'X' represents data points obtained from the finite element analysis. It is obvious that neither the waveform shape nor the magnitude correlate very well. The model shows a large harmonic in the waveform around the unstable equilibrium point. The experimental waveform shows much less of this effect. If one were to compare magnitudes only and neglect waveform shape one obtains the following results:

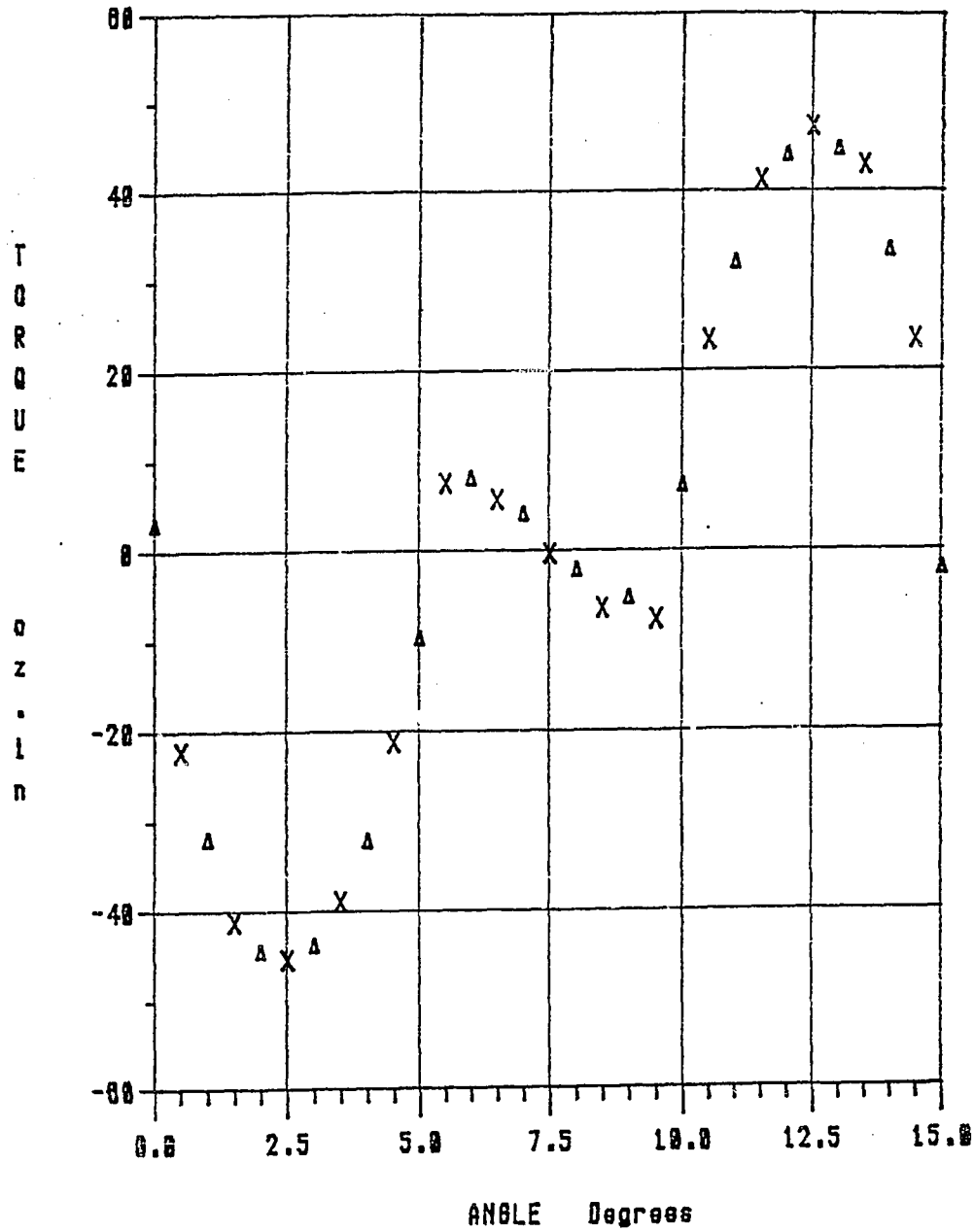

Figure III-7
Comparison of Coenergy Predicted Detent
Torque, (Triangles), and IxB Predicted
Detent Torque with DC Level Removed, (X's)

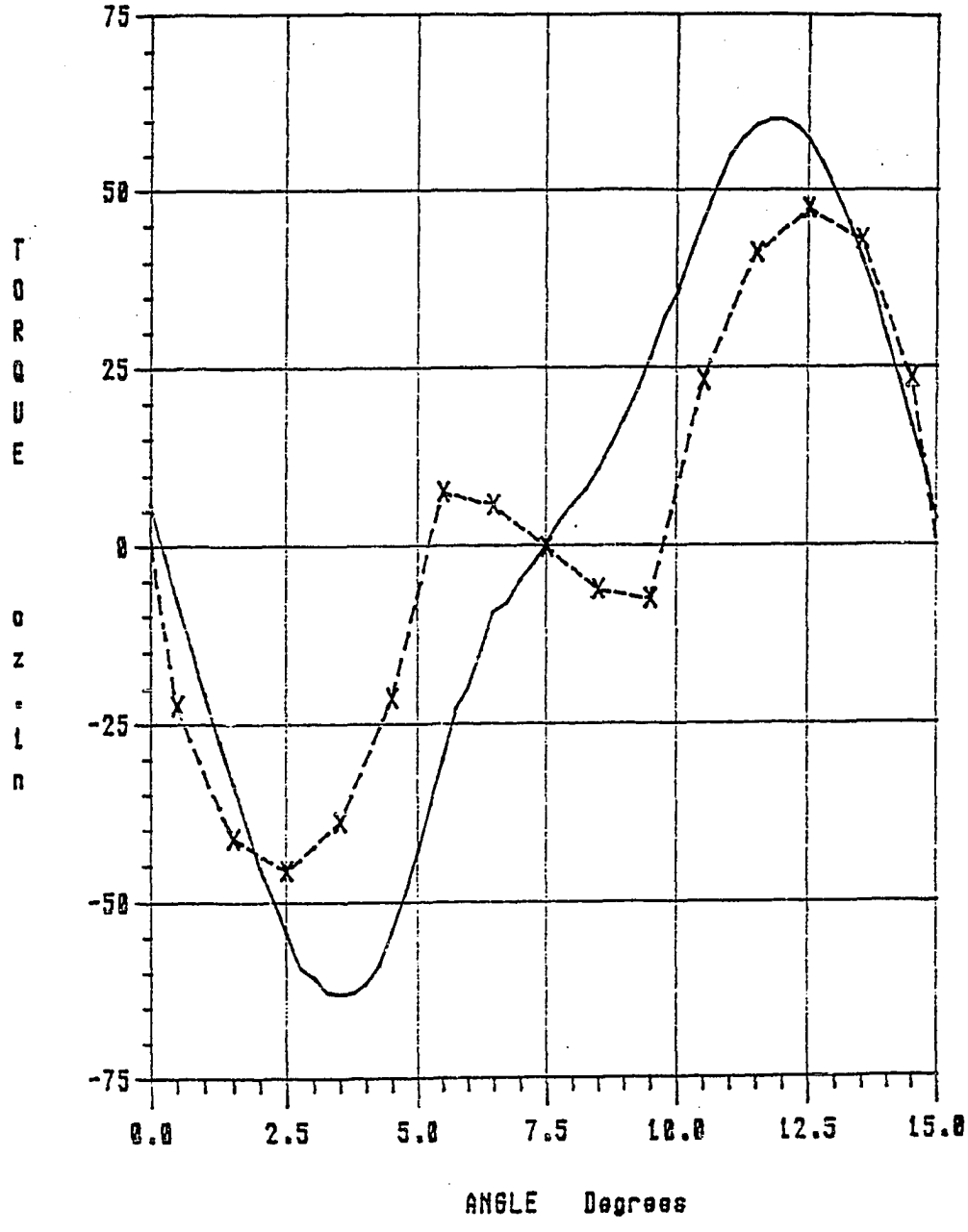

Figure III-8
Comparison of Measured, (Solid Line),
and Finite Element Predicted, (Dashed Line), Detent Torque

Peak Detent Torque (measured)	- 61.8 oz-in
Peak Detent Torque (model)	- 45. Oz-in
%error of model =	-27.2%

This is a reasonably large error. However, before any discussion or further investigations into possible causes for this error are made, the remaining motor characteristics are evaluated. The results of those evaluations lend insight into the sensitivity of predicted parameters on the FEM.

III.2a2 Calculating the Stator Torque-Angle Curve

The stator torque-angle curve can be calculated using the finite element analysis to numerically determine the torque at a variety of rotor positions. By calculating the torque over a rotor span of at least one half of an electrical cycle, the total torque versus angle relationship can be obtained. It must be remembered, however, that this contains the detent torque information as well. To obtain just the stator torque it is necessary to subtract the detent torque which was obtained from previous analysis. This process implicitly assumes, that magnetic saturation is not significant. However, if the same process of detent torque subtraction is used on both experimental and FEM results, the saturation levels should be close enough so that a valid comparison between the stator torque-angle curves can be made.

A comparison of experimental and FEA stator torque-angle curves is shown in Figure III-9. In both cases, data was obtained for a one-

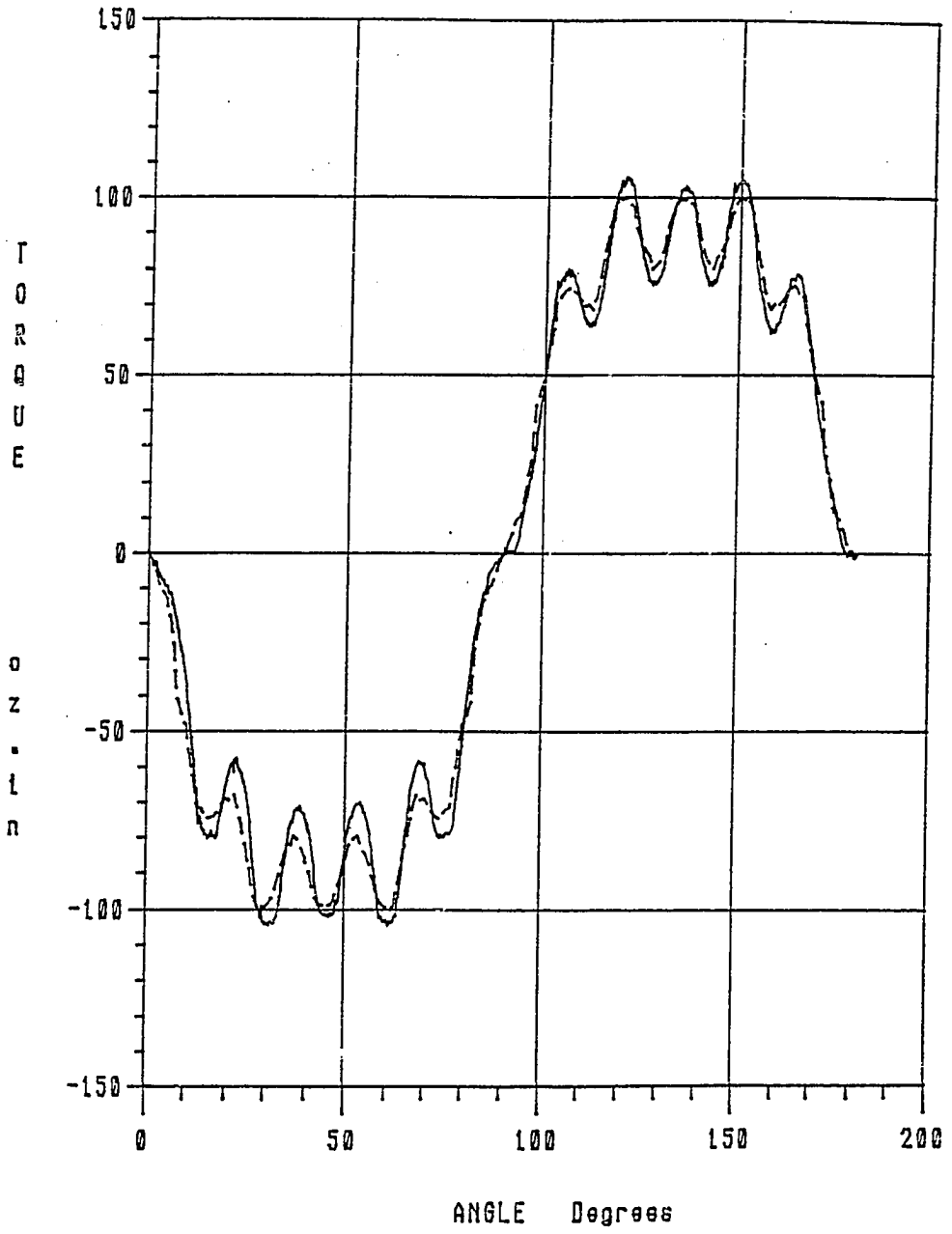

Figure III-9
Comparison of Measured, (Solid Line),
and Finite Element Predicted, (Dashed Line),
One-Phase-On Stator Torque-Angle Cuves

phase-on current of 2.0 Amps. The solid line indicates measured data and the dashed line indicates FEA data. One sees that there is very good correlation between the two curves.

III.2a3 Predicting the Torque Constant from the Finite Element Model

The finite element model was used to calculate peak stator torque for several different values of phase current. The torque values were calculated using the IxB method with the rotor 90 electrical degrees away from its stable equilibrium position.

These values were compared to the ones determined experimentally as described in Section II.4. Figure III-10 shows the comparison. The experimental data is denoted by triangles and the solid line indicates the best fit line through that data. Data obtained from the finite element model is plotted as 'X's. Calculating the torque constant from the slope of a linear least squares error fit of the finite element results yields:

$$K_{texp} = 50.23 \text{ oz-in/amp}$$

$$K_{tfea} = 49.77 \text{ oz-in/amp}$$

$$\%error = -0.92\%$$

Recalculation of the torque constant using a FEM assuming linearly magnetic iron yields no significant difference in predicted torque constant. This is in spite of the saturation observed in the flux linkage-current characteristic and the fact that the field solution shown in Figure III-5 shows portions of the iron to be at almost 2.0 Tesla.

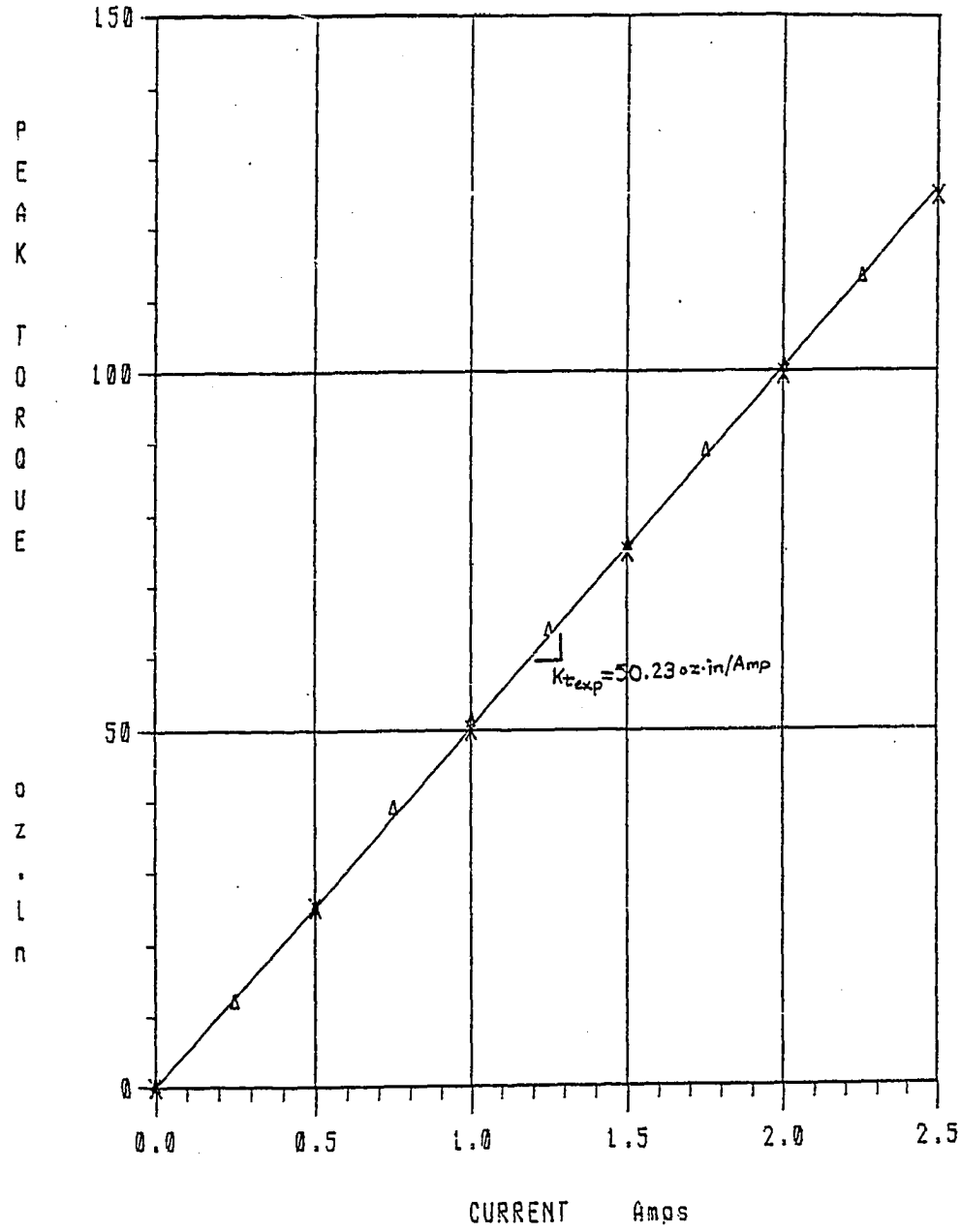

Figure III-10
Comparison of Measured, (Triangles),
and Finite Element Predicted, (X's),
Peak One-Phase-On Stator Torque versus Current

III.2b Calculating The Back Emf Waveform

The finite element analysis can be used to predict a back emf waveform that would be observed in the modeled device. Calculation of the back emf waveform proceeds in the following manner. First, field solutions for just the rotor field are found. This is done for several different rotor positions over one slot pitch. Since the field solution is cyclic with a period of one slot pitch, once it is known how the field solution changes over one slot pitch , it is known for any rotor position. The field solutions are used to determine the flux through the coil. This can be done is several different ways.

One method of finding the total flux through the coil is to use the average radial component of flux density, as a function of angle, over the region of the coil span, shown in Figure III-11. The data shown in this figure was obtained by averaging the radial component of flux density for a column of elements over a selected number of rows. (See Figure III-12). Figure III-11 shows that the flux density in each tooth shank region is nearly constant, and that the flux density in the slot regions is very small compared to that in the tooth shanks. The flux through each of the regions is determined by multiplying the average flux density in the region by the region area. A summary of those calculations is shown in Table III-2.

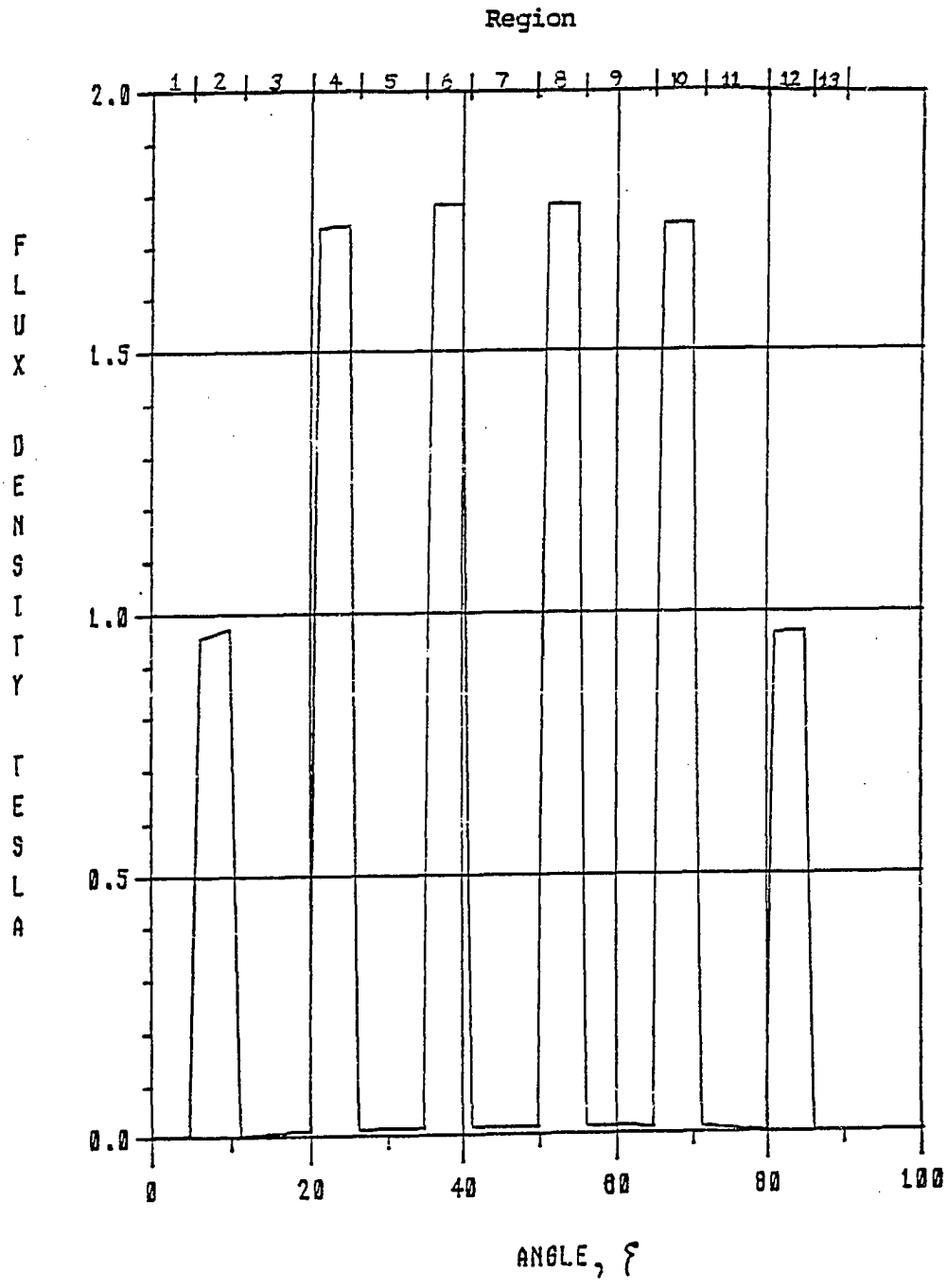

Figure III-11
Average Radial Component of
Airgap Flux Density Due to the Coil

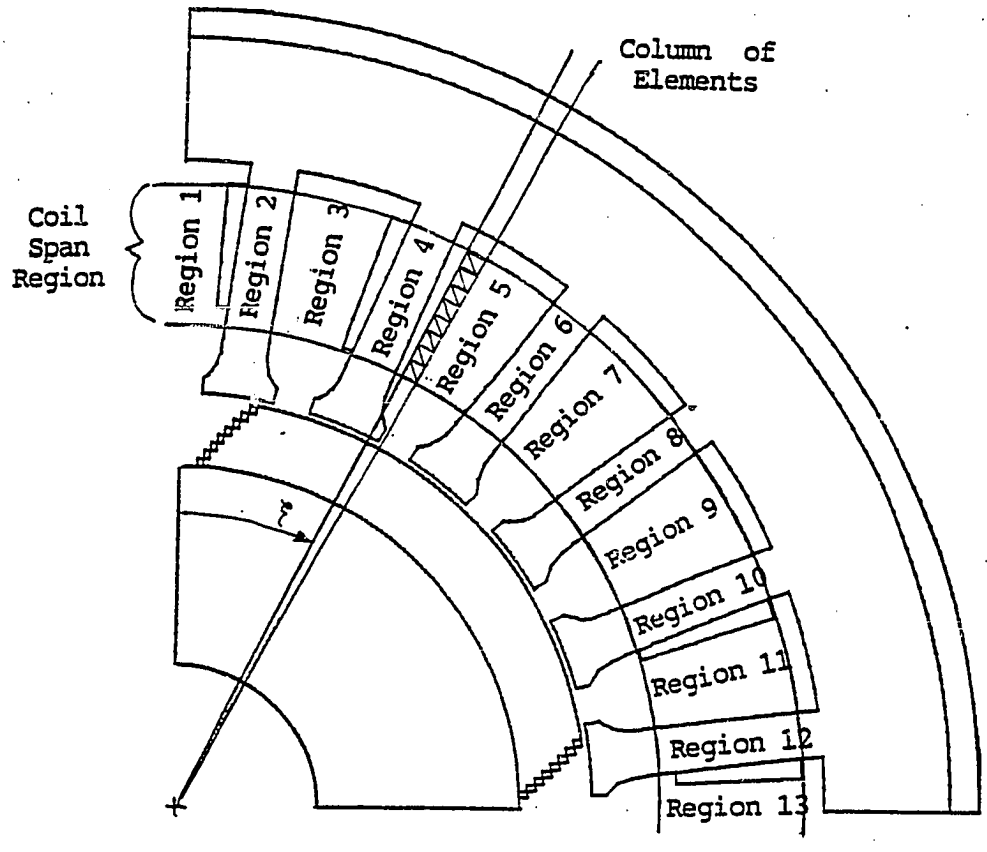

Figure III-12
Motor Outline Showing Coil Span Region

Table III-2
Flux Through Regions Shown in Figure III-10

Region	B (Telsa)	ϕ (Wb)
1	0.0	0.0
2	0.96	7.98E-05
3	0.006	9.96E-07
4	1.74	1.45E-04
5	0.013	2.16E-06
6	1.78	1.48E-04
7	0.013	2.16E-06
8	1.78	1.48E-04
9	0.0013	2.16E-06
10	1.74	1.45E-04
11	0.006	9.96E-07
12	0.96	7.98E-05
13	0.0	0.0

The flux through any slot, (an odd numbered region), is approximately two orders of magnitude less than the flux through any tooth, (an even numbered region). Therefore, the slot flux contributions are negligible.

Table III-2 tabulates, for a single rotor position, the flux found in each of the regions where constant flux density is a valid assumption. This process is repeated for several rotor positions over one slot pitch. Since the data is periodic over one slot pitch, the flux in each of these regions, and hence the total flux, is known for any rotor position.

An alternate method of calculating the flux is to use a combination of the divergence theorem and Stokes theorem to arrive at an expression which states that the line integral of the magnetic vector potential, A, around a closed contour is equal to the flux through the enclosed surface[8].

$$\Phi = \int \vec{A} \cdot d\vec{l} \qquad \text{(III-10)}$$

To find the flux through a single turn of wire of one of the coils, one would evaluate this expression around the line defined by the wire. For any planar motor problem, this can usually be broken down into four seperate line segments, shown in Figure III-13. This figure shows a closed path around a single tooth. Lines of flux run through the tooth in the plane of the tooth. The magnetic vector potential, A, is always normal to the plane of the tooth, however the magnitude and sign may vary.

Application of Equation III-10 to the path shown in Figure III-13 yields:

$$\Phi = A_1 z + 0 - A_2 z + 0 \qquad \text{(III-11)}$$

Only the line segments AB and CD have a nonzero contribution. Line segments BC and CD are perpendicular to A and therefore have no contribution. This will always be true for the planar problem. One sees that this method allows flux to be calculated in a very straightforward manner. This method can be used to find flux through large regions since no assumptions are made as to whether the flux density is constant over the region.

Once the flux through the teeth as a function of rotor angle is known, it is a simple matter to calculate the total flux linking N turns of the coil. One has simply to define the coil location and the number of turns on the coil. The total flux linking the coil is the product of the number of turns on the coil and the total flux through all of the area that the coil is wrapped around.

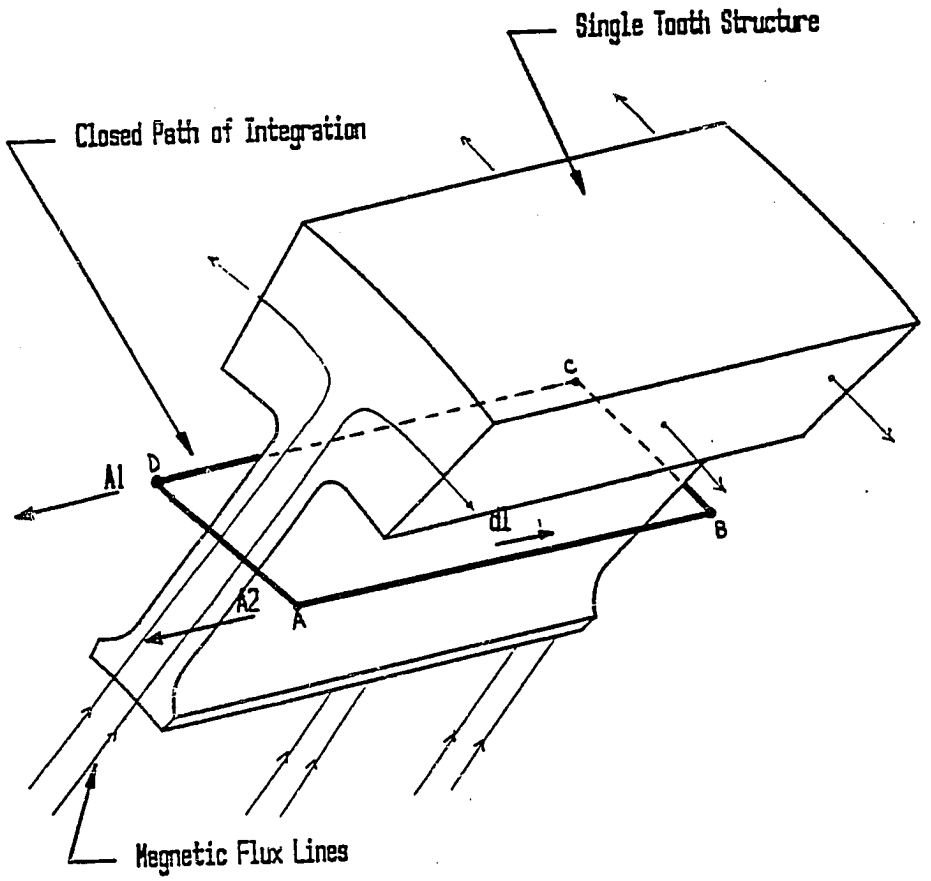

Figure III-13
Closed Path of Integration to
Find Flux Through a Tooth

A coil for this motor consists of two windings. The first winding has N_1 turns and spans teeth 2,3,4,5 in Figure III-14. The second winding has N_2 turns and spans teeth 1,2,3,4,5,6. Table III-2 showed that the flux through the slots is typically two orders of magnitude less than that through the teeth; therefore the total flux linking the coil is calculated from the tooth contributions only. Figure III-15a shows the flux in a single tooth as a function of rotor position. Figure III-15b shows the resulting plot of flux linking the coil as a function of rotor position. Numerical differentiation of the data shown in Figure 15b yields an approximation of the partial derivative of flux linkage with respect to rotor angle. As was shown in Chapter II, Equation II-4, this partial derivative term defines the back emf waveform. In order to caculate an actual back emf voltage that would appear in the coil due to a particular rotor speed, the back emf waveform must be multiplied by rotor speed. Figure III-16 shows a comparison of calculated and experimental back emf waveforms. The solid line indicates experimental data and the dashed line indicates FEM results.

III.2c Flux Linkage Curve

The flux linkage versus coil current characteristic was also calculated using the FEM. The method of determining the total flux, λ, linking the coil is the same as described in the previous section on determining the back emf waveform. In this case, however, one is determining the total flux linkage as a function of coil currents, instead of as a function of rotor position.

A comparison of experimental and FEM predicted flux linkage versus

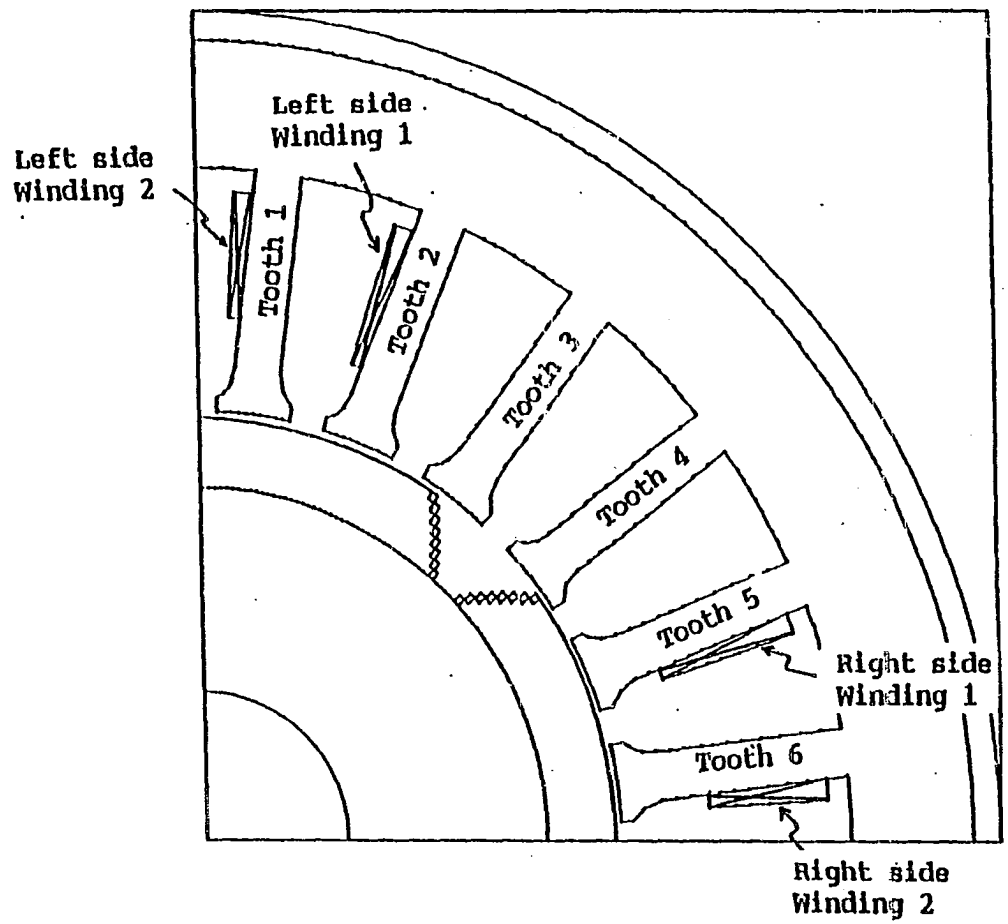

Figure III-14
Tooth Numbers and Coil Windings

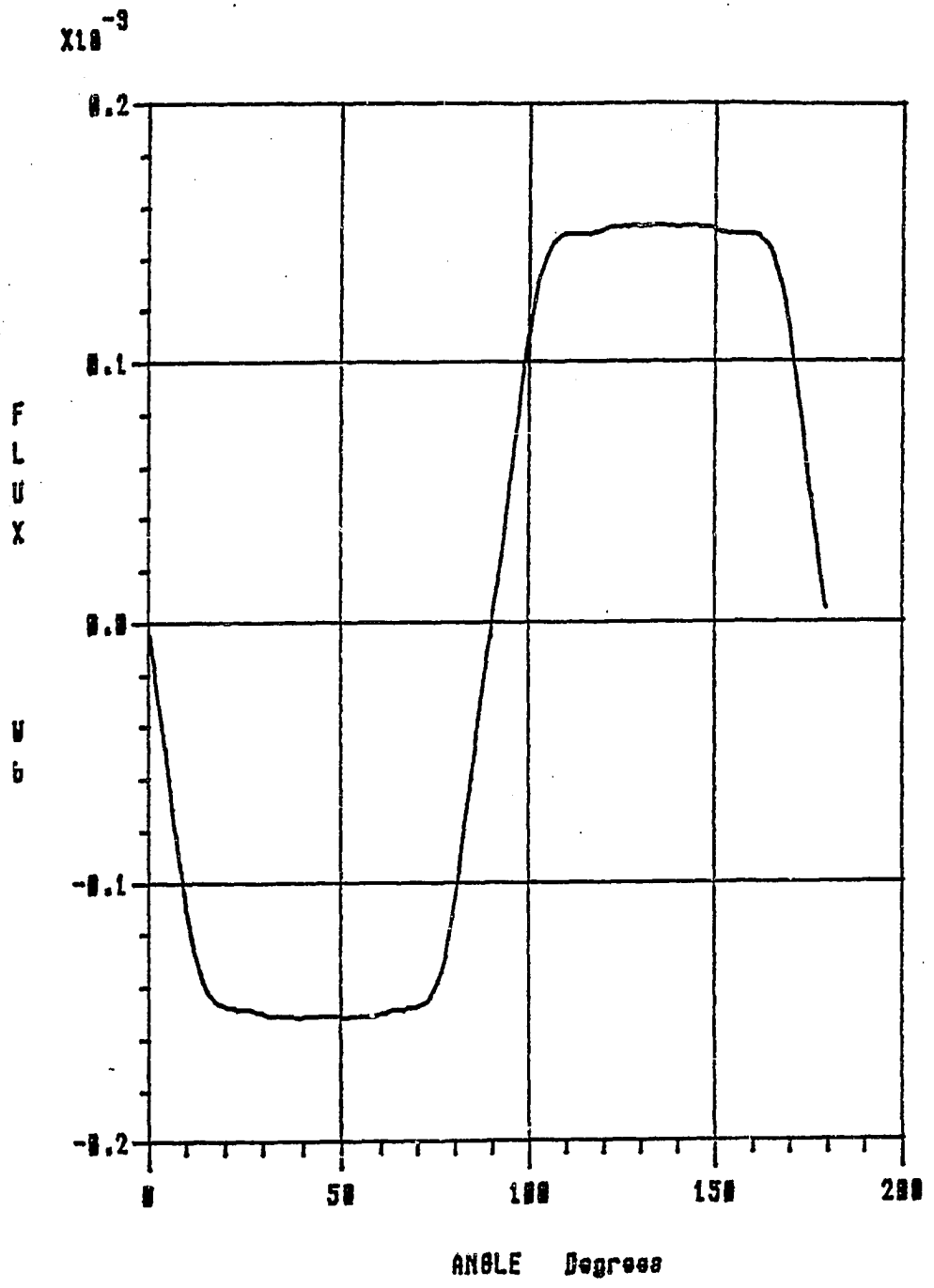

Figure III-15a
Flux in a Single Tooth as a
Function of Rotor Position

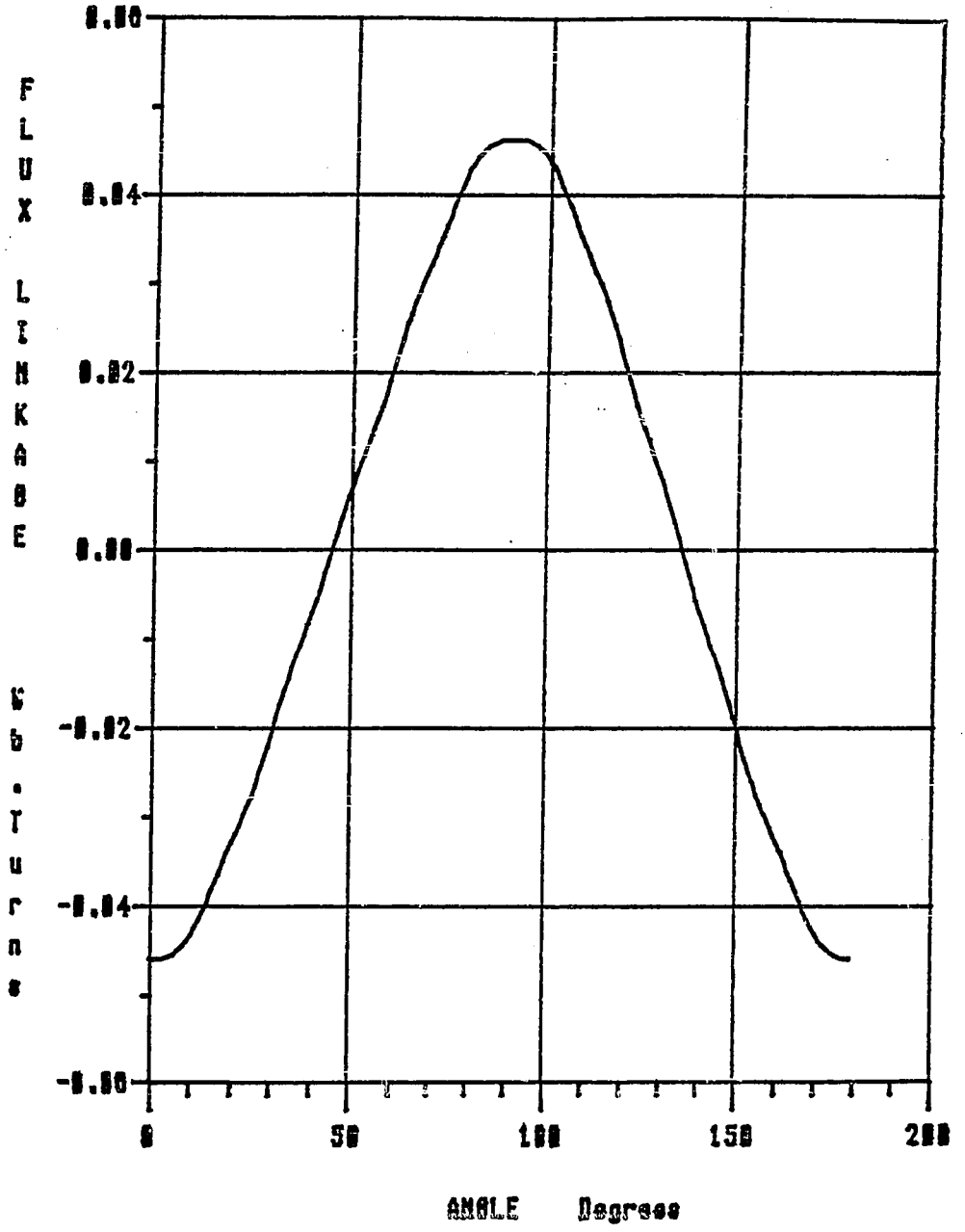

Figure III-15b
Coil Flux Linkage as a
Function of Rotor Position

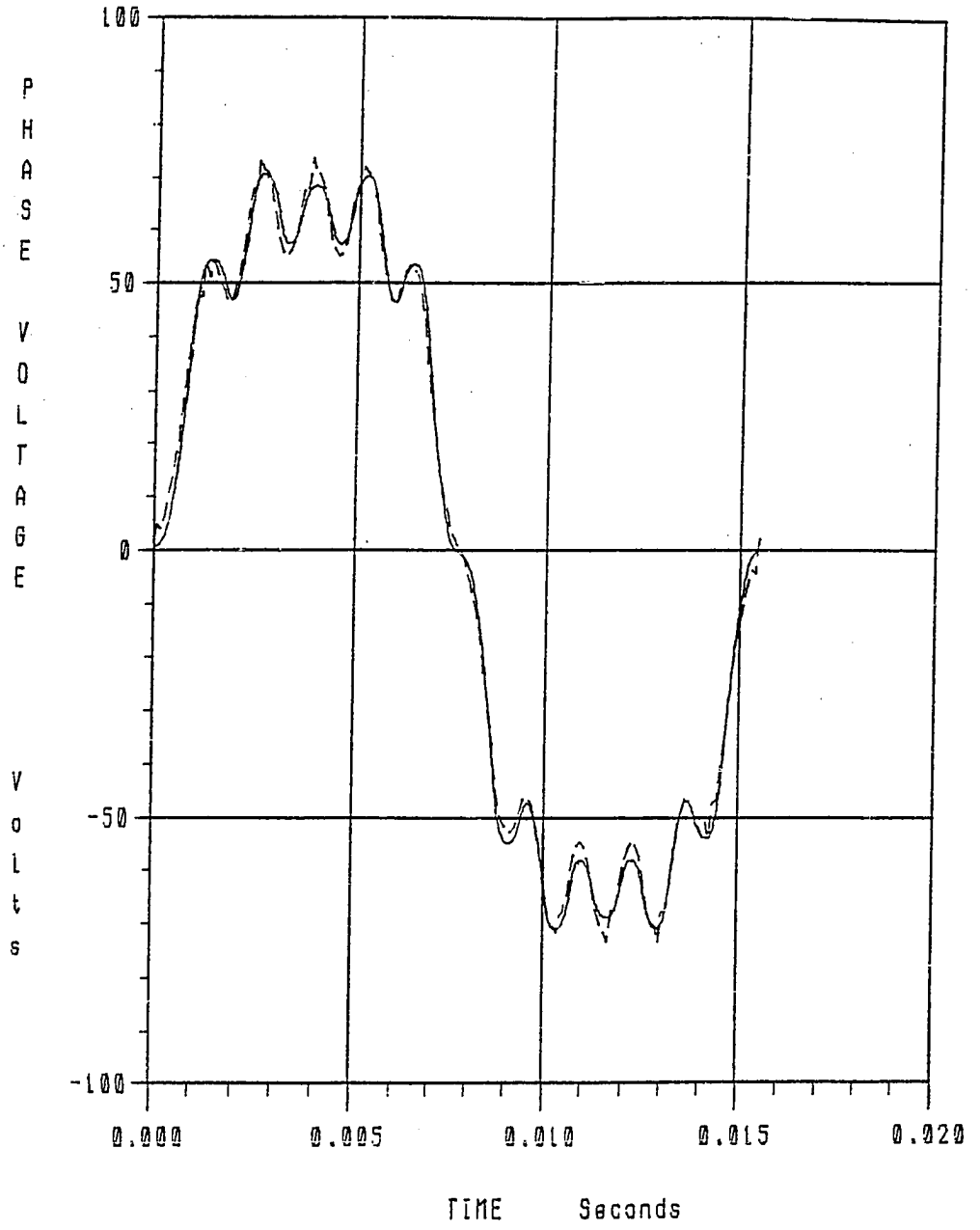

Figure III-16
Comparison of Measured, (Solid Line),
and Finite Element Predicted, (Dashed Line),
Back Emf Voltage Waveforms

current characteristics is shown in Figure III-17. Experimental data is shown as solid lines and FEM results are shown by x's, with a dashed line indicating the best fit line through the data. There are two sets of curves shown. One is for the motor with the rotor magnets in place on the rotor back iron - curves (3) and (4). The other is for the motor with just the rotor back iron in place and no rotor magnets - curves (1) and (2).

In the case where the rotor magnets were present, λ was found with the permanent magnet rotor in the stable equilibrium position for the particular coil energized. In the experimental determination, λ_o, the flux linkage at zero current, was unknown and set equal to zero. In order to compare the experimental and FEM data on an equal basis, the value of λ_o found with the FEM was subtracted from each subsequent value of λ predicted by the FEM.

In looking at Figure III-17 one sees that there is a substantial difference between the experimental and FEM results. Since both sets of data indicate a linear characteristic, the slopes, L, of each were determined and compared. Table III-3 shows the results.

Table III-3
Comparison of Flux Linkage-Current Slopes

λ-i description	Exp. slope (Henries)	FEM slope	% difference FEM from exp.
With magnet	0.0062	0.0046	-26.0
No magnet	0.0100	0.0078	-22.0

In both cases, the slope predicted by the FEM was more than 20% lower than determined experimentally. The most likely cause of this discrepancy is 'end effects'. The two dimensional FEM assumes that

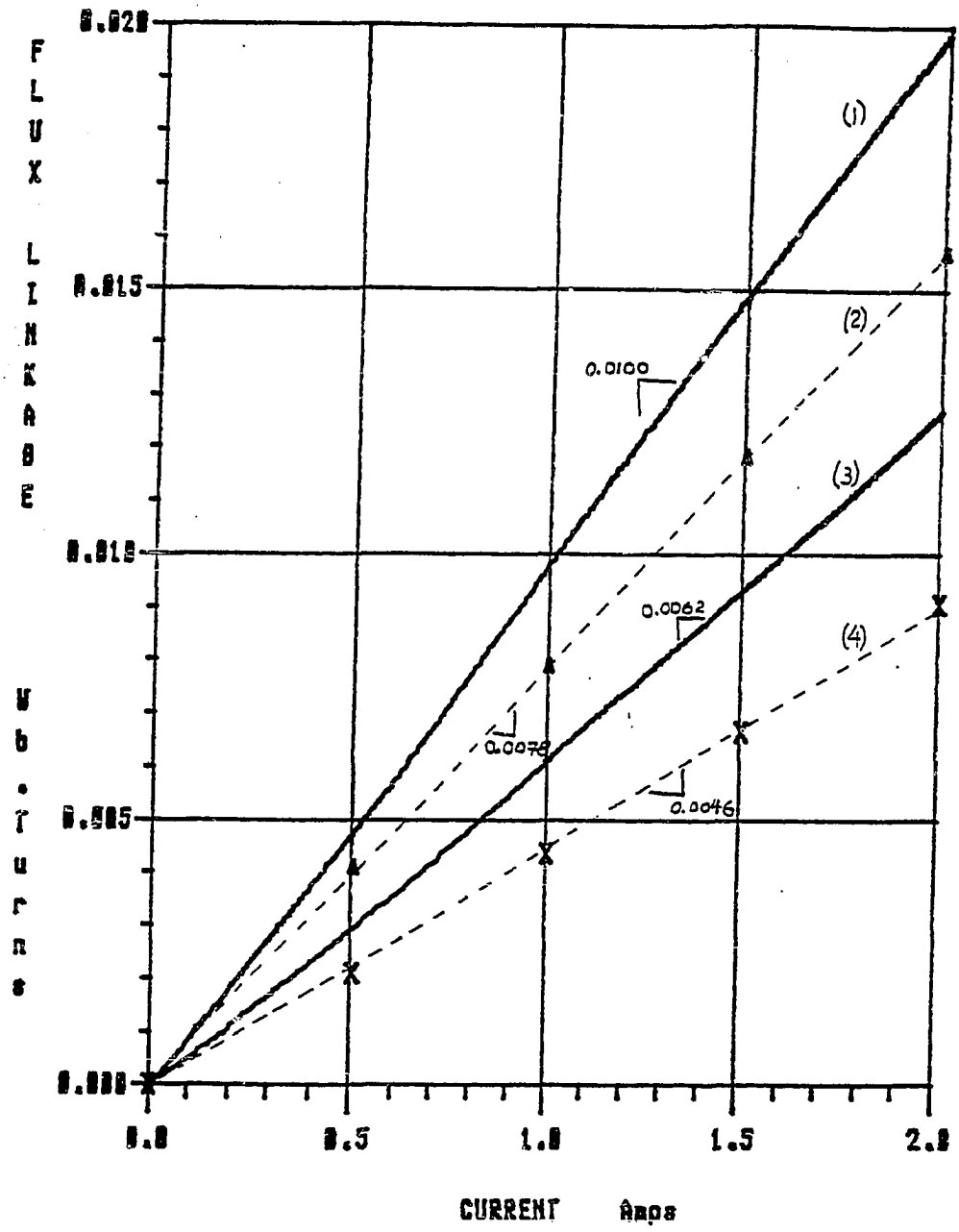

Figure III-17
Comparison of Measured and Finite Element
Predicted Coil Flux Linkage versus Current
Curve (1)- Measured Data, No Magnets on Rotor
Curve (2)- Finite Element Predicted Curve, No Magnets on Rotor
Curve (3)- Measured Data, Rotor Magnets Present
Curve (4)- Finite Element Predicted Curve, Rotor Magnets Present

the motor is infinitely long and, therefore, that the bundles of wire on the ends of the motor connecting the coils in the slots, do not effect the flux in the cross section of the device. Depending on the relative length and width of the coil, these end turns could conceivably contribute a significant amount of flux. This will be further explored in Chapter IV.

III.3 Summary of Finite Element Results

The preceeding analysis has shown that good correlation was obtained between the FEM predicted torque constant, torque-angle waveform, and back emf constant and waveform. However, it was deficient in predicting the magnitude and shape of the detent torque, and the flux linkage-current characteristic. The inaccuracy of the FEM in predicting the detent torque curve suggests an error in either the permanent magnet model or the material property model. The flux linkage-versus current errors could be due to end effects, as suggested. However, this raises several questions concerning the FEM. If end effects are significant in the flux linkage-current relation shouldn't they also have an affect on the single-phase torque, and torque constant, predictions? If the flux linkage-current errors are not due to end effects, then they must be due to material property or geometry modelling. Again the question arises, if the problem lies in the models of the material property, why does the FEM predict some of the other parameters so accuately? Furthermore, if the rotor magnet model is inaccurate and produces such poor correlation in the detent torque, wouldn't this also result in errors in predicting stator torque and back emf? Or, is it just that the detent torque is much

more sensitive to some aspects of the model? Is it possible that a poor rotor magnet model and end effects combined in such a manner as to result in the misleadingly good correlations of the torque and back emf data? Clearly, further investigation of the FEM model is necessary. Chapter IV addresses some of these questions.

CHAPTER IV

FURTHER INVESTIGATION OF THE FINITE ELEMENT MODEL

In Chapter III it was shown that the two-dimensional FEM was accurate in predicting some motor parameters, such as stator torque and back emf, but was not very successful in predicting others. As discussed, there are several possibilities that could explain the differences between FEM predicted and measured detent torques and flux linkage-current characteristics: 1) The mesh is not fine enough; 2) The material permeability models are incorrect; 3) End effects due to the three dimensional nature of the motor are not negigible; 4) The permanent magnet model is incorrect. Investigations into some of these possibilities were made and the results are described in the chapter. It was found that the principal causes of the descrepancies found and outlined in Chapter III, were end effects and the permanent magnet model. End effects were the primary source of error in the inductance calculation and the permanent magnet model was the primary source of error in the detent torque.

IV.1 Using a More Refined Mesh

One of the short comings of first order finite elements is that flux density is assumed constant over an element. A mesh which is too coarse over a region where there are actually large changes in direction and magnitude of the flux density can result in errors in torque calculations. To check for this possibility, the mesh was refined in

the region of the tooth tips, and magnet. Then, the detent torque and torque constant were re-calculated.

In the original FEM, the tooth tip was modeled by one row of finite elements, the airgap was modeled by two rows of finite elements and the magnet was modeled by eight rows of finite elements. The mesh was refined so that the tooth tips consisted of five rows of elements. The airgap was kept at two rows of elements, since these elements were already very thin, and the magnet was made to be twenty-five elements thick.

The detent torque predicted with this mesh is shown in Figure IV-1. The solid line represents the results from the original FEM of Chapter III. The dashed line represents the results from the more refined mesh. One sees that there is little difference in shape of the two curves. If peak values are compared, the more refined mesh predicts a peak detent torque that is 12% less than the original FEM predicted. Since the original FEM mesh predicted a peak detent torque value that was already 27% lower than the experimentally determined one, creating a more refined mesh is obviously not the answer to the discrepancy question.

It should be noted that not all of the difference in predicted detent torque is necessarily due to the refinement of the mesh. In using a different mesh, the placement of the edge currents representing the permanent magnet was not exactly the same as in the previous mesh. It is shown later in this chapter that detent torque is very sensitive to the location of these edge currents.

The torque versus current characteristic for both FEM's are shown in Figure IV-2. Data marked by X's are from the FEM mesh of Chapter

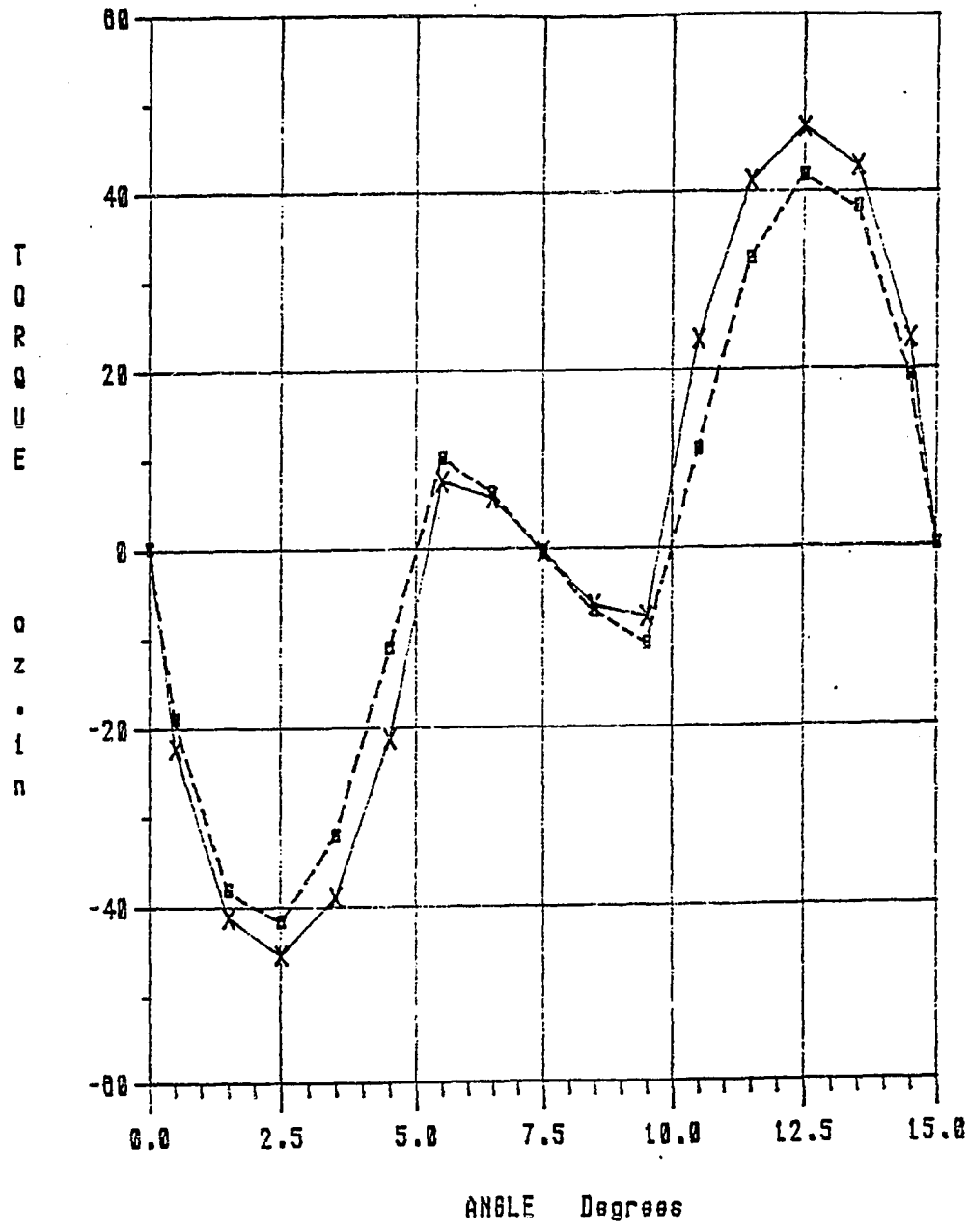

Figure IV-1
Comparison of Detent Torque versus Angle
for Original Finite Element Model, (Solid Line),
and Refined Finite Element Model, (Dashed Line)

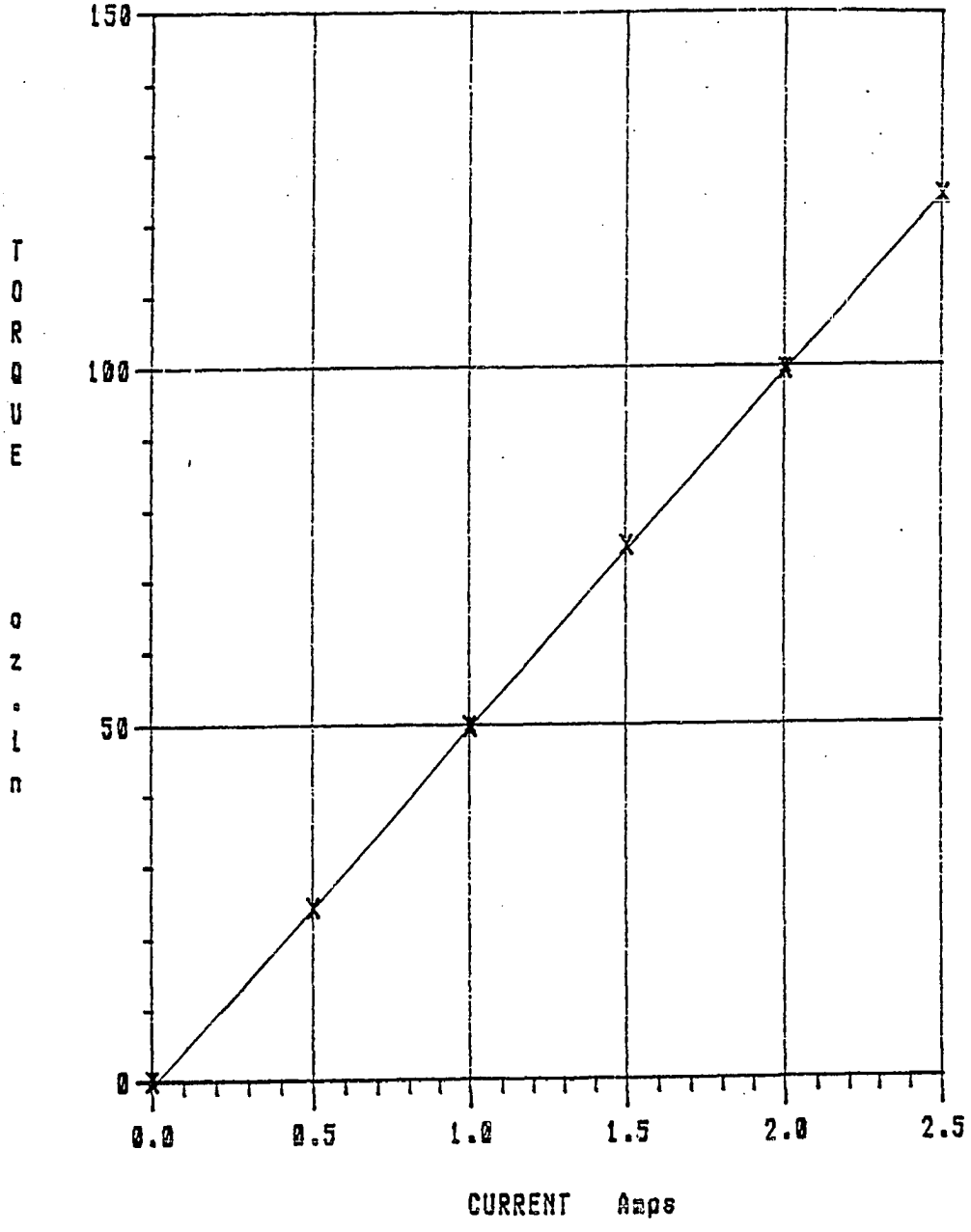

Figure IV-2
Comparison of Peak Stator Torque versus Current
for Original Finite Element Model, (X's),
and Refined Finite Element Model, (Triangles)

III. Data marked by Δ's shows results from the more refined mesh. Since previous analysis showed the torque-current relation to be very linear, only two data points were obtained with the refined mesh. One at 1.0 amps and the other at 2.0 amps. One sees that there is virtually no difference between the data obtained from the two meshes. If the data predicted with the refined mesh is used with a least squares error approach to calculate a torque constant, and this torque constant is compared to one found from the original mesh, the difference is less than 0.5%.

IV.2 Checking the Finite Element Model with a Variable Reluctance Rotor

To check the finite element model of the stator geometry and material properties, a variable reluctance, (VR), rotor was constructed. This rotor contains no permanent magnet material. It is a cylinder of iron with the same outer diameter as the permanent magnet rotor, and has four slots cut into it at 90 degree intervals. The depth of the slots was made equal to the thickness of the permanent magnet. The VR rotor was used with the prototype stator to produce a VR motor. A cross-sectional view of this VR motor is shown in Figure IV-3.

A finite element model of the VR motor was developed by using the same mesh that was constructed for the prototype BLDCM and altering the material property description of the rotor elements to fit the VR rotor instead of the permanent magnet rotor. Some finite elment nodes were also moved slightly to fit the slot geometry of the VR rotor better.

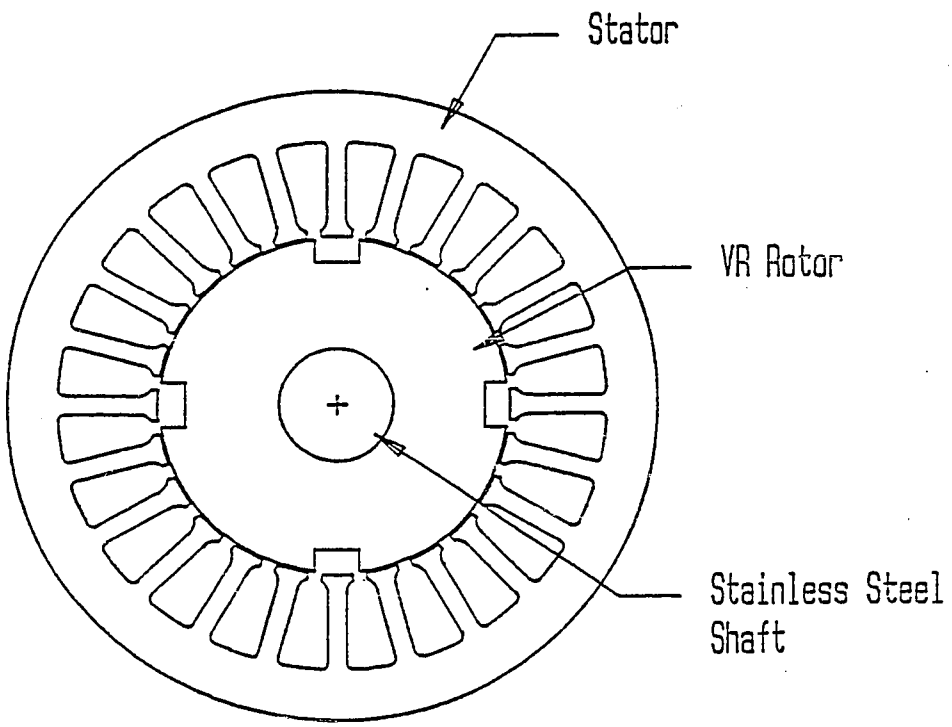

Figure IV-3
Variable Reluctance Motor
Used in Finite Element Investigation

While the VR motor has no detent torque, it does produce a torque when the stator is energized. In Figure IV-4a, the measured one-phase-on torque-angle curve, (solid line), for a phase current of 2.5 amps is compared to a finite element predicted torque-angle curve, (dashed line), for the same phase current. The excellent correlation between the waveform shapes of the two curves indicates that the model for the geometry and material properties is good. In comparing peak values, the FEM predicts a peak value that is approximately 8% greater than the experimentally determined one.

The level of phase current used in this comparison results in a flux density in the stator teeth of approximately 1.2 Tesla. This is significantly less than the 1.8 Tesla present when the permanent magnet rotor is in place. Therefore, another comparison was made at a phase current of 4.0 Amps. This was the maximum value that was felt could be used and not burn the coil insulation during the measurements. This level of phase current results in a flux density of 1.6 Tesla in the stator teeth. This value is close to that achieved with the permanent magnet rotor in place, and, since the 60% increase in phase current only results in a 30% increase in flux density, indicates that the teeth are well into saturation. The experimental and FEM torque-angle curves at this level of phase current are shown in Figure IV-4b. Again, there is good correlation between waveform shapes. A comparison of peak values reveals that the FEM predicts a peak value that is approximately 6% greater than the experimentally determined one.

Overall, the good correlation between FEM and experimentally determined torque-angle curves for the two different levels of phase

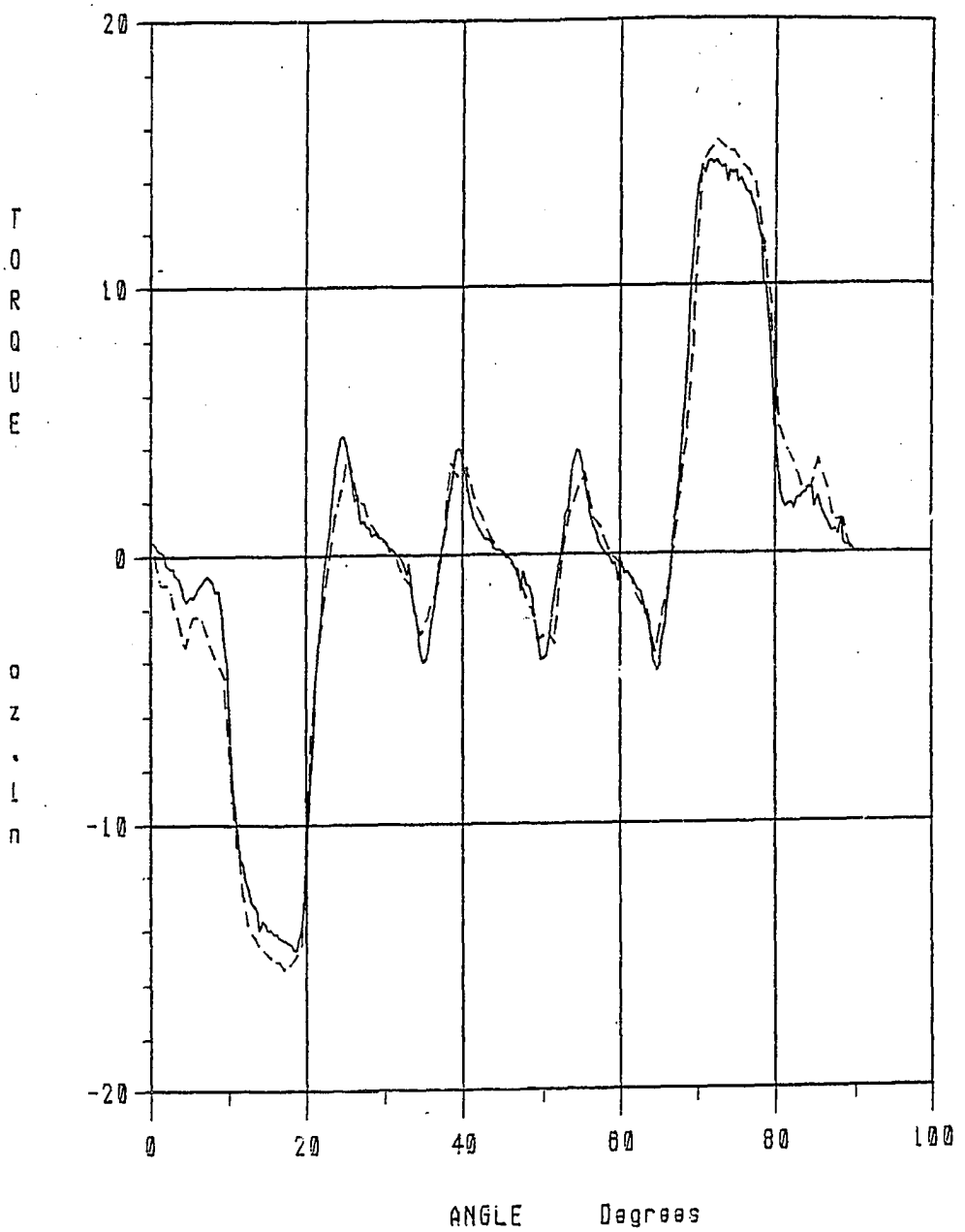

Figure IV-4a
Comparison of Measured, (Solid Line), and
Finite Element Predicted, (Dashed Line),
Variable Reluctance Stator Torque-Angle Curves, I=2.5 Amps

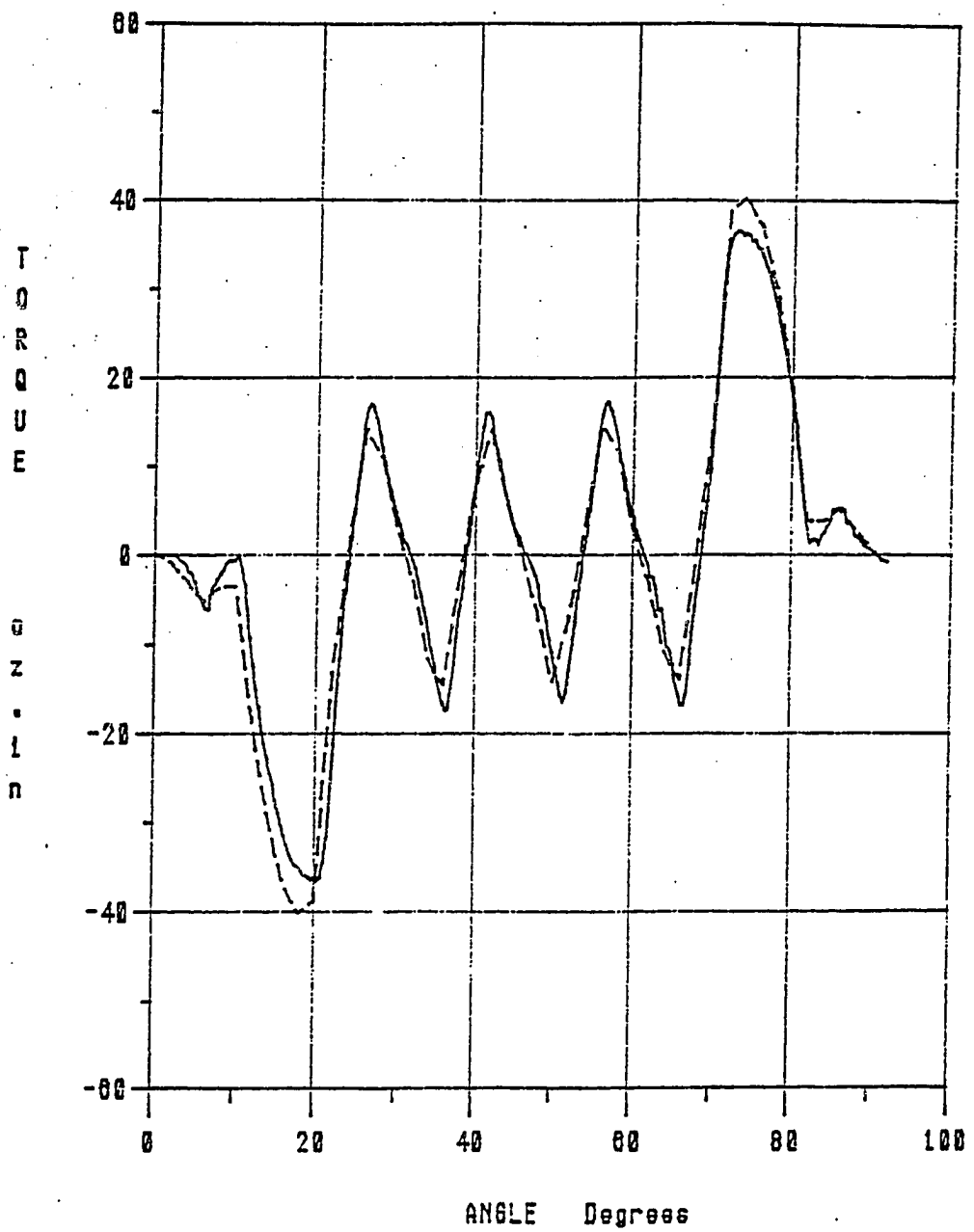

Figure IV-4b
Comparison of Measured, (Solid Line), and
Finite Element Predicted, (Dashed Line),
Variable Reluctance Stator Torque-Angle Curves, I=4.0 Amps

current indicates that the material saturation models and geometry represented by the FEM are probably good. This would lead one to believe that primary cause for the descrepancy found in Chapter III between experimental and FEM detent torque-angle curves must lie in the permanent magnet model.

IV.3 End Effects

It was suggested previously that some of the discrepancy between experimental and finite element results could be attributed to end effects. End effects is a general term used to describe the effects due to the three-dimensional nature of the problem. The consequences of these effects are not included in a two-dimensional model. The fact that a two-dimensional model was used can result in some differences between experimental and analytical results.

In order to get an idea of the possible errors introduced by using a two dimensional model, one can look at the difference in results obtained from both a two- and three-dimensional analysis of the flux density distribution and net flux through a rectangular loop of wire in air, Figure IV-5a.

The Biot-Savart Law[9] gives the far field approximation for $\vec{B}$ at a point P, in air, due to a differential piece of wire located a distance p away as:

$$d\vec{B} = \frac{\mu_o I}{4\pi} \frac{d\vec{l} \times \vec{p}}{p^2} \qquad \text{(IV-1)}$$

In this case, the tangential component of $\vec{B}$ is the only existing component. Therefore, the Biot-Savart law can be reduced to a scalar

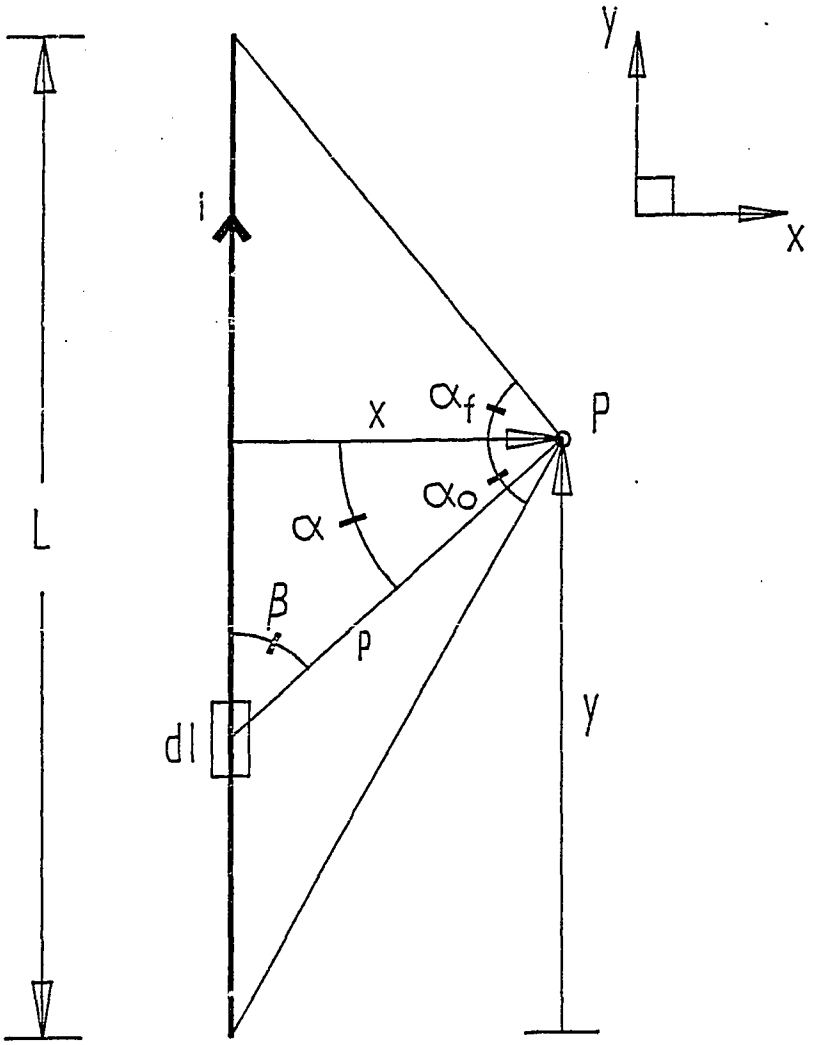

Figure IV-5a
Geometry Used for Calculation
of Flux Density at a Point P

expression, and the net B due to a straight wire of length L is:

$$B = \frac{\mu_o I}{4\pi} \int_0^L \frac{p \sin\beta}{p^2} dl \qquad \text{(IV-2)}$$

From Figure IV-5a, one sees that the following substitutions can be made in Equation IV-2:

$$dl = pd\alpha \cos\alpha$$

$$\sin\beta = x/p$$

$$\cos\alpha = x/p$$

Hence:

$$B = \frac{\mu_o I}{4\pi x} \int_{\alpha_o}^{\alpha_f} \cos\alpha \, d\alpha = \frac{\mu_o I}{4\pi x} \{ \sin\alpha_f - \sin\alpha_o \} \qquad \text{(IV-3)}$$

Where: $\alpha_o = \sin^{-1}\left\{ \frac{y}{\sqrt{x^2+y^2}} \right\}$, $\alpha_f = \sin^{-1}\left\{ \frac{L_w - y}{\sqrt{x^2+(L_w-y)^2}} \right\}$

These expressions can now be used to evaluate an expression for B within the plane defined by two infinitely long wires, (2D model), and within the plane of a rectangular coil of wire, (3D model).

Applying Equation IV-3 to the geometry shown in Figure IV-5b, yields an expression for B in the plane defined by two infinitely long wires.

$$B = \frac{\mu_o I}{2\pi} \frac{w}{x(w-x)} \qquad \text{(IV-4)}$$

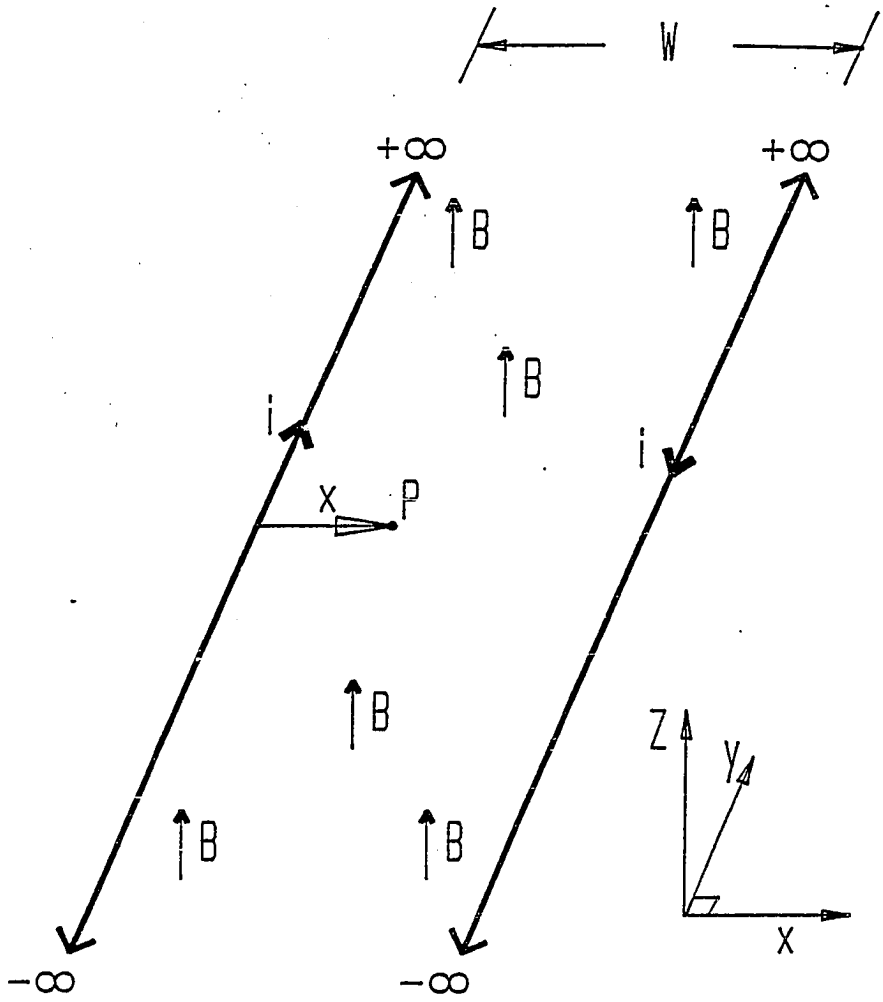

Figure IV-5b
Two Infinitely Long, Current Carrying Wires

Applying Equation IV-3 to the geometry shown in Figure IV-5c yields an expression for B in the plane defined by a rectangular loop of wire.

$$B = \frac{\mu_o I}{4\pi} \left\{ \frac{y}{x\sqrt{x^2+y^2}} + \frac{L_w-y}{x\sqrt{x^2+(L_w-y^2)}} + \frac{x}{(L_w-y)\sqrt{x^2+(L_w-y)^2}} + \right.$$

$$\frac{w-x}{(L_w-y)\sqrt{(w-x)^2+(L_w-y)^2}} + \frac{L_w-y}{(w-x)\sqrt{(w-x)^2+(L_w-y)^2}} +$$

$$\left. \frac{y}{(w-x)\sqrt{y^2+(w-x)^2}} + \frac{w-x}{y\sqrt{(w-x)^2+y^2}} + \frac{x}{y\sqrt{x^2+y^2}} \right\} \qquad \text{(IV-5)}$$

Figure IV-6a shows flux density distribution calculated from Equations IV-4&5 assuming a square loop of wire, 0.1 meter on a side. Curves (1) through (5) indicate the results from the 3D model, (Equation 5), and are for various positions along the length of the coil. Curve (6) results from the 2D model, (Equation 4), and is the same everywhere along the coil length. The net result is that the 3D model produces a flux density distribution that is always of greater magnitude. Hence, the total flux through the coil is always greater than the 2D model predicts.

Figure IV-6b shows the effects of making the current loop more rectangular. The length was increased to 0.3 meters to yield a length to width ratio of 3. One can see that there is much less of a difference between the 2D analysis- Curve (6), and the 3D analysis-

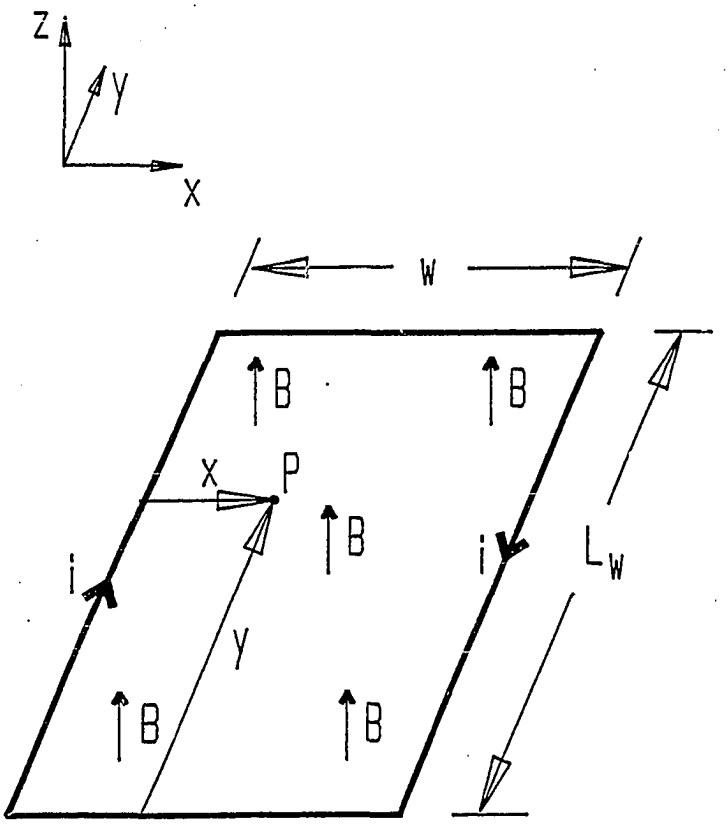

Figure IV-5c
Rectangular Loop of Wire in Air

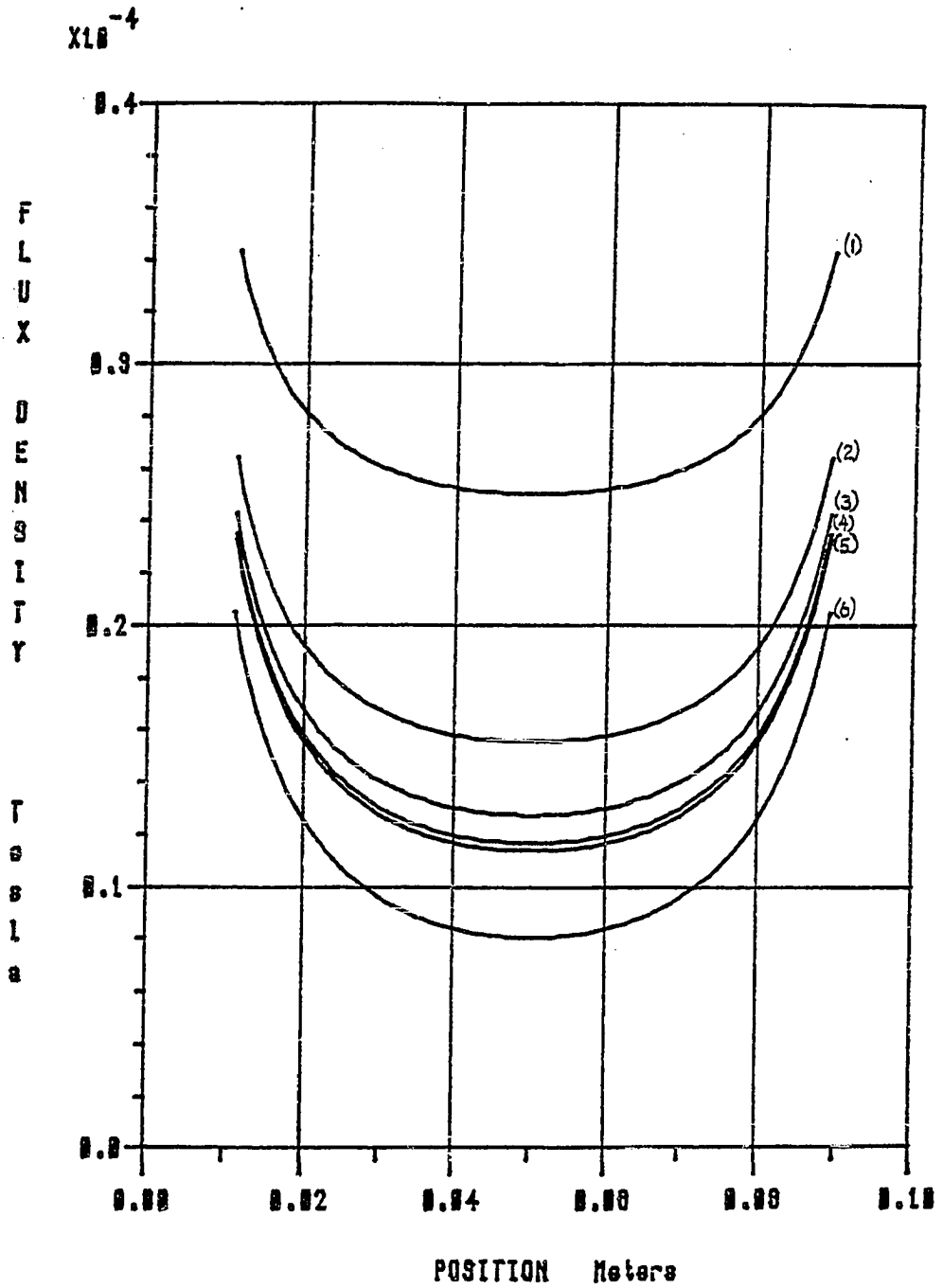

Figure IV-6a
Flux Density Distributions at Several Slices
Along the Side of a Square Wire Loop, (w=0.1m)
Curve (1)- y=0.01m; Curve (2)- y=0.02m;
Curve (3)- y=0.03m; Curve (4)- y=0.04m;
Curve (5)- y=0.05m; Curve (6)- Two-Dimensional Model

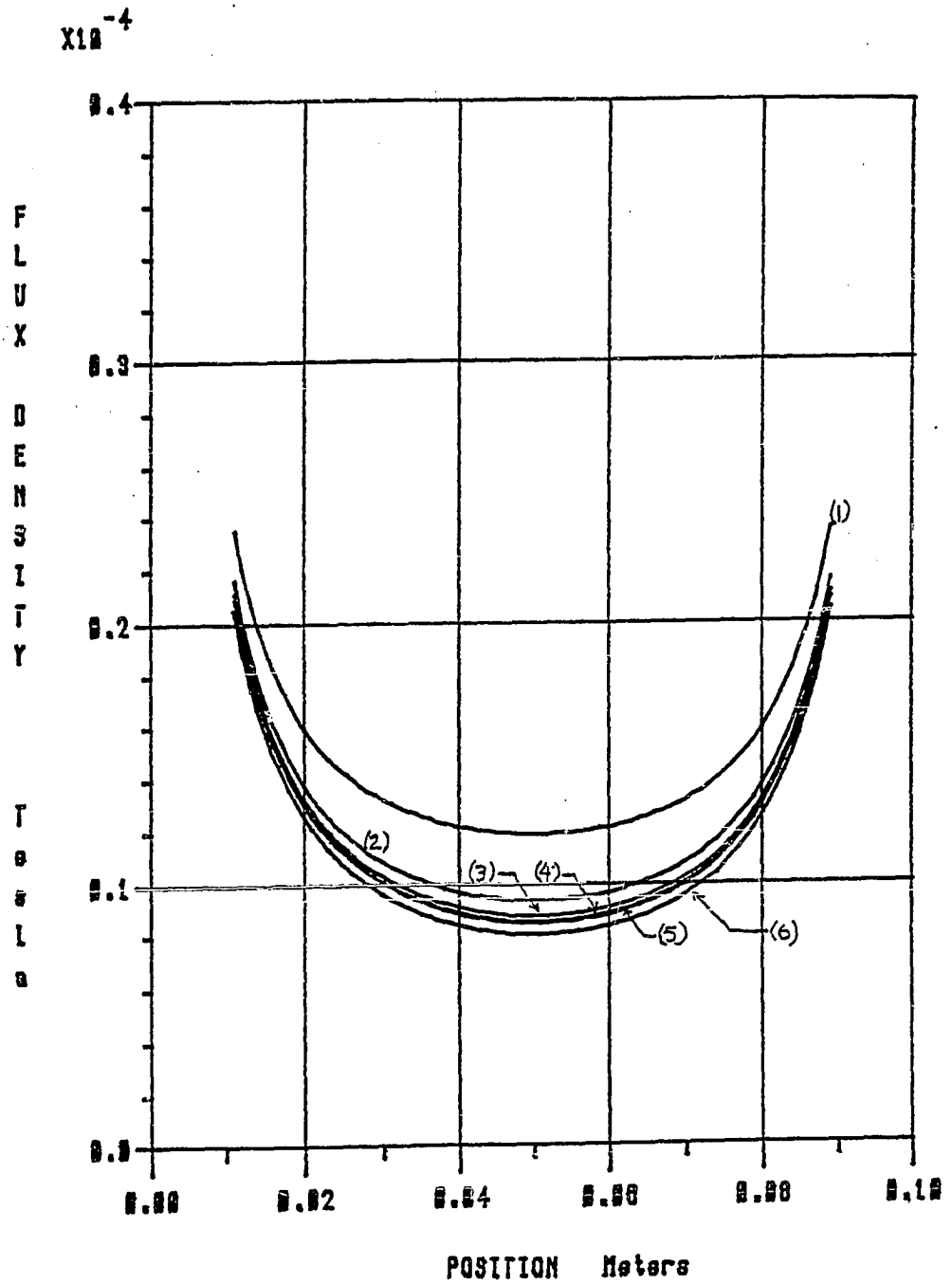

Figure IV-6b
Flux density Distributions at Several Slices Along the Side of a Rectangular Loop of Wire, (w=0.1m,Lw=0.3m)
Curve (1)- y=0.03m; Curve (2)- y=0.06m;
Curve (3)- y=0.09m; Curve (4)- y=0.12m;
Curve (5)- y=0.15m; Curve (6)- Two-Dimensional Model

Curves (1) through (5).

Unfortunately, the expressions shown in Equations 4 and 5 are for wires in air, not for wires wound around stator iron. They can not be used to evaluate how much higher the flux density will be in the real motor than the 2D FEM predicts. However, they do show the general effects; the flux density inside a rectangular coil is greater than the flux between parallel wires. Hence, end turns increase the flux through the coil.

To further explore end effects in the motor, a FEM was made of an r-z slice of the motor. Figure IV-7 shows the flux plot resulting from an analysis of the end turns. End turns are those sections of the coil which serve to connect the bundles of wire lying in the slots. These end turns are located at each end of the motor and typically lie on the surface of the end lamination. One sees in this figure that much of the flux produced due to end turns is leakage flux that does not link the air gap. In fact, counting flux lines, which delineate tubes containing equal amounts of flux, shows that approximately 60% of the flux produced by the end turns is leakage and does not link the air gap. Therefore, any flux in the motor caused by end turns would probably have the greatest effect on inductance, and a lesser effect on stator torque. In addition, knowing that flux density tends to be inversely proportional to the distance from the source, it is obvious that as the axial length of the motor increases, the flux density in middle of the motor decreases. Hence, the ratio of flux linking the air gap to end leakage flux would also tend to decrease. As the motor is made longer, end turns would have less effect on either inductance or torque.

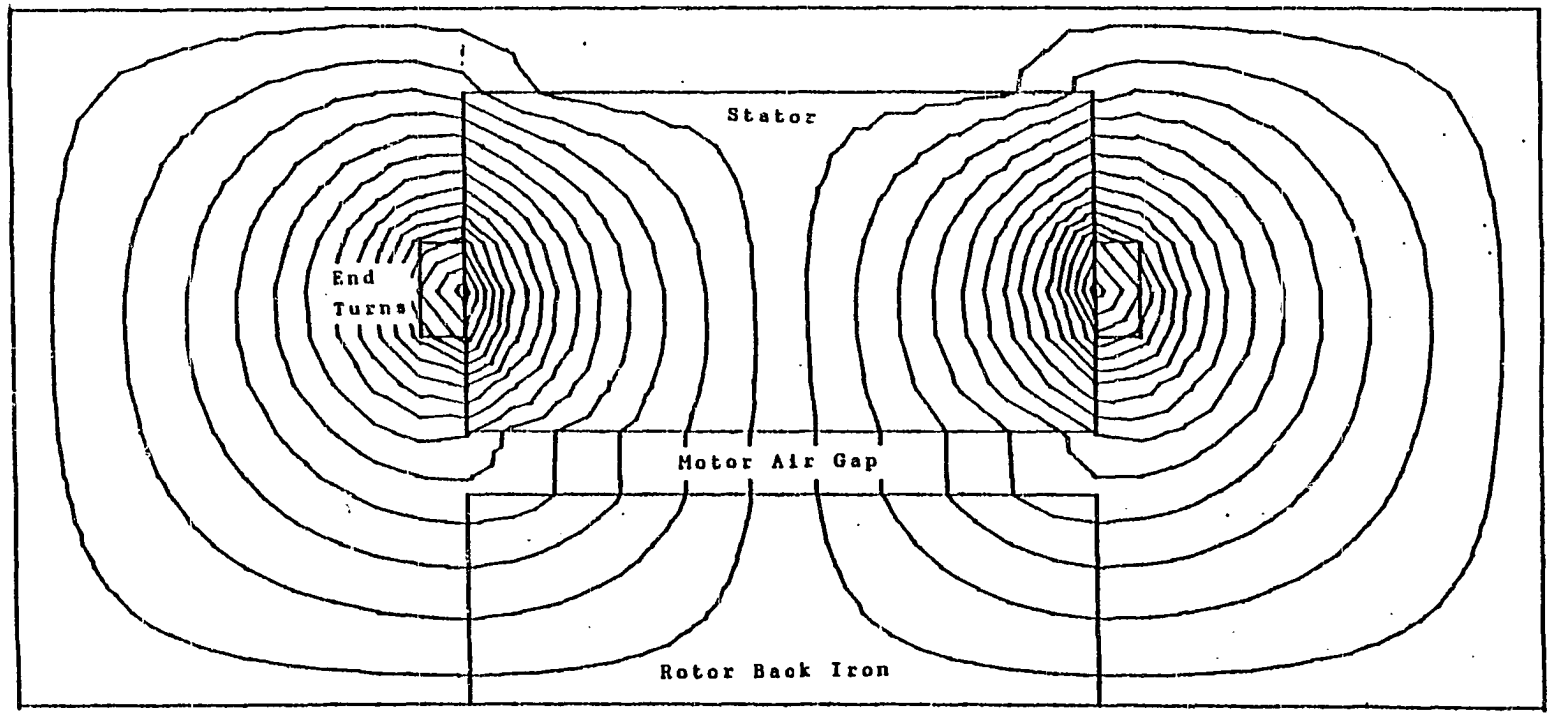

Figure IV-7
Finite Element Solution Contour Plot
of an r-Z Slice of the Prototype Motor

Further evaluation of end turn effects and its relation to motor axial length and the flux linkage-current characteristic are shown in Figure IV-8. This figure shows two solid lines that were the result of measuring two flux linkage-current charcteristics. One is for a double stack stator and rotor, (a motor of twice the normal stack length), Curve (1). The second is for a single stack stator and rotor, Curve(2). In both cases the rotor permanent magnets, (PM's), were removed and only the rotor back iron was present. This was done primarily because we did not have enough magnet segments to make a double stack rotor. Notice that the slope of the curve for the double stack is not twice the slope of the single stack curve. If end turns effects were not present, then doubling the motor length should double the slope of the flux linkage-current characteristic, as the two-dimensional FEM predicts, Curves (3) and (4), in this figure.

A summary of slope comparisons between FEM and experimental data is shown in Table IV-1. Included in this table is data from Table III-1. In comparing single and double stack length results, one sees that as the stack length is increased the two-dimensional FEM becomes more accurate.

Table IV-1

Summary of Flux Linkage-Current Slope Comparisons

λ-i description	Exp. Slope Henries	FEM Slope Henries	%Error of FEM
Single Stack PM	0.0062	0.0046	-26.0
Single Stack no PM	0.0100	0.0078	-22.0
Double Stack no PM	0.0179	0.0156	-12.8

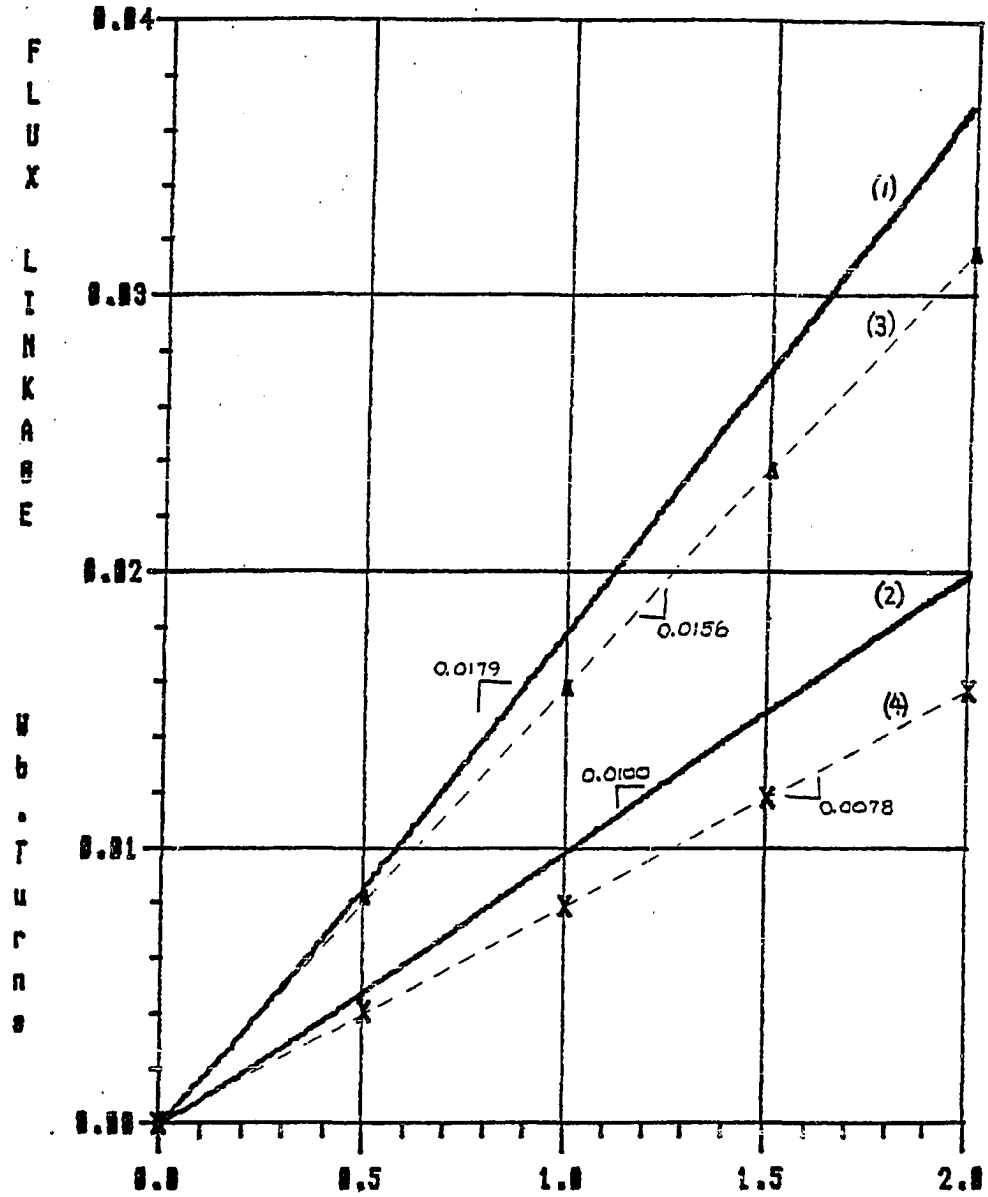

Figure IV-8
Comparison of Measured and Finite Element
Predicted Flux Linkage versus Current
Curve (1)- Measured Data, Double Stack Motor
Curve (2)- Measured Data, Single Stack Motor
Curve (3)- Finite Element Predicted Results, Double Stack Motor
Curve (4)- Finite Element Predicted Results, Single Stack Motor

If one used the single and double stack no PM data to extrapolate error based on stack length, one sees that the error is nearly halved as the stack length is doubled. Since the length to width ratio of the single stack prototype motor coil is approximately 1:1, one would need to have a motor with coil length to width ratios of 10:1 before the error in predicting inductance was less than 3%.

Given the preceeding analysis and discussion, we should see that the FEM prediction of the flux density in the motor airgap should be lower than measured values. To corroborate this, a FEM of the motor without permanent magnets mounted on the rotor back iron was used. The coil current was set to be 2.0 amps and the distribution of the radial component of flux density along the midpoint of the airgap was calculated. The same conditions were established experimentally and a gauss probe was used to measure the radial component of flux density over the tooth faces of the prototype stator. The FEM and experimental results are shown in Figure IV-9. FEM results are shown as the solid line and measured values are shown as X's. One sees that the peak FEM values are approximately 6% lower than the measured values. While this is consistent with the previous discussion on end effects, the confidence level of the measurement accuracy is not high enough for the results to be conclusive.

IV.4 Verifying the Permanent Magnet Model

To check the finite element model for the permanent magnet, it was decided to construct and model a steel annulus with an airgap large enough to allow direct measurement of the flux density in the air gap region with a hall probe. An annulus of soft steel was constructed

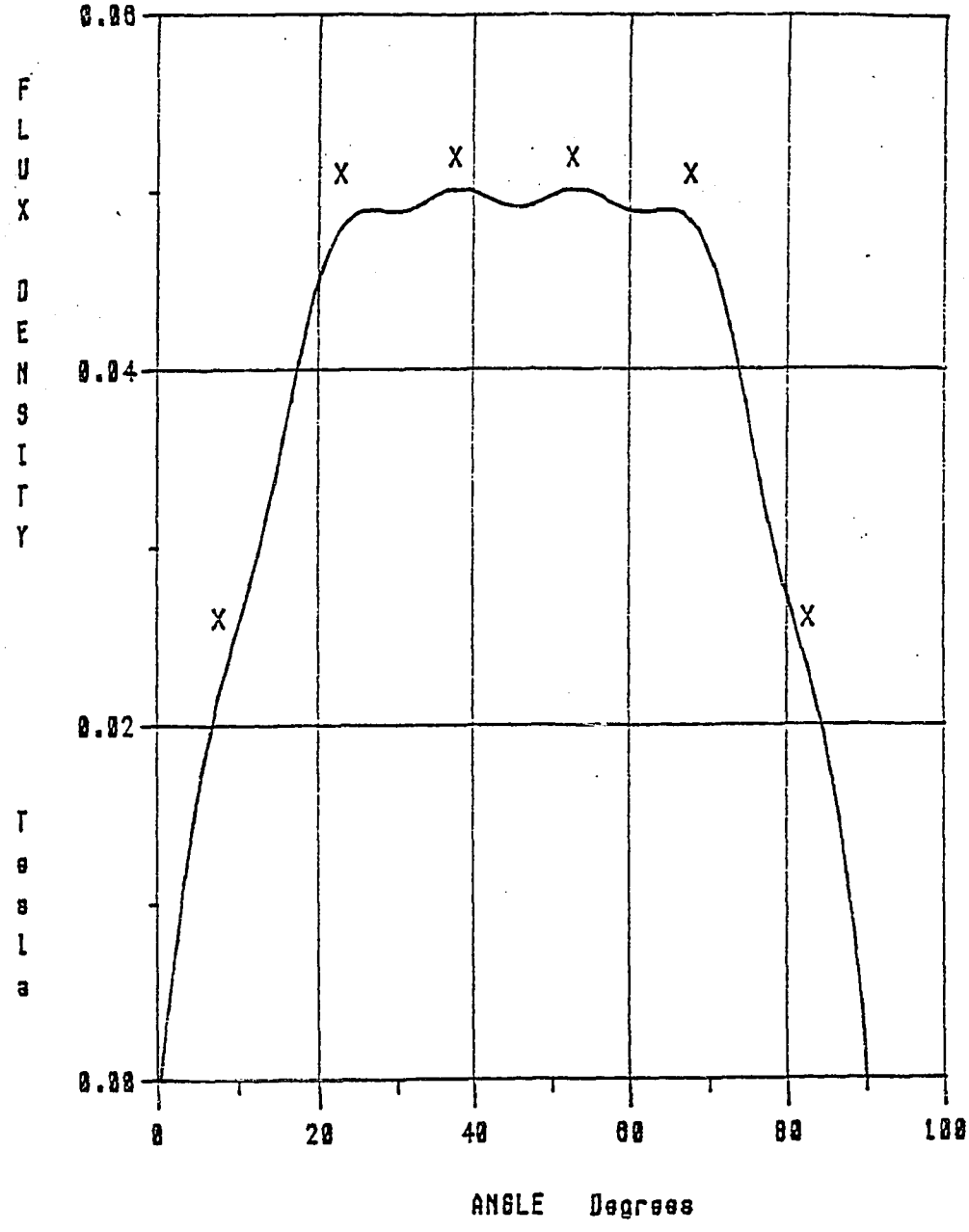

Figure IV-9
Comparison of Measured, (X's), and Finite Element
Predicted, (Solid Line), Airgap Flux Density Due to the Coil

with an outer diameter and length the same as the rotor, and with an inner diameter 0.060 inches greater than the rotor outer diameter. A Gaussmeter, (Bell model 615) was used with a transverse probe, (Bell model STJ1-0404), inserted in the air gap of this annulus and the rotor was rotated while the radial component of flux density, B_{rad}, was measured as a function of angle. The measurement was taken at the midpoint of the stack length of the rotor magnet. Probe active area was 0.040 inches in diameter and its thickness was 0.040 inches. Linearity of the device was specified as 0.1% up to 1 Tesla. The resulting measurement taken over two magnet segments, (180^0) is shown in Figure IV-10a.

In addition, a measurement of B_{rad} was taken at the center of the arc span of the magnet while the position of the probe was varied over the axial length of the rotor. This measurement is shown in Figure IV-10b.

It was necessary to compare this to a finite element model of the permanent magnet. A finite element model was constructed of a quarter section of the device, and the permanent magnet was modeled by edge currents, just as in the prototype model. This model assumes that the magnet was magnetized uniformly in the radial direction. Using the manufacturer's specification for the intrinsic strength of the magnet, the resulting finite element analysis predicts the average flux density in the air gap to be as shown in Figure IV-11. The radial component, B_{rad}, theta component, B_θ, and magnitude, $|B|$, are shown in this plot. If one compares B_{rad} shapes and magnitudes in Figures IV-10a and IV-11 there are obvious differences between the experimental and finite element model results. The finite element model

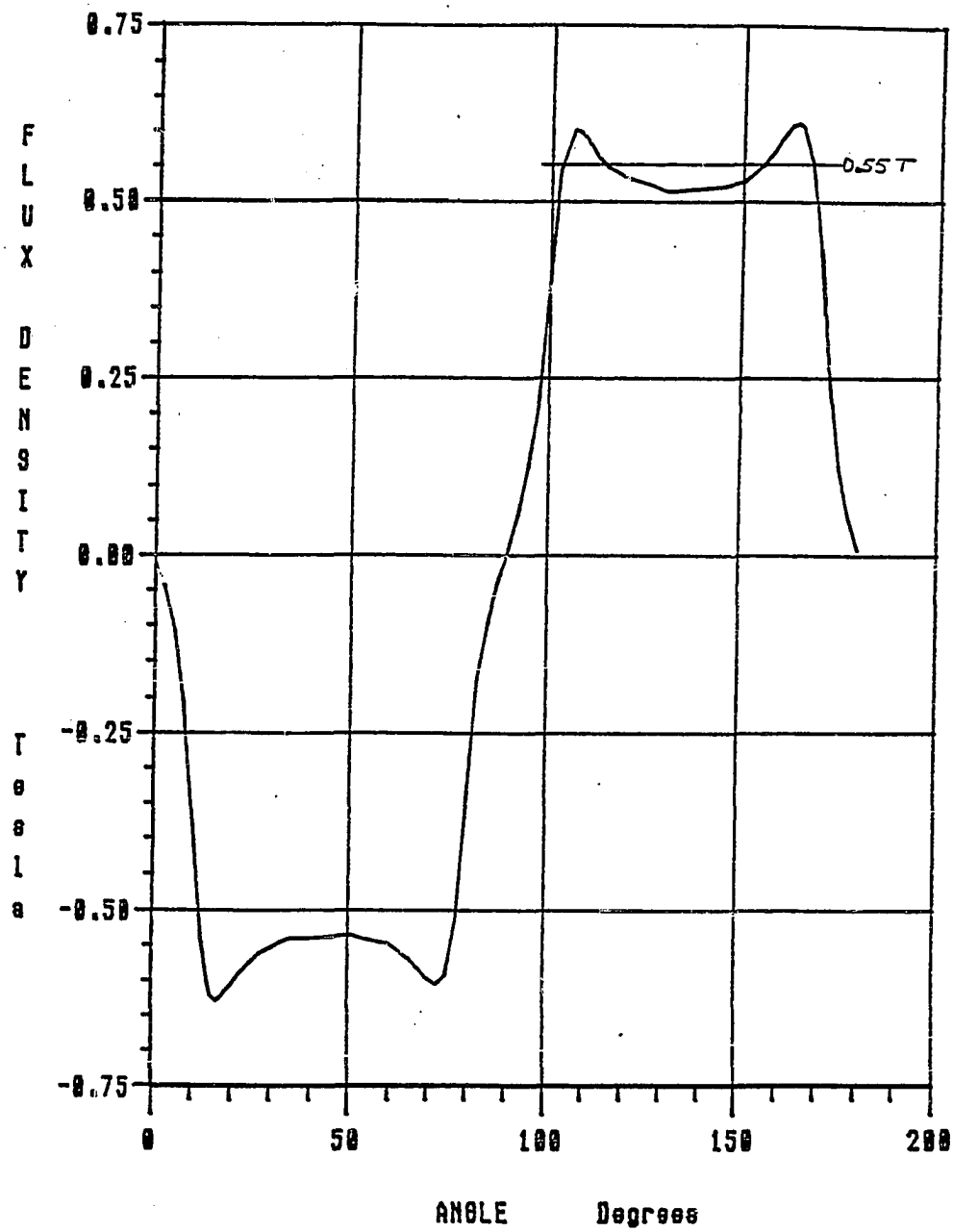

Figure IV-10a
Measured Radial Component of Airgap Flux
Density Due to Rotor in Annulus, versus Angle

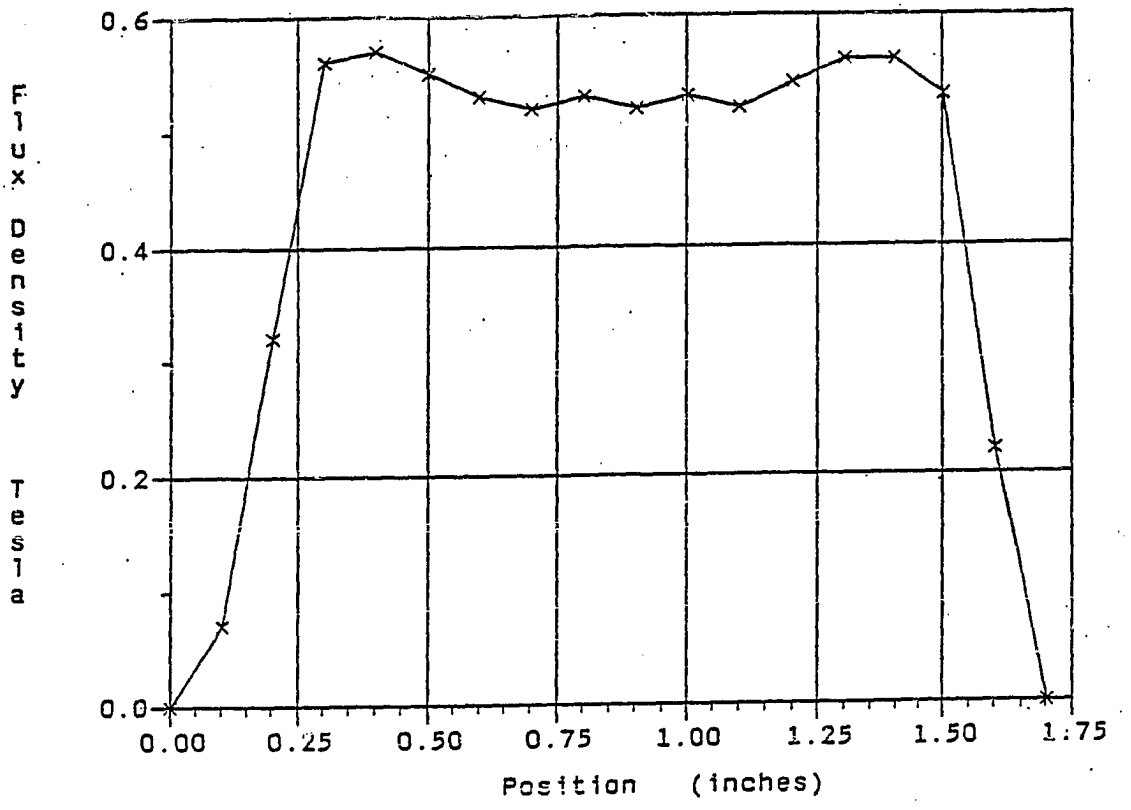

Figure IV-10b
Measured Radial Component of Airgap
Flux Density at Center of Magnet in
Annulus, as a Function of Axial Position

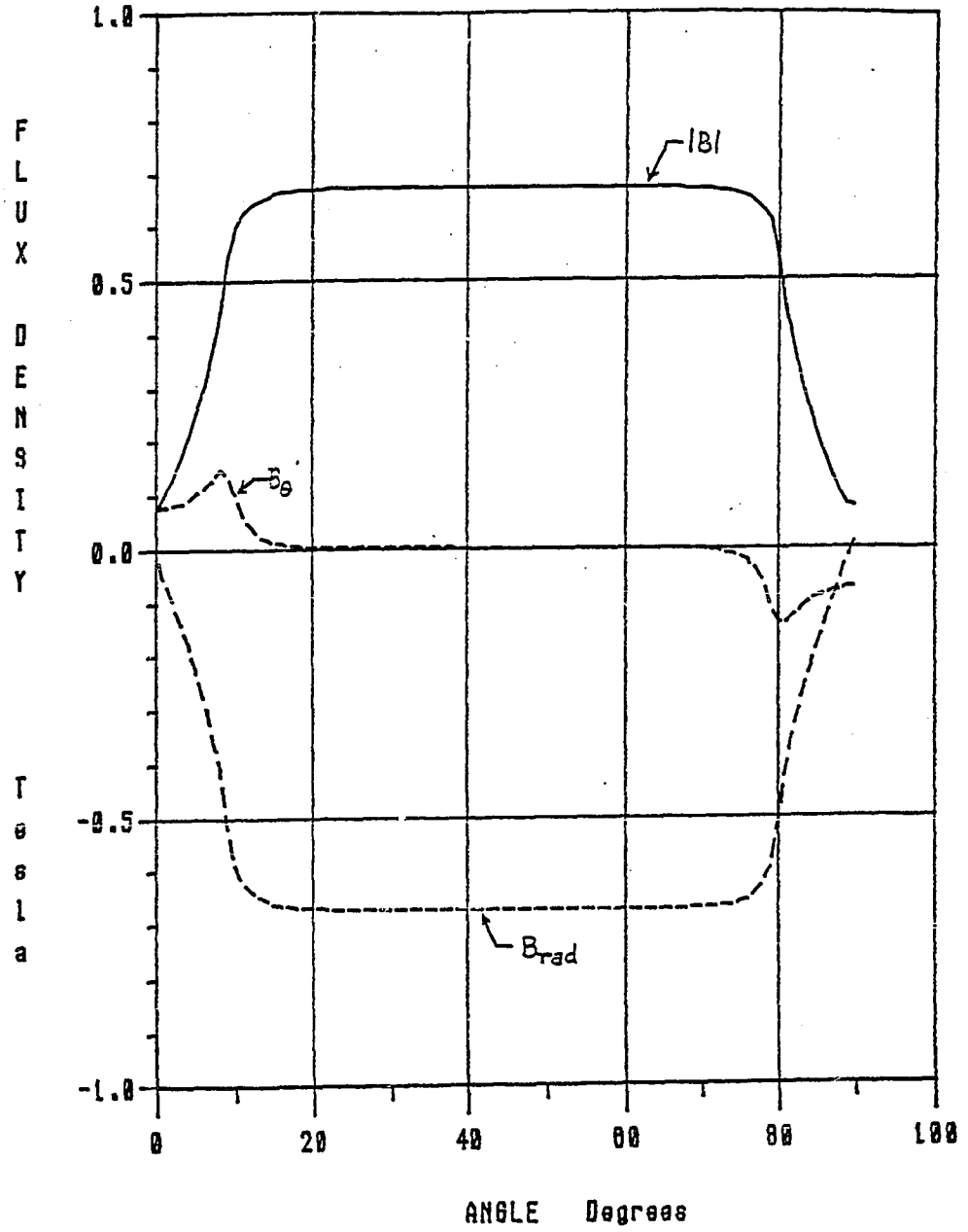

Figure IV-11
Finite Element Predicted Radial
Component of Airgap Flux Density
Due to Magnet in Annulus, versus Angle

distribution is flat topped while the experimental distribution shows 'horns'. The average value of the flat topped region found from the finite element model is 0.65 Tesla. The average value of the experimental distribution over the same region is 0.55 Tesla.

The differences in distribution 'shapes' indicates that the magnet segments are not magnetized uniformly in the radial direction. The differences in average values indicates either an inaccuracy in the saturation model for soft steel, or a variation in actual magnet magnetization from the manufacturer's specification. Since the VR analysis, performed in Section IV.2, verified the material property models, the difference must be due to the latter.

IV.5 Exploring Alternate Models for the Rotor Magnets

The previous section has shown that the magnet model used in the FEM is not accurate enough to predict the field produced by the magnet while in the annulus. Obviously, one would like to improve the permanent magnet model so that good correlation with the annulus data is obtained. Then, the new model could be used to recalculate the detent torque and torque constant. Ultimately, however, what is sought is a method of identifying, or developing, a magnet model based on some experimental measurements. If this ability could be achieved, then one could identify the magnetization model of magnets that are of unknown origin and history.

How to determine the changes necessary to improve the present magnet model is not clear. There are several approaches that could be taken. One, we could model the magnetization process of the magnet using finite elements. This would require detailed knowledge of the

magnetizer geometry, voltage levels and capacitors used, etc. It might also require a finite element analysis of the transient field because the rare earth magnets have a high iron content, allowing the presence of large eddy currents, which could effect the magnetization of the segment.

Secondly, given the measurements made in the annulus, we could try to make an intelligent guess as to the magnetization distribution of the interior of the magnet. The FEM of the annulus would be used to provide feedback and the model could be modified as necessary to make the predicted and measured flux density distributions for the annulus match. This might not be as difficult as it appears, provided we know something about the way in which it was magnetized, such as its general direction of orientation.

Third, we could simply make the average value of the distribution predicted by the FEM of the annulus match the average value of the measured distribution. It might be possible that the characteristic parameters of the motor are not overly sensitive to the magnet model, only to the average values. A precise magnet model might not be required for our purposes.

All of the preceeding options have significant drawbacks. Performing a finite element analysis of the magnetization process would require detailed information of the magnetization process. This information is usually proprietary and unavailable for rare earth magnets. In addition, it does not help us in cases where we are trying to develop a model for a magnet in which little is known about the magnetization process.

Trying to make an intelligent guess as to the internal magnetization of the permanent magnet segment is difficult because there is no way of ensuring that the guess is correct - other than using a scanning electron microscope to map the magnetic domain orientation within a sample. In addition, the distribution of the radial component of B in the annulus may not be unique; even if the distribution were forced to match there is no guarantee that the current distribution selected would be correct. This might result in significant errors in predicting some motor characteristic parameters.

Of the three methods previously mentioned for improving or altering the magnet model, the second two: guessing the magnetization and making the average values of the distributions match, were investigated. This was done because the proprietary nature of the magnetization process prevents the investigator from modeling it.

One fact we might use in developing an improved model of the magnet is that the flux density measurement of the annulus showed higher flux densities at the edges of the magnet than in the middle. The permanent magnet appears to be more strongly magnetized on the edges than in the middle. As mentioned previously, it was thought that this could be due to eddy currents having played a significant role during the magnetization process. Since the permanent magnets were probably magnetized by a pulse field, this seemed plausible. During the time that the field is building, eddy currents could be generated in the interior of the body that prevent the field from reaching levels that would completely saturate the material. This could cause the outside edges of the permanent magnet to be magnetized more strongly than the interior. If this is true, then to model the

magnetization, it would be necessary to place current densities in the interior of the permanent magnet. Since the interior magnetization is not known, the magnitude and placement of these currents would have to be determined by a trial and error process.

Recent work has shown that eddy currents do not play a significant role in the magnetization of rare earth magnets. Harned[15] performed a finite elment analysis of the transient field produced by a magnetizer. He showed that while eddy currents do appear in the rare earth material during magnetization, they do not affect the final magnetization of the material.

Another explanation for the higher strength on the edges than in the middle might lie in the manner in which a radial orientation was created. Magnet manufacturers have indicated that the combination of powder metalurgical processes, (press and sinter), and high magnetizing fields necessary for rare earths, make it very difficult to create a truly radially oriented, sintered rare earth magnet. For many materials, grain orientation is achieved by applying a low level field during the forming of the piece. However, during the pressing operation there are high amounts of friction between particles. Thus, high fields are required to produce sufficient forces to overcome the friction and allow the particles to rotate so that the easy access of magnetization of the grain is aligned with the field. Because high fields are present, any iron used to direct the field is usually saturated. Once the iron is saturated, much of one's ability to direct the field is lost. The resulting direction of magnetization could be more straight-through than radial. Again, to determine the actual direction of magnetization one would have to look at the domain

orientation within the material.

In order to produce a magnet which has some of the same external characteristics as a radially oriented magnet, the manufacturer alters the flux density distribution by remagnetizing the specimen in different ways. The manufacturer first magnetizes the material, attempting to create a radial magnetization. The actual direction of magnetization may be straight-through, or, somewhere in between a radial orientation and a straight-through orientation. The distribution of B_{rad} predicted by the FEM of the solid annulus with permanent magnets magnetized straight-through is shown in Figure IV-12. One sees that the distribution is much more sinusoidal than the one produced by the radial oriented magnets, Figure IV-11. In order to force the distribution shown in Figure IV-12 to more closely resemble that of Figure IV-11, it is obvious that the magnetization in the center of the of the specimen must be lessened. Therefore, the manufacturer applies a smaller reverse field to the middle of the segment, lessening its magnetization.

Unfortunately, the FEM of the magnet magnetized straight through requires equivalent currents of different magnitudes to be place around the entire outside boundary of the magnet. It would be very difficult with such a model to determine, by trial and error, a set of equivalent currents that would produced the B_{rad} distribution that matched the annulus data shown in Figure IV-10a. However, to determine a simple set of edge and interior currents that produces a distribution similar to the one shown in Figure IV-10a is relatively straight forward.

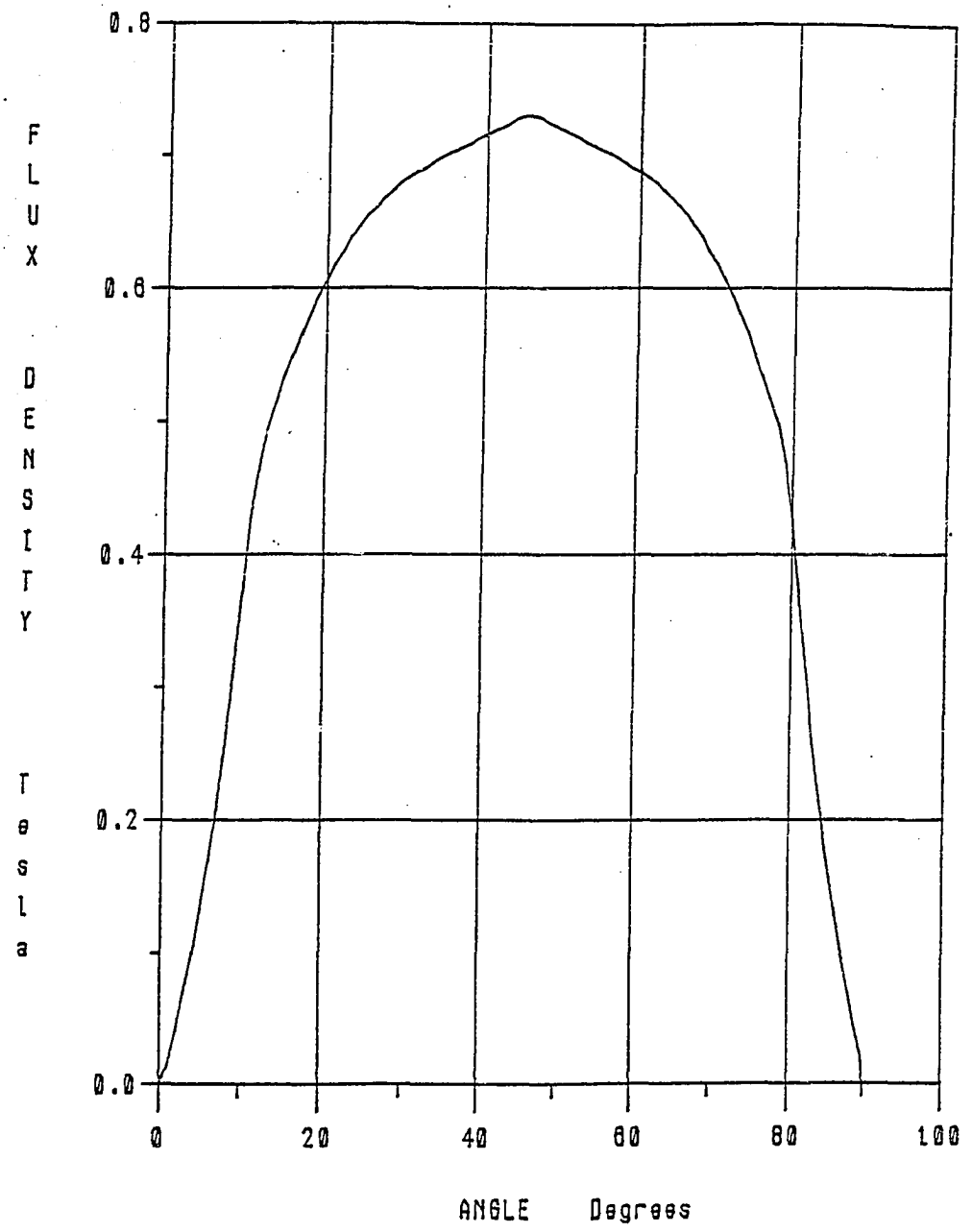

Figure IV-12
Finite Element Predicted Distribution of Radial Component of Airgap Flux Density in Annulus, for a Permanent Magnet Magnetized Straight Through

If we look at Figures IV-13, the distribution of the radial component of flux density over one of the pole faces, it appears to be the superposition of two fields. This concept is illustrated in Figure IV-14a-d. Suppose the magnetization of the permanent magnet was at two discrete levels, (M_1 and M_2 in Figure IV-14a). Then the permanent magnet could be modeled as two pairs of current sheets, one set on the outside edges and the other set in the middle. The sign and relative magnitude of the currents for this example are shown in Figure IV-14b. The larger edge currents produce a field in one direction and the lesser inner currents produce a smaller, oppositely directed field. The net distribution of B_{rad} would be the sum of the two B_{rad} distributions, (Figure IV-14c). This would result in a flux density versus position waveform with the characteristic dip observed experimentally. Of course, in the actual permanent magnet specimen, the magnetization probably would not be discontinous but would be some continous function of position within the magnet, (Figure IV-14d). Therefore, the equivalent current density distribution would vary over the interior of the magnet in a manner which depends upon the original magnetization.

Through a trial and error process, a set of current density distributions was selected for the FEM of the magnet in the annulus. These current densities resulted in a B_{rad} distribution which matched the experimental curves reasonably well. A comparison of the FEM and experimental distributions is shown in Figure IV-15. The placement of the current density distributions used to achieve the FEM produced B_{rad} distribution, are shown in Figure IV-16. The FEM which uses this set of current density distributions will be called model 1. The

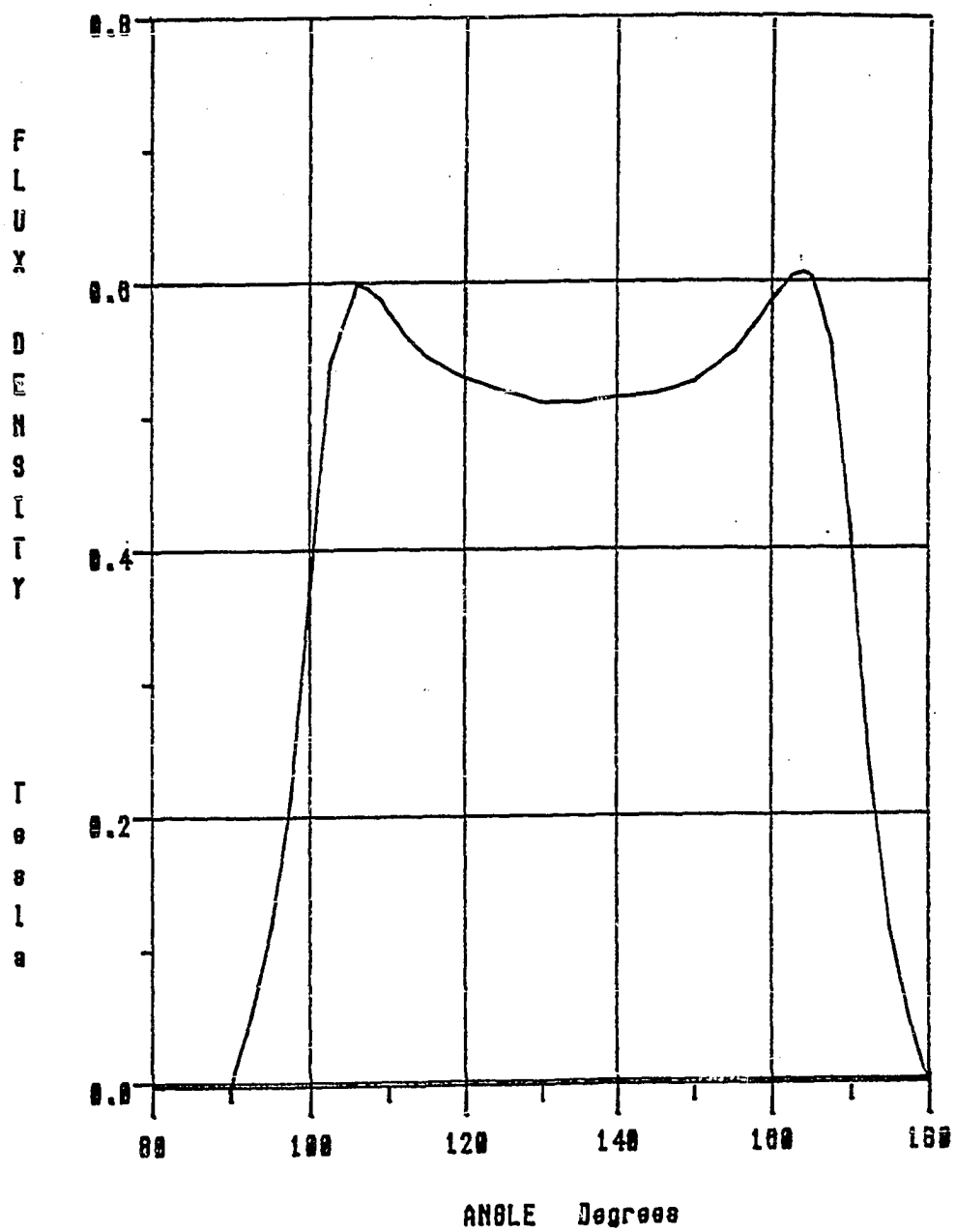

Figure IV-13
Distribution of Radial Component of
Flux Density Over One Pole Face of Rotor in Air

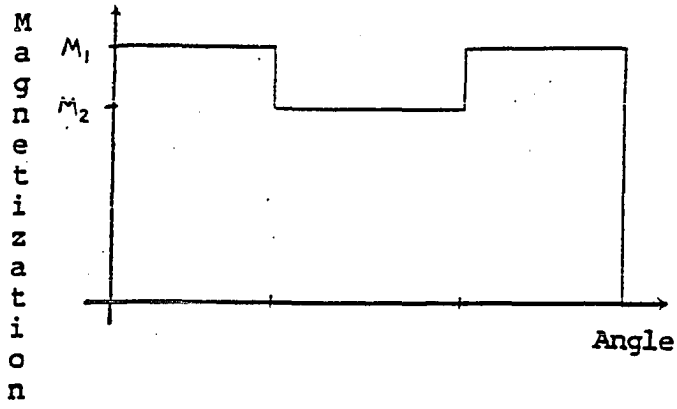

Figure IV-14a
Equivalent Current Magnetization Distribution within Magnet

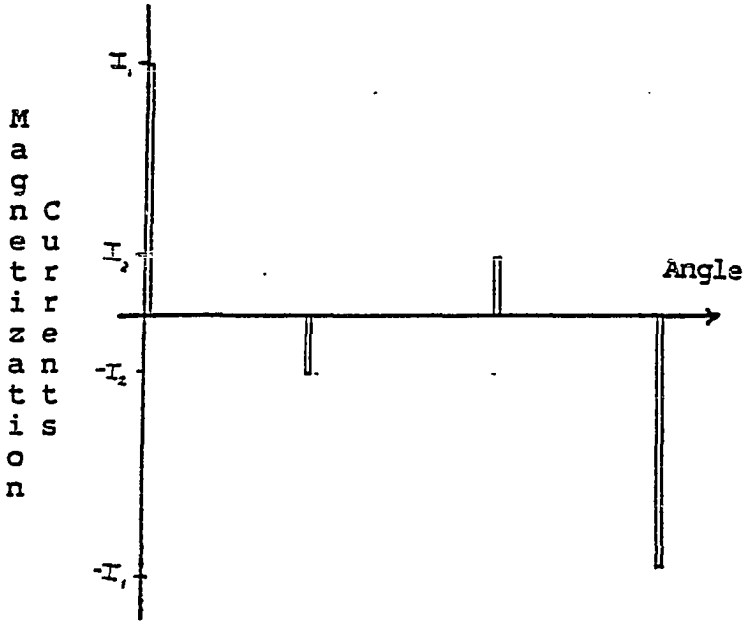

Figure IV-14b
Equivalent Current Magnetization Sheet
Currents Required to Produce Magnetization
Distribution Shown in Figure IV-14a

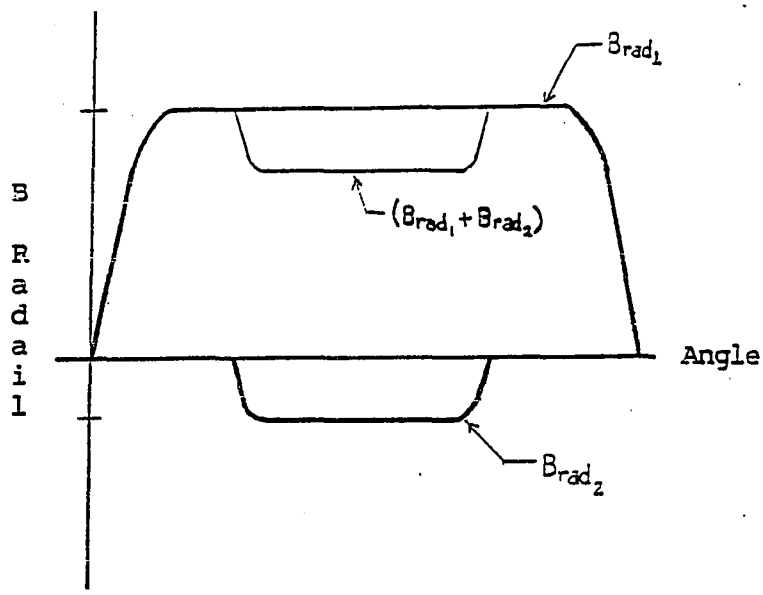

Figure IV-14c
Individual and Net Distributions of Radial Component of Flux Density Due to Outer and Inner Equivalent Magnetization Currents

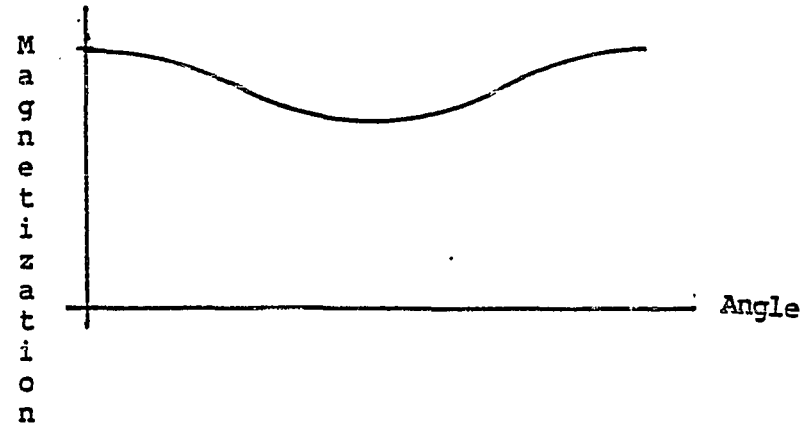

Figure IV-14d
A More Realistic Approximation for the Equivalent Current Magnetization Distribution

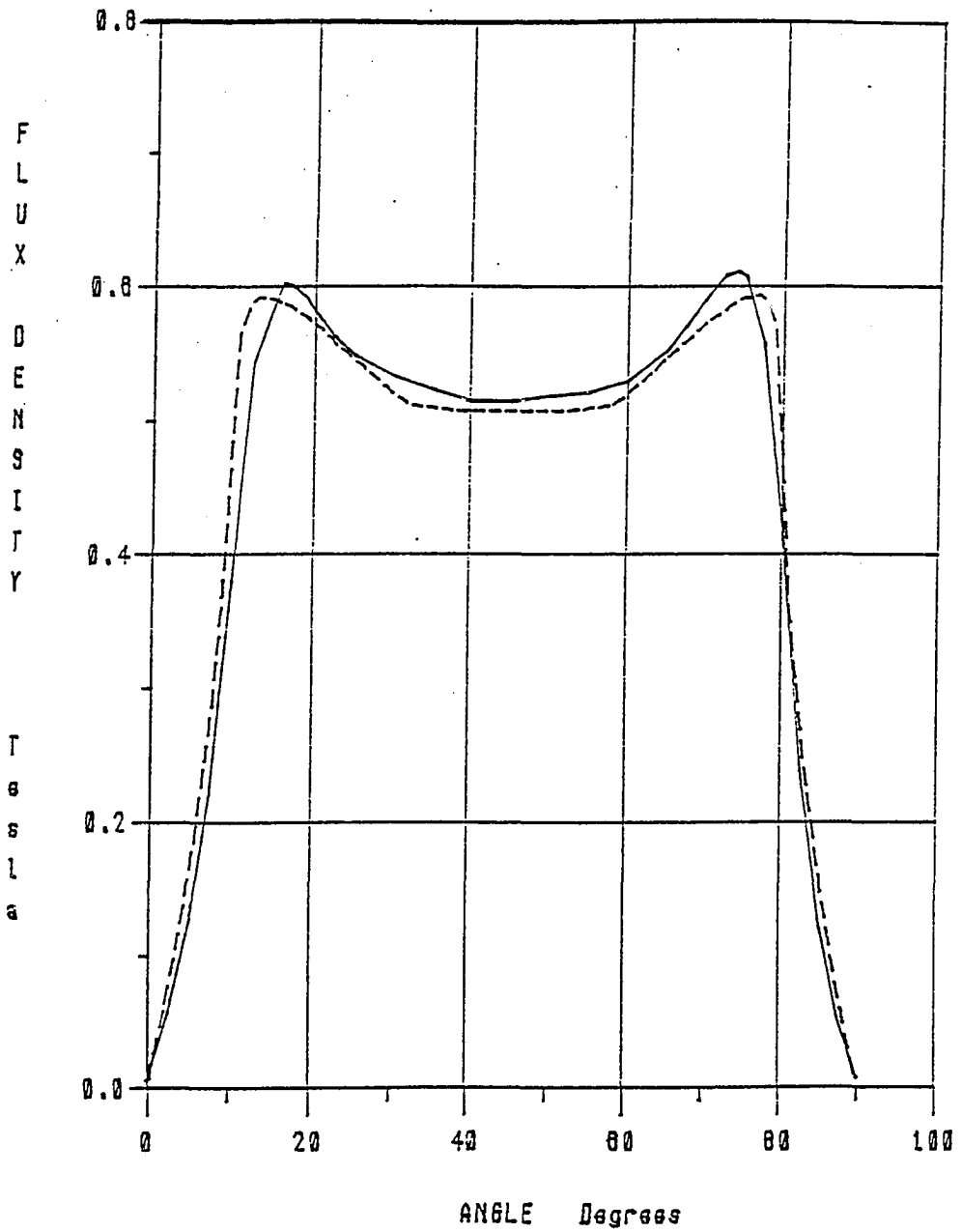

Figure IV-15
Comparison of Measured, (Solid Line), and Finite Element Predicted, (Dashed Line), Distribution of Radial Component of Airgap Flux Density Over One Pole Face of Rotor in Annulus

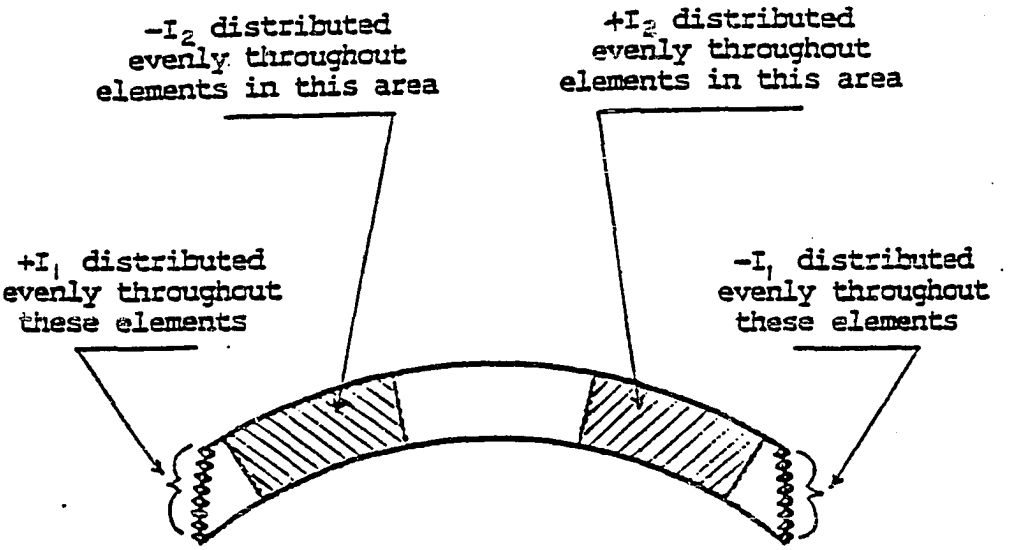

$|I_1| = 2500$ Amps

$|I_2| = 470$ Amps

Figure IV-16
Distribution of Magnetization Currents

original FEM developed in Chapter III, using just the edge currents, will be called model 0.

In addition, an FEM of the rotor and annulus was developed where the permanent magnet magnetization was assumed to be radially uniform, and the average value of the FEM predicted B_{rad} distribution was made to match the measured one, (0.56 Tesla). It was found that the edge magnetization currents neccessary to force this condition were 83% of the original equivalent currents that were based on the manufacturer's specifications for the magnet strength. This FEM will be called model 2. Comparing detent torque curves predicted by models 1 and 2 should indicate whether a high degree of precision in the magnet model is necessary, i.e. whether the detent torque is sensitive to the interior equivalent currents in the magnet model.

As further verification of model 1, a measurement was made of B_{rad}, with the rotor in air only. This measurement was compared to FEM predicted results for the same geometry. The data is compared in Figure IV-17. One sees that there is good correlation between the waveforms. This seems to indicate that the magnet current distribution developed empirically, and shown in Figure IV-16, is reasonable good.

These two models were used to find torque constants and detent torques, in order to make comparisons with measured findings to evaluate which provided the best results. They could also be compared to the orginal FEM results, (model 0), and to each other to evaluate the sensitivity of the torques to the permanent magnet representation.

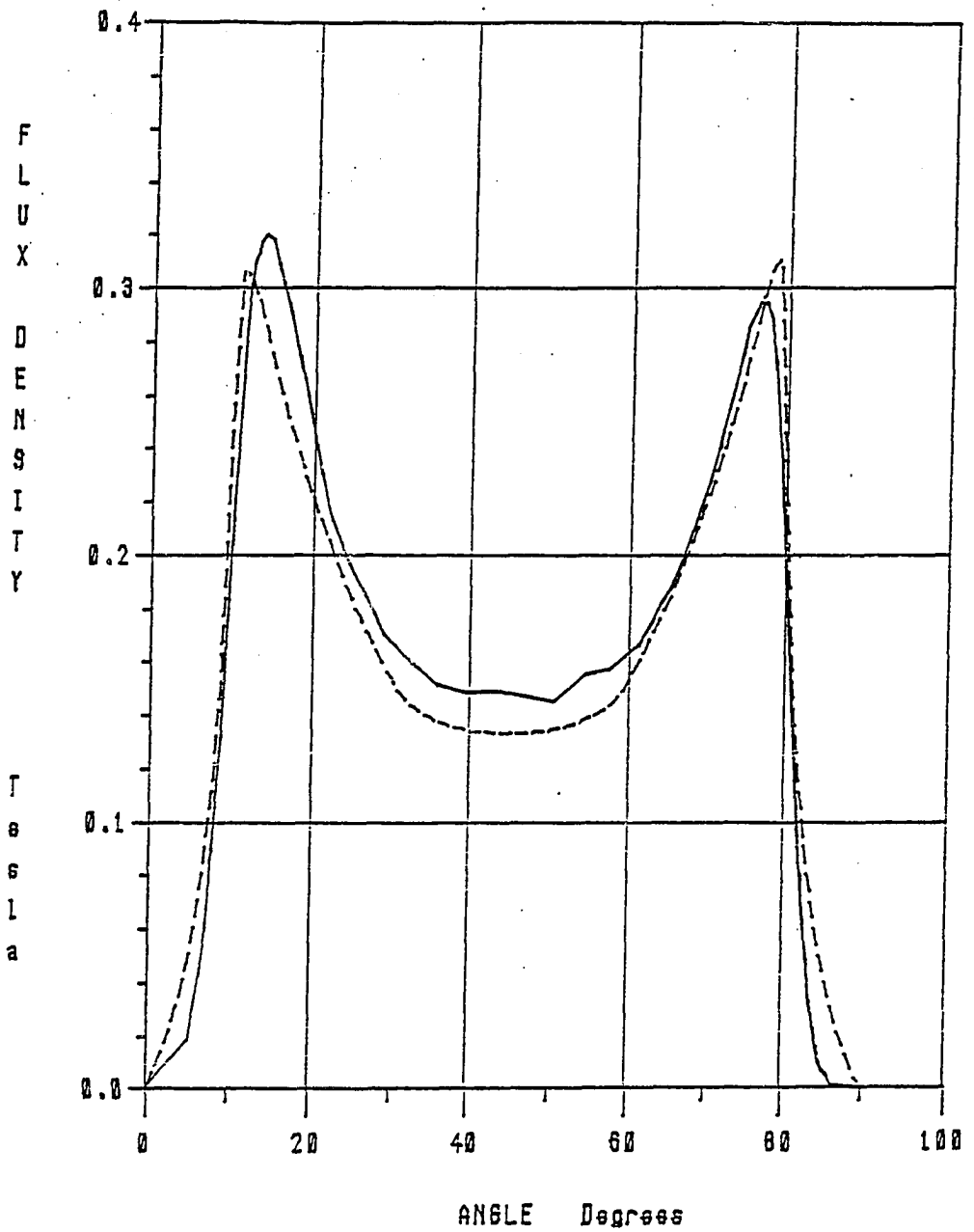

Figure IV-17
Comparison of Measured, (Solid Line), and Finite Element Predicted, (Dashed Line), Distribution of Radial Component of Flux Density Over One Pole Face of Rotor in Air

IV.5a Detent Torque Predicted by Models 1 and 2

The detent torque, as a function of angle, was calculated and compared to the experimentally measured curve. This comparison was done for both models: model 1, edge currents and interior currents; and model 2, edge currents only. The comparison is shown in Figure IV-18. The solid line is the experimentally obtained detent torque as a function of angle. The symbol 'O' represents data obtained from the finite element analysis using magnet model 1. The symbol 'X' represents data obtained from the finite element analysis using magnet model 2. It is obvious that neither the waveform shape nor the magnitude from either model correlate very well with measured data. Both models predict a severe flattening of the waveform shape around the unstable equilibrium point, (indicating a fairly large second harmonic content in the waveform). The experimental waveform shows much less of this effect. If one were to compare magnitudes only and neglect waveform shape one obtains the results shown in Table IV-2. Included in this table is Model 0; the original FEM model results from Chapter III.

Table IV-2
Comparison of Detent Torque Magnitudes

Description	Mag. of Detent oz-in	% error from experimental
Measured	61.8	---
Model 0	45.0	-27.2
Model 1	43.0	-30.4
Model 2	37.0	-40.1

One sees from Table IV-2 that the error in predicting detent torque actually increased with either model 1 or model 2, which were developed to match measured flux density within a solid annulus. In

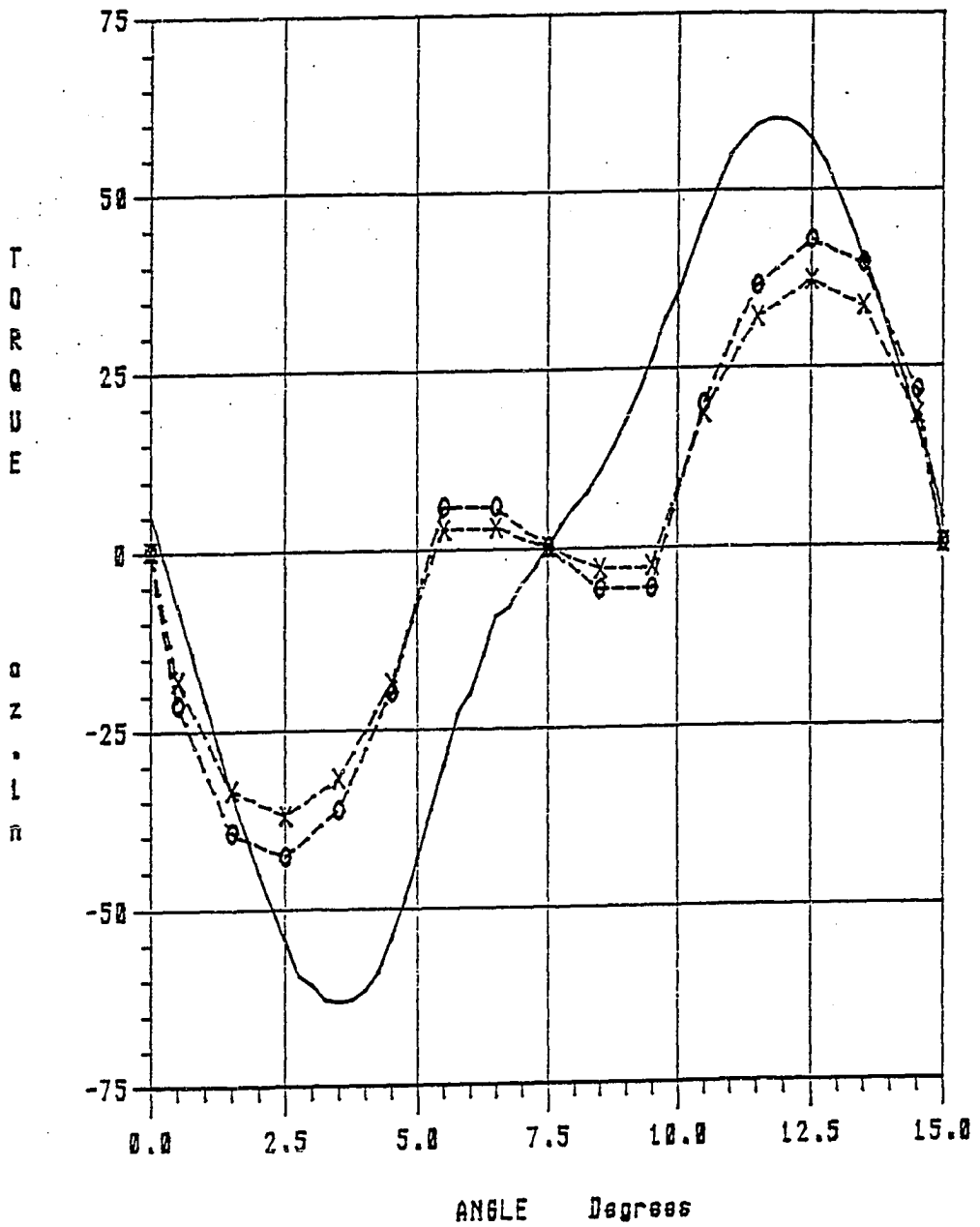

Figure IV-18
Comparison of Measured, (Solid Line), and Finite Element Model 1, (O's), and Model 2, (X's), Predicted Detent Torque versus Angle

addition, it is clear that there is not a great difference in the waveform shape of the detent torque predicted by models 1 and 2. However, the magnitude of the interior currents in model 2 were much less than edge current magnitudes. Therefore, the interior currents might not have produced a large effect on the waveform shape.

Obviously, other explanations for the differences between FEM and measured detent torque will have to be explored. These differences do not appear to be caused by the lack of refinement of the magnet model.

IV.5b Torque Constant Predicted by Models 1 and 2

Both models for the permanent magnet were used to calculate the peak stator torque for several different values of phase current. Data produced from model 1, (edge currents and interior currents), is plotted in Figure IV-19 as 'O's. Data obtained from model 2 is plotted as 'X's. The average peak stator torque values were taken from the measured torque-angle curves and plotted as a function of phase current. This is denoted by the solid line marked with triangles in Figure IV-19. Calculating the torque constant from a least squares fit of the data to find the slope for each of the three cases yields:

Table IV-3
Comparison of Torque Constants

K_{texp}	= 50.2 oz-in/amp	
K_{t0}	= 49.8 oz-in/amp	%error ≤ -1.%
K_{t1}	= 40.8 oz-in/amp	%error = -18.7%
K_{t2}	= 43.2 oz-in/amp	%error = -13.9%

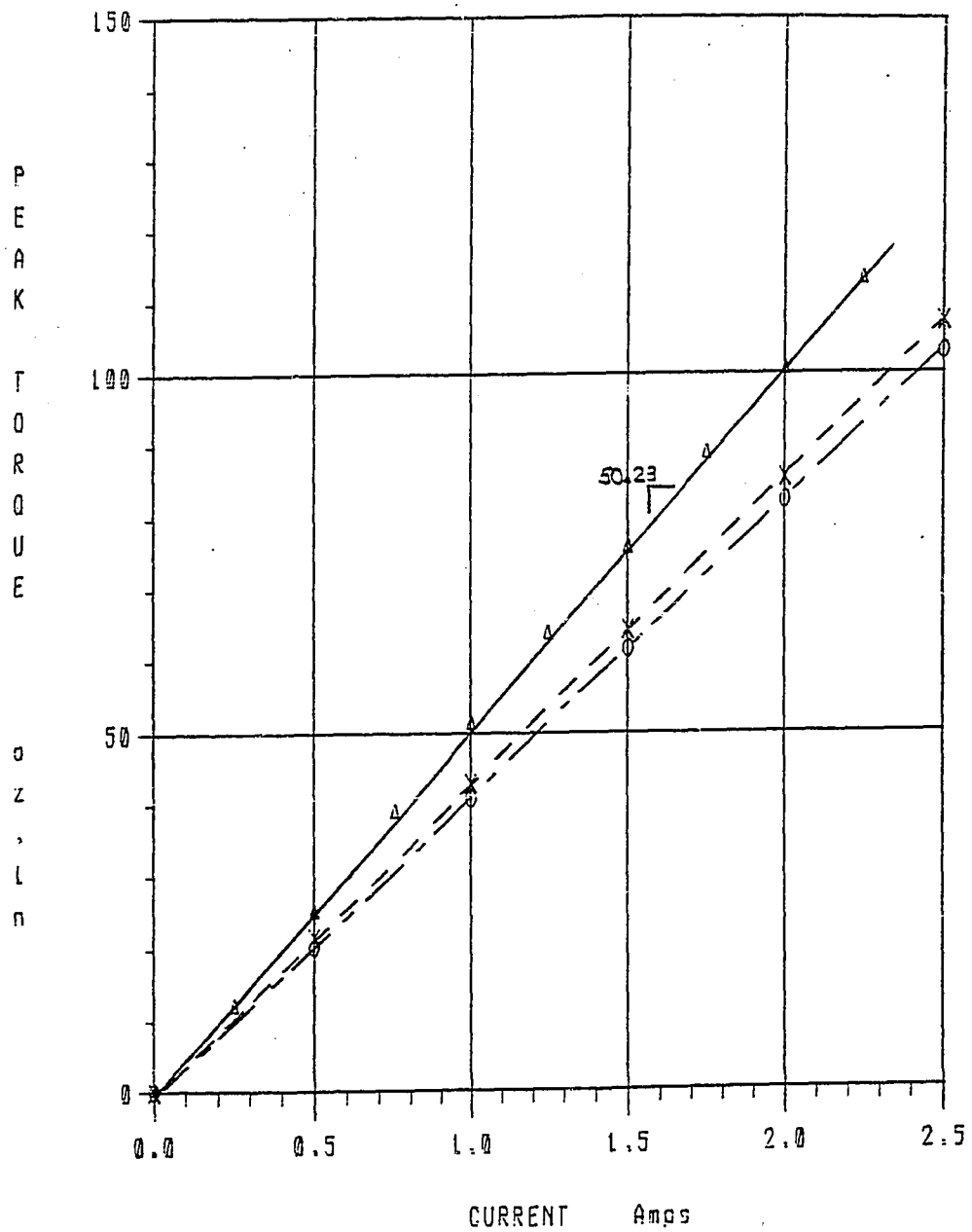

Figure IV-19
Comparison of Measured, (Triangles), and Finite Element Model 1, (O's), and Model 2, (X's), Predicted Peak Stator Torque versus Current

K_{t0} is the torque constant found from the original FEM used in Chapter III.

A comparison of the measured and FEM predicted torque constants shows that the more refined models for the rotor magnets increase the errors in torque prediction. Thus, one would suspect that there is another cause for the discrepancy and the original FEM model, model 0, compensated for most of that error to result in misleadingly good correlation between measured and FEM predicted results.

IV.6 Detent Torque Sensitivity

In searching for causes of the discrepancy between measured and predicted detent torques, the sensitivity of the detent torque to the location of the PM edge currents in the FEM was investigated. The orientation and magnitude of the edge current were held constant but the arc width of the magnet model was altered. The magnet edge currents used were those of model 0 from the FEM used in Chapter III. Detent torque curves were calculated for six different magnet arc widths. Those widths were in one mechanical degree increments. This corresponded to moving the magnet edge current in the FEM by one grid increment.

Figure IV-20 shows the resulting the detent torque-angle curves. The FEM results are shown in solid lines and the measured curve is shown as a dashed line. The change in degrees of magnet arc width from the original model is marked for each curve. The peak detent torque values for these curves are shown in Table IV-4. One sees that for an 11% decrease in magnet width the magnitude of the detent torque increased by 50%. In comparing values over the range of widths inves-

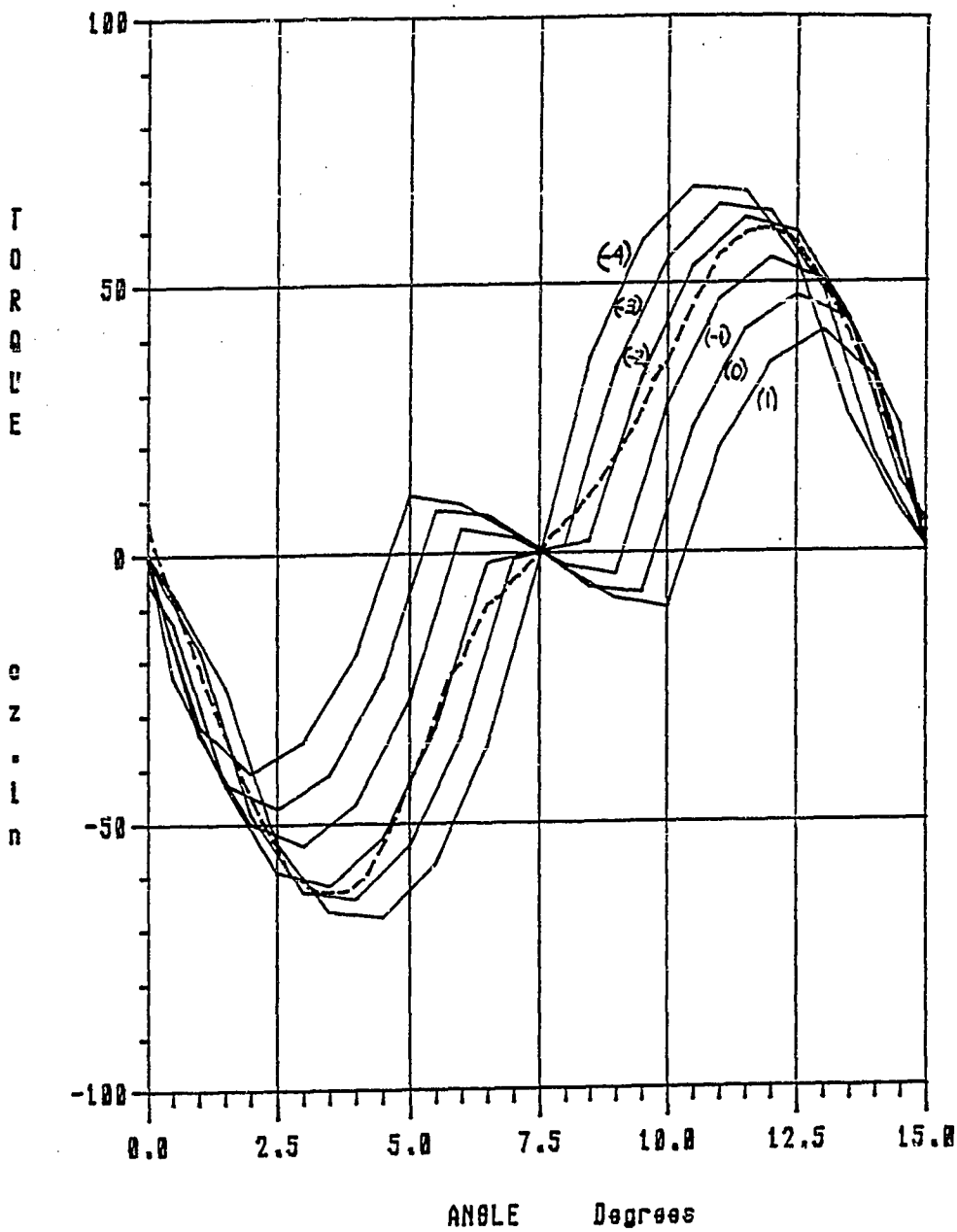

Figure IV-20
Finite Element Predicted Detent Torque-Angle Curves for Six Different Magnet Arc Widths, (75 Degrees Plus the Amount Shown for Each Curve), Measured Detent Torque is Shown as a Dashed Line

tigated, for a total change in magnet width of five degrees, the minimum width is 14% less than the maximum width, and the corresponding change in the peak detent torque is 65%.

Table IV-4
Comparison of Detent Torque Magnitudes

Arc Width change from original (deg)	% change in Arc Width	Detent Magnitude oz-in	%change in Detent Magnitude from original
+1.0	1.3	41.3	-10.2
0.0	-	46.0	-
-1.0	-1.3	54.8	+19.1
-2.0	-2.6	62.5	+35.9
-3.0	-3.9	64.5	+40.2
-4.0	-5.2	68.4	+48.7

The results of those investigations showed that better correlation between measured and FEM predicted detent torque curves could be obtained by reducing the arc width of the magnet model by 2 degrees. There is reasonable correlation between waveform shape and good correlation between the magnitudes.

There is some physical justification for the discrepancy indicated. Manufacturers indicate that there is often a layer from 0.010 to 0.020 inches on the outer surface of the magnet which has poorer magnet properties than the remainder of the magnet. This layer results from a more rapid cooling of the outer surface of the magnet compared to the inner. Sometimes it is recommended that the magnet outer surfaces be ground to obtain a more uniform magnet. If 0.020 inches were ground from both edges of the magnet, then the arc width of the magnet would be reduced by approximately three degrees.

Another reason for the discrepancy between the actual arc width of the magnet and the 'apparent' arc width could be due to inaccuracies introduced by modeling the magnet edge currents as distributed in a 'staircase' set of elements instead of in a continous line of current distributed along the actual edge of the magnet. See Figure IV-21.

A further comparison of the detent torque curve predicted by the FEM of the two-degree narrower magnet, with the experimental detent torque curve can be made by a Fourier series spectrum analysis on both sets of data. The results are shown in Table IV-5. Only those harmonics with magnitudes greater than 1% of the fundamental magnitude are shown.

Table IV-5
Comparison of Detent Torque Harmonics

Harmonic	Magnitude (oz-in)	
	FEM	Experimental
1	56.7	52.2
2	10.7	5.9
3	-4.4	-7.6

The FEM predicted detent torque has a larger second harmonic than the measured curve, resulting in the characteristic dip around the unstable equilibrium point. Unfortunately, its cause is unknown.

IV.7 Evaluating the Composite Model, Model 3

The models for the magnet from the annulus analysis, i.e: the magnet currents shown in Figure IV-16, and the detent torque sensitivity analysis, (a two degree narrower magnet), were combined into one composite FEM, (model 3). First, the distribution of B_{rad} in

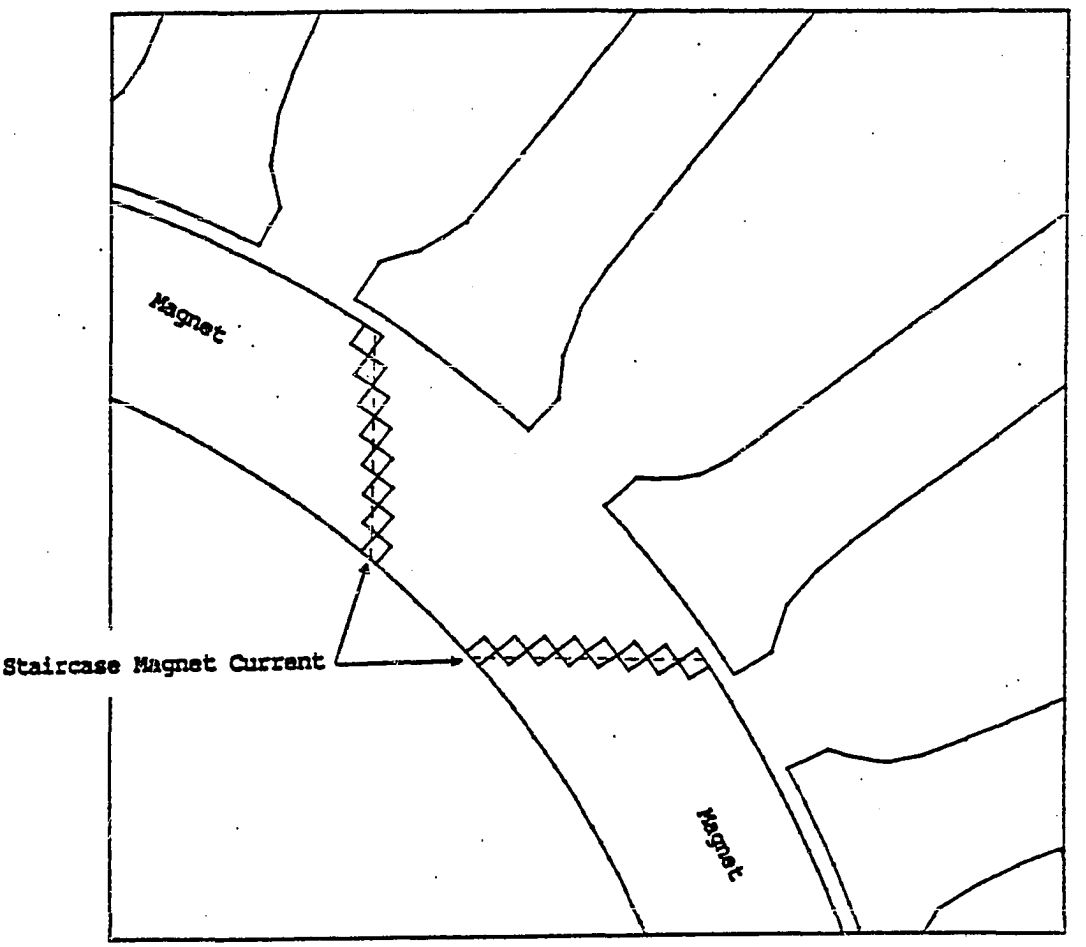

Figure IV-21
Finite Element Model Outline Showing Modeled Magnet Edges

the solid annulus was checked, Figure IV-22. Then, model 3 was used to predict detent torque, torque constant and back emf waveform, Figures IV-23,24,25 respectively. In each of these later Figures, the solid line indicates experimental data and the dashed line indicates FEM results.

Figure IV-22 shows a comparison of the distribution of B_{rad} predicted by model 3, (dashed line), with the measured B_{rad} distribution. Waveform correlation is not as good as it was previously in Figure IV-15, however it is still reasonable. The peak values at the 'horns' are now 8% larger than measured experimentally.

Figure IV-23 shows a detent torque comparison. The magnitude is still approximately 17% low. If the magnets had been made three degrees narrower instead of two, the detent would probably have matched better, and this change would have had very little effect on the torque constant. Making the magnets three degrees narrower would have helped to compensate for the smaller magnitude magnet edge currents that were used as a result of the annulus investigation.

Figure IV-24 shows a comparison of peak torque data. The torque constant predicted by the FEM is still 14% low, (43.15 oz in/amp compared to 50.2 oz in/amp). This is close to the model 1 results from Section IV.5b. There, the predicted torque constant was 18.7% low. Thus, combining the narrowing of the modeled magnets with the model that had both edge and interior equivalent currents only resulted in a 4% change in torque constant. Contrasting this with the 35% change in the magnitude of the detent torque, one sees that narrowing the magnets had little effect on peak torque.

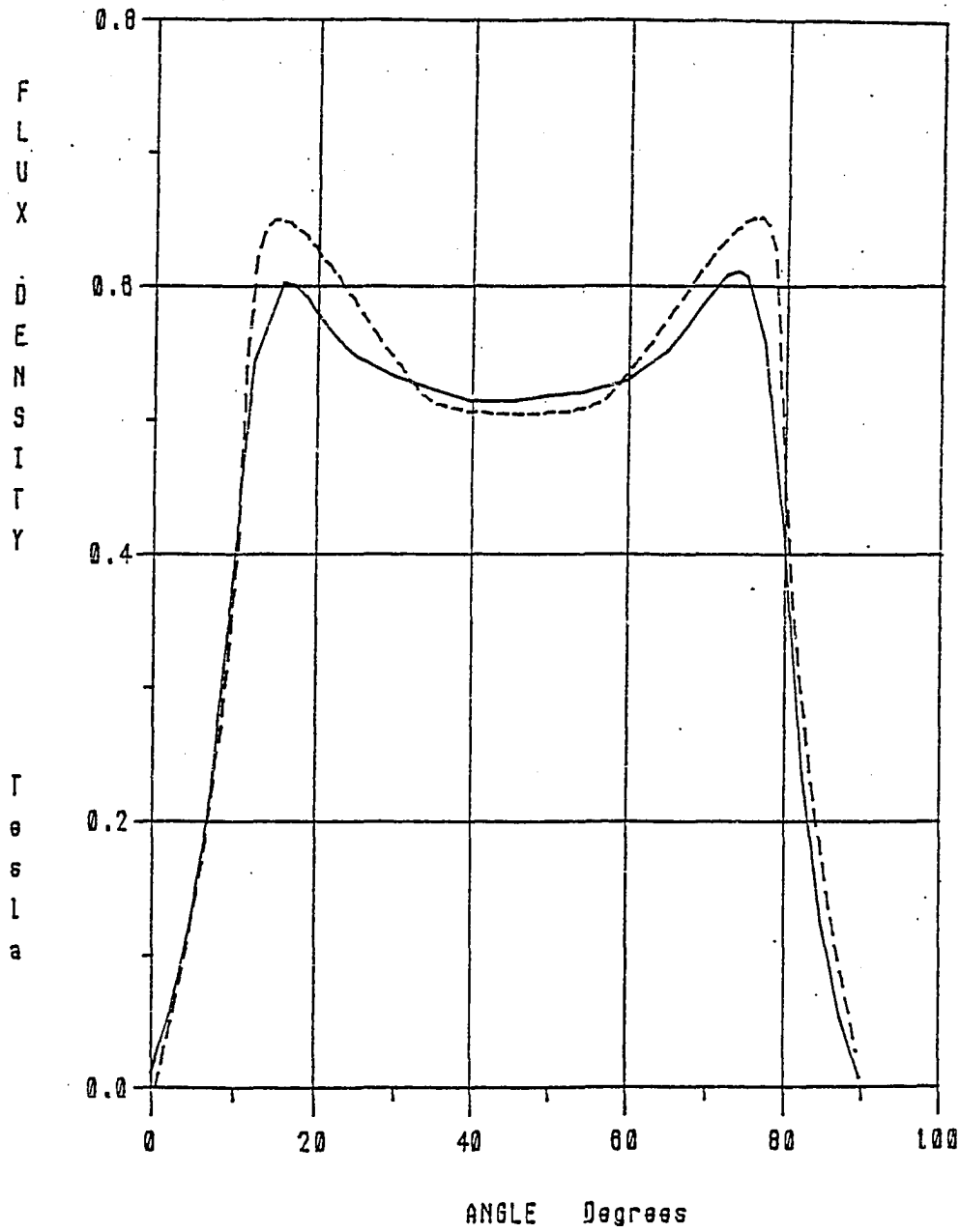

Figure IV-22
Comparison of Measured, (Solid Line), and Finite Element Model 3 Predicted, (Dashed Line), Distribution of Radial Component of Airgap Flux Density Due to Rotor in Annulus

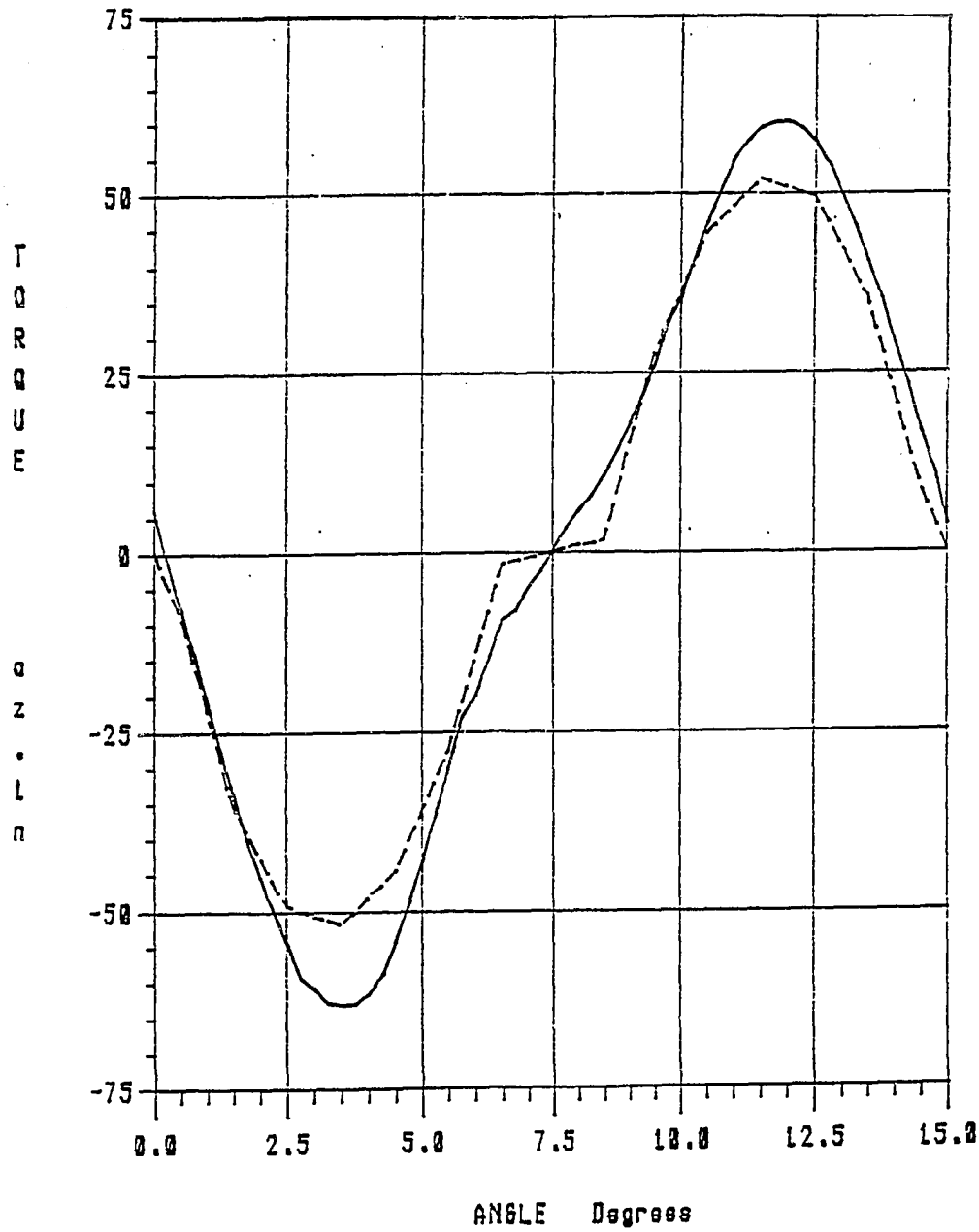

Figure IV-23
Comparison of Measured, (Solid Line), and Finite Element Model 3 Predicted, (Dashed Line), Detent Torque-Angle Curves

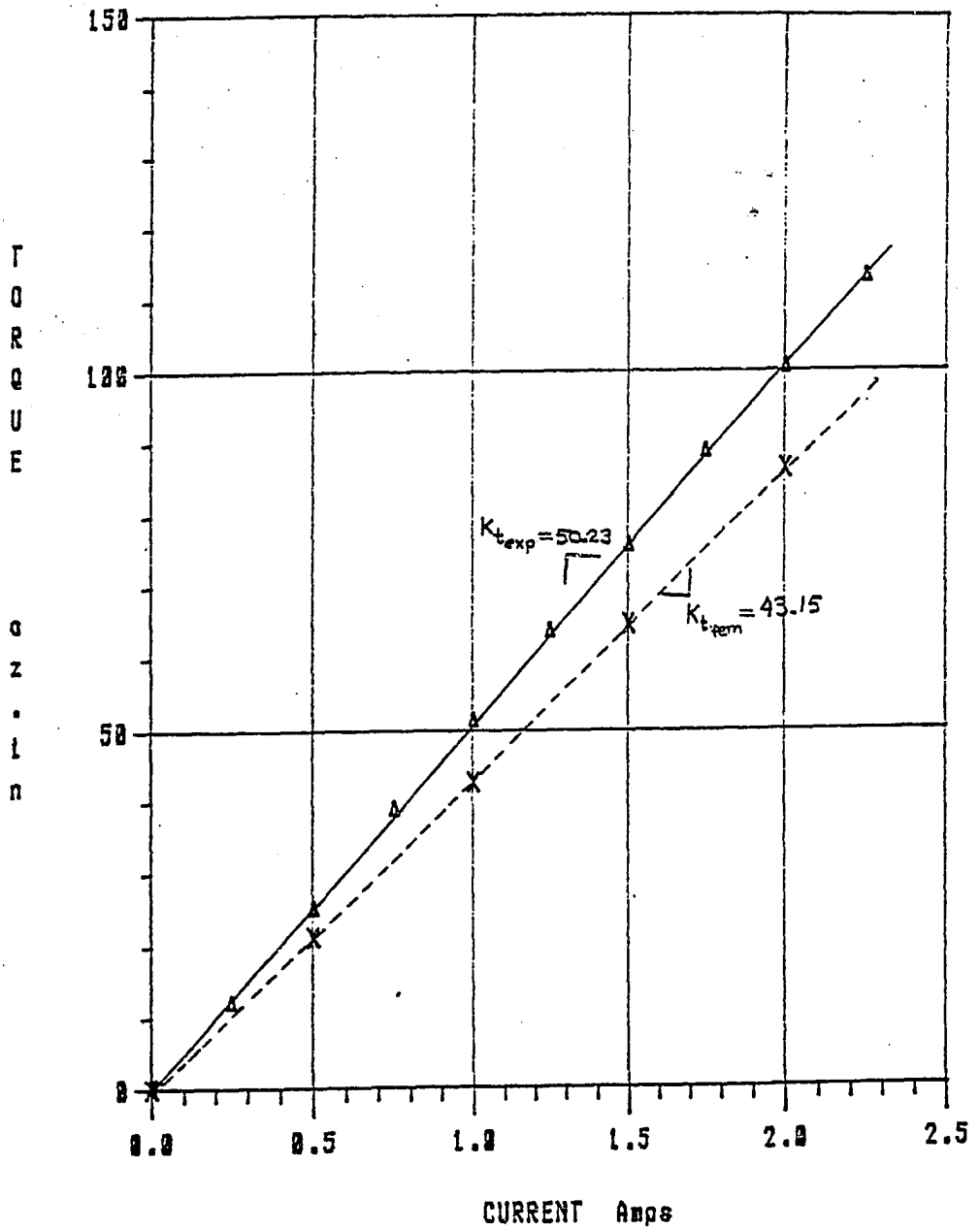

Figure IV-24
Comparison of Measured, (Triangles), and Finite Element Model 3 Predicted, (X's), Torque versus Current Characteristic

Figure IV-25 shows a comparison of FEM predicted and measured back emf waveforms at 200 rad/sec. The peak value predicted by the FEM is 11.5% lower than the experimental results. This is expected since the torque constant is also low and the back emf constant and torque constant are related. However, it should be noted that the FEM predicted back emf waveform shape still correlates well with the measured waveform. Thus, the alterations in the model have not affected the back emf waveform shape.

To summarize the evaluation of the composite model for the permanent magnet rotor, (model 3),one can say that this model predicts the peak of the B_{rad} distribution measured in an annulus within 8%; predicts the magnitude of the detent within -17%; predicts the torque constant within -15%; predicts the back emf within -11%; and shows good correlation in predicting back emf and detent torque waveforms. It is possible that another iteration of narrowing the magnet width further, until the detent torque magnitude again matched more closely, might also result in an improvement in torque constant correlation. However, it has been shown that the percentage change in torque constant which results from a change in magnet width, is not as great as the resulting percentage change in magnitude of the detent torque. In addition, the match between measured and FEM predicted B_{rad} distributions in the annulus will worsen if the magnet width is narrowed further. Therefore, one might have to use the narrower magnet model and adjust equivalent current magnitudes until annulus B_{rad} distributions again matched. Then, repeat the entire analysis.

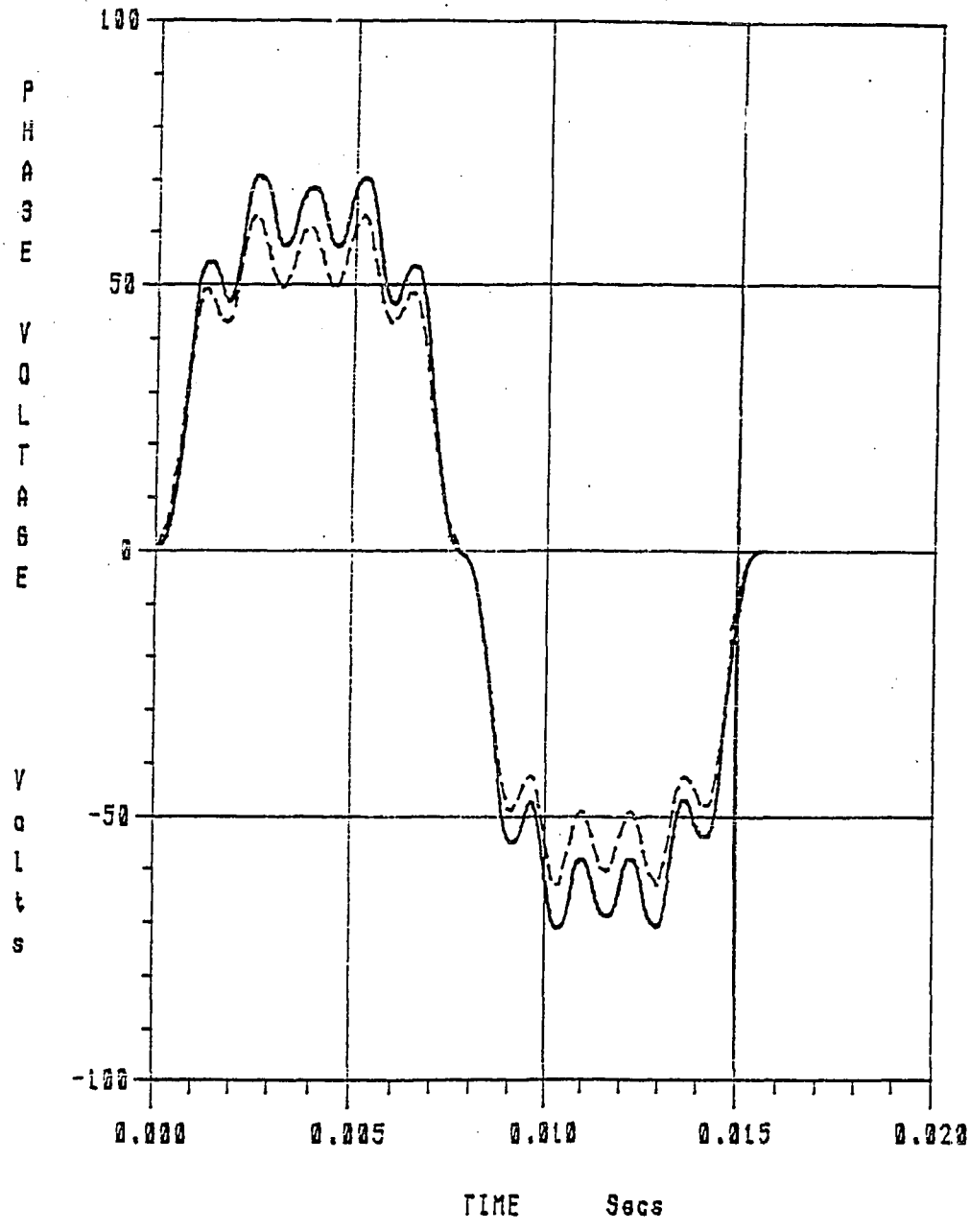

Figure IV-25
Comparison of Measured, (Solid Line), and Finite Element Model 3 Predicted, (Dashed Line), Back Emf Voltage Waveform Produced at a Rotor Speed of Approximately 200 rad/sec.

IV.8 Finite Element Model and Measurements Made on a Different Permanent Magnet Rotor

Before conclusions can be drawn concerning the accuracy of the FEM it was decided to apply the model development and verification techniques discussed in the previous sections to a different permanent magnet rotor. The second prototype permanent magnet rotor was constructed using Crucible Magnetics Nd-Fe-B magnets. These magnets were rectangular in shape and magnetized straight through. The magnet segments were mounted on a cylindrical piece of steel with flats machined on it. The resulting rotor was then ground to produce a round rotor of the same outer diameter as the original, see Figure IV-26.

First, a FEM of the new prototype rotor in the solid annulus was developed. The equivalent currents used to model the magnet were determined by geometry and the manufacturer's published data. It was assumed that the published data for the residual flux density, B_r, of the material was correct and that the magnet was magnetized straight through, as the manufacturer's data indicated. Figure IV-27 shows how the geometry was used to determine distribution of the equivalent currents. The incremental length, Δh_k, in the direction of magnetization between nodes k and k+1 was used to calculate an equivalent current for the incremental length:

$$\Delta h_k = L_{k+1} - L_k$$

$$\Delta i_k = \frac{\Delta h_k B_r}{\mu_r \mu_o} \qquad \text{(IV-6)}$$

This value of current was then distributed as a current density in

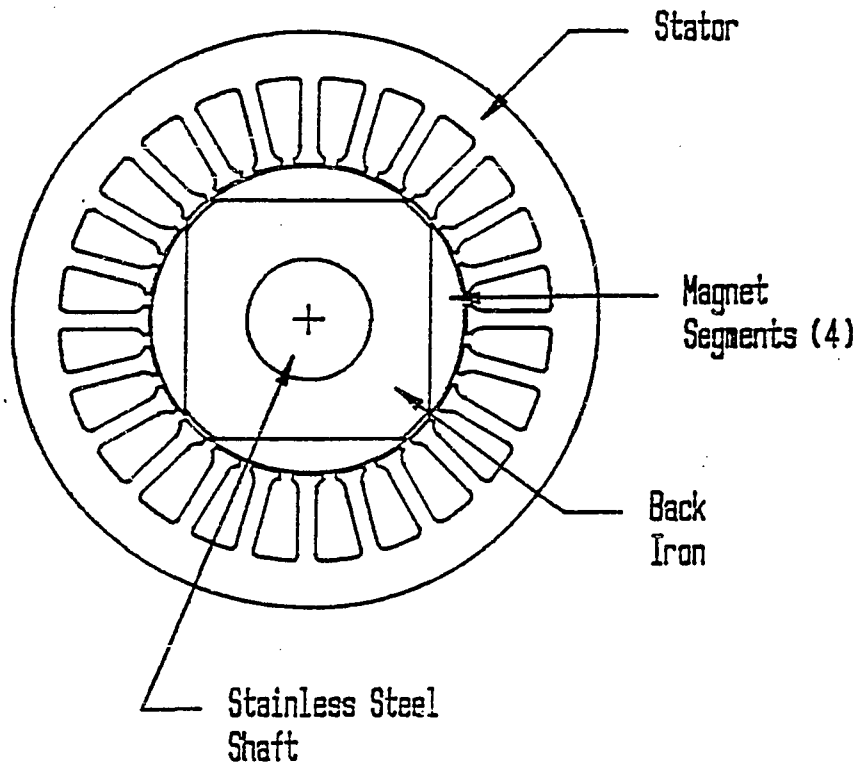

Figure IV-26
Cross-Sectional View of
Second Prototype Permanent Magnet Rotor

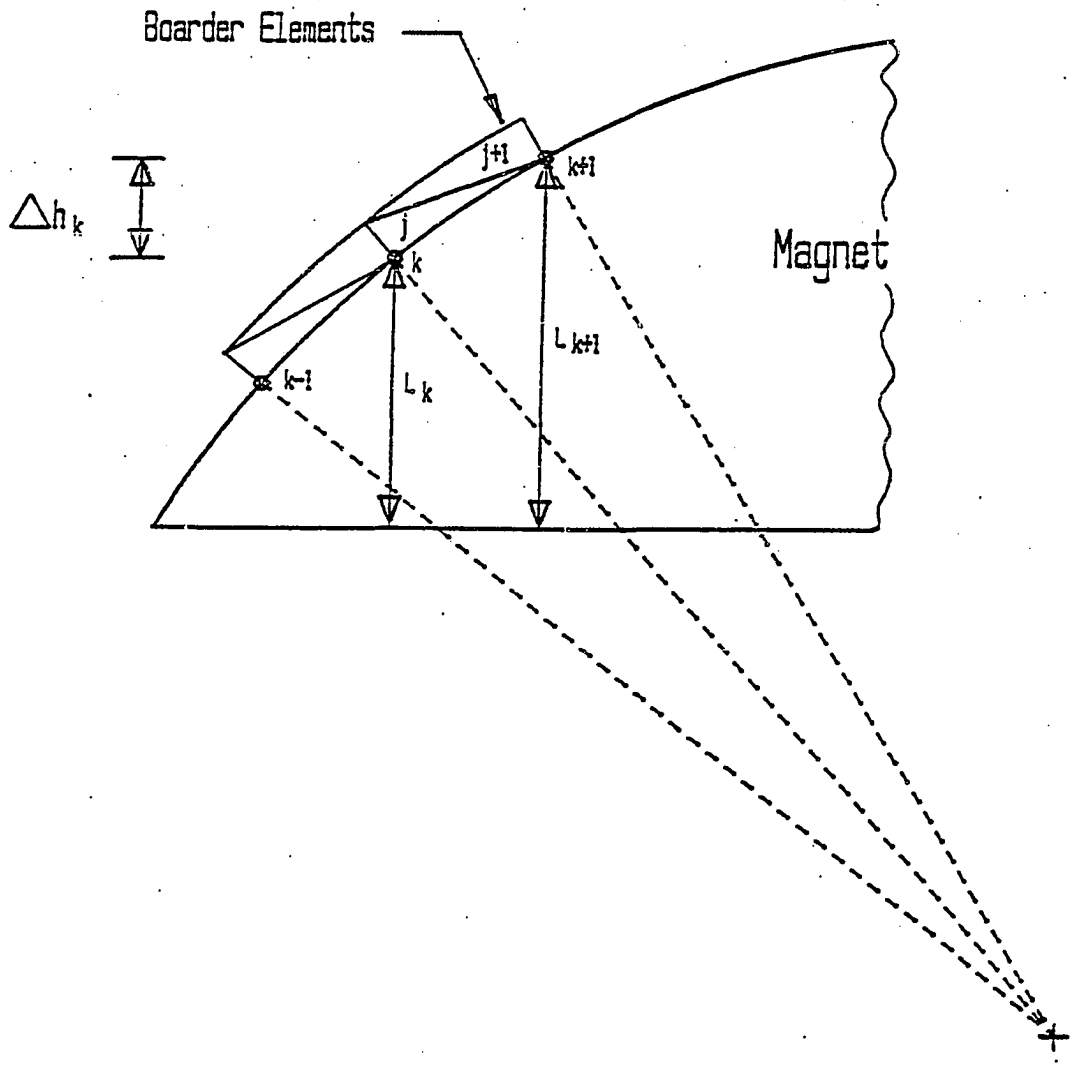

Figure IV-27
Geometry Used for Calculation of
Equivalent Magnetization Currents
of Second Prototype Permanent Magnet Rotor

elements j and j+1 as shown in Figure IV-27.

The distribution of B_{rad} was predicted and compared to measured data. Figure IV-28 shows this comparison. FEM data is indicated by the solid line, and measured data is indicated by X's. Unlike the first prototype, this data seems to correlate well. The FEM predicted waveform shape matches well and the magnitude is within 6% of the experimental value. This would indicate that the original PM model, (model 0), for the first prototype was probably incorrect since similar comparisons did not correlate as well.

Secondly, peak torque values for the new prototype were predicted and measured, Figure IV-29. The same prototype stator and FEM stator models were used for the new prototype as were used for the first prototype. A comparison of torque constants obtained from this plot yields:

$$K_{t2exp} = 65.3 \text{ oz-in/amp}$$

$$K_{t2FEM} = 55.9 \text{ oz-in/amp}$$

$$\% \text{ difference} = -14.4\%$$

This percentage error is consistent with the first prototype results once the annulus distributions matched, (-18.7% for model 1, -14.8% for model 3, the composite model).

Next the detent torque-angle waveform was measured and compared to the predicted one, Figure IV-30. One sees that like the first prototype, there is large discrepancy between the magnitudes of the two waveforms. However, the correlation between the waveform shapes is much better than it was for the first prototype. Since the previous detent torque sensitivity analysis has shown that the detent is

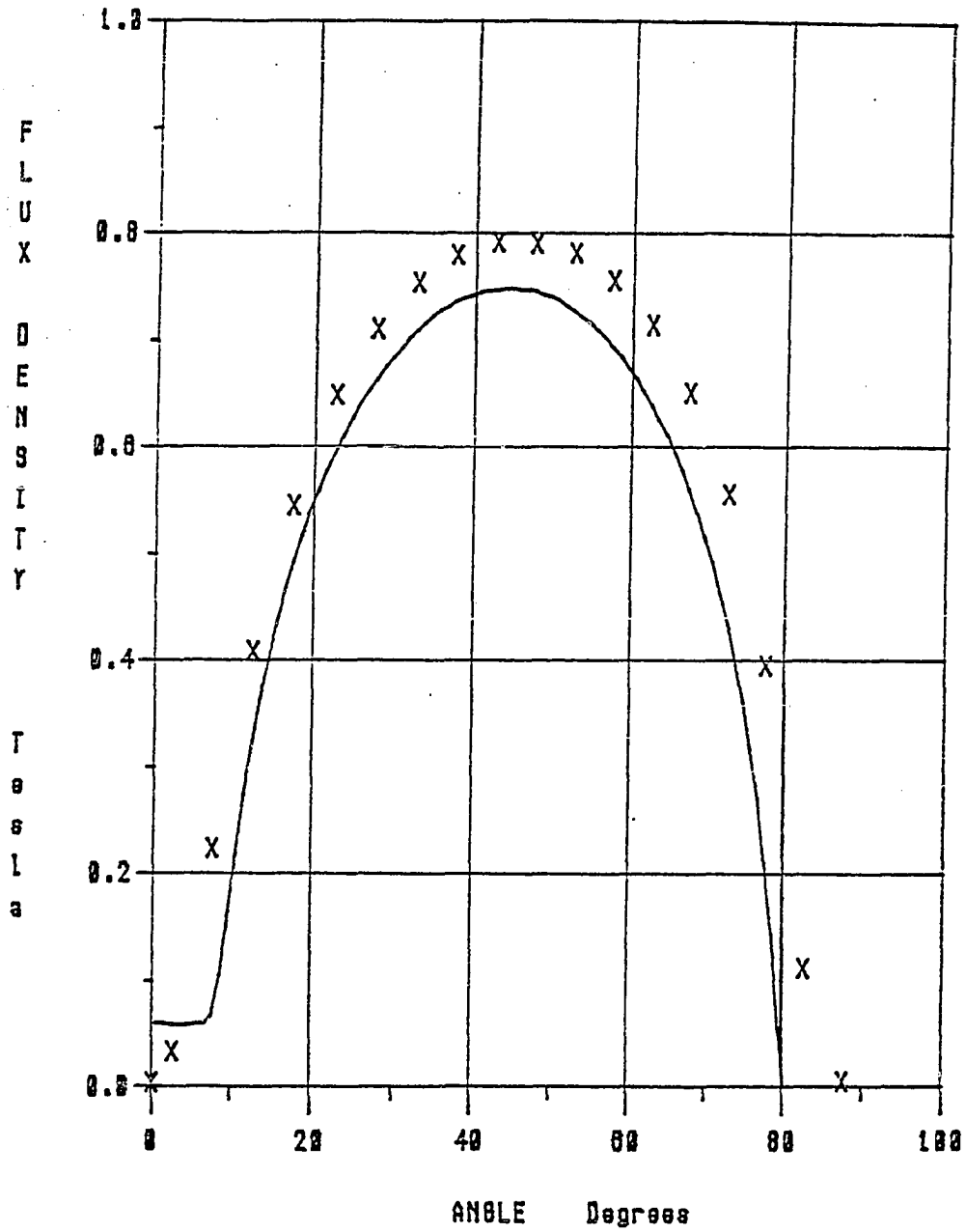

Figure IV-28
Comparison of Measured, (Solid Line), and Finite Element Predicted, (X's), Distribution of Radial Component of Airgap Flux Density over One Magnet Pole Face of Second Prototype Rotor in Annulus.

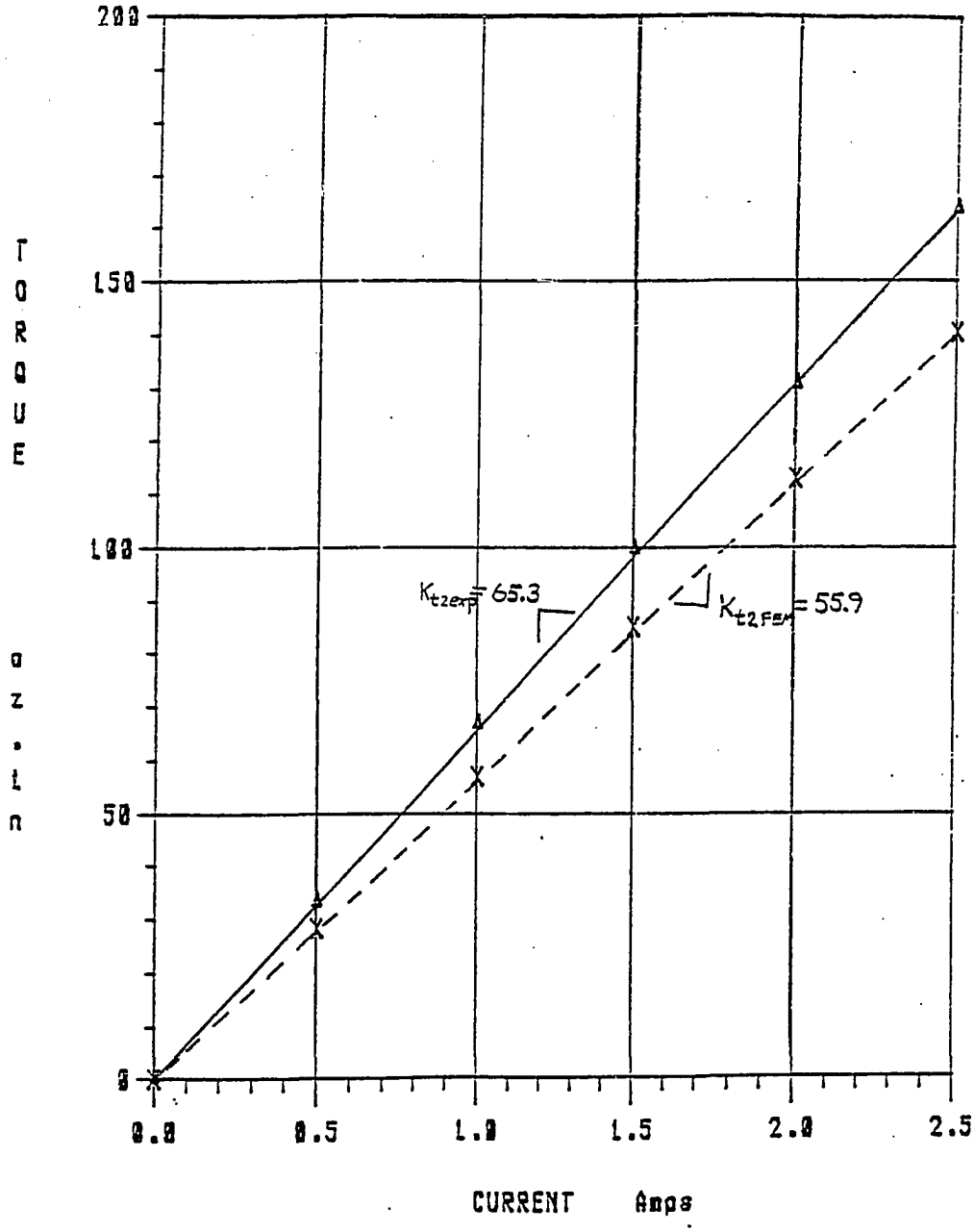

Figure IV-29
Comparison of Measured, (Triangles), and Finite Element Predicted, (X's), One-Phase-On Peak Stator Torque versus Current for Second Prototype Motor

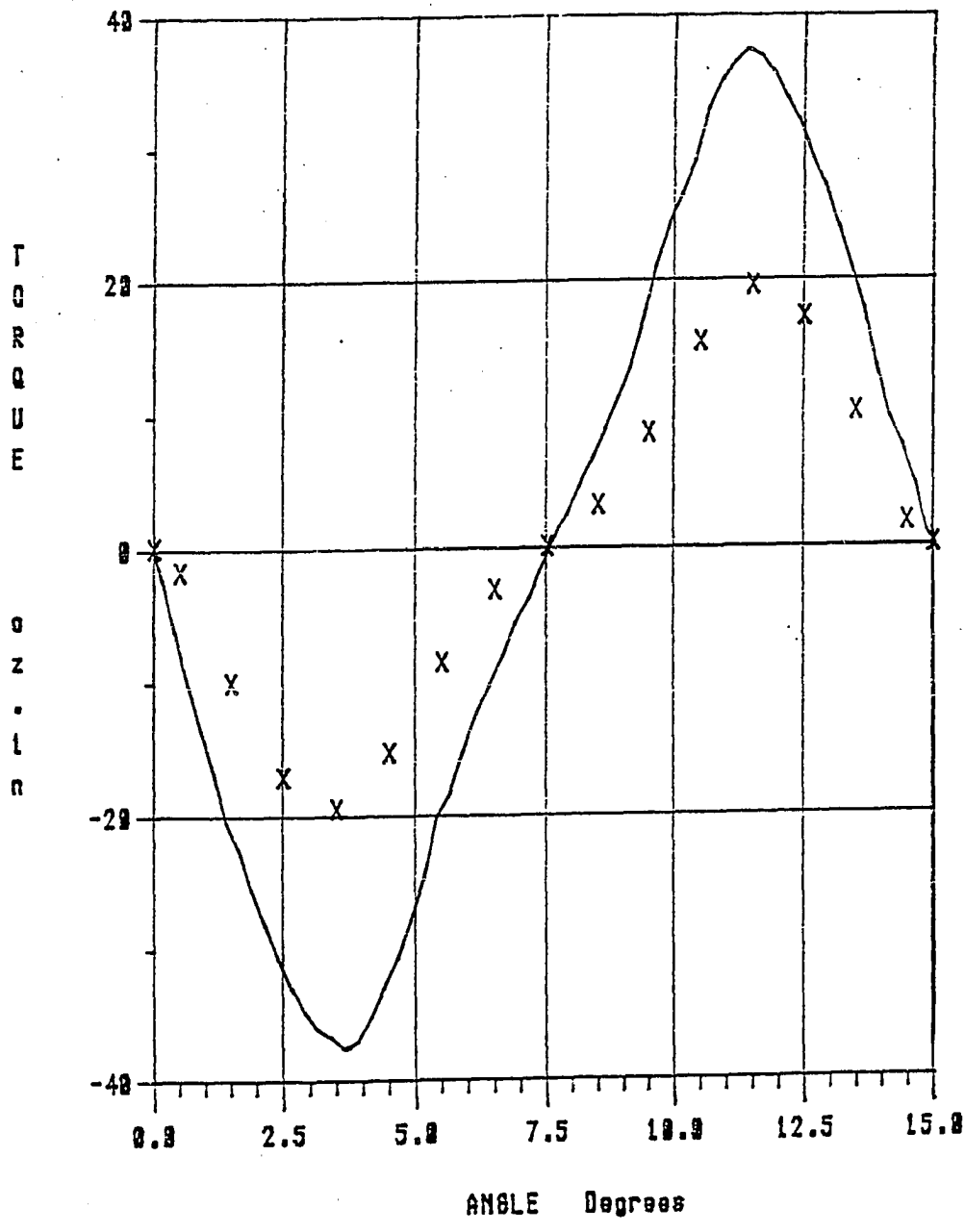

Figure IV-30
Comparison of Measured, (Solid Line), and
Finite Element Predicted, (X's), Detent Torque
versus Angle for Second Prototype Rotor

extremely sensitive to equivalent current placement, it is also assumed to be the primary cause of the discrepancy here.

IV.9 Summary

The original intent of this chapter was to attempt to answer some of the questions raised at the end of Chapter III. Those questions were prompted by discrepancies found between FEM predicted and measured, flux linkage-current characteristics, and detent torque-angle curves. While the differences in the flux linkage-current characteristics were explained by end effects, it gave one cause to wonder if other parameters were significantly influenced by end effects.

In general, the question was raised at the end of Chapter III as to how it was possible to predict some of the parameters with seemingly great accuracy, and not be able to predict other parameters, (such as the detent torque), within 50%. In light of the poor correlation between predicted and experimental detent torque and flux linkage-current characteristics, it was felt that the excellent correlation between predicted and experimental torque constants could have been coincidental. Hence, this chapter documented attempts to ascertain and evaluate reasons for poor correlation.

It was suggested at the end of Chapter III that correlation problems could be caused by coarseness of the mesh, inaccuracies in modeling material saturation properties, inaccuracies in modeling the permanent magnet, and end effects due to the three dimensional nature of the problem. In this chapter it was shown that mesh coarseness and material saturation properties were not a source of inaccuracy.

In Section IV.1 the mesh was refined and it was shown that this had little effect on the resulting torque constant. There was a small effect on the detent torque. However, in light of the subsequent discovery concerning the extreme sensitivity of the detent torque to the placement of the permanent magnet equivalent currents, it is likely that this small effect was primarily due to this sensitivity, and not due to the mesh refinement.

In Section IV.2, torque-angle curves for a VR rotor in the prototype stator were simulated and compared to measured curves. We were careful to produce approximately the same level of flux density in the stator as was attained with the permanent magnet rotor. Good correlation between simulated and experimental curves indicate that the saturation models and mesh geometry are sufficiently accurate to produce good results in the torque calculations. Thus, we are only left with evaluating the end effect and permanent magnet model investigations, and their relation to the detent torque and flux linkage-current characteristic discrepancies.

Table IV-6 summarizes some of the results found in this chapter and in Chapter III. For the VR motor model; prototype motor 1-model 0; prototype motor 1-model 3; and prototype motor 2, the following FEM predicted and experimentally measured characteristic comparisons are listed: 1) Magnitude of the peak detent torque; 2) Overall correlation of detent torque-angle curve shape; 3) Torque constant; 4) Overall correlation of back emf waveform or torque-angle curve shape; 5) Peak value of B_{rad} in the annulus; 6) Overall correlation of B_{rad} distribution shape.

Table IV-6
Partial Summary of Chapter IV Results

Model	Detent Magnitude	Detent Shape	K_t	Back Emf or T-θ shape	Annulus Pk. B_{rad}	Annulus B_{rad} shape
VR @ 4.0 Amp	-	-	6%	excellent	-	-
Proto 1 Model 0	-27%	poor	-1 %	excellent	18%	poor
Proto 1 Model 3	-17%	good	-14%	excellent	8.3%	good
Proto 2	-47.2%	good	-14.4%	good	-6.0%	good

To address the question concerning the detent torque, Section IV.5 clearly showed that detent torque is very sensitive to the placements of the equivalent currents used to model the magnet. While end effects may affect the detent torque slightly, the extreme sensitivity of the detent to the equivalent current placement would seem to be the primary cause for the discrepancy between the FEM and measured results.

This leaves the correlation between torque constants and correlation between annulus flux density distribution to be explained. Recapitulating, when the FEM and measured annulus flux density distributions matched well, (Proto 1-model 3 and Proto 2), the correlation between FEM and experimental torque constants were low by almost 15%, (see Table IV-6). It is doubtful that this could be due to coil end effects since the VR torque constants match very well. However, it could be due to permanent magnet end effects or due to the FEM of the permanent magnet.

It would seem that by making the annulus distributions match, one would include magnet end effects, to some extent. This is not

necessarily true. Making the two-dimensional FEM annulus results match the three dimensional experimentally measured results by modifying the mmf source, is analogous to adjusting the voltage in a circuit with resistance R_1 in order to get the current to match with that in a second circuit of resistance R_2. If one changes the resistances of both circuits, even by the same amount, one will no longer get the same current in both circuits. Using the annulus developed model in a different geometry is, in effect, changing the resistance of the circuit. The net resistance of the three-dimensional magnetic circuit is different from the two-dimensional one modeled. If it is very different, the annulus matching method will not yield good results.

Therefore, it would seem that the discrepancy in torque constants is probably due to a combination of end effects and permanent magnet model. If we allow that end effects will be different depending upon the geometry of the device, a particular two dimensional model of a three dimensional magnet could result in different levels of accuracy, depending upon the geometry with which it is used. Thus, based on the flux linkage analysis of Section IV.3, if the length to width ratio of the permanent magnet is less than 10:1, one should be careful in developing a magnet model based on correlation with measured data obtained from a simple geometry.

IV.10 Conclusions

As a result of the investigations discussed in this chapter the following facts and conclusions are clear.

Detent torque is extremely sensitive to the PM model, specifically

to the placement of currents used to represent the magnets. Small changes in the location of the currents can result in large changes in detent torque. This could make accurate prediction of detent for more complex magnet shapes difficult. This is further complicated by imperfect magnetization of the magnets. In addition, if one is designing motors to have specific detent torque-angle shapes, then one will have to make certain that the magnet manufacturer can produce the modeled magnet accurately and repeatably.

Peak Stator torque does not appear to be very sensitive to precise placement of magnet currents, only to the magnitudes of those currents. This should indicate that simpler magnetic lumped parameter models for peak torque can probably be developed that are of sufficient accuracy. Given the results observed in the investigations discussed in this chapter, the simplest model for the magnet that satisfies our requirements is to use the manufacturer's data for the magnet strength and make the magnet arc width two degrees narrower. This would make the detent torque, the torque constant and stator torque-angle curve, and the back emf constant and waveform match well. None of these parameters seem to be sensitive to a more involved model that predicts the annulus B_{rad} shape more accurately.

Two-dimensional finite element analysis suffers accuracy problems due to end effects. While end effects influence inductance, stator torque and back emf, they seem to have the greatest effect on inductance. Wires lying in the end turn bundles produce flux in the stator air gap. These wires also produce flux at the ends of the motor. Only airgap flux affects torque, but both contributions affect inductance. Hence, end effect flux generally increases the inductance

of the device and can not be predicted by the two-dimensional finite element model. By equivalent coil analogy, the same argument can be made for the permanent magnet. Thus, permanent magnet end effects produce additional flux which tends to produce higher torque and back emf voltages than a two dimensional FEM predicts.

A finite element model for the permanent magnet can be developed by using a trial and error process of matching finite element predicted, and experimentally determined, distributions of radial component of flux density produced by the magnet in the air gap of a simple geometry. A magnet model constructed in this manner yields reasonably good results in predicting other characteristic parameters when that same model is used in a more complicated geometry. However, care should be excerised if the geometry is radically different, or if the length to width ratio of the geometry is less than 10:1.

CHAPTER V

FACTORS AFFECTING TORQUE-ANGLE CURVE SHAPE

In Chapter III it was shown how the FEM could be used to calculate a variety of motor characteristics. In addition, the FEM was verified against experimentally determined motor charcteristics. In this chapter, the FEM is combined with other analytical techniques and used as a tool to explore the parameters which affect the shape of the torque-angle waveform. While it is obvious that one could use the methods described previously in Chapter III to determine the motor torque-angle curve shape for any alterations made in the motor design, those methods often require a large number of finite element solutions. Therefore, in this chapter, simplifying assumptions concerning the magnetic linearity of the device are made. These assumptions allow one to use the principle of superposition and the IxB method to predict torque-angle curve shape from a single FEM solution. This method allows one to develop a general understanding of the primary factors determining the basic torque-angle waveform shape.

While this chapter focuses on one-phase-on stator torque-angle curve shape, it is recognized that detent torque plays a critical role in the overall curve shape. Since many designs attempt to minimize the detent torque in order to lessen its effects, the first section of this chapter discusses some of those approaches and explains how and why they work. Then, in the second section, where the one-phase-on stator torque-angle shape is addressed, the effects of the detent

minimization techniques on the stator torque-angle curve are also included.

V.1 Detent Torque

The presence of detent torque is almost always a cause of concern in the design of BLDCMs. Often, it is desired that the motor produce smooth low speed torque. Detent torque usually adds an unwanted harmonic component to the torque-angle curve, resulting in low speed torque ripple. Therefore, in many BLDCMs, designs are created which attempt to minimize the detent torque. In the following sections, four different methods that can be used to reduce detent torque are discussed.

V.1a Reduction of Detent Torque by Skewing

The most common method of reducing the detent torque is to 'skew' either the rotor magnets or the stator lamination stack. In a skewed stator stack, each stator lamination is rotated a fixed incremental angle, ε, from the preceeding one in the stack. This is illustrated in Figure V-1. Normally, the lamination stach is skewed over one tooth pitch so that the lamination on one end of the stack is displaced from the lamination on the other end by an angular amount equal to one tooth pitch. The laminations in between are displaced by successively lesser amounts so that in looking through the stator at the teeth, the motor has the appearance of having one end twisted with respect to the other end. The magnet edge is no longer aligned with a tooth edge over the entire length of the motor.

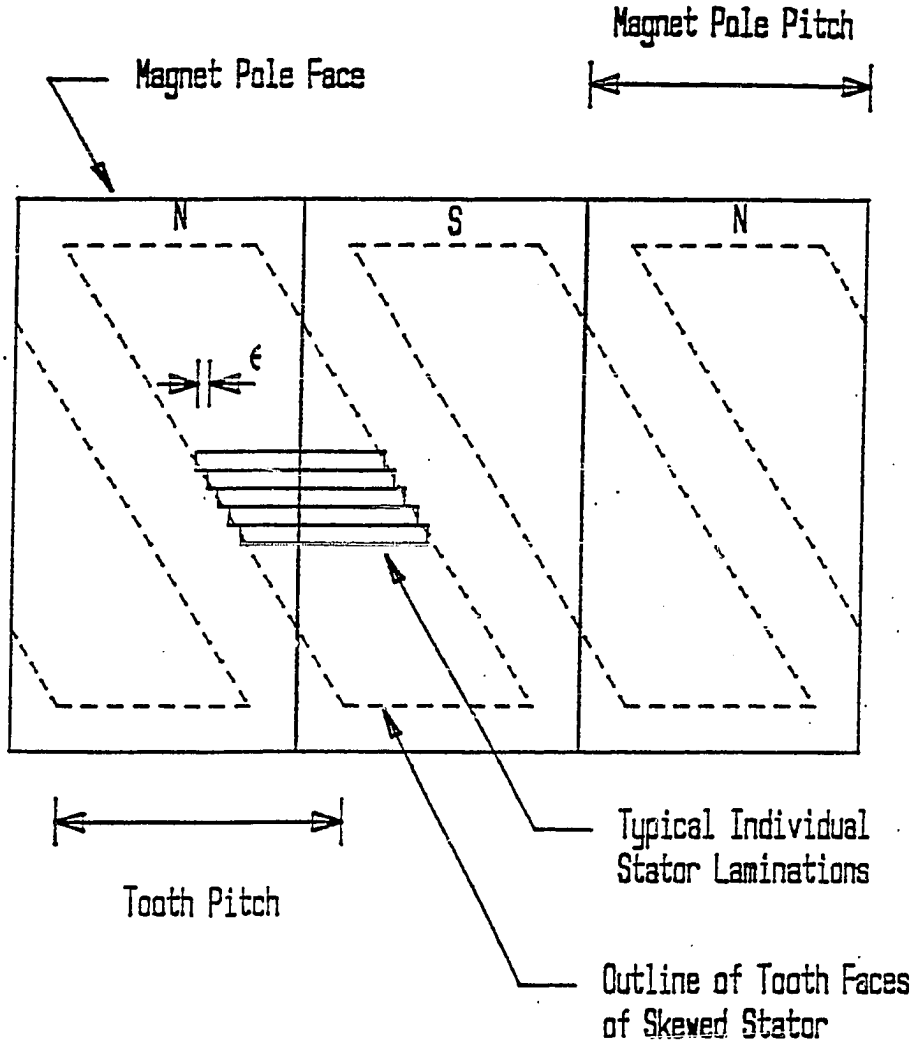

Figure V-1
Skewed Stator Stack

In the example shown in Figure V-1, the tooth pitch is equal to the pole pitch of the magnet. The tooth face outlines are shown as parallelograms but actually have jagged sides due to the finite thickness of the rectangular shaped tooth faces of the individual stator laminations.

It can be shown that skewing results in the virtual elimination of detent torque. First, assume that each of the stator laminations is infinitely thin and that the amount that each lamination is phase shifted is a linear function of the axial position of the lamination in the stack. Second, recognize that each of the stator laminations can be thought of as having a detent torque-angle curve that can be represented by a Fourier series with a fundamental period of one tooth pitch, (a 'per lamination' detent torque-angle curve). Skewing produces a set of phase shifted, per lamination, detent torque-angle curves. The total detent torque-angle curve for the skewed motor, $T_{ds}(\theta)$, due to the sum of the individual lamination contributions is given by Equation V-1. In actual devices, the stator laminations have some finite thickness. Hence, Equation V-1 is an approximation for the average phase shift of each lamination.

$$T_{ds}(\theta) = \int_0^{\ell_z} \sum_k \left[a_k \sin\left(k\left(D_m A\theta + \frac{2\pi z}{\ell_z}\right)\right) + b_k \cos\left(k\left(D_m A\theta + \frac{2\pi z}{\ell_z}\right)\right)\right] dz \qquad \text{(V-1)}$$

$$T_{ds}(\theta) = \sum_k \frac{\ell_z}{2\pi} \left\{a_k \left[\cos(kD_m A\theta) - \cos(k(D_m A\theta + 2\pi))\right] - b_k \left[\sin(kD_m A\theta) - \sin(k(D_m A\theta + 2\pi))\right]\right\} = 0$$

Where: $k \equiv$ Fourier series harmonic index

$a_k \equiv$ Fourier series sine coefficient

$b_k \equiv$ Fourier series cosine coefficient

$z \equiv$ Axial position of lamination in the stack

$\ell_z \equiv$ Axial length of lamination stack

$A \equiv$ Number of north magnet poles

$\theta \equiv$ Angular position of rotor

$D_m \equiv$ Number of stator teeth divided by the number of magnet north poles

If the laminations can be considered infinitely thin, have identical detent torque-angle curves, and the stator is skewed in a continous linear manner, then the net detent torque is zero. Physically, what occurs is that the net detent torque is a summation of the per lamination contributions that are shifted in equal phase increments over one electrical cycle. Therefore, one would expect complete cancellation. In actual practice, the three-dimensional nature of the problem, magnet 'end effects', (leakage in the axial direction from the ends of the magnets to the end laminations), and imprecise skewing result in some laminations having slightly different detent torques. Hence, the summation of all of these phase shifted detent torque curves does not result in perfect cancellation and there is usually some small residual detent torque.

In some devices, the magnet poles are skewed instead of the stator lamination stack. In this case, Equation V-1 is a very accurate description of the skew because one is considering differential slices of the magnet. The individual detent torque-angle curves that were discussed previously are no longer 'per lamination' but 'per diffe-

rential magnet slice'. However, the same analysis applies.

Two skewed stator sections were constructed for the prototype motor. One of these had a stator stack length equal to the rotor depth. The other had a stator stack longer than the rotor. In both cases the skew angle was the same. In other words, the amount of skew over the length of the rotor was the same.

Detent torques for both skewed motors were measured. It was desired to see if the longer stack skewed stator would reduce end effects. The resulting detent torque-angle curves for the single stack and long stack, respectively, are shown in Figure V-2a&b. One sees that the amplitude of the detent in these figures is approximately the same. Therefore, creating a longer skewed stator did little to reduce the end effects. On the other hand, if either of these figures is compared to the original detent for the nonskewed stator, (Figure II-6), one sees that the amplitude of the detent has been reduced from over 60 oz-in to approximately 3 oz-in. A factor of twenty!

One-phase-on stator phase torque-angle curves for the single stack skewed stator were also measured and are shown in Figure V-3a. If one compares this figure with Figure V-3b, the single phase torque-angle curves for a nonskewed stator, one sees that the twelfth harmonic has been significantly reduced by skewing. Hence, skewing not only eliminates the fundamental and harmonics of the detent, but also eliminates all harmonics of the one-phase-on stator torque that are a higher frequency than the detent torque fundamental. As current levels get higher, some of the twelfth harmonic seems to reappear; this is probably due to a combination of end effects of local saturation of the

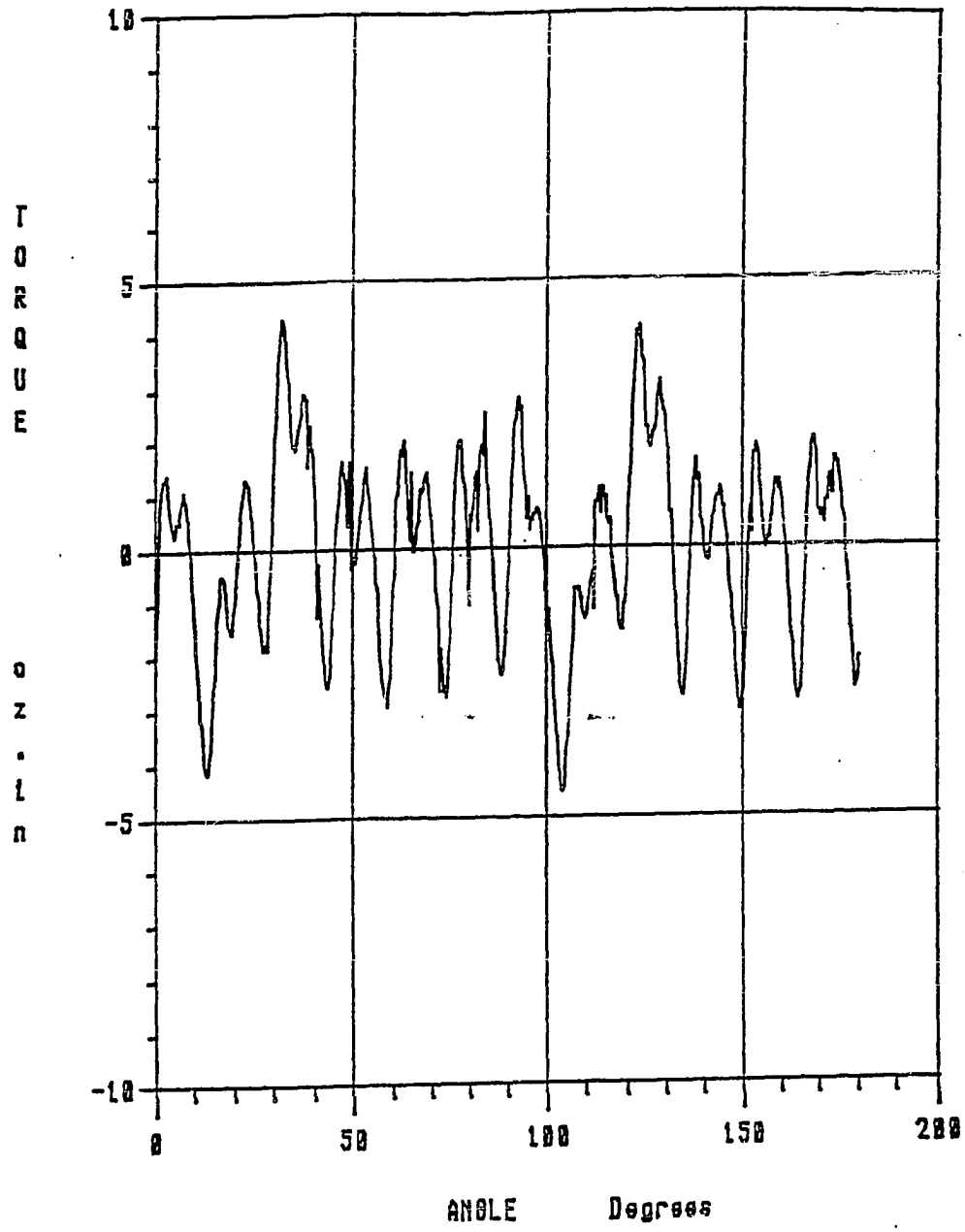

Figure V-2a
Measured Detent Torque for
Single Stack Skewed Stator

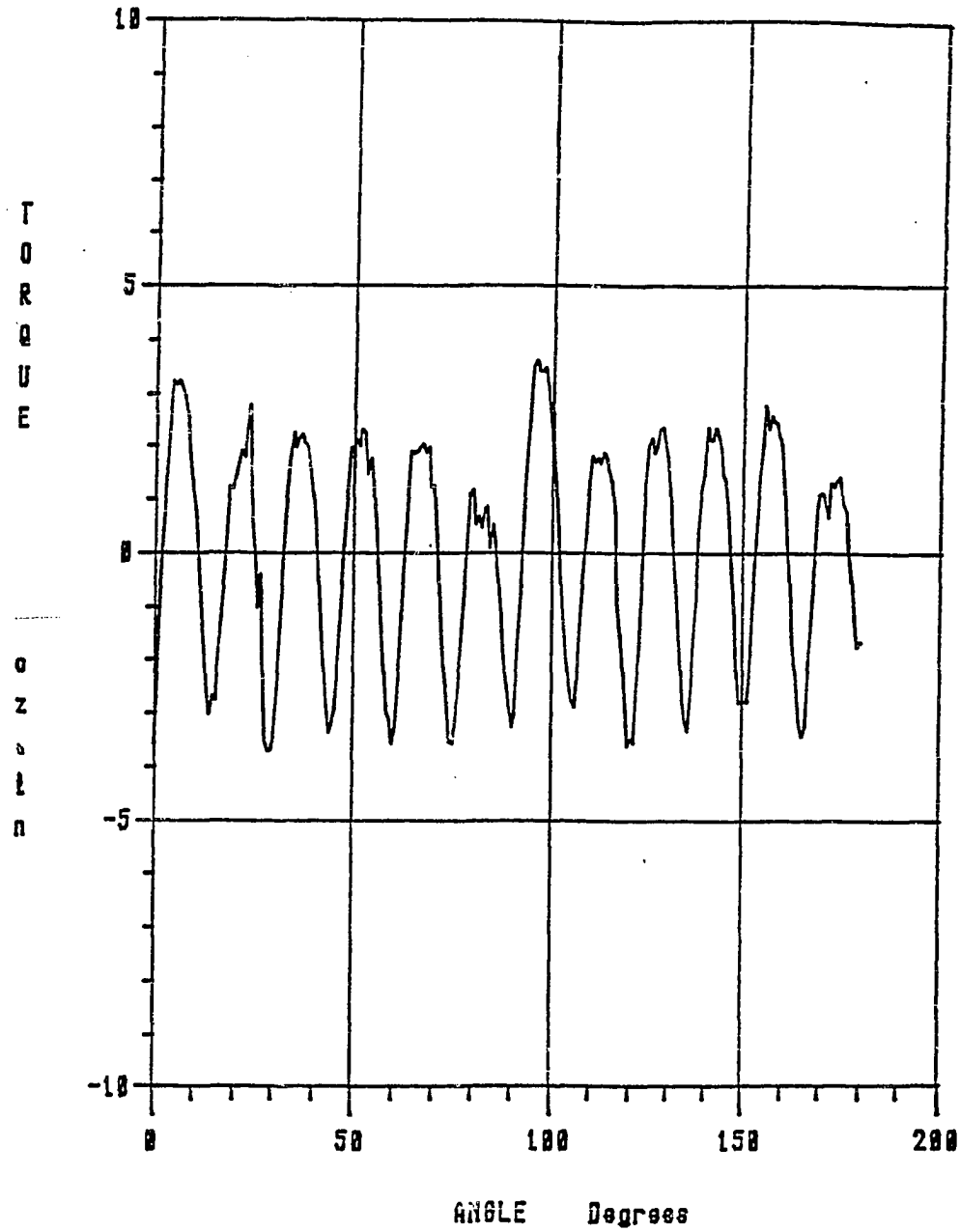

Figure V-2b
Measured Detent Torque for
Long Single Stack Skewed Stator

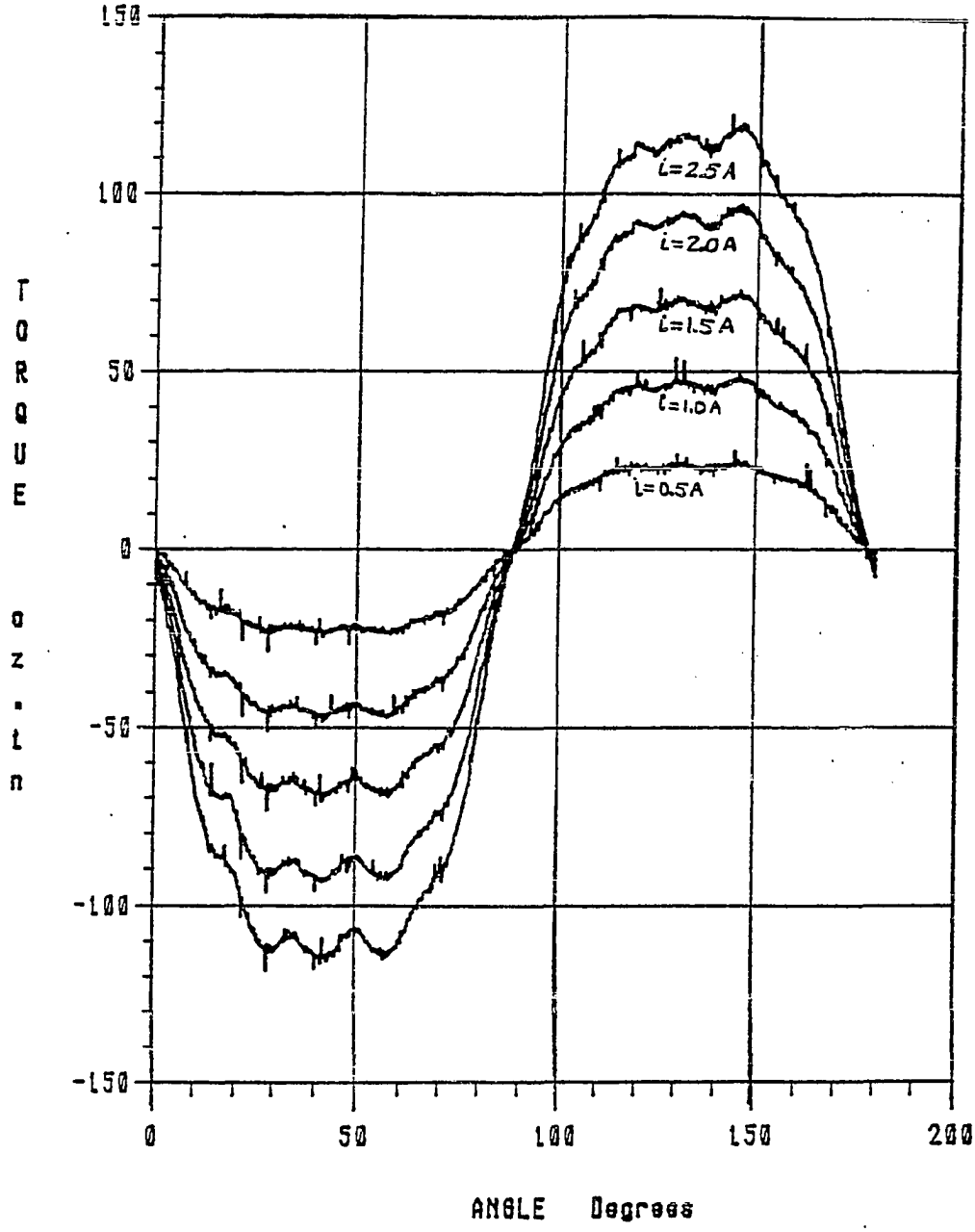

Figure V-3a
Measured One-Phase-On Stator Torque-Angle
Curves for Single Stack Skewed Stator

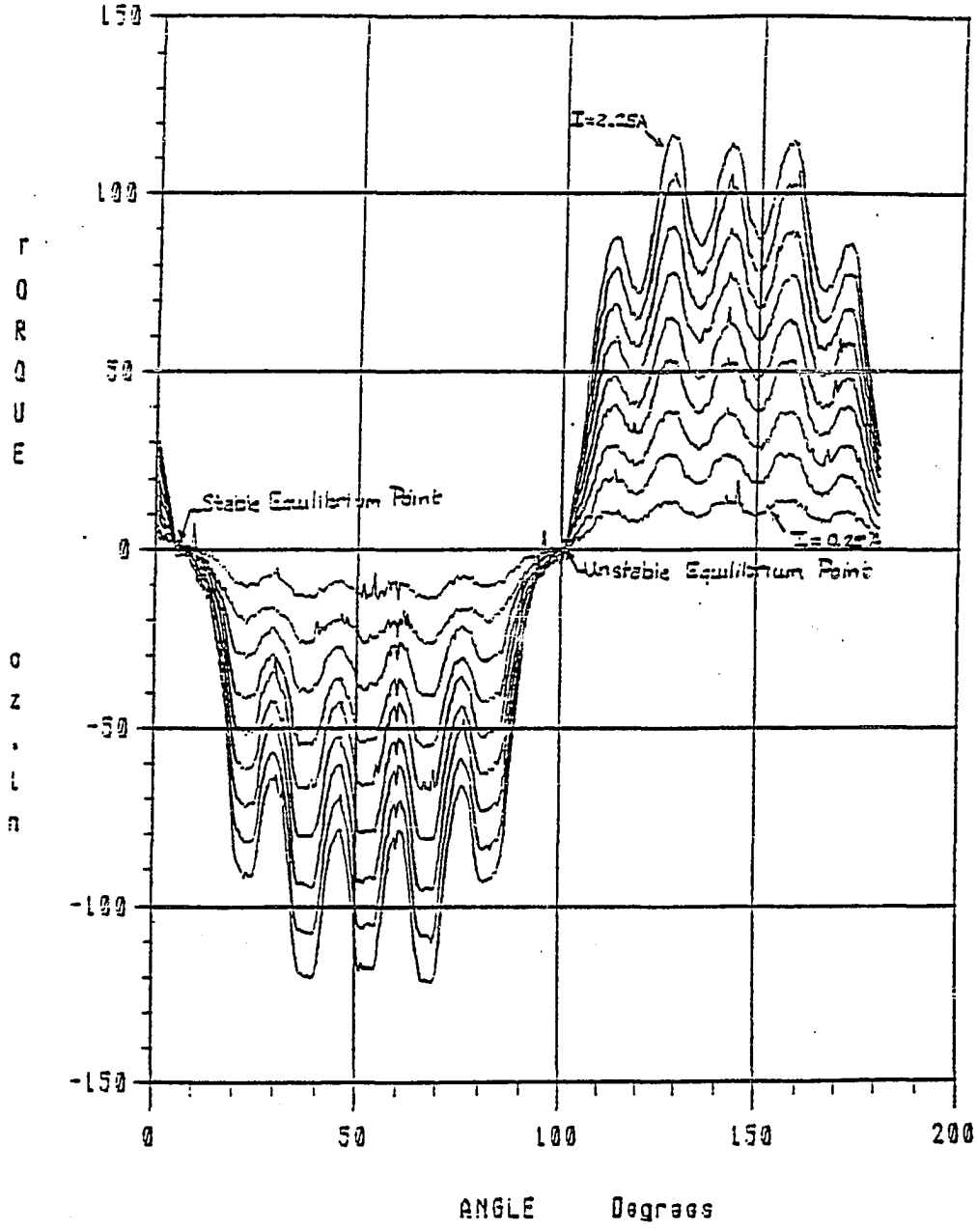

Figure V-3b
Measured One-Phase-On Stator
Torque-Angle Curves for Nonskewed Stator

tooth tips.

The peak torque data was taken from the skewed single phase stator torque-angle curves and used to find K_t for each of the skewed motors:

K_{tss} = 46.11 oz-in (Torque constant for single stack skewed motor)

K_{tls} = 48.52 oz-in (Torque constant for long stack skewed motor)

When these values are compared to the torque constant measured for the nonskewed single stack prototype motor, (K_{tns} = 50.2 oz-in), one sees that K_{tss} is approximately 8% less than K_{tns}, and K_{tls} is approximately 3% less. (To be strictly rigorous, K_{tls} should be compared to K_t for a nonskewed long stack motor.)

Theoretically, the reduction in K_t for the single stack skewed motor should be approximately 1% less than that of the nonskewed motor. This is shown by an analysis similar to Equation V-1. If the total stator torque is a linear function of stack length, (provided stator and rotor are the same length), then the 'per lamination', or differential stator torque is:

$$dT_{tot} = \frac{K_{tns}}{\ell_z} I \sin(A(\theta + \frac{\gamma z}{\ell_z})) \qquad \text{(V-2)}$$

Where: $T_{tot} \equiv$ Total torque produced

$\gamma \equiv$ amount of skew over motor length

All other parameters are as defined previously

The total stator torque for the skewed stator is found by integrating dT_{tot} over the length of the motor.

$$T_{tot} = \int_{-\ell_z/2}^{\ell_z/2} \left\{ \frac{K_{tns}}{\ell_z} I \sin(A(\theta + \frac{\gamma z}{\ell_z})) \right\} dz \qquad \text{(V-3)}$$

$$= \frac{1}{A\gamma} \sqrt{(1-\cos A\gamma)^2 + (\sin A\gamma)^2} \; K_{tns} \; I \sin(A\theta)$$

If an effective torque constant, K_{tess}, is defined for the skewed stack stator in terms of the skew angle, γ, and the torque constant of the nonskewed stator, K_{tns}, as:

$$K_{tess} = \frac{1}{A\gamma} \sqrt{(1-\cos A\gamma)^2 + (\sin A\gamma)^2} \; K_{tns} \qquad \text{(V-4)}$$

Then, for a skew angle of 15 degrees, as in the prototype skewed stator, and a 4 pole rotor, K_{tess} is:

$$K_{tess} = 0.989 \; K_{tns} \qquad \text{(V-5)}$$

This is a very small reduction in torque constant. The measured reduction was actually greater. The discrepancy could be due to nonidentical per lamination stator torque-angle curves or neglecting higher harmonics in the skewed torque constant analysis. The latter is most probably the cause. Comparison of Figures V-3a and V-3b showed that skewing eliminated a twelfth harmonic from the one-phase-on stator torque-angle curve. This harmonic added to the peak torque. Thus, the elimination of this harmonic decreased the torque constant more than would have been expected by an analysis of skewing effects on a sinusoidal single phase stator torque-angle curve. If the torque constant had been based on the average peak torque, (excluding the ripple), then the reduction in K_t would have been much less.

V.1b Reduction of Detent Torque by Staggering

In some cases, instead of skewing the magnet shape, several magnet segments are created and each of these are staggered by a certain angle, (Figure V-4). This is similar to skewing the stator laminations. When the laminations are skewed the desired continous skew is really quantized into a set of discrete angles. Staggering magnet segments is also the quantization of a continous magnet skew. The difference is that when the stator laminations are skewed, the result was a relatively fine quantization because there are usually a large number of stator laminations in a stack. However, staggering a few magnet segments produces a coarse quantization. This coarse quantization affects the net detent torque.

The net detent torque will be a function of the number of phase shifted detent torque-angle curves, i.e. the number of staggered magnet segments, and the harmonic content of each curve. For example, suppose the 'per segment' detent torque-angle curve consisted purely of a fundamental with no higher harmonics. The detent torque could be eliminated by creating two identical magnet segments that were phase shifted, or 'staggered' by one half a tooth pitch, (see Figure V-5a). Figure V-5b shows the corresponding torque-angle curves. T_{D1}, the detent torque due to magnet segment 1, is 180 degrees out of phase with T_{D2}, the detent torque due to set 2. Therefore, the net detent torque is zero.

The stator torque-angle curves, T_{S1} and T_{S2}, are also shown in Figure V-5b. These curves always have a greater period than the detent torque. Consequently, there will be a net nonzero stator torque-angle curve with a magnitude which is reduced by the process of

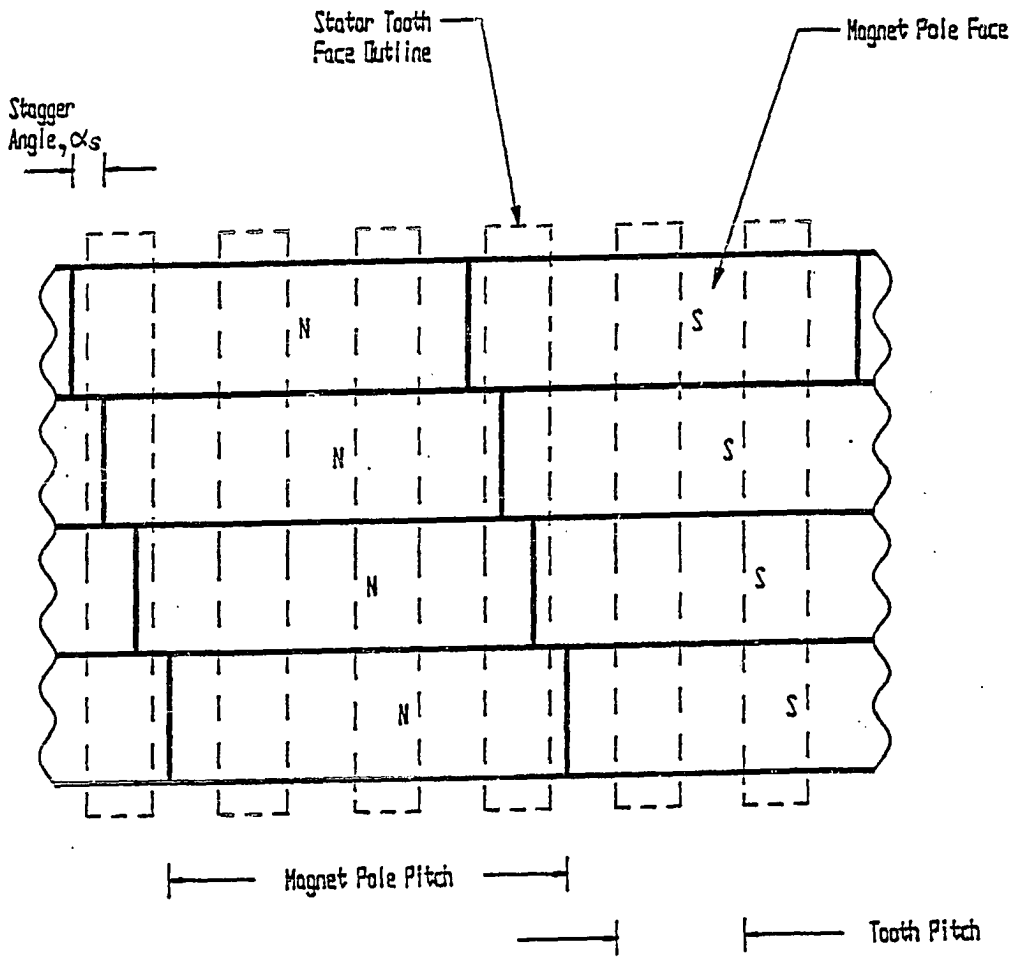

Figure V-4
Staggered Magnet Segments

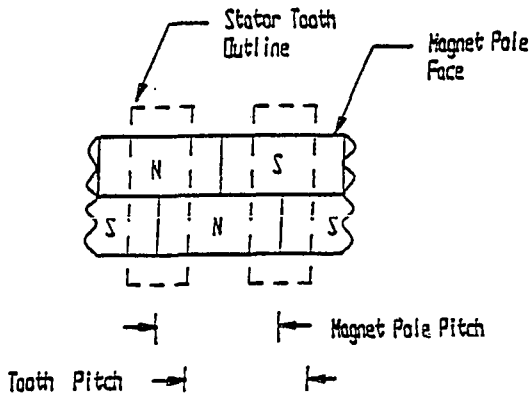

Figure V-5a
Two Staggered
Magnet Segments

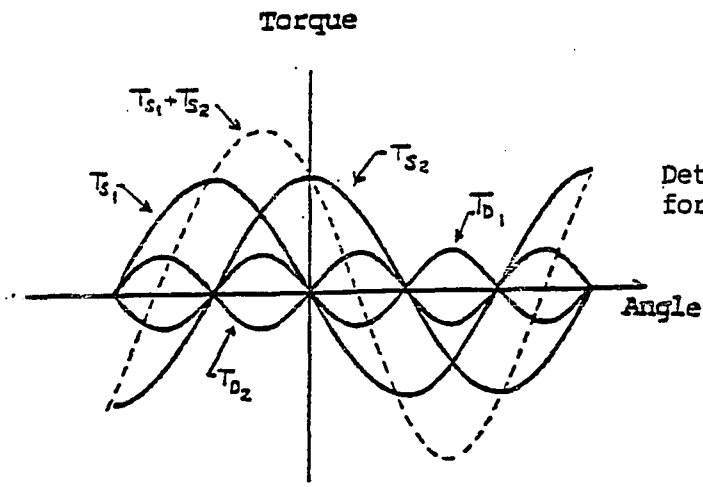

Figure V-5b
Component Stator and
Detent Torque-Angle Curves
for Two Staggered Segments

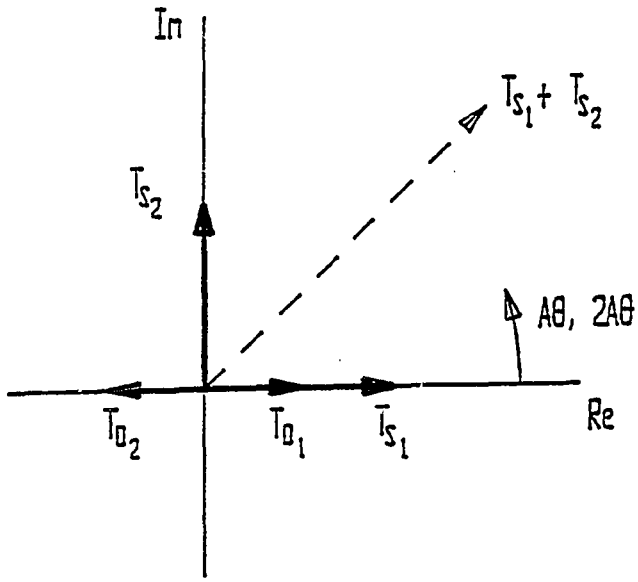

Figure V-5c
Vector
Representation
of Detent and
Stator Torque-Angle
Curves for Two
Staggered Segments

staggering. If there had been no staggering, these curves would have been in phase and the magnitude of the total torque would simply be the sum of the two magnitudes.

In general, the amount that the net stator torque magnitude is reduced, is a function of the number of staggered segments, the angle that each segment is staggered and the ratio of the number of stator teeth to rotor poles. Each of these aspects will affect the relative phase shift of the individual stator torque-angle curves which are summed.

The net detent and stator torque contributions can also be analyzed easily in a vector diagram, Figure (V-5c). This type of representation becomes more advantageous as more sets of phase shifted detent torque curves are added (i.e. more sets of magnet segments) or as higher harmonics are included, as is demonstrated in the following example.

Suppose one has the six slot, three phase, two pole motor shown in Figure V-6. The period of the stator torque, in mechanical degrees, is 360 divided by half the number of rotor poles, or 360 mechanical degrees. The period of the detent torque corresponds to the tooth pitch, which is 360 divided by the number of stator teeth, or 60 mechanical degrees in this example. Suppose further, that the rotor is divided axially into four segments which are staggered evenly over one tooth pitch, as was shown in Figure V-4. The physical stagger angle, α, in mechanical degrees is equal to the tooth pitch divided by the number of staggered segments.

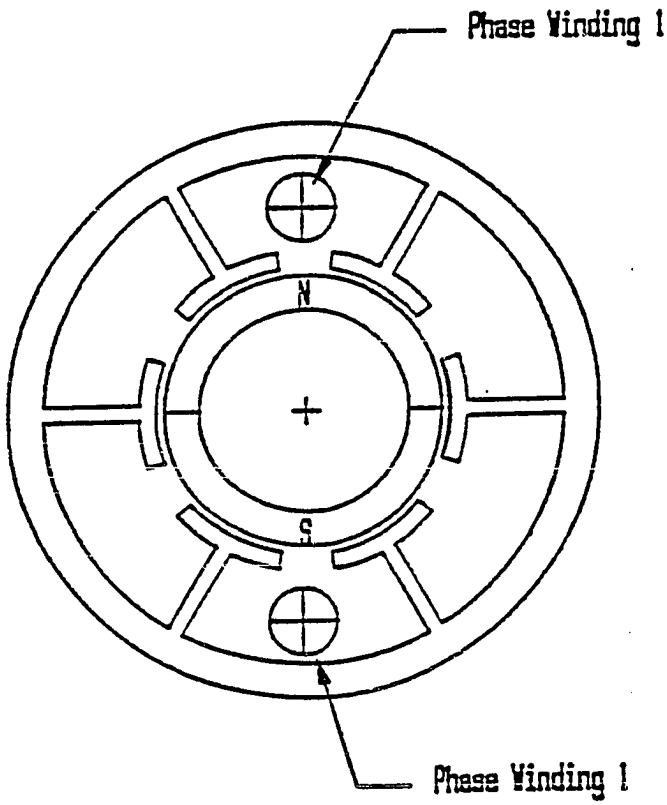

Figure V-6
Example Six Slot, Two Pole,
Three Phase Brushless DC Motor

$$\tau_s = 360/N_p/2 = 360$$

$$\tau_d = 360/N_t = 60$$

$$\alpha_s = \tau_d /N_s = 15.$$

Where: N_s ≡ Number of staggered segments (4 for this example)

τ_s ≡ Stator torque period

τ_d ≡ Detent torque period or tooth pitch

N_t ≡ Number of stator teeth (6 in this example)

N_p ≡ Number of rotor poles (2 in this example))

The result is that there are four stator torque-angle curves; one for each magnet segment. Each has a period of 360 mechanical degrees and is phase shifted by 15 electrical degrees from the torque-angle curve of the adjacent magnet segment. There are also four detent torque curves. Each of these has a period of 60 mechanical degrees and is shifted by 90 electrical degrees from the next detent torque curve. If it is assumed that there are no harmonics present in either the stator or detent torque-angle curves, then the vector representations for both of these torques are shown in Figure V-7a and V-7b. T_{D1} through T_{D4} represent the detent torques. T_{S1} through T_{S4} represent the one-phase-on stator torques. T_{Snet} is the resulting one-phase-on stator torque. It is obvious that the net detent torque is zero and the net stator torque is less than it would have been if all four vectors had been in phase. Suppose, however, that higher harmonics are added to the detent torque. The second through sixth harmonics are included and shown in Figure V-7c. The number on each vector in

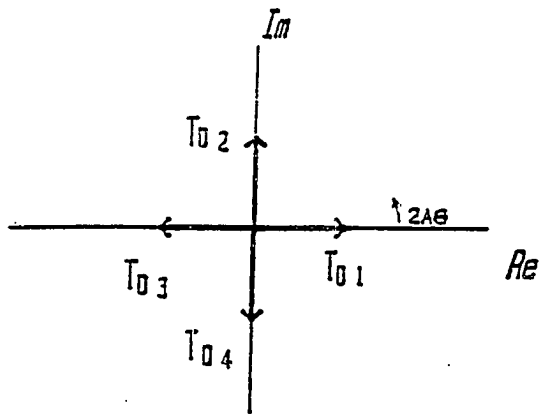

Figure V-7a
Detent Torque Vectors for Example
Motor with Four Staggered Segements

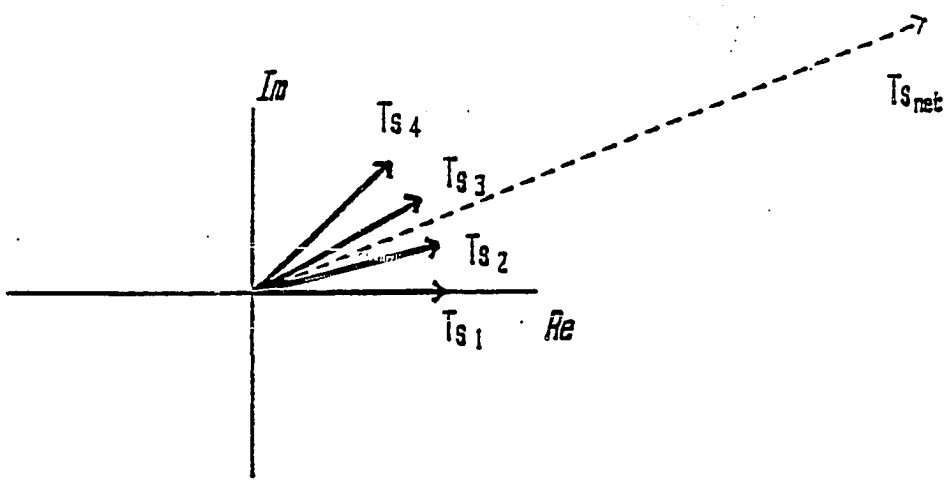

Figure V-7b
Stator Torque Vectors for Example
Motor with Four Staggered Segments

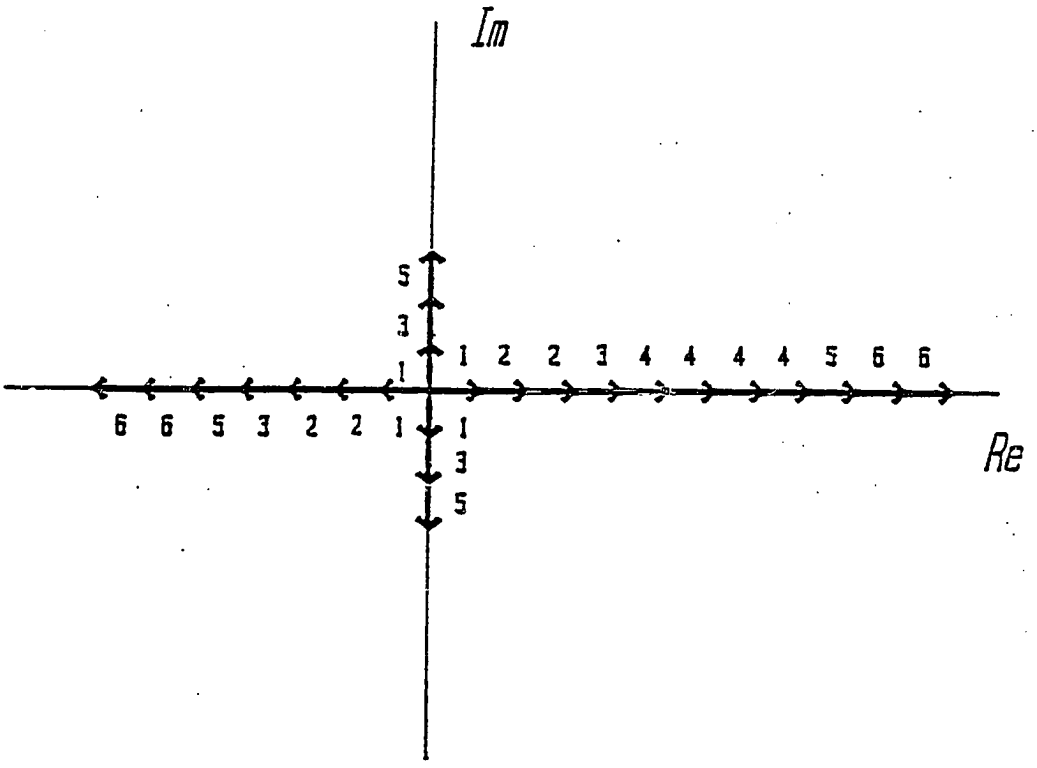

Figure V-7c
Detent Torque Vectors Including
Higher Harmonics for Example
Motor with Four Staggered Segments

this figure indicates the harmonic; there are four vectors, corresponding to the four detent torque-angle curves, for each harmonic. It is clear that the fundamental, the second, third and fifth and sixth harmonics cancel. However, the fourth harmonic is still present and its magnitude has not been reduced. If the analysis is carried further, one can see that the following generalizations can be made:

1) If the number of staggered segments, N_s, is even, all higher odd harmonics cancel.

2) If the number of staggered segments, N_s, is odd, all higher even harmonics cancel.

3) All higher harmonics that are an integer multiple of N_s will be present and their resultant magnitude will be the same as for a nonstaggered rotor.

4) The greater the ratio of stator torque period to detent torque period, the lesser the reduction in magnitude of the resultant stator torque vector.

Overall, one sees that staggering seems to be an effective means of reducing the detent torque, provided a reasonable number of staggered segments are used. Hence, one would expect to use this method on longer motors.

V.1c Reduction of Detent Torque By Altering the Magnet Arc Width

Another method exists which can be used to reduce detent torque in a permanent magnet BLDCM. It too is based upon cancellation of component detent torques. However, it is different than either stagger-

ing or skewing. Both of those methods use the fact that an incremental length of motor has a detent torque-angle curve associated with it, and that by introducing a phase shift between incremental lengths, the net detent is decreased. This method alters the detent torque by changing the magnet arc width.

In Chapter IV, Section IV.5 it was shown that the magnitude of the detent torque changed by as much as 70% for a 5 degree, (14%), change in magnet width for the prototype motor. That investigation was repeated in this section for radially oriented arc segment magnets, as shown in Figure V-8. To eliminate the effects of saturation in this investigation, a magnetically linear material model for the stator and rotor back irons was used. The resulting set of detent torque-angle curves is shown in Figure V-9a and V-9b. Figure V-9a shows a set of curves for magnet arc widths from 90 degrees to 81 degrees. Figure V-9b shows a similar set for magnet arc widths from 81 degrees to 76 degrees. One sees that at 76 degrees the detent torque is significantly reduced. In fact, it has decreased from 60 oz·in for a full width magnet, to approximately 10 oz·in.

In addition to the change in detent torque magnitude, one sees from these figures that the detent torque curve shape is most sinusoidal around 85 degrees. In the previous section, which described a component detent torque cancelation scheme, staggering magnet segements was discussed. It was shown that if the detent torque-angle curve was purely sinusoidal one would only need to have two staggered magnet segments to completely eliminate the detent torque. Obviously, the ability to alter the detent torque-angle curve shape to make it more sinusoidal is very desirable. A combination of the two schemes:

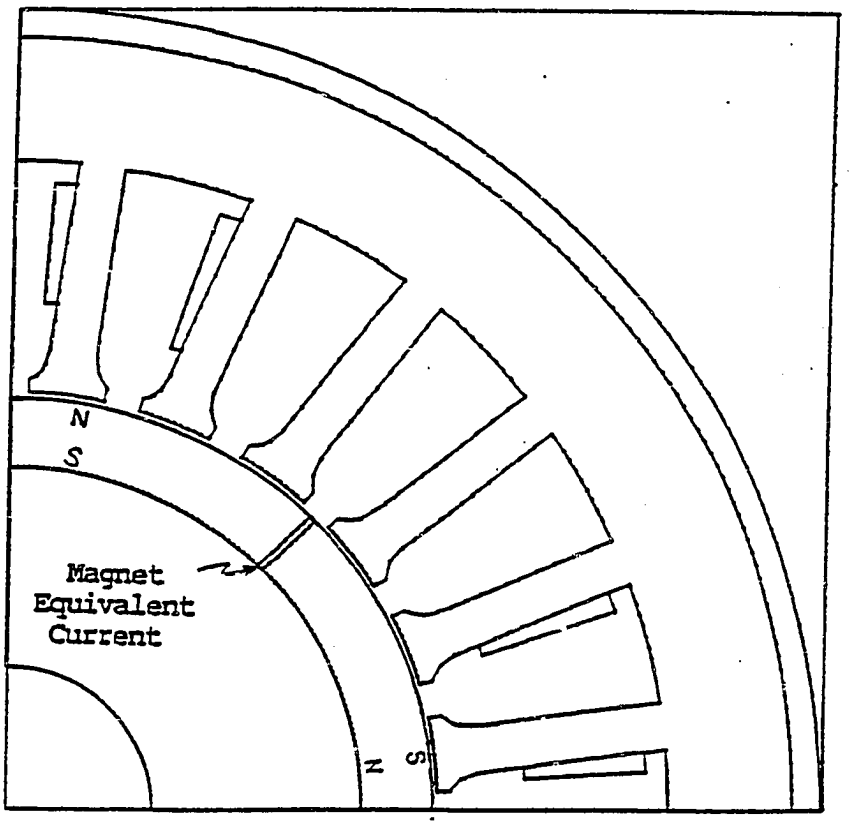

Figure V-8
Finite Element Outline for 4 Pole,
24 Slot Motor with 90 Degree Arc Shaped Magnets

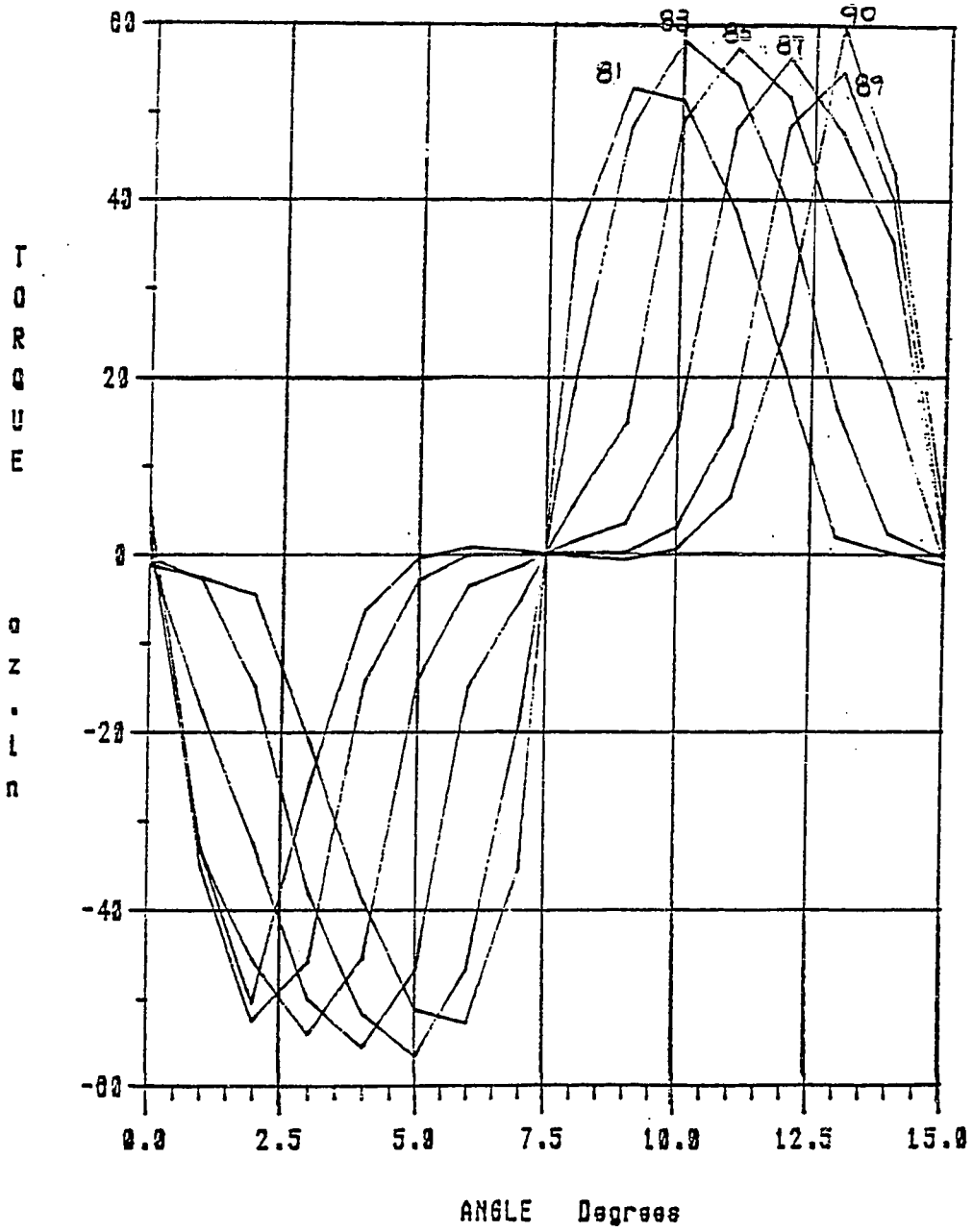

Figure V-9a
Comparison of Detent Torque-Angle Curves
for Magnet Arc Widths of 81,83,85,87,90 Degrees

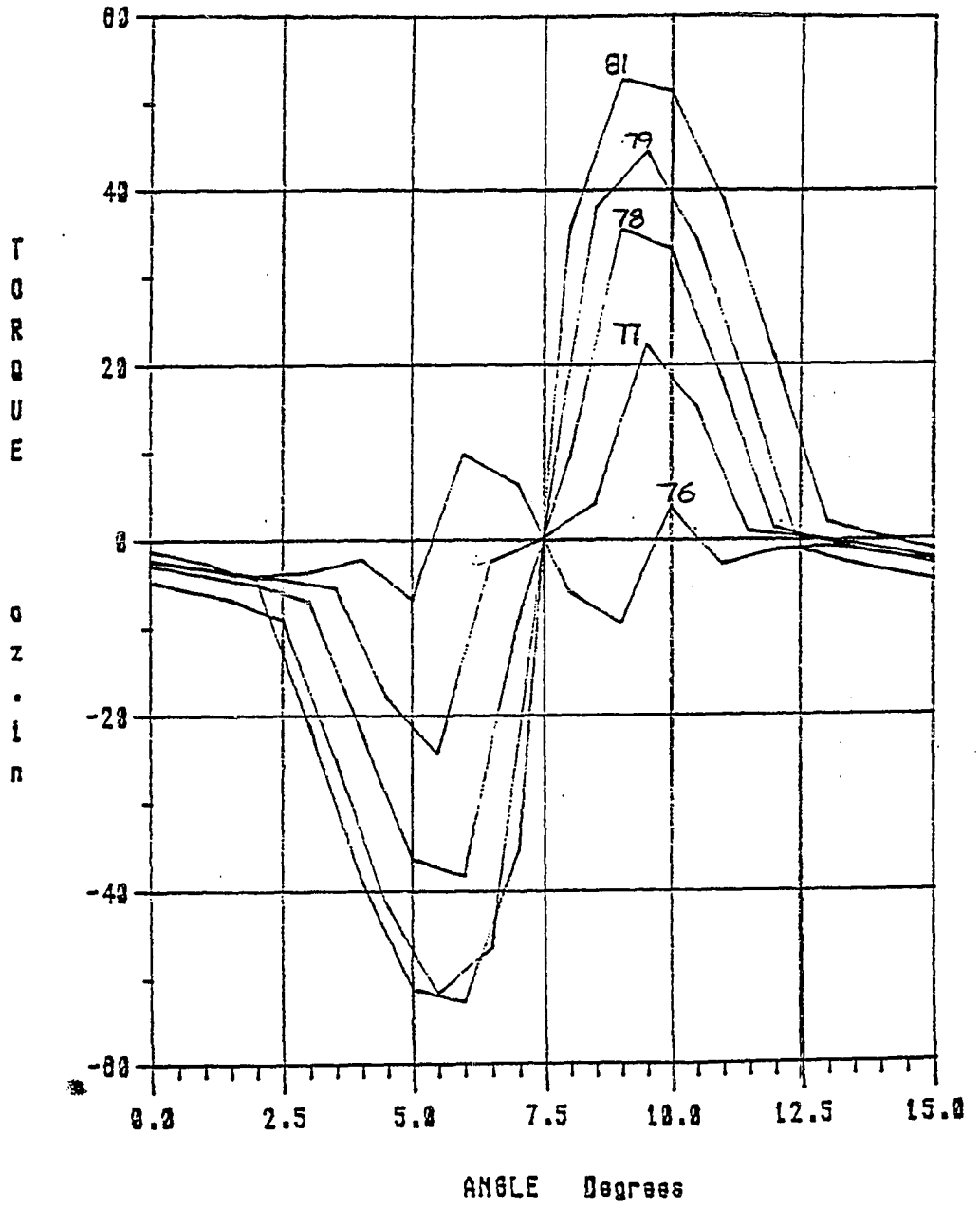

Figure V-9b
Comparison of Detent Torque-Angle Curves
for Magnet Arc Widths of 76,77,78,79,81 Degrees

altering the magnet width to achieve a more sinusoidal curve, and then staggering magnet segments, can be used to achieve a further reduction of the detent.

In trying to understand why the detent torque is significantly reduced as the magnet arc width is reduced to 75 degrees, superposition and the IxB method can be used. First, consider the sheet current used to represent the edge of the magnet. If the sheet current were placed in air, a symmetric field would be produced. Thus, any forces generated in one section of the sheet current would be canceled by equal and opposite forces generated in its symmetric counterpart. However, in the presence of iron, the field is distorted so it is not symmetric in the region of the sheet current. Therefore, a net force occurs on the sheet current that can be calculated by the IxB method. This force causes a torque to be produced on the rotor. Obviously, if more than one sheet current is present then the total detent torque on the rotor will be the sum of the total detent torque-angle curves for each sheet current.

The detent torque contributions are illustrated in Figure V-10a and V-10b. Figure V-10a shows results from a magnet arc width of 83 degrees and Figure V-10b shows results from a magnet arc width of 76 degrees. Three curves are shown in each of these figures. Curve (1) is the torque calculated by using the IxB method on sheet current 1. This curve represents one complete cycle of the detent torque-angle curve for this current sheet. Similarly, curve (2) shows the torque due to sheet current 2. Curve (3) is the net torque due to the sum of Curves (1) and (2). In both figures, curves (1) and (2) have a large DC bias. The bias results from a field in the region of each current

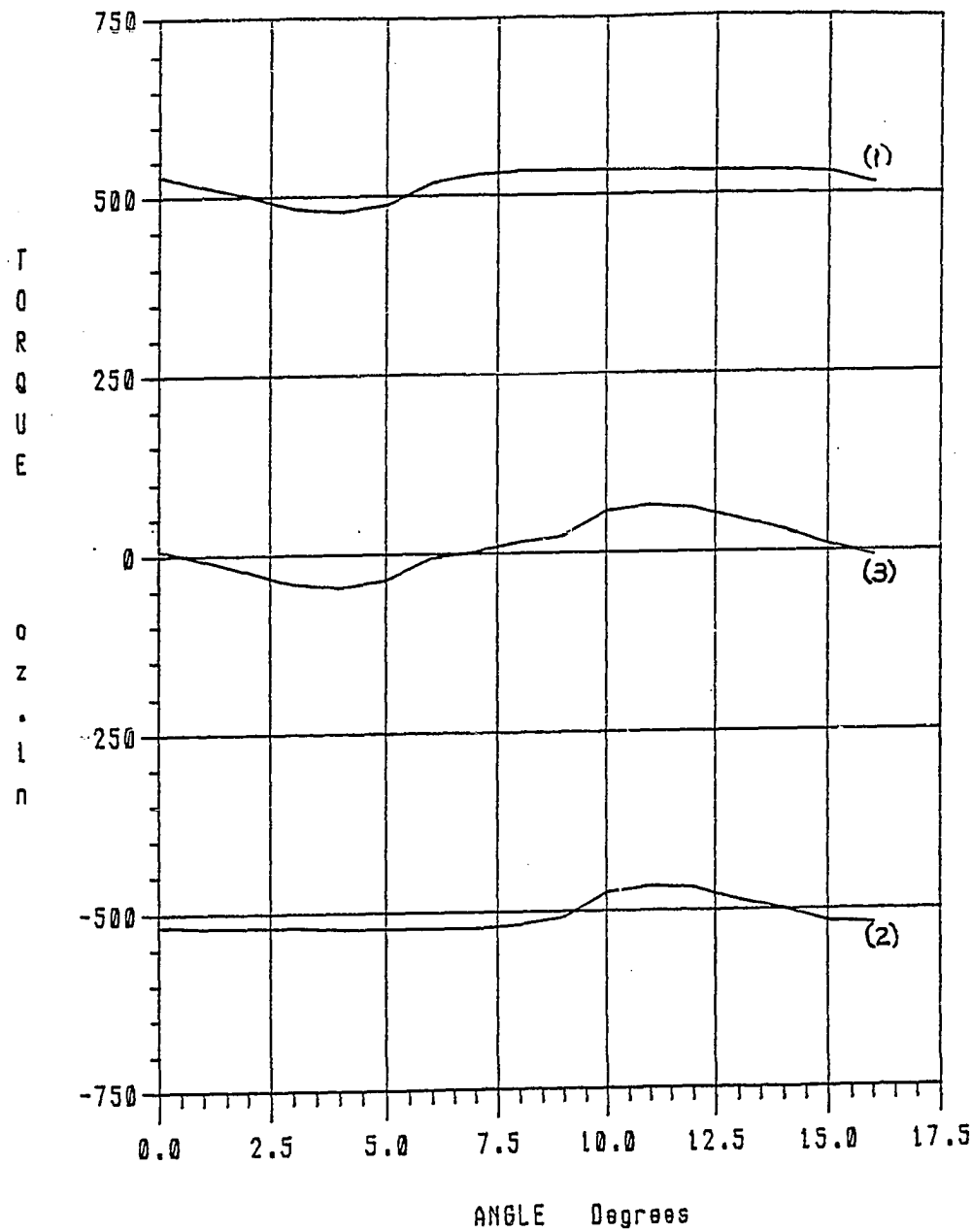

Figure V-10a
Individual Sheet Current Detent Torque
Contributions for a Magnet Arc Width of 83 Degrees
Curve (1)- Contribution Due to Sheet Current 1
Curve (2)- Contribution Due to Sheet Current 2
Curve (3)- Net Detent Torque Due to Both Contributions

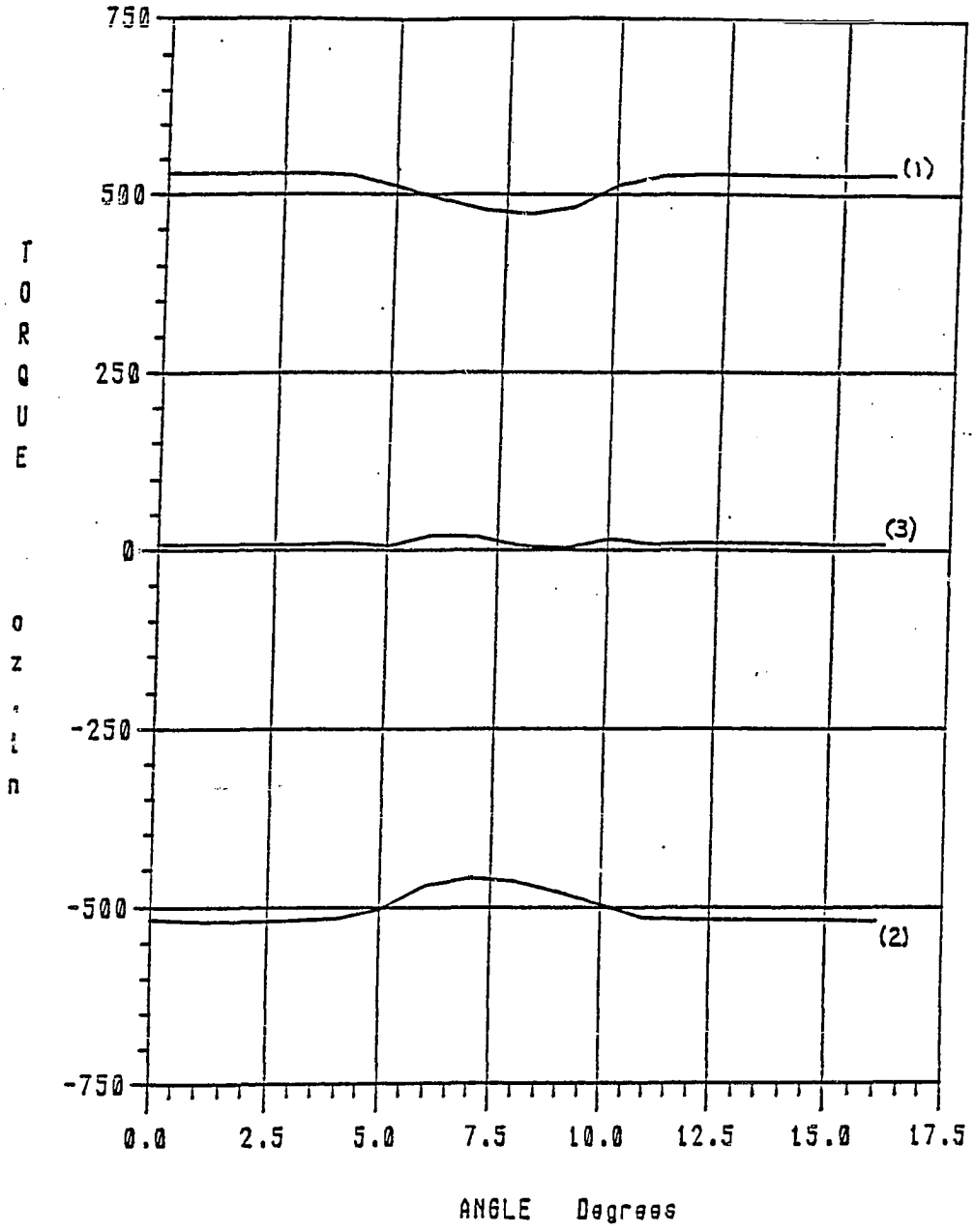

Figure V-10b
Individual Sheet Current Detent Torque
Contributions for a Magnet Arc Width of 76 Degrees
Curve (1)- Contribution Due to Sheet Current 1
Curve (2)- Contribution Due to Sheet Current 2
Curve (3)- Net Detent Torque Due to Both Contributions

sheet that is caused by the presence of the other current sheet. In the sheet current model there is an interaction between sheet currents causing forces on each other. This interaction is what prevents one from considering the detent torque resulting from a single current sheet alone, and then adding other phase shifted current sheets so that the corresponding phase shifted detent torque-angle curves add in such a manner as to achieve cancellation. Because of the interaction between current sheets, the detent torque curve resulting from one current sheet changes as a result of the location of the other current sheet.

Stated another way, the detent torque can be separated into two parts: 1) The 'self' detent torque which results from the distortion of the field in the region of the current sheet and is caused by the presence of the iron stator teeth. There are two of these contributions corresponding to the two sheet currents. 2) The 'mutual' detent torque which results from the field due to one sheet current causing a force to be generated at the other sheet current. Since each sheet current influences the other, there are also two of these contributions.

There is also a slight DC bias in curve (3), the net detent torque curve, in either Figures V-10a or V-10b. This is due to error in the field solution caused by the assymetry in the mesh triangulation. This was discussed previously in Chapter III, Section III.2a.

In Figure V-10b, curves (1) and (2) are roughly 180 degrees out of phase. Thus the net detent torque is minimized. The detent torque is not completely eliminated because the waveforms are not perfectly symmetric about 7.5 degrees in this figure. In Figure V-10a, curves

(1) and (2) are not 180 degrees out of phase, therefore the net detent torque is not minimized because there is no cancelation.

One sees that this method of anaylsis can be used to quickly understand how to minimize detent torque. Looking at individual detent torque components allows one to see what magnet width is most likely to result in component cancelation. Thus, many trial and error iterations can be eliminated.

V.1d Reduction of Detent Torque by Creating Unequal Width Magnets

Detent torque reduction can also be achieved by creating unequal width magnets. This is best understood if one thinks of each magnet interface (an adjacent set of magnet currents) as having a detent torque-angle curve associated with it. Using the methods previously described in Section V.1c, that detent torque curve should be shaped so that it is reasonably sinusoidal.

Figure V-11 shows an outline of a FEM of a half section of a motor. Three magnet segments are modeled with two magnet interfaces. The motor geometry used in this FEM is similar to that used in the previous section which showed how to alter the detent torque-angle curve shape by changing the span between magnet edge currents, i.e. changing the width of the magnet. The magnet edges in this FEM are radial and are 7^0 apart.

Figure V-12 shows the component detent torque-angle curves for each of the interfaces. Curve (1) is the detent torque produced by interface 1 of Figure V-11. Curve (2) is the detent torque produced by interface 2; it is identical to Curve (1). Curve (3) represents the net detent due to both interfaces.

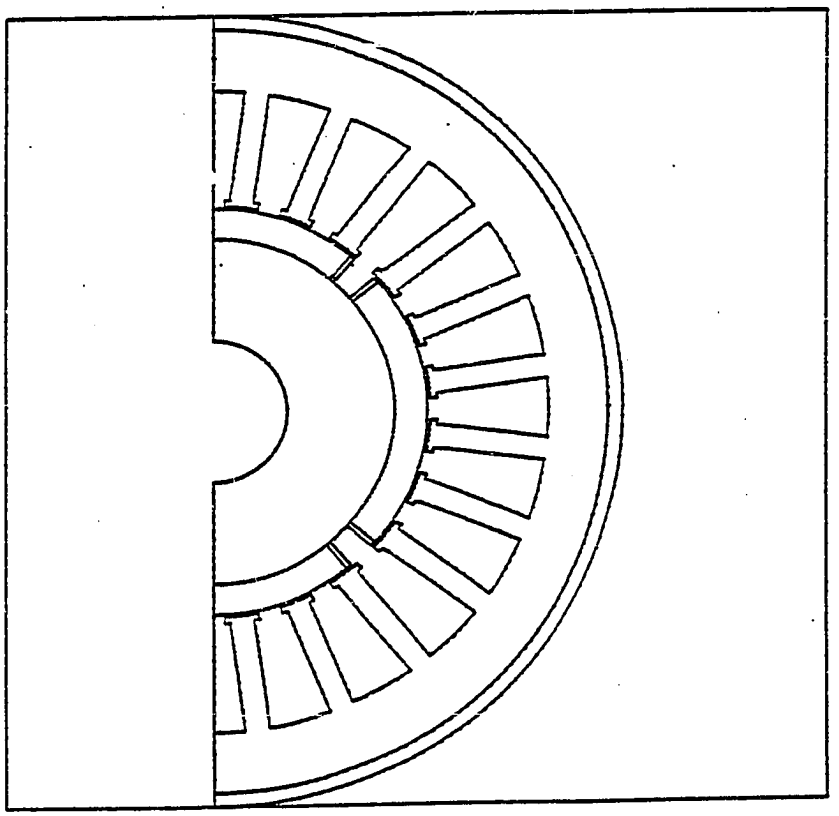

Figure V-11
Finite Element Model Outline
of 180 Degrees of the Motor

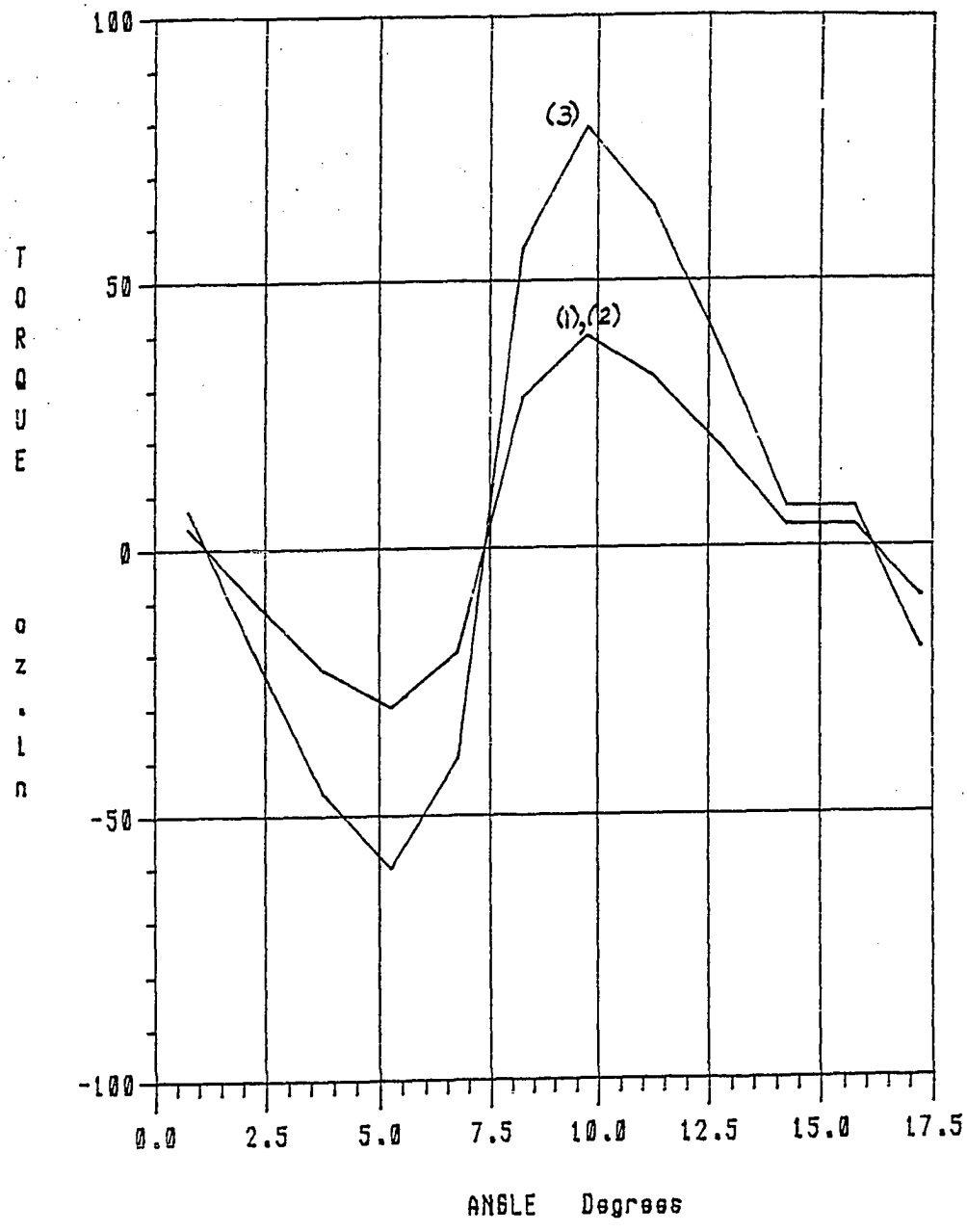

Figure V-12
Individual Sheet Current Detent Torque
Contributions for Each Magnet Interface
Curve (1)- Contribution Due to Sheet Current 1
Curve (2)--Contribution Due to Sheet Current 2
Curve (3)- Net Detent Torque Due to Both Contributions

To minimize the detent torque, interface (2) should be placed so that its detent torque curve is 180^0 out of phase with that of interface (1), (one half of a tooth pitch). This will result in cancelation of component detent torques.

The rotor constructed in this manner will have magnets which are of unequal arc widths and alternate short and long. The motor should have a high ratio of slots to poles to ensure that the presence of one interface does not have much of an effect on the adjacent one. The high ratio of slots to poles reduces the 'mutual' detent torque, (described in the previous section), between interfaces.

Figure V-13 shows a FEM outline of motor in which the interfaces have been offset as described. The resulting detent torque curves are shown in Figure V-14. Again, Curve (1) is for interface (1), Curve (2) is for interface (2) and Curve (3) is the net detent torque. One sees from comparing Curve (1) in Figures V-12 and V-14 that the shape and magnitude of the component detents has not been changed by the relocation of the adjacent interface. One also sees in comparing Figures V-12 and V-14 that the net detent torque has only been reduced by a factor of two. It has not been eliminated because the component curves were not purely sinusoidal. Hence, while the fundamental components canceled, the higher harmonics did not.

Creating these unequal arc width magnets is similar to constructing a motor stator with an odd number of slots. When one constructs a normal rotor with equal width magnets and an even number of slots the magnet interfaces are all in the same position relative to a tooth. Therefore, the detent torque curves for each interface are in phase and add. When there are an odd number of slots, the interfaces are

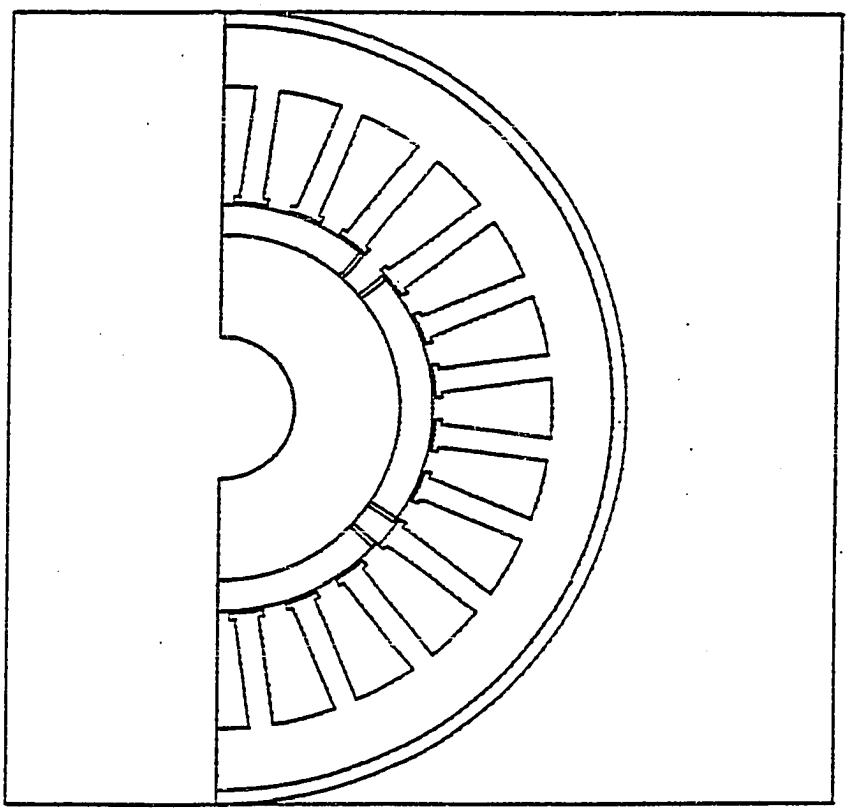

Figure V-13
Finite Element Model Outline of 180
Degrees of Motor with Unequal Arc Width Magnets

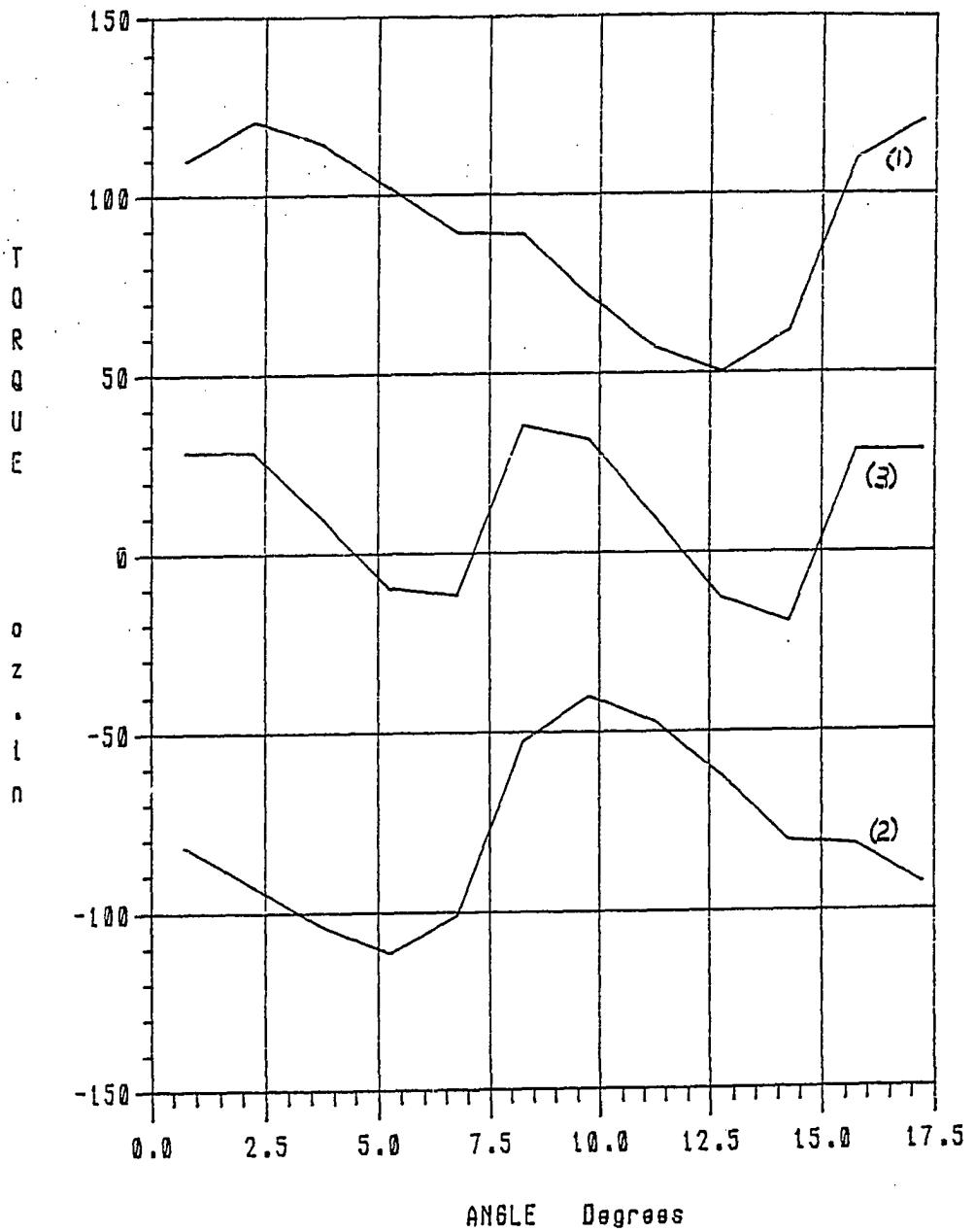

Figure V-14
Individual Sheet Current Detent Torque
Contributions for Unequal Arc Width Magnet
Curve (1)- Contribution Due to Sheet Current 1
Curve (2)- Contribution Due to Sheet Current 2
Curve (3)- Net Detent Torque Due to Both Contributions

phase shifted by an amount which depends on the relative number of slots and magnet poles. Thus, an odd number of slots can reduce the detent torque. For example, a 9 slot, 2 pole motor would have magnet interfaces which are shifted by one half a tooth pitch, or 180 electrical degrees. Thus, the magnitude of the resultant detent will be reduced because the component detents are not in phase. However, unless the component detent curves are purely sinusoidal, complete cancellation will not occur.

An additional drawback that occurs with using an odd number of stator slots is one does not obtain a symmetrical winding. For example, the portion of the coil winding that produces a magnetic north pole will not span the same number of teeth as the portion that produces a magnetic south pole. Ultimately this will affect the shape of the torque-angle curve. How the torque-angle curve is altered depends on the winding distribution and the degree to which the coil winding is assymetric.

V.2 Stator Torque-Angle Waveform

In Chapter III, the IxB method was introduced where the magnet equivalent currents were treated as true currents and used to calculate torques at different rotor positions. This method can be taken one step further if it is assumed that saturation effects are negligible. Then, superposition can be applied so that the rotor magnetic field and coil magnetic field can be separated.

Suppose one starts with a 24 slot, 4 pole motor similar to the prototype motor. An outline of one quarter of the motor is shown in Figure V-15. The coil shown consists of a single winding spaning all

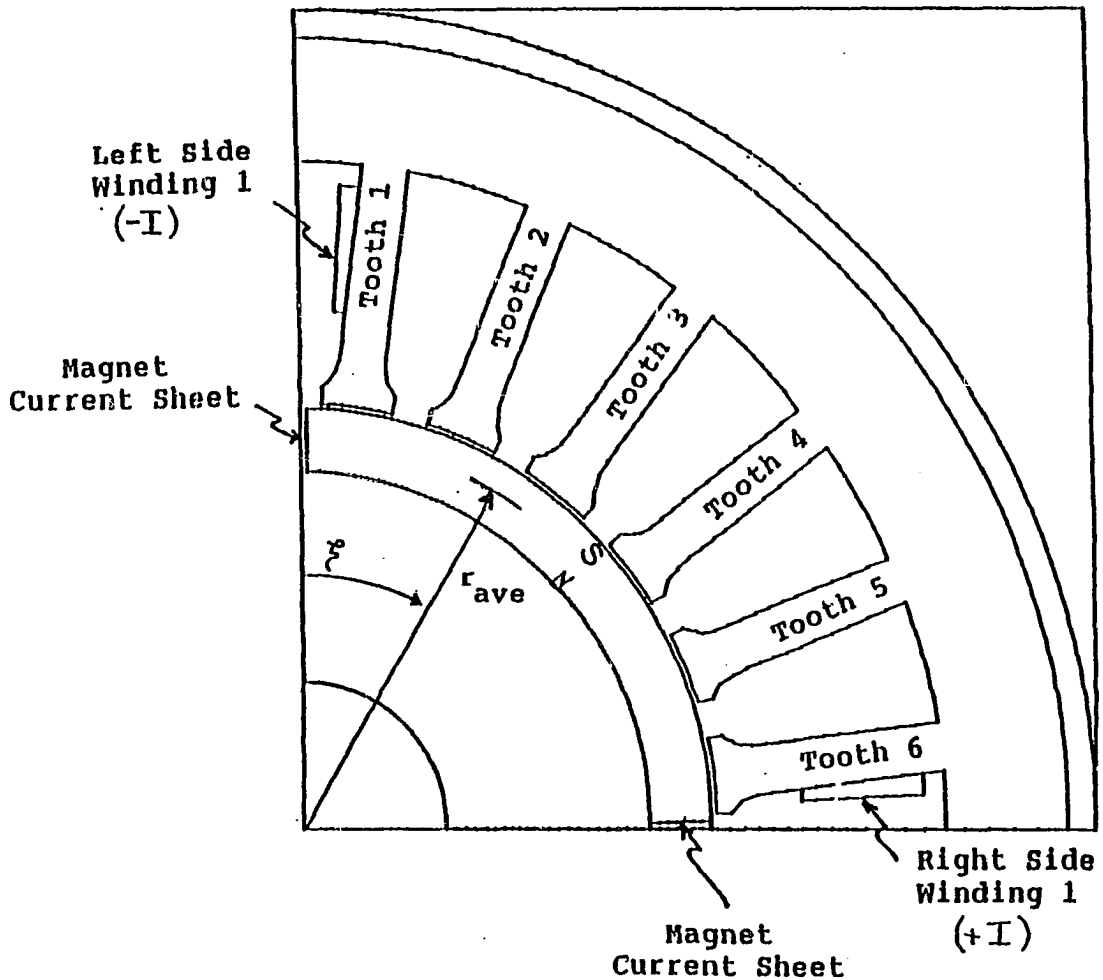

Figure V-15
Quarter Section of 4 Pole,
24 Slot, Brushless DC Motor,
Showing Coil Locations of a Simple Winding

six teeth. The rotor consists of 90 degree arc segments. If the rotor magnet currents are set to zero so that the rotor magnets are 'turned off', then the coil produced radial component of flux density distribution along any row of elements can be found. The average distribution of the radial component of flux density in the region the magnet occupies is shown in Figure V-16. This distribution was produced by a coil current of 2 amps. The distribution shown in this figure is for 180 mechanical degrees of the motor. The zero angle point is with respect to the center of slot one shown in Figure V-15. The rotor shown in Figure V-15 is in the unstable equilibrium position. The stable equilibrium point for the motor occurs when the center of the south pole aligns with the 270 electrical degree point, (45 degree mechanical angle, α), of the flux density waveform of Figure V-16. This would also coincide with the point where the center of the interface between adjacent S-N and N-S magnet segments in Figure V-15 aligns with the 90 degree angle point shown in Figure V-16.

For the rotor magnet shown in this example, the one-phase-on torque-angle curve is easily calculated. In Figure V-17 the rotor magnet has been superimposed onto the plot of flux density versus angle, and it has been displaced from the stable equilibrium by an amount θ. If the radial component of flux density at any point θ, is $B_{rad}(\theta)$, then application of the IxB method to both equivalent current sheets yields a torque expression of:

$$T(\theta) = r_{ave}\ z\ I_m\ (B_{rad}(\theta) - B_{rad}(\theta+\pi)) \qquad (V\text{-}6)$$
$$= 2\ r_{ave}\ z\ I_m\ B_{rad}(\theta)$$

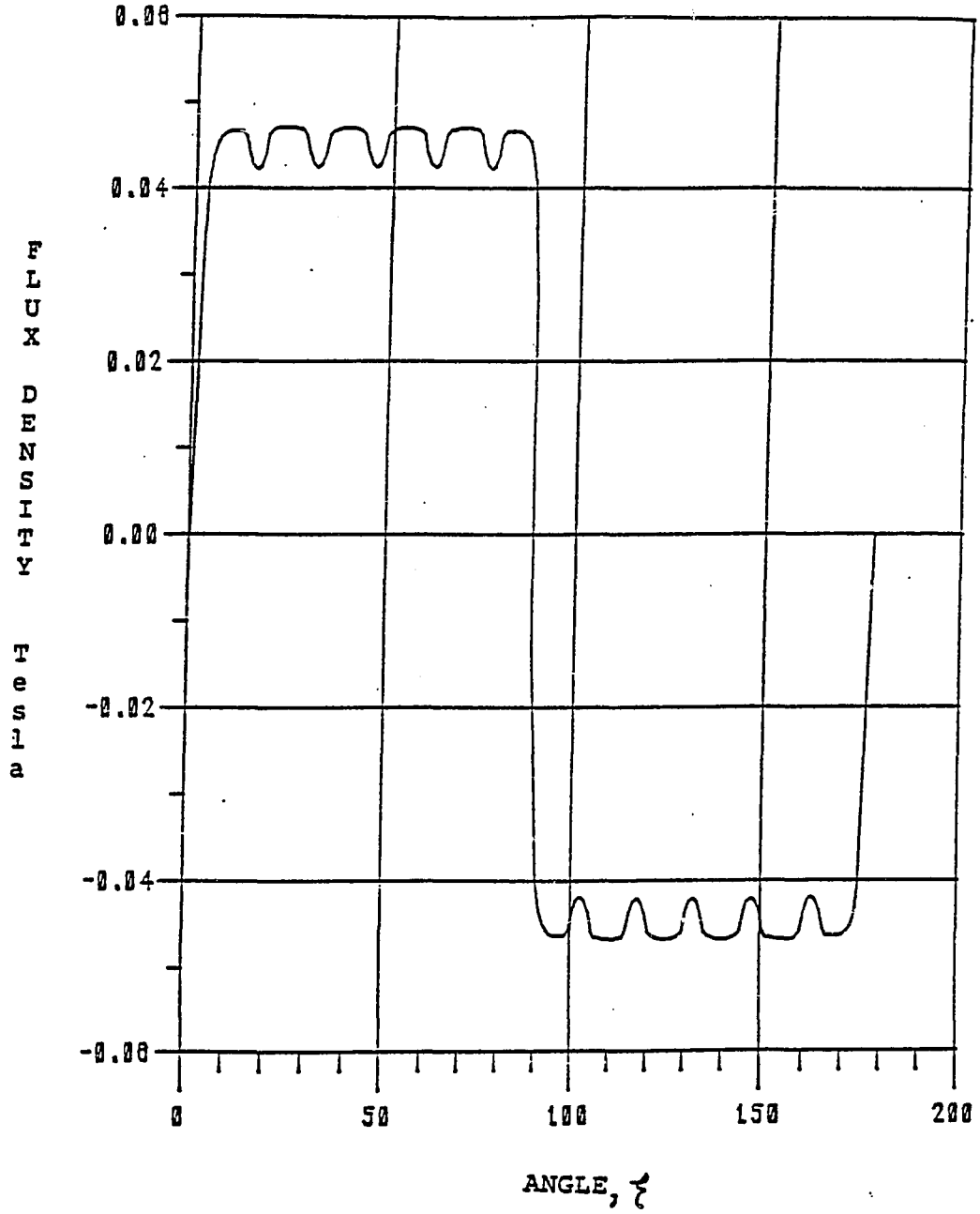

Figure V-16
Distribution of Radial Component of Airgap
Flux Density due to Simple Winding of Figure V-15

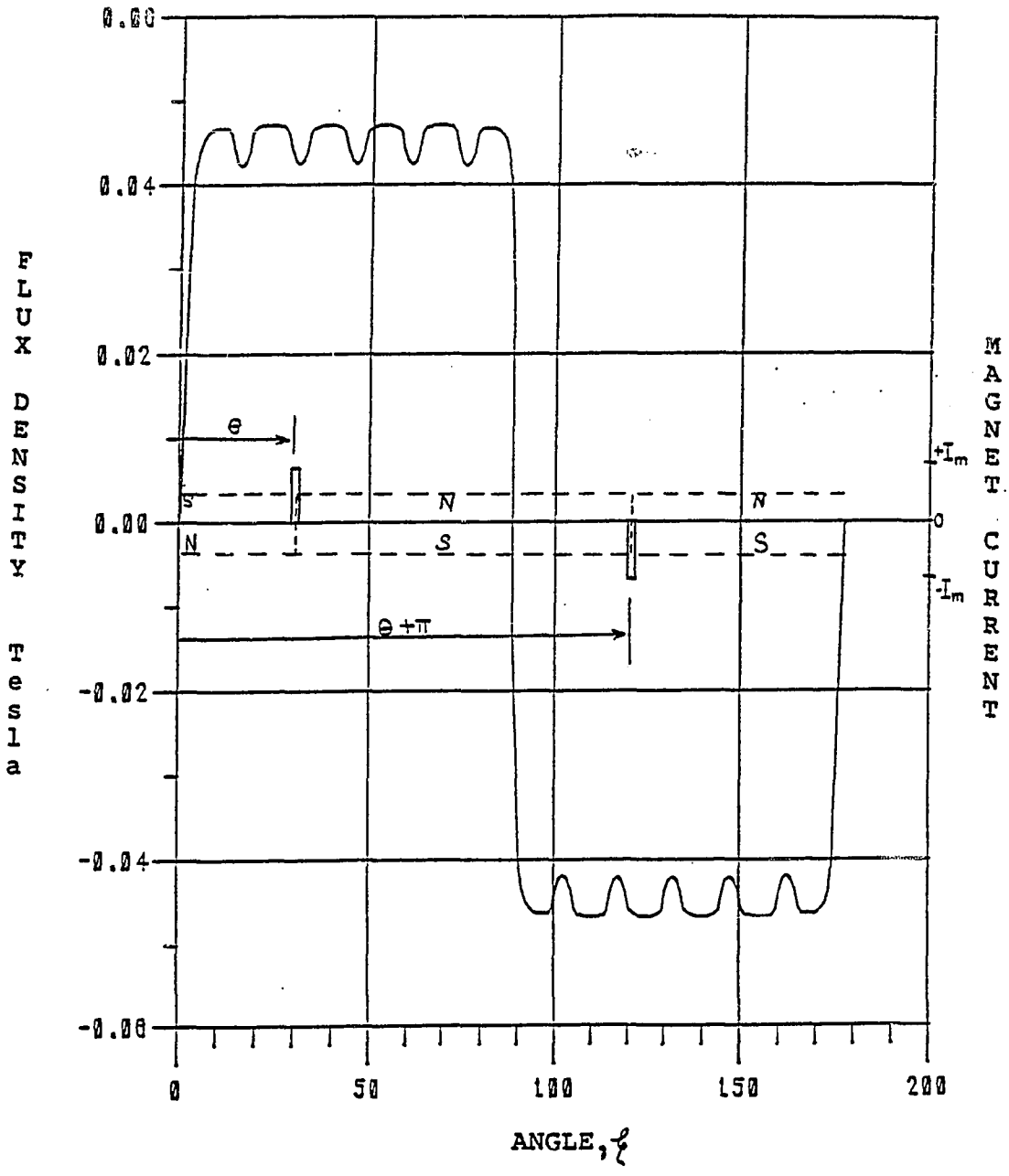

Figure V-17
Distribution of Radial Component of
Airgap Flux Density Due to Simple
Winding, and Location of Magnet Edge
Currents for an Arbitrary Rotor Position, θ

Where:

r_{ave} = average radius of the sheet current

z = axial length of the magnet segments

I_m = magnitude of the sheet current

One sees that in this example, where the magnet edge current are 180 degrees out of phase, the waveform shape of the torque-angle curve will be identical to that of the flux density.

This same method was applied to the prototype motor discussed previously in Chapters II and III, (shown in Figure III-2), with the following variation. Since the magnet edge currents used in the prototype motor are not all at the same angular location, the magnet currents in a row of finite elements were crossed with the average flux density distribution in that row. This was done because the flux density distribution in the airgap is a reasonably strong function of radius. A comparison of the distribution at the outer radius of the magnet and the inner radius of the magnet, is shown in Figure V-18a&b. In the simple example, the average distribution over the radial length of the magnet could be used since it was mathematically equivalent to crossing the magnet current in an element with the average distribution in that row of elements.

The resulting torque-angle curve obtained for the prototype motor using this method of superposition, is shown as the dashed line in Figure V-19. The full FEM generated torque-angle curve is also shown for comparison. One sees that the FEM curve shows a much larger harmonic component. This is due to saturation effects which are not included by this method of superposition. This was shown by changing the saturable steels to linear steels in the FEM. Then, a new torque-

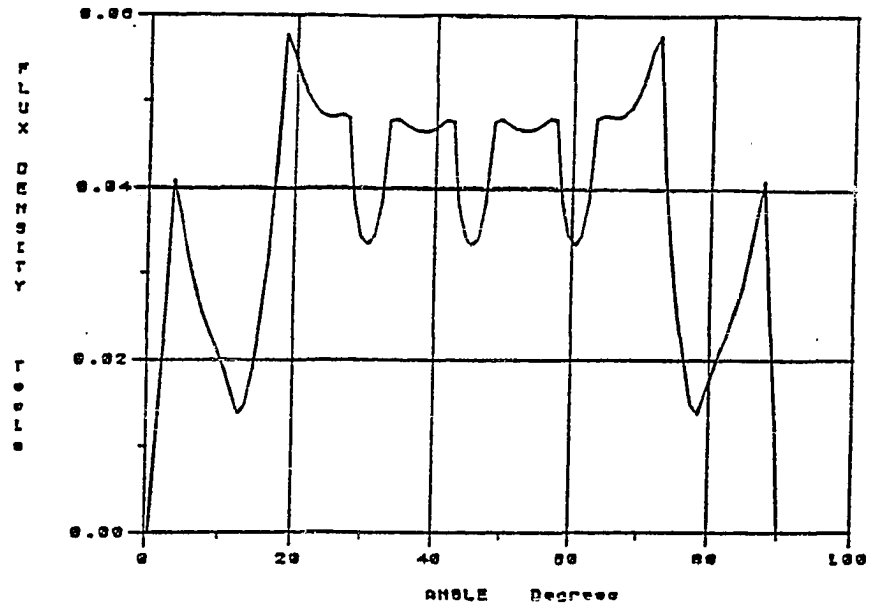

Figure V-18a
Distribution of Radial Component of
Airgap Flux Density in the Outer
Row of Elements in the Magnet Region

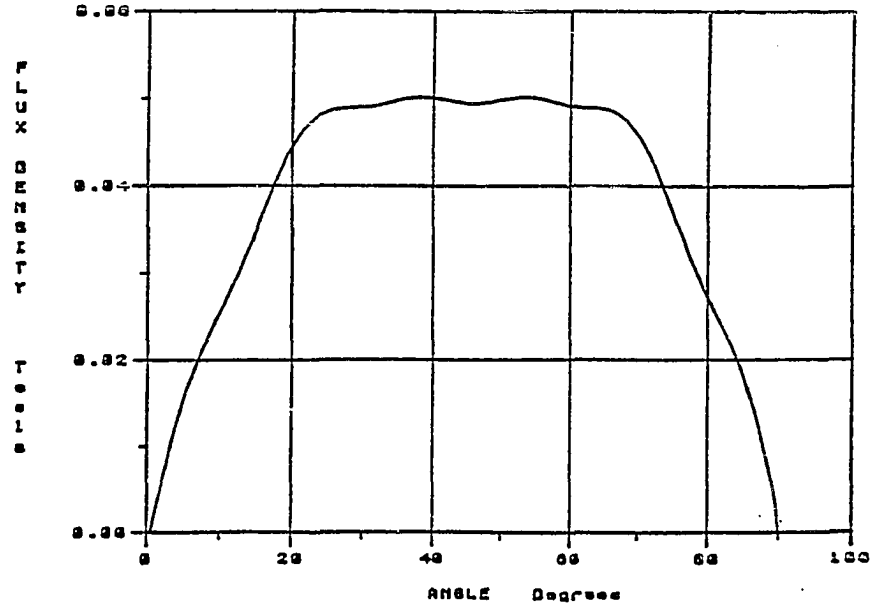

Figure V-18b
Distribution of Radial Component of
Airgap Flux Density in the Inner
Row of Elements in the Magnet Region

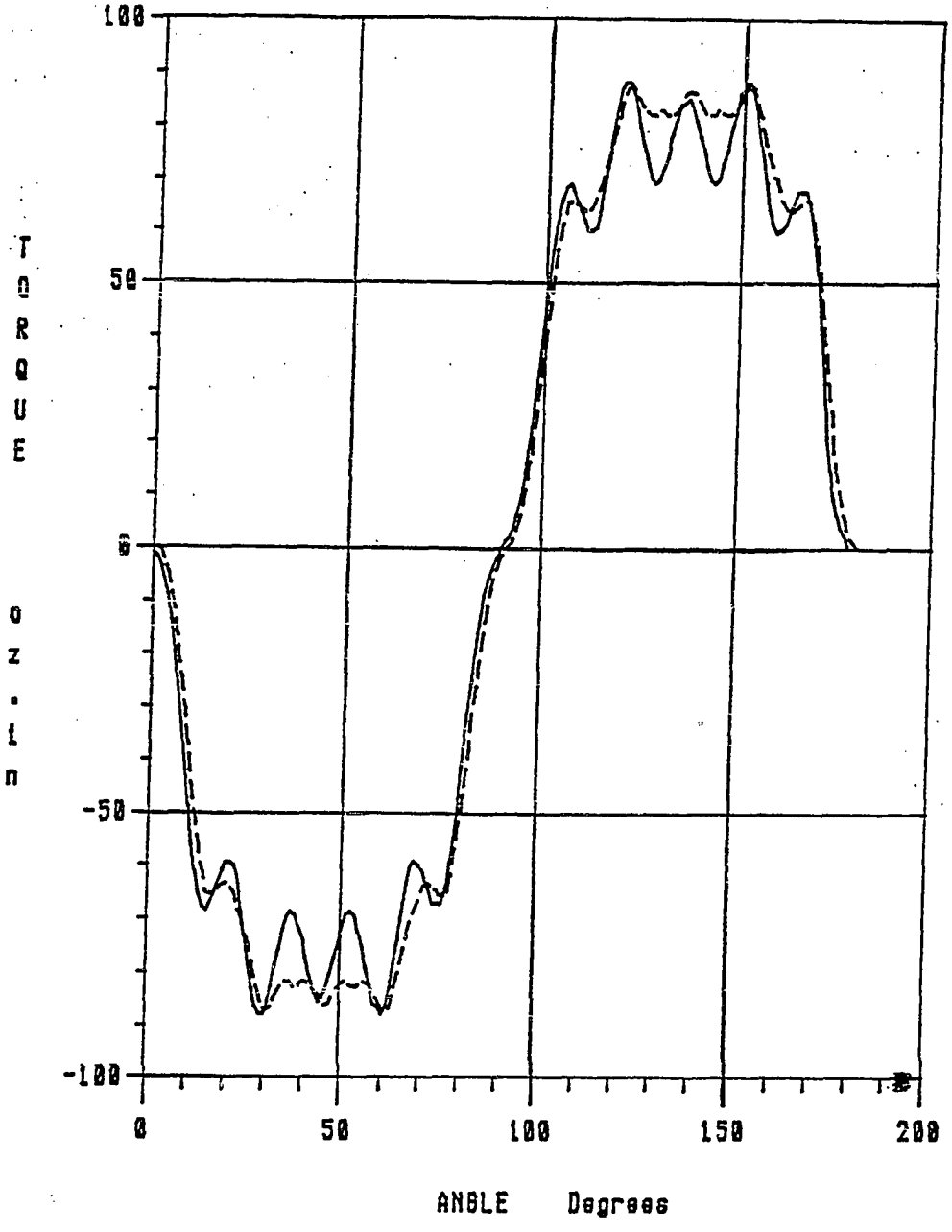

Figure V-19
Comparison of Finite Element Predicted, (Solid Line), and Ix(Coil Radial Component of Airgap Flux Density) Predicted, (Dashed Line), One-Phase-On Stator Torque-Angle Curves

angle curve was generated using the FEM. In Figure V-20 the results are compared to the torque-angle curve found by crossing magnet edge currents with the coil flux density waveform. One sees that there is excellent correlation.

The superposition IxB method allows one to easily see how the coil flux density waveform and the magnet shape influence the torque-angle waveform. Suppose one has the nondistributed winding of the simple example, Figure V-17, and an arc shaped magnet. If a magnet arc width equal to the winding half pitch, (90^0 in this figure), is used, the resulting torque-angle curve contains a harmonic that has the same period as the detent torque, but is due to the stator slots. A magnet arc width which is one half a tooth pitch less than the half winding pitch, i.e. less by half the period of the harmonic, would reduce this harmonic. The individual harmonic contributions due to the left and right magnet edge currents are now 180 degrees out of phase. However, even if this harmonic is completely eliminated there will still be a harmonic of this period in the total torque versus angle curve caused by the detent torque. Motors designed to have flat topped torque-angle curves usually have rotor or stator laminations skewed to eliminate detent torque. As was shown in the analysis on skewing, in these cases the single phase stator torque harmonic due to the slots will also be eliminated.

It is also obvious in looking at Figure V-17 that a magnet arc width less than 90 degrees, (half the winding pitch), will result in a torque-angle curve which has a flattening around both the stable and unstable equilibrium point. This is because there are times when both magnet edge currents are under a B_{rad} region of the same sign and

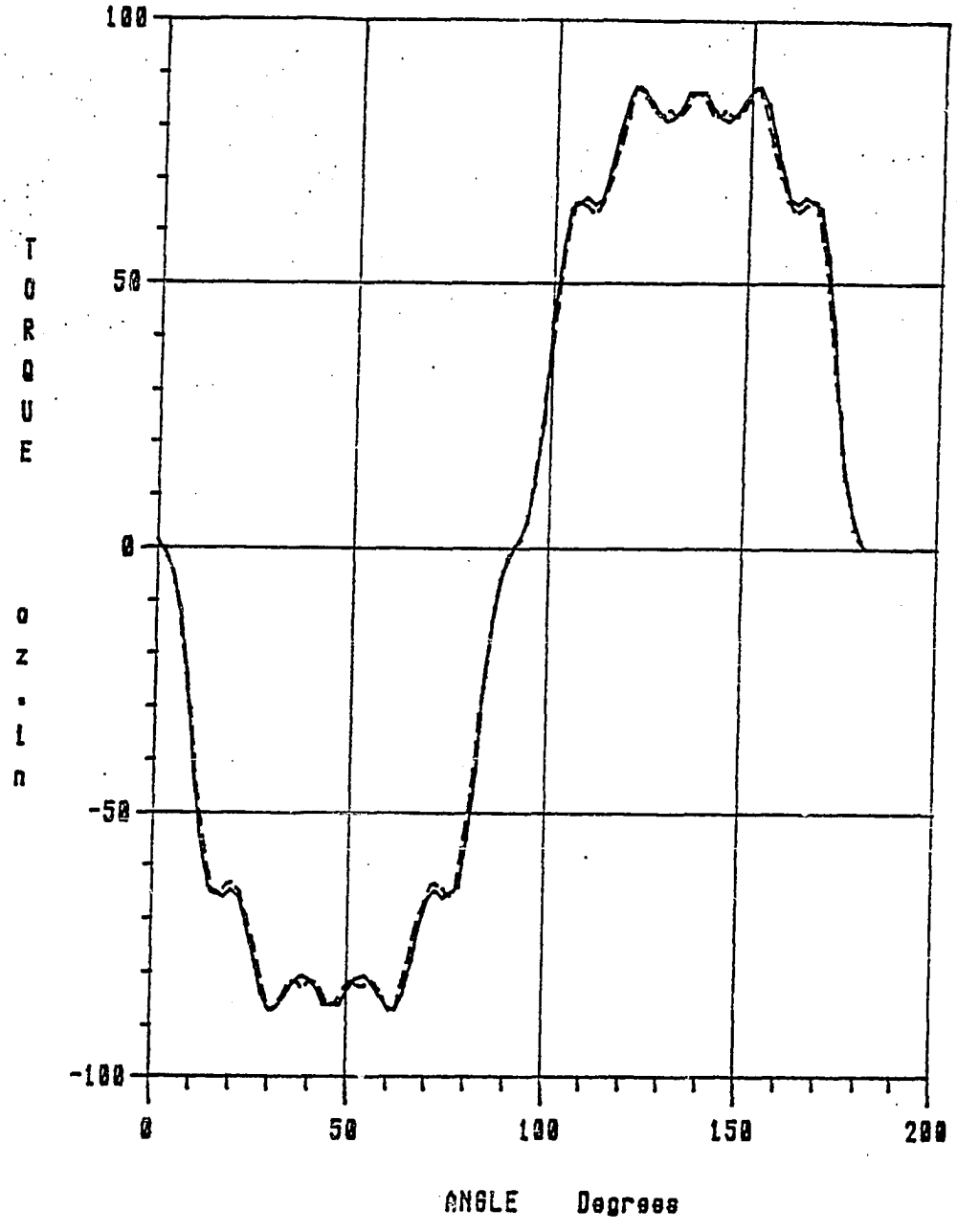

Figure V-20
Comparison of Finite Element Predicted, (Solid Line), and Ix(Coil Radial Component of Airgap Flux Density) Predicted, (Dashed Line), One-Phase-On Stator Torque-Angle Curves Assuming Linear Steel in the Finite Element Model

approximately the same magnitude. Under these conditions the net torque is close to zero. The flattening around the equilibrium points would reduce the static stiffness of a stepping motor. However, the peak torque remains relatively unchanged and so the effect on a brushless motor is minimal. This is provided the magnet arc width is not reduced to a width less than the transition of the distribution from its approximately constant positive value to its approximately constant negative value.

To illustrate the effect of magnet arc width on torque-angle curve shape, consider the ideal, flat topped, trapezoidal B_{rad} distribution of Figure V-21a. A flat topped B_{rad} distribution is ideal because it would result in a flat topped or trapezoidal torque-angle curve, (if the detent torque could be eliminated). A flat topped torque-angle curve would result in a motor with zero low speed torque ripple.

The half pitch of the distribution shown in Figure V-21a is γ_c. The transition span of the distribution is γ_t. The flat topped span of the distribution is γ_s. The pole pitch of the magnet shown as the cross-hatched area in this Figure is γ_m. The equivalent magnet currents are of magnitude I_m and are located at the magnet edges. The torque on the magnet at any position, θ, is proportional to the sum of the product of the magnitude of the magnet current, I_m, and B_{rad} at the edge current locations: $B_{rad}(\theta-\gamma_m/2)$, and $B_{rad}(\theta+\gamma_m/2)$.

Varying the magnet pole pitch, γ_m, from γ_c to 0, allows one to determine the general effects of magnet width on the shape of the stator torque-angle curve. One simply needs to assume a magnet width, use the IxB method to calculate a torque-angle curve for each current sheet, and then add the two phase shifted torque-angle curves.

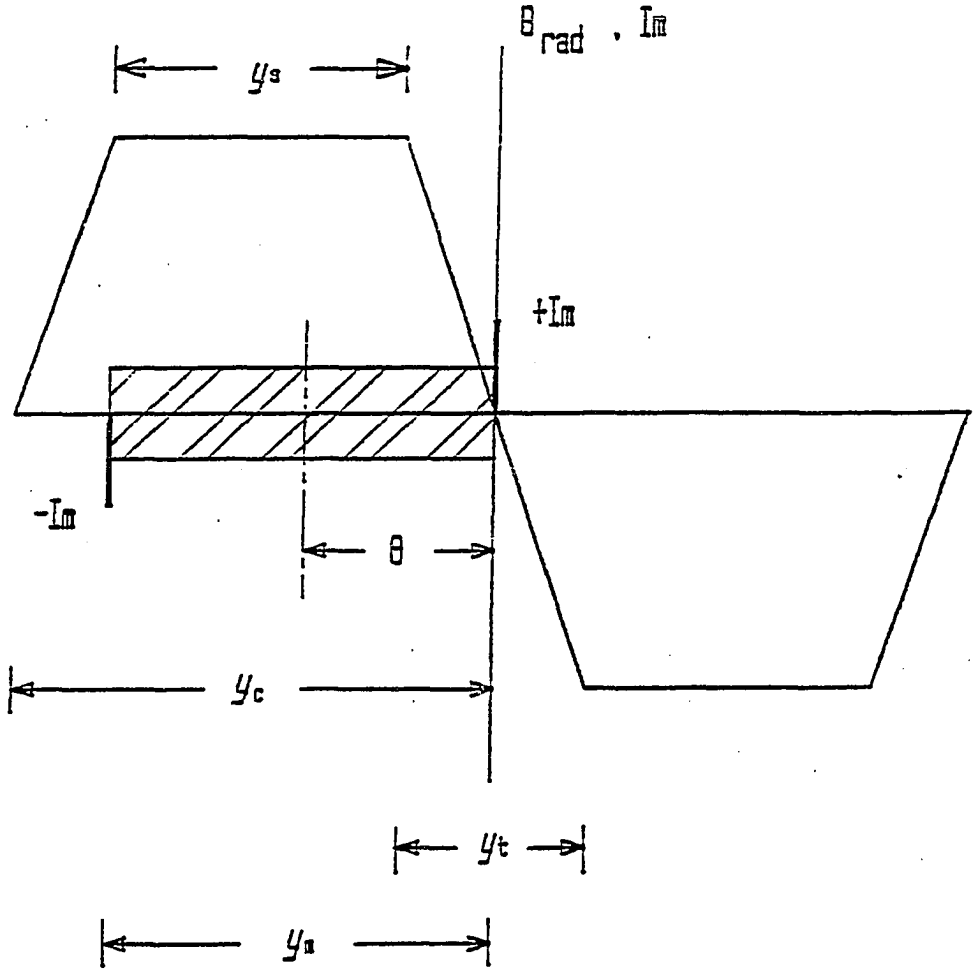

Figure V-21a
Ideal Trapezoidal Shaped Distribution of Radial Component of Airgap Flux Density, and Magnet

Figure V-21b shows two phase shifted flat topped torque-angle curves, (curves 1 and 2), such as would be produced by the combination of magnet and B_{rad} distribution shown in Figure V-21a. Curve 3 in Figure V-21b shows the net torque due to these two phase shifted curves. One sees that while the magnitude of the flat topped area is still twice that of either Curves 1 or 2, the span of the flat topped region has decreased.

Figure V-22 shows a set of torque-angle curves for a variety of different width magnets. The dashed line is the assumed ideal B_{rad} distribution. The same nomenclature used in Figure V-21 also applies here. Curve (1) is typical for a magnet width of $\gamma_t<\gamma_m<\gamma_c$. The flat top region is decreased from γ_s by an amount equal to $\gamma_c-\gamma_m$. The flat topped region shrinks to zero when $\gamma_m=\gamma_t$, Curve (2). Once γ_m is made less than γ_t, there is a decrease in the peak value of torque produced, Curve (3). Finally, if γ_m is less than γ_s, there is a flattening of the curve around the stable and unstable equilibrium points.

For the magnet shown in Figure V-21a, maximum torque is produced when one magnet edge is under the positive flat topped region of B_{rad} and the other edge is under the negative flat topped region. One sees that in order to get as large a flat topped region as possible, the magnet should be made full pitch ($\gamma_m=\gamma_c$), and the coil B_{rad} distribution needs to be made as close to a square wave as possible.

Usually, in motors where a flat topped torque-angle curve is desired, the stator laminations are skewed to eliminate the detent torque. Therefore, skewing effects on the flat topped stator torque-angle curve should be considered. If several slightly phase shifted

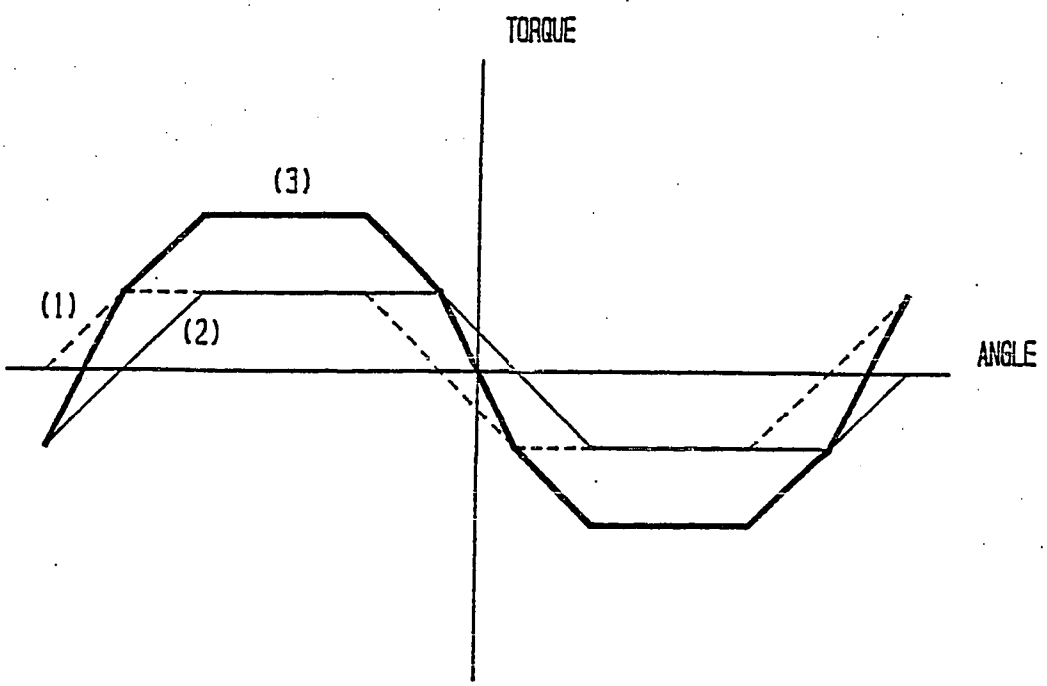

Figure V-21b
Component and Net Stator Torque-Angle Curves for the
Magnet and Flux Density Distribution Shown in Figure V-21a
Curve (1)- An Ideal Flat-Topped Torque Angle Curve
Curve (2)- A Phase Shifted Ideal Flat-Topped Torque Angle Curve
Curve (3)- Sum of Example Phase Shifted, Ideal, Flat-Topped, Curves

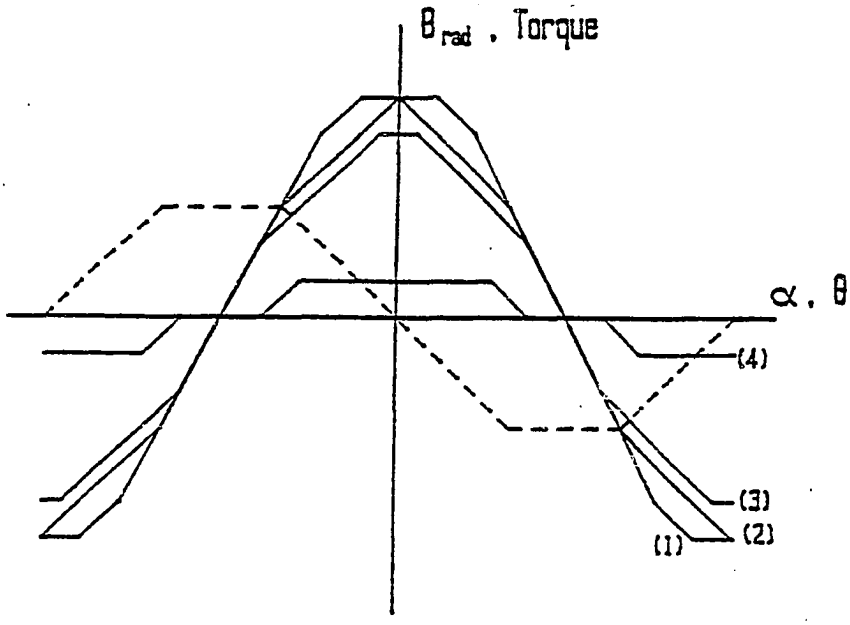

(1) $y_t < y_m < y_c$

(2) $y_m = y_t$

(3) $y_s < y_m < y_t$

(4) $y_m < y_s$

Figure V-22
Stator Torque-Angle Characteristic for the Combination of an Ideal, Trapezoidal Shaped, Flux Density Distribution and 4 Different Regions of Magnet Arc Width

flat topped torque-angle curves are summed, the flat top span decreases; this was illustrated in Figure V-21b. Two phase shifted, trapezoidal shaped torque-angle curves, (Curves 1 and 2), were summed. The result was shown as the thick solid line, Curve 3. One sees that the flat topped region of the net torque is less than the flat topped region of the component torques, Curves 1 and 2. This is consistent with the detent torque analysis that some higher harmonics are eliminated. Obviously, to maintain a large flat top span, the motor should be skewed over as small an angle as possible. Therefore, the motor should have a large ratio of slots to rotor poles. This will result in a detent torque of a much shorter period than the stator torque.

Unfortunately, if there are a large number of slots compared to rotor poles, the coil winding is usually distributed. The coil would consist of several windings distributed among a number of slots. This results in a winding flux density airgap distribution that is more sinusoidal. Figure V-23b shows an example B_{rad} distribution for the windings shown in Figure V-23a. Winding 1 produces an mmf distribution that influences the flux density in the region from zero to ninety degrees. Winding 2 produces an mmf distribution that influences the flux density in the region from fifteen to seventy-five degrees. Where the two regions overlap the net flux density will result from the sum of the two mmf sources. Hence, we see that the distributed winding serves to produce a tiered mmf distribution. This in turn produces a tiered flux density distribution. Unfortunately, there are still slot effects which cause a higher frequency harmonic to be present and tend to smooth out the flux density waveform.

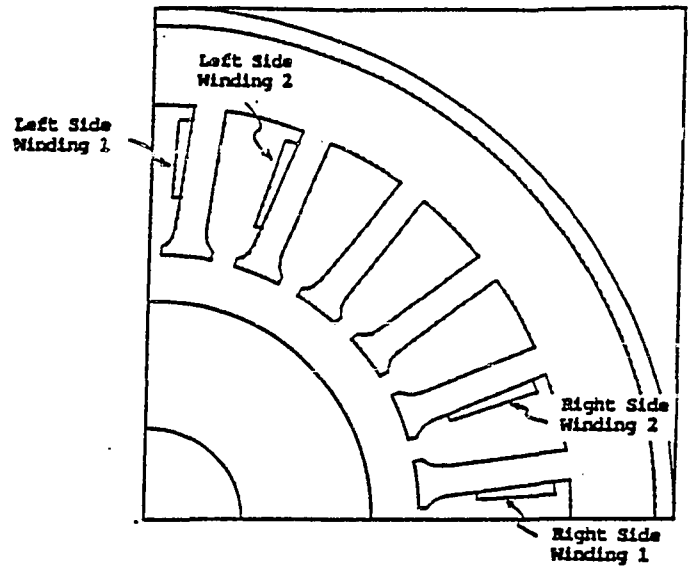

Figure V-23a
Finite Element Model Outline
Showing Distributed Windings

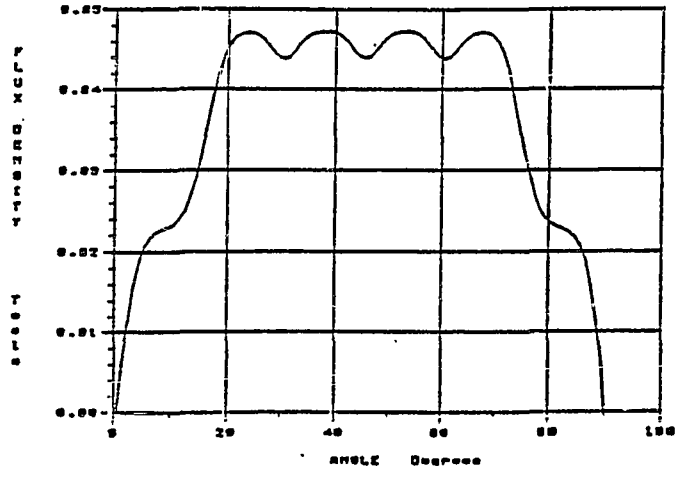

Figure V-23b
Radial Component of Airgap Flux
Density Resulting from Distributed Winding

If a full pitch arc shaped magnet was used with this winding scheme, a torque-angle curve of the same shape as the coil flux density distribution would be produced. If the magnet edge currents were distributed, such as in the prototype rotor, it would tend to smooth the effects of higher harmonics present in the distribution. The torque-angle curve produced would be more purely sinusoidal. Obviously, a combination of distributed coil windings, distributed magnet equivalent currents, and skewing will all serve to make the torque-angle curve more sinusoidal.

This analysis makes it clear that if one could precisely control the shape of the coil B_{rad} distribution and the magnetization of the magnets, then one could shape the single phase stator torque-angle curve.

V.3 Using the Back Emf Waveform as a Substitute for Finding the Torque-Angle Waveform

In Section III.2e it was shown how the back emf waveform could be calculated with the finite element model. This section addresses a method of studying the effect of the winding distribution on the back emf waveform. Calculation of the back emf waveform is important because it has the same waveform shape as the stator torque-angle curve, (provided the iron is operating in a magnetically linear state). Since the bemf waveform can be calculated in a fewer number of solutions than a one-phase-on stator torque-angle curve it represents an attractive alternative to identifying the stator torque-angle shape.

Proof that the bemf waveform and the torque-angle curve have the same shape proceeds in the following manner. Suppose that the motor magnetics are represented by a very simple linear magnetic circuit that has two sources: one due to the coil, the other due to the magnet, and that all of the reluctances can be lumped into a single effective reluctance, (Figure V-24). The total flux linking the coil is:

$$\phi_t = \frac{Ni + F_m(\theta)}{\mathcal{R}_e} \qquad \text{(V-7)}$$

Where: $N \equiv$ Number of coil turns

$\mathcal{R}_e \equiv$ Effective reluctance of magnetic circuit

$F_m \equiv$ Position, θ, dependent magnet mmf

Assuming that superposition can be applied, this is expressed as the sum of the flux due to the permanent magnet and the flux due to the coil.

$$\phi_t = \phi_m(\theta) + \phi_c(i) \qquad \text{(V-8a)}$$

Where: ϕ_t = Total flux linking the coil

ϕ_m = Flux which links coil and is due to magnet, its magnitude is rotor position dependent

ϕ_c = Flux which links coil and is due to coil, its magnitude is coil current dependent

Note in Equation V-8a that the component of flux due to the magnet is only a function rotor angle and the component of flux due to the coil is only a function of current. This assumes, of course, a linear magnetic circuit. Separating Equation V-7 into the components defined in Equation V-8a:

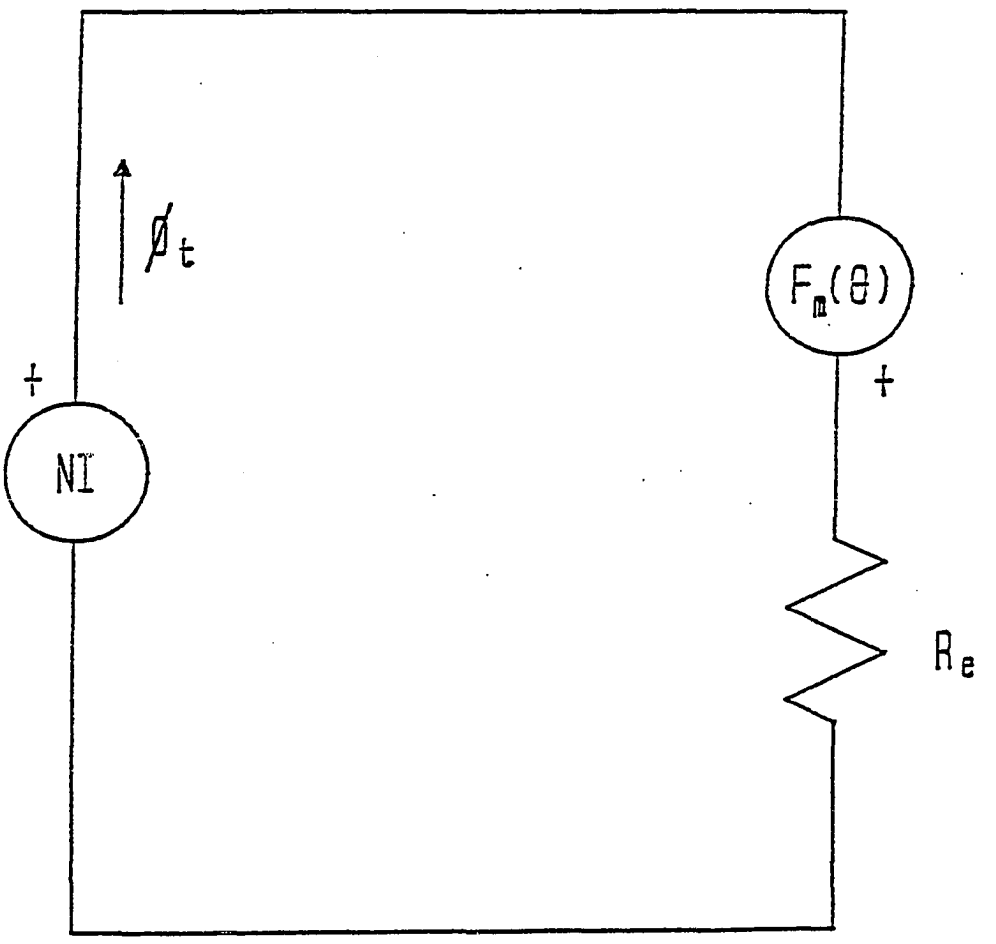

Figure V-24
Simple Lumped Magnetic Circuit Model

$$\phi_m = \frac{F_m(\theta)}{\mathcal{R}_e} \tag{V-8b}$$

$$\phi_c = \frac{Ni}{\mathcal{R}_e} \tag{V-8c}$$

The voltage induced in the coil, due to a time varying flux is:

$$\mathcal{E} = -N \frac{d\phi_t}{dt} = -N\left(\frac{d\phi_m}{dt} + \frac{d\phi_c}{dt} \right) \tag{V-9}$$

$$\mathcal{E} = -N \left(\frac{d\phi_m}{d\theta} \frac{d\theta}{dt} + \frac{d\phi_c}{di} \frac{di}{dt} \right) \tag{V-10}$$

The second term on the right hand side of Equation V-10 represents the inductive voltage. The first term represents the back emf voltage due to the spinning rotor.

$$V_{bemf} = -N\,\omega \frac{d\phi_m}{d\theta} \tag{V-11}$$

Where: ω = rotor speed

Defining flux linkage due to the magnet, λ_m, to be equal to the product of coil turns and flux:

$$\lambda_m = N\phi_m \tag{V-12}$$

yields:

$$V_{bemf} = -\,\omega \frac{d\lambda_m}{d\theta} \tag{V-13}$$

If the rotor is rotating at a constant speed, ω_o, then the back emf voltage waveform observed on the coil is proportional to the derivative of the magnet flux linking the coil as a function of angle.

The torque produced by the device is equal to the partial derivative of coenergy with respect to angle, [11].

$$T = \frac{\partial W_c}{\partial \theta} \tag{V-14}$$

The coenergy for the simple circuit is:

$$W_c = \frac{\mathcal{R}_e \phi_t^2}{2} = \frac{\mathcal{R}_e}{2} (\phi_m^2 + 2\phi_m \phi_c + \phi_c^2) \tag{V-15}$$

Thus the torque is:

$$T = \frac{\partial W_c}{\partial \theta} = \mathcal{R}_e \left(\phi_m \frac{d\phi_m}{d\theta} + \phi_c \frac{d\phi_m}{d\theta} \right) \tag{V-16}$$

The first term in this equation is the detent torque, the second term is the one-phase-on stator torque produced by the stator. Isolating the second term and using Equation V-8c and V-12 for ϕ_c and λ_m yields an expression for the one-phase-on stator torque.

$$T_s = R_e \phi_c \frac{\partial \phi_m}{\partial \theta} = i \frac{\partial \lambda_m}{\partial \theta} \tag{V-17}$$

If the coil is energized with a constant current, then from Equation V-17, the stator torque-angle curve is proportional to the derivative of magnet flux linkage with respect to angle. One sees from a com-

parison of Equations IV-13 and IV-17 that the constant current stator torque-angle waveform and the steady state back emf waveform are both proportional to the change of magnet flux with angle and therefore, both have the same shape.

To verify the preceeding analysis experimentally, the measured back emf waveform of Chapter II shown in Figure II-10 was normalized by dividing it by minus the rotor speed. In addition, the one-phase-on stator torque-angle curve for a phase current of 2 amps, shown in Figure II-7, was normalized by dividing by the stator current. The two resulting curves should be equal to the partial derivative of magnet flux linkage with respect to angle, $\partial(\lambda_m)/\partial\theta$. A comparison is shown in Figure V-25. The dashed line indicates the waveform obtained from the normalization of the back emf waveform and the solid line indicates the waveform obtained from normalization of the stator torque-angle curve. There is good correlation between the two waveforms.

The advantage of this method of calculating the stator torque-angle waveform over the method described previously in Section V.2 is that some local saturation effects are included. Thus, accuracy in predicting the one-phase-on stator torque-angle curve is improved. One sees that there is better correlation between the harmonics in the two waveforms.

There are some obvious disadvantages to this method when compared to the IxB method. A number of solutions are required to find the magnet flux waveform, which in turn is used to find the torque-angle curve. Because it is necessary to know the derivative of the waveform, the greater the number of different solutions, the better

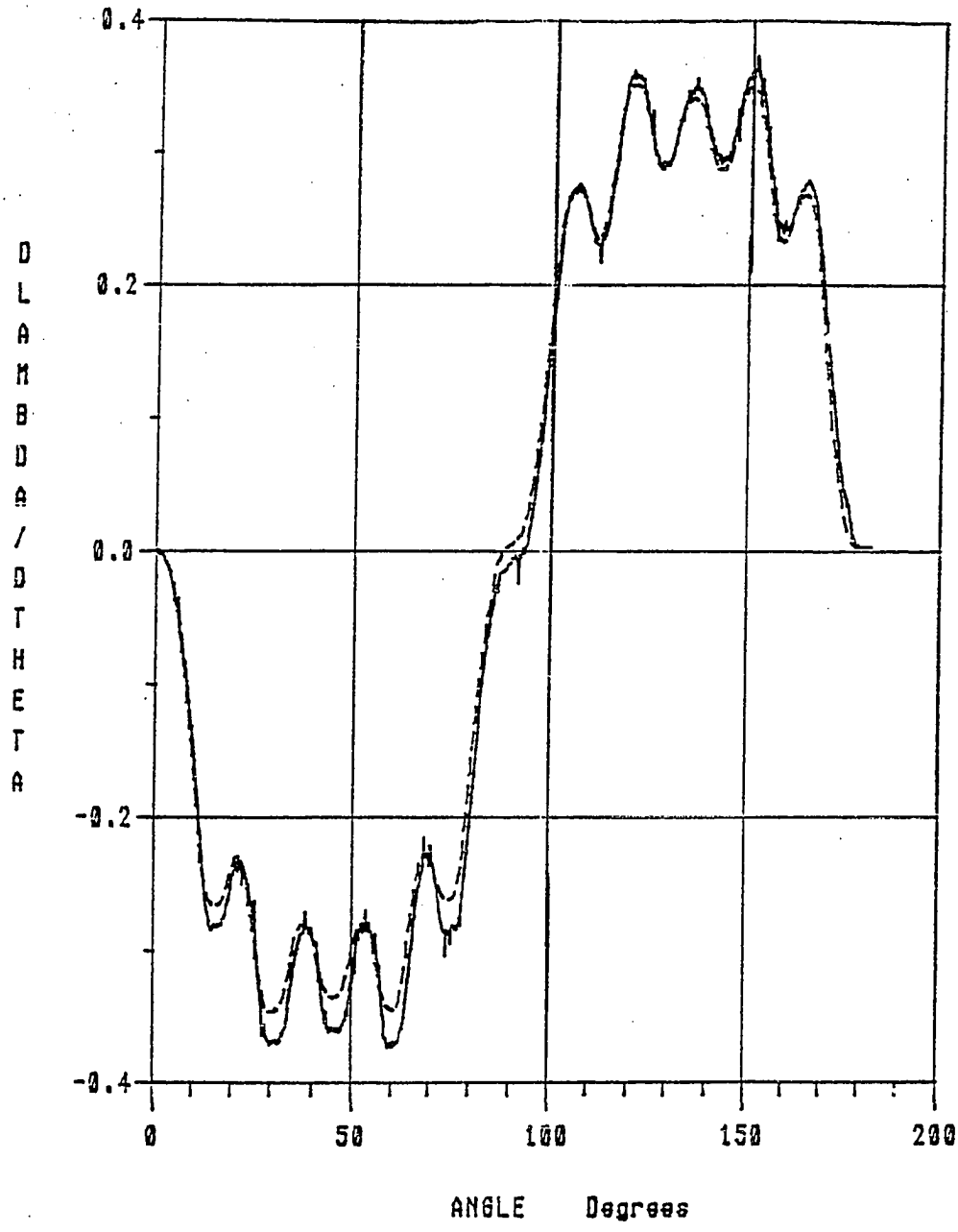

Figure V-25
Normalized Stator Torque-Angle Curve, (Solid Line),
and Back Emf Voltage Waveform, (Dashed Line)

the accuracy. Thus, there is a trade-off between accuracy and the number of solutions. Another disadvantage is if the magnet shape or magnetization is changed, the entire solution process must be repeated. One set of solutions, $\phi_m(\theta)$, can be used to study the effects of different windings but the magnet can not be altered without having to find a new solution for $\phi_m(\theta)$.

Figure V-26 shows $d\lambda_m/d\theta$ waveforms resulting from two different alternative windings. The solid line in this figure represents results from using a coil consisting of a single winding around teeth 1 through 6. The dashed line represents results from a coil consisting of three seperate windings. One winding encompassing teeth 1 through 6; the second winding encompassing teeth 2 through 5, and the third winding encompassing teeth 3 and 4. Both cases have the same total number of coil turns. Unfortunately, this motor produces a large harmonic in the flux waveform. Otherwise, one could see more clearly that the first coil type produces a squarish back emf waveform, and the second coil type produces a more sinusoidal waveform. However, one can still conclude that to achieve a flat topped torque-angle curve, one should not distribute the windings.

It is obvious that this method would be very useful in determining coil windings that produce the desired back emf/stator torque-angle waveform shape.

V.4 Summary

In light of the previous discussion, the following observations can be made concerning the design of torque-angle curves for motors without salient rotor magnet back iron.

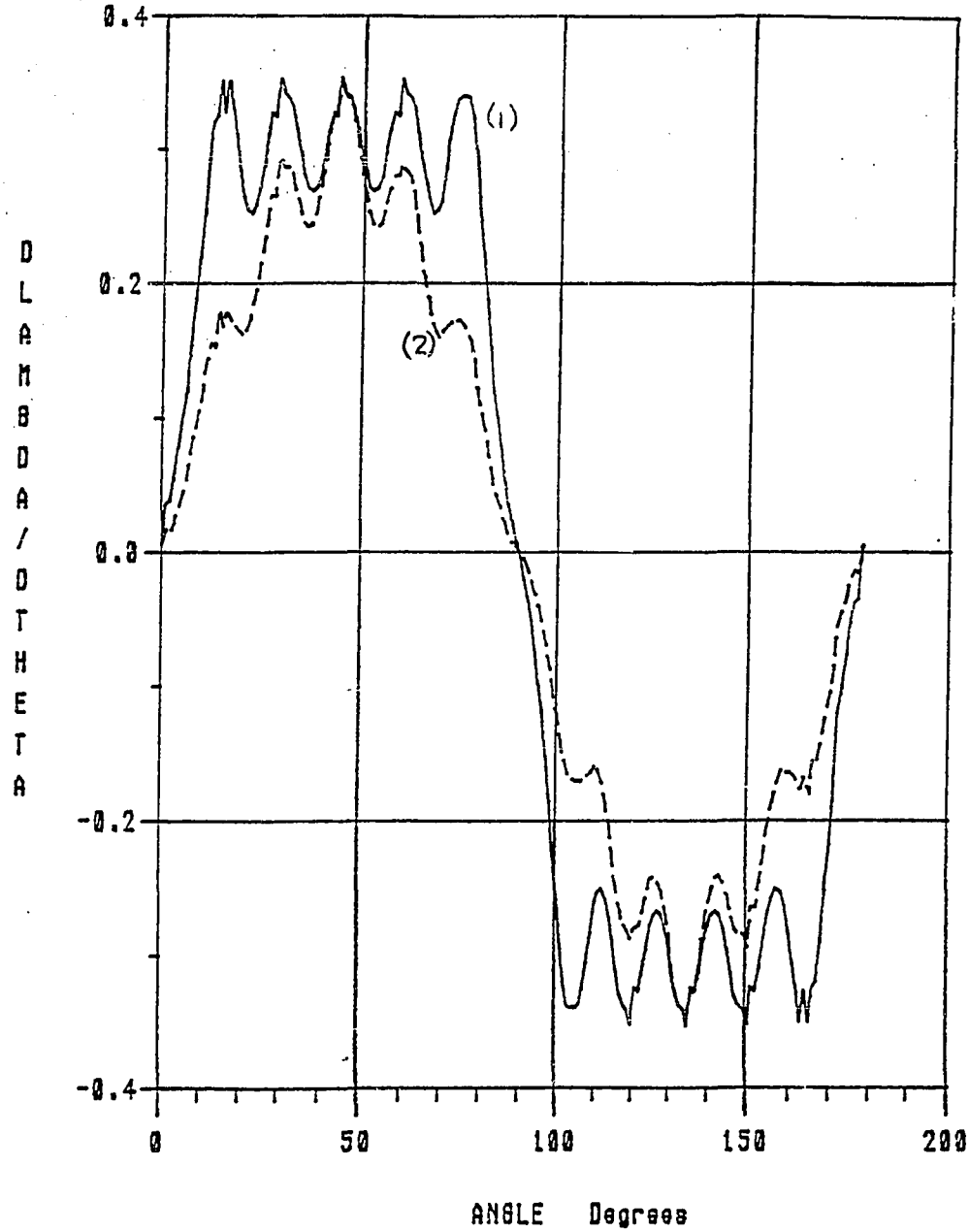

Figure V-26
Normalized Back Emf Voltage Waveform
Resulting from Two Alternative Winding Configurations
Curve (1)- Coil Around Teeth 1 Through 6;
Curve (2)- Coil Around Teeth 1 Through 6,
and 2 Through 5, and 3 Through 4

1)The effects of skewing can be analyzed as the vector sum of the detent torques due to each stator lamination. Skewing the stator will, theoretically, eliminate all detent torque; however, end effects result in some net nonzero detent torque.

2)Skewing will eliminate higher harmonics of the single phase torque-angle curve as well as the detent torque.

3)Flat topped stator torque-angle curves can be obtained by the combination of a flat topped B_{rad} distribution, a uniformly magnetized arc shaped magnet, and a skewed stator. Unfortunately, at this point it is unknown how to produce a flat topped B_{rad} distribution. As a result of this investigation, we do know that if one uses a nondistributed winding over multiple teeth, a relatively squarish B_{rad} distribution is obtained that has a harmonic due to the presence of the slots. Skewing should virtually eliminate this harmonic, but will also decrease the flat topped span of the distribution, and hence, the flat topped span of the torque-angle curve. However, using a nondistributed winding over multiple teeth does not maximize the coil mmf. Thus, the peak torque will be less than can be obtained with an identical motor and a distributed winding.

4) If one could produce a sinusoidal B_{rad} distribution then one could use uniformly magnetized, arc shaped magnets to produce a sinusoidal torque-angle curve. If the B_{rad} distribution contains harmonics, skewing will help to eliminate them from the net torque-angle curve. However, it might also be necessary to distribute the magnet edge currents as well. This would mean that the magnet edges would not be radial but would be shaped differently, more slanted perhaps. Making a sinusoidal torque-angle curve probably would be

easier than making a flat topped one. Distributed windings, distributed magnet edge currents and skewing all serve to reduce harmonics.

5) The IxB method of calculating torque is a good means of analyzing the basic factors affecting torque-angle waveform shape. However, saturation can introduce additional harmonics that are not predicted by this method.

6) Two methods of determining torque-angle shape were presented. The IxB method allows one to easily see the effects of coil distribution, magnet shape, and magnet magnetization on the torque-angle shape. The back emf method allows some nonlinear effects to be included and thus improves the accuracy of prediction.

7) Of the methods presented for reducing detent torque each has advantages and disadvantages:

Skewing the stator stack increases the difficulty of winding the coils; thus increasing winding cost. However, detent torque is virtually eliminated. Skewing the magnet segments has the same results in terms of the net detent torque. However, it is a costly manufacturing process.

Reducing detent torque by altering the magnet arc width can significantly reduce the detent torque but is not likely to result in complete elimination of the detent torque. This method is best suited to shaping the detent torque so that other cancellation shemes, such as creating staggered magnet segments, can be used to achieve further reduction. The successfulness of shaping the detent torque-angle waveform by altering the magnet shape is somewhat dependent upon the manufacturer's ability to provide a magnet with the exact magnetiza-

tion and geometry specified. At present, our confidence level in the manufacturer's ability to do this is low.

Reduction of detent torque by creating unequal arc width magnets suffers the same limitations as altering the magnet arc width.

Staggering magnet segments will effectively reduce the detent torque, provided a sufficiently large number of staggered segments are used. If a few number of staggered segments are used, the detent torque curve per segment should be primarily sinusoidal; otherwise, higher harmonics will not be eliminated. Creating a large number of staggered segments for a motor with a short stack length can be complicated by the necessity to handle a large number of small magnets.

Creating staggered magnet segments with the proper selection of magnet arc width and perhaps unequal magnet arc widths seems to be a good way of combining some of the more attractive advantages of each of those methods without completely relying on any one method.

CHAPTER VI

ONE-DIMENSIONAL, LUMPED PARAMETER MAGNETIC CIRCUIT MODELS FOR THE BRUSHLESS DC MOTOR

In previous chapters, finite element analysis has been used extensively to analyze the magnetic behavior of BLDCMs. Unfortunately, at the present level of technology, the finite element method is strictly an analysis tool. If one wishes to change the geometry of the motor, the FEM has to be altered and the entire analysis performed again. This does not lend itself well to the development of a motor design software package that would allow a motor designer to explore the effect of a particular motor design parameter on some performance parameter; for example, the effect of rotor magnet thickness on the motor torque constant.

One-dimensional magnetic circuit models are desirable because they usually either result in simple algebraic expressions which directly relate performance parameters to motor design parameters or, a set of algebraic equations, (linear or nonlinear), that can be solved to numerically relate design parameters to performance parameters. Either result can be easily incorporated into a software package that can be used to aid in motor design. Closed form expressions, however, are preferable because the equations can be manipulated directly.

One-dimensional magnetic circuit models are magnetic analogs of electric circuit models. One develops circuit networks, the same as in electric circuit analysis, that consist of elements which have

magnetomotive drops, ($\mathcal{F}$ or mmf), across them, magnetic flux, (ϕ), flowing through them, and have an inherent reluctance, ($\mathcal{R}$), associated with them. These three parameters: $\mathcal{F}$, ϕ, $\mathcal{R}$, are analogous to voltage, current and resistance, respectively, in electric circuits.

Unfortunately, modelling magnetic circuits is not as simple as modelling electrical circuits. In electrical circuits, electric flux remains principally in the intended conductive paths, there is very little leakage. In magnetic devices, however, magnetic flux is not principally confined to iron, and there is a significant amount of leakage. Often, this means that leakage paths for the flux have to be included in order to develop more accurate lumped magnetic models. Finite element analysis and resulting flux plots serve to identify leakage paths.

In this chapter, several topics are covered. First, the theoretical basis for one dimensional, lumped parameter models is reviewed with the intent of identifying the assumptions and conditions under which lumped parameter magnetic circuit analysis is valid. Keeping these assumptions in mind, some simple magnetic circuit models for the motor will be developed and results evaluated by comparision with finite element results.

The simple lumped models developed neglect iron reluctances and only include the reluctances of the airgaps. These models allow one to predict the radial component of airgap flux density due to the coil. Determination of the radial component of airgap flux density is important because one can use the results of Section V.2 to predict the stator torque-angle curve or the torque constant. It will be shown that while this simple model can be used to accurately predict

the coil induced radial component of airgap flux density, it is deficient in predicting inductance. It will be shown that accurate prediction of inductance would require a much more detailed model.

Next, it will be shown that these very simple, airgap only, lumped models can be used to predict the radial component of airgap flux density due to the permanent magnet. However, the added complication of needing some reluctances which are position dependent is required because the source is position dependent. We are trying to form flux tubes in which may change with position but have a unidirectional source.

Lastly, it will be shown that while these simple models can be used to predict the one-phase-on stator torque-angle curve, they can not be used to predict detent torque for the motor. In view of the finite element results of Chapters III and IV, it is doubtful that accurate prediction of the detent torque-angle curve is possible by lumped elements. At the very least, accurate prediction of detent torque would require additional levels of complexity that make it impractical to implement.

VI.1 Derivation of Lumped Circuit Equations

The lumped element magnetic circuit equations are derived from Maxwell's equations[8]. Equation VI-1a states that the integral of the field intensity, $\vec{H}$, around any closed path is equal to the ampere turns enclosed. Equation VI-1b states that the integral of the field intensity along a line segment represents the mmf drop, $\mathcal{F}$, in the direction of the segment. Equation VI-2a states that the total magnetic flux through any closed surface is zero. Equation VI-2b is a

subset of Equation VI-2a and states that integral of the flux density over any surface is equal to the flux through the surface.

$$\oint \vec{H}\cdot d\vec{l} = Ni \qquad \text{(VI-1a)}$$

$$\int \vec{H}\cdot d\vec{l} = \mathcal{F} \qquad \text{(VI-1b)}$$

$$\oint \vec{B}\cdot d\vec{s} = 0 \qquad \text{(VI-2a)}$$

$$\int \vec{B}\cdot d\vec{s} = \phi \qquad \text{(VI-2b)}$$

One can see that combining Equation VI-1a and VI-1b as:

$$\sum_i \mathcal{F}_i = Ni \qquad \text{(VI-3)}$$

yields an equation that is the magnetic analog to Kirchoff's voltage law. The summation of magnetomotive force drops, $\mathcal{F}$, around a closed path is equal to the source mmf.

Combining Equations VI-2a and VI-2b yields the magnetic analog of Kirchoff's node law; the sum of the flux into any node is equal to zero.

$$\sum_i \phi_i = 0 \qquad \text{(VI-4)}$$

One sees that once a circuit model consisting of reluctances and sources has been constructed, one can write equations summing the mmf drops around loops, or summing flux into nodes, to determine the flux

through any element and the mmf drop across any element.

It is the determination of the reluctances of the model that represents the real difficulty in magnetic circuit analysis. This is because BLDCMs are primarily designed to produce magnetic flux in an airgap. Iron is used to direct and carry flux to the airgap; however, the significant mmf drops occur across the airgap. Therefore, it is the reluctance of the airgaps which must be modeled accurately. This represents a difficult task since the flux field in the airgap is often two-dimensional and its direction can vary greatly with rotor position.

Reluctance is defined as the ratio of mmf to flux, (Equation VI-1b divided by VI-2b).

$$\mathcal{R} = \frac{\int \vec{H} \cdot d\vec{l}}{\int \vec{B} \cdot d\vec{s}} \qquad \text{(VI-5)}$$

This definition is easy to apply if one is trying to determine the reluctance of an airgap between two soft iron pole pieces and one knows the mmf provided by the coil as well as the total flux through the iron. However, if one is trying to evaluate the reluctance of some portion of an airgap where the geometry is complicated, this is a more difficult task.

The derivation of the reluctance of some geometry proceeds in the following manner. Starting with Equation VI-1b and assuming that $\vec{H}$ is in the direction of $\vec{l}$ yields Equation VI-6.

$$\mathcal{F} = \int H \, d\ell \qquad \text{(VI-6)}$$

Where: $\ell \equiv$ length of path in direction of flux

Substitution of the constitutive relation between B and H, (Equation VI-7) yields Equation VI-8.

$$H = \frac{B}{\mu} \tag{VI-7}$$

$$\mathcal{F} = \int \frac{B}{\mu} \, d\ell \tag{VI-8}$$

Equation VI-2b can be used to express the flux through a cross-sectional area, A_e, as:

$$\phi = \int B \cdot dS = BA_e \tag{VI-9}$$

This Equation assumes that the flux density through the cross-sectional area is constant. Solving for B in Equation VI-9 and substituting into Equation VI-8 yields:

$$\mathcal{F} = \int \frac{\phi d\ell}{\mu A_e} \tag{VI-10a}$$

If it is assumed that the cross-sectional area perpendicular to ℓ varies in a manner so that Equation VI-9 always yields a constant flux, ϕ, then ϕ can be brought outside of the integral. Thus, Equation VI-10a becomes:

$$\mathcal{F} = \phi \int \frac{d\ell}{\mu A_e} \tag{VI-10b}$$

Since reluctance has been defined as the ratio of mmf to flux then:

$$\mathcal{R} = \frac{\mathcal{F}}{\phi} = \int \frac{d\ell}{\mu A_e} \qquad \text{(VI-11)}$$

This equation defines the reluctance of a volume of space which has a constant amount of flux through it. If the reluctance path is of constant cross-sectional area then the reluctance is:

$$\mathcal{R} = \frac{\ell}{\mu A_e} \qquad \text{(VI-12)}$$

To recapitulate, there are a few assumptions, both implicit and explicit, that were made in the derivation of this expression. The first is that the derivation started with Equation VI-1b, a line integral, to derive an expression for the reluctance of some area. Strictly speaking, this equation should only be used to evaluate the mmf drop along a flux line. The use of this equation implicitly assumes that H is constant over the area or that the integral of $H d\ell$ is constant over the area.

Secondly, it was assumed that H was in the direction of ℓ, (hence, the name one-dimensional magnet circuit model). This would require one to select a reluctance path that was in the direction of the flux. If it is not in the direction of the flux, then errors will be introduced.

Thirdly, it was assumed that the flux density, B, was constant over the cross-sectional area. Finally, it was assumed that the total flux, ϕ, through a cross-sectional slice of the path, was constant along the length of the path. In some respects, this last assumption is a restatement of the fact that the reluctance path under consideration needs to be in the direction of the flux. If the side boundaries of the path under consideration coincide with flux lines, (lines of constant vector potential, A), then not only will the path be in the

direction of the flux, but the total flux through a cross-sectional slice of the path will be constant and independent of the position along the length of the path that the slice is taken.

The review of the assumptions used in developing an expression for the reluctance of a path has shown that the reluctance paths selected should be flux 'tubes'. Flux tubes are best explained by looking at a finite element flux plot, such as the one shown in Figure VI-1. As discussed previously in Chapter III, this figure shows lines of constant magnetic potential. Since flux density is tangent to any point along one of these lines,[10] these are boundaries through which no flux passes. These lines can be thought of as outlining tubes through which flux flows. Thus, the region between lines is a flux tube and this type of plot shows a set of flux tubes. By changing the number of contours of constant magnetic potential plotted, one can show either a large number of narrow flux tubes or a few wide flux tubes.

Thus, we see that if the reluctance path to be evaluated is a flux tube, then the path is in the direction of flux, and the flux through any cross-sectional slice of the path remains constant. These facts satisfy two of the four assumptions made in the derivation of the reluctance equation. The third assumption was the flux density was constant over a cross-sectional slice of the tube. If one selects a region where flux density is relatively constant as a tube, or, in order to achieve a piecewise linearization, one selects a large number of tubes in regions where the flux density varies greatly then this condition can be met. The final assumption made was that the mmf drop was constant across the tube. This assumption will be true if the tube under consideration lies between two equipotential surfaces.

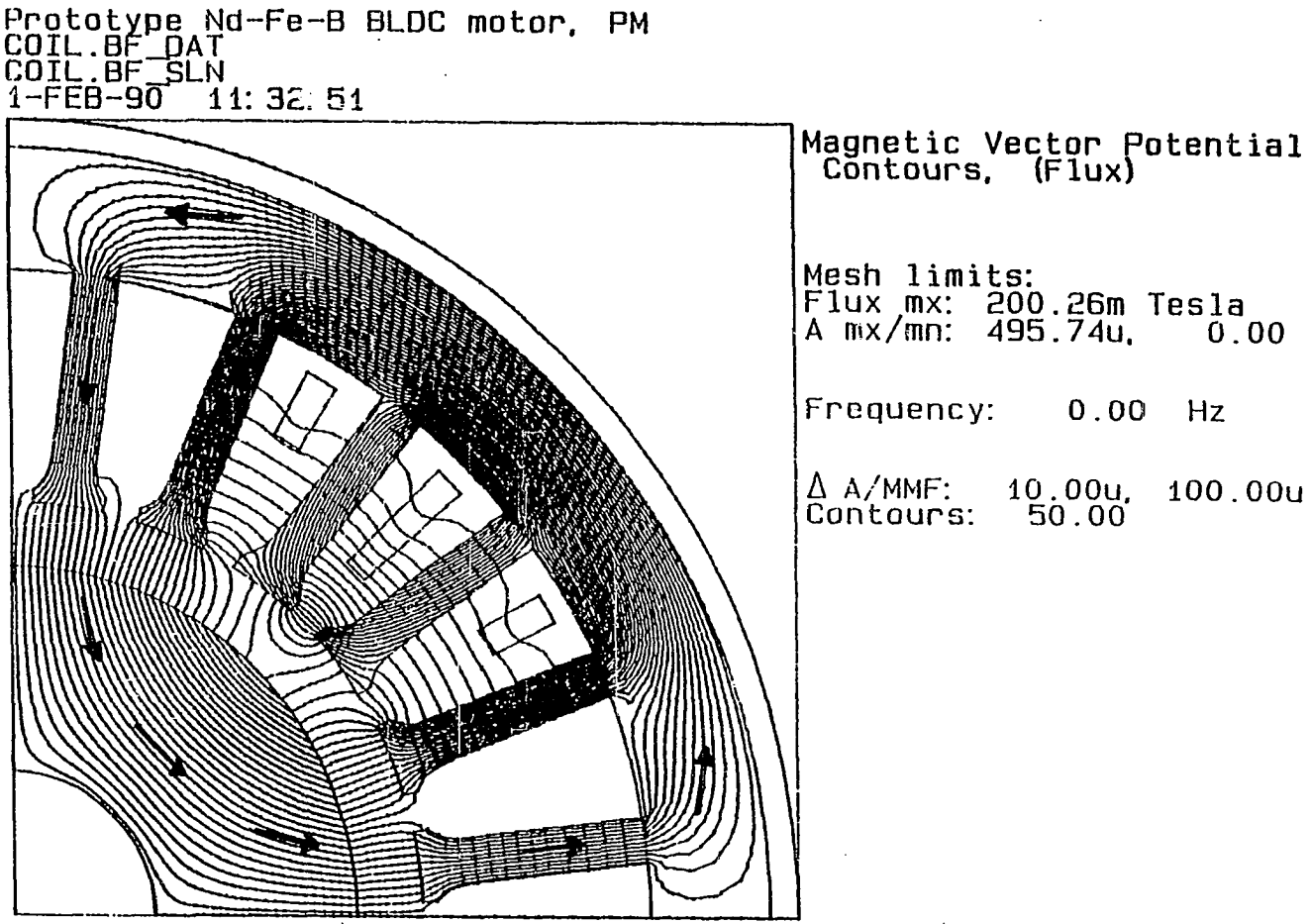

Figure VI-1
Finite Element Solution Contour Plot

Unless there is a high degree of saturation, coils wrapped around iron poles usually result in the iron surface of the pole being at a constant magnetic potential.

The previous discussion makes several points clear about using one dimensional circuit models to model the magnetics of BLDCMs. 1) One needs either to know, or at least have a good idea what the flux plot of the device will look like in order to accurately model the field produced. 2) If the flux plot changes due to changes in the permanent magnet rotor position or saturation in the iron, then the circuit model reluctances may have to change as a function of rotor position or phase excitation. 3) In regions where the field is very two-dimensional a large number of reluctance paths may be required for accuracy.

One sees that if it is desired to know the field everywhere accurately, then a fairly complicated one dimensional model is probably required. If this is the case, then finite element analysis is obviously preferable. One gains nothing by the use of a complex circuit model. The circuit model will, in all likelihood, be too complicated to yield a closed form expression for a given motor performance parameter. Thus, the model would have to be solved numerically and motor performance parameters would also have to be related to the field solution numerically. Since the primary purpose of using one dimensional circuits was to develop relatively simple expressions relating motor performance parameters to motor geometry and materials, this would be unacceptable.

In the following sections in this Chapter, simple lumped models

are developed for the BLDCM and evaluated to determine the accuracy of these models.

VI.2 Simple Lumped Model to Predict the Airgap Flux Density Due to the Coil

In this section a simple lumped parameter magnet circuit model for the flux produced by the coil is developed. In Section V.2 it was shown that by assuming magnetic linearity, superposition could be used to determine a one-phase-on torque-angle curve for the motor by first finding the coil flux density waveform in the airgap and then using the IxB method on the magnet equivalent currents. If a simple lumped parameter model could be used to find the coil flux density waveform, then the one-phase-on torque-angle curve could be found even more easily. In addition, if an expression for the peak of the torque-angle curve can be developed then one has a relationship between the torque constant and motor geometry and materials.

The simplest lumped magnetic model is one in which only the airgaps over the tooth faces are modeled. The mmf drops through iron paths are neglected. This is usually a valid assumption because the permeability of unsaturated iron is 2 or 3 orders of magnitude greater than the permeability of air. Figure VI-2 shows a very simple circuit which has been superimposed upon a FEM contour plot. Each reluctance shown is for the flux tube that encompasses the tooth face and is directed across the airgap. The flux tubes are assumed to be entirely in the radial direction. Since the flux tubes selected are only in the radial direction, the lumped parameter model will only predict the radial component of airgap flux density.

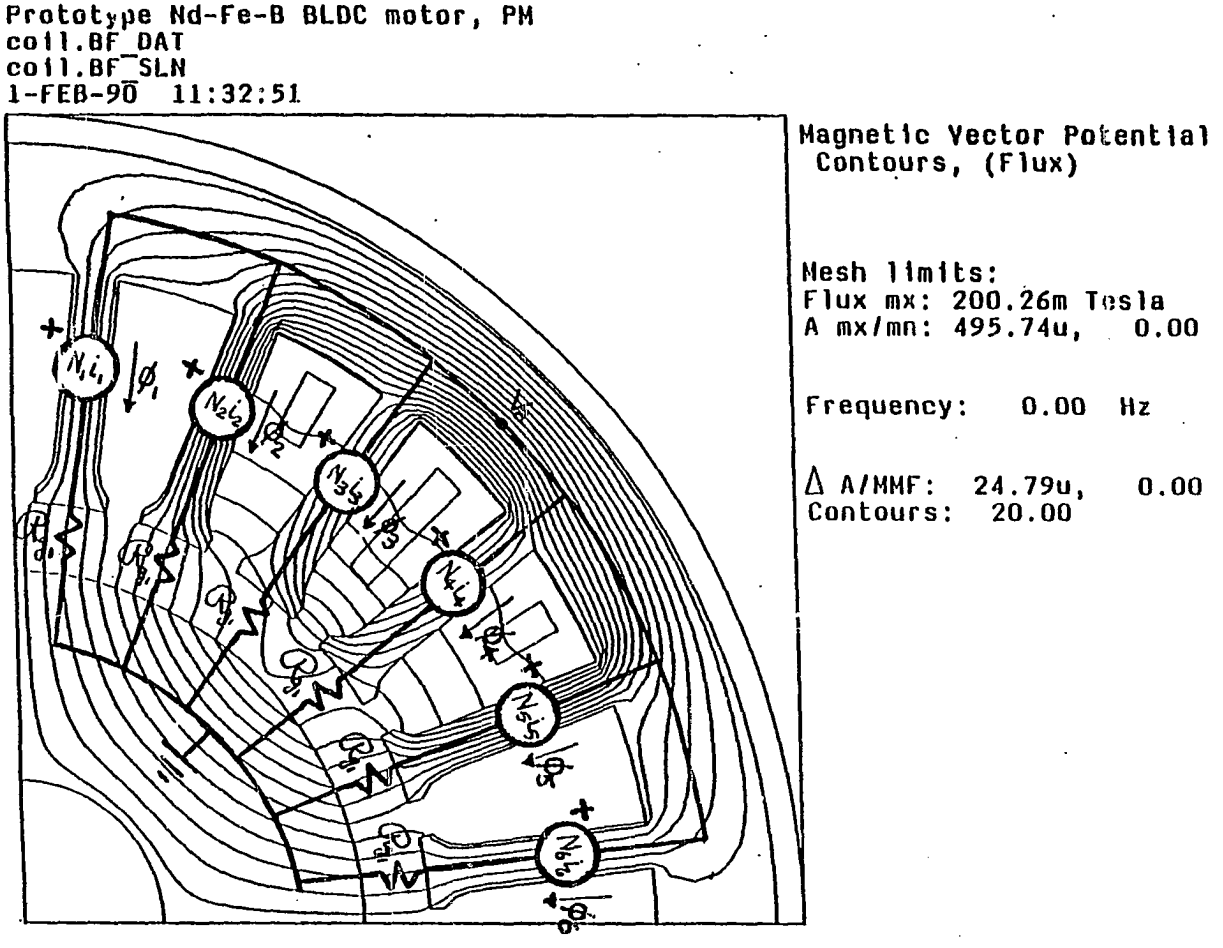

Figure VI-2
Finite Element Solution Plot for Rotor
Field and Lumped Circuit Model Superimposed

The contour plot of Figure VI-2 shows the field solution to the FEM of the prototype motor with no permanent magnets and the coil energized. Denoting the leftmost tooth as tooth 1 and the rightmost as tooth 6, one sees that the flux from tooth faces 1,2,5,6 is in the radial direction and matches the direction of the flux tubes chosen. The flux from tooth faces 3 and 4 is mostly radial but there is also a strong tangential component to the flux emanating from the right edge of tooth 3 and the left edge of tooth 4. This is leakage flux that is not included in the model. In general, the direction of the flux tubes chosen for the lumped model coincide with the direction of the flux tubes revealed by the contour plot of the field solution.

As in the finite element model, symmetry has been used to reduce the size of the lumped model to one quarter of the original problem. $\mathcal{R}_g$ is the reluctance of the airgap under the tooth face. $N_k i_k$ is the mmf source for the flux emenating from tooth k, and V_a is a unknown variable to be used with the nodal approach to solving the circuit.

Writing the nodal equations and the flux constraints for this circuit yields:

$$V_a - N_1 i_1 = \phi_1 \mathcal{R}_g \quad \text{(VI-13)}$$
$$V_a - N_2 i_2 = \phi_2 \mathcal{R}_g \quad \text{(VI-14)}$$
$$V_a - N_3 i_3 = \phi_3 \mathcal{R}_g \quad \text{(VI-15)}$$
$$V_a - N_4 i_4 = \phi_4 \mathcal{R}_g \quad \text{(VI-16)}$$
$$V_a - N_5 i_5 = \phi_5 \mathcal{R}_g \quad \text{(VI-17)}$$
$$V_a - N_6 i_6 = \phi_6 \mathcal{R}_g \quad \text{(VI-18)}$$

$$\phi_1 + \phi_2 + \phi_3 + \phi_4 + \phi_5 + \phi_6 = 0 \quad \text{(VI-19)}$$

Solving for ϕ_i in Equations VI-13 through VI-18 and substituting into Equation VI-19 yields an expression for Va:

$$V_a = \frac{N_1 i_1 + N_2 i_2 + N_3 i_3 + N_4 i_4 + N_5 i_5 + N_6 i_6}{6} \qquad \text{(VI-20)}$$

In any 4 pole 24 slot motor with a symmetric winding, such as the prototype motor, the following constraints apply:

$$N_6 i_6 = -N_1 i_1 \qquad \text{(VI-21a)}$$

$$N_5 i_5 = -N_2 i_2 \qquad \text{(VI-21b)}$$

$$N_4 i_4 = -N_3 i_3 \qquad \text{(VI-21c)}$$

Substitution of constraint Equations VI-21 into Equation VI-20 yields:

$$V_a = N_1 i_1 + N_2 i_2 + N_3 i_3 - N_3 i_3 - N_2 i_2 - N_1 i_1 = 0 \qquad \text{(VI-22)}$$

V_a will always be zero for any motor with a symmetric winding, regardless of the number of poles and stator slots. Since Va is equal to zero the fluxes in the airgaps of the prototype motor can be solved using Equations VI-13 through VI-19.

$$\phi_k = \frac{N_k i_k}{\mathcal{R}_g} \qquad \text{(VI-23)}$$

Where: k=1,2,...6

Given Equation VI-23, and the constraints for the prototype motor given in Equations VI-24, the fluxes in the airgaps are given by Equation VI-25.

$$N_6 i_6 = -N_1 i_1 \qquad \text{(VI-24a)}$$

$$N_5 i_5 = -N_2 i_2 \qquad \text{(VI-24b)}$$

$$N_3 i_3 = -N_4 i_4 \qquad \text{(VI-24c)}$$

$$N_2 i_2 = N_1 i_1 \qquad \text{(VI-24d)}$$

$$N_3 i_3 \simeq N_1 i_1/2 \qquad \text{(VI-24e)}$$

$$N_1 = N_2 = N_5 = N_6 = 2N_3 = 2N_4 \qquad \text{(VI-24f)}$$

$$\phi_1 = \phi_2 = -\phi_5 = -\phi_6 = \frac{N_1 i_1}{\mathcal{R}_g} \qquad \text{(VI-25a)}$$

$$\phi_3 = -\phi_4 = \frac{\phi_1}{2} = \frac{N_1 i_1}{2\mathcal{R}_t} \qquad \text{(VI-25b)}$$

The winding specifics of the prototype motor with a winding current of 1 Amp are used to determine the mmf sources of the circuit. Equation VI-12 and the geometry of the prototype motor can be used to calculate the reluctance, see Figure VI-3. This figure shows a flux tube over a tooth face, the tube has length ℓ and an average cross-sectional area, A_e.

If the flux found in each tube is divided by the average area of each tube, one finds the average flux density in each tube:

Table VI-1
Flux Densities Predicted by Lumped Model for Coil

$B_1 = \phi_1/A_e = 24.78$ milli-Tesla
$B_2 = B_1 = 24.78$ milli-Tesla
$B_3 = \phi_3/A_e = 12.39$ milli-Tesla
$B_4 = -B_3 = -12.39$ milli-Tesla
$B_5 = -B_2 = -24.78$ milli-Tesla
$B_6 = -B_1 = -24.78$ milli-Tesla

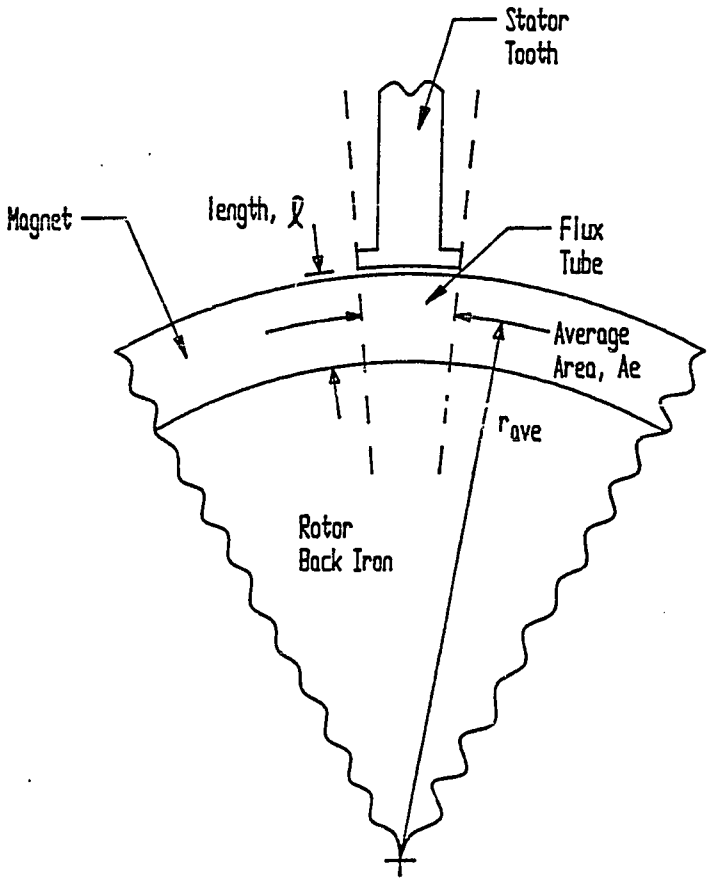

Figure VI-3
Geometry Used to
Calculate the Flux Tube Reluctance

These results can now be compared to finite element results. Figure VI-4a shows the finite element predicted distribution of the average magnitude, radial component, and theta, (tangential), component of flux density in the air gap. The data for this plot was obtained by averaging the flux densities in each column of elements over the magnet/airgap region. This is similar to plotting the flux density in a row of elements along the average radius of the magnet/airgap region. A comparison of the FEM predicted B_{rad} component with the lumped parameter predicted values is shown in Figure VI-4b. The dashed lines indicate B_{rad} results predicted for the teeth faces from the lumped model and the solid line indicates the FEM results. One sees that the correlation between B_{rad} results over the tooth faces is very good. The lumped model did not model tangential components so no comparison with that data was made. Also, the lumped model did not include models for the slot faces so no comparison was made over those regions either.

The excellent correlation between lumped and FEM B_{rad} data indicates that the lumped model can be used to predict peak torque with good accuracy. One simply needs to predict the coil flux density over the tooth faces and use the IxB method on the magnet equivalent currents to predict the peak torque.

While the distribution predicted by the lumped model correlated well with the average distribution predicted by the FEM, it should be noted that the FEM predicted distribution in any row of finite elements in the airgap is a strong function of the radius of the row of elements. Figure VI-5 shows the distribution in a row of elements along the stator teeth, and Figure VI-6 shows the distribution in a

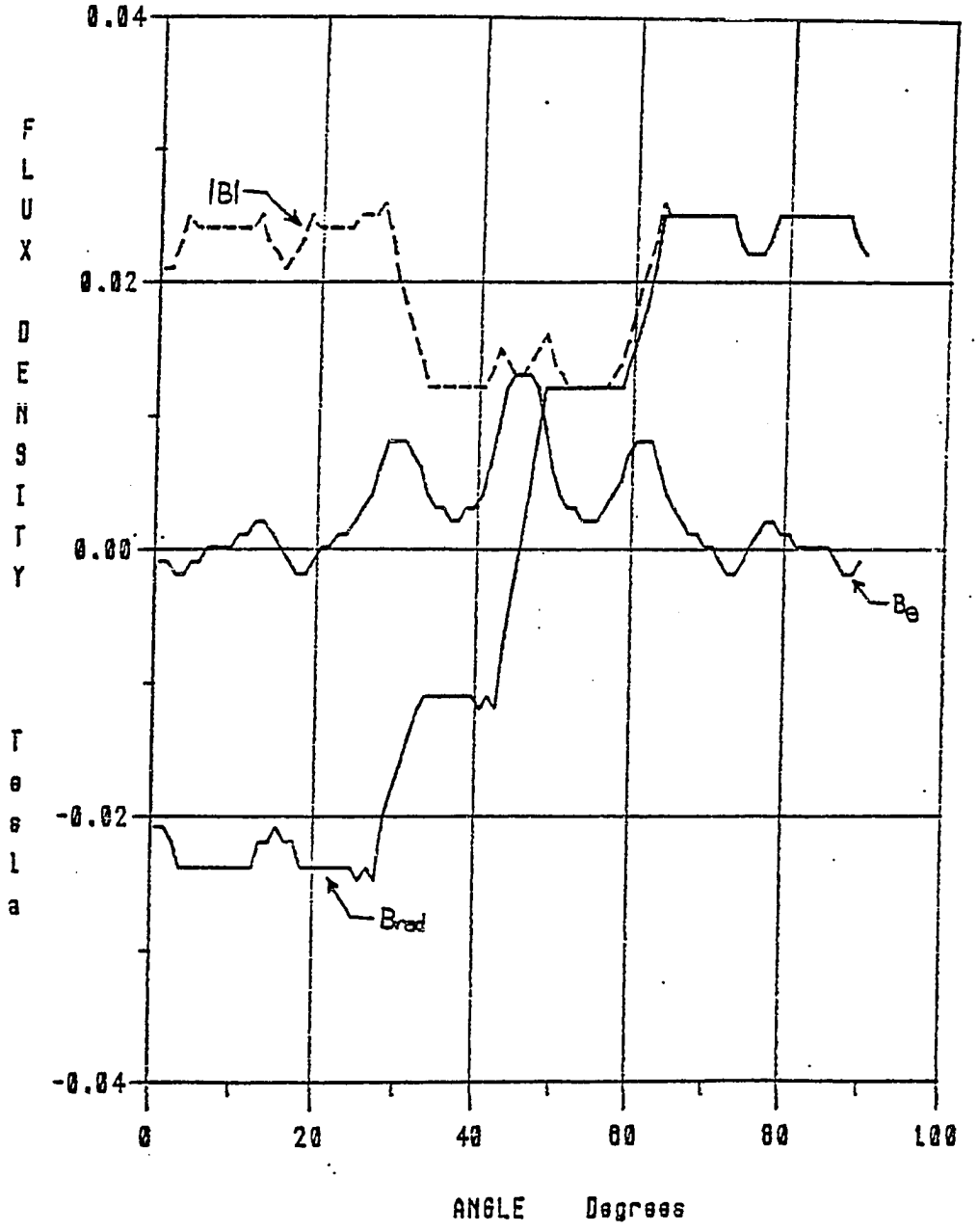

Figure VI-4a
Finite Element Predicted Average
Flux Density Distribution in Airgap

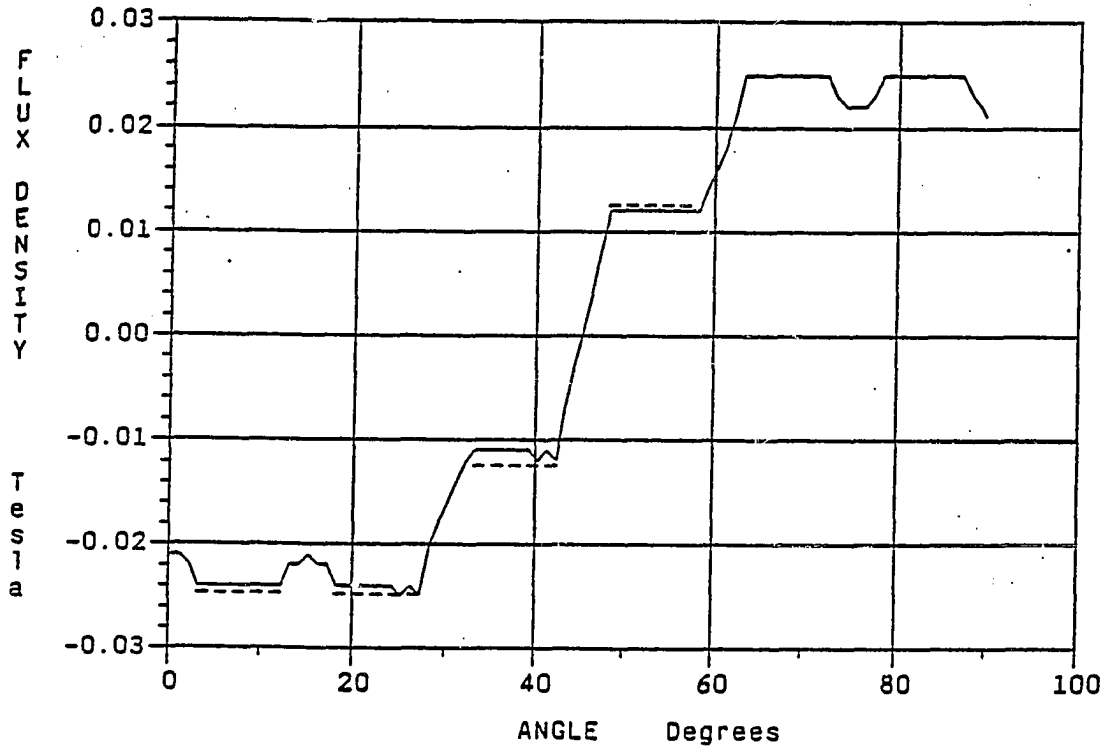

Figure VI-4b
Comparison of Finite Element, (Solid Line), and
Lumped Element Model Predicted, (Dashed Line),
Distribution of Average Radial Component
of Airgap Flux Density Distribution

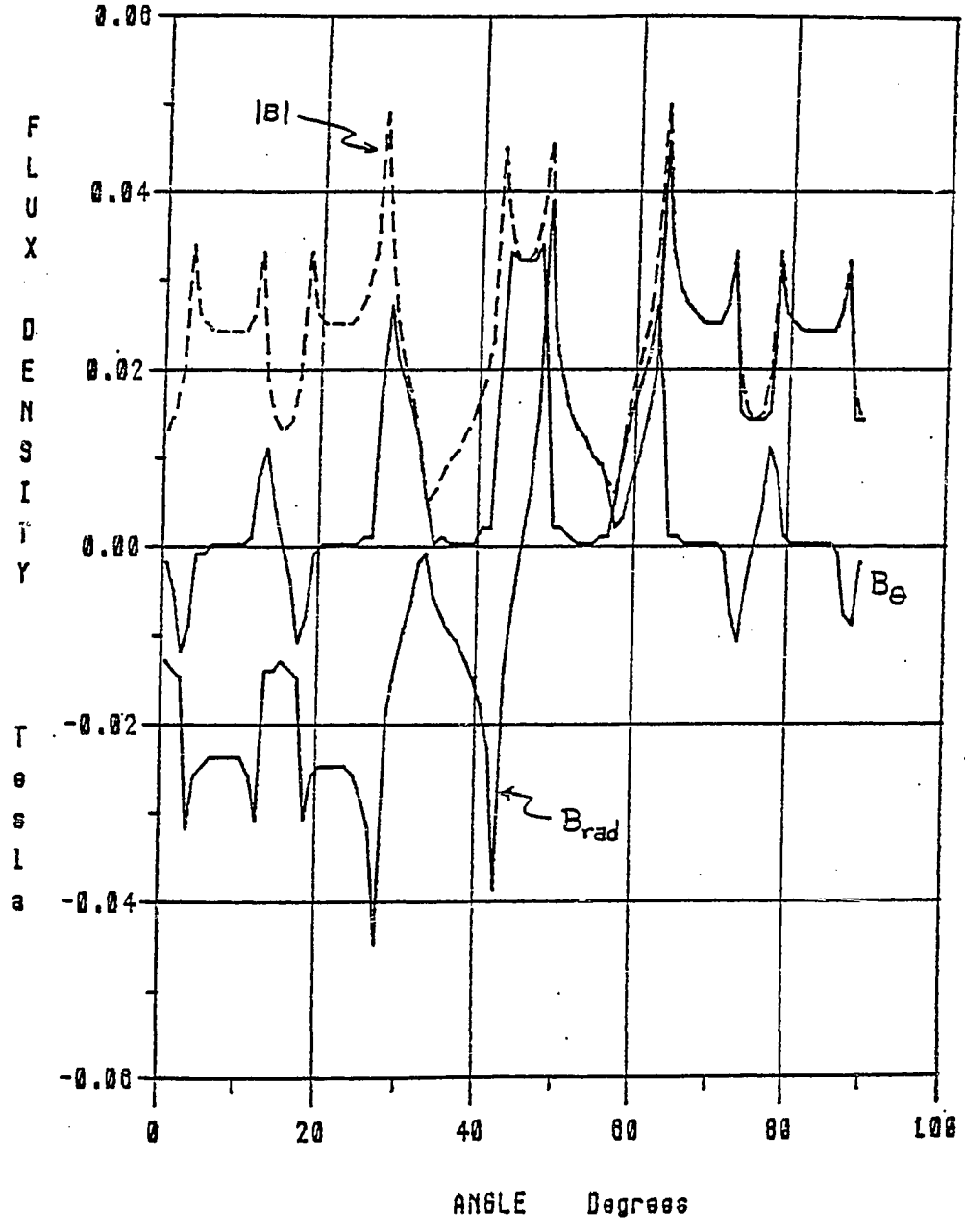

Figure VI-5
Finite Element Predicted Flux Density
Distribution in a Row of Elements Along
the Edge of the Stator Tooth Faces

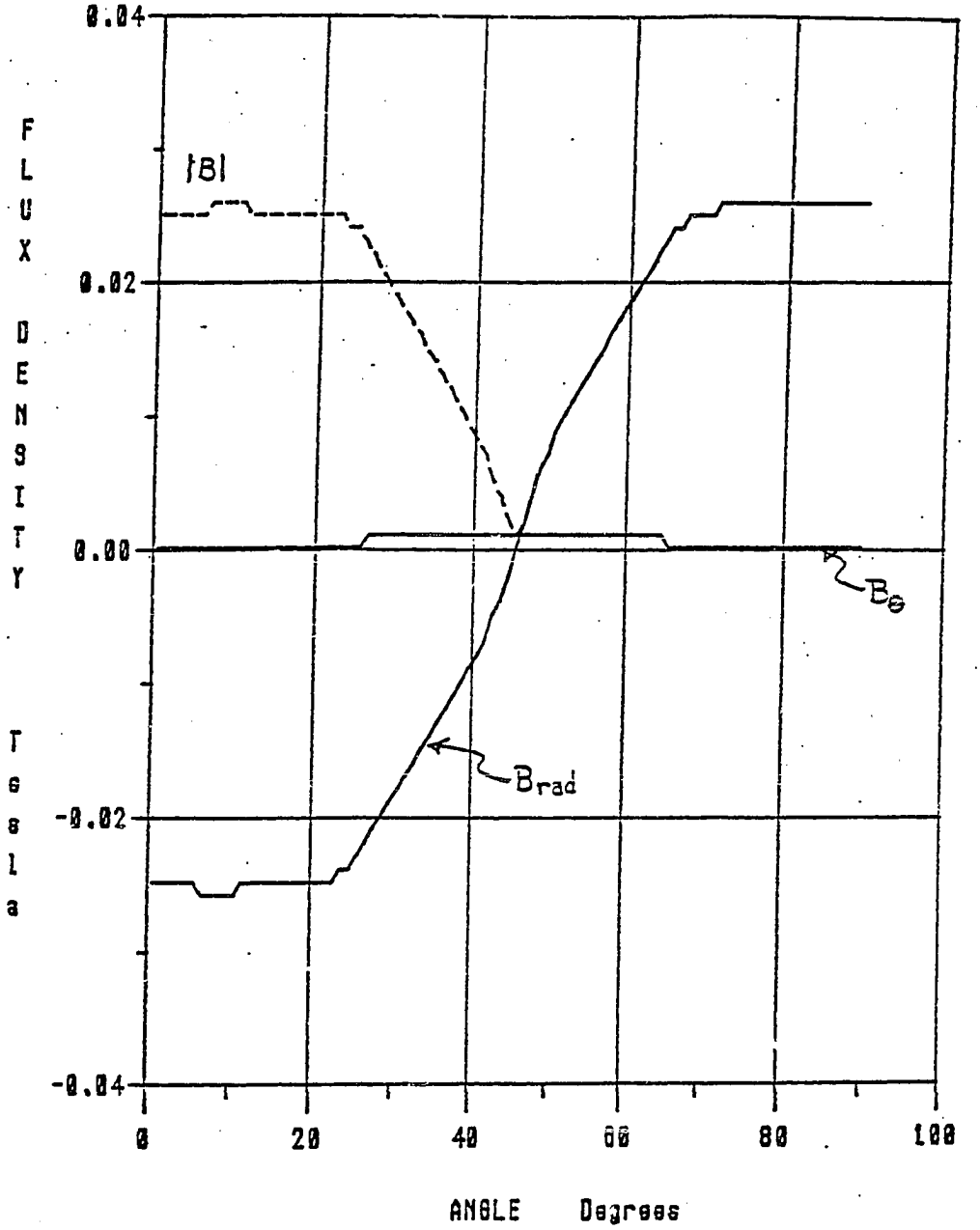

Figure VI-6
Finite Element Predicted Flux Density
Distribution in a Row of Elements Along
the Surface of the Rotor Back Iron

row of elements along the surface of the rotor back iron. One sees that there is an extreme variation between the two waveforms. While the lumped model allows the magnitude of B to change with radius within the tube, the waveform shape predicted by the lumped model cannot change unless the model is changed.

Suppose the lumped model is used to predict the coil inductance. For the linear magnetic model, inductance is defined as the coil flux linkage divided by the coil current.

$$L = \frac{\lambda_t}{i} \qquad \text{(VI-26)}$$

The total flux linkage linking the coil, (substituting the constraint Equations VI-24d&24e), is:

$$\lambda_t = 4\sum N_i \phi_i = 4(\ 2(N_1 \phi_1 + N_2 \phi_2 + N_3 \phi_3)) = 18\ N_1 \phi_1 \qquad \text{(VI-27)}$$

Substituting Equation VI-25a for ϕ_1 yields:

$$\lambda_t = \frac{18\ N_1^{\,2}\, i}{\mathcal{R}_g} \qquad \text{(VI-28)}$$

Therefore, the inductance is given as:

$$L = \frac{18\ N_1^{\,2}}{\mathcal{R}_g} \qquad \text{(VI-29)}$$

This expression is used to calculate the inductance for the prototype motor. Comparing results with the finite element and experimentally

determined results yields:

Table VI-2
Comparison of Model Predicted and Measured Inductance

L_{lumped} = 0.0037 Henries
L_{FEM} = 0.0078 Henries
L_{exp} = 0.0100 Henries

Measured and finite element inductances were obtained with having only the rotor back iron present in the motor (i.e. no magnets), thereby reducing saturation effects. The lumped parameter value is 52% lower than the finite element results and 63% lower than the experimental results. This is a large discrepancy. One would expect the inductance to be lower than the experimental value because no end leakage paths have been included. However, one would expect the model results to be closer to the finite element predicted value. This discrepancy indicates that only half the inductance is due to flux which leaves the tooth faces and crosses the airgap. The rest must be due to: flux leaving the sides of the teeth and crossing the airgap, flux leaking from tooth tip to tooth tip, and flux leaking from tooth shank to tooth shank. Each of these leakages can be examined individually to determine the relative contributions.

The first additional flux path included in the model will be the flux from the slot faces to the rotor back iron. Not only will this addition increase the accuracy of the inductance model but will also complete the model of the flux density in the airgap. Thus, a complete picture of the radial component of coil flux density in the airgap is obtained.

Figure VI-7 shows a model with paths included for flux emanating from the tooth tips and crossing the airgap over the face of the

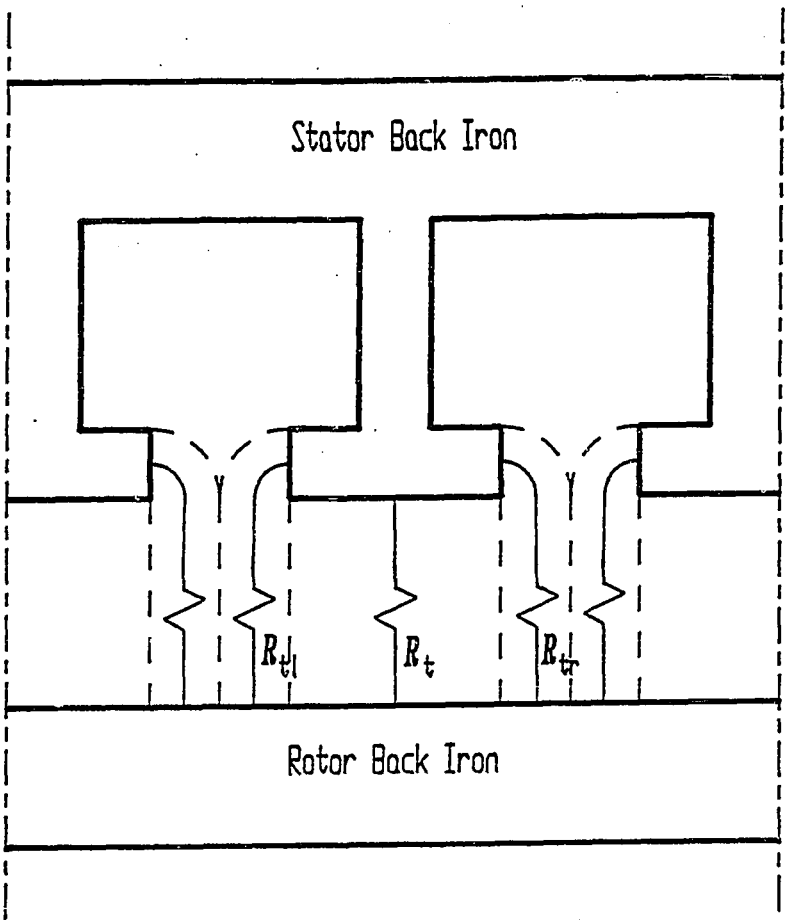

Figure VI-7
Improved Lumped Model Showing
Leakage Paths at Tooth Tips

slots. For illustrative purposes the motor shown is a linear motor. The dashed lines indicate the flux tube boundaries. The reluctances are:

$\mathcal{R}_t$ = Reluctance of tooth face

$\mathcal{R}_{tl}$ = Reluctance from left side of tooth face, (slot region)

$\mathcal{R}_{tr}$ = Reluctance from right side of tooth face, (slot region)

$\mathcal{R}_{tl} = \mathcal{R}_{tr}$

This model does not change the form of the solution found for the previous model. Now, however, $\mathcal{R}_g$ used in the previous solution is replaced by the effective reluctance, $\mathcal{R}_{eff}$, of the three reluctances: $\mathcal{R}_t, \mathcal{R}_{tl}, \mathcal{R}_{tr}$ in parallel.

$$\mathcal{R}_{eff} = \frac{\mathcal{R}_t \mathcal{R}_{tr} \mathcal{R}_{tl}}{\mathcal{R}_{tl}\mathcal{R}_{tr} + \mathcal{R}_t\mathcal{R}_{tr} + \mathcal{R}_t\mathcal{R}_{tl}} \qquad \text{(VI-30)}$$

Since the three reluctances, $\mathcal{R}_t$, $\mathcal{R}_{tl}$, $\mathcal{R}_{tr}$ are in parallel, the flux in each reluctive element is given as:

$$\phi_t = \frac{N_k i_k}{\mathcal{R}_t} \qquad \phi_{tl} = \frac{N_k i_k}{\mathcal{R}_{tl}} \qquad \phi_{tr} = \frac{N_k i_k}{\mathcal{R}_{tr}} \qquad \text{(VI-31a,b,c)}$$

Where: k ≡ the tooth number

The newly defined reluctances must be evaluated. $\mathcal{R}_t$ is actually the same reluctance that was refered to previously as $\mathcal{R}_g$. $\mathcal{R}_{tl}$, $\mathcal{R}_{tr}$ can be evaluated using the arc-straight line method[16] for the flux tube that encompasses half the slot and part of one side of the tooth. The flux density for each tooth face and each slot face of the prototype motor can be calculated by dividing the fluxes calculated in Equation VI-31 by the appropriate areas. A comparison with FEM predicted B_{rad}

data is shown in Figure VI-8. The solid line is FEM predicted data and the dashed line is lumped parameter predicted data.

Figure VI-8 shows that excellent correlation was obtained for the flux densities over the tooth faces as well as the flux density at the dip in the peak. This dip corresponds to the location of a slot. However, the transition region from maximum negative flux density at 28^0 to maximum positive flux density at 65^0, shows a much more staircase effect in the lumped predicted waveform than in the FEM predicted waveform. Thus, in a region where the field direction reverses, the field pattern becomes more two-dimensional. This is seen in Figure VI-1.

If the new lumped model is used to calculate the inductance of the coil the calculated value is:

$$L = 0.0054 \text{ Henries}$$

While this new value is 46% higher than that calculated from just the tooth face model it is still 46% lower than the measured value and 31% lower than the FEM predicted value. Obviously, leakage flux paths from tooth to tooth, and perhaps even leakage paths at the end of the motor, need to be included in order to reconcile model and FEM or experimental results.

If one looks at Figure VI-1 one sees that there is a significant amount of leaking from tooth shank to tooth shank. Since this seems to be the largest amount of leakage flux, and, hence, will have the most impact on the inductance, it will be the next set of paths included in the model.

A circuit model showing leakage paths across the tooth slots is shown in Figure VI-9. Again, a linear motor is used for illustrative

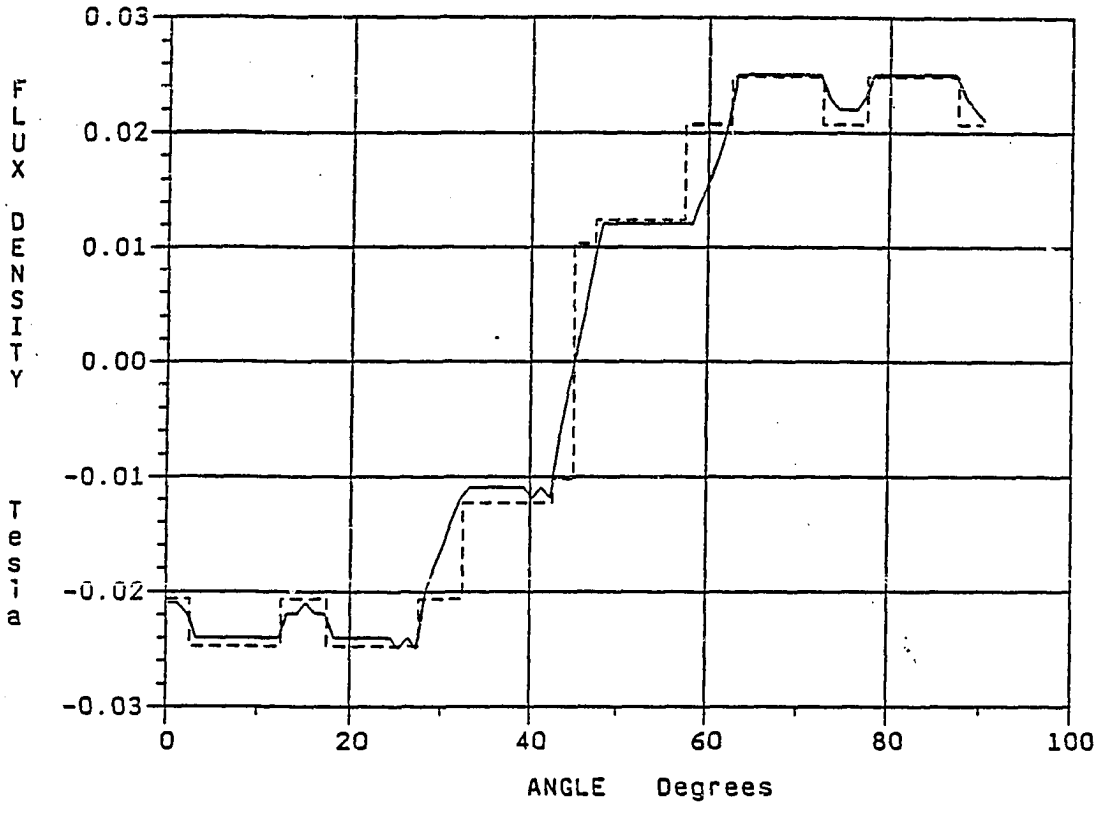

Figure VI-8
Comparison of Finite Element, (Solid Line),
and Lumped Model Predicted, (Dashed Line),
Radial Component of Airgap Flux Density

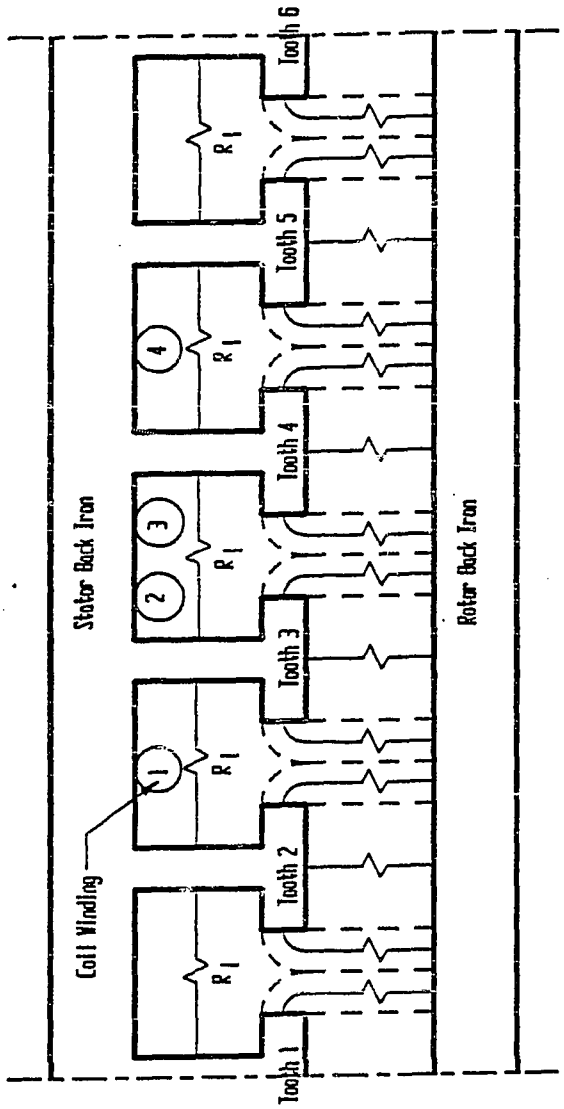

Figure VI-9
Improved Lumped Model Showing
Leakage Paths Between Tooth Shanks

purposes. The dashed lines show flux tube boundaries. $\mathcal{R}_\ell$ is the slot leakage reluctance between tooth shanks and is assumed to be equal for each of the slots. The value of $\mathcal{R}_\ell$ is calculated from the average distance between stator teeth and the average cross-sectional area of a slice through the center of the slot, (Figure VI-10). Windings are shown in Figure VI-9 as only lying in the slots between teeth 2&3, 3&4, and 4&5.

Since the leakage path is in parallel with the other flux paths, (see Figure VI-11, the equivalent circuit model), the solution found previously for the flux through the teeth and slots still applies. The total flux linking the coil is increased by the amount of flux through the leakage path. Assuming that $i_1=i_2=i_3=i_4=i_5=i_6$, and using the constraint Equations VI-24, the leakage path fluxes, ϕ_{l1}, ϕ_{l2}, ϕ_{l3}, ϕ_{l4} and ϕ_{l5} are given as:

$$\phi_{l1} = \phi_{l5} = 0 \qquad \text{(VI-32a,b)}$$

$$\phi_{l2} = \phi_{l4} = \frac{(N_2-N_3)\,i_1}{\mathcal{R}_\ell} \quad , \qquad \phi_{l3} = \frac{2N_3\,i_1}{\mathcal{R}_\ell} \qquad \text{(VI-32c,d,e)}$$

The individual flux linkage contributions of each of these paths to the total flux linking the coil are calculated in Equation VI-33.

$$\lambda_t = 8\,[\,N_1\phi_1 + N_2(\phi_2 + \phi_{l1}) + N_3(\phi_3 - \phi_{l1} + \phi_{l2})\,] \qquad \text{(VI-33)}$$

Substituting Equations VI-25 and VI-32 for the individual flux terms

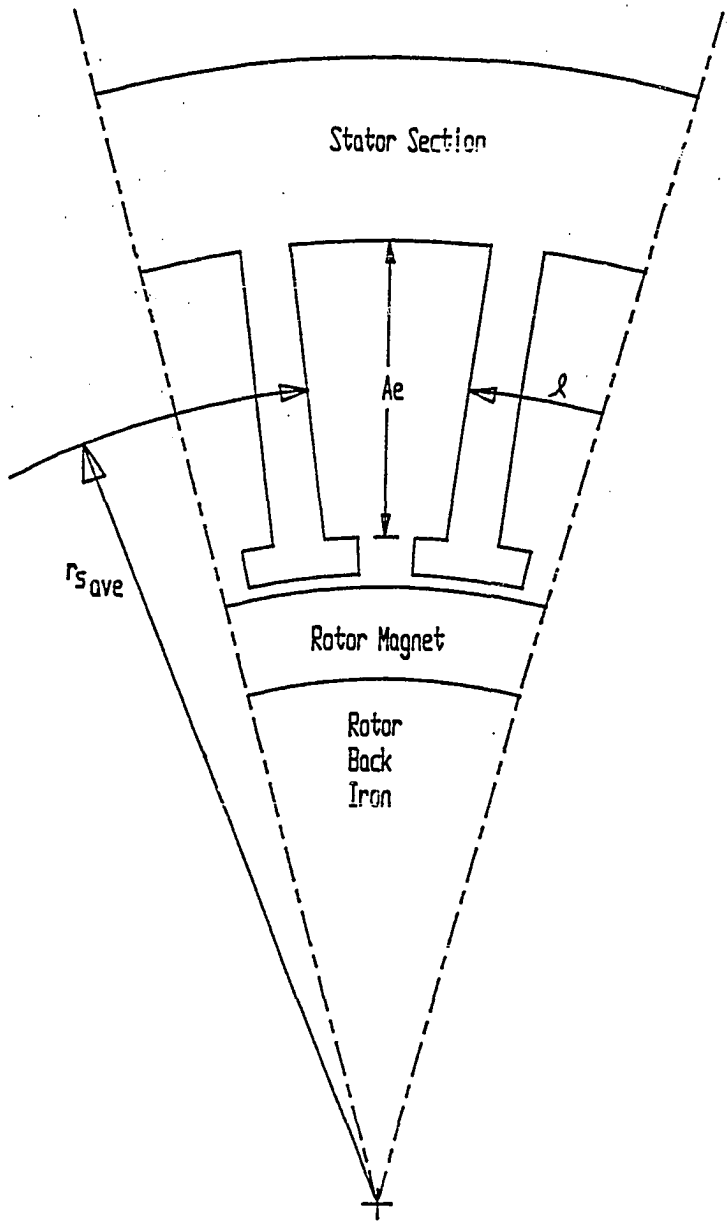

Figure VI-10
Geometry Used to Determine the
Reluctance of the Cross-Slot Leakage

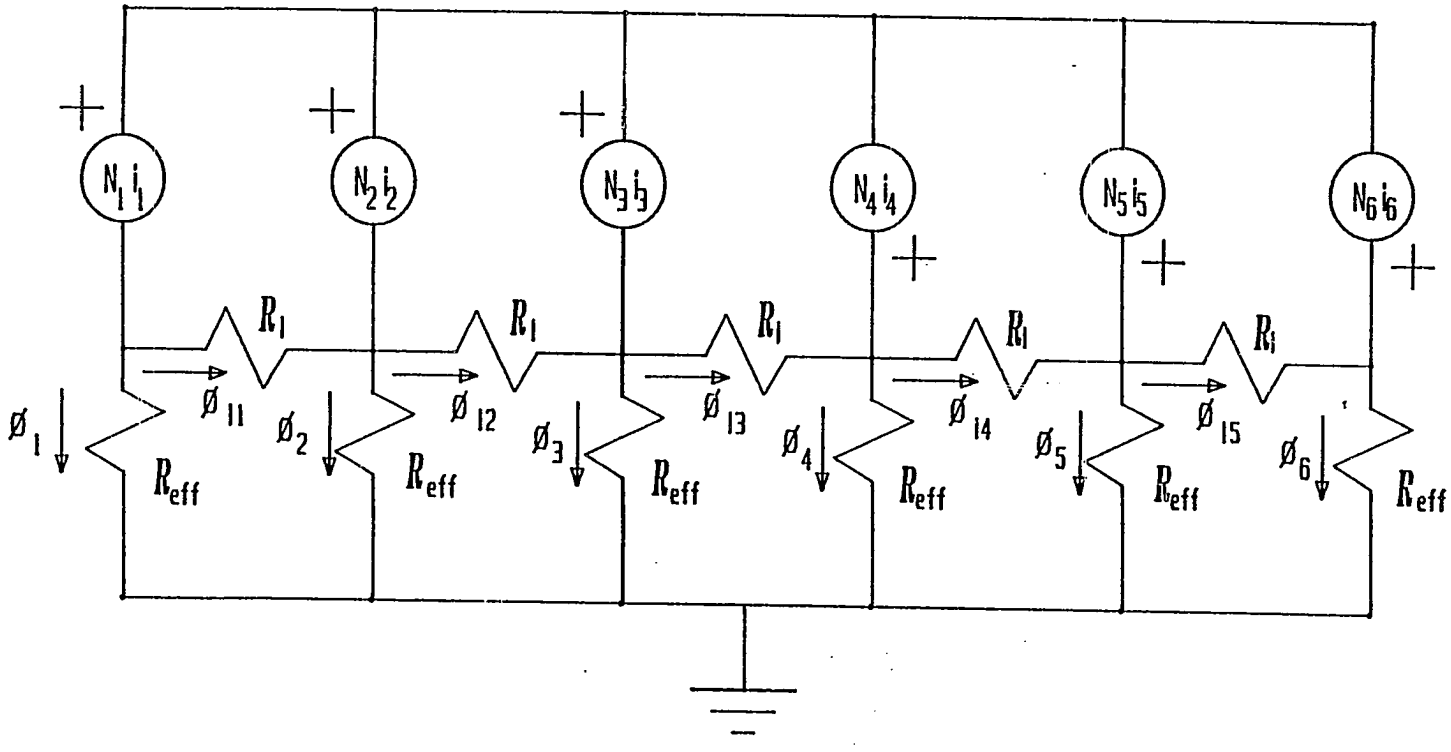

Figure VI-11a
Equivalent Circuit Network for Lumped
Model with Tooth Tip and Slot Leakage Paths

yields:

$$\lambda_t = 8 \left[\frac{N_1^2 + N_2^2 + N_3^2}{\mathcal{R}_{eff}} + \frac{N_2^2 - 2N_2N_3 + 3N_3^2}{\mathcal{R}_\ell} \right] \qquad \text{(VI-34)}$$

Substituting the constraints between number of turns, given in Equations VI-24, and applying the definition of inductance yields:

$$L = \frac{\lambda_t}{i} = \frac{18\ N_1^2}{\mathcal{R}_{eff}} + \frac{6\ N_1^2}{\mathcal{R}_\ell} \qquad \text{(VI-35)}$$

Evaluation of the expression for L, using the geometry of the EAD prototype motor yields an inductance of:

$$L = 0.0084 \text{ Henries}$$

This value is 7.7% higher than that predicted by the FEM. This new calculated inductance is higher than the FEM predicted value because the lumped model assumed that each component of leakage flux calculated linked all N turns of that winding. The FEM predicted value does not include this assumption and calculates an actual value based on the two-dimensional analysis with the winding turns distributed in the slot. If a lumped model could be developed that accounted for the distribution of the winding within the slot, then the predicted cross-slot leakage would be less.

The inclusion of paths to try to represent leakage of flux around the end turns of the motor is made difficult because of the presence of the slots. Suppose a semicircular path at the ends of the stator

is assumed as shown in Figure VI-11b. The reluctance of the tube for 1 tooth pitch is $\mathcal{R}_{\ell e}$. For each tooth pitch there are two of these reluctance paths in parallel, one for each end of the motor. Because the leakage paths are in parallel with each of the mmf sources, an expression for the end leakage flux can be written directly as:

$$\phi_{\ell e} = \frac{2\ N_k\ i_k}{\mathcal{R}_{\ell e}} \qquad \text{(VI-35b)}$$

The end leakage flux linkage, λ_e, can be expressed as:

$$\lambda_e = \frac{4}{\mathcal{R}_{\ell e}} \left(2(2N_1{}^2 i_1 + 2N_2{}^2 i_2 + 2N_3{}^2 i_3) \right) \qquad \text{(VI-35c)}$$

Substituting the constraints between the number of turns for this motor, Equation VI-24, and applying the definition of inductance yields an expression for the inductance contribution due to end leakage.

$$L_{\ell e} = \frac{36\ N_1{}^2}{\mathcal{R}_{\ell e}} \qquad \text{(VI-35d)}$$

If the slots are neglected and the reluctance is calculated assuming each tube lies only over a tooth, (see Figure VI-11c), then the end leakage inductance calculated is:

$$L_{\ell e} = 0.0003 \text{ Henrys}$$

This would only increase the total inductance for the phase by 3.6%, making it 0.0087 Henrys which is 13% less than the measured value of

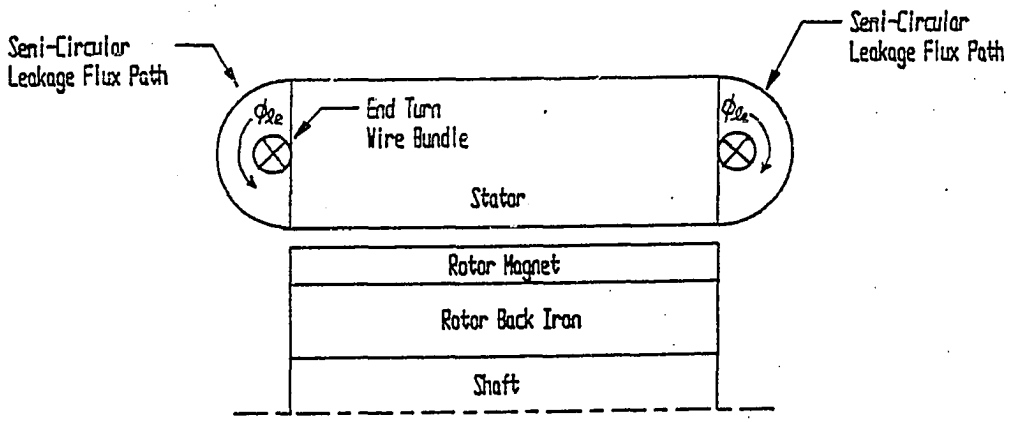

Figure VI-11b
R-Z View of Motor Showing End Turn Bundle
and Assumed Semi-Circular Leakage Flux Paths

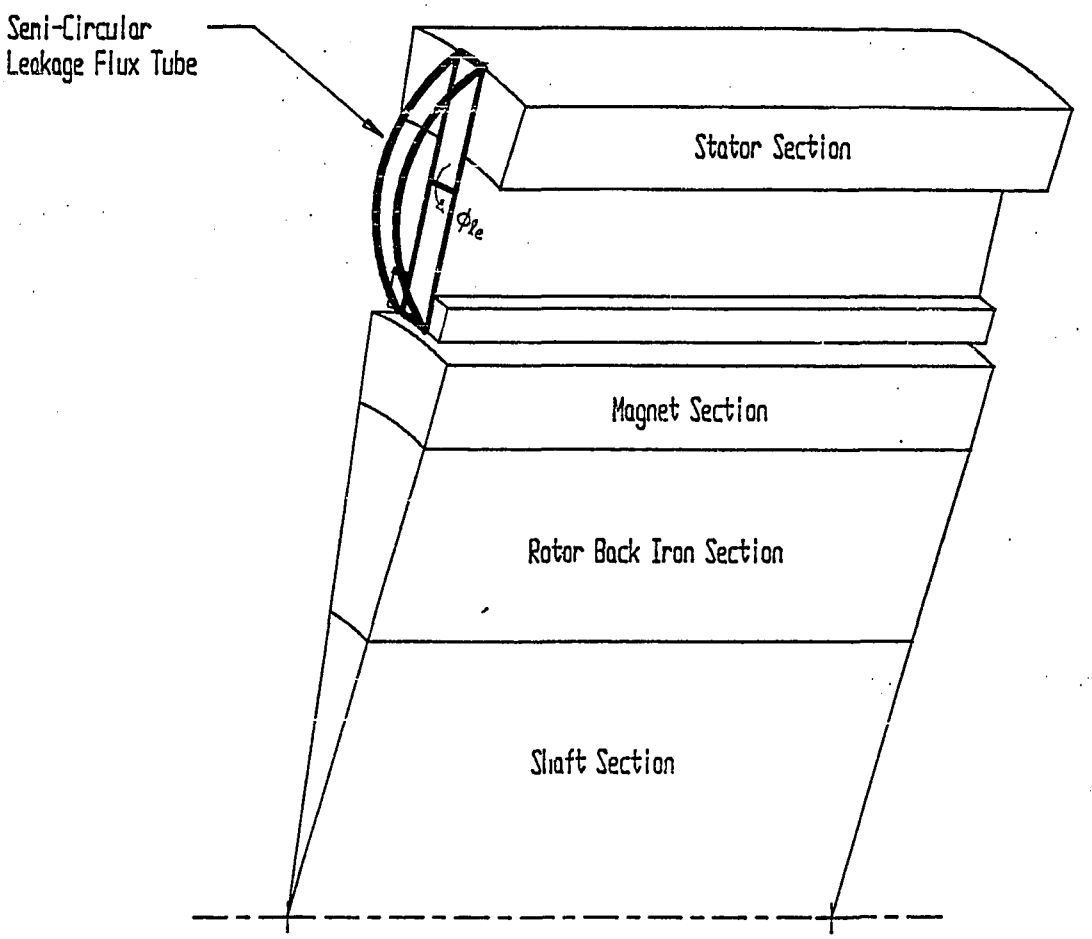

Figure VI-11c
One Tooth Pitch Slice of Motor Showing
Semi-Circular Leakage Flux Path Over Iron Tooth Shank

0.01 Henrys. On the other hand, if it is assumed that the stator is basically an annulus so that the tube encompasses both the slot and the tooth, (Figure VI-11d), the end leakage inductance calculated is:

$$L_{\ell e} = .0047 \text{ Henrys}$$

This is a 56% increase in the total inductance making it 0.013 Henrys, which is 30% higher than the measured value. Obviously, a model more complicated than either of these is necessary to model the end leakage more accurately. The development of this model is complicated by the three-dimensional nature of the field in the end turns region, as well as the partial linkage with turns.

VI.3 Simple Lumped Model to Determine the Airgap Flux Density Due to the Permanent Magnet

One can also develop a lumped model for the permanent magnet flux and compare the predicted average flux densities in the airgap to finite element results. Magnetic circuit models similar to the ones developed previously can be used; except now the mmf sources are due to the magnets instead of the coils. The physical connection between the mmf sources in the model and the magnets is not as strong in this case as it was in the model for the coil. In the coil case, because the coils were wound around iron and there was virtually no mmf drop across the iron, the surface of the iron at the tooth faces was all at the same mmf potential. In this case, the actual mmf provided by the magnet is distributed in the airgap; therefore this model is more of an approximation.

A further complication in this model is that the mmf source due to the magnet is position dependent. Figure VI-12a shows one tooth of

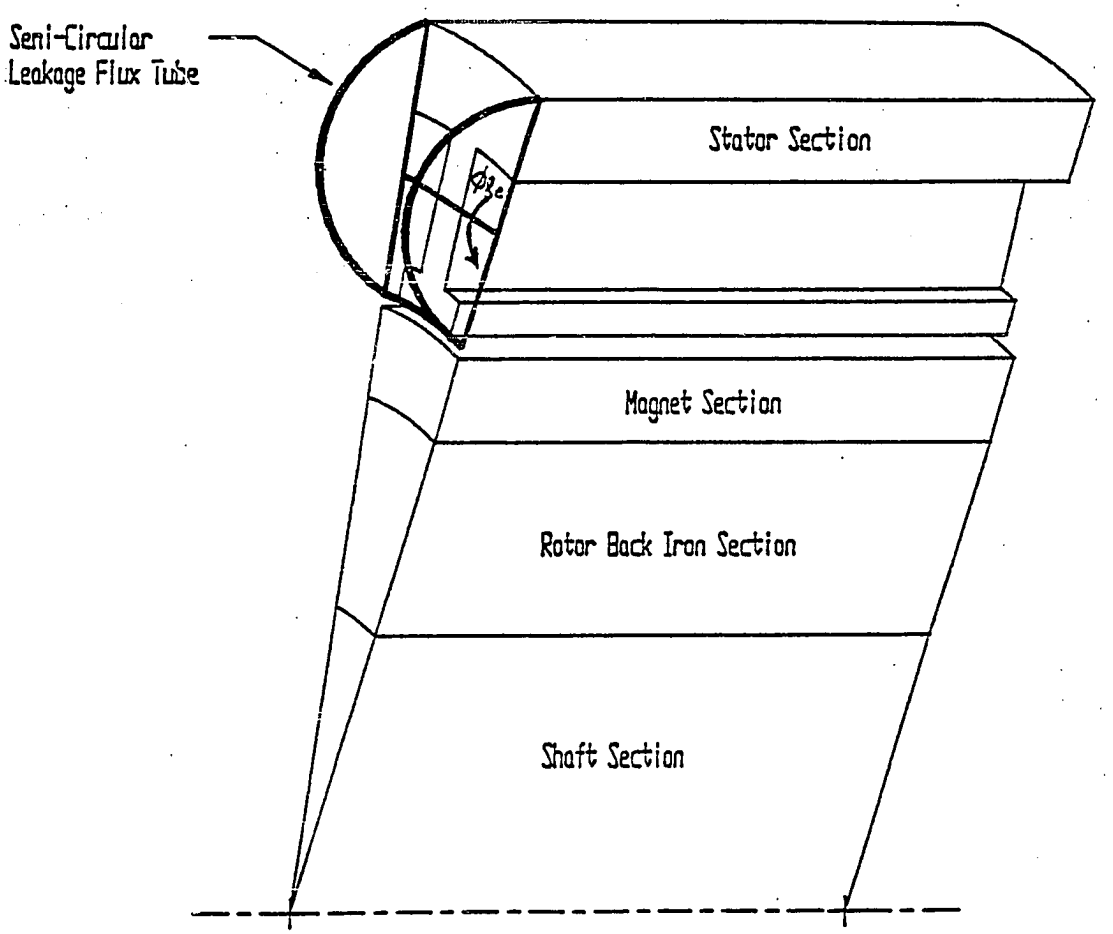

Figure VI-11d
One Tooth Pitch Slice of Motor Showing
Semi-Circular Leakage Flux Path Over
the Full Tooth Pitch Slice

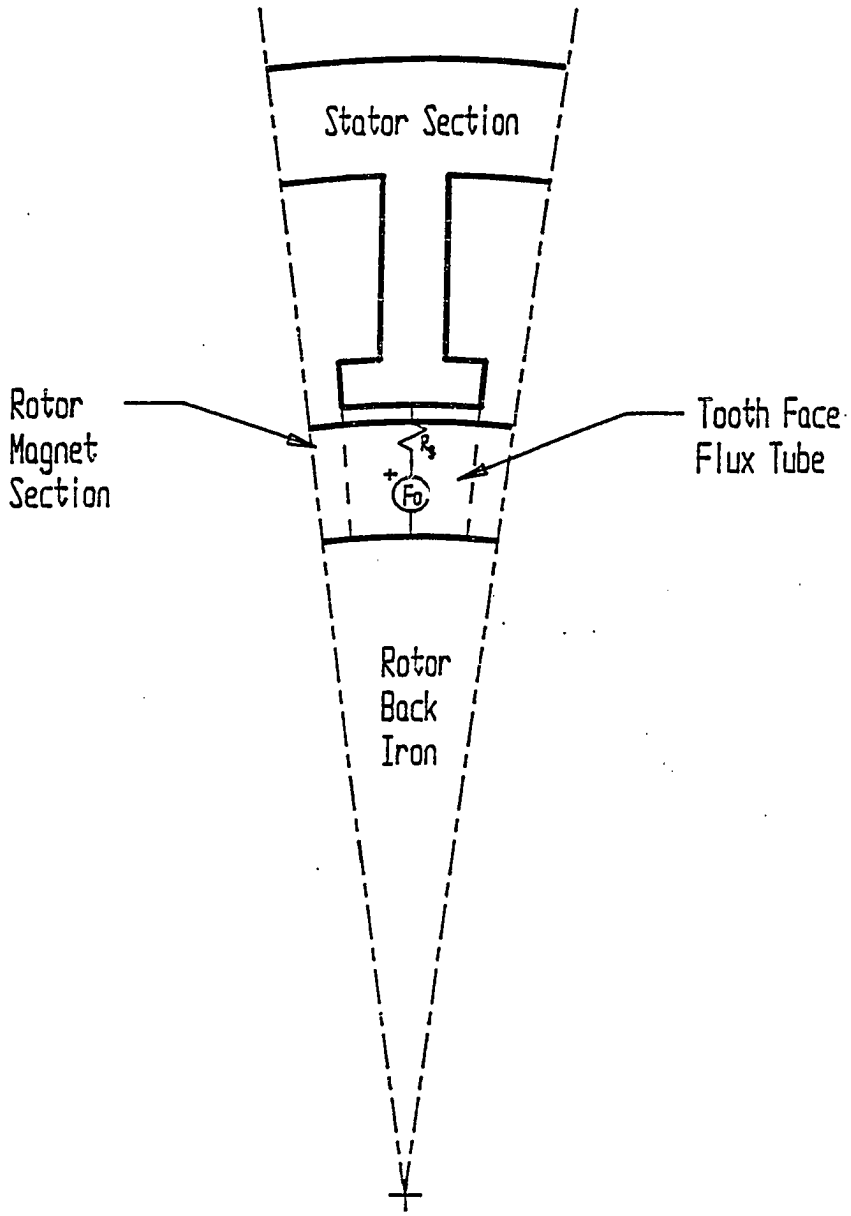

Figure VI-12a
Model for Tooth Face Airgap with Magnet MMF Source

the BLDCM with magnet and modeled mmf sources. While the magnet interface is over a particular tooth, (Figure VI-12b), the mmf source used for that lump will be the average mmf provided by the magnet. While this seems to be a reasonable assumption to make, it actually violates one of the basic assumptions outlined in the derivation of the lumped element model; namely that the integral, H·dl is constant over the element. The product H·dℓ actually changes sign over this region. However, it will be shown that a model using the average mmf provides a good approximation for the average flux through the element.

The average mmf is given as:

$$F_{ave} = \frac{1}{\tau_t} \int_0^{\theta_2} F_m(\theta)\, r_{ave}\, d\theta = \frac{F_o(\tau_t - r_{ave}\theta) - F_o r_{ave}\theta}{\tau_t} \qquad \text{(VI-36)}$$

Where: $\tau_t \equiv r_{ave}\ \theta_2$

A simple circuit model for two poles of the magnet, assuming the magnet interfaces are over teeth 1 and 7, is shown in Figure VI-13. Nodal expressions for fluxes ϕ_1 and ϕ_7 can be written:

$$\phi_1 = \frac{V_a - F_{ave}}{\mathcal{R}_g} \qquad \phi_7 = \frac{V_a + F_{ave}}{\mathcal{R}_g} \qquad \text{(VI-37,38)}$$

and a general expression for flux ϕ_2 through ϕ_6 as:

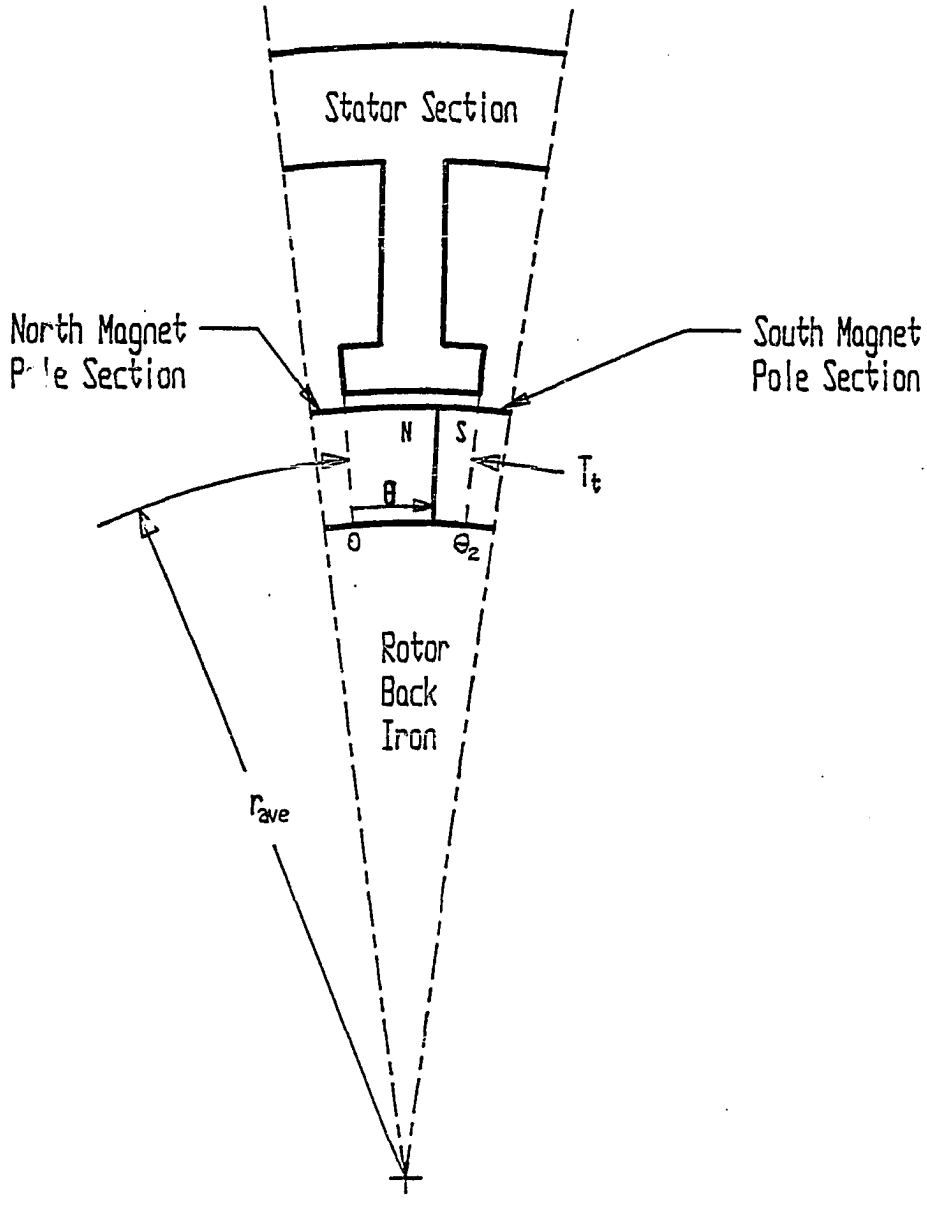

Figure VI-12b
Geometry Used for Calculation of Average MMF When
the Magnet Interface Is over a Tooth Face

$$\phi_j = \frac{V_a - F_o}{\mathcal{R}_g} \qquad \text{(VI-39)}$$

A general expression for flux ϕ_8 through ϕ_{12} is:

$$\phi_k = \frac{V_a + F_o}{\mathcal{R}_g} \qquad \text{(VI-40)}$$

Looking at Figure VI-13, symmetry can be used to argue that nodes 1 at either end of the model are the same point; the same is true for nodes 2. Using Equations VI-41 through VI-42 to write an expression for the sum of the flux into node 1 yields:

$$\frac{V_a - F_{ave}}{\mathcal{R}_g} + 5\left(\frac{V_a - F_o}{\mathcal{R}_g}\right) + \frac{V_a + F_{ave}}{\mathcal{R}_g} + 5\left(\frac{V_a + F_o}{\mathcal{R}_g}\right) = 0 \qquad \text{(VI-41a)}$$

Which reduces to :

$$V_a = 0 \qquad \text{(VI-41b)}$$

Substituting Equation VI-41b for V_a in the expressions for the flux in Equations VI-36 through VI-40 yields:

$$\phi_1 = \frac{-F_{ave}}{\mathcal{R}_g}, \quad \phi_7 = \frac{F_{ave}}{\mathcal{R}_g} \qquad \text{(VI-42a,b)}$$

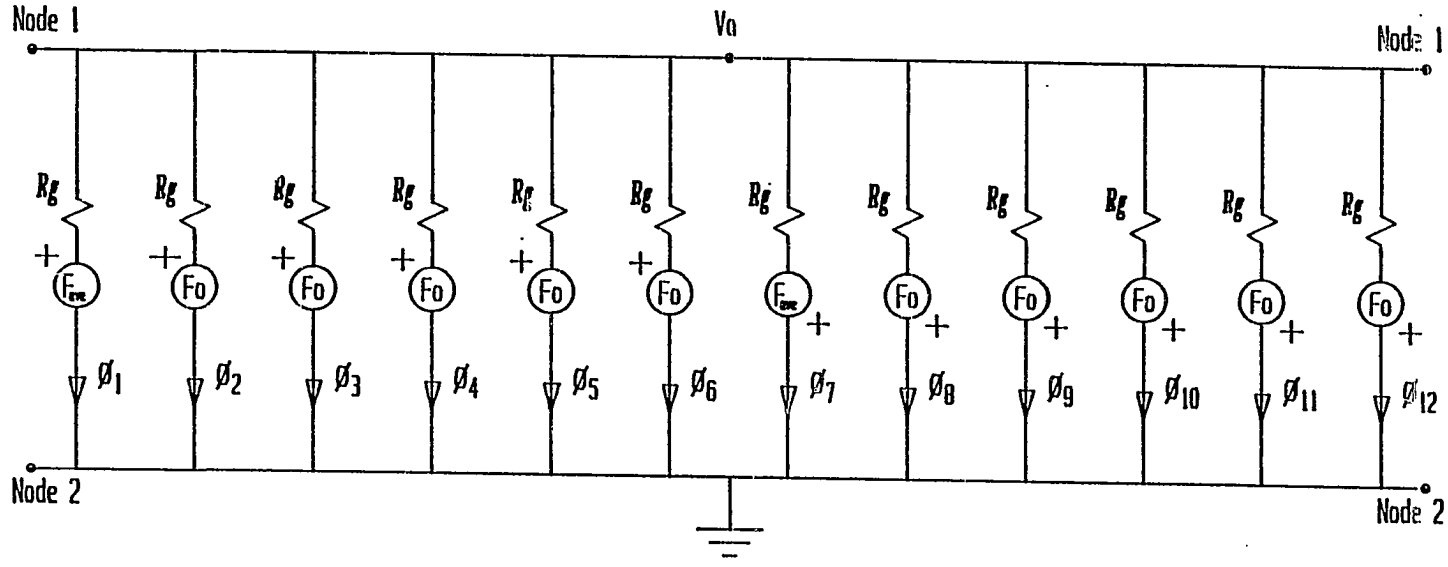

Figure VI-13
Electric Circuit Network for a Simple Model
to Determine the Airgap Flux Due to the Magnet

$$\phi_2=\phi_3=\phi_4=\phi_5=\phi_6=\frac{-F_o}{\mathcal{R}_g} \qquad \text{(VI-42c,d,e,f,g)}$$

$$\phi_7=\phi_9=\phi_{10}=\phi_{11}=\phi_{12}=\frac{F_o}{\mathcal{R}_g} \qquad \text{(VI-42h,i,j,k,l)}$$

With the rotor at $\theta=10^\circ$, the flux densities given by dividing Equations VI-42 by the average area of each element is given as:

Table VI-3
Predicted Flux Density for Lumped Magnet Model

B_1 = -0.40 Tesla,
B_2 = 0.99 Tesla
B_3 = 0.99 Tesla
B_4 = 0.99 Tesla
B_5 = 0.99 Tesla
B_6 = 0.99 Tesla
B_7 = 0.40 Tesla
B_8 = -0.99 Tesla
B_9 = -0.99 Tesla
B_{10} =-0.99 Tesla
B_{11} =-0.99 Tesla
B_{12} =-0.99 Tesla

A comparison of FEM predicted results and the lumped model results for a rotor position of $\theta=10^\circ$ is shown in Figure VI-14. Since the motor is actually quarter symmetric, data is shown for only one magnet pole face. The solid line in this figure represents FEM results and the dashed line represents lumped element results. One sees that the lumped element predicted B_{rad} value over the tooth faces is approxim-

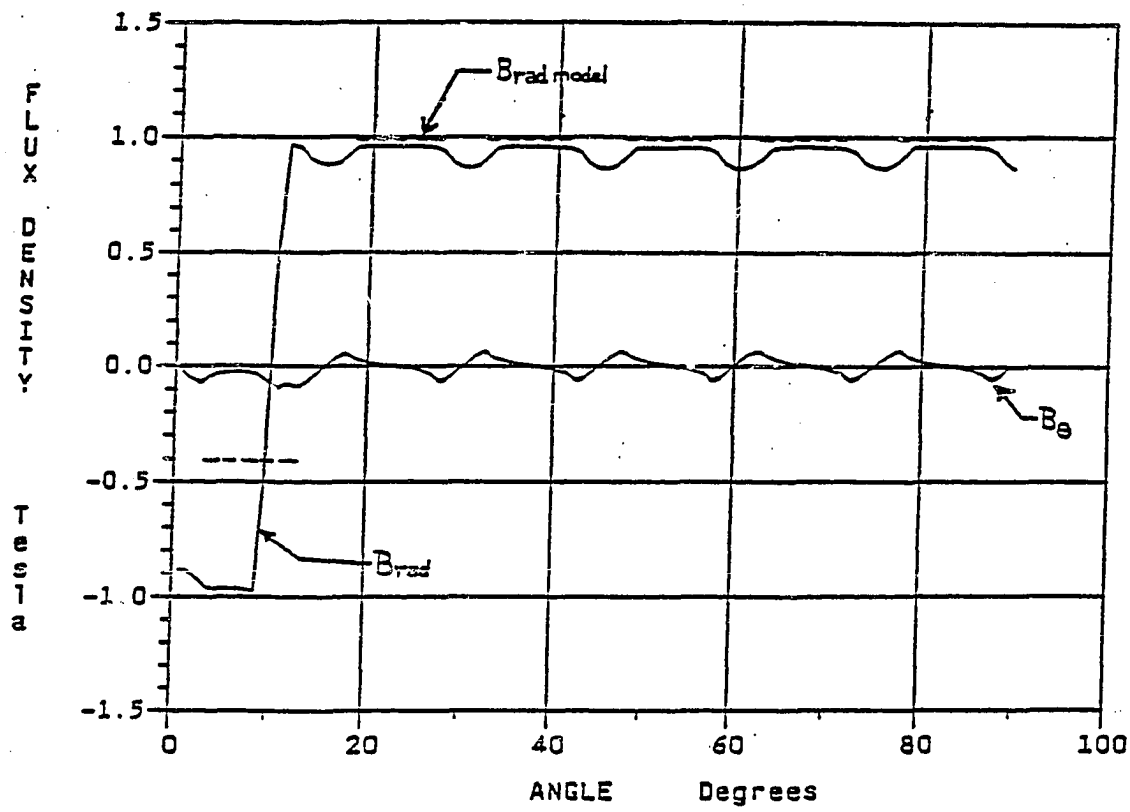

Figure VI-14
Comparison of Finite Element, (Solid Line), and
Lumped Parameter Predicted, (Dashed Line),
Distribution of Radial Component of Airgap Flux Density

ately 13.7% higher than the FEM results. Also, B_{rad} predicted for the element containing the magnet interface, element 1, is obviously in error. If one compares lumped model and FEM results on a point by point basis, over an angle from 3 to 13 degrees, one sees that the flux densities to the left and right of the interface, (at 10 degrees), are obviously of greater magnitude. This occured because the nature of the model did not allow the magnitude, (or direction), of the flux density to change over the width of the element. However, if the flux through element 1 is computed and compared, the result is:

$$\phi_{lumped} = 3.50 \times 10^{-5} \text{ Webers}$$

$$\phi_{FEM} = 3.32 \times 10^{-5} \text{ Webers}$$

The lumped model predicts the flux through the element, to be 4.5% higher than the FEM predicts. Thus, one sees that even though averaging the mmf violates one of the rules of lumped parameter analysis, it does provide a good approximation of the value of flux through the lumped element.

In the following section, it will be shown that when the mmf has both positive and negative components, using the average mmf for the lumped element can result in large errors in predicting detent torque.

VI.4 Calculation of Torque from Lumped Model

The previous sections have shown that the lumped model can be used to predict the radial component of flux density with reasonable good accuracy. Often, this type of model and the principle of virtual work, (coenergy method), have been used to predict torque. Torque is equal to the sum, over each element, of the change of coenergy with

respect to angle, (at a constant current).

$$T = \sum_{e} \frac{\partial W_{ce}}{\partial \theta} \qquad \text{(VI-43)}$$

The coenergy in a lumped circuit element is given by:

$$W_{ce} = \frac{\phi_e^{\,2}\, \mathcal{R}_e}{2} \qquad \text{(VI-44)}$$

Where: W_{ce} ≡ Coenergy of the lumped element

ϕ_e ≡ Flux in the lumped element

$\mathcal{R}_e$ ≡ Reluctance of the lumped element

This expression is based on the B-H curve for the material under consideration. B-H curves for a saturable material were shown previously in Chapter III, Figures III-4a&4b. A B-H curve for magnetically linear materials is a straight line through the origin; if the medium is air, such as in the lumped elements, then the slope of that line is μ_o, the magnetic permeability of free space.

The area under the B-H curve is the coenergy density. Integration of the coenergy density over the volume of the element yields the total coenergy of the element. The derivation of the lumped element method has shown that B is assumed to be constant over the element cross-sectional area perpendicular to its direction. However, B can vary along the length of the path. Assuming B is constant within the element, the coenergy is often expressed in terms of the flux through the element and reluctance of the element.

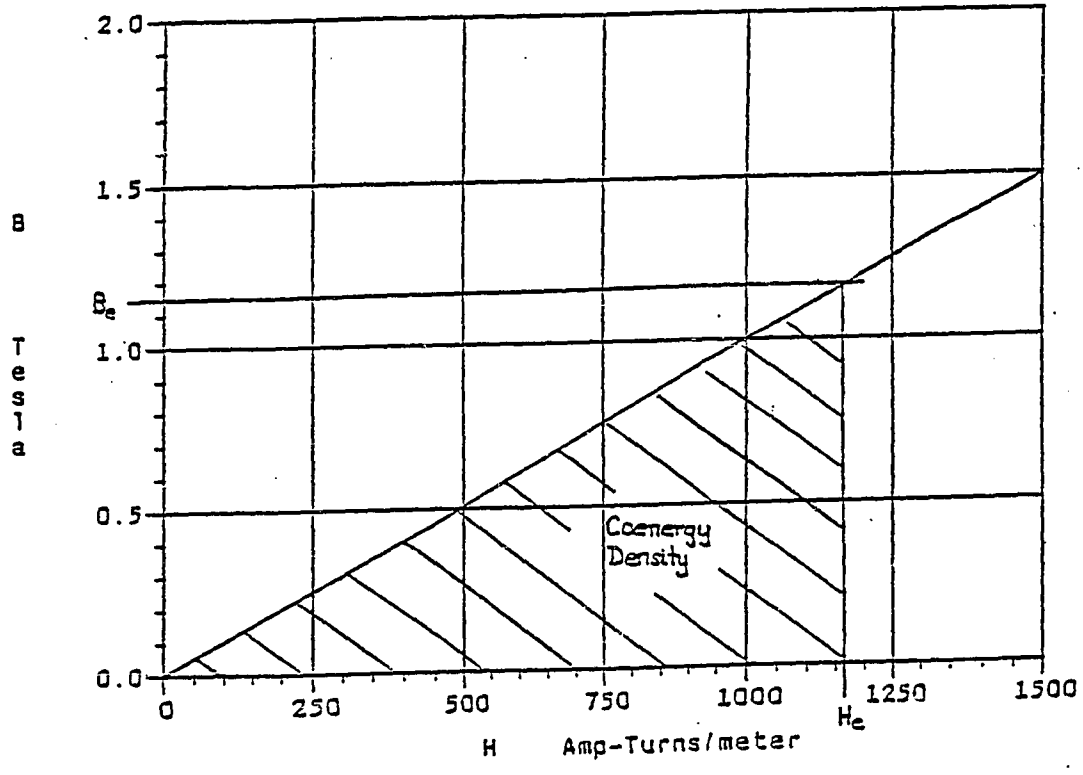

Figure VI-15
B-H Curve for a Linear Material

$$W_{ce} = \frac{1}{2} B_e H_e V_e = \frac{1}{2} \frac{B_e^2 A_e^2 \ell_e}{\mu_o A_e} = \frac{1}{2} \phi_e^2 \mathcal{R}_e \qquad \text{(VI-45)}$$

Where: $B_e \equiv$ Flux density in the lumped element

$H_e \equiv$ Magnetic Intensity of the lumped element

$V_e \equiv$ Volume of the lumped element

If the magnitude of B_e varies slightly over the length of the element, and the average B_e is used instead, this still will give a relatively good approximation. However, the direction of B must not change within the element or large errors are introduced. This is illustrated in the following example: assume the simple model shown previously in Figure VI-13, where only the reluctances of the airgaps over the tooth faces are considered. Suppose one is attempting to calculate the total torque produced by the uniformly magnetized magnet in the presence of the stator iron and the coil field. To calculate the total torque, (stator and detent), one must use the coenergy principle. Since the problem is actually quarter symmetric, we can calculate the torque for one quarter of the motor and then quadruple the magnitude of the results to obtain the total torque for the device.

The coenergy in elements 2,3,4,5,6 is given by:

$$W_{c2,3,4,5,6} = \frac{(Ni + \cdot\,)^2}{2\mathcal{R}_g} \qquad \text{(VI-46)}$$

The coenergy in element 1, where the magnet interface is positioned, is:

$$W_{c1} = \frac{(Ni + F_o(1-2r_{ave}\theta/\tau_t))^2}{2\mathcal{R}_g} \qquad \text{(VI-47)}$$

Where: $0 < r_{ave}\theta < \tau_t$

Since torque is the derivative of the coenergy with respect to angle there will only be a contribution due to the coenergy associated with element 1.

$$T = \frac{\partial W_{c4}}{\partial \theta} = \frac{2r_{ave} F_o^2}{\mathcal{R}_g \tau_t}\left(\frac{2r_{ave}\theta}{\tau_t} - 1\right) - \frac{2NIF_o r_{ave}}{\mathcal{R}_g} \qquad \text{(VI-48)}$$

The first term on the right hand side of this equation repesents the detent torque; the second term represents the stator torque. Neither of these expressions will change if the position of the magnet pole interface is over tooth 1 through 6. However, if the interface is moved to a position between teeth 7 through 12, then the coil mmf is negative and the sign of the stator torque will change. Notice that this analysis predicts the stator torque to be constant over the tooth face. The torque produced while the interface is over the slot would be less because the reluctance of the slot is higher that the reluctance of the tooth face. These results are consistent with our insight developed from the IxB method and the lumped parameter model coil B_{rad} analysis performed in one of the previous sections.

The detent torque predicted from this analysis is a sawtooth waveform which is a function of the position of the interface over the tooth face, Figure VI-16. Unfortunately, this does not agree with finite element predicted results which show that detent torque is

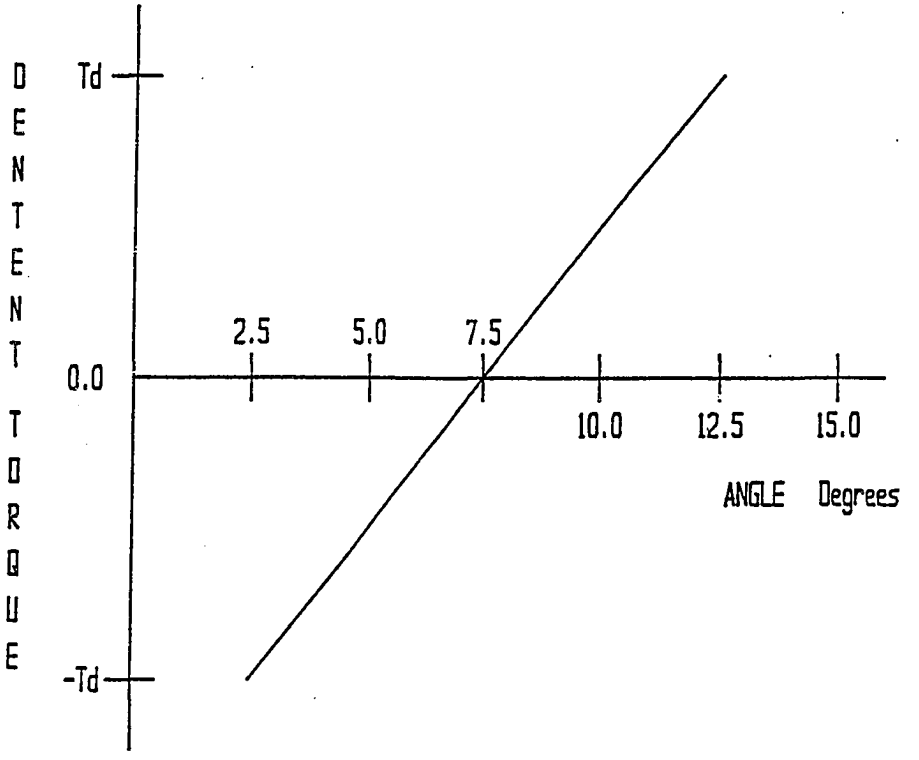

Figure VI-16
Lumped Model Predicted Detent Torque over a Tooth Face

primarily produced while the magnet interface is over the tooth slot. Figure VI-17a shows a typical FEM predicted detent torque angle curve for a full arc width, uniformly magnetized magnet. Zero degrees in this plot corresponds to having the magnet interface aligned with the center of the slot. At 2.5° the magnet interface is aligned with the edge of the stator tooth and at 12.5° the interface is aligned with the other edge of the stator tooth. One sees that while the interface is over the tooth, virtually no detent torque is produced. If a detent torque curve is obtained for a similar motor with slot widths of 5° and tooth widths of 25° one sees that the span of the 'zero' torque region increases with increasing tooth arc width, (Figure VI-17b). Thus, one can conclude from the FEM that detent torque is primarily due to the change in coenergy occuring while the magnet interface is over the slot. Furthermore, the change in coenergy only occurs when there is a change in magnet mmf in the region of the slots.

Comparison of lumped model results with finite element results is invaluable here. The finite element analysis performed previously has already shown that prediction of detent torque requires an accurate model for the magnet. By making comparisons between lumped and finite element models one can be assured that comparisons are being made between two identical representations of the magnet.

The finite element and lumped model results can be reconciled somewhat if one alters the model to comprise two flux tubes. Figure VI-18 shows a single tooth structure with the magnet interface over the tooth and two flux tubes. One flux tube is for the flux through the north magnet pole and the other flux tube is for the flux through

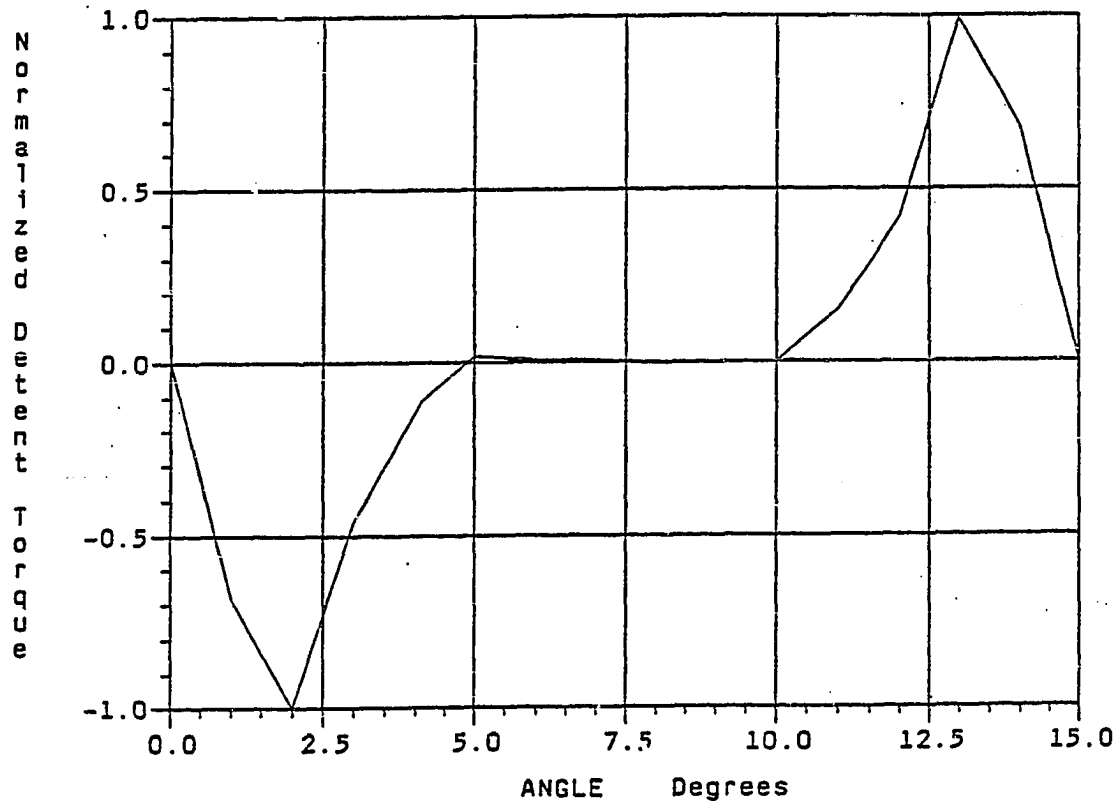

Figure VI-17a
Typical Finite Element Predicted Detent Torque
for a Full Arc Width, Uniformly Magnetized Magnet,
Tooth Width=10 Degrees, Slot Width=5 Degrees

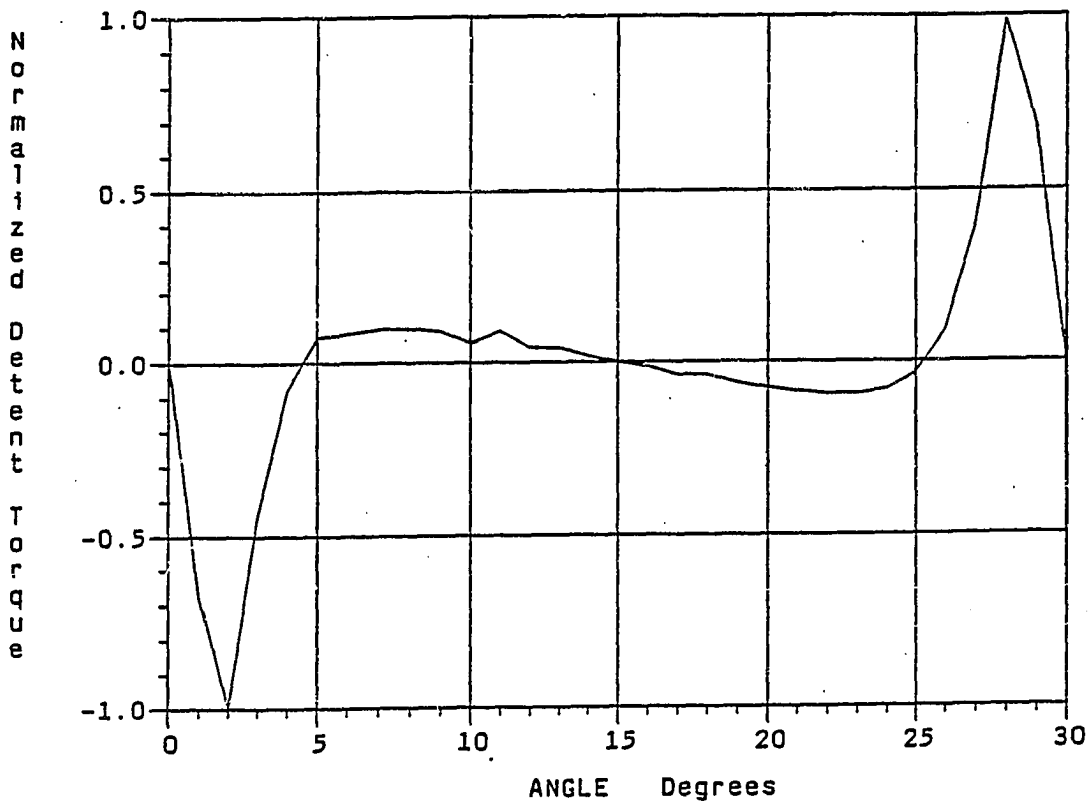

Figure VI-17b
Typical Finite Element Predicted Detent Torque
for a Full Arc Width, Uniformly Magnetized Magnet,
Tooth Width=25 Degrees, Slot Width=5 Degrees

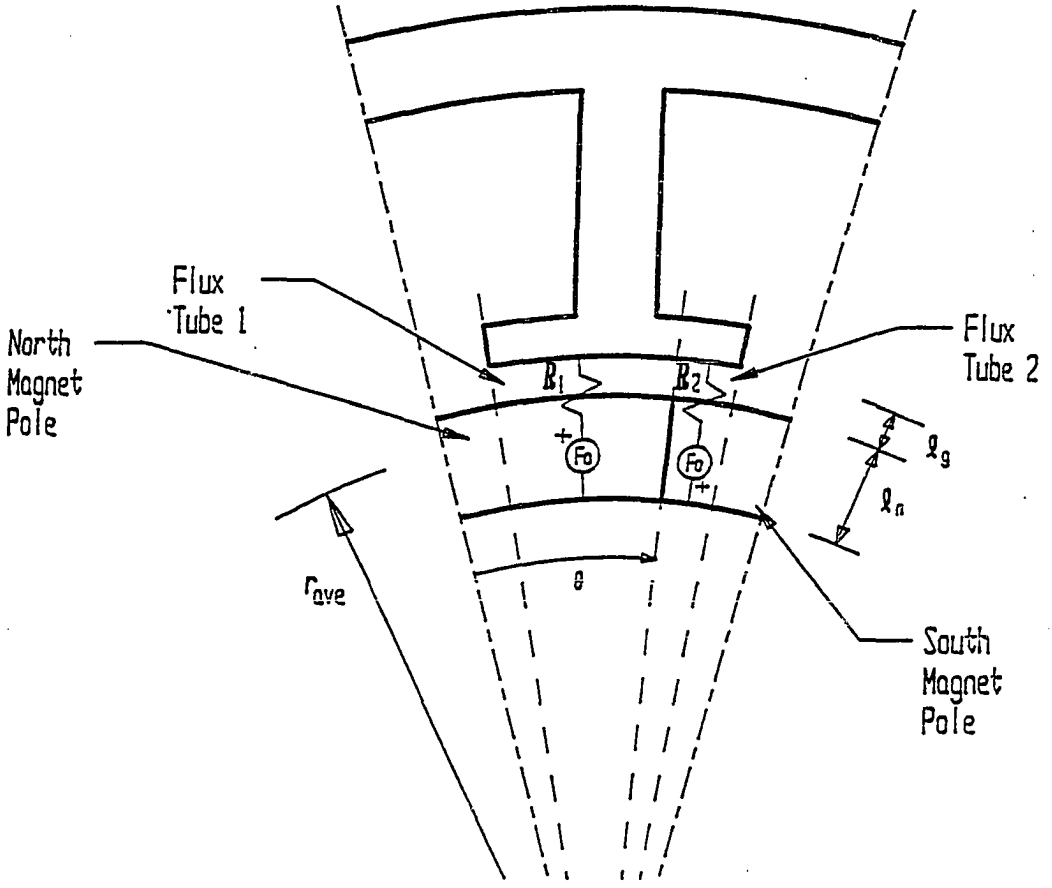

Figure VI-18
Tooth Face Lumped Model
with Position Dependent Reluctance

the south magnet pole. As the position of the magnet changes so does the cross-sectional area of the slot flux tubes. This model allows the coenergy to be calculated for regions of unidirectional flux. Thus, no assumptions relating to the derivation of the lumped element model have been violated. In addition, this model allows for correct calculation of the coenergy.

The flux in each tube is given as:

$$\phi_1 = \frac{F_o}{\mathcal{R}_1}, \qquad \phi_2 = \frac{-F_o}{\mathcal{R}_2} \tag{VI-49a,b}$$

Where F_o is the mmf of the magnet and:

$$\mathcal{R}_2 = \frac{(\ell_m + \ell_g)}{\mu_o (\tau_t - r_{ave}\theta) z}, \qquad \mathcal{R}_1 = \frac{(\ell_m + \ell_g)}{\mu_o r_{ave}\theta z} \tag{VI-50a,b}$$

The coenergy of each tube is given by:

$$W_{c2} = \frac{(-F_o)^2 \mu_o (\tau_t - r_{ave}\theta) z}{(\ell_m + \ell_g)}, \qquad W_{c1} = \frac{(F_o)^2 \mu_o r_{ave}\theta z}{(\ell_m + \ell_g)} \tag{VI-51a,b}$$

The torque is the sum of the change in coenergies for each tube.

$$T = \frac{\partial W_{c1}}{\partial \theta} + \frac{\partial W_{c2}}{\partial \theta} = \frac{-F_o^2 \mu_o r_{ave}}{\ell_m + \ell_g} + \frac{F_o^2 \mu_o r_{ave}}{\ell_m + \ell_g} = 0 \tag{VI-52}$$

One sees that the lumped model predicted net detent torque, produced while the magnet interface is over a tooth face, is zero. This is in agreement with the finite element results.

One can also apply the same approach to determine the torque predicted by the lumped parameter model while the magnet interface is over a slot. Figure VI-19 shows a flux tube for part of the slot. Because accuracy of the flux tube model is important in this case, instead of using the average permeance (inverse of the reluctance) for this portion of the slot consider the differential slice contained within the tube. The expression for the differential permeance is:

$$d\mathcal{P} = \frac{z\,\mu_o\,dx}{\ell_{ge} + \frac{\pi}{2}x} \qquad \text{(VI-53)}$$

Where: $x \equiv$ position of the magnet interface with a tube

$\ell_{ge} \equiv$ effective length of magnet/airgap

This model could also have been expressed in terms of rotor position, θ, and average airgap radius, r_{ave}: $x = r_{ave}\,\theta$. The effective permeance of the section of the tube between points x_1 and x_2 is:

$$\mathcal{P}_{eff} = z\mu_o \int_{x_1}^{x_2} \frac{dx}{\ell_{ge} + \frac{\pi x}{2}} = \frac{2z\mu_o}{\pi}\, \ell n\,(\ell_{ge}+\tfrac{\pi}{2}) \Big|_{x_1}^{x_2} \qquad \text{(VI-54)}$$

Now suppose the magnet interface was at a point x between the left edge of the slot, 0, and the right edge of the slot, S. To evaluate the coenergy, the slot tube is subdivided into two tubes, one for each side of the interface. The coenergy of the portion of the slot to the right side of the interface is:

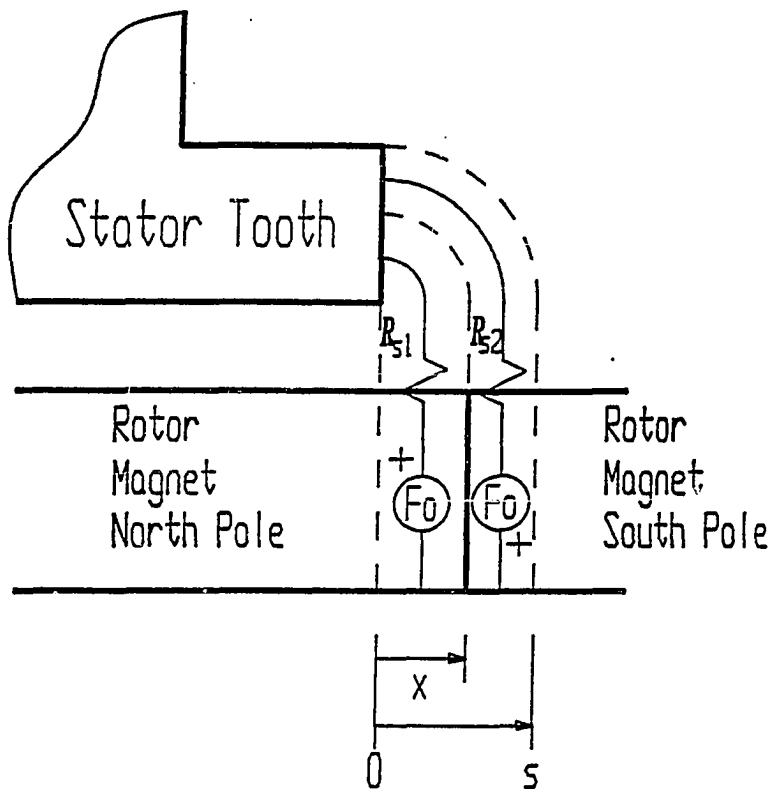

Figure VI-19
Slot Face Lumped Model
with Position Dependent Reluctance

$$W_{csr} = \frac{z\, F_o^{\,2} \mu_o}{\pi} \left[\ell n(\ell_{ge} + \frac{\pi}{2} S) - \ell n(\ell_{ge} + \frac{\pi}{2} x)\right] \qquad \text{(VI-55)}$$

$$W_{csl} = \frac{z(-F_o)^2 \mu_o}{\pi} \left[\ell n(\ell_{ge} + \frac{\pi}{2} x) - \ell n(\ell_{ge})\right] \qquad \text{(VI-56)}$$

The total coenergy for the slot tube is:

$$W_{cs} = \frac{z\, F_o^{\,2}\, \mu_o}{\pi} \left[\ell n(\ell_{ge} + \frac{\pi}{2} S) - \ell n(\ell_{ge})\right] \qquad \text{(VI-57)}$$

One sees that this expression is independent of rotor position so the lumped model would, again, predict no torque to be generated while the magnet interface is over the slot. However, we know this to be contrary to the FEM results. It seems that assuming a set of unchanging flux tubes to represent the flux produced while the magnet interface is over the slot is not accurate enough to predict the detent torque. In order to predict the detent torque using a lumped parameter model, one would need an accurate representation for the change in flux paths (i.e. changing tubes) as a function of rotor position.

Another approach might be to use the finite element results to approximate a function for the average reluctance of the magnet circuit.

$$\mathcal{R}_{mave}(\theta) = \frac{F_o}{\phi_m(\theta)} \qquad \text{(VI-58)}$$

Where: $\phi_m(\theta)$ ≡ total flux through the magnet as a function of rotor position, θ

$\mathcal{R}_{mave}$ ≡ effective average reluctance of the magnet circuit as a function of rotor position, θ

F_o ≡ mmf of the magnet

The magnet mmf remains constant. The total flux through the magnet for a rotor position, θ, would be determined by one of the methods outlined in Chapter III. Then, the effective reluctance of the magnetic circuit would be calculated. This process would be repeated for a variety of magnet positions. Curve fitting techniques could then be used to find approximating functions.

The obvious disadvantage to this technique, would be that the resulting reluctance function would only describe that particular geometry. A considerable amount of work would be necessary to try and determine if the form of the reluctance function could be related to magnet, airgap, slot, and tooth dimensions/geometry.

VI.5 Summary

This chapter has shown that some very simple lumped parameter models can be used to predict, with reasonable accuracy, the average flux density in the airgap due to either the coil or permanent magnet. It has been shown in previous chapters that if the coil flux density in the airgap can be predicted, then the flux density waveform can be crossed with the permanent magnet equivalent currents to yield the torque angle waveform of the motor. Obviously, if the peak of the torque angle waveform can be predicted then the torque constant can also be predicted. Therefore, the lumped element model is useful to

obtain a relationship between peak torque and the dominant motor parameters. This is of primary importance because the torque is usually the parameter which is of most interest in motor design.

A simple lumped model was also used to predict the inductance. A high degree of accuracy was not obtained with the model. But, it was shown that including additional leakage paths improved the prediction accuracy and finite element results were matched within reasonable accuracy limits. However, it was shown that simple models for the end leakage did not produce accurate results, and, that the results obtained, varied greatly depending upon the area of the assumed flux path. Thus, modelling leakage flux at the ends of the motor is not practical because of the difficulty in selecting leakage paths that accurately reflect the field. It was also shown in this chapter why it would be nearly impossible to predict detent torque from lumped element models. A lumped parameter model was developed that predicted the average flux density in the airgap due to the permanent magnet. This model used the average mmf provided by the magnet. However, it was shown that this same model could not be used to predict detent because the coenergy calculation results in a square of the sum of the component flux densities instead of the sum of the squares. Therefore, it would be necessary to construct a model with path lengths that were a function of rotor position.

To summarize, probably the most critical point made in this chapter is that a simple magnetic model which only includes the airgaps can be used for accurate prediction of flux densities, and hence, the energized peak stator torque of the motor. While this predicts peak torque accurately, it does not yield good accuracy in

predicting inductance because of leakage paths.

More complicated models including cross-slot leakage paths significantly improved the inductance model and produced results which closely matched finite element results. An effort to include leakeage paths for end effects did not prove successful. It should be noted that accurate prediction of the actual inductance of the device will probably not be achieved because of magnetic saturation. It was shown in Chapter II that the inductance of the prototype motor decreased by 40% when the magnets were in place. Saturation effects are extremely significant and are not included in this model.

Although no attempt was made to include reluctances of iron paths in these models, reluctance paths for the iron teeth can be included with no real additional complexity. This can be done by lumping the tooth reluctance in with the airgap reluctance. This would not be a nonlinear model and the only advantage would be that it allows one to solve for the flux density in the teeth to check and ensure that the iron is not saturated. Inclusion of saturable reluctance paths will prohibit the development of closed form expressions. To include reluctance paths for the stator back iron paths means that the mmf potential in the stator back iron is nonzero. Therefore, Equations VI-42 are no longer valid, and, it would be necessary to solve a more complicated model. As the model becomes even slightly more complicated, it quickly loses its advantage of yielding closed form expressions that are easily manipulated and lend insight directly into design.

CHAPTER VII

DESIGNING BRUSHLESS DC MOTORS HAVING SMOOTH ROTOR BACK IRON

The previous chapter showed simple models can be used to accurately predict average airgap flux densities due to the coil. Given the insights developed from using the IxB method on the magnet equivalent currents and coil B_{rad} distributions, one can infer that the torque constant for the motor can also be predicted with reasonable accuracy. This is important since one typically designs or selects a motor to produce a specified torque.

In this chapter, equations relating motor geometries and material properties to the motor torque constant, resistance, inductance, and inertia, are developed. Equations relating the magnet flux and coil flux to motor geometry are also developed. Since the problem of motor design is, in general, an under-constrained one, many of the parameters necessary to specify a design have to be chosen. A general method is presented for designing motors assuming the motor torque constant, rotor inertia and phase resistance have been specified. First, an explanation as to how a typical application might fix these particular parameters is given. Then, the design method is discussed and the necessary equations are developed. Finally, the design method is verified using the specifications for the first prototype motor described earlier, and an example design is presented.

VII.1 Specification of Motor Torque Constant, Rotor Inertia, and Phase Resistance

Motor torque constant, rotor inertia and phase resistance are parameters that might ordinarily be specified in an application. A typical application might consist of the following conditions. The motor is to be run in a wye-node-open configuration[2] with a current drive operating from a maximum supply voltage of V_{smax}. The motor must be able to run under no load conditions at a speed of $\dot{\theta}_{max}$; deliver a torque, at stalled conditions, of T_s; limit the heat dissipation due to I^2R losses to P_s; and be capable of a maximum acceleration of $\dot{\omega}_{max}$. An explanation of how these conditions fix the torque constant, inertia and resistance is given in the following.

In order for the motor to run at $\dot{\theta}_{max}$ under no load conditions, (assuming no commutation phase advance[2] is to be used), the back emf constant for the motor must limited to:

$$K_b = \frac{V_{smax}}{\dot{\theta}_{max}} \qquad \text{(VII-1)}$$

This comes from the electrical equation for a phase of the motor, Equation VII-2. It is assumed that at high speeds the phase current and phase current derivative are approximately zero, and that the motor is commutated around 90 electrical degrees so that $\sin A\theta \doteq 1$.

$$V_{smax} = iR + K_b \dot{\theta}_{max} \sin A\theta + L \frac{di}{dt} \qquad \text{(VII-2)}$$

If K_b is greater than the value given in Equation VII-1, the motor generated voltage at $\dot{\theta}_{max}$ will be larger than V_{smax}. Hence, the motor

will be functioning as a generator; no phase current will be produced and no torque generated. If the motor is to be operated in a two-phase-on mode, then this value of K_b represents the effective two-phase-on back emf constant.

The back emf constant and the torque constant are equal in the SI unit system. If the limiting value of the back emf constant is K_b, then the limiting value of the two-phase-on torque constant is also:

$$K_t = \frac{V_{smax}}{\dot{\theta}_{max}} \qquad \text{(VII-3)}$$

If the torque constant is limited to this value, and the motor must produce T_s under stall conditions, then the current at stall must be at least:

$$I_{stall} = \frac{T_s}{K_t} \qquad \text{(VII-4)}$$

Since I^2R heating is greatest at stall and increases with the square of the current, I_{stall} should not be greater than this value. The winding resistance necessary to limit the I^2R losses to P_s can then be determined:

$$R = \frac{P_s}{I^2_{stall}} \qquad \text{(VII-5)}$$

Assuming two-phase-on operation, R is the effective two-phase-on resistance. This value of R should define the 'hot' resistance, assuming the winding to be at its maximum temperature.

The limiting value of inertia for the motor can be determined from the desired maximum acceleration capability of the motor, $\dot{\omega}_{max}$, and the stall torque of the motor.

$$J_{max} = \frac{T_s}{\dot{\omega}_{max}} \qquad \text{(VII-5)}$$

This equation is derived from the differential equation describing the mechanical behavior of the motor, Equation VII-6.

$$J\dot{\omega} + B\omega + K_t i \sin A\theta = T_{load} - T_f \, sgn(\dot{\theta}) \qquad \text{(VII-6)}$$

To derive Equation VII-5, it is assumed that friction and damping losses are negligible, and the motor is operating at low speed with no external load, T_{load}. Since the motor is operating at low speed, the current is equal to the stall current. It is assumed again that the motor is commutated around 90 electrical degrees and that $\sin A\theta \doteq 1$. Therefore, $K_t i \sin A\theta = T_s$, the stall torque.

The previous discussion has shown how some of the motor characteristic parameters are specified from the motor performance requirements. Once these parameters are specified, a torque-speed curve for the motor should be simulated to determine if the dynamic torque requirements of the application can be met with these parameters. Torque-speed simulation is important because constant voltage torque-speed curves for brushless DC motors are often nonlinear[2]. Figure VII-1 shows a typical, constant voltage, brushless DC motor torque-speed curve. One sees that it can not simply be assumed that the motor torque-speed characteristic can be represented as a straight

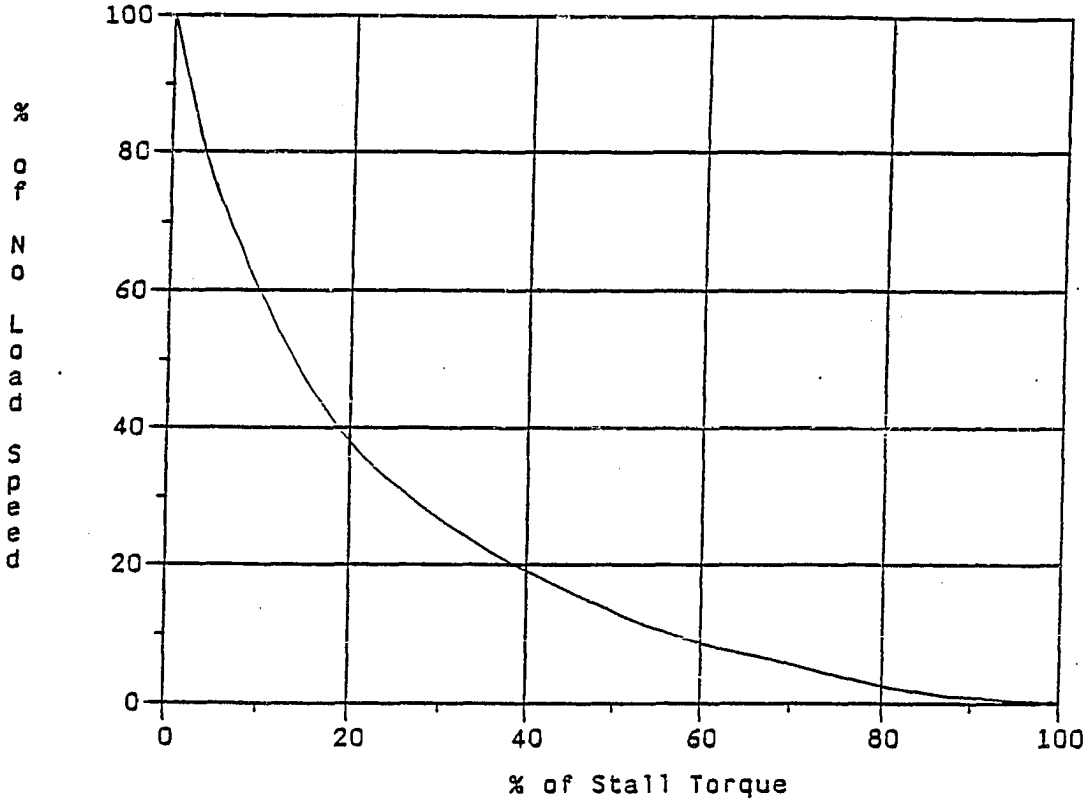

Figure VII-1
Constant Voltage Torque-Speed Curve

line drawn between the no load speed and the stall torque of the device. Thus, even though a motor design might meet the 'static' specifications, i.e: torque constant, back emf constant, resistance, etc., one can not use the static specifications and assume a linear torque-speed relationship to deduce if the motor meets the dynamic requirements.

In order to simulate the motor torque-speed curve it is also necessary to know the inductance of the motor. A typical value can be assumed from comparable motors of similar size and torque constant, or, the value of inductance used in the simulation can be varied until the dynamic torque specification is met. Then, a judgement can be made as to whether or not the value is physically realizable. Depending upon the results of this judgement, one can either proceed with the motor design or, re-evaluate the design requirements and perhaps change the performance specifications.

A torque-speed analysis is presented later in this chapter. In addition, a more detailed discussion of torque-speed simulation is presented in Appendix C. First, however, expressions for the motor phase torque constant, phase resistance, and rotor inertia, among others, are developed and used in a general approach to motor design. The approach presented allows one to develop motor designs that have smooth rotor back iron and uniformly magnetized, radially oriented, arc shaped magnets. These restrictions result from assumptions made primarily in the development of the torque constant expression. If prototypes are built, it will be important to ensure that the magnet manufacturer can provide the magnets as specified.

VII.2 Motor Design Method

VII.2a General Approach

It will be shown in this section that a motor design can be formulated by 28 equations with 58 unknowns. Therefore, many of the unknowns will have to be pre-selected. The method presented here assumes that, among other parameters selected, the torque constant, the inertia, the phase resistance of the motor, and the peak phase current have been specified. The method then consists of the following process:

1) A preliminary design to be explored is chosen. This consists of selecting such fundamental parameters as the number of stator teeth, the number of rotor poles, and the magnet material, and, other parameters such as the winding fill factor. (A general discussion of the effects of the number of stator teeth and the number of rotor poles on the motor performance parameters is presented later in Section VII.2b).

2) One solves for the combinations of rotor length and radius that satisfy the inertia constraint.

3) For every particular combination of rotor length and radius combination, the number of winding turns that will satisfy the torque constant specification is determined.

4) The maximum flux in the stator teeth due to both the magnet and coil is calculated. The widths of the stator teeth, and rotor and stator back iron necessary to carry the flux without exceeding a pre-specified flux density is also calculated.

5) For a pre-selected wire size, given the number of turns calculated in step 3, and the tooth widths calculated in step 4,

the slot outer diameter necessary to accommodate N turns of the wire is determined.

6) Winding resistance, motor outer diameter, and other performance parameters are plotted as a function of rotor radius. The designer can then view the results and make comparisons to select the design that best meets the resistance requirements and motor envelope size constraints. The process can be repeated for different wire sizes.

7) The entire process can be repeated starting at step one and selecting a different number of stator teeth and/or rotor poles. In this way, 'best' designs for different numbers of teeth and poles can be compared. Obviously, 'best' depends upon application requirements. For example, one might compare weight and size trade-offs, or trade-offs between size and stall I^2R losses.

VII.2b Slot Count and Pole Count Considerations

Initial selection of the number of stator teeth, (or equivalently the number of stator slots), and rotor poles represents the qualitative part of the design. In this section trade-offs between high and low slot and pole counts are discussed. In addition, some very simple models are used to show generic relationships between the slot and pole counts and the motor phase torque constant, inductance, resistance, and L/R time constant.

The following facts should be considered when selecting the number of slots and poles for the motor design:

1) If the stator is to be skewed to eliminate detent torque, then a high number of stator slots, relative to the number of rotor poles, makes the stator easier to wind. This is because the stator is skewed over a smaller angle. Thus, the slots openings are closer to being straight. In addition, if the stator is skewed over a smaller angle, the reduction in torque constant will be less.

2) If the motor is not skewed, then the high number of slots relative to the number of poles, results in a detent torque which has a much smaller period than the stator torque-angle curve. Therefore, the low speed ripple usually induced by the detent torque will be less, due to mechanical filtering effects by the system.

3) A motor with a high number of slots relative to the number of poles will have a more distributed winding. Distributed windings result in more sinusoidal stator torque-angle curves. This is an advantage if a sinusoidal stator torque-angle curve is desired, and a disadvantage if a more flat-topped torque-angle curve is desired.

4) A motor with a high pole count results in higher iron losses. This is due to the fact that the number of times per revolution that the magnetic field in the stator iron reverses is equal to half the pole count. Thus, a higher pole count results in a higher frequency field reversal and larger eddy currents in the motor.

5) A motor with a high number of rotor poles requires less rotor back iron to prevent saturation. In order for the rotor

back iron to be prevented from saturating magnetically, the flux which leaves from a rotor north pole and runs through the back iron to a rotor south pole, divided by the cross-sectional area of the back iron, must be less than the saturation value of flux density. Since the amount of magnetic flux from a north pole to an adjacent south pole depends on the area of the magnet, the flux is decreased by having a large number of rotor poles for a given rotor diameter.

Some very simple lumped magnetic models can be used to show, qualitatively, the effects of the number of poles, N_p, and the number of teeth, N_t, on some of the motor parameters. In order to derive expressions to evaluate the effects of N_p, and N_t on the motor parameters, assume one has motors with different numbers of poles and teeth, but with the same critical geometries: rotor magnet inner radius, rotor magnet outer radius, airgap outer radius, slot inner radius, slot outer radius, and the rotor axial length. The critical radii are shown as r_2, r_3, r_4, r_5, and r_6 in Figure VII-2. If one allows that for each combination of N_p, and N_t, the cross-sectional area of a stator tooth, (the tooth area perpendicular to the direction of flux), is designed so that it can carry its share of the magnet flux without exceeding a maximum flux density level, B_{max}, then the following statements can then be made:

1) The total iron volume occupied by the stator teeth remains constant. Figures VII-3a,b,c show a 2 pole, 6 slot; a 2 pole, 12 slot; and a 4 pole, 12 slot motor, respectively. One sees that as the number of poles, N_p, changes, or as N_t changes, the

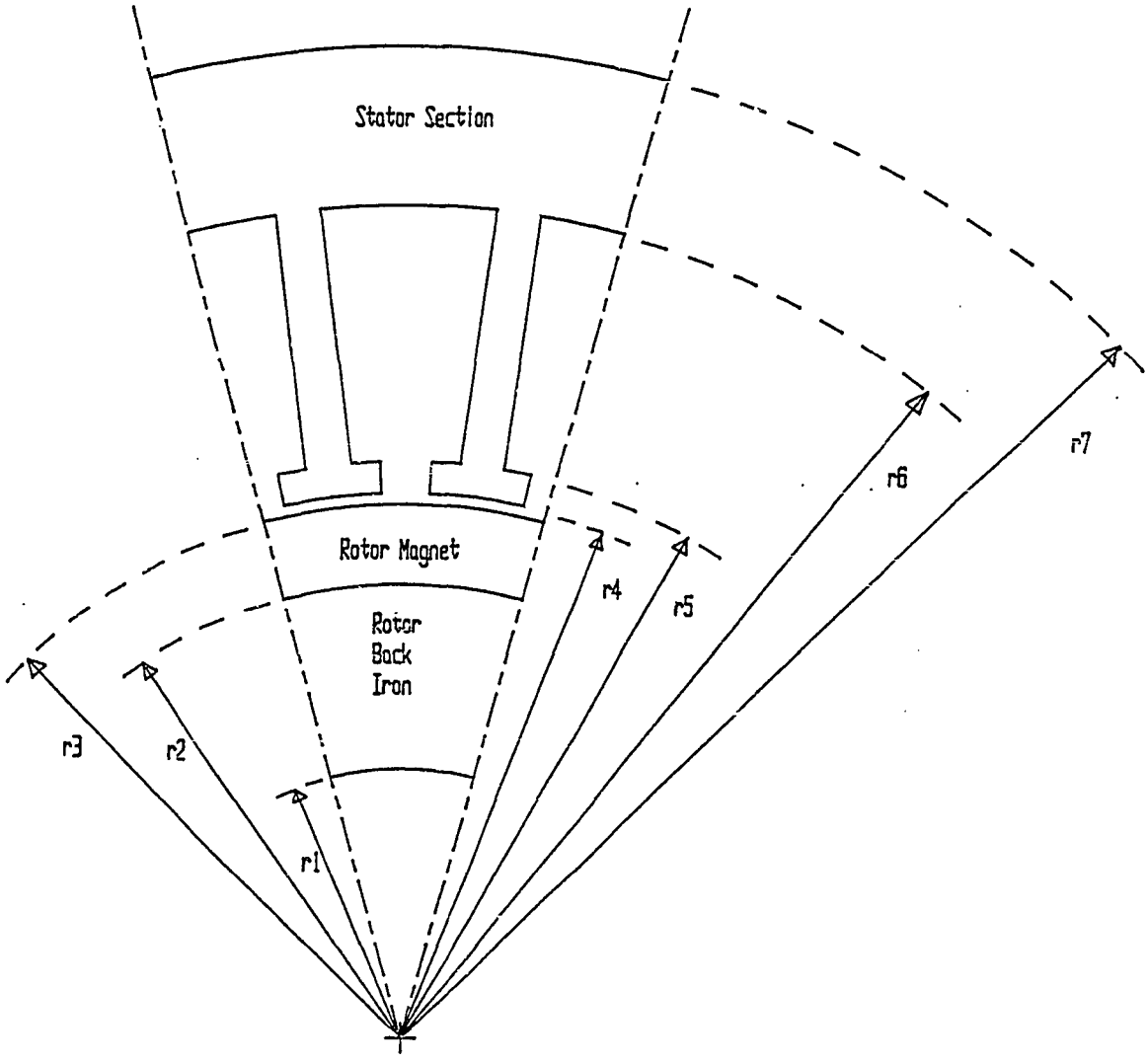

Figure VII-2
Motor Section Showing Critical Radii

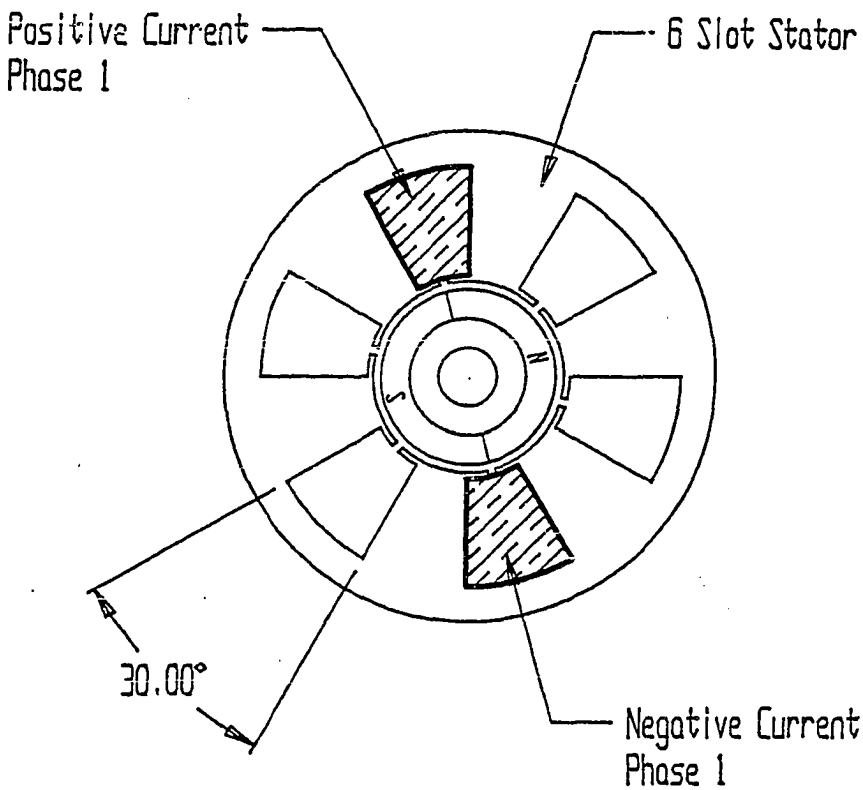

Figure VII-3a
A 2 Pole, 6 Slot Motor-
Rotor and Stator Fields Aligned,
30 Degree Arc Width Slots

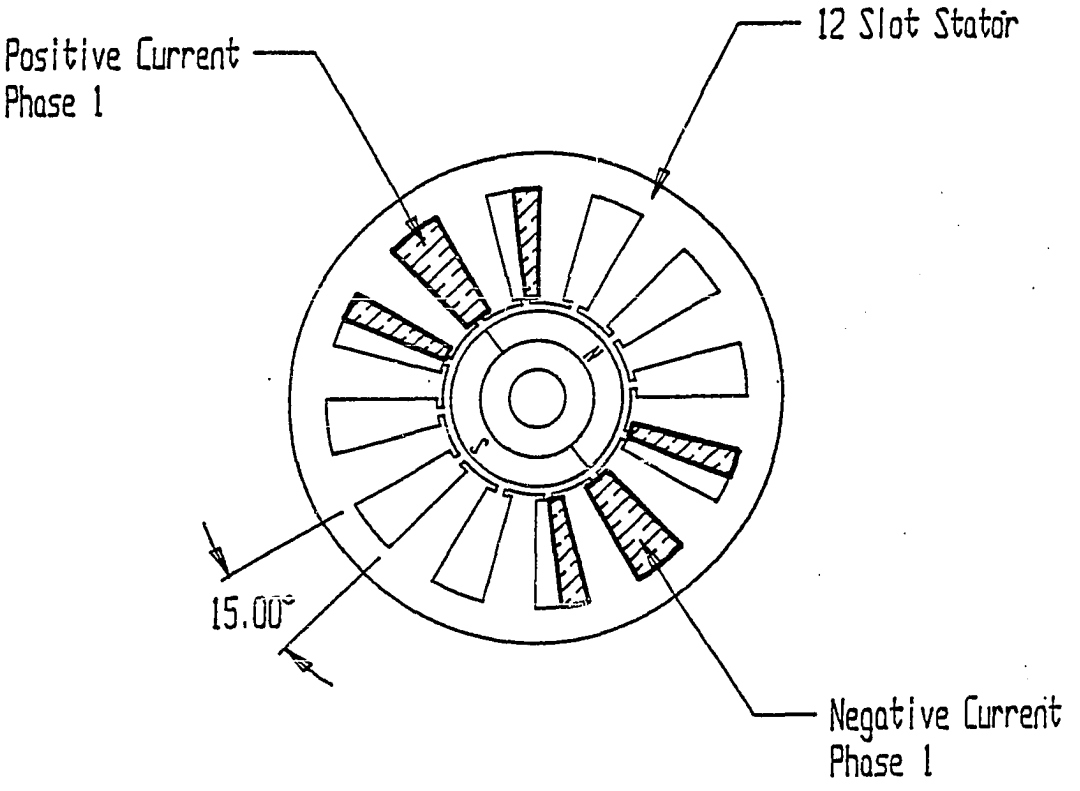

Figure VII-3b
A 2 Pole, 12 Slot Motor-
Rotor and Stator Fields Aligned,
15 Degree Arc Width Slots

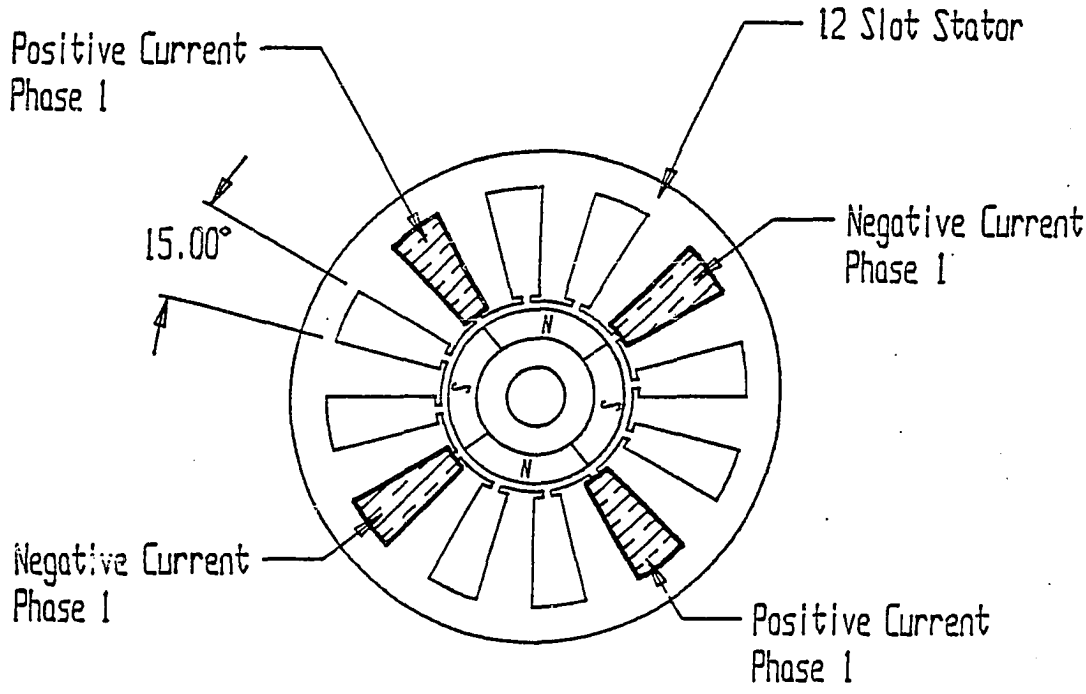

Figure VII-3c
A 4 Pole, 12 Slot Motor-
Rotor and Stator Fields Aligned,
15 Degree Arc Width Slots

total area of the slot region, (r_5 to r_6), that is occupied by the iron tooth shanks remains constant.

2) Since statement 1 is true, and assuming the fill factor of the motor, (the ratio of the slot cross-sectional area occupied by the copper wire), remains constant, then the total volume of copper in the motor remains constant.

3) Since statement 2 is true, the volume of copper available for each phase is constant. Since this volume contains wires that form pole windings, half this volume is occupied by wires carrying positive current, half with wires carrying negative current. Thus, assuming the wire size is unchanged, the resistance of each phase is independent of N_p, N_t.

Using the previous assumptions, and the descriptive geometry shown in Figure VII-2, a simple magnetic model can be constructed to determine the general relationship between K_t, L, R and N_t, N_p. To develop a magnetic model, the reluctance of the effective airgap over the pole must be determined, as well as the mmf for each pole. Then, the ixB method can be used to determine the torque constant.

Assuming that a rare earth magnet is used with a permeability approximately equal to that of air, $\mu_r \doteq 1$, the reluctance of the airgap over a tooth, $\mathcal{R}_t$, is:

$$\mathcal{R}_t = \frac{\ell_e}{\mu_o A_t} \qquad \text{(VII-7a)}$$

Where: $\ell_e \equiv$ length of the effective airgap (physical airgap+magnet length)

$A_t \equiv$ Average area of airgap over tooth pitch

In terms of the geometry shown in Figure VII-2 the effective airgap length is:

$$\ell_e = (r_4 - r_2) \tag{VII-8}$$

The average total cross-sectional area of the magnet/airgap region has been assumed constant for this comparison and equal to A_t. If the slot openings are neglected, the area of the airgap over a tooth pitch is:

$$A_t = \frac{(r_2 + r_4)\ \pi\ z}{N_t} \tag{VII-9a}$$

Where: $z \equiv$ axial length of the rotor

This can be re-written in terms of the total average cross-sectional area of the magnet/airgap region, A_{TOT}:

$$A_t = \frac{A_{TOT}}{N_t} \tag{VII-9b}$$

Where, from Figure VII-2:

$$A_{TOT} = \pi z(r_2 + r_4) \tag{VII-10}$$

Thus, the reluctance of each of N_t teeth is:

$$\mathcal{R}_t = \frac{\ell_e \, N_t}{\mu_o \, A_{TOT}} \qquad \text{(VII-7b)}$$

Assuming a symmetric winding, if each phase is wound to produce N_p poles then there are N_t/N_p teeth per coil 'pole', and each coil pole has N_t/N_p parallel branches of reluctance $\mathcal{R}_t$. This is demonstrated in Figure VII-4, for the 12 slot, 4 pole motor This motor has 3 teeth per coil pole. Thus, there are 3 parallel branches of reluctance $\mathcal{R}_t$ for each pole. The 12 slot, 2 pole motor has 6 teeth per coil pole. Thus, the effective reluctance of each coil pole, $\mathcal{R}_{cp}$, is:

$$\mathcal{R}_{cp} = \frac{\ell_e \, N_t \, N_p}{\mu_o \, A_{TOT} \, N_t} = \frac{\ell_e \, N_p}{\mu_o \, A_{TOT}} \qquad \text{(VII-11)}$$

Thus, the airgap reluctance of each coil pole increases linearly with the number of rotor poles and is independent of the number of stator teeth.

Ni_{cp}, the mmf available for each coil pole is:

$$(Ni)_{cp} = \frac{2 \, N_{TOT} \, i}{N_p} \qquad \text{(VII-12)}$$

Where: $N_{TOT} \, i \equiv$ the maximum available mmf for a 2 pole winding using all the slot area

One sees that the mmf per coil is inversely proportional to the number of rotor poles and is independent of the number of stator teeth.

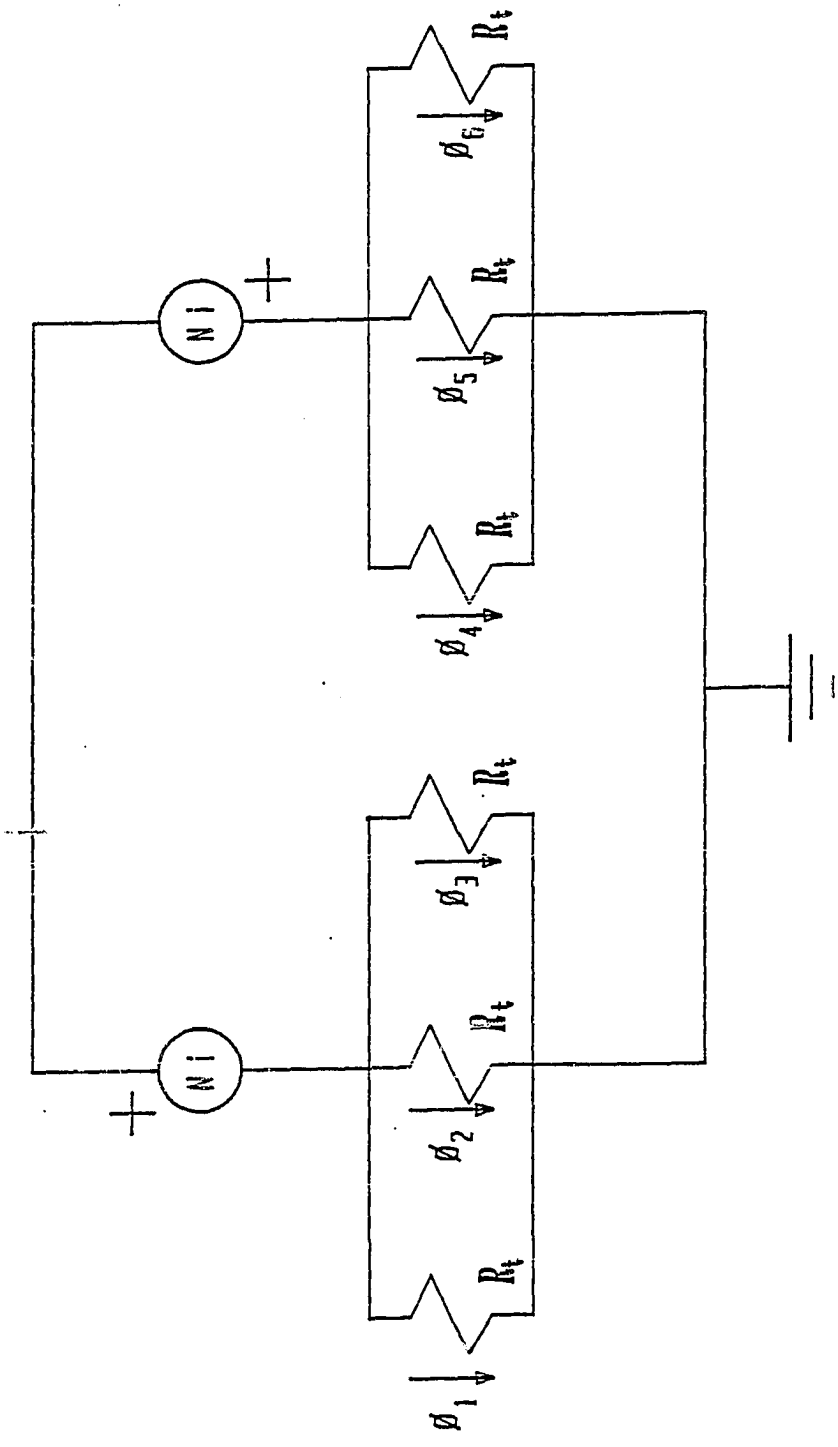

Figure VII-4
Lumped Magnetic Circuit
Model for a 2 Pole, 6 Slot Motor

Using the coil mmf and the coil reluctance, the coil flux through a coil pole can be expressed as:

$$\phi_{coil} = \frac{2\,N_{TOT}\,i}{N_p}\,\frac{1}{\mathcal{R}_{cp}} = \frac{2\,N_{TOT}\,i}{N_p}\,\frac{\mu_o\,A_{TOT}}{\ell_e\,N_p} \qquad \text{(VII-13)}$$

Thus, the flux per coil pole decreases by the square of the number of poles. The flux density in the airgap region over a coil pole is:

$$B_{coil} = \frac{\phi_{coil}\,N_p}{A_T} = \frac{2\,N_{TOT}\,i\,\mu_o}{N_p\,\ell_e} \qquad \text{(VII-14)}$$

The flux density is inversely proportional to the number of rotor poles and is independent of the number of stator teeth.

The IxB method can be coupled with the expression found in Chapter VI for the flux density in the airgap, to yield an expression for the torque constant. It has been shown that torque is equal to the product of the average radius of the magnet, r_{mave}, the equivalent current for the magnet, i_m, the radial component of flux density due to the coil, B_{crad}, and the axial length of the magnet, z.

$$T = r_{mave}\;i_m\;B_{crad}\;z \qquad \text{(VII-15)}$$

Since the model developed for the coil flux assumes the flux is only in the radial direction, Equation VII-14 represents the radial component of flux density. Thus:

$$B_{coil} = B_{crad} \qquad \text{(VII-16)}$$

Assuming full arc width magnets, and N_p poles, the total torque is $2N_p$ times as much as shown in Equation VII-15. This is due to the fact that there are N_p interfaces and 2 equivalent magnet current con-

tributions per magnet interface, (one from the right edge of the magnet to the left of the interface and the other from the left edge of the magnet to the right of the interface).

$$T = 2\ N_p\ r_{mave}\ i_m\ B_{coil}\ z \qquad \text{(VII-17)}$$

From Chapter III, Equation III-3 , an expression for the magnet currents is given by:

$$i_m = H_c \ell_m = \frac{B_r \ell_m}{\mu_o} \qquad \text{(III-3)}$$

This expression also assumes that the permeability of the magnet material is approximately the same as air. Substituting Equation VII-14 and Equation III-3 into Equation VII-17, and dividing by the phase current i, yields an expression for the torque constant as:

$$K_t = 2\ N_p\ B_r\ z \frac{\ell_m}{\mu_o} \frac{2\ N_{TOT} \mu_o}{N_p\ \ell_e}\ r_{mave} \qquad \text{(VII-18a)}$$

From the geometries shown in Figure VII-2:

$$r_{mave} = \frac{(r_2 + r_3)}{2} \qquad \text{(VII-18b)}$$

$$\ell_m = (r_3 - r_2) \qquad \text{(VII-18c)}$$

Hence:

$$K_t = 4\ z\ B_r\ N_{TOT}\ r_{mave} \frac{\ell_m}{\ell_e} \qquad \text{(VII-18d)}$$

This equation shows that the torque constant for the motor is independent of the number of poles or teeth selected.

The inductance of the motor is found from the coil flux linkage. The total flux linkages for a phase is equal to the number of turns for the coil, $(2N_{TOT}/N_p)$, times the coil flux for a coil pole, times the number of coil poles, Equation VII-19a. This equation simply calculates the inductance from the coil flux through the physical airgap and does not include the leakage paths discussed in Chapter VI.

$$\lambda_t = \frac{2\ N_{TOT}}{N_p}\ \phi_{coil}\ N_p \qquad \text{(VII-19a)}$$

Substituting Equation VII-12 for ϕ_{coil} yields:

$$\lambda_t = \frac{4\ N_{TOT}^2\ i}{N_p}\ \frac{\mu_o\ A_{TOT}}{\ell_e N_p} \qquad \text{(VII-19b)}$$

The inductance of a phase is:

$$L = \frac{\lambda_T}{i} = \frac{4\ N_{TOT}^2\ \mu_o\ A_{TOT}}{N_p^2\ \ell_e} \qquad \text{(VII-19c)}$$

Similar to the coil flux, the inductance is independent of the number of stator teeth but is inversely proportional to the number of rotor poles.

Now, using Equation VII-18d and VII-19c, as well as the fact that the resistance is independent of N_t, N_p, the effects of N_p, N_t can be

tabulated, Table VII-1.

Table VII-1

Summary of N_p, N_t Effects on Motor Performance Parameters

Parameter	N_p	N_t
K_t	*NE	NE
L	$\frac{1}{N_p^2}$	NE
R	NE	NE
L/R	$\frac{1}{N_p^2}$	NE

* NE ≡ no effect

None of the parameters shown in this table depend on the number of stator teeth. One sees that only the inductance and L/R time constant are dependent on the number of poles. These results can be used to deduce the effect of the pole count on the motor torque-speed curve. The no-load speed for the motor is only dependent upon the supply voltage and the back emf constant; therefore, the no-load speed will be independent of pole count. Also, the stall torque will not be dependent on the pole count because the torque constant is independent of the number of rotor poles. However, the shape of the torque speed curve between these two points does depend on the pole count. Taft[2] has shown that the concavity of a torque-speed curve depends on a factor he terms the commutation or 'C' factor of the motor. C is approximately the L/R time constant divided by the time between

commutations at the no load speed. As C becomes greater than 1 the torque speed curve is more concave.

$$C = \frac{V_s \; N_p \; L}{2 \; K_b \; R} \qquad \text{(VII-20)}$$

Since V_s, K_b and R are indpendent of the number of poles, one sees that as L decreases by $1/N_p^2$, C decreases by $1/N_p$. Thus, the motor is easier to commutate. A physical explanation is as follows: In order for the motor shaft to turn at a speed $\dot{\theta}_o$, the motor must be commutated at a rate which is proportional to N_p, (e.g. an N_p pole, 3 phase motor, running from a bi-polar drive is commutated $3N_p$ times, per revolution). As the pole count increases, the duration of the commutation interval shortens proportionaly; allowing less time for current to build in the winding. However, the inductance decreases by $1/N_p^2$; resulting in a faster current rise time and a greater average current in the winding over the commutation interval. Therefore, the motor with the higher pole count produces more average torque over the midrange speeds.

The penalty one pays for this increased torque is increased heating due to iron losses. Iron losses tend to increase with the square of the commutation frequency.

Given the previous discussion, one sees that selection of the number of teeth and poles should be determined by consideration of the torque-speed curve shape, iron losses, ease of winding, detent torque period, and winding distribution, as discussed previously in Section VII.2b. It should be reiterated that the effects shown in Table VII-1 assume a fixed space for stator iron and copper. If the outside dim-

ensions of the motor are allowed to change, then the fill factor, or the total amount of copper in the motor, will change and the results derived in this section do not necessarily apply.

VII.2c Development of Equations Used in Design Process

In this section, general expressions for inertia, torque constant, resistance, coil and magnet flux, slot area and others are developed. These equations will be used to formulate a method of motor design.

VII.2c1 Torque Constant

A simple expression for the torque constant was derived in Equations VII-15 through VII-18. A slightly more complicated equation can be derived by starting again with Equation VII-17, (substituting Equation III-3 directly for i_m).

$$T = 2\, B_r z \frac{\ell_m}{\mu_r \mu_o}\, B_{coil}\, N_p\, r_{mave} \qquad \text{(VII-17)}$$

It should be noted that B_r, the remanent flux density of the magnet is temperature dependent. B_r could be modeled as:

$$B_r = B_{ro}\ (\ 1 - C_{Tm}\ \Delta T) \qquad \text{(VII-21)}$$

Where: $\Delta T \equiv$ is the change in magnet temperature over ambient

$C_{Tm} \equiv$ is the reversible temperature coefficient of the magnet material

$B_{ro} \equiv$ remanent flux density of magnet material at ambient temperature

Care must be taken not to exceed the temperature range of the reversible temperature coefficient or the material could be permanently demagnetized. For Samarium Cobalt, this is about 350°C; for Neodymium Iron Boron, it can be as low as 125°C.

An expression for B_{coil}, in Equation VII-17 can be found by creating a model for a differential flux tube over a tooth face, (Figure VII-5). The differential coil flux through the tube is given by Equation VII-22. This equation assumes a symmetric winding; therefore the coil mmf is divided equally across the airgaps and V_a, in this figure, is zero. Thus, all paths are in parallel and one can write an expression for the differential flux directly.

$$d\phi_{coil} = \frac{Ni}{dR} = \frac{Ni \; dA}{\frac{\ell_m}{\mu_o \mu_r} + \frac{\ell_g}{\mu_o}} \qquad \text{(VII-22)}$$

From Figure VII-2:

$$\ell_g = (r_4 - r_3) \qquad \text{(VII-22a)}$$

$$\ell_m = (r_3 - r_2) \qquad \text{(VII-22b)}$$

Since the flux density is the derivative of flux with respect to area, the flux density is given by:

$$B_{coil} = \frac{Ni}{\frac{\ell_m}{\mu_o \mu_r} + \frac{\ell_g}{\mu_o}} \qquad \text{(VII-23)}$$

Substituting Equation VII-23 into Equation VII-17, and normalizing with respect to phase current i, yields an expression for the torque constant as:

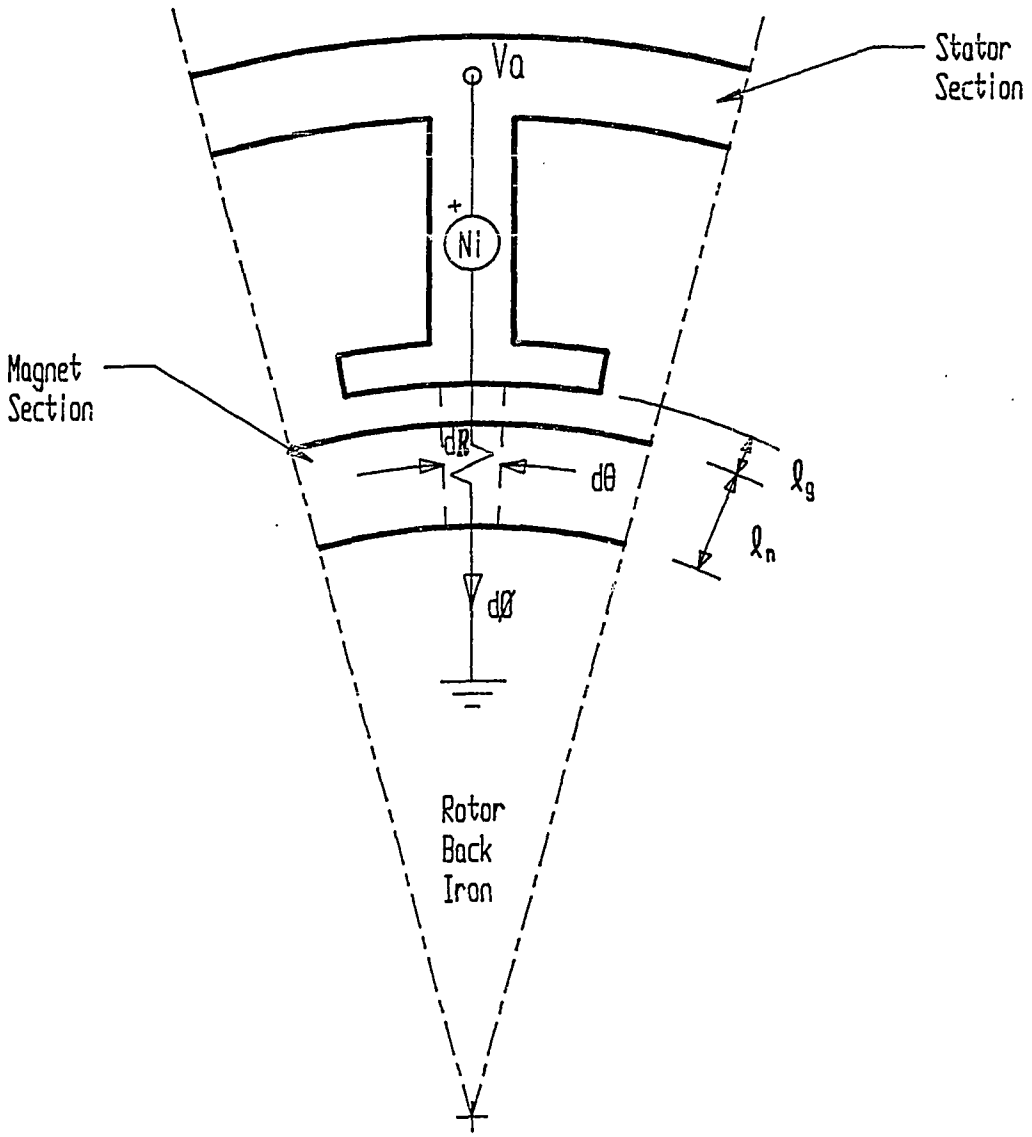

Figure VII-5
Motor Section Showing Differential Flux Tube

$$K_t = \frac{B_r}{\mu_r \mu_o} \quad \frac{2 N_p \ell_m N r_{mave} z}{\frac{\ell_m}{\mu_o \mu_r} + \frac{\ell_g}{\mu_o}} \qquad \text{(VII-24)}$$

If the torque constant expression is rearranged, one obtains:

$$K_t = 2 B_r r_{mave} N_p N z \frac{\ell_m/\ell_g}{\frac{\ell_m}{\ell_g} + \mu_r} \qquad \text{(VII-25)}$$

This expression was derived under the assumption of magnetic linearity. Equation VII-25 shows that the torque constant will increase linearly with the number of rotor magnet poles, the number of coil turns, the axial length of the motor, the residual flux density of the magnet material, and the average radius of the magnet. It is also a nonlinear function of the ratio of magnet radial length to physical airgap length. If it is assumed that the average magnet radius remains constant and the ratio of magnet to airgap length is varied, then the effect on the torque constant can be explored. First, Equation VII-25 is normalized with respect to r_{mave}, B_r, N_p, N and z:

$$\bar{K}_t = \frac{K_t}{2 r_{mave} B_r N_p N z} = \frac{\ell_m/\ell_g}{\ell_m/\ell_g + \mu_r} \qquad \text{(VII-26)}$$

For rare earth magnets $\mu_r \doteq 1$. If $\ell_m/\ell_g \gg 1$, then $\bar{K}_t = 1$. Figure VII-6 shows a plot of $\bar{K}_t$ versus the ratio ℓ_m/ℓ_g. The solid line represents Equation VII-26. As ℓ_m/ℓ_g reaches a value of approximately 7, the normalized value of K_t is 0.87. At $\ell_m/\ell_g = 10$, $\bar{K}_t$ is 0.90, an increase to $\ell_m/\ell_g = 20$ yields $\bar{K}_t = 0.92$, obviously there is a diminishing return.

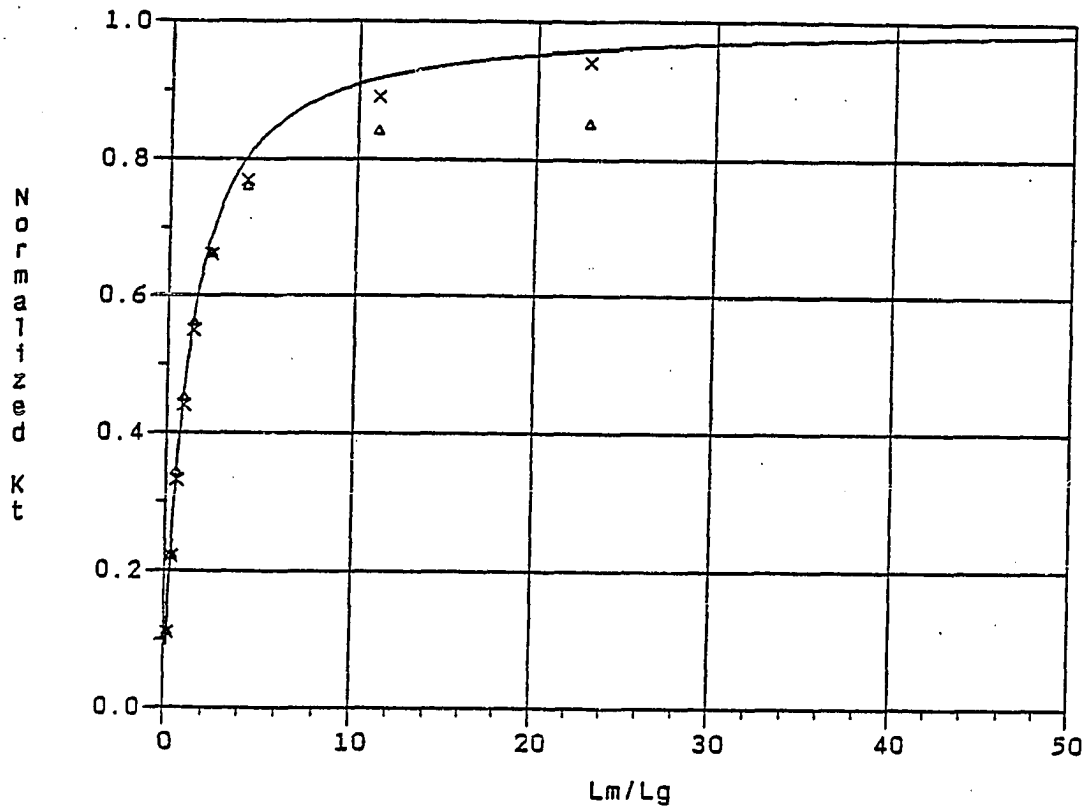

Figure VII-6
Normalized Torque Constant versus Ratio
of Magnet Length to Physical Airgap Length
Solid Line- Theoretical value
X's - Finite Element Predicted with Linear Iron Model
Triangle's - Finite Element Predicted with Saturable Iron Model

Since the physical air gap length, ℓ_g, is usually fixed by the mechanical tolerences, increasing the ratio ℓ_m/ℓ_g directly increases the magnet length and hence magnet costs.

For comparison, finite element results are also shown in Figure VII-6. The X's show results obtained using a magnetically linear iron within the model. The magnet thickness was increased from a small percentage of the airgap to a point where it completely filled the airgap, $(\ell_m/\ell_g=\infty)$. The maximum value of K_t found was used to normalize the torque constants found for the lesser values of ℓ_m/ℓ_g. These results agree closely with the results predicted by Equation VII-26. The triangles are data obtained with the finite element model using a saturable iron. The maximum K_t found using the linear iron was used to normalized the torque constants found for the saturable steel. This was done to eliminate saturation effects in determining the normalized torque constant. One sees that for this motor saturation prevents the motor from producing its maximum possible torque constant.

Therefore, one sees that for a given design, if one selects a magnet length to airgap length ratio greater than seven, the increase in torque constant probably does not justify the increase in magnet cost. However, the increase in effective airgap could have an affect on other parameters, such as decreasing the inductance.

VII.2c2 Rotor Inertia

The simplest model for rotor inertia is to assume that the rotor is a solid cylinder, no air spaces in the interior of the rotor, and that the magnet segments used were full arc span, with no air gaps between adjacent magnet segments. See Figure VII-7. The rotor inertia, J_r, is the sum of the inertia due to the magnet, the back iron, and the nonmagnetic stainless steel shaft.

$$J_r = J_{mag} + J_{back} + J_{shaft} \qquad \text{(VII-27)}$$

Since the shape of each of these sections is cylindrical, the expression describing the inertia of each, J_k, is given as:

$$J_k = \frac{1}{2} \rho_k \pi z (r_{ok}^4 - r_{ik}^4) \qquad \text{(VII-28)}$$

Where:

r_{ok} ≡ outer radius of annular section k

r_{ik} ≡ inner radius of annular section k

ρ_k ≡ density of annular section k

The density of the stainless steel shaft, the rare earth magnet material, and the steel rotor back iron are all approximately equal. Therefore the inertia of the rotor is given as:

$$J_r = \frac{1}{2} \rho_s \pi z r_3^4 + J_{se} \qquad \text{(VII-29)}$$

Where:

r_3 ≡ outer radius of magnet, as shown in Figure VII-2

J_{se} ≡ inertia of the shaft extension which extends from the end of the rotor and out the front of the motor.

ρ_s ≡ density of steel

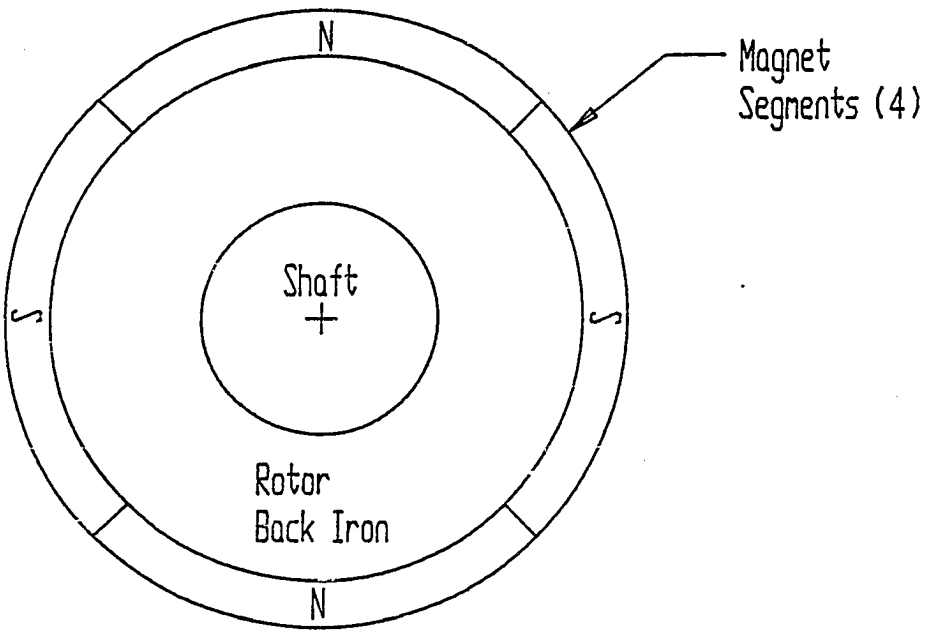

Figure VII-7
Cross-Sectional Configuration of Assumed Rotor

VII.2c3 Phase Resistance

An expression for the resistance of a phase of the motor can be developed in the following manner. The resistance of a length of wire is given as:

$$R = N\ell_t \rho_{pf} \qquad \text{(VII-30)}$$

Where: $N \equiv$ Number of turns per phase

$\ell_t \equiv$ length of wire per turn

$\rho_{pf} \equiv$ the resistivity per foot of the wire

Temperature effects can be taken into consideration in this equation by making ρ_{pf} temperature dependent. A material such as copper has a resistivity that is a reasonably linear function of temperature. Hence, the resistivty per foot could be modeled as:

$$\rho_{pf} = \rho_{pfo} \ (1 + C_{Tc} \Delta T) \qquad \text{(VI-31)}$$

Where: $\rho_{pfo} \equiv$ the resistivity per foot at 25^0C

$C_T \equiv$ the temperature coefficient of the material ($0.0039\ \Omega/^0$C for copper)

$\Delta T \equiv$ change in temperature of copper over ambient

The model would be particularly useful if thermal models were included as part of the design. However, the design process discussed in this work calculates resistance at ambient temperature only.

If a turn is considered to be the length of wire necessary to wind a single turn for all windings of a phase, then an expression for the length per turn is given in Equation VII-32. Figure VII-8 shows an example winding scheme for a single phase of a 4 pole, 3 phase, 24 slot motor. One sees from this figure that there are 4 coils to correspond to the 4 poles. A coil has been defined as the windings over a pole face. For this motor there are 2 windings per coil. A

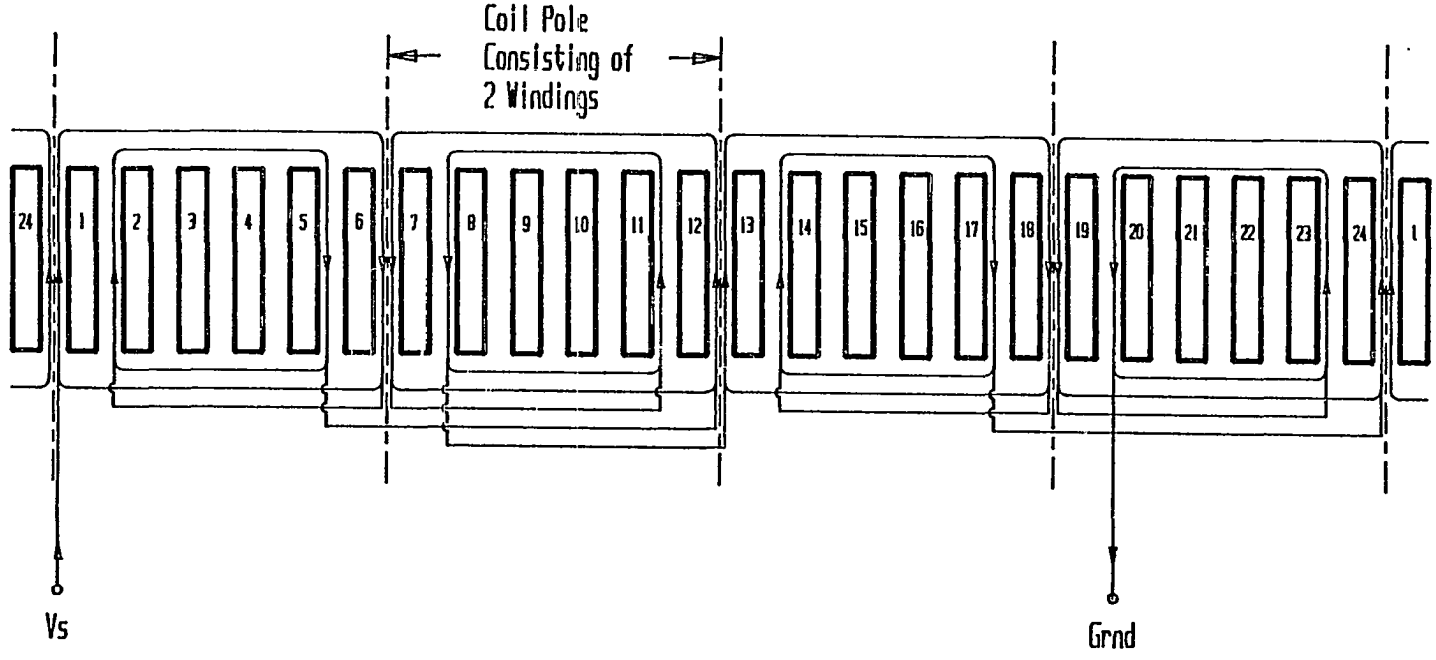

Figure VII-8
Example Wiring Diagram for
1 Phase of a 4 Pole, 24 Slot Motor

single turn, as defined above, is the length of wire necessary to wind the eight loops shown in this figure.

$$\ell_t = 2\, N_{wp} N_p (z+e) + 2r_{save}\left(\frac{2\pi}{N_p}\right) N_p N_{wp} \qquad \text{(VII-32)}$$

Where: $N_p \equiv$ number of poles
$N_{wp} \equiv$ number of windings per coil
$z \equiv$ axial length of the motor
$e \equiv$ wire axial overhang over stator stack length
$r_{save} \equiv$ average radius of stator slot

The number of windings per coil is given by the expression:

$$N_{wp} = \left(\frac{N_t}{3N_p}\right) \qquad \text{(VII-33)}$$

Combining Equations VII-30,32 & 32 yields an expression for the resistance of a phase of the motor as:

$$R = 2N\rho_{pf}\left(\frac{N_t}{3N_p}\right)\left\{N_p (z+e) + 2\pi r_{save}\right\} \qquad \text{(VII-34)}$$

VII.2c4 Tooth Width and Back Iron Thicknesses

The stator tooth width and stator and rotor back iron thickness can be determined from the coil and magnet flux, and, a limiting value of flux density. Once the coil and magnet flux is determined, one can find the cross-sectional areas of the stator teeth, and rotor and stator back iron, needed to carry that amount of flux without exceeding the pre-specified level of flux density.

First, one finds the maximum coil flux through one of the teeth.

the reluctance of the airgap region over each tooth, $\mathcal{R}_{tth}$, is given in Equation VII-35.

$$\mathcal{R}_{tth} = \frac{\ell_m}{\mu_o \mu_r A_m} + \frac{\ell_g}{\mu_o A_g} \qquad \text{(VII-35a)}$$

Where:

$$A_g = \pi z (r_4 + r_3)/N_t \qquad \text{(VII-35b)}$$

$$A_m = \pi z (r_3 + r_2)/N_t \qquad \text{(VII-35c)}$$

The area used in this expression is the cross-sectional area over one tooth pitch, rather than the cross-sectional area over the tooth face. In this manner, the flux through the airgap over the slot face is taken into account. The path length of the flux through slot airgap is actually longer than this model indicates; in Chapter VI the path extended into the slot opening through a semi-circular path to the edge of the tooth tip. Ignoring the tooth tip path does not significantly affects the results.

The maximum coil flux through a tooth, ϕ_{ctth}, is then given by:

$$\phi_{ctth} = \frac{N_{wp} N I_{max}}{\mathcal{R}_{tth}} \qquad \text{(VII-36a)}$$

In a similar manner, the maximum magnet flux through a tooth is:

$$\phi_{mtth} = \frac{B_r \ \ell_m}{\mu_r \mu_o \mathcal{R}_{tth}} \qquad \text{(VII-36b)}$$

A constraint can be introduced between the stator tooth widths and back iron and the magnet and coil flux. The constraint will limit the flux density in these sections to prevent saturation. First, one needs to calculate the maximum total flux through a tooth due to both coil energization and magnet. The maximum total flux through each tooth is the sum of the maximum flux due to two coils, (for two-phase-on operation), and the magnet, divided by the number of teeth per pole. This is a worse case condition, occuring when the rotor and stator fields are aligned.

$$\phi_{maxtth} = 2\phi_{ctth} + \phi_{mtth} \qquad \text{(VII-37a)}$$

The necessary width of the tooth, w_t, to support a prespecified level of flux density, B_{max}, is:

$$w_t = \phi_{maxtot}/(zB_{max}) \qquad \text{(VII-37b)}$$

This expression assumes a linear magnetic steel. To ensure that the steel remains in the linear region, the prespecified level of flux density must be below or near the knee of the saturation curve.

The necessary width of the stator and rotor back iron must also be determined. Figure VII-9 shows a contour plot of the field solution for the motor when the magnet and stator fields are aligned. One sees that both the rotor and stator back iron thicknesses should be selected so that each will support half the total flux through a pole. Therefore, an expression for the total magnet flux and coil flux through one pole is needed.

The number of turns, N_k, and the number of ampere-turns, $N_k I_{max}$, driving flux across the airgap over each tooth face is known from the

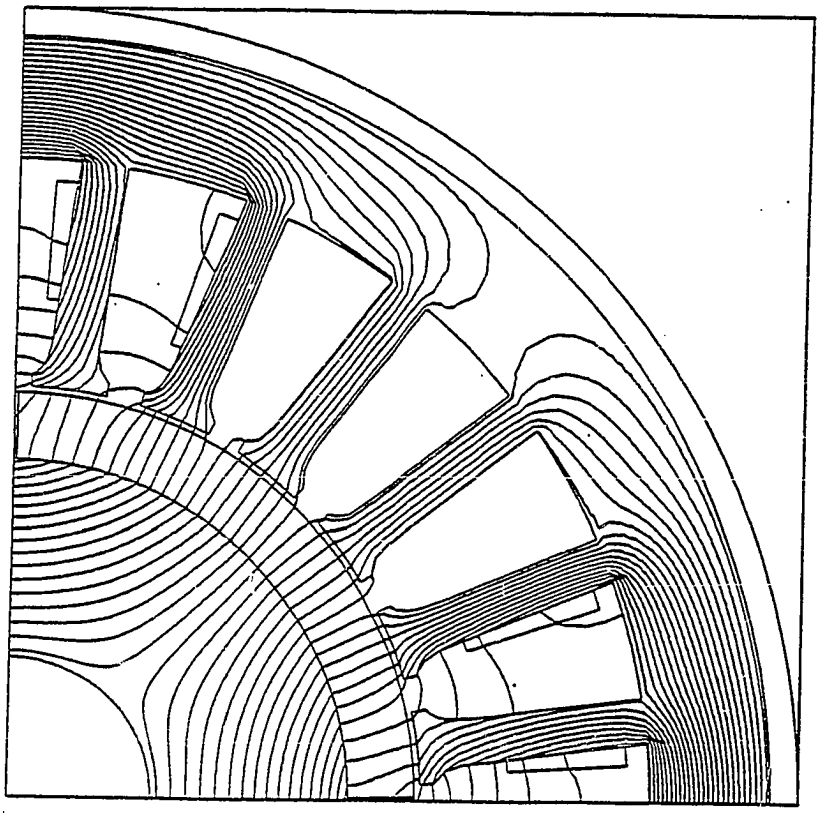

Figure VII-9
Field Solution Plot for
Rotor and Stator Fields Aligned

number of turns for each winding, N, and the number of windings per coil, N_{wp}. $N_k I_{max}$ corresponds to the source, $N_k i_k$, used in each branch of the coil flux circuit model developed and shown in Chapter VI as Figure VI-11. Since the current is the same for each of the sources, one can simply sum the turns to find the total effective turns for each branch.

$$N_k = \sum_{j=1}^{N_{wp}} \sum_{k=j}^{N_t/N_p - j + 1} N \qquad \text{(VII-38)}$$

The total coil flux through a pole is:

$$\phi_c = \sum_{k=1}^{N_t/N_p} N_k \, I_{max} \, / \, \mathcal{R}_{tth} \qquad \text{(VII-39a)}$$

The total magnet flux through a pole is:

$$\phi_m = \frac{N_t}{N_p} \, \phi_{mtth} \qquad \text{(VII-39b)}$$

The maximum total flux through a pole when two phases are energized and both the rotor and stator fields are aligned is:

$$\phi_{maxtot} = 2\phi_c + \phi_m \qquad \text{(VII-39c)}$$

Therefore, the maximum allowable backiron thickness, b_t, is:

$$b_t = (2\phi_c + \phi_m)/(2B_{max}) \qquad \text{(VII-40)}$$

The necessary rotor and stator back iron thicknesses, b_{tr}, b_{ts}, are equal.

$$b_{tr} = b_{ts} = b_t \qquad \text{(VII-40a,b)}$$

VII.2c5 Calculation of Slot Area and Stator Geometry

Given the number of turns, and a user selected wire size to try, the slot area necessary to accommodate N turns of the wire can be calculated. Incorporated in this calculation is a fill factor which relates the actual copper area of the total amount of wire that can be placed in the slot to the total avaliable slot area. The available slot area is equal to the total slot area minus any slot liners and forms to hold bundles in place. Typically, this fill factor is 40%-50%; slightly larger values may be used if the motor is to be wound by hand.

The necessary available slot area is given as:

$$A_{sn} = 2\ N\ A_{wt}/ff \qquad \text{(VII-41)}$$

Where:

A_{wt} ≡ total coated area of a strand of the copper wire

ff≡ area slot fill factor

The slot must accommodate 2N turns of wire. This is because there must be 2 bundles in each slot, where each bundle contains N turns. One bundle is one side of a north pole coil the other bundle is one side of a south pole coil. This can be seen by looking back at Figure VII-8.

Given the slot area necessary, the slot outer diameter can be calculated. First, an expression for the slot area is written in terms of the slot dimensions. Figure VII-10 shows the geometry of the slot, as well as the descriptive geometry.

$$A_s = \frac{\pi r_6^2 - \pi r_5^2}{N_t} - w_t (r_6 - r_5) \qquad \text{(VII-42)}$$

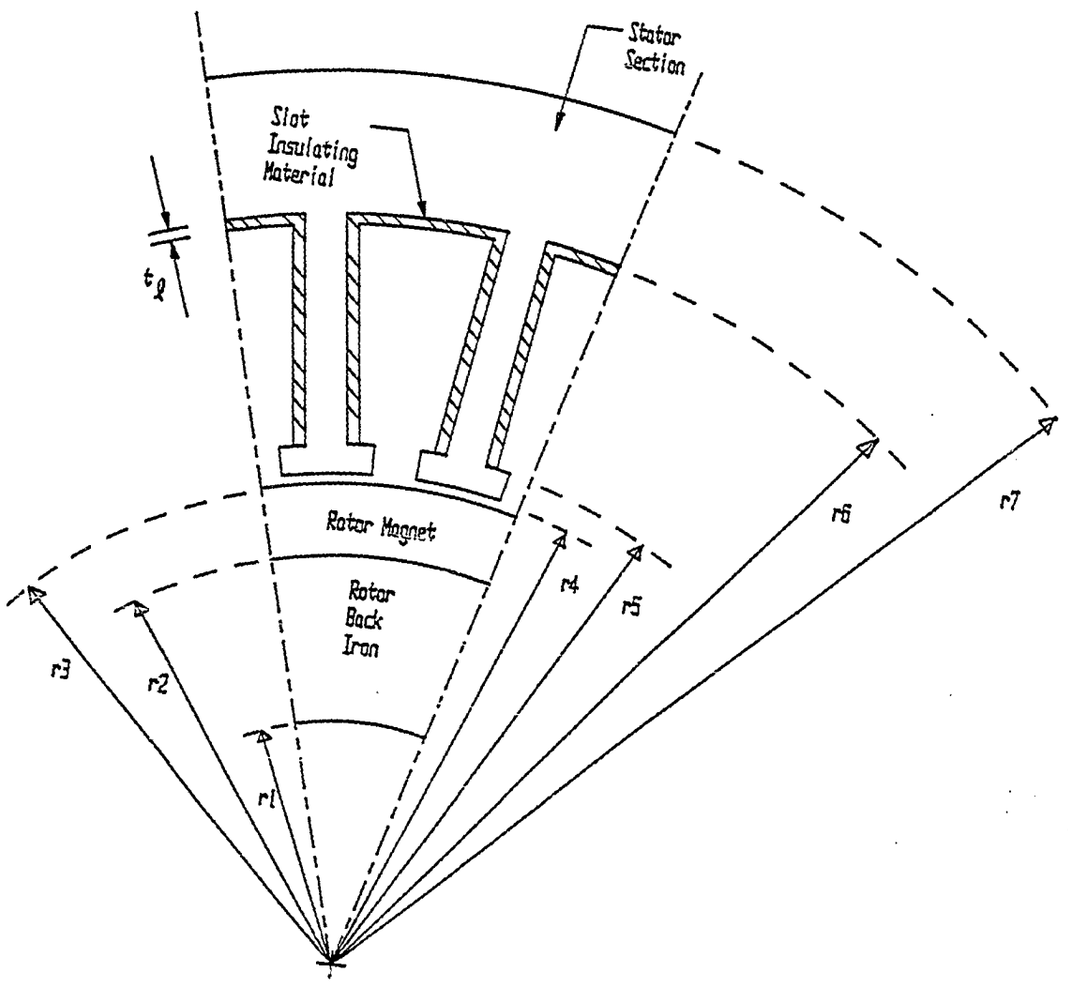

Figure VII-10
Motor Section Showing Descriptive Geometry

The slot area available, A_{sa}, is equal to the slot area minus the area occupied by the slot liner.

$$A_{sa} = A_s - \left[\frac{2\pi r_6}{N_t} - w_t\right]t_\ell + 2t_\ell(r_6 - r_5) \qquad \text{(VII-43)}$$

Where: $t_\ell \equiv$ the thickness of the slot liner

Substituting for A_s, and setting A_{sa} equal to the necessary available slot area, A_{sn}, from Equation VII-41, yields a quadratic expression for r_6:

$$r_6^2 - r_6\left[\frac{N_t w_t}{\pi} + 2t_\ell + \frac{2N_t t_\ell}{\pi}\right] + \left[\frac{w_t t_\ell N_t}{\pi} + \frac{A_{sn}N_t}{\pi} + \frac{w_t r_5 N_t}{\pi} + \frac{2r_5 t_\ell N_t}{\pi} - r_5^2\right] = 0 \qquad \text{(VII-44)}$$

Assigning some temporary variables, r_6 is given as:

$$r_6 = -\frac{b}{2} + \sqrt{\frac{b^2}{2} - c} \qquad \text{(VII-45)}$$

Where:

$$b = -(N_t w_t + 2N_t t_\ell + 2\pi t_\ell)/\pi$$

$$c = (-\pi r_5^2 + N_t w_t r_5 + 2N_t t_\ell r_5 + N_t t_\ell w_t - N_t A_{sn})/\pi$$

$$r_4 = r_3 + \ell_g \qquad \text{(VII-46)}$$

$$r_5 = r_4 + tt \qquad \text{(VII-47)}$$

Once the outer shaft radius is known, it can be used with the backiron thickness to determine the stator outer diameter.

$$r_7 = 2(r_5 + t_b) \qquad \text{(VII-48)}$$

VII.2c6 Calculation of Iron Losses

Iron losses due to eddy currents and hysteresis are dependent on the stator lamination material, the weight of the stator, the motor speed, and stator iron flux density. Often, a manufacturer will supply a set of curves showing loss per pound as a function of flux density and frequency, such as in Figure VII-11. These curves will vary with material type and the thickness of the lamination. The loss per pound, L_s, can be modeled as:

$$L_s = k_o \ (B_{max})^{k1} \ f^{k2} \qquad \text{(VII-49)}$$

B_{max} is the maximum flux density in the iron due to the magnet and phase winding. f is the frequency of the alternating field and is a function of the number of rotor poles and the speed of the motor. The unknown coefficients k_o, k_1, k_2, can be found by applying regression techniques to the data shown in Figure VII-11. For example, typical value for k_o, k_1, k_2 for M19 electrical grade steel were found to be:

$$k_o = 0.0012, \ k_1 = 1.88, \ k_2 = 1.50$$

After the geometry of the stator has been found, the iron losses, IL, in the stator are calculated by multiplying the loss coefficient, L_s, given by Equation VII-49, by the weight of the stator iron.

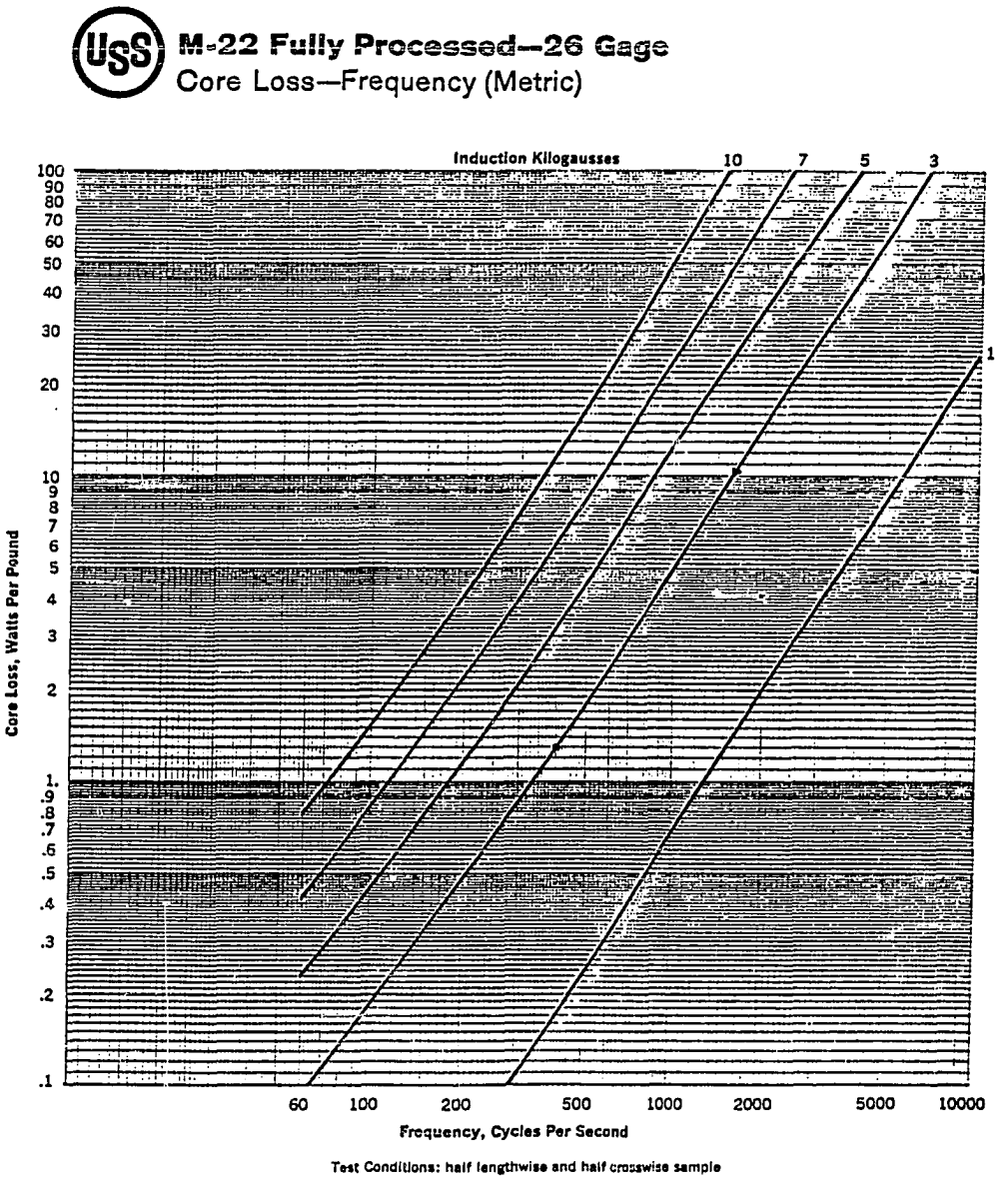

Figure VII-11
Lamination Steel Manufacturer's Data for Core
Loss as a Function of Flux Density and Frequency
(From US Steel's Non-Oriented Electrical Steel Catalogue)

$$f = \frac{N_p \dot{\theta}_c}{120} \qquad \text{(VII-50)}$$

$$IL = L_s \text{ vol } \rho_\ell \qquad \text{(VII-51)}$$

Where: vol ≡ the volume occupied by the stator iron

ρ_ℓ ≡ density of the lamination material

$\dot{\theta}_c$ ≡ maximum continuous operating speed of the motor

The volume of the stator iron is given by:

$$\text{vol} = (r_7^2 - r_6^2)\pi z + N_t (r_6 - r_4) w_t \qquad \text{(VII-52)}$$

VII.2c7 Constraint on Slot Width

Obviously, the slot opening in any design must be large enough to allow wires to be inserted. The maximum width of the slot opening is given by:

$$w_s = \frac{2\pi r_4}{N_t} - w_t - 2t_\ell \qquad \text{(VII-53)}$$

Often, to overcome the combination of a narrow slot opening and a relatively large diameter wire, a number of strands, N_{ps}, of a smaller diameter wire are wound together and connected in parallel. The number and size of these smaller diameter wires is selected so that the total copper cross-sectional area of N_{ps} strands of the smaller diameter wire, is equal to the cross-sectional area of one turn of the larger diameter wire. In this way, one obtains an equivalent winding, i.e: same resistance and inductance, yet, it is easier to insert in

the slot. There is a practical limit, however, to the number of strands that can be wound in parallel. Winding more than eight strands in parallel can be cumbersome and difficult.

The slot opening should be at least twice the diameter of the wire. This value could even be made larger to make winding insertion easier. Given the wire size and the ratio between wire diameter and slot opening, the minimum slot width, w_s, can be defined as:

$$w_s \geq \frac{wtd}{N_{ps}} \sqrt{\frac{4A_{wt}}{\pi}} \qquad \text{(VII-54)}$$

Where: A_{wt} ≡ coated wire area
N_{ps} ≡ maximum number of parallel strands
wtd ≡ specified minimum slot width to wire diameter ratio, (should be at least 2)

Slot widths less than this value are not wide enough to allow the wire to be inserted. For convience, a slot width ratio can be defined by expressing Equation VII-54 as a ratio, χ:

$$\chi = \frac{w_s}{\frac{wtd}{N_{ps}} \sqrt{\frac{4A_{wt}}{\pi}}} \qquad \text{(VII-55)}$$

If χ is greater than 1, the wire will fit through the slot because the ratio of slot width to wire diameter is equal to the specified ratio, wtd, (given the desired number of parallel strands).

VII.2c8 Calculation of Inductance

The inductance is calculated using the expressions derived previously in Chapter VI. In Chapter VI it was shown that accurate prediction of inductance by a simple lumped parameter model is difficult. It was necessary to include flux leakage paths between slots in order to predict the inductance with any accuracy. It was also shown in Chapter VI that the total inductance is the sum of the contribution due to the coil flux crossing the airgap/magnet region and the contribution due to the cross-slot leakage flux. The expressions determined for the inductance applied specifically to the 24 slot, 4 pole prototype motor. In this chapter, a more general expression is desired which is applicable to any motor having symmetric windings.

First, an expression for the inductance due to the coil flux crossing the airgap will be written. Using the number of turns, N_k, for the mmf source associated with each tooth, yields an expression for the flux through the airgap over a tooth, k, as:

$$\phi_{c_k} = \frac{N_k \; I_{max}}{\mathcal{R}_{tth}} \qquad \text{(VII-56a)}$$

Where: $\mathcal{R}_{tth}$ is the reluctance defined previously in Equation VII-35

N_k is the number of turns defined previously in Equation VII-38

The inductance contributions, L_{gap}, due to the airgap flux is:

$$L_{gap} = \sum_{k=1}^{N_t/N_p} \frac{N_k \, \phi_{ck}}{I_{max}} \qquad \text{(VII-56b)}$$

Substitution of Equation VII-56a yields:

$$L_{gap} = \sum_{}^{N_t/N_p} \frac{N_k^{\,2}}{\mathcal{R}_{tth}} \qquad \text{(VII-56c)}$$

The inductance of the cross-slot leakage path is determined in a similar manner. The cross-slot leakage reluctance is shown in Equation VII-56d.

$$\mathcal{R}_{cs} = \frac{\frac{2\pi(r_4+r_6)}{2\,N_t} - w_t}{\mu_o \, z \, (r_6 - r_4)} \qquad \text{(VII-56d)}$$

In this expression, it has been assumed that the teeth are straight sided with no tooth tips. Alternatively one could use r_5 instead of r_6 in this equation and then also calculate the additional reluctance from tooth tip to tooth tip and add the two reluctances in parallel. The simpler model was used here because it did not significantly affect the results. The total flux crossing the tooth tips is much less than that crossing the slot.

The inductance, L_{cs}, due to the cross-slot leakage is now given as:

$$L_{cs} = \frac{2N_1^{\,2}}{\mathcal{R}_{cs}} + \sum_{k=1}^{N_{wp}-1} \frac{2N_k}{\mathcal{R}_{cs}} (N_k - N_{k+1}) \qquad \text{(VII-57a)}$$

The total phase inductance, L_p, for N_p coils connected in series is N_p

times the sum of the gap and cross-slot leakage inductances.

$$L_p = N_p \left(L_{gap} + L_{cs} \right) \qquad \text{(VII-57b)}$$

This model is simplistic in that it is only a linear model including the airgap path and a leakage path. Saturation and end effects in the actual motor can significantly affect the inductance; making the accuracy of any linear model questionable. It was shown in Chapter VI that end effects are difficult to account for because of three dimensional effects. Saturation, at least, will always tend to decrease the inductance. In this respect the results obtained from this type of model will be a worse case analysis.

VII-2c9 List of Equations

For completeness, the equations developed in the previous sections are listed below. Some algebraic manipulation and substitution has been performed. Twenty-one equations are listed as Equations VII-58 through VII-78. The 51 variables used in these Equations are listed immediately afterward in Table VII-2.

Phase torque constant:

$$K_t = B_r \frac{N_p \ell_m N (r_4 + r_3) z}{\ell_m + \ell_g \mu_r} \qquad \text{(VII-58)}$$

Where:

$$B_r = B_{ro} (1 + C_{rm} \Delta T) \qquad \text{(VII-59)}$$

Rotor inertia:

$$J_r = \frac{1}{2} \rho_s \pi z r_3^4 + J_{se} \qquad \text{(VII-60)}$$

Phase resistance:

$$R = 2N \frac{\rho_{cu}}{A_{wb}} \left(\frac{N_t}{3N_p}\right)\left\{N_p (z+e) + \pi(r_5+r_6)\right\} \qquad \text{(VII-61)}$$

Where:

$$\rho_{cu} = \rho_{cuo} (1 + C_{Tc} \Delta T) \qquad \text{(VII-62)}$$

Reluctance of airgap over a tooth pitch;

$$\mathcal{R}_{tth} = \frac{\ell_m}{\mu_o \mu_r A_m} + \frac{\ell_g}{\mu_o A_g} \qquad \text{(VII-63)}$$

Average area of air gap region over a tooth pitch:

$$A_g = \pi z(r_4 + r_3)/N_t \qquad \text{(VII-64)}$$

Average area of Magnet region over a tooth pitch:

$$A_m = \pi z(r_3 + r_2)/N_t \qquad \text{(VII-65)}$$

Maximum coil flux through a single tooth:

$$\phi_{ctth} = \frac{N_t \; N \; I_{max}}{3 \; N_p \; \mathcal{R}_{tth}} \qquad \text{(VII-66)}$$

Magnet flux through a tooth;

$$\phi_{mtth} = \frac{B_r \; \ell_m}{\mu_r \mu_o \; \mathcal{R}_{tth}} \qquad \text{(VII-67)}$$

Maximum allowable tooth width:

$$w_t = \frac{(2\phi_{ctth}+\phi_{mtth})}{(N_t/N_p)zB_{max}} \qquad \text{(VII-68)}$$

The number of turns for each mmf source:

$$N_k = \sum_{j=1}^{N_t/3N_p} \sum_{k=j}^{N_t/N_p-j+1} N \qquad \text{(VII-69)}$$

The total coil flux through a pole:

$$\phi_c = \sum_{k=1}^{N_t/N_p} N_k \; I_{max} \; / \; \mathcal{R}_{tth} \qquad \text{(VII-70)}$$

The total magnet flux through a pole:

$$\phi_m = \frac{N_t}{N_p} \; \phi_{mtth} \qquad \text{(VII-71)}$$

The maximum allowable backiron thickness:

$$b_t = (2\phi_c+\phi_m)/(2B_{max}) \qquad \text{(VII-72)}$$

Stator slot outer radius:

$$r_6 = -\frac{b}{2} + \sqrt{\frac{b^2}{2} - c} \qquad \text{(VII-73)}$$

Where:

$$b=-(N_t w_t + 2N_t t_\ell + 2\pi t_\ell)/\pi$$

$$c=(-\pi r_5^2 + N_t w_t r_5 + 2N_t t_\ell r_5 + N_t t_\ell w_t - N_t A_{sn})/\pi$$

Necessary slot area:

$$A_{sn} = 2\ N\ A_{wt}/ff \qquad \text{(VII-74)}$$

Stator slot inner radius:

$$r_5 = r_4 + tt \qquad \text{(VII-75)}$$

Airgap outer radius:

$$r_4 = r_3 + \ell_g \qquad \text{(VII-76)}$$

Magnet outer radius:

$$r_3 = r_2 + \ell_m \qquad \text{(VII-77)}$$

Magnet inner radius:

$$r_2 = r_1 + b_t \qquad \text{(VII-78)}$$

Outer motor radius:

$$r_7 = r_6 + b_t \qquad \text{(VII-79)}$$

Slot opening width ratio:

$$\chi = \frac{2\pi r_4/N_t - w_t - 2t_\ell}{\frac{wtd}{N_{ps}}\ \sqrt{\frac{4A_{wt}}{\pi}}} \qquad \text{(VII-80)}$$

Stator iron losses:

$$IL = k_o (B_{max})^{k1} \left[\frac{N_p \dot{\theta}_c}{120}\right]^{k2} \left\{\pi z(r_7^2 - r_6^2) + N_t w_t (r_6 - r_4)\right\} \rho_\ell \qquad \text{(VII-81)}$$

Cross-slot leakage reluctance:

$$\mathcal{R}_{cs} = \frac{\frac{2\pi(r_4 + r_6)}{2\ N_t} - w_t}{\mu_o\ z\ (r_6 - r_4)} \qquad \text{(VII-82)}$$

Inductance due to gap flux:

$$L_{gap} = \sum_{k=1}^{N_t/N_p} \frac{N_k^2}{\mathcal{I}_{max}} \qquad \text{(VII-83)}$$

Inductance due to cross-slot leakage flux:

$$L_{cs} = \frac{2N_1^2}{\mathcal{R}_{cs}} + \sum_{k=1}^{N_{wp}-1} \frac{2N_k}{\mathcal{R}_{cs}} (N_k - N_{k+1}) \qquad \text{(VII-87)}$$

Phase inductance:

$$L_p = N_p (L_{gap} + L_{cs}) \qquad \text{(VII-88)}$$

The preceeding summary has shown the design problem to be formulated by 28 equations with 58 unknowns. The unknowns are listed in Table VII-2. In order to solve the 28 equations listed, one needs to select, or specify, 30 of these variables. Of the 58 variables listed in Table VII-2, ρ_s, ρ_{cuo}, C_{Tc} can be treated as constants and

Table VII-2

List of Variables

A_g ≡ cross-sectional area of airgap region

A_m ≡ cross-sectional area of magnet region

A_{sn} ≡ necessary slot area

A_{wb} ≡ cross-sectional area of bare wire

A_{wt} ≡ cross-sectional area of coated wire

• B_{max} ≡ maximum flux density allowed in stator back iron

B_r ≡ remanent flux density of magnet at ΔT above ambient

• B_{ro} ≡ remanent flux density of magnet at 25^0C

b_t ≡ thickness of backiron

k C_{Tc} ≡ temperature coefficient for change in resistivity

• C_{Tm} ≡ reversible temperature coefficient of magnet material

• e ≡ overhang of wires

• ff ≡ slot area fill factor

IL ≡ stator iron losses

I_{max} ≡ maximum phase current

J_r ≡ rotor inertia

• J_{se} ≡ Inertia of shaft extension

• k_o ≡ lamination iron loss coefficients

• k_1 ≡ lamination iron loss coefficients

• k_2 ≡ lamination iron loss coefficients

K_t ≡ Phase torque constant

• ℓ_m ≡ magnet radial thickness

• ℓ_g ≡ radial length of air gap

L_{cs} ≡ inductance due to cross slot leakage

L_{gap} ≡ inductance due to the coil flux across the gap

L_p ≡ inductance of a phase

N ≡ number of turns for a coil

N_k ≡ number of turns for mmf source k

• N_p ≡ number of rotor poles

• N_{ps} ≡ maximum number of parallel strands

• N_t ≡ number of teeth

R ≡ phase resistance

(Table VII-2, Continued)

r_1 ≡ rotor backiron inner radius
r_2 ≡ rotor magnet inner radius
r_3 ≡ rotor magnet outer radius
r_4 ≡ rotor airgap outer radius
r_5 ≡ stator slot inner radius
r_6 ≡ stator slot outer radius
r_7 ≡ stator outer radius
• ΔT ≡ change in magnet temperature above ambient, assumed to also be change in coil temperature above ambient
• t_ℓ ≡ thickness of slot liner
• tt ≡ tooth tip thickness
w_t ≡ thickness of stator teeth
• wtd ≡ slot width to wire diameter ratio
z ≡ axial length of the rotor/stator
ϕ_c ≡ flux due to coil
ϕ_{ck} ≡ coil flux through airgap over a single tooth
ϕ_{ctth} ≡ maximum coil flux through a single tooth
ϕ_m ≡ flux due to magnet
ϕ_{mtth} ≡ magnet flux through a single tooth
• μ_r ≡ relative permeability of magnet material
k ρ_s ≡ density of steel - a constant
• ρ_ℓ ≡ density of lamination material
ρ_{cu} ≡ resistivity of copper at ΔT above ambient
k ρ_{cuo} ≡ resistivity of copper at ambient 25^0C
• $\dot{\theta}_c$ ≡ maximum continous operating speed of the motor
$\mathcal{R}_{cs}$ ≡ reluctance of the cross slot leakage path
$\mathcal{R}_{tth}$ ≡ reluctance of airgap over a tooth face
• χ ≡ slot width opening ratio

are marked by a 'k' in the first column of the table. There is little variation in the density of steel from one type of iron to another. The resistivity of copper is constant and relatively independent of wire size. (However, one might want to use aluminum wire instead, which has a different resistivity).

There are 22 variables in Table VII-2 that are marked with a '•' in the first column. These can usually be specified in advance, either because of a limited number of choices, or because it is known in advance that the effects on the design are not significant. An explanation of these choices follows.

B_{ro}, μ_r, C_{Tm} are fixed once one selects a magnet material. Here there are a limited number of choices. For example, if a sintered rare earth magnet is desired, usually B_r is approximately 1 Tesla and $\mu_r \doteq 1.0$.

ΔT is the maximum change in continuous temperature of the wire over ambient. This is a difficult number to determine without an involved thermal model which includes heat transfer paths specific to the application. If one assumes that ΔT is zero, then one obtains the characteristics at ambient temperature; this would not account for the increased I^2R losses and the decrease in magnet remanent flux density. Alternatively, one can assume the temperature of the winding is equal to the maximum temperature rating of the winding insulation. In this way, one can look at a worse case temperature condition. This analysis also assumes that the temperature of the magnet and the temperature of the winding are the same.

Once one selects a lamination material, ρ_ℓ is specified. In addition, B_{max}, the maximum flux density in the material before the onset of saturation, is specified. Selection of the lamination thickness fixes the loss coefficients k_o, k_1 and k_2.

The airgap length, ℓ_g, is usually fixed by the tolerence that is to be held between the rotating and nonrotating member. The magnet radial length, ℓ_m, can be specified once ℓ_g is specified. The analysis performed in Section VII-2c1 showed that ℓ_m/ℓ_g ratios of 7 were best for getting the most torque constant for the amount of magnet. Thus, a ratio of seven would typically be a good value to assume initially. Subsequently, this value might be changed slightly to refine the design.

The application will determine the geometry of the shaft extension. Therefore, J_{se}, will be fixed.

There are a limited number of teeth/pole combinations, N_t, N_p, that result in symmetric windings like those being considered in this design. The consequences of selecting the number of teeth and poles on some of the fundamental parameters were discussed in Section VII-2b.

The wire overhang, e, is a parameter that is fixed by the winding process and is specified by experience. This value will typically range from 0.5 to 1.0 inch. To some extent, however, this value depends on the size of the wire and the number of turns.

The thickness of the slot liner is fixed by the choice of slot liner material, this value is usually between 0.0075 and 0.015 inches.

Tooth tip thickness is another parameter specified from experience. The tooth tip serves the purpose of supporting wedges to hold

windings in place and to allow the field to fringe in the airgap and distribute the flux. Typically, this thickness is about 0.050 inches.

The fill factor, ff, for slots usually runs between 0.4 and 0.5. These are usually the maximum ratios of the copper area to slot area that can be inserted into the slots.

The slot opening width to wire diameter ratio, wtd, and maximum number of parallel strands are fixed by practical considerations and costs. The more difficult a motor is to wind, the more costly the process. Thus, for most typical applications, a value of wtd of 4, and a value of N_{ps} of 4 are desirable. If these constraints are satisfied then χ will be equal to 1.

$\dot{\theta}_c$ is the maximum continuous speed of the motor and is usually known in advance as part of the application requirements.

From the preceeding arguments one sees how 25 of the 58 variables listed in Table VII-2 can be pre-specified in initial designs. Combining these with the 28 equations requires 5 additional variables to be specified. Then, all the variables listed in Table VII-2 can be determined. By displaying a graphical comparison for some of these parameters as a function of rotor diameter, a motor design can be selected which meets the application requirements. The graphical comparison is an important part of this design process because some additional constraints might be imposed that can be thought of as 'soft' constraints. These would constrain a parameter to be within an approximate range. For example, it might be desired to constrain iron loss to be below a specified value at maximum motor speed. If the problem is solved to exactly yield the limiting value of iron

losses, designs might be overlooked which would yield slightly higher iron losses with less I^2R loses.

The design process described in Section VII-2a assumes that K_t, J_r, I_{max}, R are specified; therefore, only one additional variable needs to be fixed to specify a design. The design process described in the beginning of this section assumes the designer will select either the rotor length or the rotor diameter as that addition variable. In this manner the designer can use graphical methods to develop a more global understanding of parameter variations as a function of rotor length and diameter.

The design process described is illustrated in the following. If the specified inertia of the motor rotor, J_r, is specified as J_{sp}, and one assumes a particular length and diameter shaft extension, Equation VII-60 can be manipulated into:

$$zr_3^4 = 2\ (J_{sp}-J_{se})/\pi\rho_s \qquad \text{(VII-79)}$$

Relating the axial length, z, to the outer rotor radius, r_3, by a length to radius ratio, η, the outer radius of the rotor necessary to satisfy the inertia specifications is given as:

$$r_3 = [2(J_{sp}-J_{se})/\pi\rho_s]^{.2}/\eta \qquad \text{(VII-80)}$$

$$z=\eta r_3 \qquad \text{(VII-81)}$$

Relating the length to radius by the ratio η allows one to explore designs based on the ratio η, which is usually within a range from 0.1 to 20. (However, one can explore any range of interest). This allows the designer to explore immediately, a range of designs that are within a reasonable range of lengths to radius ratios.

For a particular value of η, r_3 given by Equation VII-80 can be used with Equation VII-58 to solve explicitly for the number of turns

necessary to meet the torque constant and inertia specification.

$$N = \frac{3K_t (\ell_m + \ell_g)}{(r_3 - \ell_m/2)(2\eta r_3 B_r N_t \ell_m)} \qquad \text{(VII-82)}$$

Since this expression will result in fractional values of turns, one needs to use the closest larger integer value. Once the number of turns is known, Equation VII-59 through VII-78 can be used to determine the remaining motor parameters. Graphical methods can be used to find a design which satisfy the resistance by a trial and error selection of different wire sizes.

VII.3 Application of the Design Process

VII.3a Application of the Design Process to the Prototype Motor

The design method described above is illustrated by applying the process to design a motor with the same torque constant and inertia as the prototype motor discussed previously in this work. This was done as a verification of the design process. Therefore, the parameter specifications made are ones which will result, hopefully, in a matching design. However, these parameters may not result in an optimum design with respect to weight or volume, for example.

The initial design parameters and constraints used are shown in Table VII-3.

Table VII-3

List of Specified Parameters for Example Design

Inertia,	$J = 7.738E-03$ in-lb-s^2
Torque constant,	$K_t = 50$ oz-in/Amp
Magnet Br,	$B_r = 1.08$ Tesla
Physical airgap,	$\ell_g = 0.011$ inches
Magnet radial length,	$\ell_m = 0.121$ inches
Number of rotor poles,	$N_p = 4$ poles
Number of stator teeth,	$N_t = 24$ teeth
Copper fill factor,	$ff = 0.3$
Tooth tip thickness,	$tt = 0.025$ in.
Phase resistance,	$R = 5.4$ ohms
Maximum phase current,	$I_{max} = 2.0$ Amps
Maximum allowable iron flux density,	$B_{max} = 2.0$ Tesla

Figure VII-12 shows a plot of combinations of rotor outer diameter and rotor length that will satisfy the inertia requirement for the prototype motor. These combinations correspond to a range of rotor length to radius ratio, η, of $0.5<\eta<25$. Combinations that lie above this line will result in motor inertias greater than the specified value. Combinations lying below the line result in lesser inertias.

Figure VII-13 shows a plot of the number of turns necessary to satisfy the torque constant constraint, versus rotor diameter. It is important to remember that in this plot, and in similar ones to follow, although the parameter is plotted versus rotor diameter, length is not a constant. The length is changing with diameter in a manner to satisfy the inertia constraint. Figure VII-14 shows the number of turns necessary to satisfy the torque constant constraint plotted versus rotor length. Given the particular combination of

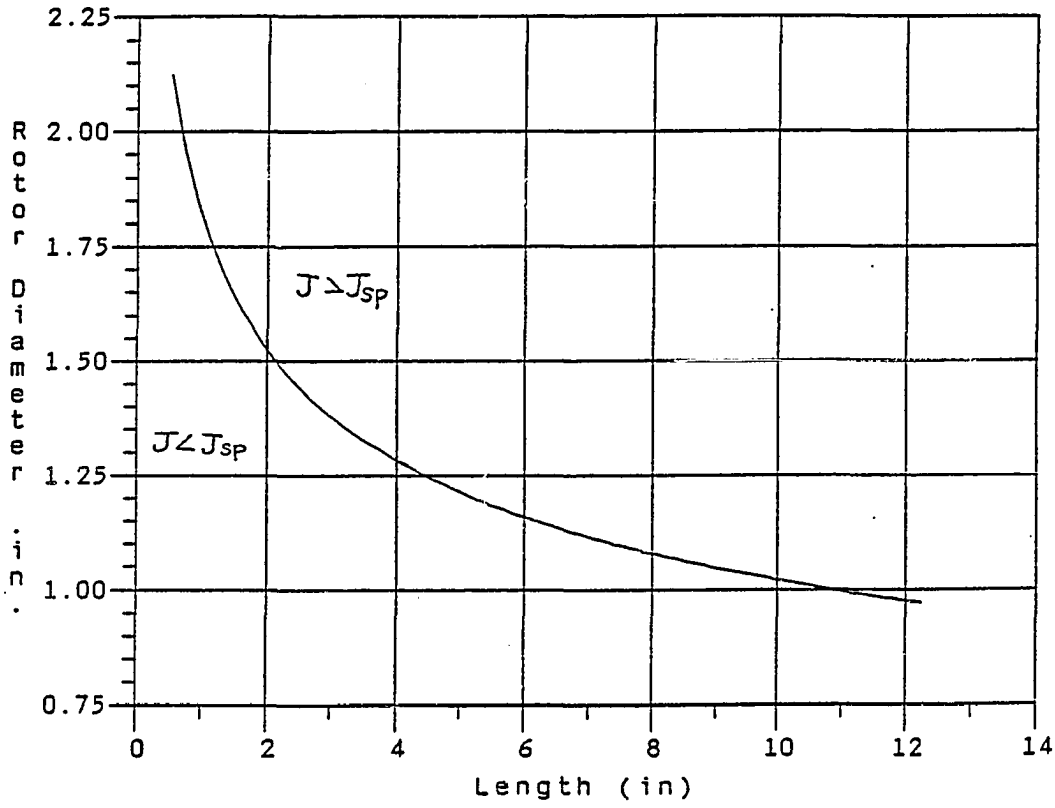

Figure VII-12
Rotor Diameter and Length Combinations
that Satisfy the Inertia Constraint

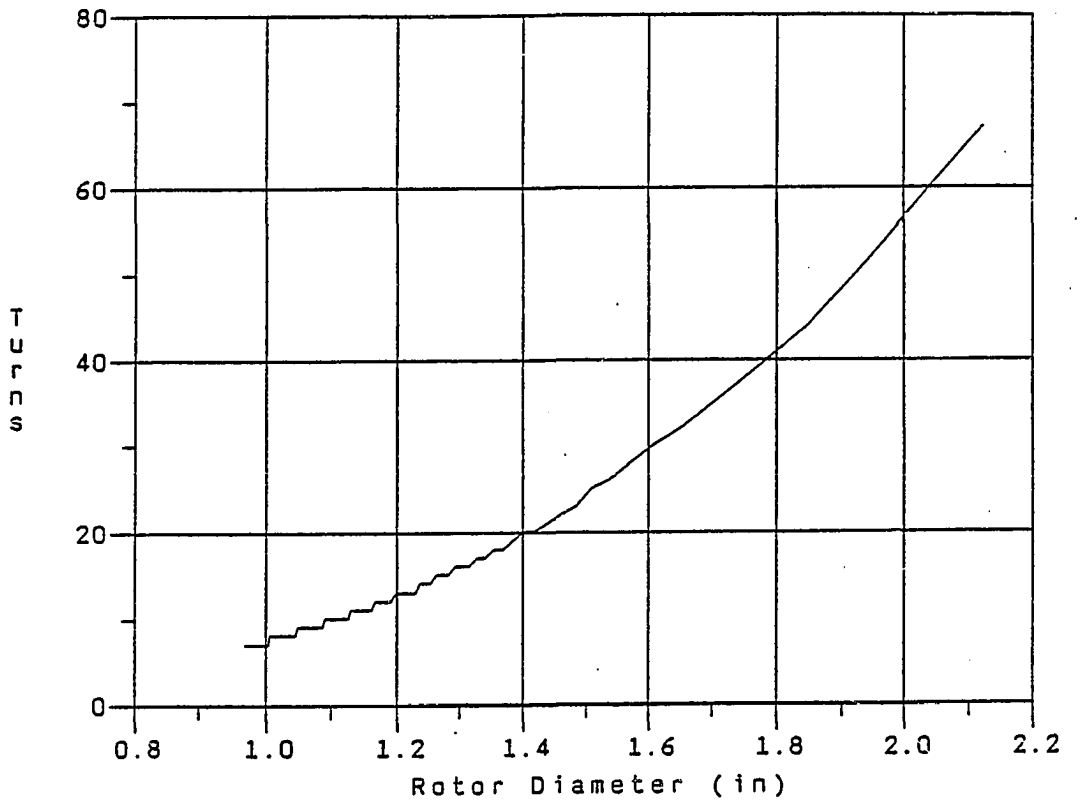

Figure VII-13
Number of Turns Necessary to Satisfy the Inertia
and Torque Constant Requirements, versus Rotor Diameter

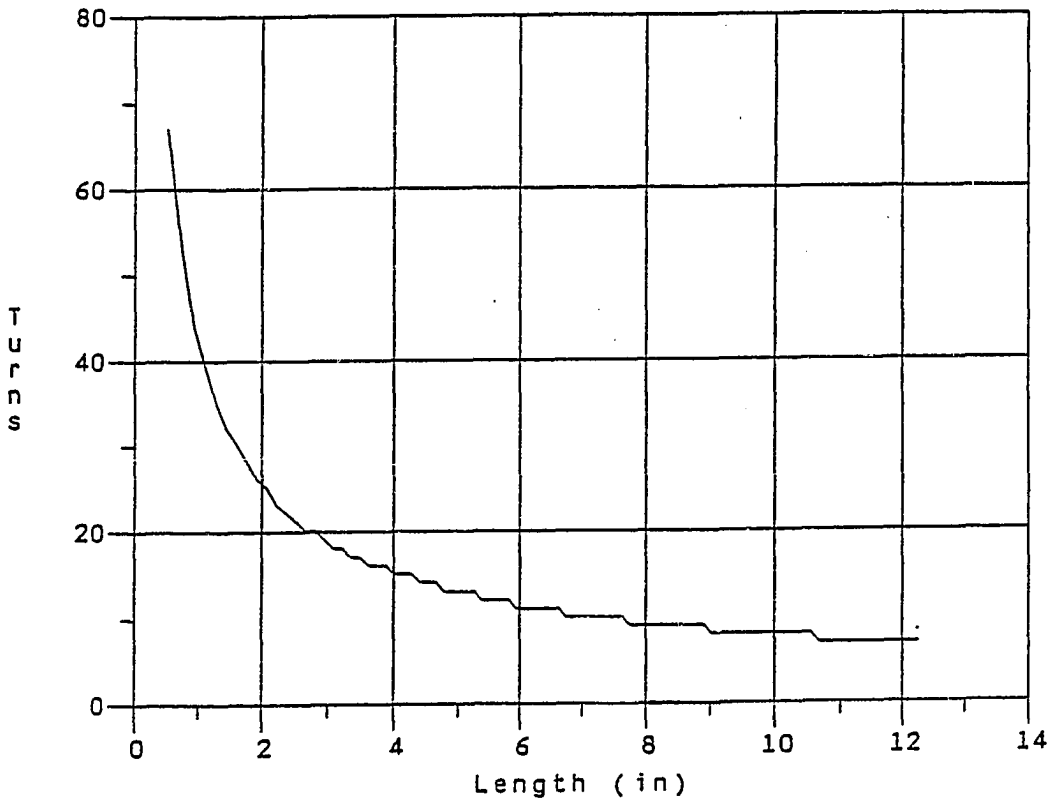

Figure VII-14
Number of Turns Necessary to Satisfy the Inertia
and Torque Constant Requirements, versus Rotor Length

rotor diameter and length, and the number of winding turns, the remaining motor geometry and performance parameter can be determined.

Both Figures VII-13 and VII-14 show 'steps', this is due to the fact that the number of turns can only be an integer. When one solves for the number of turns necessary to meet a specified torque constant, the closest integer value is used. Therefore, any subsequent plots shown which depend on the number of turns will not be smooth.

To start the design process, one should first look at the diameter available in the center of the rotor to place the nonmagnetic stainless steel shaft. This parameter is determined by taking the rotor outer diameter and subtracting the magnet thickness and calculated necessary rotor back iron thickness. The remainder is space available to accommodate a nonmagnetic shaft. Figure VII-15 shows such a plot. One sees from this figure that if a 0.625, (5/8), inch shaft is required, the rotor diameter must be larger than approximately 1.37 inches in diameter. If a 0.625 inch diameter shaft is to be used, and the rotor diameter is smaller than 1.37 inches, the rotor back iron thickness will be less than was determined to be necessary to avoid saturation. This could affect the torque constant of the motor. Hence, this plot allows one to determine the minimum rotor diameter that satisfies this additional constraint. If the back iron thickness constraint is violated, the actual motor torque constant might be less than designed.

Whether or not the torque constant is significantly decreased depends upon the added saturated back iron reluctance to the airgap flux circuit. If the added reluctance of the saturated back iron is a very small percentage of the total circuit reluctance, then the coil

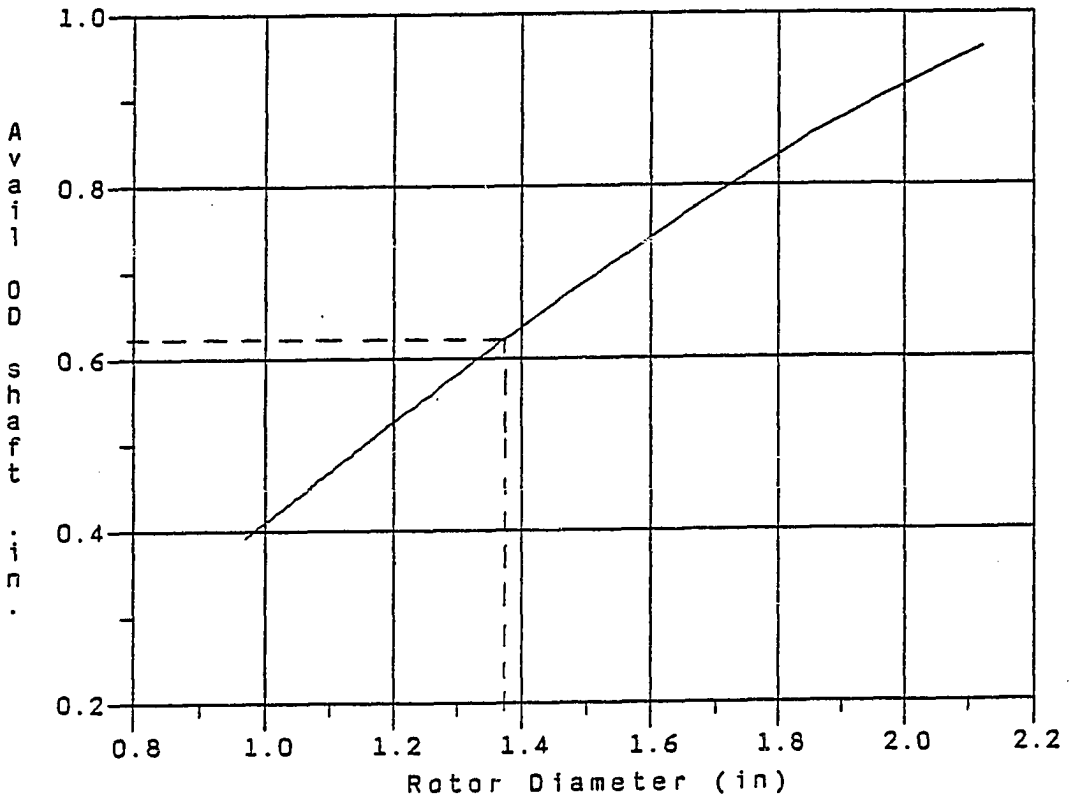

Figure VII-15
Available Diameter Remaining in Rotor
Back Iron to Accomodate a Shaft

flux will only change by a small percentage. Given the permanent magnet IxB method, we can deduce that the torque and torque constant will change by a corresponding percentage.

The reluctance of the back iron is a function of its length, area, and permeability (as shown previously in Equation VII-7a). If the back iron path has a low permeability due to saturation, but, the length of the saturated path is short, the saturated reluctance will be small. Hence, even though a portion of the path experiences some degree of saturation, the net effect on the torque constant could be negligible.

The next step in this design process depends upon which performance parameter is more important to the user. Suppose the user is to use a current drive and has to meet a resistance specification to limit the I^2R heating losses of the motor. Suppose further, that the resistance is to be limited to 5.4 ohms, the resistance of the prototype motor. By selecting several different values of wire size, the resistance of each combination of r_o and η for each wire size selected can be determined.

A plot of resistance versus diameter for wire sizes AWG 24,25,26 is shown in Figure VII-16. If a line is place on this plot indicating the specified resistance limit of 5.4 ohms, one sees that in order to meet this specification with a wire size of AWG 25, the rotor diameter must be limited to approximately 1.68 inches or less. Wire size AWG 24 would meet the resistance specification for diameters < 1.86 inches and AWG 26 would meet it for diameters < 1.45 inches. The use of a large diameter wire, (smaller AWG number), would allow the use of a larger diameter rotor diameter. However, the larger the diameter of

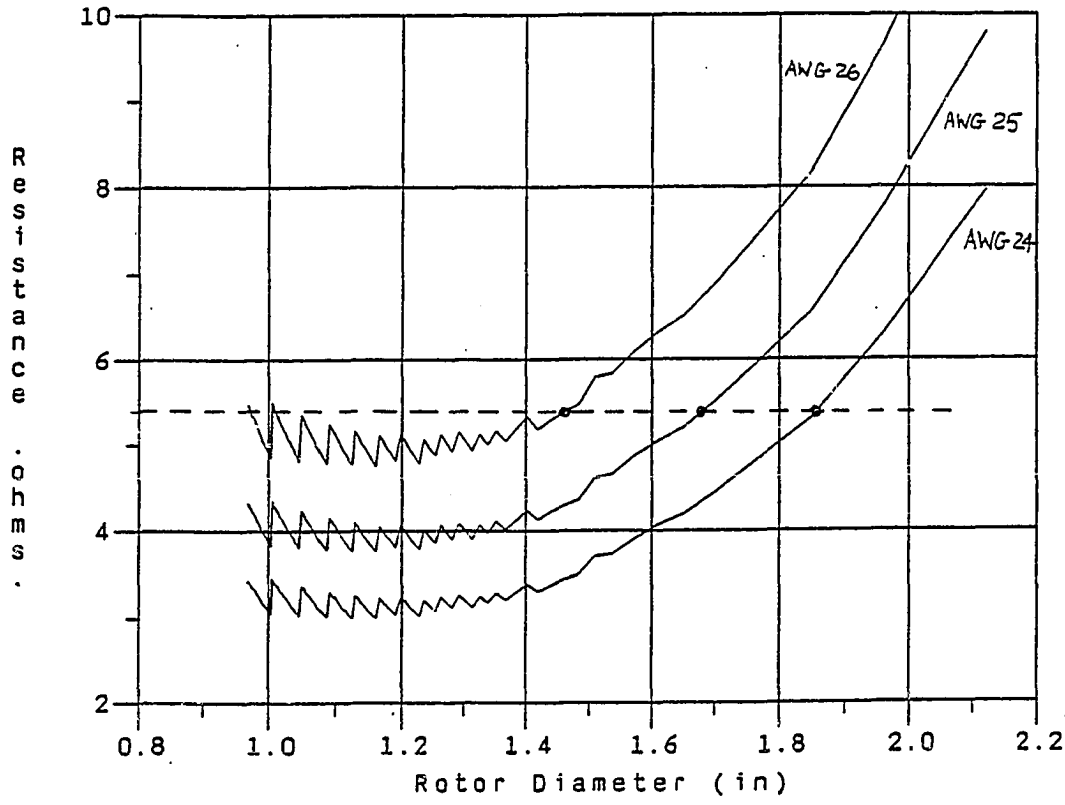

Figure VII-16
Resistance versus Rotor Diameter
for Wire Sizes AWG 24, 25, and 26

the wire, the greater the outer diameter of the motor.

Figure VII-17 shows a plot of motor outer diameter versus rotor diameter for the three different wire sizes. One sees that for a fixed rotor diameter, the larger the wire diameter, the larger the motor outer diameter. The information learned from the shaft and resistance plots can be transfered to the plot of motor outer diameter. Due to back iron considerations the minimum rotor diameter allowable is 1.37 inches. A wire size of AWG 26 or less is necessary to meet the resistance specifications. If its desired to minimize motor outer diameter then one should select wire size AWG 25 and rotor diameter of 1.45 inches. A '•' marks the maximum diameter that can be used in each wire size and still meet the resistance specifications. An arrow marks the direction of decreasing phase resistance. One can deduce that use of a wire size higher than AWG 26 would not meet both the shaft and resistance requirements.

If minimization of resistance is more important then, again, one should select a rotor diameter of 1.45 inches and decide upon a maximum allowable motor outer diameter. Then one selects the largest diameter wire possible that results in a motor outer diameter within the predetermined limits. For example, if one selects a rotor diameter of 1.45 inches and AWG 24 instead of AWG 25, the resistance is reduced from 4.7 ohms to 3.0 ohms. The penalty is an increase in motor outer diameter from 2.9 inches to 3.17 inches. This is a 9% increase in motor diameter for a 36% decrease in resistance and resistive losses.

Figure VII-18 shows a plot of motor weight versus rotor diameter. If similar trade-offs for weight are to be considered for the previous

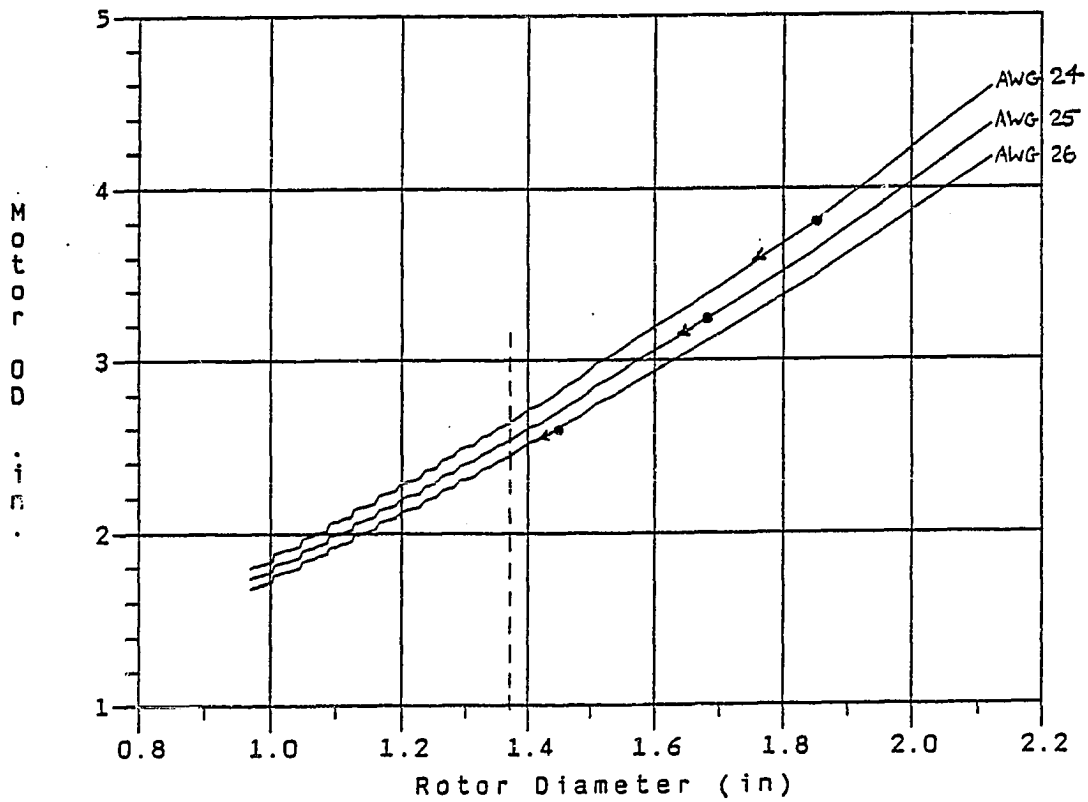

Figure VII-17
Motor Stator Outer Diameter versus Rotor Diameter for Wire Sizes AWG 24, 25, and 26

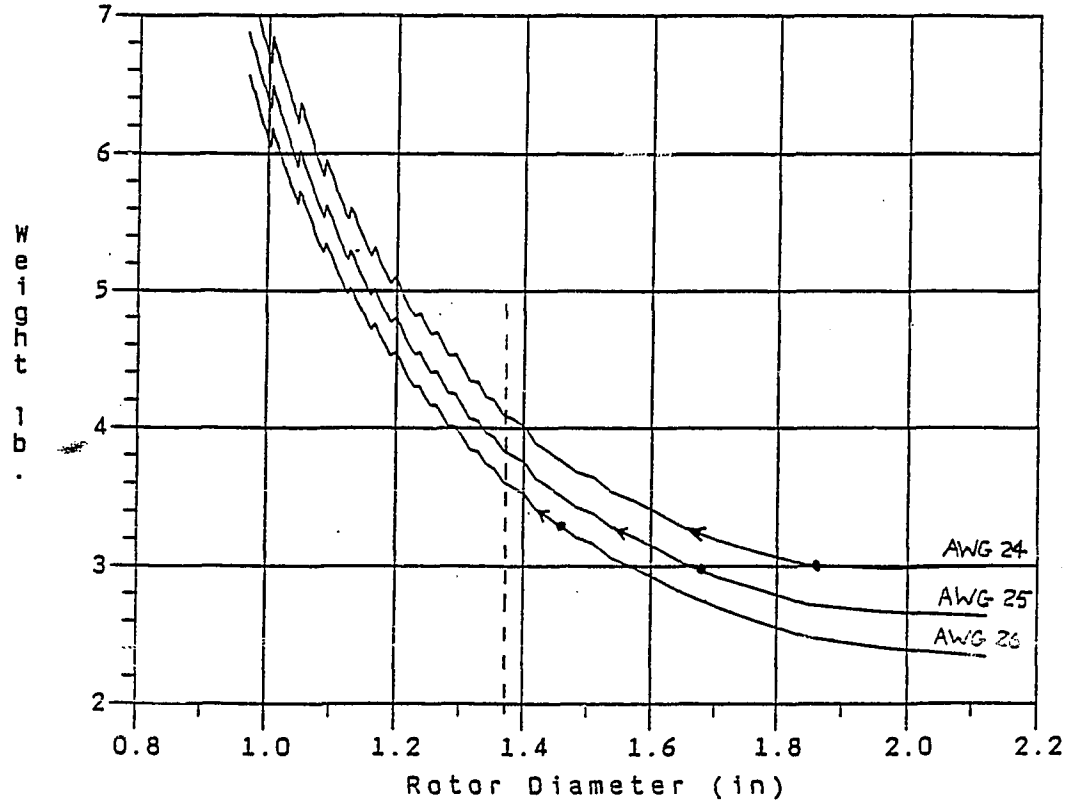

Figure VII-18
Motor Weight versus Rotor Diameter
for Wire Sizes AWG 24, 25, and 26

example, one sees an 11% increase in weight for the 36% reduction in resistance. Overall, if weight represents a penalty, then one sees that the rotor diameter should be made as large as possible. A comparison of the three design points shows a 17% difference between a design using AWG 25 and AWG 26.

One should also examine the slot opening width ratio to determine the ease of winding. Figure VII-19 shows that for all designs, the slot opening is at least 6 times the wire diameter. Since the minimum acceptable ratio is usually in the range 2~2.5, slot opening width ratio is not a concern in these comparisons.

Figure VII-20 shows a plot of estimated iron losses at 1000 rpm versus rotor diameter; the no load speed for the motor operating from a 100 volt supply would be approximately 1500 rpm. Overall, iron losses decrease with increasing rotor diameter. While this might seem counter-intuitive, one has to remember that length is simultaneously changing to maintain a constant inertia. Since inertia is a function of the diameter to the fourth power, as rotor diameter increases slightly, length decreases dramatically. This reduces the volume and weight of the stator iron, and, thus, the iron losses.

A comparison of the three design points considered, show about a 23% increase in iron losses with an AWG 26 design compared to the AWG 24 design. The losses shown here are negligible compared to the stall I^2R losses of 43.2 watts. It is possible, however, to use commutation phase advance to run the motor at speeds higher than the no load speed. The iron losses could then become significant.

Motor volume might also be considered. This is shown in Figure VII-21. The volume shown is simply calculated from the stator outer

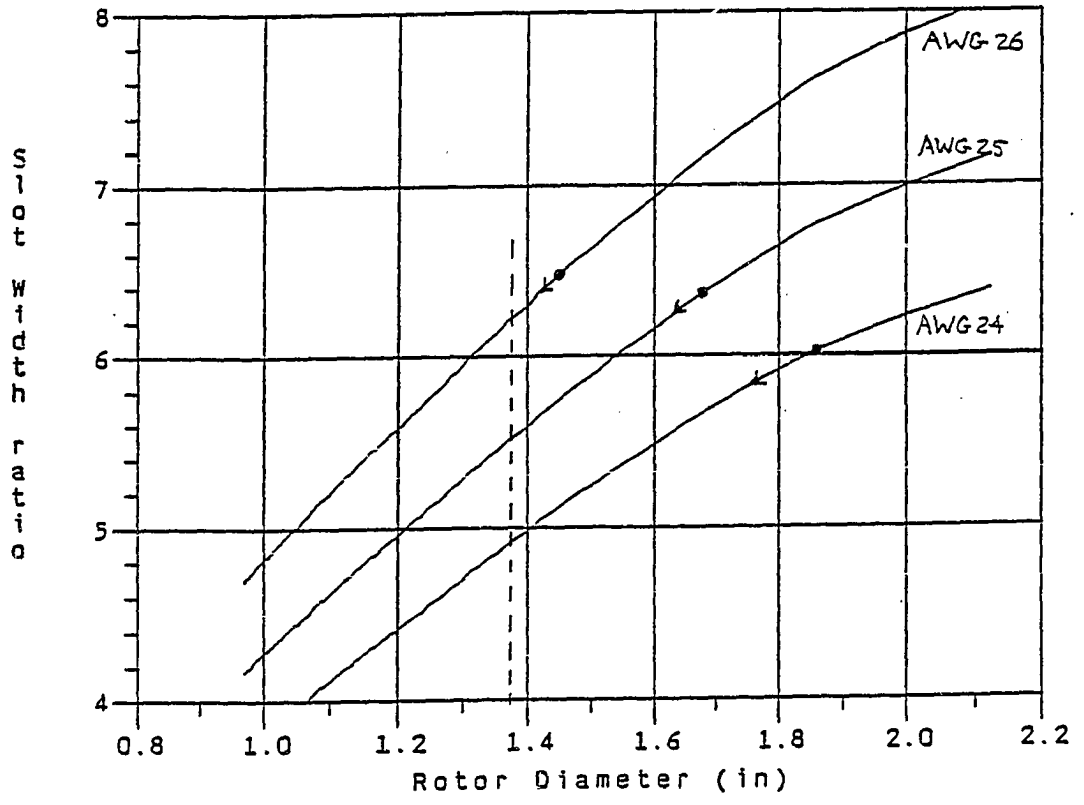

Figure VII-19
Slot Width versus Rotor Diameter
for Wire Sizes AWG 24, 25, and 26

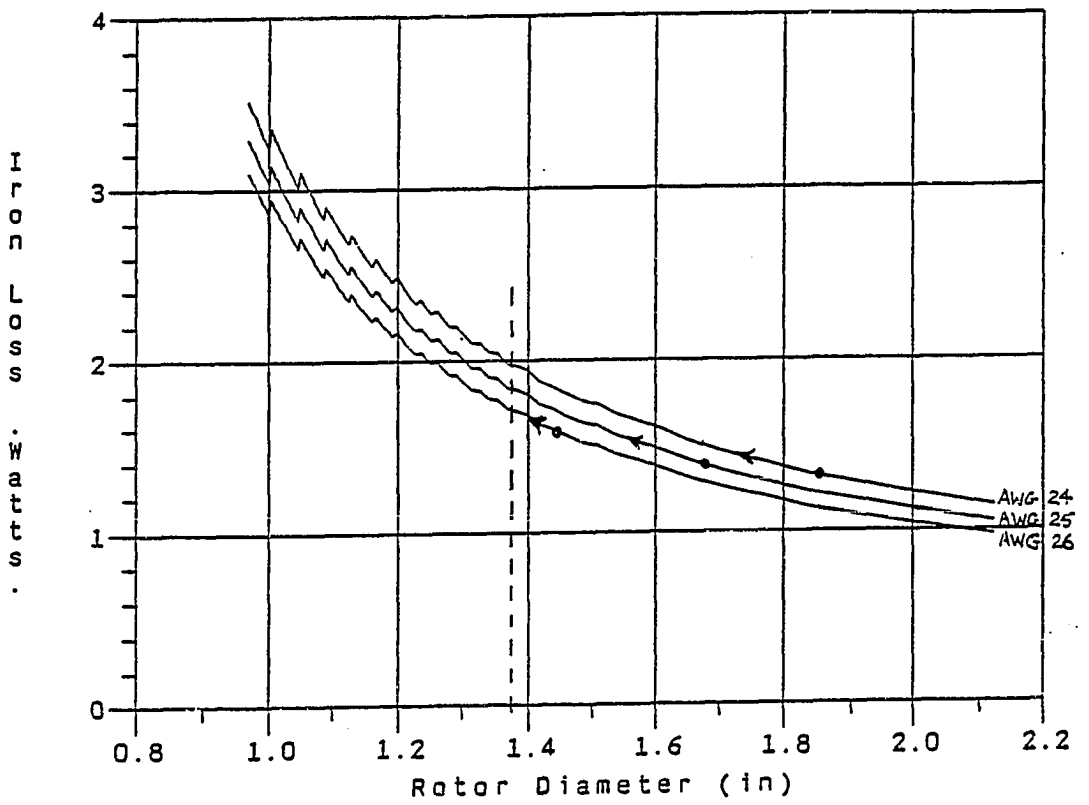

Figure VII-20
Iron Losses versus Rotor Diameter
for Wire Sizes AWG 24, 25, and 26

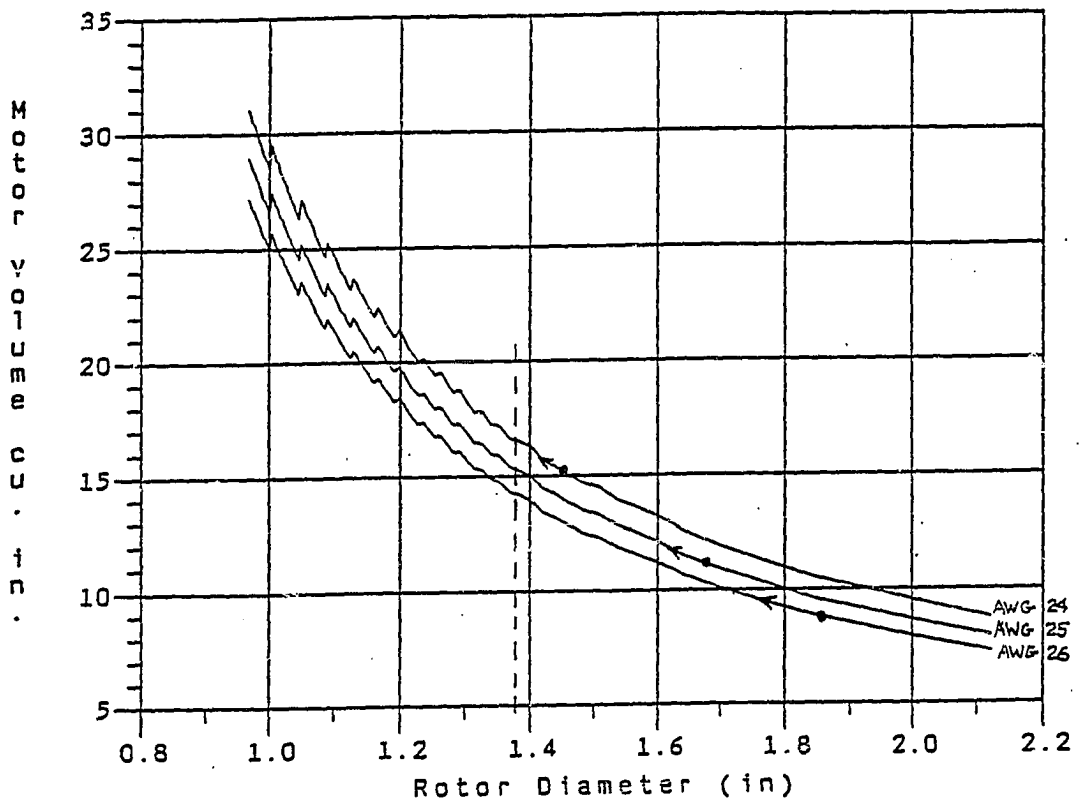

Figure VII-21
Motor Volume versus Rotor Diameter
for Wire Sizes AWG 24, 25, and 26

diameter and length; it does not include winding end turns, wire overhang, end caps, external housing or sensors.

Obviously, the previous methods of comparison allows the designer to obtain both qualitative and quantitative assements of trade-offs between parameters. Comparisons for designs of the same inertia, torque constant, and resistance are tabulated in Table VII-4.

Table VII-4

Comparison of Designs Having the Same Inertia, Torque Constant and Resistance

Parameter	AWG 24	AWG 25	AWG 26	Max/Min
Motor Outer diameter (in)	3.82	3.20	2.61	1.47
Motor Weight (lbs)	3.0	3.0	3.5	1.17
Slot Width Ratio	6.0	6.3	6.4	1.07
Iron losses at 1,000 rpm (watts)	1.33	1.39	1.64	1.23
Motor Volume (in^3)	10.54	11.26	14.07	1.33
Inductance (Henrys)	0.0096	0.0070	0.0045	2.13
Length (in)	0.92	1.40	2.65	2.88
Rotor Diameter (in)	1.85	1.66	1.42	1.30

Table VII-4 shows the parameters discussed and a ratio of maximum to minimum values for designs using the three wire sizes considered. One sees that by selecting the design using AWG 24, one obtains the design with the least volume and least weight. The penalty paid lies in an inductance which is approximately twice that of the design using AWG 26. If inductance is determined to be a critical factor, then compromises would have to be made. Inductance constraints can be determined in advance by torque-speed simulation.

VII.3b Verification of the Design Equations Using the Prototype Motor

To complete the verification of the design process against the prototype motor, a design is selected from these plots for wire size AWG 25 and the diameter of the prototype rotor, (1.665 inches). The resulting parameters predicted are then given as shown in Table VII-5. The actual parameters used in the prototype EAD motor are also shown for comparison in this table.

Table VII-5

Comparison of Predicted and Actual Parameters

Parameter	Design Predicted	Actual Motor
diameter	1.665 in.	1.665 in.
length	1.400 in.	1.40 in.
rotor back iron thickness	0.320 in.	0.3325 in.
stator back iron thickness	0.320 in.	0.250 in.
number of turns	33	34
K_t calculated	50.5 oz-in/A	50.0 oz-in/A
wiresize	25	25
rotor back iron ID	0.770 in.	0.625 in.
tooth width	0.108 in.	0.095 in.
slot inner diameter	1.740 in.	1.73 in.
slot outer diameter	2.560 in.	2.625 in.
motor outer diameter	3.200 in.	3.127 in.
phase resistance	5.33 ohms	5.40 ohms
phase inductance	0.078 H	0.010 H (no PM's)
Stator iron weight	1.63 lbs	1.35

Selecting a design with the same rotor diameter as the prototype motor allows a comparison to be made between the calculated design and the actual design. Of course, since the same design criteria were not used to design the stator backiron and tooth widths of the prototype motor, one cannot expect perfect correlation.

Rotor diameter and length, torque constant and phase resistance have all been forced to match. A comparison of the remaining

parameters yields the following:

1) The stator back iron thickness in the prototype is 23% less than the predicted. Thus, a higher degree of saturation will be present. This higher saturation means the torque constant might have been higher if the back iron was made thicker. The same is true for the stator teeth, which are 12% thinner than predicted. Both of these factors could contribute to the saturation effects observed in Chapter II, where the inductance increased by 22% with the magnets removed. It is doubtful that the torque constant would increase by 23% because a significant proportion of the inductance is due to leakage between teeth. However, one might expect to see a 5% to 10% increase in torque constant if these iron pieces were made thicker.

2) The number of turns predicted is 1 turn less, (3%), than used in the prototype motor. Thus, the same torque constant was obtained using one less turn in the motor winding.

3) The predicted motor outer diameter is 2% larger than the actual; however, this includes the thicker stator back iron discussed previously. A comparison of slot outer diameters reiterates this. The predicted slot outer diameter is less than the prototype.

4) A comparison of stator iron weights shows the design to be 24% heavier than the prototype. Again, the difference is due to the thicker back iron and teeth. This could result in 24% more iron losses, depending upon the relative flux density levels in the two stator irons. Losses are roughly a function of the square of the flux density.

5) The inductance comparison was made between the predicted and the prototype with no permanent magnets on the rotor. This is done in order to make a more fair comparison. We know that in the prototype motor, saturation effects significantly alter the inductance. The simple model used in the design does not account for this. The inductance predicted by this equation yields a lower value of inductance than the model developed earlier in Chapter 6. This is due to the fact that the inductance predicted is for the proposed design geometry, not for the actual motor geometry. Hence, the slot geometry is different, and, therefore, the cross-slot leakage inductance is also different.

Overall, one sees that the design process produces a motor design that meets the design specifications and is of comparable size and weight to the prototype motor. This proves that the models developed and used in the design process are reasonably accurate.

VII.3c An Example Design

In this section an example design is presented starting with the application requirements and ending with final selection of the design and torque-speed simulation. The design method used is slightly different than the one outlined. In this example, instead of calculating the maximum phase resistance from the allowable power losses, it is recognized that heating due to iron hysteresis and eddy current loss can be significant. Therefore, a design is selected based on the maximum total loss in the motor.

Suppose, for this example, that a given application requires a motor which produces an average stall torque of 13.5 in-lbs and will deliver 7 in-lb at 6000 rpm. It is to be operated in a wye-node-open configuration[2] using a current drive with a maximum continuous current rating of 5 amps. The supply voltage is 220 volts DC obtained from rectified 240 AC. The maximum acceleration capability required is 16,666 rad/sec^2, which yields an maximum allowable inertia of 0.000778 in-lb-sec^2. Furthermore, it has been estimated that 50 watts can be dissipated through the mounting without the motor windings exceeding the rated temperature.

This power dissipation estimate is critical to the process of selecting a design; however, future work on this design process should include thermal models from motor winding to motor case and motor case to ambient. Then, given the effective thermal resistance of the heat sink, (or apparatus/fixture), the motor is mounted to, the models can be used to determine winding temperature for various wire sizes as a function of rotor diameter and length. Designs can then be directly selected so that the winding temperatures do not exceed the limits of the wire insulation. Because this model does not include thermal models, the loss analysis presented here for illustration simply used the cold resistance values. However, a worse case winding temperature could have been assumed and used to increase the resistance by a fixed percentage, (see Equation VII-62).

The torque constant can be calculated from the stall torque and maximum phase current, as shown previously in Equation VII-4. This equation yields the two-phase-on torque constant. The one-phase-on torque constant will be $1/\sqrt{3}$ times less. The back emf constant can be

inferred from the torque constant. This leaves the following design specifications.

V_s = 220 volts

I_{max} = 5 Amps

K_t = 1.572 in-lb/amp

K_b = 0.177 V/rad/sec

J_{max} = 0.000778 in-lb-sec^2

Max Power Losses = 50 watts

Some preliminary designs were investigated assuming: a 4 pole, 24 slot motor, a magnet length to airgap length ratio of 7, a physical airgap length of 0.020 inches, M19 stator iron, and a rare earth magnet, a maximum allowable flux density in the iron of 2.0 Tesla and a winding fill factor of 0.4. The total losses are investigated first, Figure VII-22a. Total losses consist of I^2R losses and iron losses at a rotor speed to be 6000 rpm, (Figures VII-22b,c respectively). The I^2R losses are calculated assuming the average winding current remains at 5 amps, even at 6000 rpm. This is a 'worse case' scenario. The curves shown are for wire sizes AWG 10,12,14,16,18 20. These wire sizes were selected after a some preliminary trials showed these sizes to result in acceptable losses over a limited range of rotor diameters. Wire sizes less than 10 and higher than 20 would have resulted in even greater losses. However, additional sizes between 10 and 20, including half sizes, could also result in acceptable loss limits and could be explored. Although none of these designs show losses less than 50 watts, resistive losses are

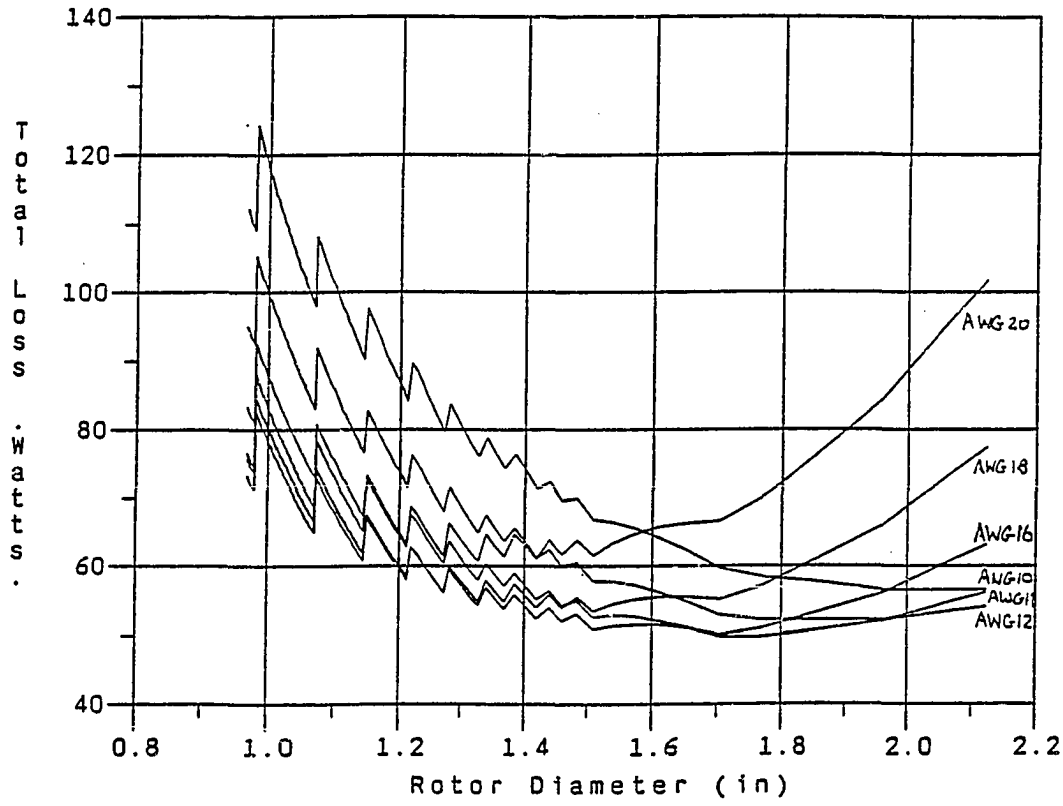

Figure VII-22a
Total Resistive and Iron Losses versus Rotor Diameter for Wire Sizes AWG 10,12,14,16,18 and 20

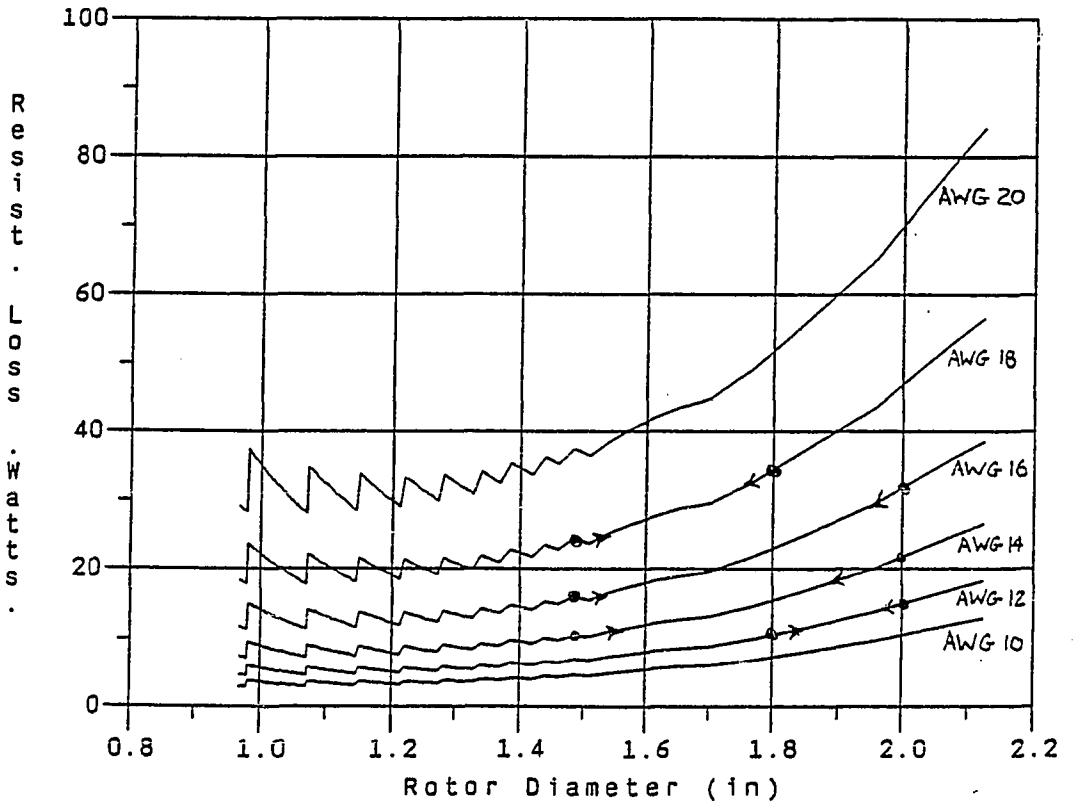

Figure VII-22b
Resistive Losses versus Rotor Diameter
for Wire Sizes AWG 10,12,14,16,18 and 20

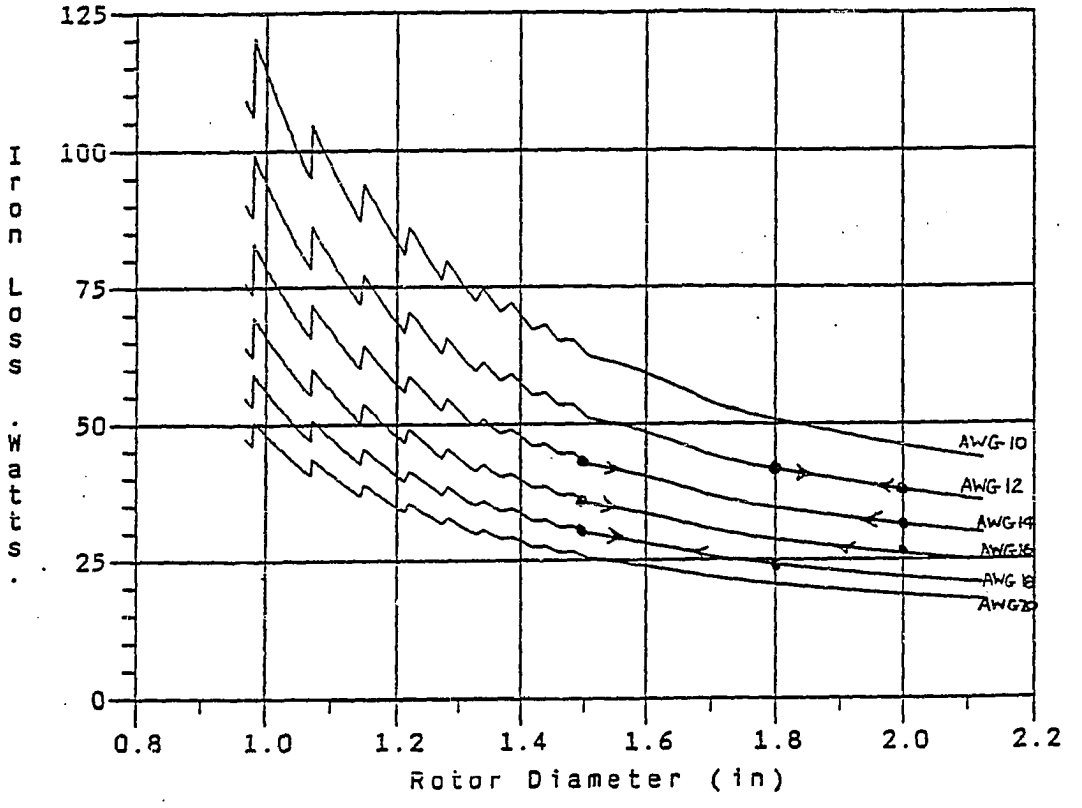

Figure VII-22c
Iron Losses versus Rotor Diameter
for Wire Sizes AWG 10,12,14,16,18 and 20

included which assume the windings carry 5 amps at 6000 rpm. If the drive is no longer current regulating, the average current could be less. Therefore, it is possible that there is some margin in these loss estimates. Hence, a more accurate estimate of the losses, including drive limitations, made later by torque-speed analysis, shows this initial estimate to be reasonably good.

Given that the minimum total losses are 50 watts and above for the four pole motor selected, the maximum allowable number of rotor poles is probably four. If a six pole motor had been selected the losses would have more than doubled because the commutation frequency would have increase by a factor of 1.5. Losses increase with the square of the frequency. A two pole motor could have been used and the iron losses would have decreased. However, initial analysis showed that a two pole motor using radially oriented full arc width magnets would have resulted in insufficient back iron thickness to meet the flux density limit: the model predicted a negative available shaft diameter. Therefore, saturation is likely to be present which could cause significant errors between the model predicted parameters and the actual motor parameters.

From the loss analysis of Figure VII-22a, one sees that losses can be minimized using wire sizes AWG 12 to 18, in the range of rotor diameters, D_r, $1.5<D_r<2.0$. If AWG 12 is used, the range should probably be narrowed to $1.8<D_r<2.0$. If AWG 18 is used, the range should probably be narrowed to $1.5<D_r<1.8$. Clearly, before a final design can be selected, further investigation of trade-offs for wire sizes and rotor diameters in the ranges outlined is necessary.

Figure VII-23 shows the phase resistance versus rotor diameter for the six wire sizes considered. In this figure, and subsequent plots to follow, the endpoints of the acceptable range, (discussed above), for each wire size is marked with a '•'. One sees that the phase resistance ranges from roughly 0.2 to 0.7 ohms. This information yields a 'ball park' value for the resistance that can be used in a torque-speed analysis.

Assuming a phase resistance of 0.45 ohms, a torque-speed curve was simulated for the potential design. The phase inductance was varied, assuming a current drive with no phase advance, until a maximum value was found that would allow the motor to reach its dynamic specification of 7 in-lbs of torque at 6000 rpm. The resulting torque-speed curve is shown in Figure VII-24. The solid line represents the torque-speed behavior. The short dash, medium dash, and long dash lines represent the average current over a commutation interval for phases 1, 2 and 3 respectively. The maximum allowable inductance was found to be 8.5 milli-Henrys. As long as the design yields a winding inductance less than 8.5 mHenrys, the dynamic specification will be met. (There will be some variation in the maximum inductance due to variations in resistance with individual designs).

Figure VII-25 shows inductance vs rotor diameter. One sees that over the range of designs under consideration the inductance is well within the 8.5 milli-Henry limit found by torque-speed simulation. In addition, a reasonable margin is present to allow for a slightly larger inductance due to end effects in the actual device.

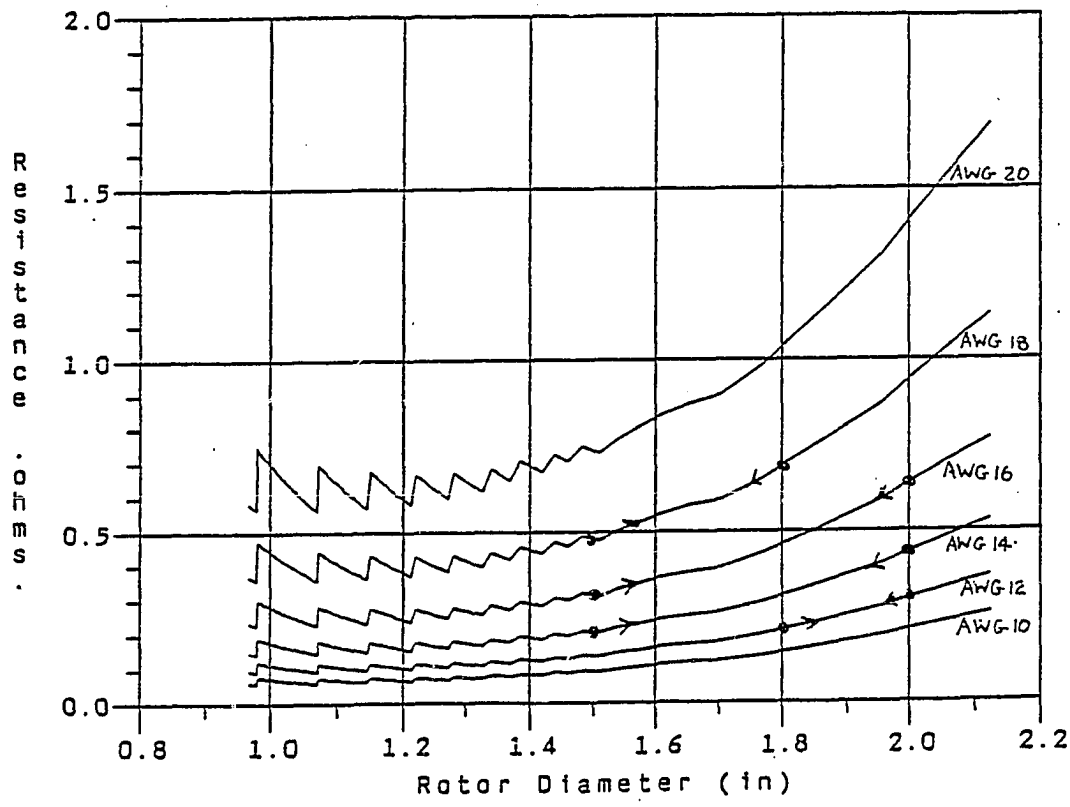

Figure VII-23
Resistance versus Rotor Diameter for
Wire Sizes AWG 10,12,14,16,18 and 20

WYE OPEN

KT	=	1.5600	KB	=	0.176000	CY	=	0.0000	TF	=	0.0000	B	=	0.000000
VS	=	220.000	R	=	0.4500	L	=	0.008500	IC	=	5.0000	CF	=	0.0000
A	=	2.0000	BD	=	0.0000	OA	=	0.0000	VD	=	500.0000	VT	=	500.0000

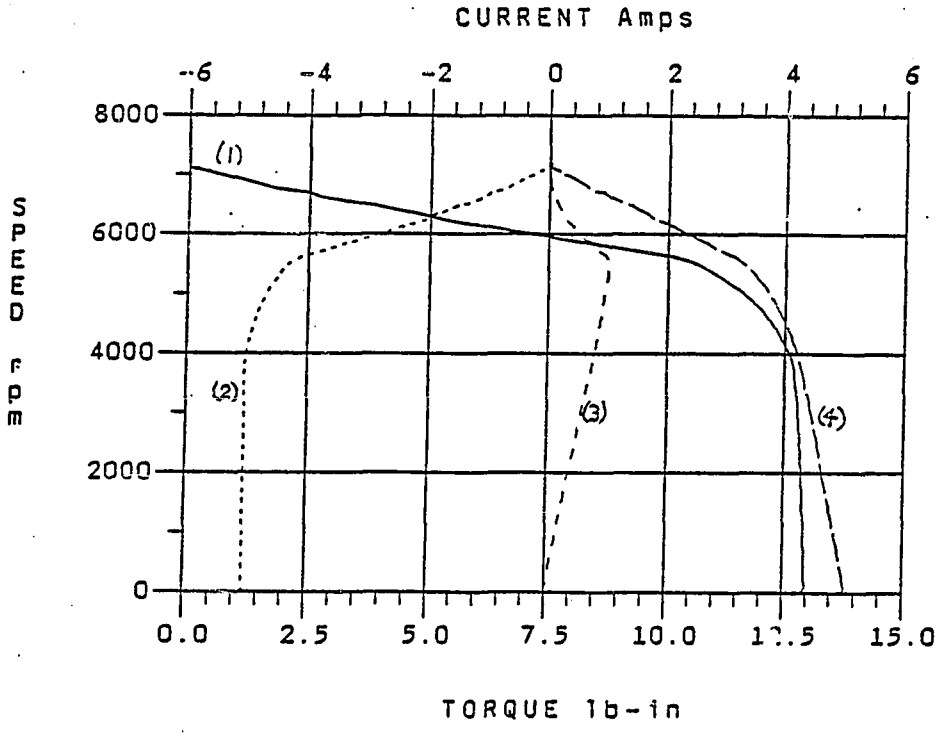

Figure VII-24
Torque-Speed Characteristic for Example Design
Assuming a Phase Inductance of 0.0085 Henrys
Curve (1)- Average Torque Over a Commutation
Curve (2)- Average Current in Phase 1 Over a Commutation
Curve (3)- Average Current in Phase 2 Over a Commutation
Curve (4)- Average Current in Phase 3 Over a Commutation

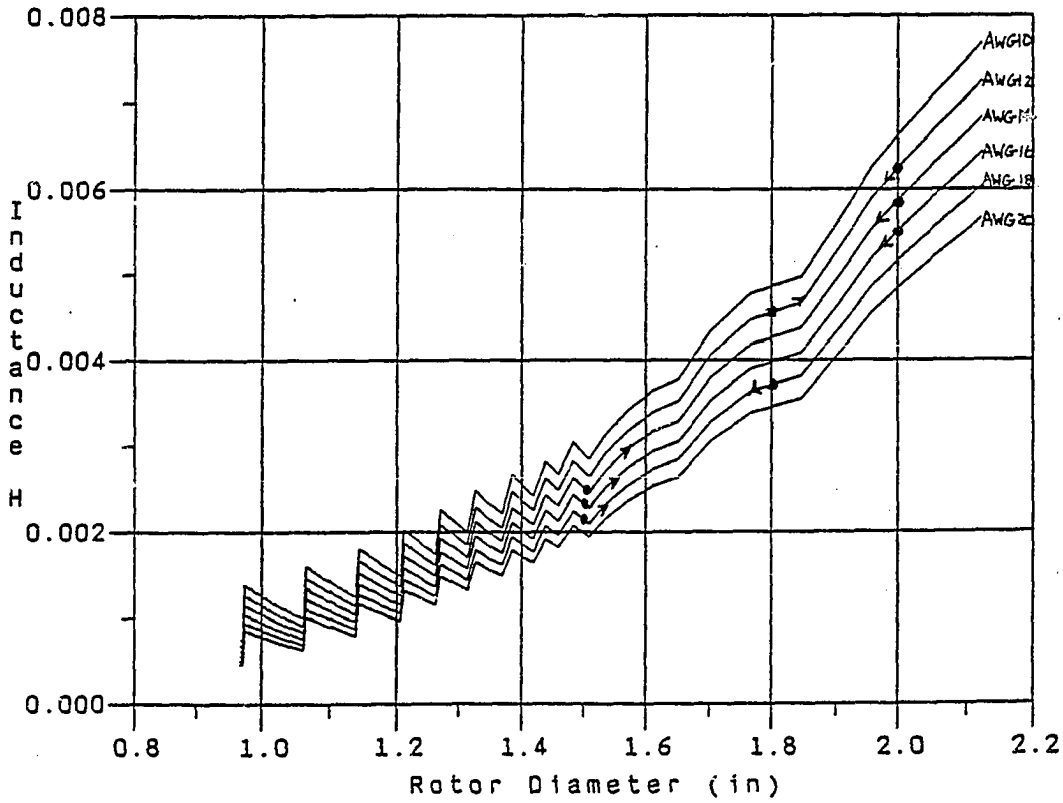

Figure VII-25
Predicted Inductance versus Rotor
Diameter for Example Design

Figure VII-26, shows shaft diameter versus rotor diameter. One sees that if a 0.5 inch diameter shaft is required the rotor diameter should be greater than 1.55 inches.

Slot width ratio is shown in Figure VII-27. The slot width ratio over the diameter range of interest varies from 1.5 to 2.9. If a ratio of 2 is used as a cutoff point, of the designs under consideration only a design using AWG 18 would be acceptable. The winding is still difficult to insert at this ratio. Ratios of 4 are more common, making the wire easier to insert and lessening the likelihood of damage to the wire insulation during insertion. A slot width ratio constraint of 4 would seem to exclude any of the designs; however, windings consisting of parallel strands of wire can be used to increase the slot width ratio and yet have the same winding resistance, torque constant, and inductance. Therefore, designs with an effective wire size of AWG 12-16 can still be considererd. The worse case would be a design using AWG 12 which has a slot width ratio of about 1.5 over the range of diameters of interest. If one decides the ratio is to be increased to 4.0 by winding parallel strands, it would require a wire diameter that is 0.375 times the diameter of the original wire. This would correspond to a wire which was 0.14 times the area of the original wire. In order to keep the resistance of the set of parallel strands, the same as the resistance of the single original wire, the total cross-sectional areas of the two must be the same. Thus, 7.11 parallel strands would be required. In order to use an integer number of identical strands, 7 parallel strands could be used with less than a 2% change in the original wire area, and thus less than a 2% change in the resistance of the phase.

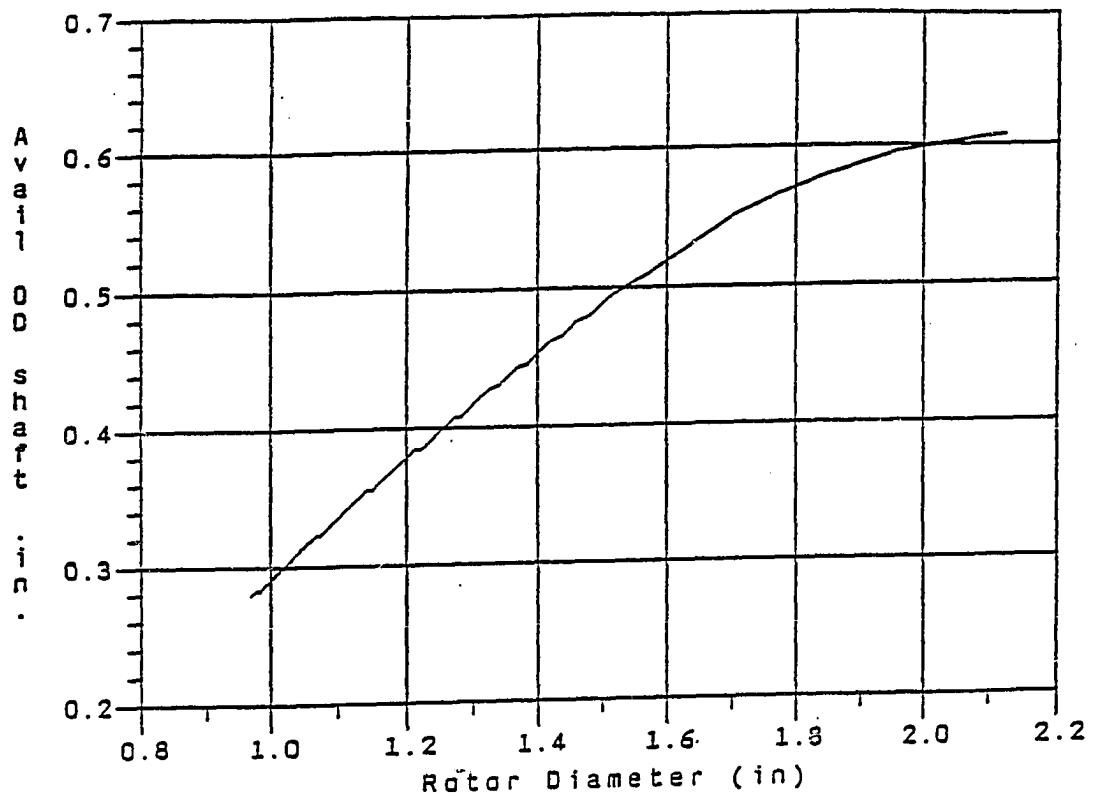

Figure VII-26
Inner Diameter of Rotor
Back Iron Available for Shaft

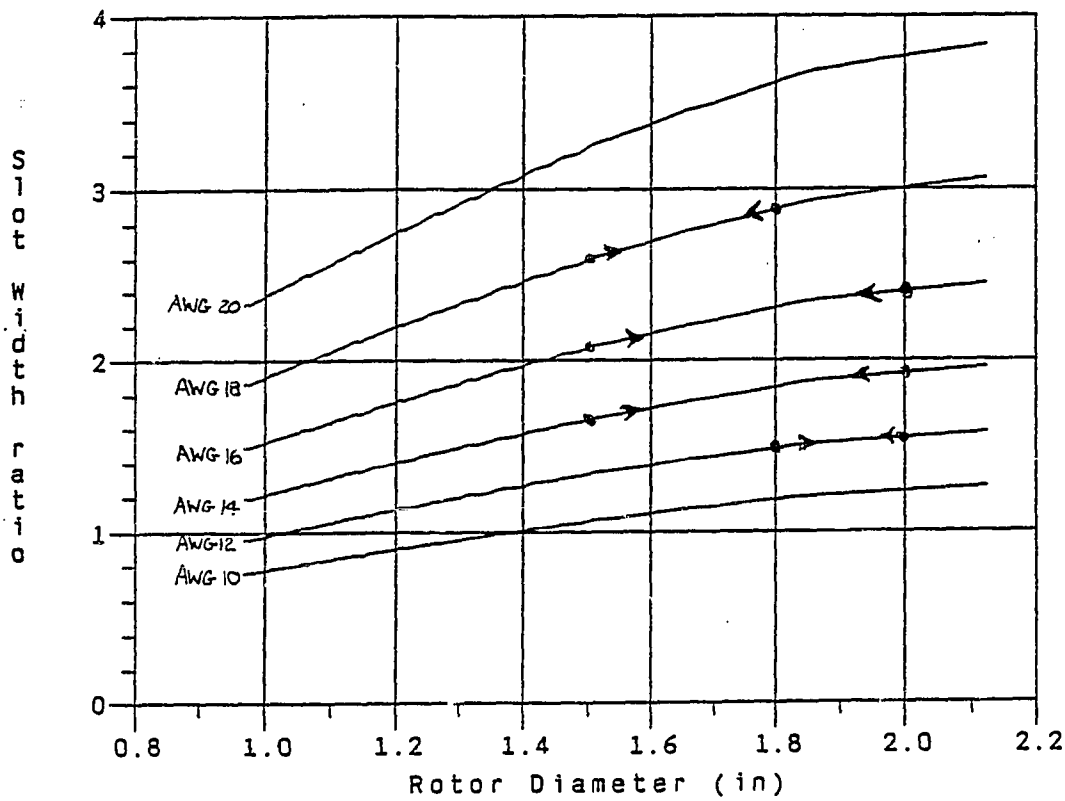

Figure VII-27
Ratio of Slot Opening Width to Wire Diameter
for Wire Sizes AWG 10,12,14,16,18 and 20

It should be noted that there is a limit on the number of parallel strands that can be used, trying to wind more than 8 parallel strands becomes difficult from a manufacturing standpoint.

An alternative to the parallel strand method would be to change the motor design to be a 4 pole, 12 slot motor. The analysis performed at the beginning of this chapter showed the number of stator teeth to have no effect on the phase resistance, inductance or torque constant. By using 12 slots, the slot width ratio would double, halving the necessary number of parallel strands for all of these cases.

Motor volume and weight are shown in Figures VII-28 and VII-29 respectively. Motor volume is minimized by using a high wire size and a large diameter motor. Motor weight is minimized by using a high wire size; design minimization within each wire size depends on the wire size.

Given the previous analysis and discussion, Table VII-6 lists some specific resistance, inductance, loss, weight and volume data for eight different combinations of wire size and rotor diameter. These designs were selected as representative of potential designs which result in total losses of 50 watts(±). Although all of the designs listed in this table were within the loss limits, the weights varied by 40%, (minimum to maximum), and the volumes varied by 33%. Given loss, weight and volume considerations, one sees from this table that a design using AWG 17 with a rotor diameter of 1.65 inches, is probably the best choice.

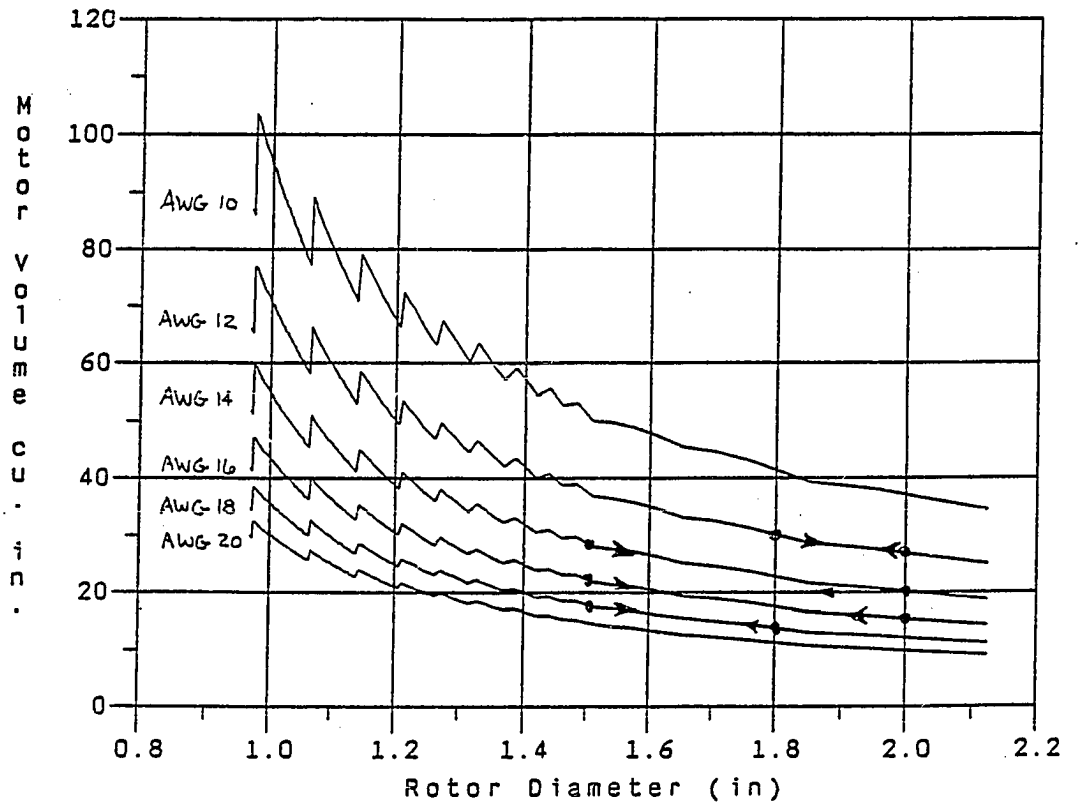

Figure VII-28
Motor Volume versus Rotor Diameter for
Wire Sizes AWG 10,12,14,16,18 and 20

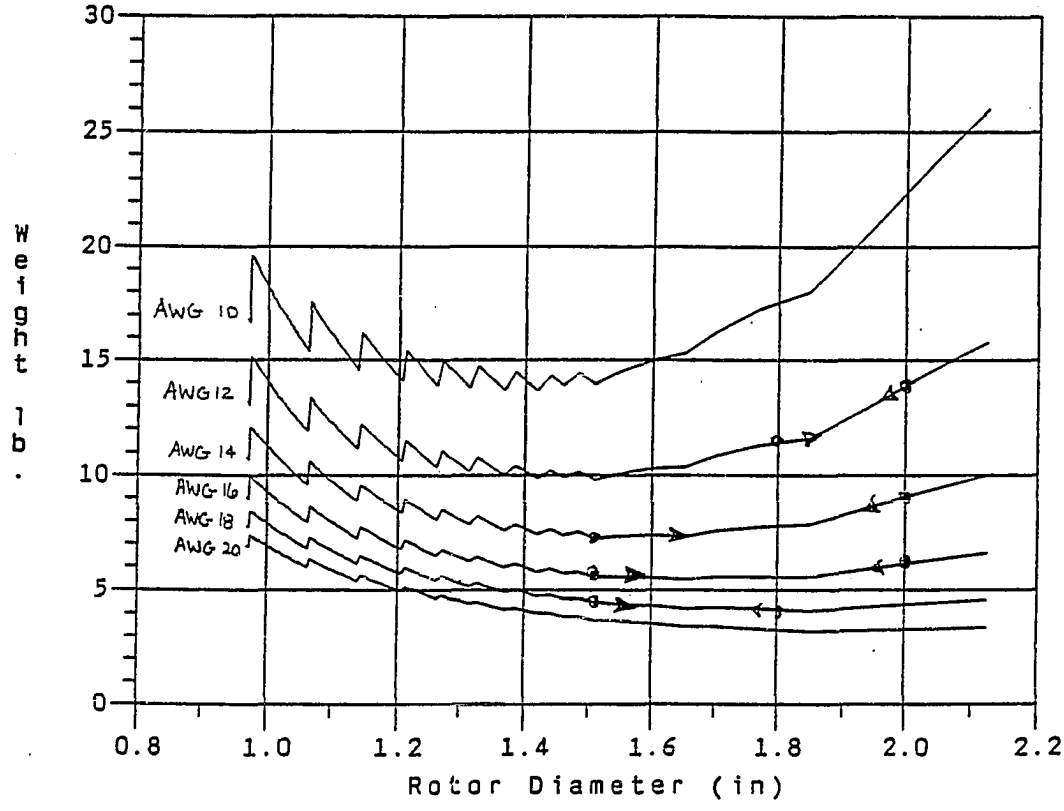

Figure VII-29
Motor Weight versus Rotor Diameter for
Wire Sizes AWG 10,12,14,16,18 and 20

Table VII-6

List of Representative Potential Designs

AWG	D_r (in.)	R (Ohms)	L (mHenrys)	Total Loss(Watts)	Total Wt.(lbs)	Volume (in^3)
14	1.6	0.23	3.2	51.3	7.4	26.6
14	1.7	0.26	3.8	50.3	7.6	24.7
14	1.8	0.30	4.4	49.6	7.8	22.7
14	2.0	0.40	5.5	50.6	8.7	19.6
16	1.6	0.35	3.0	50.2	5.6	20.5
16	1.7	0.40	3.6	50.4	5.5	18.9
16	1.8	0.45	4.1	50.9	5.6	17.4
17	1.55	0.38	2.4	49.6	4.8	18.6
17	1.65	0.44	3.0	50.5	4.8	17.2
18	1.50	0.46	2.1	52.3	4.5	17.8

A design selection using AWG 17 and a rotor diameter of 1.65 inches results in a phase resistance of 0.44 Ohms, an inductance of 0.0030 Henrys, and a stator iron weight of 2.32 lbs. Using these values, a torque-speed and loss-speed curve can be generated for the design, (Figures VII-30 and VII-31 respectively). Figure VII-30 shows that the stall torque and dynamic torque requirements have been met with no phase advance. In fact, because the inductance was lower than 8.5 mHenrys, at 6000 rpm the current drive is regulating for a large portion of the commutation interval. Thus the motor produces approximately 11 in-lb at 6000 rpm.

Figure VII-31 shows the losses for the motor as a function of speed. The solid line represents the total losses; the short dash line represents the iron losses and the long dash line represents the I^2R losses. One sees that the motor does generate 43 watts of heating loss at 6000 rpm. The heating loss are less than expected because the design model assumed that the rms I^2R losses had not fallen off at 6000 rpm from the stall values. While the drive continues to current

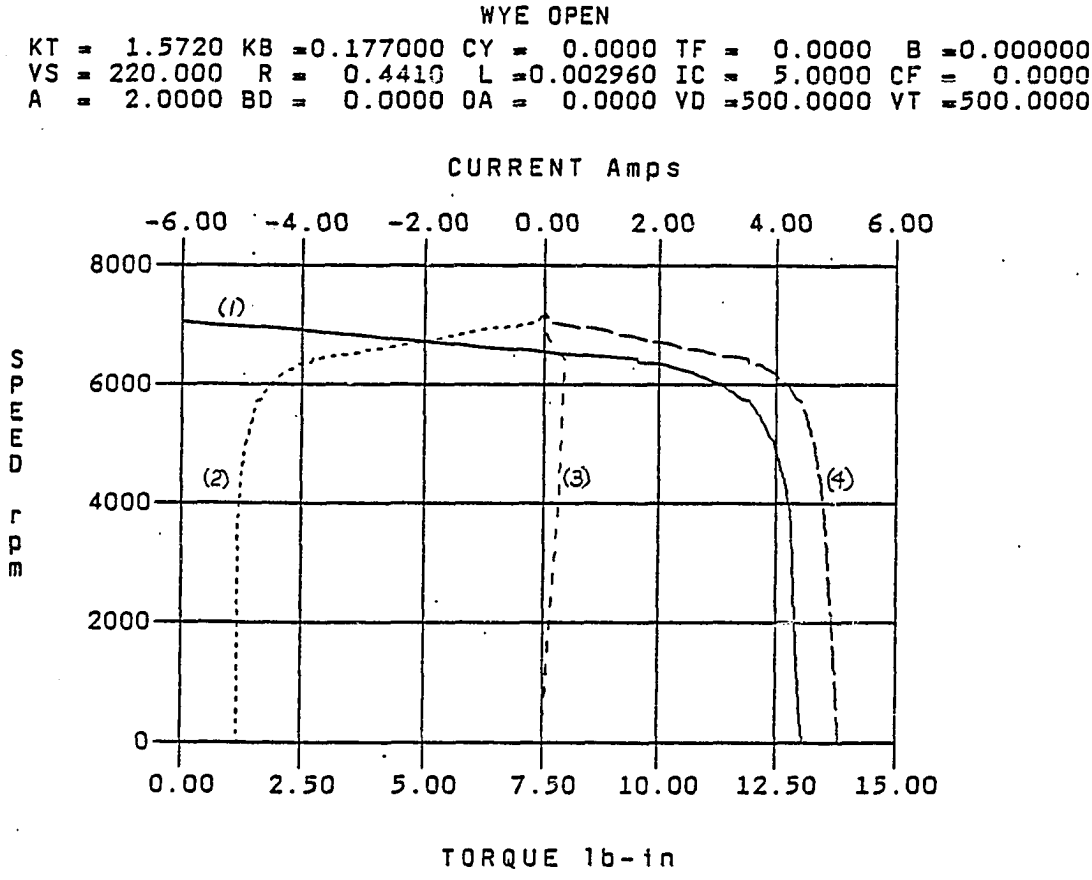

Figure VII-30
Torque-Speed Curve for Example Design
Using the Model Predicted Parameter Values
Curve (1)- Average Torque Over a Commutation
Curve (2)- Average Current in Phase 1 Over a Commutation
Curve (3)- Average Current in Phase 2 Over a Commutation
Curve (4)- Average Current in Phase 3 Over a Commutation

WYE OPEN

KT	=	1.5720	KB	=0.177000	CY	=	0.0000	TF	=	0.0000	B =0.000000
VS	=	220.000	R	= 0.4410	L	=0.002960	IC	=	5.0000	CF	= 0.0000
A	=	2.0000	BD	= 0.0000	OA	=	0.0000	VD	=500.0000	VT	=500.0000

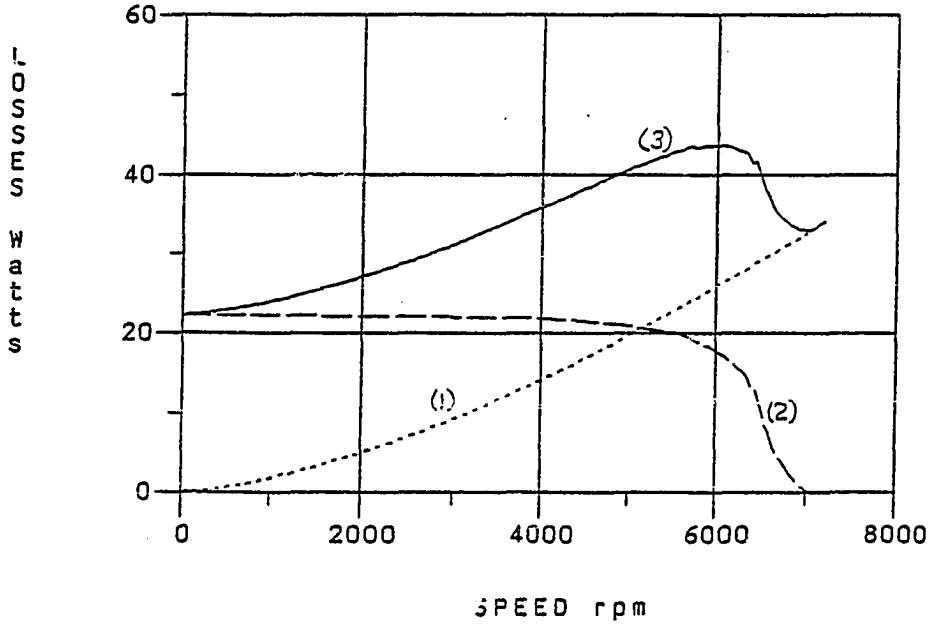

Figure VII-31
Losses as a Function of Speed for Example
Design Using the Model Predicted Parameter Values
Curve (1) - Iron Losses
Curve (2) - I R Losses
Curve (3) - Total Losses

regulate at 6000 rpm, inductive effects are not completely negligible and result in a decrease in the rms current over the commutation interval.

VII.4 Summary

This chapter showed how the back emf constant, torque constant, stall current and resistance are often specified given the no load speed, supply voltage, stall torque and maximum allowable I^2R losses. Given these motor parameters, a process was presented that allowed the designer to develop a motor design to meet those specifications. The method presented represents a reasonable approach to specifying a set of motor parameters that will meet the application requirements. However, this is not the only approach that could be made.

If commutation phase advance is to be used, the motor can be run at speeds much higher that the no load speed. However, the process of identifying allowable back emf and torque constants is less clear. One possible method would be trial and error torque-speed simulation. Given an idea of the maximum supply voltage available and at least one torque-speed point that must be met, one could check the torque-speed curve to see if it meets the requirements. If it does not, then parameters could be modified by visual feedback obtained from the torque-speed simulation, until the requirements are met. Those parameters then serve as the design specifications for the motor.

This chapter also outlined the effects of the number of rotor poles and the number of stator teeth for a motor, assuming the stator iron and copper volumes did not change. It was demonstrated that torque constant, back emf constant and resistance are independent of

the number of poles and teeth. But, inductance decreases with the square of the number of poles. Since the inductance limits the speed at which the motor phases can be commutated, this implies that a motor with a higher pole count can run faster. Of course, in order for a higher pole count to run at the same speed as a lower pole count motor the commutation frequency must be proportionally higher. However, the combination of the two effects, higher commutation frequency and lower inductance, still results in the current rise time being a proportionally smaller percentage of the commutation time for the higher pole count motor. This is counter-intuitive. Commonly, one thinks of a lower pole count motor as being able to run faster bacause the eddy current losses are less. However, this really relates to the thermal aspects of the design. As long as the motor can safely dissipate the higher losses, a higher pole count is desirable for high speed operation.

An extensive set of equations was developed to describe many different motor parameters. This development resulted in a set of 28 equations with 58 unknowns. Therefore, 30 unknowns had to be selected in advance. It was shown that the range of choices on 25 of these unknowns was somewhat restricted. Often, many of the unknowns were constrained to one another through material properties. For example, by choosing a particular type of magnet material the residual flux density, relative permeability and reversible temperature coefficient are fixed. The presented discussion outlined how rational choices could be made for these 25 unknowns, and how one could anticipate some of the effects of alternative choices for these parameters. For example, it was shown how torque constant varied as a function of the

ratio of magnet length to physical airgap length.

Assuming the pre-selection of the 25 unknowns listed, there remained 5 additional variables to be specified. The design method presented assumed that these would be inertia, torque constant, resistance, maximum phase current, and either length or diameter. Really, however, only inertia, torque constant and maximum phase current were necessary to begin the solution process and determine possible motor geometries. After these parameters are specified, most any other two parameters, such as volume and weight, or total losses and weight can be used to zero in on a design.

The design process was verified against the prototype motor used in this investigation, by predicting a design for a motor with the same rotor dimensions, material properties, wire size and tooth/pole counts. The process resulted in a design with the same torque constant, resistance, and inductance, a 3% larger outer diameter and a 6% larger volume.

A second example design was also presented that used the total losses as a constraint. It was shown that while iron losses decrease with increasing rotor diameter, resistive losses increase. Thus, there existed a range of rotor diameters where total losses were minimized. If heat dissipation is a concern, then the design should take advantage of this mimimum.

It was also shown how torque-speed simulation could be used to determine additional constraints such as the maximum inductance that would still allow the motor to meet its torque-speed requirements. It should be emphasized becaused BLDCM's can have very nonlinear torque-speed curves, torque-speed simulation is a very important part of any

BLDCM design. Torque-speed simulation is an important tool. Not only because it is essential to identify torque-speed shape, but also as an aid to identifying additional parameter constraints required in order for the motor to meet torque-speed requirements.

CHAPTER VIII
CONCLUSIONS AND FUTURE WORK

Review of Chapters

Chapter II was concerned with the experimental determination of characteristic parameters for the prototype motor. While the primary purpose of the chapter was to determine parameters for later comparison against finite element results, some interesting characteristics were identified that can be considered typical of motors having rare earth magnets. It was shown that the detent torque was extremely large compared to the peak one-phase-on stator torque of the motor. The inherently high detent torque probably represents one of the foremost problems in using rare earth magnet materials in brushless DC motors. In order for the motor to be useful and produce smooth low speed torque the detent torque will have to be reduced by either skewing or proper design of the magnet geometry.

Chapter II also showed the torque-current relation for the prototype motor to be very linear. One might be inclined to use this as a basis to argue that there is no magnetic saturation in the device. However, we know from the flux linkage evaluation that this is not true. The absence of the permanent magnet resulted in a 60% increase in the slope. This would seem to indicate a high degree of saturation. One might think that the 60% change in slope of the flux-linkage curve means that the torque constant could be increased 60% by eliminating saturation. However, analysis performed in this thesis has shown that inductance, and hence the flux-linkage current

characteristic, has significant components due to end effects and cross-slot, cross-tooth tip flux leakage. Local saturation of the tooth tips by the presence of the permanent magnet could significantly decrease the cross-tooth tip leakage contributions. The saturated tooth tips would have little effect on the torque constant because the increase in effective airgap would be small. Hence, the decrease in flux in the airgap would be small, as would the decrease in coil flux density in the region of the magnet. We know from insights developed from the IxB method, that if the radial component of coil flux density in the region of the magnet is not significantly affected, then neither is the torque.

Finite element analysis showed parts of the motor to be at 2.0 Tesla. Even though this is considerably higher than the 1.3 Tesla which is commonly used as an indicator of saturation, the torque-current characteristic was linear and showed none of the curvature usually associated with saturation. The flux linkage-current curves were also linear. One reason saturation is not reflected in these curves is that the coil mmf is small compared to the magnet mmf, (less than 6% for the prototype motor). The magnet mmf provides a large DC bias in the material B-H curve so that the flux linkage versus current curve then gives an idea of the average permeability of the material as it deviates from the operating point established by the magnet.

In general, one can see that BLDCM's having rare earth magnets may have linear torque-current curves despite the presence of high levels of flux density within the iron portions of the device. The rare earth magnet effectively 'presaturates' the iron; the coil mmf produces a small change in flux density compared to that produced by

the magnet mmf. Thus, the linear nature of the torque-current curve may simply indicate the linearized behavior of the torque-current characteristic around the operating point established by the magnet.

In Chapter III, methods of predicting different motor parameters were presented. Probably the most important of these was the IxB method of determining torque from the radial component of flux density in the airgap and the magnet equivalent currents. Torque calculated by this method was shown to compare well with the data obtained from coenergy method. However, when used to predict the detent torque-angle curve, the IxB method was shown to produce a small DC level in the curve. It was felt that this DC level was due to small errors caused by triangulation and the approximation of constant flux density over the element. Small errors in the solution can be magnified in using this method to predict the detent torque because the net detent torque is the sum of large opposing component torques calculated from the flux density and current density in several individual elements. This is the classical problem of determining a parameter by subtracting two large numbers of approximately the same value. The coenergy method, on the other hand is more of an averaging method, using the coenergy calculated from all of the elements.

Despite the small errors in predicting detent torque (the DC level that appeared) the IxB method is useful in finite element analysis because it allows for relatively accurate prediction of the energized torque from a single FEA solution. This facilitates the generation of torque-current curves. Although, application of the IxB method is restricted to devices which have no variable reluctance effects. However, the largest advantage by far of the IxB method lies in

predicting energized stator torque-angle curves by assuming superposition and directly crossing the magnet equivalent currents with the distribution of coil radial component of flux density in the magnet region, (as discussed in Chapter V). Not only are many finite element simulations avoided by using this method, but, this tool also allows one to visualize the effects of magnet arc shape and the coil flux density distribution on the resulting stator torque-angle curve. Thus, allowing the motor designer to quickly gain insight into the consequences of magnet shape and winding distribution selection. Unfortunately, the superposition IxB method is, of course, limited to cases where magnetic saturation does not significantly affect the torque.

The purpose of Chapter III was two-fold; one was to show the different methods of predicting motor parameters. This was because questions pertaining to motor design are not answered by finding the field solution. Certainly, a plot of the field solution provides the motor designer with a clear picture of the flux paths - intended and otherwise - within the device. In addition, it can be used to provide a picture of the distribution of a number of field parameters: flux density, field intensity or energy-coenergy, for example. However, motors are not designed or built to be flux producers; they are designed to be torque producers. One is almost always primarily interested in determining the parameters which affect the performance of the device: typically, the detent torque, torque constant, torque-angle waveform, back emf characteristic, and inductance. This chapter described at least one method of determining each of these from finite element results.

The other purpose of this chapter was to evaluate the two-dimensional, nonlinear, finite element model as a means of determining the parameters listed previously. While this is not the first time such an evaluation has been performed, the evaluation presented here was very detailed and thorough. In addition, such an evalution was necessary if the two-dimensional finite element model was to be used as a substitute for prototyping motors in the verification of design theory.

Overall, the finite element analysis performed in Chapter III showed two-dimensional finite element analysis to be reasonably accurate in predicting motor parameters with the exception of predicting detent torque and flux linkage/inductance. A number of investigations were performed to determine reasons for the discrepancies observed between measured and predicted values for these parameters. The results of these investigations were presented in Chapter IV.

It was found that end effects appear to be the principal cause of discrepancy in predicting inductance. End turns result in a significant contribution of flux to the coil, much of which does not link the airgap. Since much of it does not link the airgap and permanent magnet, this end flux has larger effects on the inductance than it does on the torque constant.

An extensive investigation into the detent torque was also performed in Chapter IV. It was shown that detent torque was extremely sensitive to the location of the permanent magnet equivalent currents. It was shown that an 11% change in magnet arc width resulted in almost a 50% change in the magnitude of the detent torque. While this change was specific to the particular motor geometry

tested, i.e. the specific tooth widths and magnet geometry, the geometry was certainly typical of common motor designs -the lamination used was selected from a lamination catalogue. This has several important implications. The first is that accurate prediction of the detent torque by the finite element analysis is difficult. Accurate prediction will require a reasonably fine mesh in order to model the magnet geometry, i.e. edge current placement, accurately. Since detent torque is very sensitive to edge current placement, and detent torque is primarily generated while the magnet interfaces (edge currents) are over a slot, the tooth and slot geometry will also have to be modeled accurately. One will also have to be careful to model the 'magnetic' dimensions accurately, as opposed to just modelling the physical geometry of the magnet.

Another consequence of the detent torque sensitivity lies in trying to design motors having low detent torque. If designs are developed based on precise control of the magnet geometry, extreme care must be taken to ensure the magnet manufacturer can magnetize the magnet as required and, that the magnet segments can be positioned accurately on the rotor.

Another implication of the results of the detent torque investigation is that if one has difficulty in predicting detent torque by finite element means, because of the sensitivity problem, then, certainly, predicting detent torque by a lumped parameter model would probably be even more difficult. After all, the first order finite element model is nothing more than a very complicated two-dimensional lumped element model.

To summarize the detent torque investigation, it was concluded that the magnetic geometry of the magnet was different than the physical geometry. In order to accurately predict detent, it is more important to model the magnetic geometry. How one determines the magnetic geometry is unclear; except, perhaps, through working with the magnet manufacturer to determine tolerances in the homogeneaity of the magnetic material resulting from different sintering and cooling processes, and, the uniformity of magnetization from the magnetizing process.

Another point brought to light by the investigations presented in Chapter IV was that the magnet segments did not appear to be truly radially oriented. Therefore, a method was developed to identify a magnet model. That method consisted of making measurements of the airgap flux density distribution produced by placing the magnet in a known uniform airgap. Then, finite element predicted data was made to match measured data by trial and error placement of magnet edge and interior current distributions. Making finite element predicted and measured annulus radial component of flux density data match gave a good approximation for the magnet model. Good correlation was obtained between finite element predicted and measured flux density distributions when the magnets were placed in a different, larger airgap. However, when that same model was used to predict the torque constant, back emf constant, torque-angle and back emf waveforms, the finite element results were 10%-15% low. These numbers were consistent in both the first and second prototype rotors investigated. It was concluded that end effects can vary as a function of the airgap. When the rotor is placed in the relatively small airgap of

the motor, magnet end effects are increased over what was accounted for in the development of the magnet model. This, combined with a certain amount of coil end effects, tend to make the measured torque constant higher than that predicted by the finite element model.

This data, taken into consideration with the analysis of a rectangular loop of wire in air and two infinitely long wires in air leads one to expect errors in using the two-dimensional finite element analysis to model coils and magnets with length to width ratios less than 10:1. However, practical experience has shown that the two-dimensional analysis can be used to accurately predict trends. If, for example, the two-dimensional finite element analysis predicts a 10% increase in torque constant by making the back iron 20% thicker to relieve saturation, experimental evidence bears it out. Thus, even though absolute values may be in error for motors with low length to widths, trends can be accurately predicted without the need for three-dimensional finite element analysis.

In Chapter V methods of reducing detent torque in brushless DC motors were presented. The methods presented were: skewing, staggering, altering the magnet arc width, and creating unequal arc width magnets.

Skewing is a technique commonly used by many motor manufacturers. Peak stator torque will be reduced by an amount dependent upon the skew angle. While all of the methods presented depend upon component detent torque cancellation in one way or another, skewing is probably the least sensitive to magnet positioning and magnetization because of the large number of phase shifted components it utilizes to achieve cancelation. Skewed magnets effectively use an infinite number of

phase shifted component detent torque-angle curves. Skewing typically suffers from end effect problems. The laminations at the ends of the motor have slightly different detent torque-angle characteristics. Thus, complete component detent is not achieved, resulting in some residual detent. It is often necessary to skew over an angle slightly different than one tooth pitch to optimize the detent torque reduction.

Unless there is a high ratio of teeth to poles the motor must be skewed over a relatively large angle, making the winding difficult to insert. Typically there is not a high number of teeth per pole. Therefore, the motor is skewed over an angle which represents a significant portion of the torque-angle curve. Therefore, skewing tends to eliminate most higher harmonics making the torque-angle curve very sinusoidal. This is an advantage if a sinusoidal torque-angle curve is desired. For example, if one is using a three phase sine wave current excitation to drive the motor and require sinusoidal torque-angle curves to produce smooth low speed torque. However, usually the phases are driven by applying constant voltages to the phases and one relies on flat-topped torque-angle curves to produce smooth low speed torque. Obviously in the latter case, the sinusoidal torque-angle curves produced by skewing are a disadvantage.

The manner in which staggered magnet segments reduces detent torque was shown to be very similar to skewing, except the quantization of phase shift between component detent torque-angle curves was not as fine. However, a large number of higher harmonics are eliminated. Staggering also results in a reduction of the peak torque. Similar to skewing, the reduction depends upon the amount of

stagger. More complete elimination of detent torque is achieved by using a large number of staggered segments. Therefore, this method would be best for longer motors because there is usually a limit to the allowable thinness of the magnet material because of its brittleness.

Altering magnet arc width seems to be best suited as a means of shaping the detent torque-angle curve. This method probably will only result in a partial elimination of detent. Complete elimination, as in the skewing and staggering schemes, is not assured, at least not with radial arc segments. However, it is possible that the magnets may be shaped differently to provide a reasonably low detent torque motor.

Probably it is best to combine altering magnet arc width with staggered magnet segments. The magnet arc width should be selected to produce as sinusoidal a detent torque-angle curve as possible. Then, staggering can be used to achieve phase shifted component detent torques. Obviously, if a purely sinusoidal component detent torque is achieved, it would only be necessary to stagger two segments by one half a tooth pitch to eliminate detent.

It was also shown that staggering does not eliminate or reduce harmonics that are integer multiples of the number of staggered segments. Therefore, it is advisable to use several staggered segments. Then, at least, the harmonic that is passed through will be of a higher frequency and, because of mechanical filtering effects, have less of an effect on low speed torque ripple.

Overall, one sees that there are advantages and disadvantages to the different reduction schemes. I think that a combination of proper

selection of magnet arc width and staggered arc segments is one of the best ways of reducing detent. Problems relating to consistency of magnet magnetization and magnet positioning can probably be more easily overcome than the end effect problems encountered in skewing.

Chapter V presented a superposition method of crossing magnet edge currents with finite element predicted distribution of radial component of coil flux density. Since this method does rely on superposition, saturation effects are not included. As was shown in this chapter, saturation can significantly affect the torque ripple predicted. However, the usefulness of this method lies not so much in its use to precisely predict the torque-angle waveform but as a tool to obtain global insight into the relationship between coil windings and magnet shape on the resulting torque-angle curve. In the past, this relationship has been little understood. It was commonly felt that small changes in magnet geometry or slot width could result in large changes in torque. The work presented in this thesis has helped to illuminate this relationship. We now know that small changes in geometry can result in large detent torque changes but do not have much affect on the energized torque. The IxB method has also helped to provide an understanding of how to achieve either a more sinusoidal or more flat topped torque-angle curve. If a sinusoidal torque-angle curve is desired, distribute the winding and distribute the magnet edges so that higher harmonics are averaged out. Neither of these should be done if one desires a more flat-topped curve. Motors with lower numbers of teeth per pole will have more flat-topped torque-angle curves because the windings are distributed.

The final topic presented in Chapter V was the use of the back emf waveform as a substitute for finding the energized stator torque-angle waveform. This method complements the IxB method because the IxB method assumes the windings are unchanged and allows one to vary magnet width. The back emf method assumes the magnet is unchanged and allows one to vary the winding distribution. While this method does not give as good a mental picture of the relationship as the IxB method, it does include more saturation effects because, in a rare earth magnet motor, the saturation is more likely to be caused by the presence of the permanent magnet as opposed to the coil.

In Chapter VI one-dimensional lumped parameter magnetic models for the brushless DC motor were explored. The primary goal of this chapter was to identify the simplest model that would predict torque and other performance parameters within the accuracy limits required. These models had to be simple enough to provide closed form solutions for design synthesis. More complicated models that provide higher degrees of accuracy but were not tractable were not desired because the finite element method is a good analysis tool. A second analysis tool was not necessary.

The basic theory of lumped parameter magnetic models was developed first in this chapter to identify any fundamental assumptions that could be inadvertently violated during the development of a lumped model. It was shown that in order for the lumped elements to predict the flux in any region, the elements selected must be flux 'tubes' in which a constant amount of flux flows.

This chapter showed that a simple lumped model including only the mmf drops acoss the airgaps can be used to predict the radial

component of coil flux density. Thus, this simple model can be combined with the IxB method described in Chapter V to predict the stator torque-angle waveform. Obviously, if the stator torque-angle waveform can be predicted, then the peak torque can also be predicted and used to predict the torque constant.

While the relatively simple model was accurate in predicting the radial component of coil flux density, it was over 30% in error in predicting inductance. In order to predict an inductance value within 10% of the finite element results, cross-slot leakage paths had to be included. This produced an inductance value which was 7.7% higher than the finite elment predicted value. However, this value was still 16% less than the measured results. This is not surprising considering the investigations into finite element prediction of inductance made previously in Chapter IV. We know that leakage paths significantly affect the inductance, and, some of those leakage paths are due to end effects. In order to predict inductance accurately, lumped parameter models would require paths for end turn leakage; I feel this model would be complicated because of the three-dimensional nature of the end turn leakage. Once again, this is contrary to the basic goal of developing a simple model to be used for design synthesis.

A simple model was developed to predict the radial component of flux density due to the permanent magnet. It was shown that where the basic rules of lumped parameter models were not violated, the results matched well with finite element results. When average mmfs were used, the total flux through the element correlated well with finite element results, even though the distribution of radial component of

flux density did not. This would indicate that this simple model could be used with the back emf method to predict the back emf and stator torque-angle waveforms.

Finally, the use of a lumped element model to predict detent torque was investigated. It was shown that any model which uses an averaging technique to represent the mmf of the magnet, while the magnet interface is over the element, will produce erroneous detent torque values because it uses an incorrect expression for the coenergy. When the model was corrected so that the coenergy was calculated properly, it predicted zero detent torque while the magnet interface was over the tooth. This agrees closely with finite element results which showed little detent torque produced while the magnet interface is over a tooth face. An attempt was made to include lumped elements for the slot and calculate detent but this also showed no detent torque to be generated. This is in direct contradiction to finite element results which predict most of the detent to be generate in this region. It is my conclusion that detent torque is primarily a consequence of leakage flux from the magnet to the slot sides and tooth tips. Therefore, in order for the lumped model to predict the detent torque, the model would have to include leakage paths which change length and direction as a function of magnet position. Besides being impractical, from a design standpoint this is not really possible since one does not know the tooth geometry a priori; the tooth geometry is one of the parameters to be determined. Also, in terms of the global picture, if one is designing a higher performance motor, knowing the detent torque is not critical since one of the

schemes outlined in Chapter IV will probably be used to eliminate detent.

The simplest models developed in Chapter VI were used as a basis for the development of a motor design method and presented in Chapter VII. The method presented assumed that at least the torque constant, inertia, resistance and stall current for the motor had been specified. First, an explanation of how those parameters are typically determined from the supply voltage, no-load speed, and maximum power dissipation capabilites of the application was given. The design method presented actually only requires the torque constant, maximum phase current and inertia to be specified in advance. A variety of different designs can then be explored and trade-offs considered. The final design selected can then be based on the results of those comparisons. The final selection may be one which produces minimum I^2R losses, or minimum weight, minimum volume, or an acceptable combination of several different parameters.

A preliminary investigation of the number of stator teeth and rotor poles was also performed. It was shown that if one simply changes the number of teeth and poles, keeping all radii, (slot inner radius, slot outer radius, magnet outer radius, etc.) constant, then the number of teeth selected has no effect on the torque constant, the inductance or the resistance of the device. While the number of poles also has no effect on the torque constant or resistance, the inductance appears to decrease by the inverse of the square of the number of poles. This implies that a higher pole count motor can be run faster because the electrical time constant has decreased by the inverse of the square of the poles, while the commutation rate has

only increased proportionally. However, there is an additional penalty paid. The heating due to iron losses theoretically increases by the square of the excitation frequency.

Given that a basic understanding of the consequences of pole count and slot count selection was developed, the design method outlined assumed that the designer had pre-selected the number of poles and slots. Equations relating performance parameters and motor geometry were then developed; 28 equations with 58 unknowns were formulated. Arguments were presented for the pre-selection of 25 of these unknowns based on material constraints and physical limitations of choices. For example, choice of a magnet technology limits the residual flux density; sintered rare earth magnets have B_r values ranging from 1.0 - 1.2 Tesla, and relative permeabilities ranging from 1.03 - 1.1. There are a number of similar examples.

It was also shown that the degree of maximization of the torque constant can be determined prior to completion of the design. A normalized torque constant expression was developed which showed that while the maximum torque constant is obtained by having a ratio of magnet length to airgap length of infinity, 91% of the maximum is obtained at a ratio of 10:1, and 83% of the maximum is obtained at 5:1. Finite element results were shown that substantiated these findings. The torque constant-length ratios findings are important because the consequences of using a particular magnet length to airgap length ratio are now known in advance. Given a particular airgap that can be held by manufacturing tolerences, the motor designer can select the magnet thickness, balancing maximization of torque constant against cost -a function of magnet volume; and inductance, which

decreases with increasing combined magnet/airgap length.

The basic approach of the design method presented, fixes the rotor size to meet an inertia constaint and then allows the stator dimensions to grow until the slots are sufficiently large to accommodate enough turns to produce the desired torque constant. Consideration is given to ensure that saturation of iron parts does not occur. One of the basic premises of the method is that the designer does not want to design a motor which operates in a magnetically saturated state. It is my feeling that for any motor where saturation has caused a decrease in the potential torque constant, a motor of comparable weight and size could have been designed using less magnet, and therefore less cost.

Consideration is also given to the slot opening widths to make sure that the wire can be inserted. The design method allows the designer to compare trade-offs between inductance, weight, resistance, resistive losses, and iron losses at a given speed. These comparisons can be made for a variety of different wire sizes, and rotor diameters and lengths, giving the designer a global idea of parameter variation for a range of design selection variations.

The design method was verified against the prototype motor discussed throughout this work. A design was developed that produced the same torque and resisitance; was 2% greater in diameter and had a stator iron weight that was 20% heavier. The heavier weight was due to the thicker stator back iron. It is possible that the flux density limits allowed in the stator back iron were conservative. Allowing a higher level of flux density would result in a thinner back iron, weighing less. Overall, the dimensions of the design correlated well

with the prototype motor.

Lastly, in this chapter, an example design was performed for a motor to be driven from a current drive with a large over voltage ratio. Motor-drive combinations with large over-voltage ratios typically have very nonlinear constant voltage torque-speed curves. Consideration of the torque-speed behaviour should always be undertaken before a design is prepared. This is necessary to ensure the desired torque-speed behaviour can be achieved given the specified motor characteristics. The example design presented allowed the designer to develop a design which met the running torque specifications within the dissipation envelope. Both the verification and the example design show the design process presented to be a viable means of producing reasonable designs for brushless DC motors. The verification proves that the simple airgap models are sufficient to use as a basis for the magnetic portion of the motor design. Final designs could then be 'fine tuned' by finite element analysis to further minimize stator iron volume. Thereby reducing weight while investigating saturation effects to ensure the torque constant requirement is maintained.

Future Work

I believe that the research documented in this thesis has answered many questions relating to basic motor design, and, helped to lend considerable insight into the magnetic behavior of the device. I also believe that it has provided a foundation for motor design. However there remains much to be done.

The motor structure which was analyzed and used as a basis for motor design assumed radially oriented arc shaped magnets. Many

brushless DC motors commercially available have rotors of the form shown as prototype 2 in Chapter IV. These consists of squared-off rotor back irons with permanent magnet segments which are oriented straight through. These types of rotor designs have the advantage of being less costly to prototype. Rectangular magnet segments magnetized straight through are readily available in prototype quantities. These segments are mounted to the square rotor back irons and then, via a grinding operation, are turned down to produce a round rotor. Prototype rotors of this type can be produced much more quickly and tend to be less costly than motors with radial oriented arc segments.

Some preliminary work performed by the author has shown that the torque constant of each of these types of design is approximately the same when each are of the same axial length, are used in the same stator, and have equal magnet cross-sectional areas. However, additional comparisons should be made between these two basic design types. It seems to me that the rotor with the square rotor back iron would have less detent torque and be more sinusoidal in nature because the edges of the magnet are more distributed. The distributed magnet edges would also result in a more sinusoidal stator torque-angle curve. These speculations, however, are based on insight gained by the IxB method, which is not strictly applicable in the case of the squared-off rotor back iron.

The development of a simple model to predict the magnetic characteristics of the motor rotor with the square rotor back iron will be made difficult by the variable reluctance effects of the square rotor back iron. Since the IxB method will no longer be a

valid means of calculating torque; it may be necessary to develop other methods.

Apart from an investigation into these other types of rotors, there are three primary areas that I think should be focused on in the future: an analysis of hysteresis and eddy current losses; the development of a thermal model for the device; and a thorough investigation into the effects of saturation.

A very simple method of including iron losses was used in the design equations presented in Chapter VI. That approach simply used the manufacturer's loss per pound curves. Those curves are based on an AC excitation and assume a uniform field is present throughout the iron. The field present in the motor iron is much more complicated. Different parts of the iron see different field levels and there are a number of different AC components which are due to the rotating permanent magnets, the fundamental phase current, harmonics due to pulse width modulation of the drive, and iron nonlinearities.

It is not clear to me that the total losses can be determined by using the manufacturer's loss curves to find the losses due to each of the AC components, and then using superposition to find the total losses. Investigation is necessary to determine if a more complicated model is needed to account for each of these contributions in various sections of the iron because iron losses can be a significant source of heating in the motor. Further experimental work to verify the models is also necessary.

A more complete model for the iron losses could be coupled with a thermal model for the motor. In order to truly optimize the system design, the motor design should include thermal considerations for the

application. The heat transfer characteristics vary for each application; whatever the motor is mounted to acts as a heat sink, and, the heat transfer characteristics of the mount are a function of its size, material properties and adjoining pieces. In addition, the motor can be mounted in an enclosure, submersed in a fluid, or have a fan blowing air over it. Modelling the heat transfer characteristics of the motor/application as a system is important because the continuous torque required for an application is a function of the torque constant and the maximum continuous current. The continuous current rating is based on the amount of heat that can be transfered away from the winding. Obviously, the higher the continous current is, the lower the necessary torque constant is to meet a certain stall torque. The thermal characteristics represent an additional degree of freedom in the design of the system.

The development of simple models for the thermal resistance from stator windings to motor housing and housing to ambient would be a first start in the analysis of the thermal characteristics of the motor. The thermal resistance from winding to housing would, at least, be useful for those applications that do not blow air, or force fluids down through the airgap between the stator and rotor. With the exception of these cases, the significant heat transfer path is outward through the case; thus thermal resistance of this path would be fixed for a given motor. In many applications, the thermal resistance from housing to ambient is of limited use, other than as a basis for comparison between motor. Once the motor is mounted, there are usually other heat transfer paths which tend to dominate the thermal characteristics of the motor.

In some cases, optimal motor design will require a lumped thermal model that describes the dynamic thermal behavior of the motor/application system; not just a quasi-static model. This will be important in applications that require large output power from small package sizes for short periods of time, (e.g. missle applications).

The work presented in this thesis has made no attempt to incorporate a thermal model into this design. Development of some generic thermal models is necessary to complete the analysis of the device as a part of the system.

Saturation is another important issue which needs to be addressed. The simple models developed neglect saturation and assume that the motor is to be designed to operate in a magnetically linear state. From strictly a torque production standpoint, it is my opinion that one never wants to design a motor that operates in a region of saturation. A nonlinear torque-current characteristic is undesirable because at high current levels the torque constant is saturated and the stall torque is reduced. At low current values the torque constant, and hence the back emf constant, is high, decreasing the noload speed of the motor. Magnetic saturation of the torque constant will result in a nonoptimal use of magnet material. However, there may be trade-offs between decreases in torque and decreases in inductance. Local saturation might have a more significant effect on inductance than on the torque constant. Decreasing the inductance could improve the high speed torque capability of the device.

Including saturation in the model will certainly make the design process more complicated. However, I feel that it might be possible to model saturable paths and base the design so that the mmf drops across

the saturable paths do not exceed a certain percentage of the airgap mmf drops. This would result in a more optimal use of the iron paths. Mmf drops through the iron are a function of the reluctance of the path. The path reluctance is a function of the path length and the saturable reluctivity of the iron. In regions where the flux paths were short, higher flux densities would be allowed. Longer flux paths through the iron would limit the flux density to lower values. In this manner one is not concerned with the flux density levels in the iron so much as with the undesired mmf drops. The flux densities would be whatever value necessary to make the mmf drops be as specified.

LIST OF REFERENCES

REFERENCES

1. Taylor, E.O., Say, M.G., Direct Current Machines, John Wiley & Sons Inc, New York, NY, 1980

2. Taft, C.K., Gauthier, R.G., Harned, T.J., Huard, S.R., "Brushless Motor System Design and Anaylsis", Workshop Text- Univeristy of New Hampshire, 1989

3. Huard, S.R., "A Quasi-Static Torque Versus Speed Model For A Three Phase Brushless DC Motor", Masters Thesis- University of New Hampshire, 1988

4. Zienkiewicz, O.C., The Finite Element Method, McGraw Hill (UK) Ltd, London England, 1977

5. Burke, H.E., Handbook of Magnetic Phenomena, Van Nostrand Rienhold Inc, New York, 1986

6. Ploncey, R., Collins, R.E., Principles and Applications of Electromagnetic Fields, McGraw Hill, New York, 1961,

7. Brauer, J.R., Larkin, L.A., Overbye, V.D., "Finite Element Modeling of Permanent Magnet Devices", Journal of Applied Physics, March 1984

8. Lorrain, P., Corson, D.R., Electromagnetism: Principles and Applications, W.H. Freeman and Company, San Fransico, California, 1979

9. Zahn, M., Electromagnetic Field Theory: A Problem Solving Approach, Robert E. Krieger, Malabar, Florida, 1987

10. Brauer, J.R., "Conference Record of Applied Magnetics Workshop", IEEE No 75ch099-MAG, 1975

11. Woodson, H.H., Melcher, J.R., Electromechanical Dynamics: Part I, John Wiley & Sons, New York, 1968

12. Woodson, H.H., Melcher, J.R., Electromechanical Dynamics: Part II, Robert F. Krieger, Malabar Florida, 1985

13. Bodmer, J.H., Limbert, D.E., "Force Computation By the Magnetizing Current Method", Proceedings: Nineteenth Annual Symposium on Incremental Motion Control Systems and Devices, Champaign, Illinois, 1990

14. Aronson, E.A., Brauer, J.R., "Magnetic Torque Or Force Calculuation By Direct Differentiation of Finite Element Coenergy", IEEE Transactions on Magnetics, Vol. 25, No. 5, September 1989

15. Harned, T.J., "Transient Finite Element Analysis of Permanent Magnet Magnetization", Proceedings: Nineteenth Annual Symposium on Incremental Motion Control Systems and Devices, San Jose, California, 1990

16. Chai, H.D., "Permeance Model and Reluctance Force Between Tooth Structures", Proceedings: Second Annual Symposium on Incremental Motion Control Systems and Devices, Champaign, Illinois, 1973

17. Harned, T.J., Prina, S.R., "Finite Element Analysis of Electromechanical Devices", Proceedings: Sixteenth Annual Symposium on Incremental Motion Control Systems and Devices, Champaign, Illinois, 1987

18. Vemuri, V. and Karplus, W.J., Digital Computer Treatment of Partial Differential Equations, Prentice Hall, New Jersey, 1981

19. Chari, M.V.K., "Finite Element Solution of Magnetic and Electric Field Problems in Electrical Machines and Devices",- Finite Elements in Electrical and Magnetic Field Problems, John Wiley & Sons, New York, 1980

20. Silvester, P., Chari, M.V.K., "Finite Element Solution of Saturable Magnetic Field Problems", IEEE Transactions on Power Apparatus and Systems, PAS-89 No. 7, 1989

21. Brauer, J.R., "Saturated Magnetic Energy Functional For Finite Element Analysis of Electric Machines", IEEE Power Engineering Society Winter Meeting, New York, 1975

22. Hoole, S.R.H., Computer-Aided Analysis of Design of Electromechanical Devices, Elsevier, New York, 1989

23. Silvester, P. and Ferrari, R., Finite Elements for Electrical Engineers, Cambridge University Press, 1983.

24. Catalogue: "USS Non-Oriented Steel Sheets", United States Steel Co, Pittsburgh, PA

25. Prina, S.R., Taft, C.K., "The Design and Analysis of Brushless DC Motors Having Smooth Rotor Back Iron", Proceedings: Nineteeth Annual Symposium on Incremental Motion Control Systems and Devices, Champaign, Illinois, 1990

APPENDICES

APPENDIX A

DEVELOPMENT OF A NONLINEAR MAGNETIC FINITE ELEMENT MODEL

A first order, nonlinear, two-dimensional finite element magnetic model was used to model the motors shown in this thesis. In this appendix that finite element model will be developed. The material presented in this appendix is excerpted from a paper written by the author and Dr. T.J. Harned of Eastern Air Devices, Dover NH and presented at the 1987 IMCS Conference[17].

The types of problems usually thought of as two-dimensional are really three-dimensional with certain constraints. These problems are axisymmetric ones that can be modeled by assuming that the geometry varies in the plane of the device and is uniform in the axial direction.

A.1 Nonlinear Magnetic Materials

Magnetic materials found in electromechanical devices are usually highly nonlinear. Their magnetic characteristics are described by a B-H curve, (see Figure A-1). The B-H curve relates the magnetic flux density, **B**, produced in the material due to an applied magnetic field intensity, **H**. Figure A-1 shows that magnetic materials are nonlinear, and they also exhibit hysteresis. Modelling the hysteretic characteristic of the material requires information about the past history of the magnetic field, making such modelling impractical. Hence, the magnetic materials are usually modeled using their

magnetization curve. This curve is single valued, as shown in Figure A-1. Thus, Equation A-1 can be used to describe the magnetic properties of the material.

$$\mathbf{B} = \mu \mathbf{H} \qquad \text{(A-1a)}$$

Or:

$$\mathbf{B} = \frac{\mathbf{H}}{\upsilon} \qquad \text{(A-1b)}$$

Where: μ is the permeability of the material

υ is the reluctivity of the material

In a saturable material, such as most ferromagnetics, the permeability and the reluctivity are nonlinear functions of either the flux density or the field intensity.

A.2 The Magneto-Static Field Equation

The partial differential equation, (PDE), describing the static magnetic field can be derived using Maxwell's fourth equation[8], in differential form, and the magnetic material properties. Maxwell's fourth equation, for time invariant problems, is shown in Equation A-2.

$$\nabla \times \mathbf{H} = \mathbf{J} \qquad \text{(A-2)}$$

This equation states that the curl of the magnetic intensity equals the total current density, **J**, within the field region. If the magnetic material relation given in Equation A-1a is substituted into this equation then Equation A-3 results.

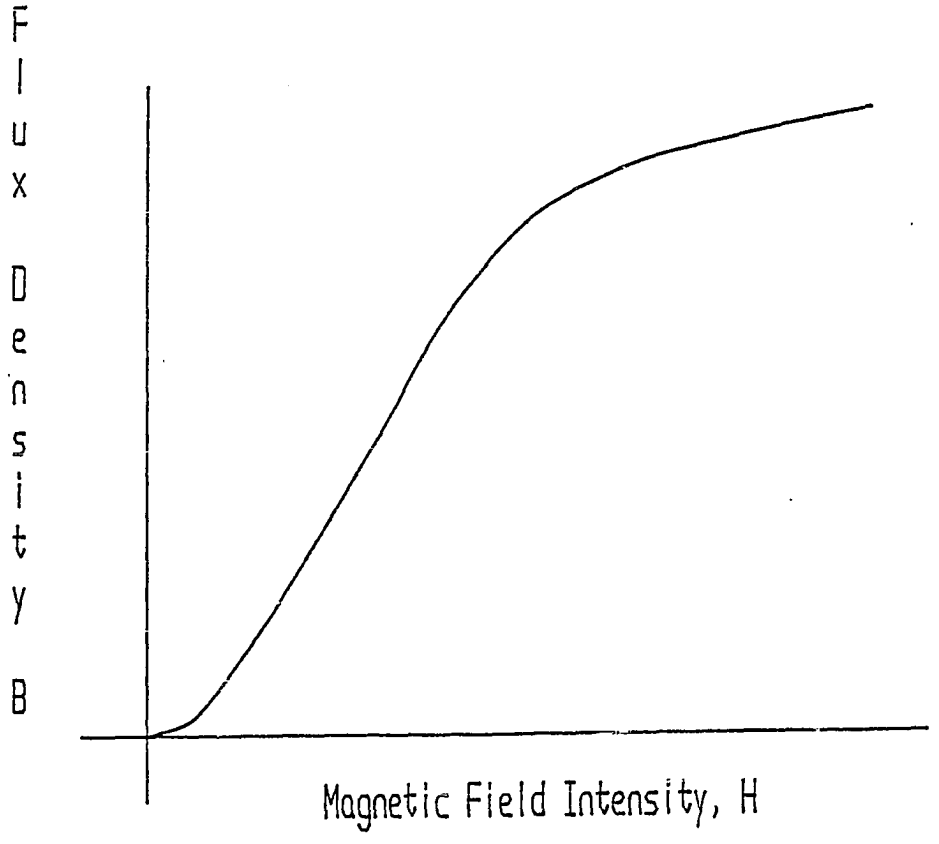

Figure A-1
Typical Virgin Steel B-H Magnetization Curve

$$\nabla \times \frac{\mathbf{B}}{\mu} = \mathbf{J} \tag{A-3}$$

In solving two-dimensional problems, it is convenient to define a vector magnetic potential, **A**, such that:

$$\mathbf{B} = \nabla \times \mathbf{A} \tag{A-4}$$

This definition is convenient for the two-dimensional case because if **B** is to have components only in the x and y directions, then **A** must have components only in the z direction, (A_z). Since the vector potential **A** has only the component A_z, then the vector PDE reduces to a scalar PDE. Examining the two-dimensional case by substituting Equation A-4 into Equation A-3 results in Equation A-5.

$$\frac{\partial}{\partial x}\left[\frac{1}{\mu}\frac{\partial A_z}{\partial x}\right] + \frac{\partial}{\partial y}\left[\frac{1}{\mu}\frac{\partial A_z}{\partial y}\right] = -J_z \tag{A-5}$$

It can be seen from Equation A-5 that the vector differential equation has been reduced to a nonlinear scalar PDE. Equation A-5 is then solved for A_z using finite element methods. Once A_z is obtained, **B** can be calculated using Equation A-4.

A.3 Finite Element Formulation

Finite element methods present a way of discretizing a system and using approximating functions to describe the parameter of interest over the element. Primarily, there are two approaches to the development of a finite element model. One, is through the method of weighted residuals. The other is the variational approach. The weighted residual method will be described briefly, then the variational method will be used to derive the finite element model in detail.

In the weighted residual method the residual is the amount by which the approximating function misses satisfying the governing differential equation. This residual is multiplied by some weighting function and then integrated over the domain. By setting this integral equal to zero, one forces the residual to be zero, in an average sense, over the domain. Some classical weighted residual procedures are: Collocation, Least Squares and Galerkin[18]. Galerkin's method, in which the weighting function is chosen to be identical to the approximating function, is one of the most popular.

In the variational approach[19], the stationary value, i.e. extremum, of some definable functional provides the solution to the differential equation. The functional often represents some physical quantity in the problem, such as the potential energy in the magnetostatic case. It also contains lower order derivatives than the differential equation, which means that lower order approximating functions can be used. The variational approach allows one to treat more complicated derivative boundary conditions, such as natural boundary corditions. In addition, it always leads to a symmetric system of algebraic equations.

In the following, the variational approach is used to develop a finite element model for two-dimensional, nonlinear magnetic field problems. It should be noted, however, that a development using the Galerkin method of weighted residuals would result in an identical set of algebraic equations.

The nonlinear magnetic field problem described by Equation A-5 can be expressed in the variational approach as an energy functional, Equation A-6. This functional was first derived by Chari and

Sylvester[20] and later modified by Brauer[21], and was shown by them to satisfy the necessary conditions required in order for it be a true functional formulation of Equation A-5.

$$F(U(B)) = \int_{\Omega} W(U)\ d\Omega - \int_{\Omega} \mathbf{J}\cdot\mathbf{U}\ d\Omega - \int_{S} \mathbf{U}\cdot\frac{\partial \mathbf{U}}{\partial n}\ dS \qquad \text{(A-6)}$$

W(U) is the energy density associated with the approximate, or trial solution, U, of the vector potential, A. The energy density for both linear and nonlinear anisotropic magnetic materials is given by Equation A-7, and is the area which lies to the left of a B-H curve for the material. (See Figure A-1).

$$W(U(B)) = \int_{0}^{B_0} |H|\ d|B| \qquad \text{(A-7)}$$

Using Equation A-1b, and expressing the reluctivity as a function of the magnitude of the flux density, the energy density can be expressed as shown by Equation A-8.

$$\mathbf{H} = \upsilon(|\mathbf{B}|)\ \mathbf{B} \qquad \text{(A-1b)}$$

$$W(U(B)) = \int_{0}^{B_0} \upsilon(|B|)\ |B|\ d|B| = \int_{0}^{B_0} \upsilon(|B|)\ |B|\ d|B| \qquad \text{(A-8)}$$

|B|, in this equation, is the magnitude of the flux density and is defined by Equation A-9.

$$|B| = \sqrt{\left[\frac{\partial U_z}{\partial x}\right]^2 + \left[\frac{\partial U_z}{\partial y}\right]^2} \qquad \text{(A-9)}$$

Equation A-9 is valid only for two-dimensional magnetic problems where both U and J have components in the z-direction only. The functional can now be written as shown in Equation A-10.

$$F(U(B)) = \int_{\Omega} \left[\int_{0}^{B_o} \upsilon(|B|)|B| \, d|B| - J_z \, U_z \right] d\Omega - \int_{S} \frac{\partial U_z}{\partial n} \, dS \qquad \text{(A-10)}$$

It should be noted that by setting the line integral on the right hand side of Equation A-10 to zero, natural boundary conditions, (homogeneous Neumann), are implicitly satisfied by this formulation[22]. Therefore, on mesh boundaries where the potential is unspecified, contours of constant potential will be perpendicular to the boundary.

At this point, the energy density will be rewritten in terms of the square of the flux density. This makes the mathematics slightly more convenient. A new reluctivity function can be formed that is a function of the square of the flux density. The reluctivity expression usually comprises a seres of cubic splines approximating the reluctivity-flux density data, it is no more difficult to reformulate the function as a set of cubic splines approximating the reluctivity-flux density squared data.

$$\upsilon(|B|) = \upsilon(|B|^2)$$

To rewrite the energy density in terms of the square of the flux density the following definitions are made:

$$\tilde{B} = |B|^2 \qquad \text{(A-11a)}$$

$$d\tilde{B} = 2|B| \, d|B| \qquad \text{(A-11b)}$$

$$\int_0^{B_o} \upsilon(|\mathbf{B}|)\,|\mathbf{B}|\;d|\mathbf{B}| = \frac{1}{2}\int_0^{\tilde{B}_o} \upsilon(\tilde{B})\;d\tilde{B} \qquad \text{(A-11c)}$$

Substitution of Equation A-11c into Equation A-10 and setting the line integral to zero, produces the functional expression shown in Equation A-12.

$$F(\mathbf{U}(\mathbf{B})) = \int_{\Omega} \left[\frac{1}{2}\int_0^{\tilde{B}_o} \upsilon(\tilde{B})\;d\tilde{B} - J_z U_z\right] d\Omega \qquad \text{(A-12)}$$

If the domain is discretized into a set of N_e nonoverlapping finite elements, and the potential is defined within an element by an interpolative approximation, then the functional becomes a summation of integrals over each and every element, Equation A-13. A general form for the interpolative approximating function is shown in Equation A-14. N_o is the number of nodes on the element, $U_{z\,i}$ is the potential at node i and N_i is the shape or basis function associated with node i.

$$F(\mathbf{U}(\mathbf{B})) = \sum_{k=1}^{N_e} \int_{\Omega_e} \left[\frac{1}{2}\int_0^{\tilde{B}_o} \upsilon(\tilde{B})\;d\tilde{B} - J_z U_z\right] d\Omega_e \qquad \text{(A-13)}$$

$$U_z = \sum_{i=1}^{N_o} U_{z\,i} N_i \qquad \text{(A-14)}$$

The energy functional is then minimized by setting the partial derivatives of the functional, with respect to each of the unknown nodal, potentials equal to zero.

$$\frac{\partial F}{\partial U_{z\,i}} = 0 \qquad \text{(A-15)}$$

Since the energy functional is a summation of integrals over each element, the minimization process can be applied to a single element to produce a set of algebraic equations in terms of its unknown nodal potentials. Once this procedure has been applied to all of the elements, the result will be a system of N_n equations for the N_n unknown nodal potentials.

Applying the minimization to a single element, Equation A-15 requires the condition shown by Equation A-16.

$$0 = \frac{1}{2} \int_{\Omega_e} \frac{\partial}{\partial U_{z\,i}} \left[\int_0^{\tilde{B}} \overset{\circ}{\upsilon}(\tilde{B})\, d\tilde{B} \right] d\Omega_e - \int_{\Omega_e} \frac{\partial}{\partial U_{z\,i}} (J_z U_z)\, d\Omega_e \qquad \text{(A-16)}$$

Substitution of the interpolative approximation for the potential over the element, defined by Equation A-14, into the second integral of Equation A-16, yields the result shown in Equation A-17.

$$\int_{\Omega_e} \frac{\partial}{\partial U_{z\,i}} \left(J_z \sum_{k=1}^{N_n} U_{z\,k} N_k \right) d\Omega_e = \int_{\Omega_e} J_z N_i \, d\Omega_e \qquad \text{(A-17)}$$

Application of the chain rule to the first integral of Equation A-16, which is the energy density, W, in Equation A-18, produces the following result.

$$\frac{\partial}{\partial U_{z\,i}} W(\tilde{B}(U_z)) = \frac{\partial}{\partial U_{z\,i}} \frac{1}{2} \int_0^{\tilde{B}_o} \upsilon(\tilde{B})\, d\tilde{B} = \upsilon(\tilde{B}) \frac{\partial \tilde{B}}{\partial U_{z\,i}} \qquad \text{(A-18)}$$

The remaining partial derivative term in this integral can be eliminated by using the fact that $\tilde{B}$ is the square of the magnitude of the flux density, (Equation A-9 and A-11a). The square of the flux density magnitude is as shown in Equation A-19a.

$$\tilde{B} = |B|^2 = \left(\frac{\partial U_z}{\partial x} \right)^2 + \left(\frac{\partial U_z}{\partial y} \right)^2 \qquad \text{(A-19a)}$$

The partial derivative of $\tilde{B}$ with respect to the axial component of vector potential at node i is:

$$\frac{\partial \tilde{B}}{\partial U_{z\,i}} = 2 \frac{\partial U_z}{\partial x} \frac{\partial^2 U_z}{\partial U_{z\,i}\, \partial x} + 2 \frac{\partial U_z}{\partial y} \frac{\partial^2 U_z}{\partial U_{z\,i}\, \partial y} \qquad \text{(A-19b)}$$

The partial derivative of the vector potential can be evaluated by substitution of the interpolative approximation, Equation A-14.

$$\frac{\partial U_z}{\partial x} = \sum_{k=1}^{N_n} U_{z\,k} \frac{\partial N_k}{\partial x} \qquad \text{(A-19c)}$$

$$\frac{\partial U_z}{\partial y} = \sum_{k=1}^{N_n} U_{z\,k} \frac{\partial N_k}{\partial y} \qquad \text{(A-19d)}$$

and,

$$\frac{\partial}{\partial U_{z\,i}} \left(\frac{\partial U_z}{\partial x}\right) = \frac{\partial N_i}{\partial x} \qquad \text{(A-19e)}$$

$$\frac{\partial}{\partial U_{z\,i}} \left(\frac{\partial U_z}{\partial y}\right) = \frac{\partial N_i}{\partial y} \qquad \text{(A-19f)}$$

Therefore,

$$\frac{1}{2} \frac{\partial \tilde{B}}{\partial U_{z\,i}} = \left[\sum_{k=1}^{N_n} U_{z\,k} \frac{\partial N_k}{\partial x} \right] \frac{\partial N_i}{\partial x} + \left[\sum_{k=1}^{N_n} U_{z\,k} \frac{\partial N_k}{\partial y} \right] \frac{\partial N_i}{\partial y} \qquad \text{(A-20)}$$

Substitution of the results from Equation A-17, A-18 and A-20 into Equation A-16 yields Equation A-21.

$$\int_{\Omega_e} \upsilon(\tilde{B}) \left\{ \left[\sum_{k=1}^{N_n} U_{z\,k} \frac{\partial N_k}{\partial x} \right] \frac{\partial N_i}{\partial x} + \left[\sum_{k=1}^{N_n} U_{z\,k} \frac{\partial N_k}{\partial y} \right] \frac{\partial N_i}{\partial y} \right\} d\Omega_e -$$

$$\int_{\Omega_e} J_z N_i \, d\Omega_e = 0 \qquad \text{(A-21)}$$

This equation is applied for each nodal potential $U_{z\,i}$ on the element for all N_o nodes on the element. This will result in N_o equations which can be restated in matrix form as shown in Equation A-22.

$$[S]_e \{U\}_e = \{\tilde{J}\}_e \qquad \text{(A-22)}$$

$\{U\}_e$ is the vector of unknown nodal potentials, $U_{z\,i}$, of the element. The individual entries of the $[S]_e$ matrix and $\{\tilde{J}\}_e$ vector are given by

Equations A-23a and A-23b.

$$\tilde{J}_i = \int_{\Omega_e} J_{zi} N_{zi} \, d\Omega_e \qquad \text{(A-23a)}$$

$$S_{ij} = \int_{\Omega_e} \upsilon(\tilde{B}) \left(\frac{\partial N_i}{\partial x} \frac{\partial N_j}{\partial x} + \frac{\partial N_i}{\partial y} \frac{\partial N_j}{\partial y} \right) d\Omega_e \qquad \text{(A-23b)}$$

This represents the general equation which can be applied to any type of finite element selected to discretize the region.

In the finite element work discussed in this appendix, first order triangular elements with 'regular' node numbering on a 'regular' mesh are used to analyze electric machines. A 'regular' mesh was shown in Chapter III, Figure III-1. It will be shown here, that these types of meshes result in matrix equations which are banded and sparse. This, combined with the fact that the variational method produces a symmetric set of equations, results in a very compact set of equations.

Consider the example element, e, in Figure A-2 with vertices, or nodes, labeled j,k,l. The interpolative approximating function which will be used to describe the approximate vector potential, U_z, within the element is:

$$U_z = N_j U_{zj} + N_k U_{zk} + N_l U_{zl} \qquad \text{(A-24)}$$

The functions N_i are basis functions for the natural, or area coordinate system of the triangle[18]. The transformation between cartesian and natural coordinates is given by the following relationship:

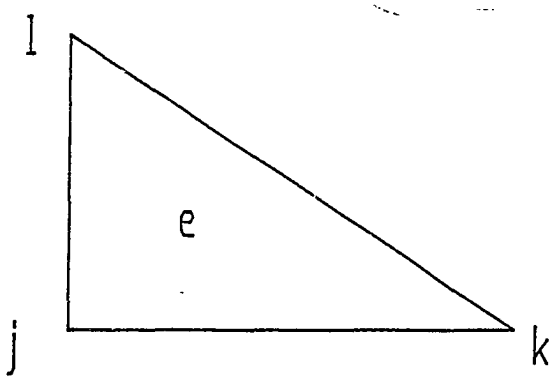

Figure A-2
A Single Triangular Finite Element

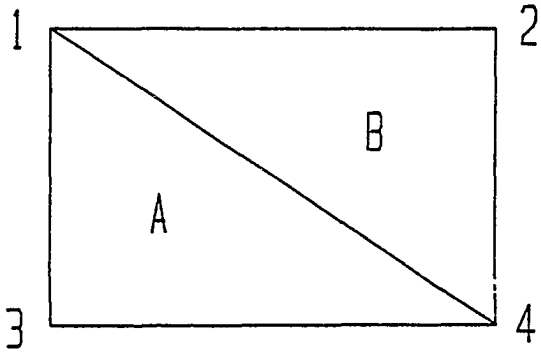

Figure A-3
A Two Element Example

$$N_i = \frac{1}{2\Delta_i} (p_i + q_i x + r_i y) \qquad \text{(A-25)}$$

Where:

$i \equiv j,k,l$

$\Delta_i \equiv$ triangle area

$p_j \equiv x_j y_k - x_k y_l$

$q_j \equiv y_l - y_k$

$r_j \equiv x_k - x_l$

Similar expressions for p_k, q_k, r_k and p_l, q_l, r_l can be found by the rotation scheme shown below.

$$\begin{array}{ccc} j & k & l \\ \downarrow & & \\ k & l & j \\ \downarrow & & \\ l & j & k \end{array}$$

Applying equations A-23a&b to find the individual entries of the $[S]_e$ and $\{\tilde{J}\}_e$ matrix for the example element, produces the matrix Equation A-26.

$$\frac{1}{4\Delta_e}\nu(\tilde{B}_e)\begin{bmatrix} (q_j^2+r_j^2) & (q_j q_k+r_j r_k) & (q_j q_l+r_j r_l) \\ (q_k q_j+r_k r_j) & (q_k^2+r_k^2) & (q_k q_l+r_k r_l) \\ (q_l q_j+r_l r_j) & (q_l q_k+r_l r_k) & (q_l^2+r_l^2) \end{bmatrix}\begin{Bmatrix} U_{z\,j} \\ U_{z\,k} \\ U_{z\,l} \end{Bmatrix} = \frac{-J_z \Delta_e}{3}\begin{Bmatrix} 1 \\ 1 \\ 1 \end{Bmatrix} \qquad \text{(A-26)}$$

One should bear in mind that this assumes that the current density is constant over the element. Furthermore, since U_{zi} was assumed to vary linearly over the element, the flux density, and hence the reluctivity, are also constant over the element.

One can see that the individual elements of the matrix are only functions of the geometry of the triangle. One can also see the symmetry which results from this type of formulation.

Now consider the two elements A and B with nodes 1,3,4 and 1,2,4 respectively, shown in Figure A-3. If the matrix $[S]_A$ is formed for element A, then the matrix equation A-27 results. For clarity, the individual entries are expressed as $s^{\#}_{ij}$ where the superscript, #, corresponds to the element.

$$\frac{1}{4\Delta_A}\,\nu_A \begin{bmatrix} s^A_{11} & 0 & s^A_{13} & s^A_{14} \\ 0 & 0 & 0 & 0 \\ s^A_{31} & 0 & s^{A3}_{33} & s^A_{34} \\ s^A_{41} & 0 & s^A_{43} & s^A_{44} \end{bmatrix} \begin{Bmatrix} U_{z1} \\ U_{z2} \\ U_{z3} \\ U_{z4} \end{Bmatrix} = \frac{-J_{zA}\Delta_A}{3} \begin{bmatrix} 1 \\ 0 \\ 1 \\ 1 \end{bmatrix} \qquad \text{(A-27)}$$

Note that the second row and column entries in the matrix $[S]_A$ are zero because node 2 is not contained in element A.

In a similar manner, the matrix equation for the potentials for element B is given by Equation A-28.

$$\frac{1}{4\Delta_B}\,\nu_B \begin{bmatrix} s^B_{11} & 0 & s^B_{13} & s^B_{14} \\ 0 & 0 & 0 & 0 \\ s^B_{31} & 0 & s^{B3}_{33} & s^B_{34} \\ s^B_{41} & 0 & s^B_{43} & s^B_{44} \end{bmatrix} \begin{Bmatrix} U_{z1} \\ U_{z2} \\ U_{z3} \\ U_{z4} \end{Bmatrix} = \frac{-J_{zB}\Delta_B}{3} \begin{bmatrix} 1 \\ 0 \\ 1 \\ 1 \end{bmatrix} \qquad \text{(A-28)}$$

The matrix equation which describes the entire system of elements A and B, Equation A-29, is formed by adding the two individual matrix equations.

The assembly of the system of equations for a large number of elements proceeds in exactly the same manner as for this two element example. The elements are dealt with one at a time, calculating the individual $s^{\#}_{ij}$ and $\tilde{J}$ components, and then adding them into the system matrix. Once the component calculations for all the elements have been completed, all that remains is to solve the matrix equation, A-30.

$$[S]\{U\} - \{\tilde{J}\} = 0 \qquad \text{(A-30)}$$

It must be remembered, however, that this equation is nonlinear, due to the fact that the reluctivities used in forming the [S] matrix are functions of the flux densities within the elment.

It is obvious that for a large number of nodes, N_n, not only is a large amount of memory required for storage of the N_n by N_n matrix [S], but also that the solution of Equation A-30 will be computationally expensive. Computational costs are increased even more by the fact that this is a nonlinear system requiring an iterative technique to find the solution. Therefore, it would be advantageous if the nodes were numbered in such a manner as to make the matrix [S] as banded and as sparse as possible; thereby allowing the use of a solution technique which takes advantage of these properties.

It was stated previously that the use of regular node numbering on a regular mesh would result in a coefficient matrix that was banded and sparse. By regular node numbering and regular mesh, we mean one

like that shown in Figure A-4.

The node numbering on this mesh is regular in the sense that the numbering starts in the upper right corner and successive nodes are numbered in increasing order in going along the top boundary from left to right. Then,the second row of nodes is numbered in the same manner. The mesh is considered regular because there are the same number of nodes, N_x, along each row. If this type of numbering and meshing scheme is used, then any interior node, i, is always conected to six other nodes and forms the set of connected nodes given in Equation A-31. The interconnection of nodes that lie along a boundary will form a subset of these.

$$[\ (i-N_x-1),\ (i-N_x),\ (i-1),\ i,\ (i+1),\ (i+N_x),\ (i+N_x+1)\ ] \qquad \text{(A-31)}$$

As a result of this regular numbering scheme, the matrix [S] has the structure shown in Figure A-5. Since the matrix is symmetric, it is only necessary to store the diagonal terms and the three off diagonal terms that lie above it. Therefore, for N_n unknown potentials, one does not need to be able to store a full N_n by N_n matrix, only one that is N_n by four. This is a significant savings, and when coupled with an efficient algorithm for solving the equations, allows one to model structures that require a large number of nodes and elements.

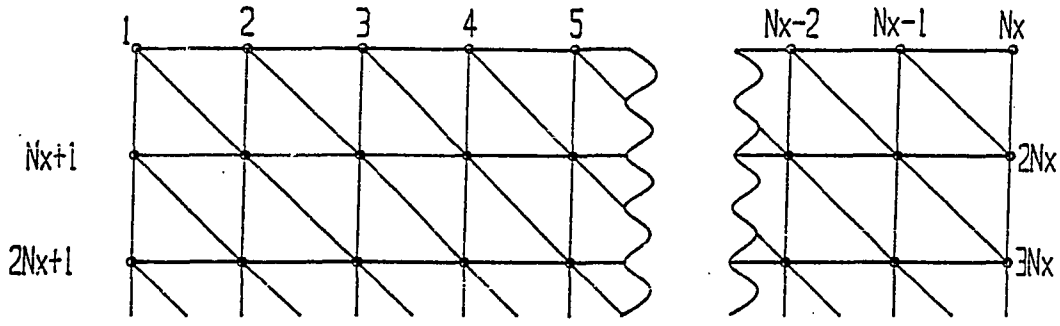

Figure A-4
'Regular' Mesh with 'Regular' Node Numbering

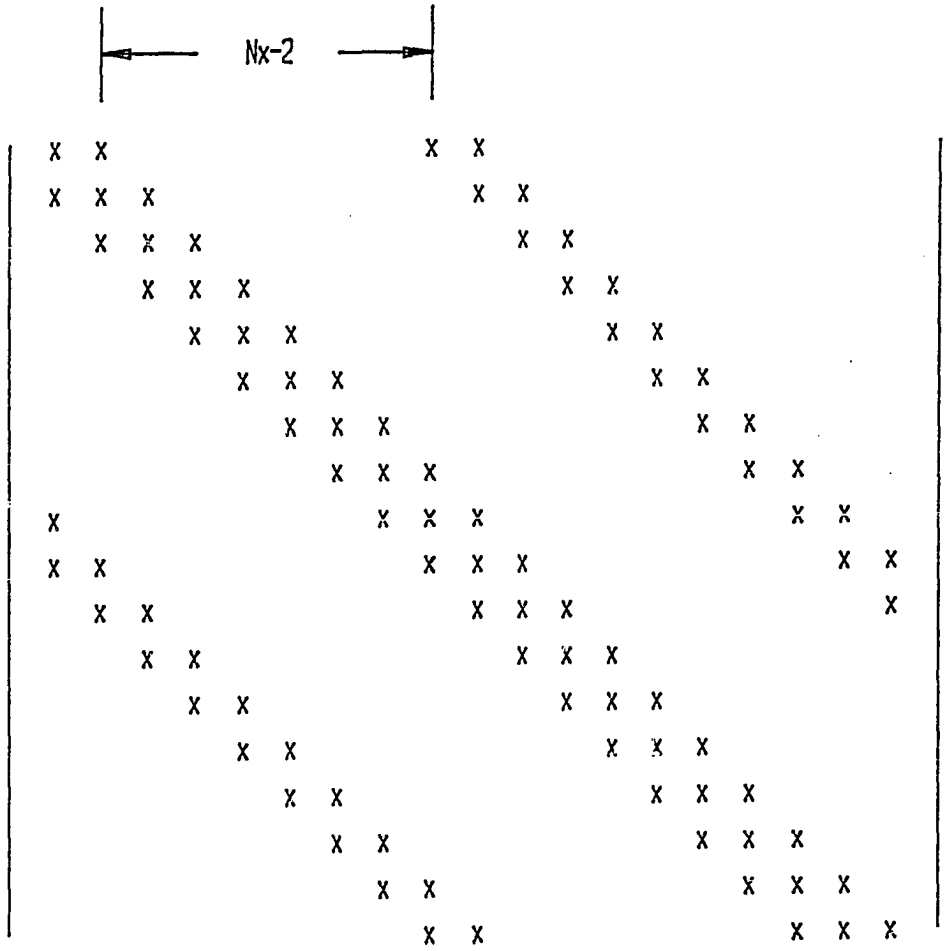

Figure A-5
Sparse, Banded Matrix Structure
Resulting from 'Regular' Mesh and Numbering

APPENDIX B

SOLUTION OF THE FINITE ELEMENT MODEL NONLINEAR MATRIX EQUATION

In Appendix A, the finite element method was developed, and the governing partial differential equation was reduced to a set of simultaneous, nonlinear, algebraic equations. Once the symmetric, banded coefficient matrix has been set up, the problem is reduced to solving the set of nonlinear equations. Solving the nonlinear matrix equations is a two-step iterative process. First, an outer, nonlinear loop must be developed that will cause the nonlinear properties to converge on their correct values. Then, for each iteration, it is necessary to solve the linear matrix equation. This process, as it applies to the set of equations developed in Appendix A, was discussed in detail in reference [17] and is repeated here for completeness.

One of the most popular methods for solving the nonlinear portion of the problem is the Newton-Raphson iteration scheme. The Newton method is popular because it is unconditionally stable, provided the B-H characteristic is monotonic. In addition, the convergence rate for the process becomes quadratic near the solution point[18].

During each iteration, the Newton method evaluates the nonlinear equations at an operating point. This results in a set of linear equations valid at that operating point. The linear equations can then be solved using one of several different techniques and a new operating point is determined. The iteration process is repeated until a satisfactory solution is obtained.

B.1 Solution of the Nonlinear Equations by the Newton-Raphson Method

The Newton process can be formulated as follows[23]. Given that $\{A_z\}$ is the exact solution and $\{U_z\}$ is an approximate solution which is close to $\{A_z\}$ but misses by $\{\delta U_z\}$, then $\{U_z\}$ can be expressed as:

$$\{U_z\} = \{A_z\} - \{\delta U_z\} \tag{B-1}$$

In Appendix A it was required that the gradient of the energy functional be zero to provide a solution for $\{U_z\}$. Each component of the gradient of $F(U)$, (i.e. Equation A-15), can be expanded in a Taylor Series near U_i, as shown in Equation B-2.

$$\frac{\partial F}{\partial U_{zi}} = \frac{\partial F}{\partial U_{zi}}\bigg|_{U_{zi}} + \sum \frac{\partial^2 F}{\partial U_{zj}\,\partial U_{zi}}\bigg|_{U_{zi}} \delta U_{zj} + \text{H.O.T.} \tag{B-2}$$

(H.O.T. signifies "higher order terms".)

Equation A-15 required that each component of the gradient must be equal to zero. Therefore, if the higher order terms of the Taylor series are neglected, the matrix equation, B-3a, results. The deviation of $\{U_z\}$ from $\{A_z\}$ can be expressed as in Equation B-3b.

$$0 = \{V\} + [P]\{\delta U_z\} \tag{B-3a}$$

$$\{\delta U_z\} = [P]^{-1}\{V\} \tag{B-3b}$$

$[P]$ in these equations is the Jacobian matrix of the Newton-Raphson iteration. Its individual components are given by Equation B-4. $\{V\}$ contains the components of the gradient of $F(U)$ at U_i, as shown in Equation B-5.

$$P_{ij} = \frac{\partial^2 F}{\partial U_{zi}\,\partial U_{zj}} \tag{B-4}$$

$$V_j = \frac{\partial F}{\partial U_{i,j}} \tag{B-5}$$

The components of $\{V\}$, V_j, are the partial derivatives of the functional. In Appendix A, the minimization process required that these terms be set equal to zero in order to produce the solution $\{U_z\}$. This resulted in the matrix equation, $[S]\{U_z\}-\{\tilde{J}_z\} = 0$. If $\{U_z\}$ is not the exact solution to the equation then $\{V\}$ will represent the residual values of the equation.

The Newton iterative method proceeds as follows: an initial $\{U_z\}$ is assumed and $\{\delta U_z\}$ is calculated, $\{\delta U_z\}$ is then added to the assumed $\{U_z\}$ to form a better estimate. The recursive relation is given by either Equation B-6a or B-6b.

$$\{U\}^{k+1} = \{U\}^k - ([P]^{-1})^k \{V\}^k \tag{B-6a}$$

$$\{U\}^{k+1} = \{U\}^k + \{\delta U\}^k \tag{B-6b}$$

In order to implement the Newton process described by Equation B-6b, [P] must be evaluated and the matrix equation B-3a solved. To form [P], the partial derivatives expressed in Equation B-4 must be evaluated. This can be done on an element by element basis.

If one takes the partial derivative with respect to U_j of Equation A-16, after first having substituted the results from Equation A-18, (as shown in Equation B-7), then Equation B-8 results.

$$\tilde{B} = |B|^2 \tag{A-11a}$$

$$\frac{\partial F}{\partial U_i} = \sum^{N_e} \int_{\Omega_e} \frac{1}{2} \upsilon(\tilde{B}) \frac{\partial \tilde{B}}{\partial U_{z\,i}} d\Omega_e + \int_{\Omega_e} J_z N_i \, d\Omega_e \tag{B-7}$$

$$\frac{\partial F}{\partial U_{z\,j}\,\partial U_{z\,i}} = \sum^{N_e} \int_{\Omega_e} \frac{\upsilon}{2} \frac{\partial^2 \tilde{B}}{\partial U_{z\,j}\,\partial U_{z\,i}} d\Omega_e + \int_{\Omega_e} \frac{1}{2} \frac{\partial \upsilon}{\partial \tilde{B}} \frac{\partial \tilde{B}}{\partial U_{z\,j}} \frac{\partial \tilde{B}}{\partial U_{z\,i}} d\Omega_e \tag{B-8}$$

In the second integral on the right hand side of Equation B-8, the partial derivative of υ must be evaluated from the B-H data. This is why it is more efficient to use curves relating the reluctivities to the square of the flux density ($\tilde{B}$), instead of the classical B-H curve.

The first integral in Equation B-8 can be evaluated by taking the partial derivative of Equation A-20, which results in Equation B-9.

$$\int_{\Omega_e} \frac{\upsilon}{2} \frac{\partial \tilde{B}}{\partial U_{z\,j}\,\partial U_{z\,i}} d\Omega_e = \int_{\Omega_e} \upsilon \left[\frac{\partial N_j}{\partial x} \frac{\partial N_i}{\partial x} + \frac{\partial N_j}{\partial y} \frac{\partial N_i}{\partial y} \right] d\Omega_e = S_{i\,j} \tag{B-9}$$

If one refers back to Equation A-23b, one sees that the right hand side of Equation B-9 is really just an element of [S].

At this point it is convenient to define a new coefficent, $\tilde{S}_{i\,j}$, as shown in Equation B-10.

$$S_{i\,j} = \upsilon \, \tilde{S}_{i\,j} \tag{B-10}$$

One sees from comparing Equations A-23b and B-10 that $\tilde{S}_{ij}$ is what remains once υ has been taken outside of the integral. This is valid because, for first order triangular elements $|\mathbf{B}|$, and hence υ, is constant over the element. In addition to defining $\tilde{S}$, let an temporary vector, $\{E\}$, be defined as in Equation B-11.

$$E_i = \sum_{k=1}^{N_o} \tilde{S}_{ik} U_k \tag{B-11}$$

Now, return to the second integral in Equation B-8. If the expressions for the partial derivatives of B^2, derived earlier in Equation A-19, are substituted and the terms expanded and collected, one finds that the second integral reduces to:

$$\int_{\Omega_e} \frac{1}{2} \frac{\partial \upsilon}{\partial \tilde{B}} \frac{\partial \tilde{B}}{\partial U_{zi}} \frac{\partial \tilde{B}}{\partial U_{zj}} d\Omega_e = \frac{2}{\Delta_e} \frac{d\upsilon}{d\tilde{B}} E_i E_j \tag{B-12}$$

Therefore, the individual elements of the Jacobian matrix [P] are given by Equation B-13.

$$P_{ij} = \upsilon(\tilde{B})\tilde{S}_{ij} + \frac{2}{\Delta_e} \frac{d\upsilon}{d\tilde{B}} E_i E_j \tag{B-13}$$

The complete Jacobian matrix is assembled by cycling through all of the elements and adding the contributions. In actuality, $[P]_e$, $\{V\}_e$, $[S]_e$ and $\{\tilde{J}\}_e$ for each element are assembled at the same time. $[S]_e$

and $\{\tilde{J}\}_e$ are calculated first, then the residual, $\{V\}_e = [S]_e\{U\}_e - \{J\}_e$, as well as $[P]_e$. Once all the elements have been cycled through, [P] and {V} are complete and $\{\delta U_z\}$ can be calculated using Equation B-3a. The result can then be used in the recursive relation B-6b. The equation is iterated until some convergence criteria, which is usually based on the vector norm of {V}, is reached. This algorithm[23] is shown in Figure B-1.

The Newton method outlined above linearizes Equation B-3 about the operating point of the current iteration. $\{\delta U_z\}$ is not usually found via Equation B-3b because of the necessity of inverting [P]. Instead, $\{\delta U_z\}$ is usually found by an iterative solution method. Any one of a number of iterative techniques[18] could be used, such as Gauss-Seidel, Jacobi or successive overrelaxation. The finite element program used in this research uses a preconditioned conjugate gradient method.

B.2 Solution of the Linear Problem

In previous sections we have dealt with the nonlinear magnetic field problem. The linear magnetic field problem is merely a subset of the nonlinear problem. The variational derivation shown in Appendix 1 is valid for both the nonlinear and linear case. If the materials are linear then the Newton-Raphson method yields the solution in one iteration.

Alternatively, one can solve the linear field problem directly by solving the matrix equation that was derived in Appendix A, Equation A-30.

$$[S]\{U\} - \{\tilde{J}\} = 0 \qquad \text{(A-30)}$$

This can be solved by either direct methods or any of the iterative methods mentioned previously.

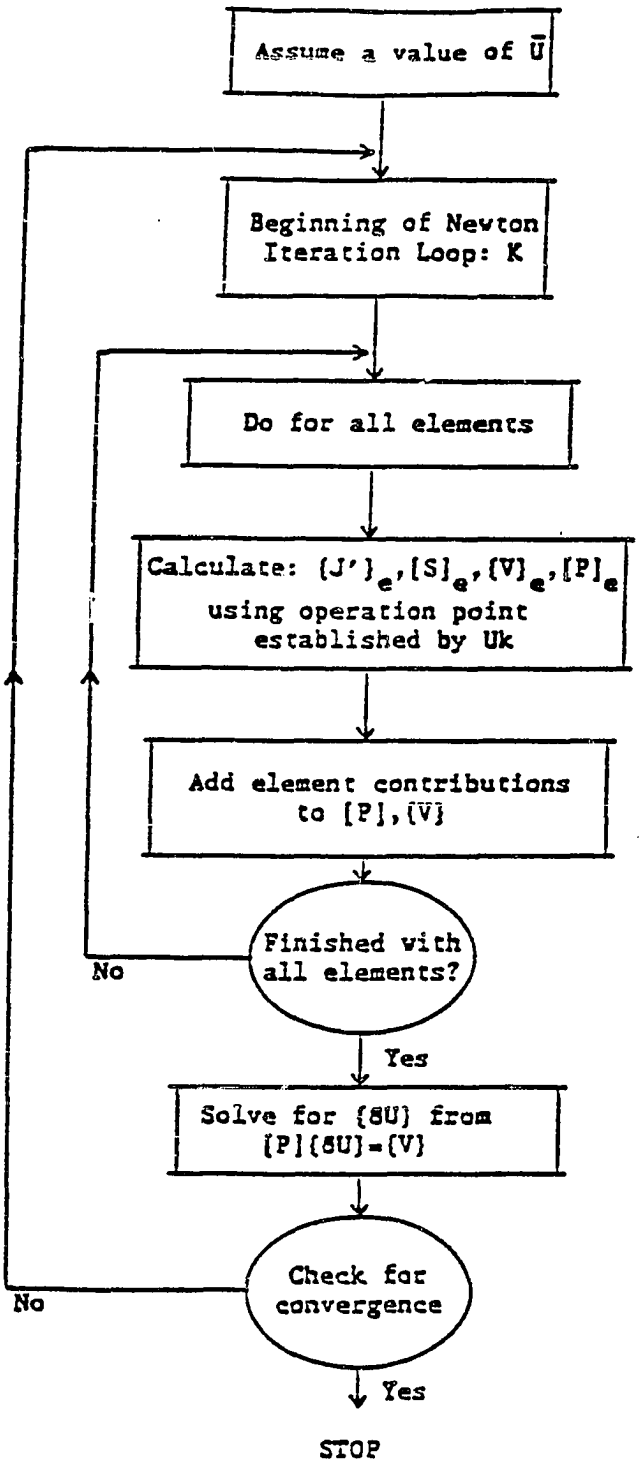

Figure B-1
Flow Diagram for Newton-Raphson Method

APPENDIX C

DERIVATION OF TORQUE SPEED EQUATIONS

In general, Brushless DC motor constant voltage torque-speed curves are nonlinear. It should not be assumed that the torque-speed characteristic can be represented by a straight line drawn between the no-load speed and the stall torque. The torque-speed characteristic should be determined from a model of the steady state speed behavior of the motor. Huard[3] has investigated constant voltage drive torque-speed behavior of Brushless DC motors by assuming sinusoidal back emf and torque-angle waveforms and developing closed form expressions for the currents during the commutation interval. The approach described in this appendix is a numerical one. A phase model is developed and the equations are numerically integrated. Because it is a numerical method, many nonlinear effects can be included in the analysis: nonsinusoidal torque-angle and back emf waveforms; saturation of the torque constant, the back emf constant and inductance; and angular variations of inductance. The numerical approach also allows one to simulate pulse width modulated current drives as well as different diode breakdown conditions.

In this appendix, the equations describing the steady state speed versus torque behaviour of the brushless DC motor are derived. Average torque for a commutation interval is calculated assuming the motor is running at a constant speed. This derivation assumes that the BLDCM is a three phase motor being driven with a wye connected

drive, (see Figure C-1). This figure shows that one end of each phase is connected in common. The other end of each phase is connected to a half bridge so that it can be connected to either supply or to ground. Protection diodes are shown for each transistor; these may be an integral part of the transistor package or they may be external. The blocking diodes shown may or may not be present.

An electrical model for the motor phases is shown in Figure C-2. Each phase model consists of a connection to a supply voltage, a back emf voltage generator, a resistance, and an inductance which is mutually coupled to each of the other phases. If the center node is assigned the unknown voltage V_c, the following three nodal equations can be written:

$$V_1+V_{b1}-V_c = L_1\frac{di_1}{dt} - M_2\frac{di_2}{dt} - M_3\frac{di_3}{dt} + i_1R_1 \qquad (C-1)$$

$$V_2+V_{b2}-V_c = -M_1\frac{di_1}{dt} + L_2\frac{di_2}{dt} - M_3\frac{di_3}{dt} + i_2R_2 \qquad (C-2)$$

$$V_3+V_{b3}-V_c = -M_1\frac{di_1}{dt} - M_2\frac{di_2}{dt} - L_3\frac{di_3}{dt} + i_3R_3 \qquad (C-3)$$

In addition, one can also use Kirchoff's nodal law to sum the currents into the center node.

$$i_1+i_2+i_3 = 0 \qquad (C-4)$$

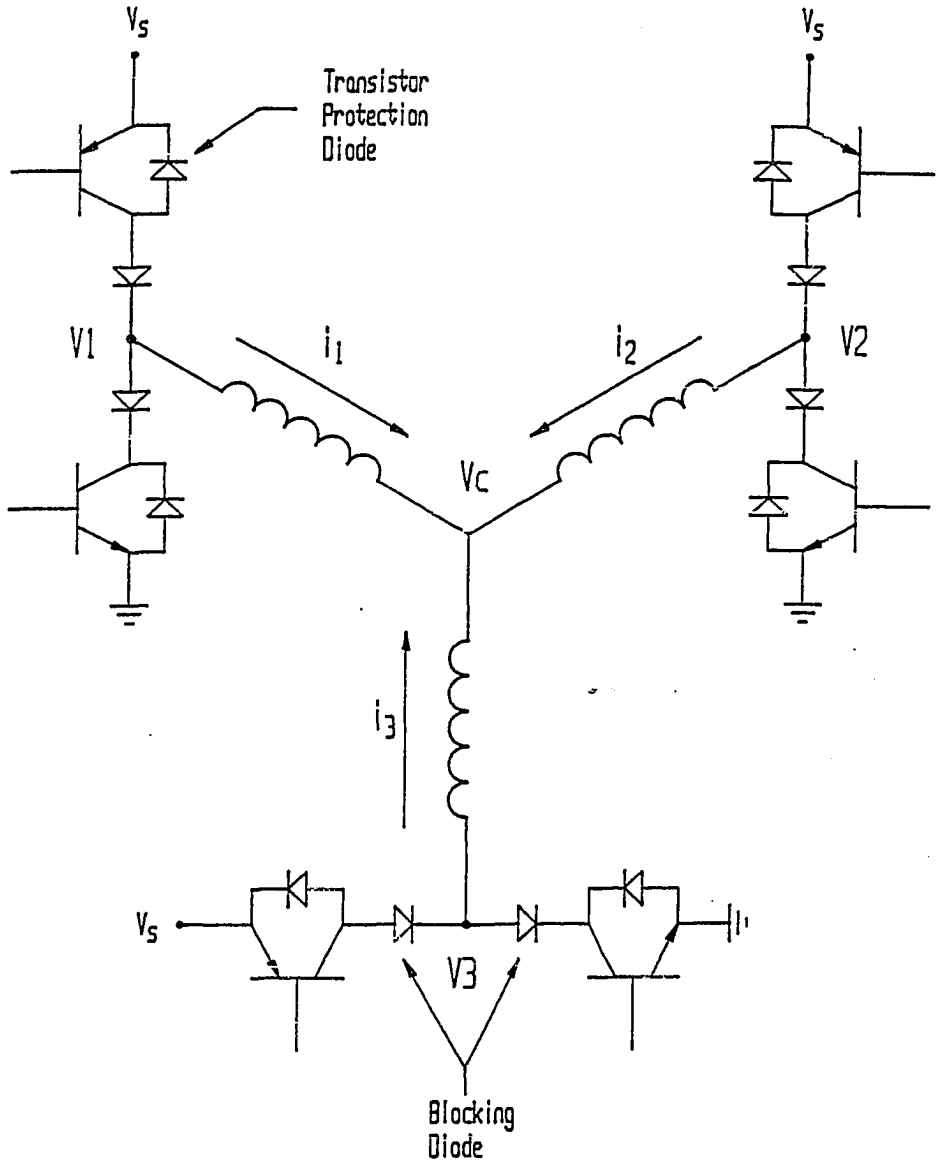

Figure C-1
Half Bridge Connections for
a Wye Connected Drive

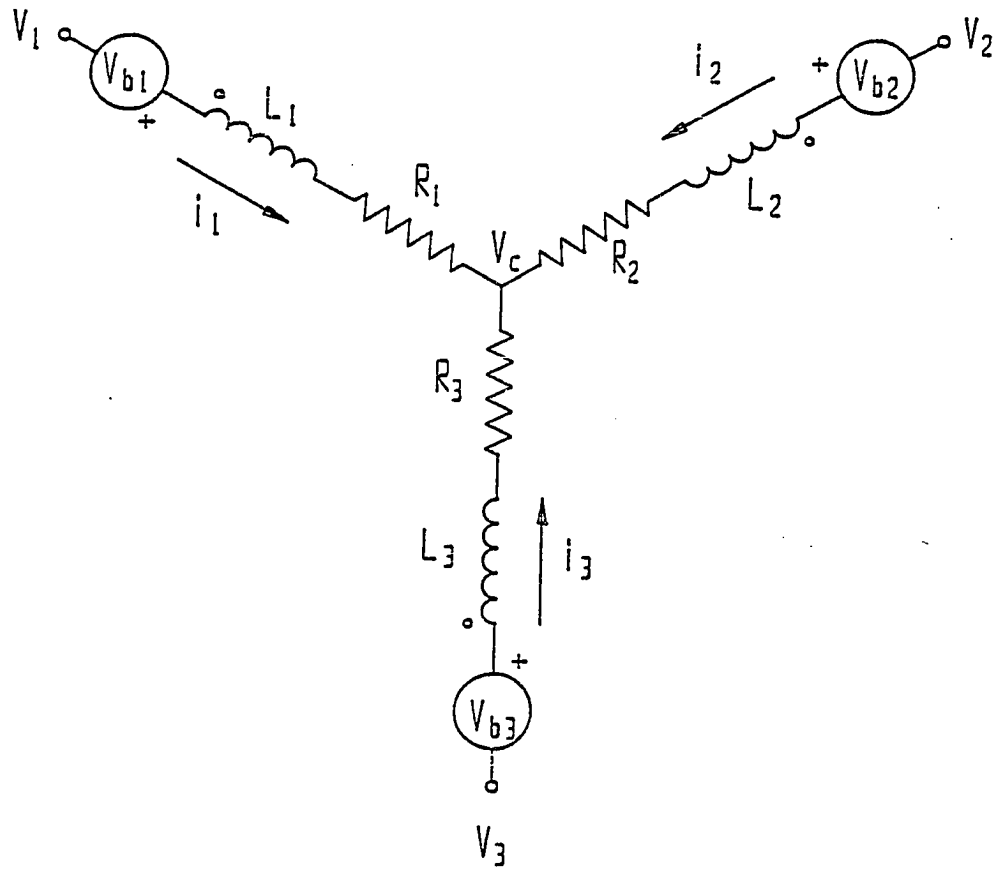

Figure C-2
Circuit Model for a Wye Connected Drive

Equation C-1 can be used to solve for V_c explicitly:

$$V_c = V_1 + V_{b1} - L_1\frac{di_1}{dt} + M_2\frac{di_2}{dt} + M_3\frac{di_3}{dt} - i_1R_1 \qquad (C\text{-}5)$$

Substituting Equation C-5 into Equation C-2 and C-3 to eliminate the unknown variable V_c:

$$V_2 - V_1 + V_{b2} - V_{b1} = R_2 i_2 - R_1 i_1 - \frac{di_1}{dt}(L_1 + M_1) + \frac{di_2}{dt}(L_2 + M_2) \qquad (C\text{-}6)$$

$$V_3 - V_1 + V_{b3} - V_{b1} = R_3 i_3 - R_1 i_1 - \frac{di_1}{dt}(L_1 + M_1) + \frac{di_3}{dt}(L_3 + M_3) \qquad (C\text{-}7)$$

Asuming symmetry within the motor:

$$M = M_1 = M_2 = M_3 \qquad (C\text{-}8)$$

$$L = L_1 = L_2 = L_3 \qquad (C\text{-}9)$$

$$R = R_1 = R_2 = R_3 \qquad (C\text{-}10)$$

Substituting Equations C-8 through C-10 into Equations C-6 and C-7, and rearranging terms yields:

$$-\frac{di_1}{dt} + \frac{di_2}{dt} = [V_2 - V_1 + V_{b2} - V_{b1} - R(i_2 - i_1)]/(L+M) \qquad (C\text{-}11)$$

$$-\frac{di_1}{dt} + \frac{di_3}{dt} = V_3 - V_1 + V_{b3} - V_{b1} - R(i_3 - i_1)]/(L+M) \qquad (C-12)$$

In addition, the constraint equation, C-4, can be differentiated to produce:

$$\frac{di_1}{dt} + \frac{di_2}{dt} + \frac{di_3}{dt} = 0 \qquad (C-13)$$

Equations C-11,12,13 can be expressed in the matrix form shown in Equation C-14; where the variables a,b represent the right hand sides of Equations C-11 and C-12 respectively.

$$\begin{bmatrix} -1 & 1 & 0 \\ -1 & 0 & 1 \\ 1 & 1 & 1 \end{bmatrix} \begin{Bmatrix} di_1/dt \\ di_2/dt \\ di_3/dt \end{Bmatrix} = \begin{Bmatrix} a \\ b \\ 0 \end{Bmatrix} \qquad (C-14)$$

This matrix can be solved by any of the standard techniques: Gaussian elimination or Cramers rule for example, to yield explicit expressions for the derivative of the current in each phase, (Equation C-15).

$$\begin{Bmatrix} di_1/dt \\ di_2/dt \\ di_3/dt \end{Bmatrix} = \frac{1}{3} \begin{Bmatrix} -a-b \\ 2a-b \\ 2b-a \end{Bmatrix} \qquad (C-15)$$

Substitution of the definitions for a,b yields:

$$\frac{di_1}{dt} = \frac{(2V_1 - V_2 - V_3) + (2V_{b1} - V_{b2} - V_{b3}) - R(2i_1 - i_2 - i_3)}{3(L+M)} \qquad (C\text{-}16)$$

$$\frac{di_2}{dt} = \frac{(-V_1 + 2V_2 - V_3) + (-V_{b1} + 2V_{b2} - V_{b3}) - R(-i_1 + 2i_2 - i_3)}{3(L+M)} \qquad (C\text{-}17)$$

$$\frac{di_3}{dt} = \frac{(-V_1 - V_2 + 2V_3) + (-V_{b1} - V_{b2} + 2V_{b3}) - R(-i_1 - i_2 + 2i_3)}{3(L+M)} \qquad (C\text{-}18)$$

These equations can be further reduced if one uses the constraint equation, C-4, and the fact that phase relation of the back emf voltages is such that their sum is zero, (Equation C-19)

$$i_1 + i_2 + i_3 = 0 \qquad (C\text{-}4)$$

$$V_{b1} + V_{b2} + V_{b3} = 0 \qquad (C\text{-}19)$$

$$\frac{di_1}{dt} = \frac{(2V_1 - V_2 - V_3) + 3V_{b1} - 3Ri_1}{3(L+M)} \qquad (C\text{-}20)$$

$$\frac{di_2}{dt} = \frac{(V_1 - 2V_2 - V_3) + 3V_{b2} - 3Ri_2}{3(L+M)} \qquad (C\text{-}21)$$

$$\frac{di_3}{dt} = \frac{(V_1 - V_2 - 2V_3) + 3V_{b3} - 3Ri_3}{3(L+M)} \qquad (C\text{-}22)$$

Given the equations for the derivatives of the phase currents, one can integrate these numerically to find the current in each phase as a

function of time. The currents can then be used with Equation C-23 to determine the instantaneous torque produced by the motor for any combination of phase currents.

$$T = -K_t\,(i_1 \sin(A\theta)+i_2 \sin(A\theta-2\pi/3)+i_3 \sin(A\theta-4\pi/3) \qquad \text{(C-23)}$$

This torque is averaged over the commutation interval, (60 electrical degrees), to yield the average torque as a function of speed:

$$T_{ave} = \frac{3}{\pi} \int_{\theta_1}^{\theta_2} T \, d\theta \qquad \text{(C-24)}$$

First, however, in order to simulate the phase currents, initial current conditions need to be determined. Figure C-3a shows a commutation squence for a Wye node open drive. If the node voltages are switched according to the sequence shown in this figure, one obtains the static torque vectors shown in Figure C-3b. Commutation at the proper position will result in a unidirectional torque produced by the motor.

Instead of simulating the commutation and switching through the sequence shown in Figure C-3, it is only necessary to simulate one commutation. If the motor is running at a constant speed, the instantaneous torque waveform and the average torque are the same for every commutation. However, in order to determine the correct currents and torque by simulating a single commutation interval, one needs to have a means of determining the appropriate initial currents

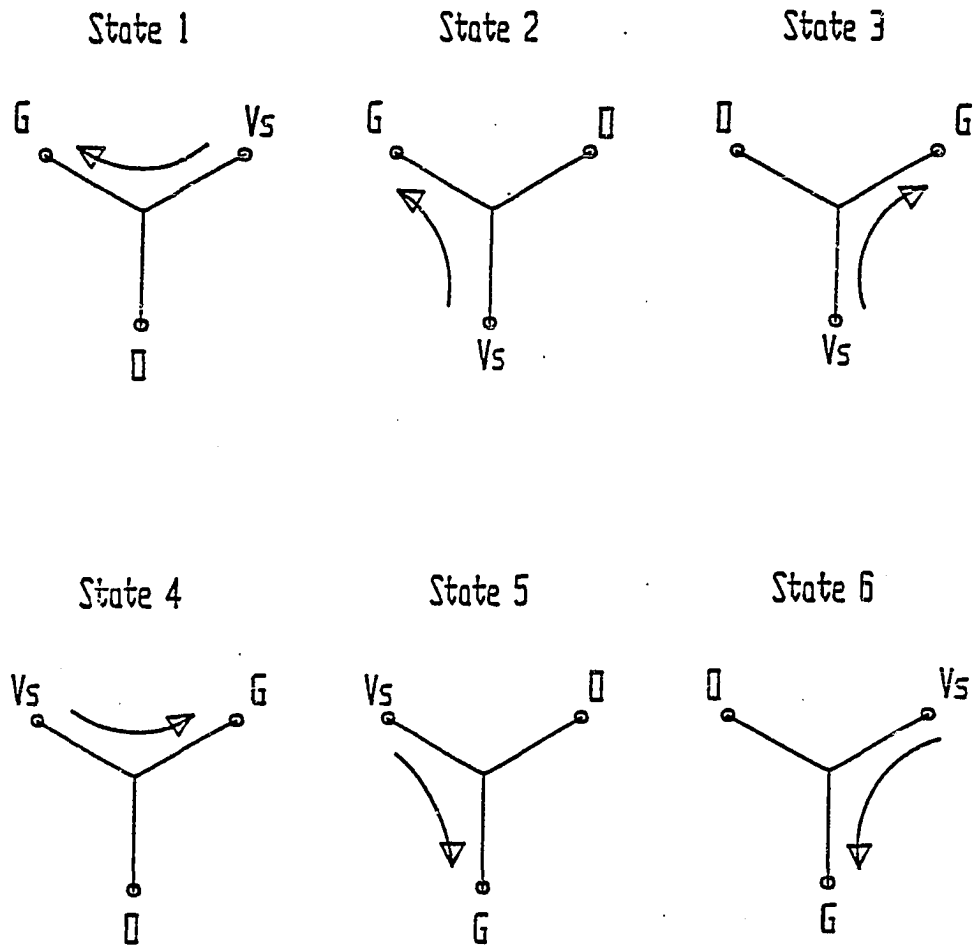

Figure C-3a
Node Voltages for the Six
Different Commutation States

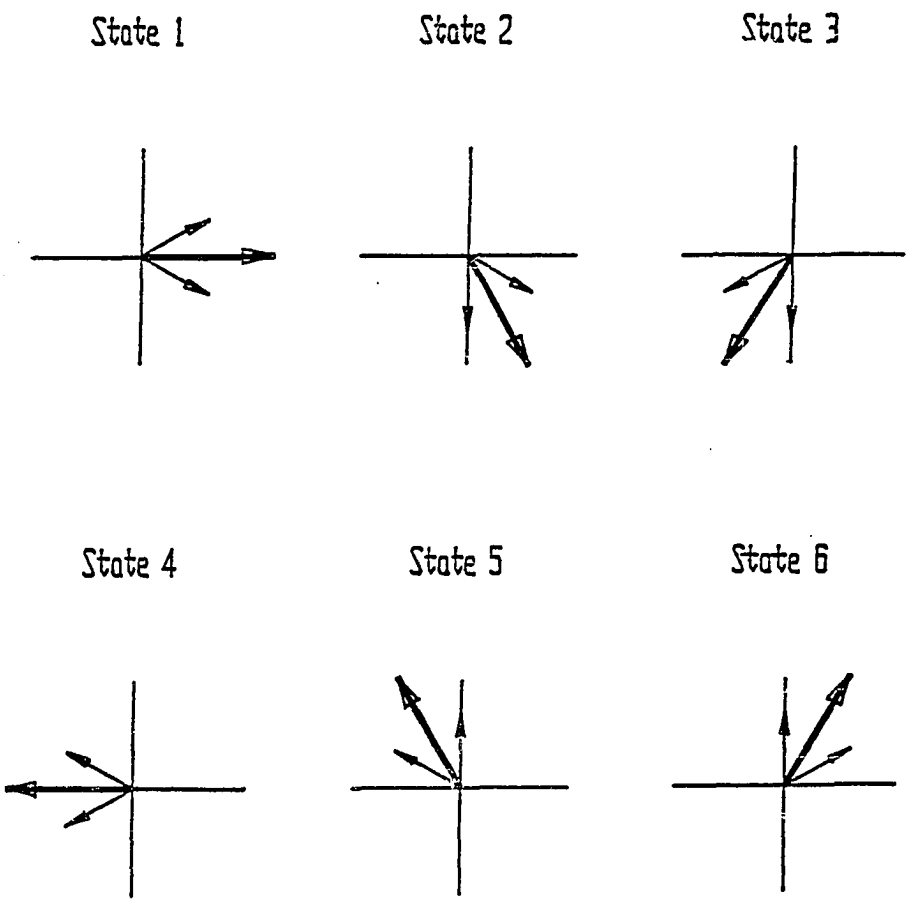

Figure C-3b
Torque Vectors Corresponding to
the Six Different Commutation States

to use. This is not necessary if one simulates the switching sequence because one can simply assume zero current initial conditions and simulate the response until equilibrium conditions have been reached, (i.e. no change in the average torque or pattern of current waveforms from one commutation interval to the next).

In simulating just one commutation interval, the initial current for a phase at the beginning of the commutation interval, is equal to the final current in the phase at the end of the last commutation interval. But, the final current in the phase at the end of the last commutation interval is unknown. However, it should be possible to find a relationship between the final currents of interval n and the initial currents of interval n. This should be possible because the final currents of interval n-1 become the initial currents of interval n, and the current waveform patterns are repeated from one commutation interval to the next. This will be shown later

Analogous currents between commutation state n-1 and commutation state n can be determined by looking at the switching sequence. In order for the currents to be analogous they must have gone through the same switching sequences. Table C-1 lists the voltage switching sequence for a wye-node-open drive. The sequence starts at state 1 and ends at state 6; states 1 through 6 correspond to those shown in Figure C-3a and C-3b.

Table C-1
Commutation Switching Sequence

phase \ state	1	2	3	4	5	6
1	0	g	g	0	V_s	V_s
2	g	0	V_s	V_s	0	g
3	V_s	V_s	0	g	g	0

Suppose, for example, one needs to find a current in commutation state 1 that went through the same sequence of node voltage changes as a current in state 2 did. The switching sequence for the five states prior to state 2 is given in Table C-2

Table C-2
Switching Sequence Ending at State 2

phase \ state	3	4	5	6	1	2
1	g	0	V_s	V_s	0	g
2	V_s	V_s	0	g	g	0
3	0	g	g	0	V_s	V_s

Now looking at state 1 and constructing a similar table, as shown in Table C-3:

Table C-3
Switching Sequence Ending at State 1

phase \ state	2	3	4	5	6	1
1	g	g	0	V_s	V_s	0
2	0	V_s	V_s	0	g	g
3	V_s	0	g	g	0	V_s

Defining a notation for the currents as $i_{(state),(phase)}$, a comparison of these two switching sequences shows that the sequence for $i_{1,3}$, (Table C-3), is the same as for $i_{2,1}$, (Table C-2), except that ground and supply are swapped. This change would produce an oppositely directed set of currents, but, the switching transients would be the same. Thus, the analogous current condition is given as:

$$i_{2,1} = -i_{1,3} \tag{C-25a}$$

Similar analogies can be made for $i_{2,2}$ and $i_{2,3}$.

$$i_{2,2} = -i_{1,1} \tag{C-25b}$$

$$i_{2,3} = -i_{1,2} \tag{C-25c}$$

These analogies apply for corresponding instants in time during the commutation. For example, the current in phase 1, Δt seconds into state 2, is equal to the negative of the current in phase 3, Δt seconds into state 3. Since the initial current for any phase of state 2 is also equal to the final current of the same phase of state 1, the following equations can be written:

$$i_{2,1_i} = i_{1,1_f} \tag{C-26a}$$

$$i_{2,2_i} = i_{1,2_f} \tag{C-26b}$$

$$i_{2,3_i} = i_{1,3_f} \tag{C-26c}$$

Where: i_{j,k_f} ≡ final current of commutation interval for state j, phase k

i_{j,k_i} ≡ initial current of commutation interval for state j, phase k

The analogies defined in Equations C-25 can be used to replace the final currents of state 1 in Equations C-26 with the equivalent final currents of state 2. Thus, a mapping of final currents to initial currents within the same state is established.

$$i_{2,1_i} = -i_{2,3_f} \quad \text{(C-27a)}$$

$$i_{2,2_i} = -i_{2,1_f} \quad \text{(C-27b)}$$

$$i_{2,3_i} = -i_{2,2_f} \quad \text{(C-27c)}$$

While these initial conditions were established for a wye node open drive a similar analysis can be used to show that they also hold for wye node closed drive.

Given that the mappings for the initial current conditions have been identified; one also needs to determine the appropriate voltages to apply to nodes 1,2,3. If it could be assumed that phase currents could be shut off instantaneously, then one could simply apply the voltages from the sequence table for the appropriate state. State 2, for example, would require node 1 to be at ground, node 2 to be floating and node 3 to be at supply. However, current transients that occur when the transistors are switched can have a significant effect on the net average torque predicted when modelling the high speed behavior of the motor. The transient conditions can be included by

modelling transistor and diode breakdown voltages.

Figure C-4 shows two half bridge circuits connected to phase ends. The half bridges include blocking diodes that may or may not be present in a particular drive. Figure C-4a shows a half bridge connected to a phase carrying positive current. In Figure C-4b the half bridge is connected to a phase carrying negative current. The dashed lines in both figures show possible current breakdown paths.

When a phase is switch to the 'open' state and both transistors are switched off, inductive effects cause a voltage spike that will always be of sufficient magnitude to cause a breakdown condition to occur. At t_o, when either transistor Q1 or Q2 is shut off, if $i_p \neq 0$ then shutting off the transistor causes a large inductive voltage spike to occur. This, in turn, reverse biases either the transistor protection diode or the blocking diode, (if present), and causes it to enter the breakdown region. The diode with the lower breakdown voltage conducts first; i_p decays to zero and then the diode prevents further current flow. The rate of current decay as it flows through one of these breakdown paths depends, among other things, on the magnitude of the breakdown voltage.

The breakdown path the current follows depends on the sign of the current and the 'critical' breakdown voltage. For a given case of either positive or negative current, the path the current follows will depend on which path has the lower magnitude breakdown voltage. The will be the critical breakdown voltage.

While a diode is in its breakdown region, the voltage seen at node

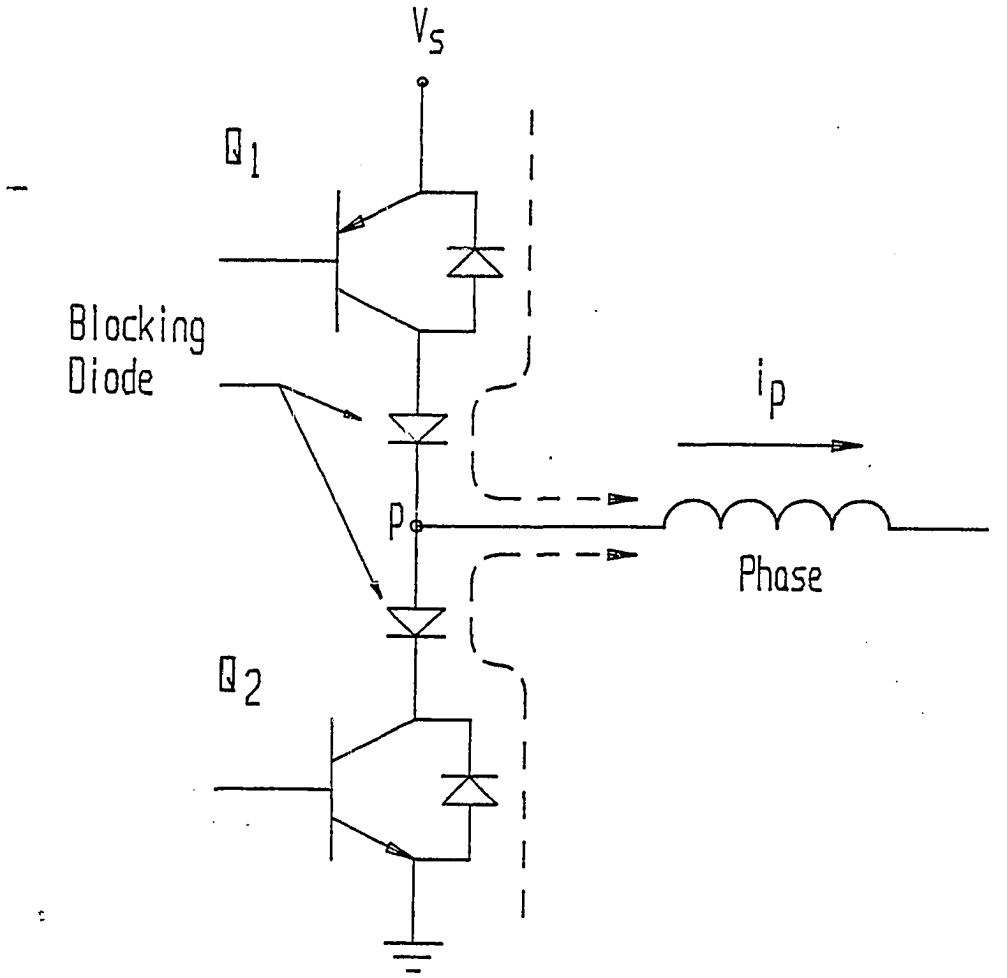

Figure C-4a
Half Bridge Connected to a
Phase Carrying Positive Current

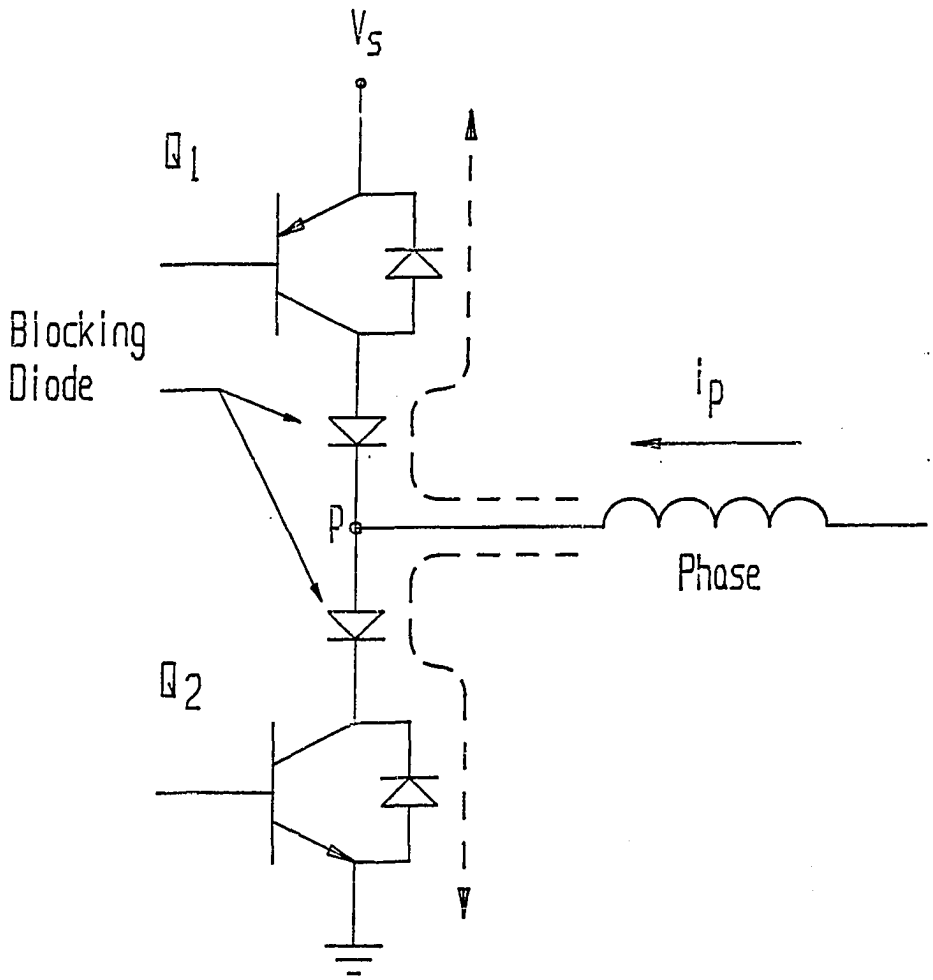

Figure C-4b
Half Bridge Connected to a
Phase Carrying Negative Current

p is equal to voltage necessary to cause the diode to breakdown. Thus, the critical breakdown voltage should be used as the 'supply' voltage seen by the node. The breakdown voltage conditions should be maintained until the current reaches zero and the breakdown path shuts down. Once i_p decays to zero, the voltage at node p floats at a level determined by the back emf voltage, and center node voltage.

The breakdown voltages are determined in the following. First, the following parameters are defined:

$V_s \equiv$ supply voltage

$V_{trv} \equiv$ transistor reverse bias breakdown voltage

$V_{tfv} \equiv$ transistor forward bias voltage

$V_{drv} \equiv$ diode reverse bias breakdown voltage

$V_{dfv} \equiv$ diode forward bias voltage

$V_{ubpd} \equiv$ upper leg breakdown voltage for positive current with blocking diodes

$V_{lbpd} \equiv$ lower leg breakdown voltage for positive currents with blocking diodes

$V_{ubpn} \equiv$ upper leg breakdown voltage for positive current no blocking diodes

$V_{lbpn} \equiv$ lower leg breakdown voltage for positive currents no blocking diodes

$V_{ubnd} \equiv$ upper leg breakdown voltage for negative current with blocking diodes

$V_{lbnd} \equiv$ lower leg breakdown voltage for negative current with blocking diodes

$V_{ubnn} \equiv$ upper leg breakdown voltage for negative current no blocking diodes

$V_{lbnn} \equiv$ lower leg breakdown voltage for negative current no blocking diodes

The upper and lower leg breakdown voltages for positive current with blocking diodes present are:

$$V_{ubpd} = V_s - V_{trv} - V_{dfv} \quad \text{(C-28a)}$$

$$V_{lbpd} = - V_{dfv} - V_{drv} \quad \text{(C-28b)}$$

If no blocking diodes are present then these breakdown voltages are given by:

$$V_{ubpn} = V_s - V_{trv} \quad \text{(C-29a)}$$

$$V_{lbpn} = -V_{dfv} \quad \text{(C-29b)}$$

The breakdown voltages for negative current with blocking diodes are:

$$V_{ubnd} = V_{drv} + V_{tfv} + V_s \quad \text{(C-30a)}$$

$$V_{lbnd} = V_{dfv} + V_{trv} \quad \text{(C-30b)}$$

The upper and lower leg breakdown voltages for negative current with no blocking diodes are:

$$V_{ubnn} = V_{tfv} + V_s \quad \text{(C-31a)}$$

$$V_{lbnn} = V_{trv} \quad \text{(C-31b)}$$

The critical voltage in each of the four cases is the breakdown voltage with the lesser magnitude. The appropriate breakdown voltage used, depends upon whether the current is negative or positive and, whether or not there are blocking diodes present in the circuit. The blocking diode condition is an input at the beginning of the simulation. The direction of the current is checked at each integration time step. Thus, there is a critical breakdown voltage for negative current, and one for positive current. Given the current directions and the critical breakdown voltages, logical conditions can

be set up to determine the appropriate nodal voltages to be applied to each of the phase nodes at each time step of the integration.

Given that appropriate initial conditions, switching conditions, breakdown voltages and nodal voltages can now be applied. One can now simulate a single commutation interval instead of simulating the switching sequence and waiting for transients to pass. An algorithm for determining the torque-speed behavior proceeds as follows:

1) The zero speed steady state currents are calculated. These are used to determine the average torque, (stall torque), of the motor.

2) A speed is assumed which is some small fraction of the no load speed. The currents from step 1 are used as initial conditions via the mapping strategy of Equations C-27. The currents are simulated by numerical integration over the duration of the commutation interval.

3) The final current values found from step 2 are now used to determine the new initial conditions and the current waveforms are re-simulated. Since these final currents are dependent on speed they are not quite correct, but are a good first approximation. An iterative procedure can then by entered, using the change in final currents as a convergence criteria; this step is repeated until convergence has been satisfied.

4) An incrementally larger speed is assumed and step 3 is repeated. In this manner, small steps in speed can be taken so that

the starting initial current conditions are not much in error.

Figure C-5 shows a set of current waveforms simulated for one commutation interval using this method. The solid line represents the instantaneous torque produced by the currents in all three phases. The short dash line represents phase 1 current, the medium dash line is phase 2 current, the long dash line represents the current in phase 3. One sees that the initial-final current relation outlined by Equations C-27 holds.

Figure C-5 also shows the effects of the noninstantaneous shutoff of current in phase 2. For this simulation, no blocking diodes were included; therefore, the breakdown path for current 2 is through the forward biased protection diode in the lower leg of Figure C-4a.

One sees in Figure C-5 that as the current in phase 2 is driven down by the temporary connection to ground, the current in phase 3 is driven up quickly and the current in phase 1 is driven down quickly. The stored field energy that was associated with the current in phase 2 is now associated with the current in phases 1 and 3. This occurs because the stored field energy cannot change instantaneously. Thus, phase currents 1 and 3 adjust accordingly. One also sees from this figure that if the transient had occured almost instantaneously, the initial currents for both phases 1 and 2 would have been approximately half their final values. This is in aggreement with Huard's theoretical prediction. However, if that were the case, then the initial torque would have been less; resulting in a lower average

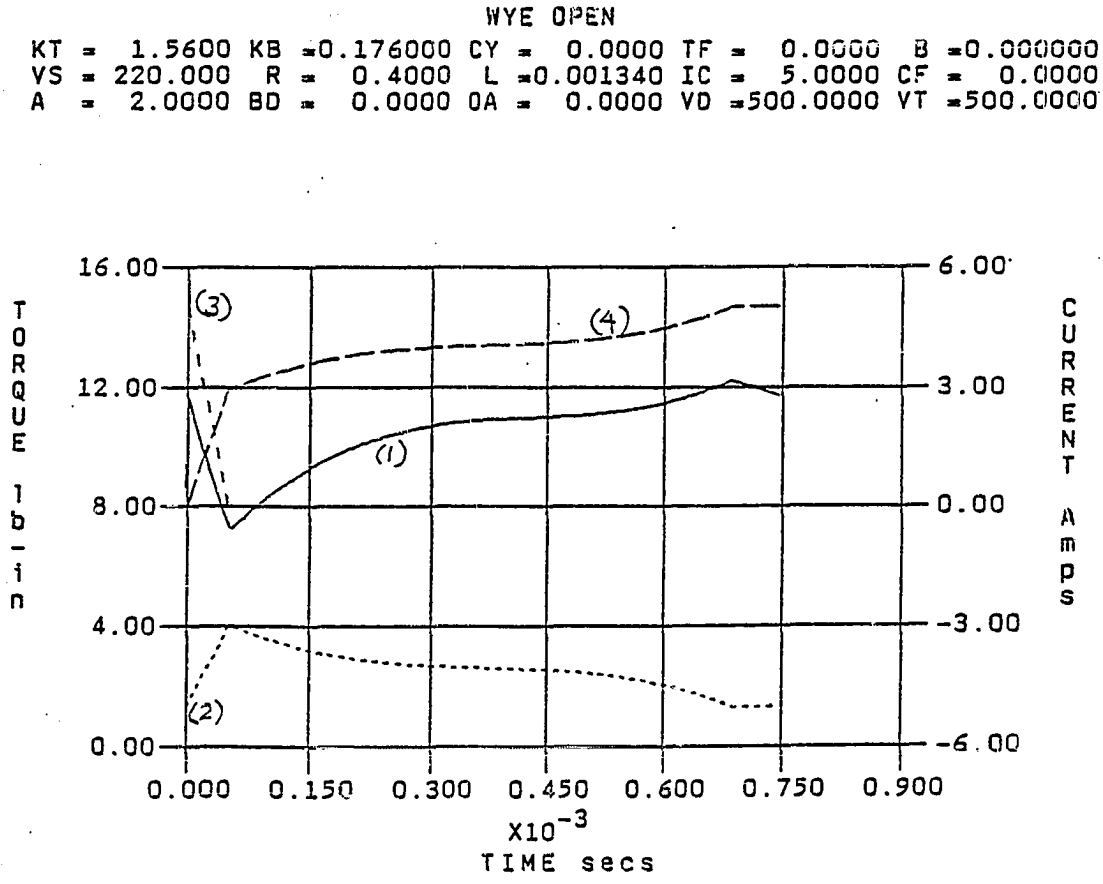

Figure C-5
Instantaneous Current and Torque
Waveforms Over a Commutation Interval
Curve (1)- Instantaneous Torque
Curve (2)- Instantaneous Current in Phase 1
Curve (3)- Instantaneous Current in Phase 2
Curve (4)- Instantaneous Current in Phase 3

torque over the interval. Therefore, it appears as if the transient decay has increased the average torque at this speed. this is not always the case. If the decay time became a significant portion of the commutation time, it is possible that the torque produced by that phase would be negative over some portion.

The three currents shown in Figure C-5 can be used to reconstruct an entire cycle of the current waveform. This is shown in Figure C-6; it represents 6 commutations. Again, notice that at the end of commutation 3, the transients associated with switching caused the current to drop.

The torque-speed simulation method discussed here was verified against analytical and experimental work performed by Huard. Figure C-7a shows a comparison of analytical and experimental results obtained by Huard[3], for commutation phase advance angles of 0^0 and 45^0. The results obtained from the simulation method presented in this appendix for the same motor parameters and phase advance angles are shown in Figure C-7b. One sees that the method presented here yields better correlation at low torque-high speed points. This is due to the fact that the simulation used here included models for the diode breakdown effects of both the blocking diodes and transistor protection diodes, which were not included in Huards analytical model.

The torque-speed simulation method presented here can be used easily to simulate pulse width modulated, (PWM), current drives. A PWM current drive might typically control the current by controlling the connection to ground of one of the transistor legs. The PWM

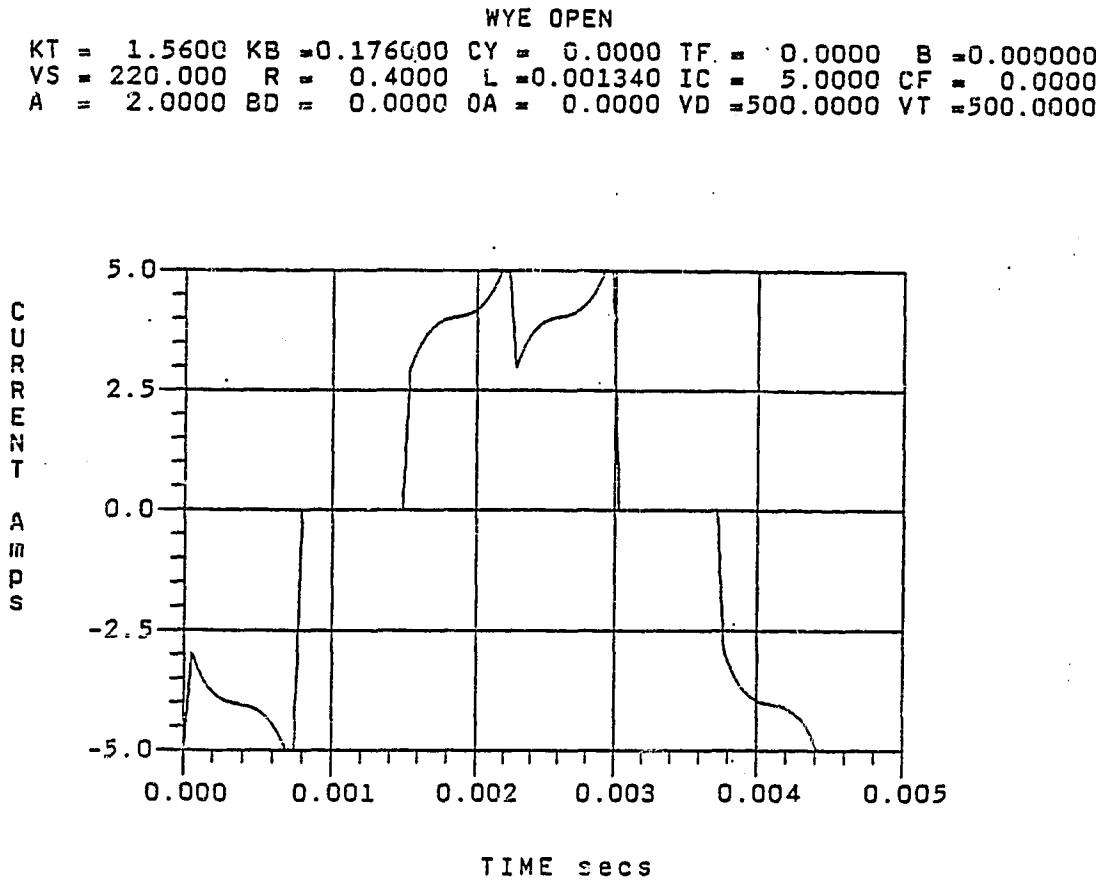

Figure C-6
Current Waveform for a Phase for
Six Commutation Intervals

Wye Open

KT = 4.9000 KB =0.039000 A = 2.0 TF = 1.0000 B =0.003200
R = 1.1400 L =0.000304 Cd = 0.1960 Vs = 28.000

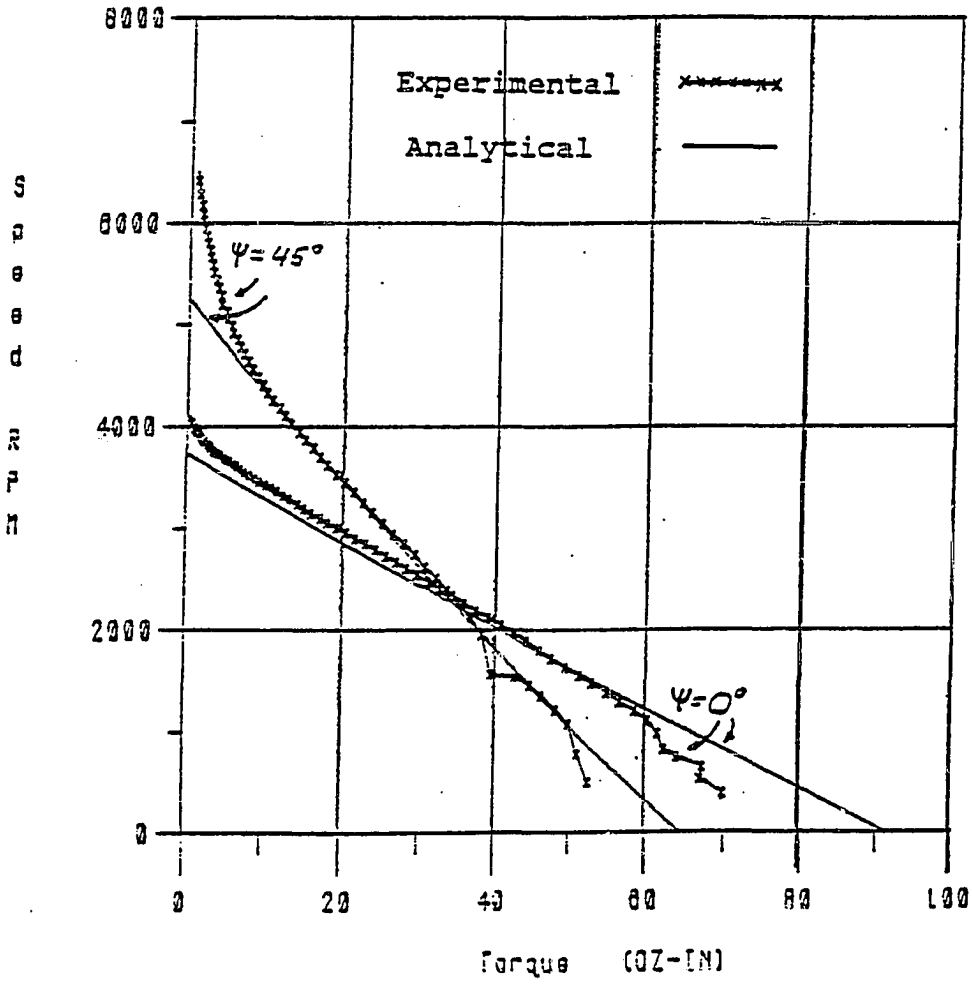

Figure C-7a
Figure 2.15 from Huard's Thesis-
Comparison of Experimental and Analytical Results
for Phase Advance Angles of 0 Degrees and 45 Degrees

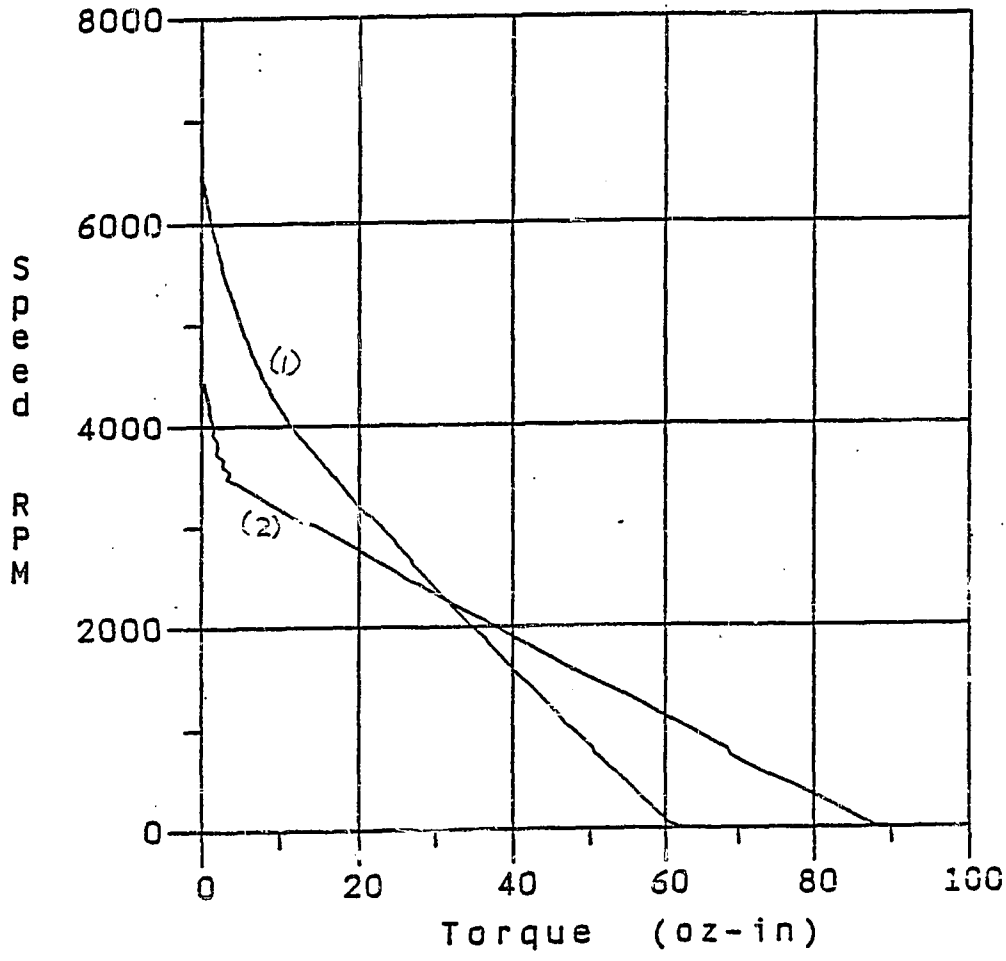

Figure C-7b
Torque-Speed Characteristic Predicted for the
Same Motor Parameters as in Figure C-7a
Curve (1)- 45 Degrees Phase Advance
Curve (2)- 0 Degrees Phase Advance

current drive controls current by sampling the voltage across a sense resistor, (which indicates current), and comparing it to a reference level. The sampling is usually done at a fixed frequency, (typically 10-20kHz).If the sense voltage is less than the reference level it turns on the lower transistor leg connecting the phase to ground. If the sense voltage is greater than the reference level it turns off the lower transistor breaking the ground connection.

Figure C-8a shows current and torque waveforms for one commutation interval of a motor being driven at 5000 rpm with a PWM drive chopping at 20kHz. Figure C-8b shows one full cycle of one of the phase current waveforms. For comparison, Figures C-9a and 9b show corresponding current waveforms resulting from an 'ideal' PWM drive chopping at an infinite frequency. The finite chop frequency of the real PWM drive obviously introduces current and torque ripple into the system. The simulation method presented here can be used to determine the magnitude of the ripple. This is important because these higher frequency ripple components can cause an increase in iron losses and effect the low speed velocity ripple.

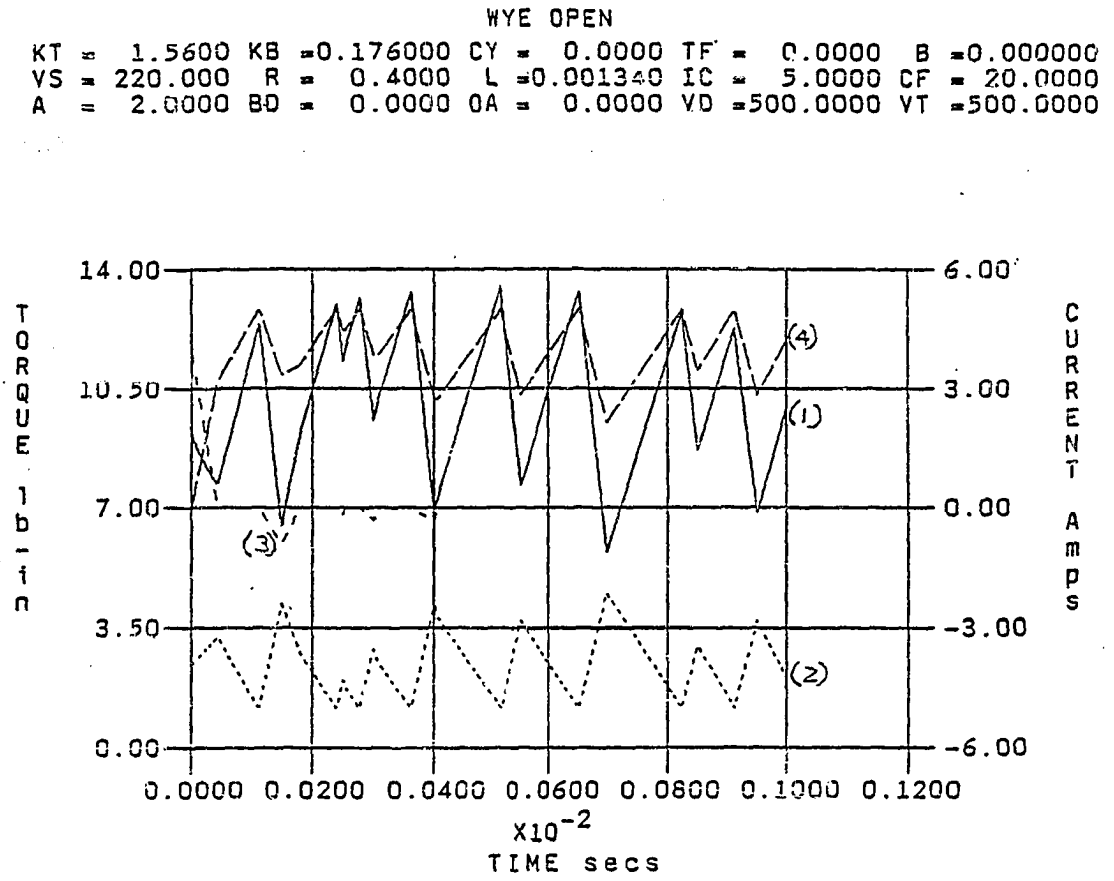

Figure C-8a
Instantaneous Current and Torque Waveforms Produced
by 20kHz Pulse Width Modulated Current Drive
Curve (1)- Instantaneous Torque
Curve (2)- Instantaneous Current in Phase 1
Curve (3)- Instantaneous Current in Phase 2
Curve (4)- Instantaneous Current in Phase 3

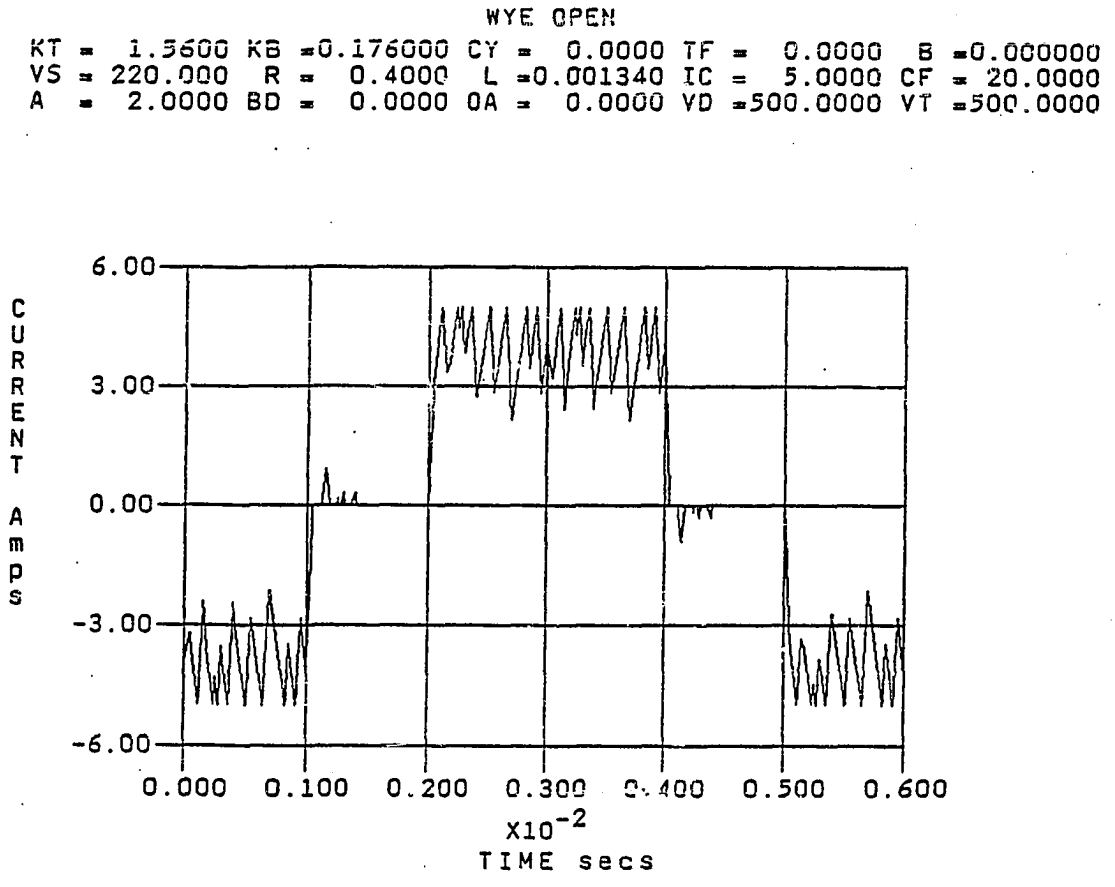

Figure C-8b
One Full Cycle of a Phase Current Produced by
a 20kHz Pulse Width Modulated Current Drive

WYE OPEN

KT = 1.5600 KB =0.176000 CY = 0.0000 TF = 0.0000 B =0.000000
VS = 220.000 R = 0.4000 L =0.001340 IC = 5.0000 CF = 0.0000
A = 2.0000 BD = 0.0000 OA = 0.0000 VD =500.0000 VT =500.0000

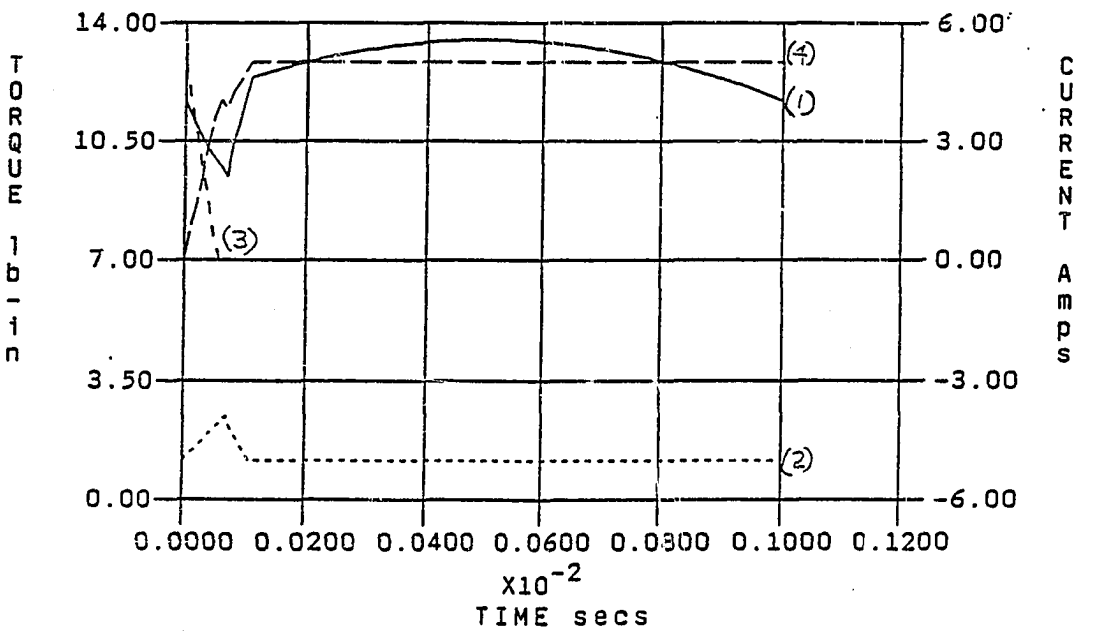

Figure C-9a
Instantaneous Current and Torque Waveforms
Produced by an Ideal Current Drive
Curve (1)- Instantaneous Torque
Curve (2)- Instantaneous Current in Phase 1
Curve (3)- Instantaneous Current in Phase 2
Curve (4)- Instantaneous Current in Phase 3

WYE OPEN

KT =	1.5600	KB =	0.176000	CY =	0.0000	TF =	0.0000
VS =	220.000	R =	0.4000	L =	0.001340	IC =	5.0000
A =	2.0000	BD =	0.0000	OA =	0.0000	VD =	500.0000

B =	0.000000		
CF =	0.0000		
VT =	500.0000		

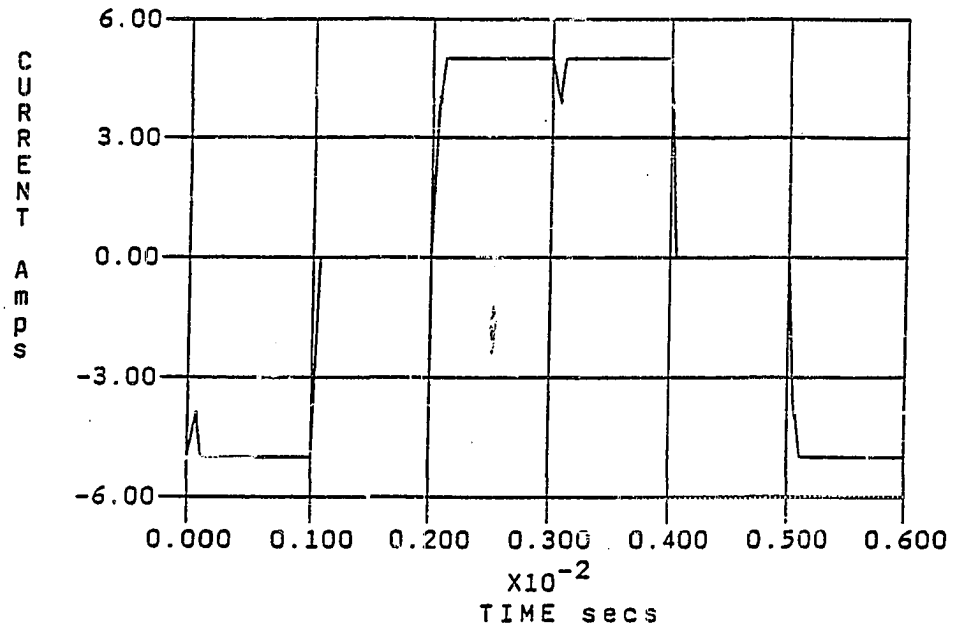

Figure C-9b
One Full Cycle of a Phase Current Produced
by an Ideal Current Drive